Detection and localisation of drug molecules in biological samples using Secondary Ion Mass Spectrometry (SIMS)

A thesis submitted to The University of Manchester for the degree of Doctor of Philosophy in the Faculty of Science and Engineering

2019

Samar Abdullah Aldossari

The University of Manchester
Faculty of Science and Engineering
School of Natural Sciences
Department of Chemistry

Contents

Word count: 75,919

List of Figures

List of Tables

List of Equations

Abbreviations

SIMS	Secondary ion mass spectrometry
BNCT	Boron neutron capture therapy
BPA	Boronophenylalanine
NanoSIMS	Nano- secondary ion mass spectrometry
BioToF-SIMS	Bio- Time-of-Flight secondary ion mass spectrometry
GBM	Glioblastoma multiform tumour
BAT	Brain around Glioblastoma-multiform tumour
MSI	Mass spectrometry imaging
LMIG	liquid metal ion gun
MALDI	Matrix-assisted laser desorption/ionization
DESI	Desorption electrospray ionization
2D	Two-dimensional
3D	Three-dimensional
MS	mass spectrometry
LAESI-MS	Laser Ablation Electrospray Ionization mass spectrometry
LESA-MS	liquid extraction surface analysis mass spectrometry
LA-ICP-MS	Laser ablation inductively coupled plasma mass spectrometry
FT-ICR-SIMS	Fourier transform-ion cyclotron resonance-mass spectrometry
TRIFT-TOF-SIMS	triple ion focusing time-of-flight
RSF	Relative sensitivity factor
^{10}BPA-f	10boronophenylalanin-Fructose
ToF	Time-of-Flight
LToF	linear ToF mass spectrometer
RToF	Reflectron time-of-flight
MCP	Microchannel plate
DC	Direct current
MRP	Mass resolving power
ICP-MS	Inductively coupled plasma mass spectrometry
FI/ESI-MS/MS	flow- injection electrospray tandem mass spectrometry
DCP-AES	direct current plasma atomic emission spectroscopy
L- DOPA	L-3, 4-dihydroxyphenylalanin
LAT-1	L-amino acid transporter-1
[^{18}F]-FBPA	2-[18F] fluoro-4-borono-L-phenylalanine
BCH	2-aminobicyclo-(2,2,1)-heptane-2-carboxylic acid
ICP-AES	inductively coupled plasma atomic emission spectroscopy
IMT	123I-a-methyl-L-tyrosine
SPECT	Single photon emission computed tomography
BrdU	Bromodeoxyuridine
BPA-f	Boronophenylalanin-Fructose

F-BPA	fluorinated p-boronophenylalanine
BSH	Sodium borocaptate
laser-SNMS	laser post-ionization secondary neutral mass spectrometry
H&E	Hematoxylin and Eosin
FoV	Field-of-view
ABCPC	1-amino-3- bronocyclopentanecarboxylic acid
SD	Standard deviation
T	Tumour mass
IT	Tumour cells infiltrating the normal brain around tumour
UHV	Ultra-high vacuum
cryo-ToF-SIMS	Cryostage ToF-SIMS
PBS	Phosphate-buffered saline
GA	Glutaraldehyde
D1	aperture
SEM	Scanning electron microscopy
HMR	high mass resolution
ROI	Region of interest
CCD	charge-coupled device
MIMS	Multi-isotope Imaging Mass Spectrometry
WF	Wien filter
SE	Secondary electron
Q1	First quarter
Q3	Third quarter
IQR	The interquartile range
EDX	Energy-dispersive X-ray microanalysis

Abstract

Mass spectrometry imaging (MSI) can be used in the investigation of biological tissue in detecting elements, metabolites, lipids, peptides and proteins. Secondary ion mass spectrometry (SIMS) is the most mature technique used in MSI. SIMS is characterized by its ability to provide high spatial resolution and high-sensitivity imaging of elements (in dynamic mode) and small–medium mass molecules (in static mode), potentially making it a very powerful tool in drug distribution studies that are vital to developing and validating new therapies.

Primary malignant brain tumours are universally fatal and glioblastoma multiforme (GBM) is the most frequent and severe type. Boron neutron capture therapy (BNCT) is a form of targeted radiotherapy based on the preferential accumulation of ^{10}B in the tumour core and infiltrating cells relative to contiguous normal cells. Validation of BNCT relies, therefore, on imaging boron at the cellular level within biological tissue.

This study focused on assessment of the imaging capabilities of dynamic and static SIMS instruments (CAMECA NanoSIMS 50L and BioToF-SIMS) in detecting the relative concentration and localisation of ^{10}B from the BNCT agent boronophenylalanine (BPA) in primary cell cultures and in imprint samples of tissue biopsies from GBM human brain tumours and the border around the tumours (BAT). The samples received BPA *in vitro* and, *in vivo* respectively, and were used for the first time in this project. In addition, the effect of tyrosine preloading and efflux treatment on ^{10}BPA uptake was investigated in primary cell cultures. The performance of both instruments was compared in terms of spatial resolution, sensitivity and quantitative measurement. The results show that the use of the NanoSIMS 50L with a Cs^+ beam provided greater spatial resolution in the imaging of ^{10}B distributions at the cellular and sub-cellular levels in the samples and higher sensitivity in the detection of ions of low abundance when compared with BioToF-SIMS with an Au^+ beam, whereas the performance of the two instruments was similar in terms of the quantitative measurement. NanoSIMS 50L images also showed that the ^{10}B from BPA accumulated in GBM tumour samples at a higher concentration than for BAT samples. In cell cultures, pre-loading of tyrosine did not improve the BPA uptake while exposure to the efflux process led to a decrease the BPA level in the cells. The images also showed the preferential accumulation of ^{10}B in cell nuclei compared with the cytoplasmic areas in the cell culture samples, which is an important factor in the success of BNCT.

Declaration

No portion of the work referred to in the thesis has been submitted in support of an application for another degree or qualification of this or any other university or other institute of learning.

Copyright Statement

Acknowledgements

I would like to acknowledge King Saud University and the Ministry of Education in Riyadh in Saudi Arabia for giving me the opportunity to complete my postgraduate degree and for funding my PhD study.

Great thanks and gratitude go to my supervisors, Dr. Nicholas Locker and Dr. Katie Moore, for their outstanding efforts in supervision, guidance, support and encouragement during my PhD project.

Special thanks to Dr. Allah Detta of the Molecular Neuro-Oncology Laboratory at the Queen Elizabeth Neuroscience Centre in University Hospitals Birmingham in the UK for providing me with samples for the thesis and for help in interpreting the data.

I would also like to thank the former Senior Experimental Officer in NanoSIMS and Electron Microscopy, Dr. Greg McMahon, for his help and guidance with the experiments, and thanks to Dr. Alex Henderson for assistance with technical issues and data processing.

Furthermore, I would like to thank former members of the Lockyer group: Dr. Giles Edwards, Dr. Ewa Szula and Dr. Huriyyah Alturaifi, for their continued support.

My deep thank also go to the members of the NanoSIMS group: Prof. Ian Lyon, Dr. Romain Tartese, Yasser, Christopher, Rebecca and Connaugh, for the useful meetings and good times we shared together.

Finally, I would like to express my sincere thanks and my great gratitude to all my family for their love, encouragement and support throughout my studies, especially my Mum. My deep appreciation also for my Dad, who no longer exists in life and was the first to encourage me.

1 Introduction

Imaging studies have received extensive attention in the fields of biological [1], medical [2], and pharmacological [3] research and material sciences [4] to investigate the distribution and localisation of elements and molecules in different samples, alongside quantitative measurement. Secondary ion mass spectrometry (SIMS) is one of the techniques used for this purpose and a number of analytical instruments are based on the principle. SIMS instruments differ among themselves in terms of the mass spectrometry method, instrument geometry and type of primary ion beam used in the analysis. This difference in design has led to a diversity in the capabilities of SIMS instruments in terms of spatial resolution, mass resolution, and sensitivity, thus creating multiple imaging methods that are complementary to each other, rather than competitive, offering great flexibility in analysing various types of samples.

In recent years, studies have increased on the discovery of drug distribution and localisation within tissues and cells to determine whether the drug reaches the target of interest, which has an impact in various fields such as drug manufacturing and design [5][6], medical applications [7], pharmacokinetic studies [8], and to understand the therapeutic effect on biological systems in terms of toxicity [9] and efficacy [10]. Boron neutron capture therapy (BNCT) is one of the cancer treatments, its effectiveness depends on the preferential localisation of BNCT agents such as 10boronophenylalanine (^{10}BPA) in the core of infected cells [11]. It is therefore necessary to verify the location of ^{10}BPA in biological samples to understand how the treatment is managed successfully.

1.1 Aim of the study

The aim of the study presented in this thesis is to assess the imaging capabilities of the CAMECA NanoSIMS 50L and BioToF-SIMS instruments in terms of spatial resolution and sensitivity in detecting the distribution and localisation of drug molecules in biological samples. In addition, the sub-cellular distribution and quantitative uptake of ^{10}BPA in two types of human brain samples will be determined. First, primary cell cultures of glioblastoma multiform tumour (GBM) and brain around tumour (BAT) were investigated to understand the effect of tyrosine preloading and efflux treatment on ^{10}BPA uptake, the effect of tyrosine preloading was included in this study due to differing results presented in the literature depending on the sample-type. Secondly, imprints from GBM-tumour and BAT tissue biopsies were investigated. To the best of the researcher's knowledge, this is the first time these types of human brain tumour samples have been studied with SIMS imaging, rather

than cell lines and animal models (*in vitro*) or murine (*in vivo*) used by previous studies. This study demonstrates the potential of the SIMS technique for BNCT research and drug distribution studies more generally.

Chapter 1 gives the theory and a description of the SIMS process in terms of its principle of operation, methodologies and quantitative aspects. Other mass spectrometry imaging (MSI) techniques are also discussed. A description of the BioToF-SIMS and NanoSIMS 50L instruments are also given in Chapter 1. Chapter 2 presents a literature review of the ^{10}BPA drug, and localisation studies using SIMS, as well as the methods of preparation of biological samples for SIMS experiments. The experimental methodology, tuning of the instruments used for this project and preliminary experiments are discussed in Chapter 3.

Chapters 4 and 5 present the experiments on localisation and distribution of ^{10}BPA drug in GBM tumour and BAT samples from human patients with a high grade of brain tumours. The samples were prepared and treated with ^{10}BPA in two forms: primary cell cultures (*in vitro*) which are presented in Chapter 4, and imprints of the tissue biopsies (*in vivo*) that are presented in Chapter 5. In both Chapters, the BioToF-SIMS experiments were run with an Au^+ beam of liquid metal ion gun (LMIG) and the NanoSIMS 50L experiments were run with a Cs^+ beam to obtain high spatial resolution during imaging. A chemical imaging approach was used to analyse the samples with the two instruments in dynamic mode to obtain 2D images that in turn represent data collected from several atomic layers in the sample (3D-data collection). The images were processed and the results analysed quantitatively. The performance of the SIMS instruments in the determination of the drug localisation of ^{10}BPA in the tumour samples was compared.

Finally, the most important conclusions drawn from this study are presented in Chapter 6 with suggestions for future study.

1.2 Principle of secondary ion mass spectrometry

SIMS is an analytical technique based on the principle of bombarding a sample surface using primary ion beams with an energetic impact of between ~ 0.1–50 keV [12]. There are different types of primary ion beam: atomic ions (Ga^+, Cs^+, Ar^+), small cluster ions (O_2^-, Au_3^+, Bi_3^+) and polyatomic ions (C_{60}^+, SF_5^+, Ar_{2000}^+). As a result of the ion bombardment process, a variety of secondary particles are emitted from the surface such as electrons, neutral species and positive or negative ions (atomic and clusters) depending on the chemical surface composition; only charged species can be measured directly and are called secondary ions [13]. Secondary ions are separated using a mass analyser according to the values of the mass-to-charge ratio (*m/z*); their relative abundance is then measured for each of their signals separately using a detector [14]. Secondary ions provide important data that characterizes the chemical composition of samples in three typical forms: mass spectra, spatial distribution images and depth-profile (**Figure 1.1**). SIMS occupies an important place in academic studies and industrial fields due to its ability to detect all elements in the periodic table from hydrogen to uranium, measure low concentrations of a sample to parts per billion (ppb), distributional mapping of the elements, molecules or isotopes in the sample solid, and ease of sample preparation for non-hydrated samples [12].

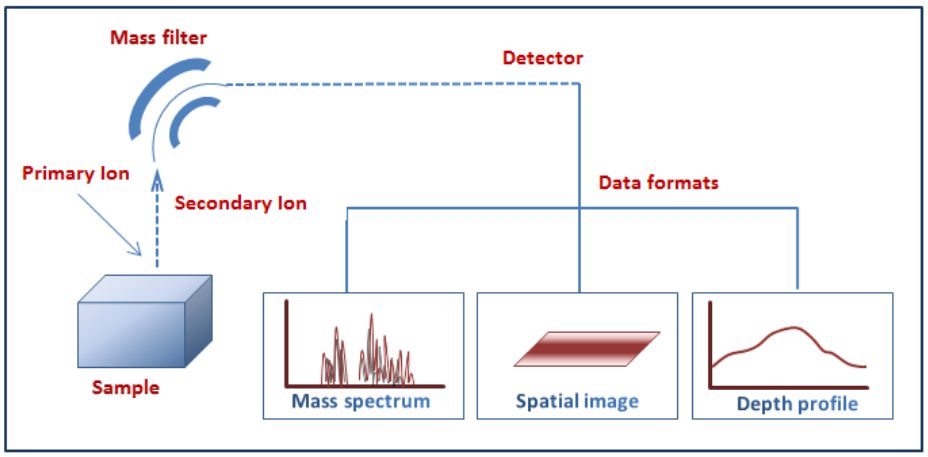

Figure 1.1: Schematic diagram of the SIMS process. A primary ion beam bombards the sample surface, leading to sputtering of secondary particles. Only secondary ions (+ and -) are separated, then measured using a mass analyser and detector, respectively. Data are extracted in three forms: mass spectra, spatial imaging and depth profiling. Modified from [12].

1.3 Secondary ion formation

A number of theories and approaches have been suggested in an attempt to understand how secondary ions are generated [4][15][16]. A summary of these theories shows that the formation of secondary ions occurs as a result of two main processes: sputtering and ionization. Both types of processes are given in the following sub-sections.

1.3.1 Sputtering

Sputtering is the first step in the generation of secondary ions, as described by Sigmund in his linear cascade theory in 1981[15]. A solid surface is bombarded with a beam of the incident particle, which has a suitable kinetic energy, leading to the transmission of energy to the target atoms to cause a series of collision cascades within the target atoms through almost 30Å of the surface [13][15]. The incident particle energies are always in the keV range; hence, highly energetic direct collisions with the atoms in the target lead to extensive fragmentation and bond breaking near the impact site and the result is emission of atomic particles. Furthermore, as the collision series moves away from the impact site, it becomes less energetic, leading to a reduction in bond breaking and fragmentation and molecular fragments emission. If the amount of energy in the particles in the top 2–3 monolayers of the sample is enough to overcome the surface binding energy, this leads to sputtered neutral atoms, molecules and ions (positive and negative) leaving the surface (**Figure 1.2**) [17].

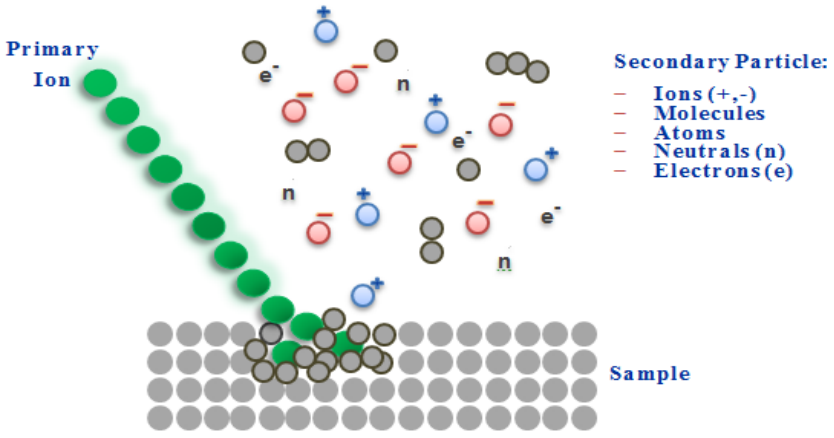

Figure 1.2: Schematic illustrating the sputtering process and secondary particle emission, modified from [17].

It should be mentioned that sputter yield (*Y*) is defined as the total number of particles (neutrals and positive or negative ions) that are removed from the surface per incident particle (primary ion beam) in the sputtering process. This yield is influenced by a number of factors, including: gradual linear increases with the flux of the incident particle; non-linear increases with increasing mass, charge and energy of the incident particle; the angle between the incident particle and the target surface; and the target mass and surface nature in terms of topography, crystallinity, components and contamination [18]. The type of incident particle is also important; polyatomic cluster primary ions increases the sputter yield of molecules [13]. Garrison and Postawa illustrated that the energy of the cluster projectiles, such as Au_3^+, is distributed on a few atoms and thus penetrates the chemical surface deeply enough to cause significant subsurface damage, while polyatomic projectiles, such as C_{60}^+, deposit their energies on the surface, with less damage and produce more molecular ion particles than Au_3^+ [19].

1.3.2 Ionization

The sputtering process referred to above produces a very small amount of ions (~1%) and the largest amounts are neutral particles (~99%). In general, sputtered particles are exposed to ionization, either during emission, in the near-surface region or by direct interaction with primary ions [13]. The ionization of sputtered atoms produces positive and negative secondary ions, depending on the ionization energy and electron affinity of the atoms, respectively [20][21]. Molecular species ionization is influenced by many factors, more details can be found in the following references [22]–[25].

Secondary ion yield refers to the number of secondary ions produced during the sputtering process per primary ion impact [26]. This yield is affected by the electronic and chemical states of the surface [24]. The primary ion source also plays an important role in the enhancement of secondary ionic yield; for example, O^- and Cs^+ beams enhance the generation of positive and negative ions, respectively [27]–[29]. Moreover, the use of primary beams of large cluster size increases the secondary yield of molecular ions. Projectile chemistry appears to play a role also in polyatomic bombardment. It was recently demonstrated that a water cluster $(H_2O)_{1000}^+$ beam is more effective than argon Ar_{1000}^+ beam at enhancing ionization in biological samples through a proton reaction, thus increasing ion yields with much less damage on the surface [30].

1.4 Classification of SIMS methodologies

1.4.1 Static SIMS

SIMS operating methods are grouped into two classes based on the ion beam dose (fluence) used in the sputtering of the sample surface [31]. The first class is static SIMS, which was proposed and developed by Benninghoven in 1970 [32] and subsequently by Vickerman and co-workers [13]. The main objective of static SIMS is to reduce the proportion of chemical damage that occurs on the sample surface during the bombardment process by placing a static limit on the primary beam dose. The static SIMS method provides spectral information using a low dose of the primary beam, not exceeding 10^{13} ions/cm^2 (static limit), to generate secondary species from less than 1% of the upper layer of the surface; this means that statistically, no specific point on the analysis area is hit more than once by the primary beam, (**Figure 1.3 - A**) [13][31][33]. The operation of static SIMS is usually accompanied by the use of a time-of-flight (ToF) analyser and a primary beam in pulsed mode [34]. The use of low-energy polyatomic ion projectiles in the analysis (SF_5^+ and C_{60}^+) leads to reduced damage on the surface, thus enhancing its use beyond the static limit. Cluster ions (Au_n^+, Bi_n^+) provide a higher molecular ion yield than an atomic beam (Ga^+, Cs^+) [13][35]–[37].

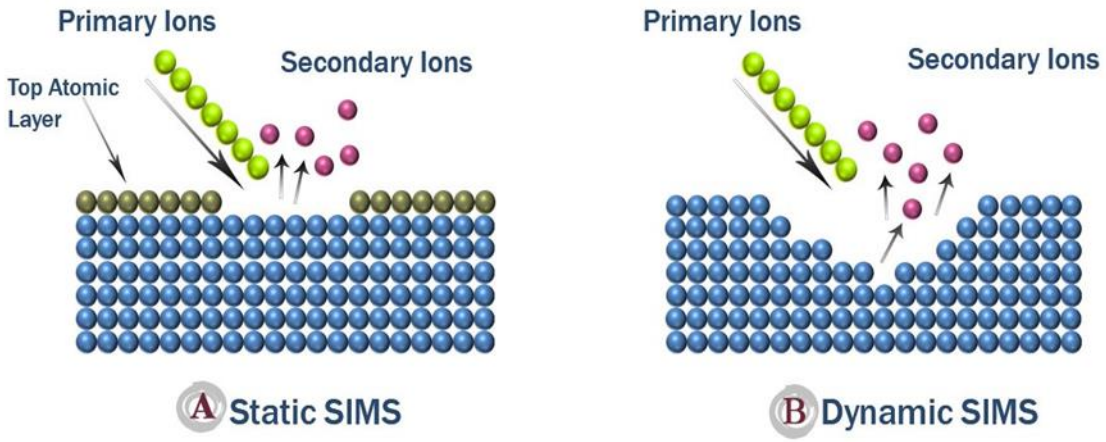

Figure 1.3: Simplified scheme of static and dynamic SIMS methods, redrawn [33].

1.4.2 Dynamic SIMS

Dynamic SIMS is the second classification of SIMS methods and uses a high dose of the primary ion beam, exceeding the static limit > 10^{13} ions/cm^2, causing erosion when sputtering the material from the surface. Dynamic SIMS is destructive on the surface because the primary beam penetrates the surface layers deeply enough (a few nanometers) to generate a high ion yield of small ion fragments (less than *m/z* 100), as well as some atomic and elemental species; thus, dynamic SIMS is typically used for depth profiling [31][38] (**Figure 1.3 - B**) [33]. Depth profiling is an application of the dynamic SIMS method that works by the removal of several atomic or molecular layers in each analysis cycle to provide chemical information from that depth [39].

Caesium (Cs^+) and oxygen (O_2^+ and O^-) beams are the most commonly used primary ion sources in dynamic SIMS [38]. The sources have been successful in studying the depth profiling and elemental composition of various materials (inorganic [40], organic [35] and biological samples [41]). Although atomic beams cause damage to the surface, a highly focused beam increases the ability to create images with high spatial resolution, leading to the development of imaging studies and particularly the localisation of drugs [42] and toxins [38] in biological samples. The primary beam is often run in continuous mode to generate secondary ions continuously [43]. Instruments with a dynamic SIMS system commonly use a quadrupole or magnetic sector analyser or both [43].

1.4.3 Mass spectrometry imaging

Mass spectrometry imaging (MSI) is a methodology used to determine the spatial distributions of elements and molecules by providing an image of the surface and sub-surface of different samples [39][44]. The intensity distribution in the images is represented using a colour bar [39]. MSI is widely used in the investigation of biological tissues to detect metabolites, peptides, proteins [44], lipids [45], pathology [44][46], and elements [44][47].

Images of a surface are created using one of two modes: microprobe or microscope, which were developed by Respectively Liebel in 1967 [48], then Castaing and Slodzian in 1984 [49]. The two approaches differ from each other in how they detect spatial distributions.

In the microprobe imaging mode, a moveable and focused primary ion beam (or laser beam) is focused onto a small area (pixel) of the sample surface. The resulting ions are separated in the analyser then measured by the detector. Thus, a mass spectrum is obtained from an individual pixel and stored. The previous analysis process is then repeated on an adjacent

area, pixel by pixel, until the completion of the measurement of the whole sample, and the previous spectra are collected and translated into images. The aim of using a highly focused beam is to obtain the best possible image resolution. Microprobe imaging is characterized by flexibility and ease of use with all types of mass analysers and most desorption-ionization techniques [45][50][51].

In the microscope imaging mode, a large area of the sample surface is exposed to a defocused primary ion beam (or laser beam). Desorption ions maintain their positional information during extraction and detection by the mass analyser. After that, ion images are formed on a position-sensitive detector. This method produces a set of images, each image represents those ions with the same *m/z* ratio and thus spatial information is obtained. For matrix-assisted laser desorption/ionization (MALDI) and desorption electrospray ionization (DESI), the microscope mode gives higher spatial resolution than the microprobe mode as there is no need to focus or move the beam and is not limited by the large probe beam size. The resolution is defined by the quality of the secondary ion optics and the pixel size on the detector. The most important disadvantage is that the microscope mode is only compatible with specialised mass analysers [45][50]–[52]. **Figure 1.4** shows the difference between the microprobe and microscope methods of image acquisition [45].

MSI is usually performed by three well-established desorption and ionization techniques: SIMS, MALDI, and DESI, in addition to other complementary techniques which are reviewed in the following sub-sections.

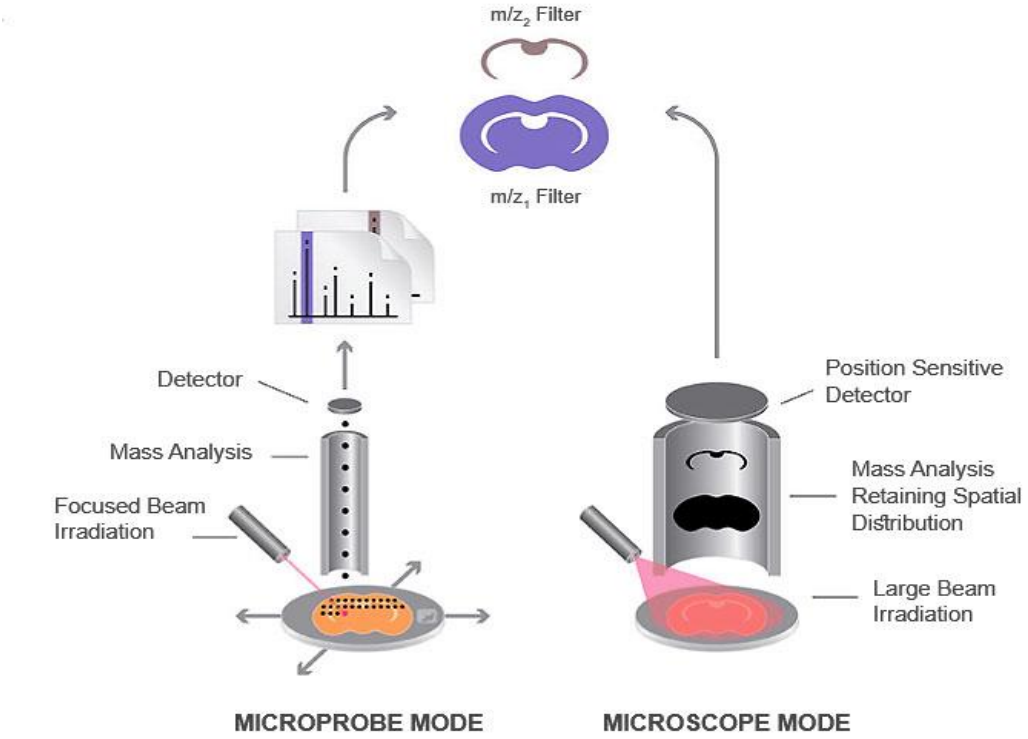

Figure 1.4: Showing the difference between the mechanisms of the microprobe and microscope methods in obtaining images from samples, modified from [45], with permission from Springer Nature.

1.4.3.1 Imaging SIMS

In 1960, SIMS was first used for MSI, in which it was employed extensively in the study of inorganic materials [45]. In 1999, Pacholski and Winograd demonstrated rapid progress in the use of SIMS imaging in various bio-applications [53]. Static SIMS is typically used in qualitative imaging [31], while dynamic SIMS is often utilized in quantitative imaging [46]. SIMS is characterized by its ability to provide the highest spatial resolution of the MSI techniques, high sensitivity and the detection of isotopes, elements and molecules, making it an effective tool in imaging [44]. In SIMS, data are acquired from the surface by two methods: two-dimensional (2D) and three-dimensional (3D) imaging. These methods are described in the following sub-sections.

1.4.3.1.1 Two-dimensional imaging (2D)

2D imaging is used to determine the spatial distributions of materials from the surface and sub-surface. A comprehensive image of a sample is taken, consisting of a number of pixels,

such as 256 × 256 on two axes, x and y. Each pixel provides ions with a specified *m/z* value, which are collected together to represent the full spectrum and images [54].

A large number of 2D imaging studies have been performed to detect lipids in mouse or rat brain tissue because of the presence of a large number of lipids in living cells, which, in turn, has high potential for ionization and is easier to identify than other biomolecules [54][55].

1.4.3.1.2 Three-dimensional imaging (3D)

3D imaging follows the same method of depth profiling (dynamic-SIMS) in which 2D images are taken for each layer in the depth direction *z* (voxel). The 2D images are then collected together and stacked sequentially to create a 3D image which has a cubic shape of the data (*m/z* ratios). 3D imaging is capable of detecting atomic and molecular ions from the first surface layer until reaching the substrate [39][54][56]. 3D imaging has drawn great attention in the fields of biology and medicine in determining the localisation and distribution of various ions through the use of high spatial resolution beams [56][57].

The first attempt to demonstrate the ability of ToF-SIMS in the 3D molecular imaging of biological systems was published by Fletcher *et al.* in 2007. A *Xenopus laevis* oocyte, a single cell with a diameter of ~1 mm, was studied. A BioToF-SIMS instrument was used with a C_{60}^+ primary ion beam (as a function of the depth). 3D maps were obtained successfully and displayed the distribution of the different biomolecular types with good sensitivity. The main drawback was that the time of analysis was very long using a pulsed C_{60}^+ primary ion beam (**Figure 1.5**) [56].

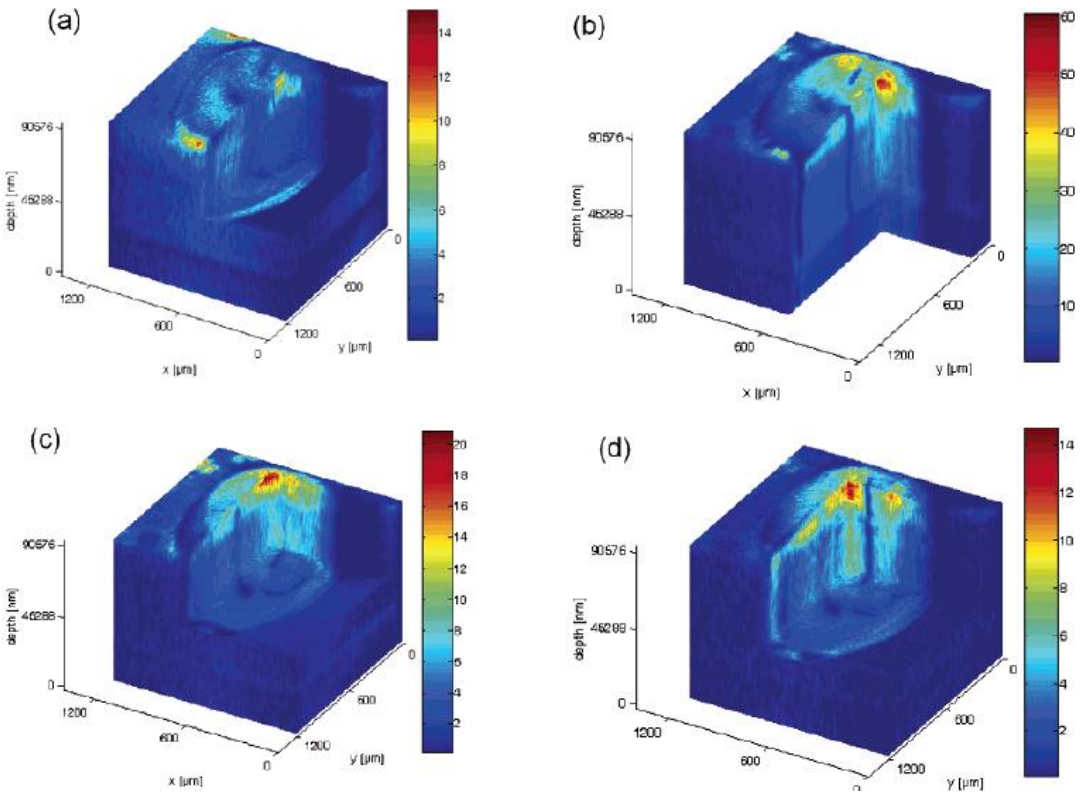

Figure 1.5: 3D biochemical imaging by BioToF-SIMS of a *Xenopus laevis* oocyte (freeze dried) with a C_{60}^{+} primary ion beam. The analysis was performed in positive mode with 1×10^{15} ions/cm^2 in 256×256 pixels. **a**: peaks at *m/z* 58, 86, 166, and 184 for phosphocholine; **b**: peaks at *m/z* 548, 574, and 576 for phosphatidylcholines (PC) with fatty acid; **c**: other lipids at *m/z* 815-960; and **d**: cholesterol peak at *m/z* 369. Scale bar: red indicates the high intensity sites of the ion, while light blue indicates sites of lower intensity. Reprinted with permission from [56]. Copyright (2019) American Chemical Society.

1.4.3.2 MALDI

MALDI imaging was introduced in 1997 when Caprioli *et al.* published a successful imaging study for each of the pancreatic tissues in rats to determine insulin, rat pituitary to determine hormone peptides, as well as protein in the mucosa cells with 25 µm spatial resolution [58]. In 2001, Stoeckli *et al.* published the first paper to image peptides and proteins in mammalian brain tissue (human and mouse) using 25 - 100 µm spatial resolution [47]. Since then MALDI-MSI has been widely used in the analysis of lipids [59][60], proteins [61][62], peptides [63][64], and pharmaceutical compounds [65]–[68].

MALDI-MSI technique is based on coating the sample by matrix capable of absorbing the laser beam energy, resulting in desorption of analytes to the gas-phase [14][69]. After that, the ionization process occurs often through proton transfer mechanism either prior to

desorption or in the gas-phase. There are also other ionization mechanisms proposed for MALDI that have been discussed in more detail in references [70]–[72]. The resulting ions accelerate under the influence of an electrostatic field towards the mass analyser where they are separated and then detected based on their *m/z* ratios [45]. Multiple types of mass analysers can be used with MALDI and time of flight (ToF) analyser is being the most common [45][73][74].

MALDI-MSI is characterized by sensitivity down to ~10^{-15} mol, the laser wavelength does not require modifying for each different analysis, and it allows analysis of a wide range of molecular masses from < 1 kDa up to 300 kDa [14][75]. In addition, the use of a matrix to absorb laser energy helps to transfer energy to the sample and allows soft desorption with reduced fragmentation. A major challenge for MALDI is that the type of matrix used noticeably affects the type and intensity of molecular signals generated from the sample, several references illustrate the classification of commonly used matrices according to chemistry of the material to be detected [69][76]–[78]. Furthermore, a good spatial resolution of MALDI-MS imaging can be achieved by improving the laser spot size from 300 μm to 5 μm [79], but this is accompanied by a decrease in sensitivity and only limited detection of the abundant molecules in cells such as membrane lipids [80]–[82]. Recently small peptides, lipids and metabolites were imaged with MALDI-MS with a spatial resolution of 1.4 μm [83].

The soft desorption process in MALDI generates molecular ions with masses of a few hundred Dalton and more [80]. Thus, the shortcoming of MALDI-MSI is that it is unsuitable for determining the localisation of small molecules and elements. In contrast, SIMS imaging can provide a spatial resolution (up to 50 nm) much higher than MALDI-MSI. SIMS does not require the addition of a matrix, thereby reducing the probability of diffusion of ions [84][85]. Thus, SIMS is an exciting tool for imaging elements and small molecules less than 1000 Da [86].

1.4.3.3 DESI

The desorption electrospray ionization - mass spectrometry (DESI-MS) technique was developed in 2004 by Cooks *et al.* [87]. DESI-MS has been used in imaging studies to detect biomolecules of proteins [88][89], peptides [90], lipids [91]–[93], phospholipids [94][95] and drugs molecules in tissue sections [96]–[98].

DESI's performance is based on the use of an electrospray source to generate charged and energetic solvent droplets [80], which in turn are used to desorb molecules from the analyte

surface as free or dissolved ions in solvent droplets, along with a large proportion of uncharged species [69][99]. This process occurs in ambient atmospheric pressure [69][99]. The resulting ions are drawn to the mass spectrometer under the influence of a pressure differential at the capillary inlet [69]. All types of mass spectrometers can be operated with DESI to analyse ions [45]. The sensitivity of DESI is affected by the angle of the spray and the position of the capillary and mass spectrometer with the sample [79]. Chemical ionization for specific compounds can be enhanced by changing the type of spray liquid, which then affects the solubility and desorption of analyte from the sample surface [69]. The molecules that have relatively weak bonds with the surface are often the easiest to detect using this technique [69].

DESI-MS is characterized by its use in investigations that do not require sample preparation, such as drug detection and forensic tests where the analysis can be conducted at ambient pressure [69][100]. DESI-MS in imaging mode typically provides a spatial resolution > 100 µm [101], but the spatial resolution of DESI has been improved to 40 µm by improving the spray design [45][102], and to 10 µm with nano-DESI that included further modifications to the spray source [103][104]. DESI does not require the application of a matrix, making it free from the issues of co-crystallization between the analyte and matrix that occur in MALDI [80][104].

In terms of shortcomings, the desorption process of species in DESI is soft, as in MALDI, and less energetic than SIMS [69], which makes DESI suitable for detecting molecular ions from masses up to 2000 Da but not for elements and small ions [103]. Despite the capability of DESI to provide useful spatial information, spatial resolution is still lower than that provided by SIMS and MALDI imaging [96][105]. In addition, the operation of SIMS and MALDI systems under high vacuum provides high efficiency in the ion collection and transmission to the mass spectrometer leading to better sensitivity compared to the DESI system under ambient pressure conditions [69][105].

1.4.3.4 Other MSI techniques

Other complementary MSI techniques employed in the analysis of biological samples are reviewed below. Laser Ablation Electrospray Ionization mass spectrometry (LAESI-MS) and liquid extraction surface analysis mass spectrometry (LESA-MS) are techniques developed from DESI, so they are similar to DESI in terms of providing soft ionization in ambient atmospheric pressure [103][106], along with the simplicity of sample preparation without the need to add a matrix [101][106].

LAESI-MS is based on ablation of the target molecules from the sample surface using mid-infrared laser followed by electrospray ionization, more detail about its operation is given in references [103][107]. This technique achieves a spatial resolution of ~ 50 - 200 μm [101]. LAESI-MS was used in imaging small and large biomolecules of lipids, proteins, peptides and metabolites [101][107].

LESA-MS is a combination of liquid extraction from the tissue surface and ionization by nano-electrospray respectively, more detail about its operation is given in references [106][108]. The tool has been used for 2D imaging of tissue sections with low spatial resolution (1 mm) [109]. LESA-MS is highly sensitive, but at the expense of poor spatial resolution, allowing the detection of compounds that cannot be analysed by other MSI techniques [109][110]. Therefore, LESA-MS is a preferred tool to analyse the entire body section of animals but not well suited for thin sections analysis [106]. LESA-MS has been used in multiple studies to detect proteins [111][112], lipids [113] and drug compounds [110][114]. Although LAESI-MS and LESA-MS are valuable techniques, their applications in biological imaging are still limited [103].

Laser ablation inductively coupled plasma mass spectrometry (LA-ICP-MS) can also be used in the quantitative measurement and imaging of elements and isotopes in biological and biomedical materials [45][105][115]–[120], along with wide applications in other scientific fields [121]. With this technique, the sample surface is eroded using a 10 - 100 μm UV laser to generate the ablation plume, which is transported to the plasma using argon gas where it is hard ionized in ambient pressure. The resulting ions are separated and detected in the mass spectrometer [103][105]. The technique is discussed in greater detail in references [119][121]. LA-ICP-MS is characterized by simple sample preparation, high sensitivity, and detection of low concentrations (ng/g) for most elements of the periodic table [105][117][122]. LA-ICP-MS also provides faster analysis and higher ionization of the elements than SIMS [103][117]. However, SIMS provides higher spatial resolution compared with LA-ICP-MS [38][123][124]. The distribution of *p*-boronophenylalanine-fructose (BPA-f) in human tumour liver tissue sections were determined quantitatively using LA-ICP-MS with a spot size of 50 μm. The results showed a homogeneous distribution of ^{10}B in the samples, and that the $^{10}B/^{11}B$ ratio in tumour-free tissue was almost double that detected in tumour tissues [125].

The 3D Orbi-SIMS is one of the newer SIMS instruments that combines both Orbitrap and ToF mass analysers (Tandem MS/MS) [126]. In this tool, the sample surface is rastered either using Bi LMIG or Ar gas cluster ion beams. The resulting secondary ions are separated

by mass either using a TOF analyser or Orbitrap analyser or both together for conducting 2D and 3D imaging, depth profiling, and obtaining surface spectra [127]. Thus, 3D Orbi-SIMS combines the high spatial resolution of a ToF analyser (~ 2 μm of Ar beam and 200 nm of Bi beam), with the high mass resolution (> 240,000 at 200 *m/z*) of an Orbitrap analyser [126]–[128]. Due to the operation of 3D Orbi-SIMS under high-vacuum, the best way to prepare the samples by freeze-drying, although the tool is capable of analyzing frozen hydrated tissues sections [126]. Many compounds can be detected in a single measurement, it has been used to detect the metabolites and lipids of tissue sections and single cells [126][127].

Developments in SIMS have led to the birth of several instruments that show potential for bioimaging of molecules in tissues and single cells with submicrometer spatial resolution [126][129] such as the J105-ToF-SIMS [130], Fourier transform-ion cyclotron resonance-mass spectrometry (FT-ICR-SIMS) [131], and a triple ion focusing time-of-flight (TRIFT-TOF-SIMS) with 200 nm spatial resolution [129].

1.5 Resolution

Resolution in SIMS has three different meanings: spatial, depth and mass resolution, as described in the following sub-sections.

1.5.1 Spatial resolution

Spatial or lateral resolution is a term that expresses the precision of the chemical imaging of samples. In microprobe mode it is governed by the use of a primary beam with a small diameter to bombard the surface [132]. The size of the pixels in each image and the number of sites utilized to analyse the target should be proportional to the size of the ion beam spot in order to avoid degradation of spatial resolution [50].

Achieving high resolution in an image makes it possible to distinguish the chemical distributions of the various elements present in the sample. It is possible to reduce the spot size of the ion beam to a reasonable size in the instrument by decreasing the aperture size used for the primary ion source, as well as increasing the focus of the beam through the ion optic system. However, very high spatial resolution is accompanied by a decrease in secondary ion signal, which inevitably leads to reduced sensitivity. This can be overcome either by increasing the diameter and therefore current of the primary beam slightly in order to maintain part of the sensitivity and form a balance between them, or by lengthening the

acquisition time (dwell time) and the use of a long pulse of the primary beam in some instruments, such as a ToF-SIMS, but this last solution renders the experiment very lengthy and reduces the mass resolution [133]–[135].

The nature of the ion source used in the investigation also affects the spatial resolution, as it is difficult to focus multi-atomic ion beams to less than 1 μm [134][135], unlike atomic beams, which can be focused to much less than that, such as caesium and oxygen (50 nm) [38][136][137]. An LMIG (Au, Bi) source is characterized by its ability to offer high resolution, ranging from 100 to 200 nm, due to its extreme brightness (high current) [50][124], while gallium is the best source of spatial resolution in an LMIG as it can provide a focused beam of 20 nm [135][138].

1.5.2 Depth resolution

Depth resolution is the crater depth resulting from the escape of the secondary particles caused by the primary ion beam when hitting the surface at a depth of about 1 nm [132].

The collision cascade and the increased energy of the primary ion beam causes atomic mixing in the lower layers in depth, and in cracks and erosion features [50][132][138]. In addition, the topography and the uneven-thickness layers in the sample contribute to the reduction of the depth resolution [139].

The degradation of depth resolution can be limited by reducing the beam energy used, as well as using multi-atomic beams, as the energy is distributed over a large number of atoms, thus reducing its effect on the site of impact. In addition, a dual-beam method can be used as a methodology for depth analysis, with a high-energy focused beam being used for data acquisition (analysis), while another low-energy beam is used to remove the effect of the analysis beam in depth. This method was used to conduct imaging using ToF-SIMS [50][132][138].

1.5.3 Mass resolution

Mass resolution refers to the ability of an instrument to distinguish ion peaks having very similar *m/z* values that are almost overlapping [50][140]. An example of ions having the same nominal mass is $^{31}P^{+}$ and $^{30}Si^{1}H^{+}$ which are separated by a mass of only 0.0078 [141]. The mass resolution (R) is expressed by Equation1.1:

$$R = \frac{M_1}{M_1 - M_2} = \frac{M}{\Delta M} \qquad \text{Equation 1.1}$$

Where:

M_1: target ion mass M_2: adjacent ion mass

The mass resolution can be calculated at the 10% valley when the interference between peaks is low, whereas, a large interference between the peaks is calculated from 50% of the height of the peaks and is known as the full width at half height (FWHH) [142]. Achieving accurate mass measurements increases the confidence level in the assignment of peaks to the correct ions and determines the elemental components of the sample. At present, the vast majority of imaging instruments in mass spectrometry use a ToF analyser, which provides high mass resolution up to 5,000 [50][143]. With ToF-SIMS, mass resolution can be increased using a short pulse length for the primary beam (ns) [24].

Moreover, a mass spectrometer designed with a magnetic sector analyser, such as a NanoSIMS, provides a higher mass resolution than ToF, up to 10,000, thus overcoming more mass interferences, especially in depth-profiling studies [132][134]. With a magnetic sector instrument, high resolution in mass can be achieved by using slits that act on the ion beam by cutting the edges and flattening the top of peaks, as in **Figure 1.6**, producing narrower and more separated peaks, but this leads to a decrease in secondary ions and thus reduced transmission and sensitivity [144][145]. In addition, **Figure 1.6** shows the ion interference between $^{12}C^{14}N^-$, $^{12}C^{13}C^1H^-$ and [$^{13}C_2^-$] at mass 26 Da in a coral tissue spectrum, where it is possible to distinguish easily between $^{12}C^{14}N^-$ and $^{12}C^{13}C^1H^-$ but difficult to separate [$^{13}C_2^-$], which needs mass resolution up to 7,200 to distinguish it from the other ions; thus, when selecting the $^{12}C^{14}N^-$ ion, the carbon peak site [$^{13}C_2^-$] is avoided by tuning the detector at the site of the dashed line *a* [145].

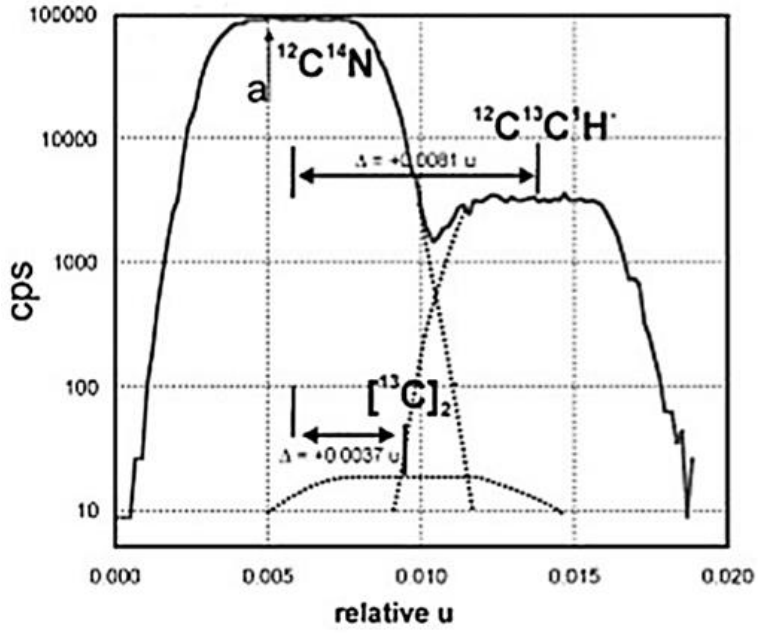

Figure 1.6: NanoSIMS scan of a coral tissue sample at mass 26 Da showing the interference between $^{12}C^{14}N^-$, $^{12}C^{13}C^1H^-$ and [$^{13}C_2^-$] peaks. Dashed line (**a**) shows the most appropriate site to tune the detector at $^{12}C^{14}N^-$ so that the [$^{13}C_2^-$] peak site is avoided [145]. Reprinted with permission from John Wiley and Sons.

1.6 Quantitative chemical information in SIMS

1.6.1 The SIMS equation

In SIMS, the formation of secondary ions passes through two stages: sputtering and ionization, processes which were discussed in 1.3section 1.3. During these two stages, the resulting secondary ion current is influenced by a variety of factors expressed in the following SIMS Equation 1.2 [13]:

$$I_m = I_p y_m \alpha^+ \theta_m \eta \qquad \text{Equation 1.2}$$

Where,

I_m: secondary ion current (often positive ions) of sample particles *m*.

I_p: primary ion current flux.

y_m: sputter yield (total number of secondary neutrals/ions per primary ion)

α^+: ionization probability to positive ion (or negative ion).

θ_m: fractional concentration of the chemistry of particles *m* in the surface.

η: transmission of the analyser and detector system.

The current of secondary ions is strongly affected by the electronic state of the samples under analysis, which complicates quantitative analysis. Thus, in this equation, both y_m and α^+ represent the most significant parameters in SIMS performance. The two parameters are affected by the characteristics of the primary ion beam used in the sputtering process, such as the flux, mass, charge, energy and angle of the primary beam on the sample. Moreover, the sputter yield is affected by the nature of the surface, such as the target mass, topography, crystallinity, and types of components and contamination [13][18]. Sputter yield was discussed in section 1.3.1. Furthermore, the ionization probability of particles (atomic and molecular) depends on both the sample chemistry and the matrix effect [146].

The transmission parameters strongly depend on the type of analyser selected for the analysis and its sensitivity in detecting the ions required. A comparison of the types of analysers used in this project was presented later in **Table 1.1** [12][24][45][147].

1.6.2 Yield

The sputter yield (*Y*) represents the total number of secondary particles sputtered from the surface per primary ion impact [148], as expressed in Equation 1.3 [149]:

$$Y = \frac{number\ of\ sputtered\ particles}{number\ of\ primary\ ion} = \frac{Sdpq}{I_P t} \qquad \text{Equation 1.3}$$

Where

S: analysed area

d: depth of the crater

ρ: atomic density

q: particle charge

I_p: primary ion particles

t: time spent for analysis.

The primary ion beam characteristics affect the yield (for more details, see sections 1.3 and 1.6.1). Moreover, the yield is affected by the surrounding matrix, the surface topography, the concentration of the elements in the sample, and surface type, such as insulating samples. These effects are described below [148].

1.6.2.1 Matrix effects

The matrix effect is the term given to the sensitivity of a specific element in multiple samples that vary in structure, crystallinity and composition, which, in turn, affects both ionization efficiency and yield [44]. This effect complicates quantitative analysis in SIMS, whether measuring the element concentration in the sample or at the interface between the sample and the substrate, which becomes more difficult when using a reactive primary beam [24].

The matrix effect has been considered in some mass spectrometry techniques that involve dissolving the analyte in a suitable matrix, such as MALDI. In contrast, SIMS has the ability to analyse samples without the need to add a matrix, labelling or using separation methods [44][150]–[152]. Molecular ion yields in SIMS can also be enhanced using multi-atomic ion beams [24]. Nonetheless, diverse chemical modifications can be made in SIMS to reduce the matrix effect and achieve high ionization [153][154].

The effect of a matrix is very complicated in biological systems due to the diversity of density and the elemental composition of biological materials [155]. Nevertheless, quantitative analysis of these systems has been carried out. For example, Jackson *et al.* presented a quantitative study of certain purines, such as inosine monophosphate (IMP) dissolved in trehalose as a matrix. Measurement was conducted using ToF-SIMS with a C_{60}^+ primary beam. The study demonstrated the possibility of measuring concentrations at the biological level, whereby trehalose showed the importance of a matrix in maintaining intact quasimolecular ion concentrations [156].

1.6.2.2 Surface Topography

Sputter yield is greatly affected by topography, as rough surfaces form a high yield and fluctuate between suppressing and enhancing the secondary ions when compared with flat surfaces [157]. The presence of holes or pores in the sample surface reduces the sputter yield because these features trap species and the crater edge causes a rise in yield [158]. Therefore,

the use of flat samples with an intact surface is important in obtaining reliable SIMS information [38]. The crystallization of a sample surface also affects the sputter rate due to different crystalline layers [24].

In depth-profiling experiments, the crater bottom is usually rough, resulting in the generation of ions from different vertical positions and thus a reduction in depth resolution [159]. The sputter rate also varies from one element to another and, therefore, when a sample consists of multiple elements, the element with the lowest sputtering rate will concentrate at the sample surface until a steady state situation is reached whereby sputter rates are constant [24][160].

1.6.2.3 Sample charging

Insulating samples suffer from ionization difficulties, whereby the bombardment of these samples by positive primary ions leads to the accumulation of positive charge on the surface, thus suppressing negative ion generation, then loss of spectrum and image information [13]. To overcome charging, the insulating sample can be coated with a thin layer (a few nanometres) of metal, such as Au, Ag or Pt [161][162]. This layer is exposed to sputtering before starting the sample analysis. An electron flood gun can also be used to compensate the charge, whereby a low-energy electron beam is used to irradiate the sample and return it to a neutral state [13].

1.6.3 Ionization efficiency

The ionization efficiency in SIMS is a term that refers to the ionized portion of the atoms and molecules emitted from the surface during the sputtering process. The number of secondary ions formed is very low for most materials and typically represents <1% of the total number of sputtered secondary particles, whereas uncharged species represent the vast majority of the yield and cannot be detected directly. Secondary ion yield is affected by several factors, the most important being the element characteristics in terms of the tendency of electronic loss and the forming of positive ions or electron affinity in forming negative ions [13][20]. The type of ion beam used to bombard a sample surface also has a significant role in influencing ionization efficiency. Reactive ion sources can significantly increase ionization efficiency. For instance, the use of an oxygen beam increases the generation of positive ions. When a sample surface is bombarded with an oxygen primary beam, oxygen–metal bonds are formed in the impact area. During ionization, these bonds break and, therefore, the oxygen atoms tend to acquire a negative charge because of their possession of

high electron affinity, which leads to enhancing the formation of positive ions (M^+) from the sample [20][163]. Moreover, selecting a caesium beam for sample analysis (or implantation step) reduces the surface work function, thus providing a large number of excited electrons on the surface, which, in turn, increases the probability of gaining electrons and the formation of negative ions (M^-) from the sample [20][164].

In comparison, the use of a multi-atomic ion beam increases the chances of obtaining molecular information. Therefore, when using these sources, the choice of ion beam depends on the kind of ions required to be detected as well as the beam's effect on ionization. Methodologies of the experiments in SIMS (spectrum from the surface, depth profiling and imaging) also affect the selection of the primary beam. For example, imaging experiments require the use of a highly focused primary beam in order to achieve high spatial resolution in the images, an LMIG is the best source for imaging experiments [135][138][165][166].

1.6.4 Sensitivity – Transmission - Detection limits

Sensitivity in SIMS depends on two properties, the secondary ion yield [38], and the transmission through the ion optics of the instrument. Transmission is expressed as the actual number of ions measured in the detector divided by number of ions produced from the sample surface. This means that a portion of ions may be lost during transport in the optical system. An increase in the mass resolution by introducing apertures and slits to restrict the path of secondary ions leads to a decrease in transmission, which, in turn, negatively affects sensitivity. Moreover, increasing spatial resolution using a primary beam with a small probe size also leads to decreased sensitivity. Therefore, sensitivity, transmission, mass resolution and spatial resolution are interrelated factors, whereby an increase in one leads to a drop in another [13][38][144], so it is usually preferable in experiments to use intermediate conditions that combine these factors at reasonable levels.

The limit of detection is the minimum quantity or concentration of a sample that will generate useful signal levels, which can be distinguished by at least 10 times background noise [14]. The useful yield is expressed by the number of ions detected divided by the number of sputtered atoms from the sample, and is affected by ionization efficiency, transmission through the optical system and the efficiency of the detector [144][149][167].

1.6.5 Relative sensitivity factors in quantification

Quantification in SIMS is often required to convert the intensities of secondary ions into concentrations, but this process is difficult due to each element and molecular ion being emitted from the sample surface with different yields [168]. Quantitative measurement can instead be made using a relative sensitivity factor (RSF). The RSF depends on the measurement of the ratio of the secondary signals (molecules or elements) recorded to the matrix signals in the same experiment and then compared with a reference material, also known as an internal standard. The reference material used should contain the same species of interest as the sample at a known concentration and have the same matrix as the sample [12][24][169].

Modification can be made using the RSF and concentration is expressed by the following Equation 1.4 [169]:

$$C_E = RSF \cdot \frac{I_E}{I_M} \qquad \text{Equation 1.4}$$

C_E: concentration required for measurement (of the element or molecule)

I_E: intensity of the secondary signals of the target whether an element or molecular species

I_M: signal intensity from the matrix element or molecular

Each element associated with the matrix has a specific RSF value that is different from that of the other elements. There are a number of reference tables for RSF values, which differ from each other depending on the primary ion beam type used in the analysis, such as oxygen or caesium, and the type of matrix used, such as silicon, or other semiconductors, such as gallium nitride (GaN). These tables provide a useful indicator of possible ion yields when preparing experiments [168]–[170]. Quantitative measurement of the elemental distribution in SIMS is very important to fulfilling the requirements of the semiconductor electronics industry [171].

Chandra *et al.* performed quantitative measurements on human glioblastoma cells (T98G) treated with 110 ppm 10boronophenylalanin-Fructose (^{10}BPA-f) to determine boron concentrations in cellular compartments [172][173] using an RSF of $^{10}B^+$ to the $^{12}C^+$ cell matrix signals [174], more details on these studies will be given in sections 2.3.1 and 2.3.1.1.

1.7 Instrumentation

In the field of analytical science, there are multiple types of SIMS instruments, each with its own advantages and disadvantages. Often, the main differences between the instruments are the mass analyser used and the primary ion source. When selecting a SIMS instrument, the most appropriate mass analyser is determined based on the requirements of mass resolution and sensitivity; the primary ion source is selected according to the requirements of spatial resolution, chemical damage, and mass range (atomic or molecular ions). The following is a review of the types of primary ion sources and mass analysers used in this project.

1.7.1 Primary ion source types

1.7.1.1 Liquid metal ion beams

A liquid metal ion gun (LMIG) is a source that emits positive primary ion beams from liquid metal [24]. The source structure and the primary ion beam extraction system in the LMIG gun column are described elsewhere [24][165][175]. The source provides monoatomic or multi-atomic ion beams, such as indium (In^+) [176], gallium (Ga^+), bismuth (Bi_3^+, Bi_1^+) and gold (Au^+, Au_2^+ and Au_3^+) [177]. LMIG is one of the main ion sources for performing imaging experiments with an ~100 nm - 10 µm probe size [123]. The LMIG was developed by Ionoptika Ltd (Southampton, UK) and UMIST by using Gold:Germanium alloy (Au:Ge) as a Au primary ion source, which melts easily at a temperature of 400 °C, rather than a pure gold source, which melts at temperatures above 1000 °C. The low melting temperature gives the eutectic source a long life and protects it from evaporation, as well as reducing the erosion of the source substrate [165]. The LMIG is widely used in ToF-SIMS analysis (for imaging and depth profiling) because it stimulates high secondary ion yield. A comparative study of primary ion beams of Au^+, Au_n^+ (n = 2–3) and Ga^+ performed on gramicidin (a biological sample) and polyethylene terephthalate (PET) showed that molecular ion fragment yields were greater when using Au_3^+ than Au^+, the latter in turn yielding more than Ga^+. [165].

An LMIG is characterized by the possibility of analysis using small-sized spots (< 100 nm) with a high-intensity focused current (very bright ion source), stable operation in dynamic and pulsed modes with higher energy (> 25 keV) and a long lifetime. Its disadvantage lies in the damage to the surface as a result of the bombardment by a beam consisting of a few atoms with high energy, whereby the damage volume exceeds the sputter volume [124][177][178].

1.7.1.2 Atomic ion beam

Atomic ion sources are widely used in dynamic SIMS applications (depth profiling and imaging) as they offer reactive primary ion beams for the bombardment of samples as explained in section 1.6.3. The most prominent types of this source are Cs^+ beam to produce negative ions and O^- beam to produce positive ions [24][177]. Both sources are needed in NanoSIMS instrument because of the use of a coaxial optical system, which requires an opposite polarity between the primary ion beam and secondary ion beam. This is discussed in more detail in [144][179].

In this project, only the Cs^+ beam was used for analysis, generated from a surface ionization source. The source design is explained in [177][180]. Cs^+ sources offer a high current density with a small spot size (spatial resolution) down to 50 nm, low energy spread and a good level of brightness but not better than an LMIG. However, the most prominent drawback is that Cs^+ beam cause damage to the surface [24][144][177].

1.7.2 Mass analysers

1.7.2.1 Time-of-Flight analyser (ToF)

Stephens introduced the concept of a ToF mass analyser in 1946 [181]. In 1955, Wiley and McLaren designed the first commercial tool based on Stephens' concept: the linear ToF (LToF) mass spectrometer [182]. The ToF analyser separates the secondary ions in the flight tube (1–2 m in length) depending on their velocity, which in turn depends on their mass-to-charge ratios *(m/z*, where $z = 1$, usually) [14][183]. The ToF mass analyser has an intrinsic advantage in its ability to measure all *m/z* of the ions using parallel detection [184] with good mass resolution and high sensitivity [183]. The performance of ToF analyser is shown in **Table 1.1** [12][24][45][147].

ToF is a common type of analyser for SIMS, used in a wide range of applications to analyse surfaces of materials and structures in various research fields, such as chemistry, biochemistry [185], genetics [186], and immunology [187]. The Bio-ToF mass spectrometer has been improved using a two-stage reflectron [143], to be called a reflectron time-of-flight (RToF) mass spectrometer [188]. A two-stage reflectron is a sequence of electrostatic fields that creates the 'retard' and 'reflect' voltage along a series of electrodes, this improves the mass resolution and sensitivity, more details about LToF and RToF are described in [14][183][188].

The separated secondary ions by ToF analyser are accelerated under a potential of ~ -8 kV by a post-acceleration detector into a microchannel plate (MCP) detector, which in turn is characterized by its ability to detect a large number of ions at the same time; extraction and response time is sub-nanosecond. The detector used in this study combines the output of a single MCP with a phosphor scintillator and an electron multiplier to provide an overall gain ~10^7. MCP-based detectors provide high sensitivity and high time-resolution and are ideal for ToF-SIMS measurements [189][190]. The ionic signals detected are translated into 1 ns time bins by a transient digitizer (PX1500-2 Signatec Inc., Philadelphia, USA) [191].

1.7.2.2 Magnetic sector analyser

The NanoSIMS instrument has a double focusing mass spectrometer in a Mauttach-Herzog design, which consists of a spherical electrostatic sector placed at 90° to the asymmetric magnet [192]. This design is commonly used when high sensitivity is required [193]. The electrostatic sector compensates for the kinetic energy variation of the secondary ions before entering the magnetic sector and therefore improves the mass resolution [194]. The magnetic sector separates the secondary ions that come through the optical system depending on their *m/z* ratio [194]. Magnetic sector analysers can only analyse a limited number of secondary ions in parallel [193]. More details of the magnetic sector design/operation are given in [192][194]. Furthermore, this design has good transmission, allows high spatial resolution and the ability to analyse with high mass resolution using a small probe size [195], making it preferable for use in dynamic SIMS and depth profiling. Magnetic sector also works with a continuous beam (duty cycle is unity), so is not suitable for static SIMS due to the probability of damaging the sample [14]. **Table 1.1** shows the performance of the magnetic sector analyser compared to the ToF analyser.

For the NanoSIMS 50L, the secondary ions separated by the magnetic sector are detected using seven detectors in the multicollection chamber. There are six moveable trolleys that allow detectors to be positioned at the masses of interest. Each trolley is equipped with both an electron multiplier (EM), which can measure ion signals of low intensity, and a Faraday cup (FC) for higher counts rates [144]. The main advantages of the magnetic sector on the NanoSIMS are discussed in section 1.7.3.2.

Table 1.1: The performance and capabilities of the mass analysers used in SIMS [12][24][43] [144][147].

	Type of analyser	
	Time of flight	**Magnetic sector**
Mass range	1000–10,000	< 10,000
Mass resolution	> 1000	10,000
Mass accuracy (ppm)	10	10
Mass detector	Parallel	Sequential
Ion production	Pulsed	Continuous
Transmission	<100%	< 50 % (classic) < 100% (double focusing)
Relative sensitivity	10,000	10
Used in	Dynamic and static SIMS	Dynamic SIMS

1.7.3 SIMS Instrumentation

The instruments used in this research, a BioToF-SIMS and a CAMECA NanoSIMS 50L, are explained in the following sections then compared with each other.

1.7.3.1 BioToF-SIMS instrument

The BioToF-SIMS is a microprobe imaging tool. Its characteristics make it reliable for analysing various types of biological, organic and inorganic samples [43][143]. A BioToF-SIMS was constructed at UMIST in the late 1990s, and represented the collective work of the Winograd group at Penn State University (USA) and the Vickerman group at the University of Manchester (UK), in addition to collaborative endeavours with Kore Technology Ltd (Cambridge, UK) and Ionoptika Ltd (Southampton, UK) [143][196].

The BioToF-SIMS instrument is equipped with a LMIG source and ToF analyser explained in sections 1.7.1.1 and 1.7.2.1 respectively. There are two methods for using the BioToF-SIMS instrument. First, the SIMS method is used to detect either positive or negative ions which are emitted from the surface during bombardment using a 25 kV LMIG Au_n^+ beam (n = 1 - 3), which in turn can be operated in two modes: direct current (DC) and pulsed [143][178]. The second method uses post-ionization, in which a laser is used to ionize the

neutral particles in the plume of sputtered species. The result of laser ionization is usually the formation of positive ions which increases the signal intensity and then the intensity of the signal can in some cases be increased in the spectrum [143]. The aim of constructing a BioToF-SIMS instrument was to find a successful way to analyse and image biological surfaces and cells using both SIMS and laser post-ionization while maintaining sensitivity and high mass resolution [196][197]. In this project, the BioToF-SIMS was operated without laser post ionization. **Figure 1.7** shows a schematic drawing of a BioToF-SIMS instrument [143]. The design and operation of the instrument are described in detail in references [143].

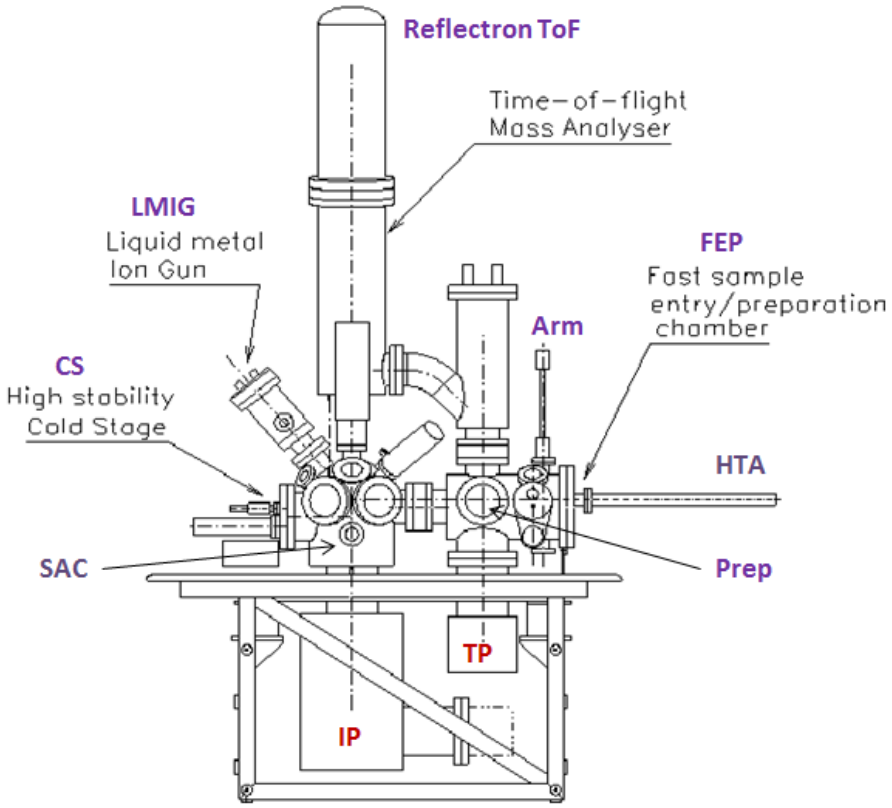

Figure 1.7: Schematic diagram of the BioToF-SIMS instrument showing its main parts. **Prep**: preparation chamber. **IP**: an ion pump to create ultrahigh vacuum inside the instrument. **TP**: a turbo pump to maintain a vacuum within Prep of less than 10^{-8} mbar. Arm: to insert the sample through fast entry port (**FEP**) into the Prep. HTA: a horizontal transfer arm to transfer the sample to cold stage (**CS**) in the surface analysis chamber (**SAC**). **LMIG**: liquid metal ion gun. **Reflectron ToF**: a reflectron time-of-flight analyser [143]. Reprinted with permission from John Wiley and Sons.

1.7.3.2 CAMECA NanoSIMS 50L instrument

The CAMECA NanoSIMS 50L is a dynamic microprobe SIMS instrument that uses a primary focused beam of caesium or oxygen ions in DC mode, which makes it a destructive technique. The instrument can perform depth profiling and 2D and 3D imaging in order to track and analyse elements, isotopes and small generated fragments [198]. The instrument was developed by Slodzian *et al*. in the early 1990s, with the aim of improving the spatial resolution and sensitivity of SIMS imaging while preserving high mass resolution and strong transmission, up to 100% [167]. The unique capabilities of the NanoSIMS have led to new applications and developments in various fields, such as cell biology [145][199], material science [200], microbiology [201][202], pharmacology [203], plant and soil science [204][205], geology and space science [144], cosmetics [206] and cosmochemistry [207].

The Manchester NanoSIMS 50L is shown in **Figure 1.8**. NanoSIMS 50L is equipped with atomic ion beam sources and a magnetic sector analyser reviewed in sections 1.7.1.2 and 1.7.2.2 respectively. The design and operation of the instrument are described in detail in references [144][179]. The main advantage of the design of the magnetic sector for the NanoSIMS is the ability to focus ions of seven different masses on one flat plane at the same time, which allows the use of a flat detector system to create images for each ion from the same sputtered volume [167][193], more detail about ion detectors in [144]. This results in greater precision in image recording and more accurate isotope ratio measurements [167][193].

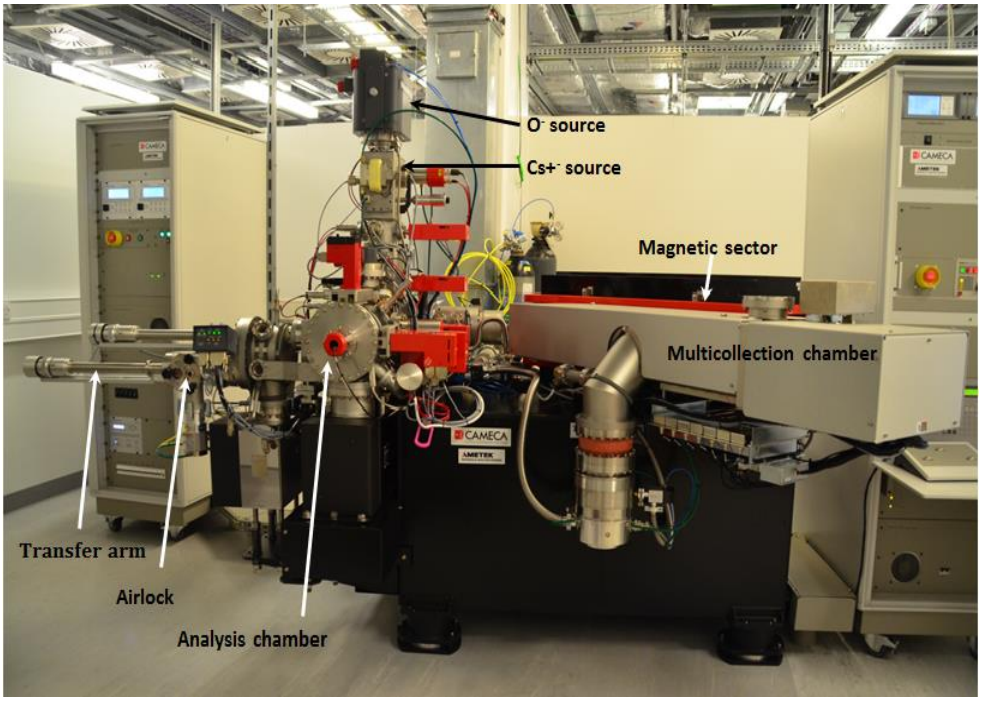

Figure 1.8: Manchester NanoSIMS 50L instrument.

1.7.3.3 Comparison between BioToF-SIMS and CAMECA NanoSIMS 50L

Secondary ion mass spectrometry is one of many techniques used to study and image the distribution of elements at the cellular and sub-cellular level for example to understand the relationship between the distribution of a drug and its impact on health and disease treatment in living organisms. NanoSIMS and BioToF-SIMS were used in this research as imaging methods, as each technique has individual characteristics and advantages that distinguish it from the other [1][208].

The NanoSIMS technique is characterized by the following:

- High spatial resolution down to 50 nm with a Cs^+ or O^- beam, , which requires a high-density primary beam [209][210].

- High sensitivity to concentrations down to the ppb level for some elements [211] and the ability to distinguish between ions of almost equal mass, such as $^{12}C^{15}N^-$ and $^{13}C^{14}N^-$ [209].

- The ability to analyse all elements and isotopes, from hydrogen to uranium, in the periodic table [209] except the noble gases. Elements such as Cd, Zn and Mn are challenging [198] because of the stability of the last filled valence orbitals and, therefore, do not easily form ions.

- The ability to achieve high transmission and high mass resolution [38]. For example, $^{13}C^-$can be resolved from $^{12}C^1H^-$, which needs a mass resolving power (MRP) of almost 3000 [144]. With a MRP of 3500, full transmission (100 %) can still be achieved, but the transmission drops to 25 % with a MRP of 9600 [179].

- Fast acquisition with a DC primary ion beam and the ability to collect up to seven masses simultaneously (parallel detection) from one pixel, which allows the measurement of precise isotope ratios and with perfect registration of ion images. It is also possible to analyse insulating samples [212].

- NanoSIMS instrument has a working distance of ~ 400 µm between the ion extraction lens and sample surface in order to obtain high sensitivity, improve collection efficiency and reduce the dispersion time resulting from ion movement. This means only flat samples can be analysed [143][144].

- The main disadvantage of the NanoSIMS is that it uses the same coaxial optic group to focus the primary ion beam and extract the secondary ions at the same time, which requires

that the two ion beams have opposite polarity [144]. This feature requires the instrument to be equipped with two different sources to generate positive and negative primary ions [213]. Other disadvantages of NanoSIMS are that it is a destructive technique, it is expensive, it works only in dynamic mode and cannot be operated in static mode so information is limited to atomic or small molecular ions. Nor is it suitable for analysing frozen-hydrated samples because it does not contain a cryogenic stage.

In comparison, BioToF-SIMS is characterized by the following:

- Good spatial resolution that reaches the sub-micron level down to 100 nm with an Au^+ beam, and < 10 μm for a C_{60}^+ beam [123][144].

- The ability to detect in parallel all secondary ions that have the same polarity originating from one analysis point, thus providing information on atomic and molecular ions [144].

- It causes less chemical damage compared with NanoSIMS [214]. It is also possible to run it in static mode, dynamic mode and in laser post-ionization experiments [143].

- Good transmission with reasonable mass resolution and good sensitivity, to ppm levels [143].

- The primary ion gun can be changed to any type of ion gun suitable for the analysis question [176][215], it is less expensive than NanoSIMS and can be used to analyse frozen-hydrated biological samples because it contains a cryogenic stage [167], minimizing possible water desorption and thus maintaining the integrity of the chemical information and surface sensitivity [143].

- In a BioToF instrument, the ion extraction lenses are placed at a distance of 10 mm from the sample surface in order to facilitate laser post-ionization experiments and analyse morphologically rough samples without causing distortions in the mass spectral signals [143].

The most obvious limitation in BioToF-SIMS is the difficulty in using it to measure and track isotopes due to the low ion signals produced compared with NanoSIMS. Another disadvantage of BioToF-SIMS is the limited spatial and mass resolution [144], the instrument is controlled manually before and during image acquisition, due to the large extraction gap it is difficult to determine the area of interest with high precision *via* the optical image, and the detection of all ions sometimes leads to a lower measurement accuracy of the elements. **Table 1.2** shows a comparison between the characteristics of NanoSIMS and BioToF-SIMS.

Table 1.2: Comparison of the capabilities and features of NanoSIMS and BioToF-SIMS.

Technique features	**NanoSIMS**	**BioToF-SIMS**
Primary beam sources	Cs^+ , O^- [144]	Au^+, Au_3^+ , C_{60}^+ [143]
Ion collection	Positive or negative ions; up to seven masses in parallel [144]	Positive or negative ions; collect all ions of one polarity, post-ionization [143]
Ions detected	Elements, isotopes, small ion fragments [144]	Elements, small ion fragments, molecular ion fragments [143]
SIMS mode	Dynamic SIMS [144]	Static and dynamic SIMS [143]
Ion optical system	Co-axial [179]	50° angle [43]
Mass range (a.m.u)	~250 [123]	2000 [123] (theoretically unlimited)
Analyser	Double focusing: magnetic and electrostatic sector [192]	Reflectron ToF [143]
Mass resolution	~5,000 [38][179]	~ 5,000 [143]
Spatial resolution	50 nm (Cs^+) 200 nm (O^-) [38]	> 100 nm (Au^+) ~ 10 μm to 2 μm (C_{60}^+) [123][124]
Transmission	60 – 80 % [38][179]	60% [143]

1.8 Summary

SIMS instruments provide many useful capabilities for surface analysis and offer reliable spatial and mass resolution in detecting elemental and molecular species at concentrations down to ppb. SIMS also provides great flexibility in dealing with different samples in various chemical, biological, pharmaceutical and medical science research areas.

The 2D and 3D imaging of biological samples is one of the forefront areas of SIMS application, which is the subject of the work presented in this thesis. Imaging allows for chemical mapping of the distribution and localisation of elements and molecules in tissues and cells at the sub-cellular level. Achieving high resolution in imaging experiments requires the use of high energy focused primary ion beams. The primary ion beam is selected for analysis based on the type of ion yield required. For example, a monoatomic ion beam is more focused for a small size probe, such as Au^+, Cs^+, O^- and Ga^+, and is more suited to the

detection of elemental species and small molecules, while a multi-atomic beam, such as C_{60}^{+}, is usually used to detect large molecules, such as lipids. To verify inner layers (3D depth profiling), it is advisable to use the microprobe imaging technique to focus the beam in small areas, thus obtaining better imaging resolution. 2D imaging is usually used to obtain molecular information from the surface with the use of either a microprobe or a microscope instrument when considering the use of an unfocused ion beam with less energy.

SIMS imaging is often run in dynamic mode which exceeds the static limit in order to penetrate surface layers sufficiently to generate high signals from small ionic fragments or elements. The diversity of SIMS possibilities in imaging makes it a valuable tool in quantitative bioanalytical applications.

1.9 References

[1] D. J. Hare, E. J. New, M. D. De Jongee, and G. McColl, "Imaging metals in biology: balancing sensitivity, selectivity and spatial resolution," *Chem. Soc. Rev.*, vol. 44, pp. 5941–5958, 2015.

[2] C. Quintana, T. D. WU, B. Delatour, M. Dhenain, J. L. Guerquin-Kern, and A. Croisy, "Morphological and Chemical Studies of Pathological Human and Mice Brain at the Subcellular Level: Correlation Between Light, Electron, and NanoSIMS Microscopies," *Microsc. Res. Tech.*, vol. 70, pp. 281–295, 2007.

[3] L. E. Wedlock, M. R. Kilburn, J. B. Cliff, L. Filgueira, M. Saunders, and S. J. Berners-Price, "Visualising gold inside tumour cells following treatment with an antitumour gold(I) complex," *Metallomics*, vol. 3, no. 9, pp. 917–925, 2011.

[4] D. S. McPhail, "Applications of Secondary Ion Mass Spectrometry (SIMS) in materials science," *J. Mater. Sci.*, vol. 41, no. 3, pp. 873–903, 2006.

[5] M. C. Davies, A. Brown, J. M. Newton, and S. R. Chapman, "SSIMS and SIMS Imaging Analysis of a Drug Delivery System," *Surf. Interface Anal.*, vol. 11, no. 12, pp. 591–595, 1988.

[6] A. Nilsson, R. J. A. Goodwin, M. Shariatgorji, T. Vallianatou, P. J. H. Webborn, and P. E. Andrén, "Mass spectrometry imaging in drug development," *Anal. Chem.*, vol. 87, no. 3, pp. 1437–1455, 2015.

[7] P. Malmberg, E. Jennische, D. Nilsson, and H. Nygren, "High-resolution, imaging TOF-SIMS: novel applications in medical research," *Anal. Bioanal. Chem.*, vol. 399, no. 8, pp. 2711–2718, 2011.

[8] A. Bodzon-Kulakowska and P. Suder, "Imaging Mass Spectrometry: Instrumentation, Applications, and Combination with other Visualization Techniques," *Mass Spectrom. Rev.*, vol. 35, pp. 147–169, 2016.

[9] M. K. Passarelli *et al.*, "Single-Cell Analysis: Visualizing Pharmaceutical and

Metabolite Uptake in Cells with Label-Free 3D Mass Spectrometry Imaging," *Anal. Chem.*, vol. 87, no. 13, pp. 6696–6702, 2015.

[10] A. M. Judd, D. J. Scurr, J. R. Heylings, K.-W. Wan, and G. P. Moss, "Distribution and visualisation of chlorhexidine within the skin using ToF-SIMS: A potential platform for the design of more efficacious skin antiseptic formulations," *Pharm. Res.*, vol. 30, no. 7, pp. 1896–1905, 2013.

[11] R. D. Alkins, P. M. Brodersen, R. N. S. Sodhi, and K. Hynynen, "Enhancing drug delivery for boron neutron capture therapy of brain tumors with focused ultrasound," *Neuro. Oncol.*, pp. 1–11, 2013.

[12] P. V. D. Heide, *Secondary Ion Mass Spectrometry: : An Introduction to Principle and Practice*, vol. 1. Canada: John Wiley & Sons, Inc., 2014.

[13] J. C. Vickerman and D. Briggs, "Prologue: ToF-SIMS-An evolving mass spectrometry of materials," in *ToF-SIMS: Materials Analysis by Mass Spectrometry*, 2nd ed., IM Publications, 2013, pp. 1–10.

[14] E. De Hoffmann and V. Stroobant, *Mass Spectrometry - Priniples and Applications.*, 3rd ed., vol. 29, no. 6. England: John Wiley & Sons Ltd, 2007.

[15] P. Sigmund, *Topics in Applied Physics: Sputtering by particle bombardment I*. Verlag Berlin Heidelberg: Springer, 1981.

[16] G. J. Leggett and J. C. Vickerman, "An empirical model for ion formation from polymer surfaces during analysis by secondary ion mass spectrometry," *Int. J. Mass Spectrom. Ion Process.*, vol. 122, no. C, pp. 281–319, 1992.

[17] A. M. Belu, D. J. Graham, and D. G. Castner, "Time-of-flight secondary ion mass spectrometry: Techniques and applications for the characterization of biomaterial surfaces," *Biomaterials*, vol. 24, no. 21, pp. 3635–3653, 2003.

[18] V. S. Smentkowski, "Trends in sputtering," *Prog. Surf. Sci.*, vol. 64, no. 1, pp. 1–58, 2000.

[19] B. J. Garrison and Z. Postawa, "MD simulations, the theoretical partner to dynamic cluster SIMS experiments," in *TOF-SIMS: Materials analysis by mass spectrometry*, 2nd ed., Manchester: IM Publications, 2013, pp. 170–173.

[20] A. Benninghoven, "The history of Static SIMS-A personal perspective," in *TOF-SIMS: Materials analysis by mass spectrometry*, 2nd ed., Manchester: IM Publications, 2013, p. 61.

[21] V. R. Deline, C. A. Evans, and P. Williams, "A unified explanation for secondary ion yields," *Appl. Phys. Lett.*, vol. 33, no. 7, pp. 578–580, 1978.

[22] E. A. Jones, N. P. Lockyer, J. Kordys, and J. C. Vickerman, "Suppression and Enhancement of Secondary Ion Formation Due to the Chemical Environment in Static-Secondary Ion Mass Spectrometry," *J. Am. Soc. Mass Spectrom.*, vol. 18, no. 8, pp. 1559–1567, 2007.

[23] A. Benninghoven, "Some aspects of secondary ion mass spectrometry of organic compounds," *Int. J. Mass Spectrom. Ion Phys.*, vol. 53, pp. 85–99, 1983.

[24] J. C. Vickerman and I. S. Gilmore, "Chapter 4:Molecular Surface Mass Spectrometry by SIMS," in *Surface Analysis – The Principal Techniques*, 2nd ed., 2009, pp. 121–

122, 127–137.

[25] L. D. Detter, O. W. Hand, R. G. Cooks, and R. A. Walton, “Interfacial chemical reactions accompanying desorption ionization mass spectrometry,” *Mass Spectrom. Rev.*, vol. 7, no. 5, pp. 465–502, 1988.

[26] E. R. Fuoco, G. Gillen, M. B. J. Wijesundara, W. E. Wallace, and L. Hanley, “Surface Analysis Studies of Yield Enhancements in Secondary Ion Mass Spectrometry by Polyatomic Projectiles,” *J. Phys. Chem. B*, vol. 105, no. 18, pp. 3950–3956, 2001.

[27] K. Wittmaack, “Implication in the use of reactive ion bombardment for secondary ion yield enhancement,” *North Holl. Publ. Co.*, vol. 9, pp. 315–334, 1981.

[28] S. Seki, H. Tamura, and W. Saitoh, “Ion image enhancement using in-situ implantation of Cs^+ and O_2^+ ions,” *Appl. Surf. Sci.*, vol. 203–204, pp. 832–835, 2003.

[29] R. N. S. Sodhi, “Time-of-flight secondary ion mass spectrometry (TOF-SIMS):—versatility in chemical and imaging surface analysis,” *R. Soc. Chem.*, vol. 129, pp. 483–487, 2004.

[30] S. S. Née Rabbani, I. B. Razo, T. Kohn, N. P. Lockyer, and J. C. Vickerman, “Enhancing ion yields in time-of-flight-secondary ion mass spectrometry: A comparative study of argon and water cluster primary beams,” *Anal. Chem.*, vol. 87, no. 4, pp. 2367–2374, 2015.

[31] L. Hanley, O. Kornienko, E. T. Ada, E. Fuoco, and J. L. Trevor, “Surface mass spectrometry of molecular species.,” *J. Mass Spectrom.*, vol. 34, no. 7, pp. 705–723, 1999.

[32] A. Benninghoven, “The analysis of monomolecular layers of solids by secondary ion imission.,” *Z. Phys.*, vol. 230, pp. 403–417, 1970.

[33] J. C. Vickerman, “Introduction,” in *Surface Analysis– ThePrincipal Techniques*, A John Wiley and Sons, 2009, pp. 1–8.

[34] M. S. Wagner and D. G. Castner, “Analysis of adsorbed proteins by static time-of-flight secondary ion mass spectrometry,” *Appl. Surf. Sci.*, vol. 231–232, pp. 366–376, 2004.

[35] J. Brison, S. Muramoto, and D. G. Castner, “ToF-SIMS Depth Profiling of Organic Films: A Comparrison between Single Beam and Dual-beam Analysis,” *J. Phys. Chem.*, vol. 114, no. 12, pp. 5565–5573, 2010.

[36] S. Sun, C. Szakal, N. Winograd, and A. Wucher, “Energetic ion bombardment of Ag surfaces by C_{60}^+ and Ga^+ projectiles,” *J. Am. Soc. Mass Spectrom.*, vol. 16, no. 10, pp. 1677–1686, 2005.

[37] G. Gillen and S. Roberson, “Preliminary evaluation of an SF_5^+ polyatomic primary ion beam for analysis of organic thin films by secondary ion mass spectrometry.,” *Rapid Commun. Mass Spectrom.*, vol. 12, no. 19, pp. 1303–12, 1998.

[38] J.-L. Guerquin-Kern, T. Wu, C. Quintana, and A. Croisy, “Progress in analytical imaging of the cell by dynamic secondary ion mass spectrometry (SIMS microscopy),” *Biochim. Biophys. Acta*, vol. 1724, pp. 228–238, 2005.

[39] P. V. D. Heide, “Data collection and processing,” in *Secondary Ion Mass Spectrometry: An Introduction to Principle and Practice*, Canada, 2014, pp. 204–251.

[40] H. Gnaser and H. Oechsner, “SIMS Depth Profile Analysis Using MCs^+ Molecular-Ions,” *Fresenius J. Anal. Chem.*, vol. 341, no. 1–2, pp. 54–56, 1991.

[41] J. S. Fletcher, X. A. Conlan, N. P. Lockyer, and J. C. Vickerman, “Molecular depth profiling of organic and biological materials,” *Appl. Surf. Sci.*, vol. 252, no. 19, pp. 6513–6516, 2006.

[42] D. Touboul *et al.*, “Tissue Molecular Ion Imaging by Gold Cluster Ion Bombardment,” *Anal. Chem.*, vol. 76, no. 6, pp. 1550–1559, 2004.

[43] D. Weibel, S. Wong, N. Lockyer, P. Blenkinsopp, R. Hill, and J. C. Vickerman, “A C_{60} Primary Ion Beam System for Time of Flight Secondary Ion Mass Spectrometry: Its Development and Secondary Ion Yield Characteristics,” *Anal. Chem.*, vol. 75, no. 7, pp. 1754–1764, 2003.

[44] E. R. Amstalden van Hove, D. F. Smith, and R. M. A. Heeren, “A concise review of mass spectrometry imaging,” *J. Chromatogr. A*, vol. 1217, no. 25, pp. 3946–3954, 2010.

[45] J. Pól, M. Strohalm, V. Havlíček, and M. Volný, “Molecular mass spectrometry imaging in biomedical and life science research,” *Histochem. Cell Biol.*, vol. 134, no. 5, pp. 423–443, 2010.

[46] S. Chandra, D. R. Smith, and G. H. Morrison, “Sub cellular image by dynamic SIMS ion microscop,” *Anal. Chem.*, pp. 104–114, 2000.

[47] M. Stoeckli, P. Chaurand, D. E. Hallahan, and R. M. Caprioli, “Imaging mass spectrometry: A new technology for the analysis of protein expression in mammalian tissues,” *Nat. Med.*, vol. 7, no. 4, pp. 493–496, 2001.

[48] H. Liebl, “Ion microprobe mass analyzer,” *J. Appl. Phys.*, vol. 38, no. 13, pp. 5277–5283, 1967.

[49] R. Castaing and G. Slodzian, “Analytical microscopy by secondary ion imaging techniques,” *J. Phys. E.*, vol. 14, no. 10, pp. 1119–1127, 1981.

[50] L. A. McDonnell and R. M. A. Heeren, “Imaging mass spectrometry,” *Wiley Period.*, vol. 26, pp. 606–643, 2007.

[51] R. M. A. Heeren, D. F. Smith, J. Stauber, B. Kükrer-Kaletas, and L. MacAleese, “Imaging Mass Spectrometry: Hype or Hope?,” *J. Am. Soc. Mass Spectrom.*, vol. 20, no. 6, pp. 1006–1014, 2009.

[52] S. L. Luxembourg, T. H. Mize, L. A. McDonnell, and R. M. A. Heeren, “High-spatial resolution mass spectrometric imaging of peptide and protein distributions on a surface,” *Anal. Chem.*, vol. 76, no. 18, pp. 5339–5344, 2004.

[53] M. L. Pacholski and N. Winograd, “Imaging with Mass Spectrometry,” *Chem. Rev.*, vol. 99, no. 10, pp. 2977–3006, 1999.

[54] J. S. Fletcher and J. C. Vickerman, “A new SIMS paradigm for 2D and 3D molecular imaging of bio-systems,” *Anal. Bioanal. Chem.*, vol. 396, no. 1, pp. 85–104, 2010.

[55] D. Touboul, A. Brunelle, F. Halgand, S. De La Porte, and O. Laprévote, “Lipid imaging by gold cluster time-of-flight secondary ion mass spectrometry: application to Duchenne muscular dystrophy,” *J. Lipid Res.*, vol. 46, no. 7, pp. 1388–1395, 2005.

[56] J. S. Fletcher, N. P. Lockyer, S. Vaidyanathan, and J. C. Vickerman, “TOF-SIMS 3D biomolecular imaging of Xenopus laevis oocytes using buckminsterfullerene (C_{60}) primary ions,” *Anal. Chem.*, vol. 79, no. 6, pp. 2199–2206, 2007.

[57] P. Sjövall, J. Lausmaa, and B. Johansson, “Mass spectrometric imaging of lipids in brain tissue,” *Anal. Chem.*, vol. 76, no. 15, pp. 4271–4278, 2004.

[58] R. M. Caprioli, T. B. Farmer, and J. Gile, “Molecular Imaging of Biological Samples: Localization of Peptides and Proteins Using MALDI-TOF MS,” *Anal. Chem.*, vol. 69, no. 23, pp. 4751–4760, 1997.

[59] M. E. Dueñas, J. J. Essner, and Y. J. Lee, “3D MALDI Mass Spectrometry Imaging of a Single Cell: Spatial Mapping of Lipids in the Embryonic Development of Zebrafish,” *Nature*, pp. 1–9, 2017.

[60] S. N. Jackson *et al.*, “Imaging of lipids in rat heart by MALDI-MS with silver nanoparticles,” *Anal Bioanal Chem*, vol. 406, no. 5. pp. 1377–1386, 2014.

[61] M. Dilillo *et al.*, “Ultra-High Mass Resolution MALDI Imaging Mass Spectrometry of Proteins and Metabolites in a Mouse Model of Glioblastoma,” *Nature*, vol. 7, no. 1. 2017.

[62] J. Frank *et al.*, “MALDI mass spectrometry imaging of proteins exceeding 30,000 daltons,” *Med Sci Monit*, vol. 16, no. 9, pp. 293–299, 2010.

[63] H. C. Diehl *et al.*, “The challenge of on-tissue digestion for MALDI MSI — a comparison of different protocols to improve imaging experiments,” *Anal Bioanal Chem*, vol. 407, pp. 2223–2243, 2015.

[64] M. Stoeckli, D. Staab, A. Schweitzer, J. Gardiner, and D. Seebach, “Imaging of a β-Peptide Distribution in Whole-Body Mice Sections by MALDI Mass Spectrometry,” *J Am Soc Mass Spectrom*, vol. 18, pp. 1921–1924, 2007.

[65] I. H. Bartelink *et al.*, “Heterogeneous drug penetrance of veliparib and carboplatin measured in triple negative breast tumors,” *Breast Cancer Res.*, vol. 107, no. 19, pp. 1–17, 2017.

[66] B. Prideaux, M. S. ElNaggar, M. Zimmerman, J. M. Wiseman, X. Li, and V. Dartois, “Mass spectrometry imaging of levofloxacin distribution in TB-infected pulmonary lesions by MALDI-MSI and continuous liquid microjunction surface sampling,” *Int. J. Mass Spectrom.*, vol. 377, pp. 699–708, 2015.

[67] N. Sun *et al.*, “Pharmacokinetic and pharmacometabolomic study of pirfenidone in normal mouse tissues using high mass resolution MALDI-FTICR-mass spectrometry imaging,” *Histochem Cell Biol*, vol. 145, pp. 201–211, 2016.

[68] A. Bouslimani, N. Bec, M. Glueckmann, C. Hirtz, and C. Larroque, “Matrix-assisted laser desorption/ionization imaging mass spectrometry of oxaliplatin derivatives in heated intraoperative chemotherapy (HIPEC)-like treated rat kidney,” *Rapid Commun. Mass Spectrom.*, vol. 24, no. 11, pp. 415–421, 2010.

[69] J. C. Vickerman, “Molecular imaging and depth profiling by mass spectrometry—SIMS, MALDI or DESI?,” *Analyst*, vol. 136, pp. 2199–2217, 2011.

[70] R. Knochenmuss and R. Zenobi, “MALDI Ionization: The Role of In-Plume Processes,” *Chem. Rev.*, vol. 103, p. 441−452, 2003.

[71] R. Zenobi and R. Knochenmuss, “Ion formation in MALDI mass spectrometry,” *Mass Spectrom. Rev.*, vol. 17, no. 5. pp. 337–366, 1998.

[72] K. Dreisewerd, “The Desorption Process in MALDI,” *Chem. Rev.*, vol. 103, no. 2, p. 395−425, 2003.

[73] D. J. Douglas, A. J. Frank, and D. Mao, “Linear ion traps in mass spectrometry,” *Mass Spectrom. Rev.*, vol. 24, no. 1, pp. 1–29, 2005.

[74] P. J. Trim and M. F. Snel, “Small molecule MALDI MS imaging: Current technologies and future challenges,” *Methods*, vol. 104, pp. 127–141, 2016.

[75] M. W. Duncan, H. Roder, and S. W. Hunsucker, “Quantitative matrix-assisted laser desorption/ionization mass spectrometry,” *Briefings Funct. Genomics Proteomics.*, vol. 7, no. 5, pp. 355–370, 2008.

[76] J. G. Swalesa, G. Hamma, M. R. Clenchb, and R. J. A. Goodwin, “Mass spectrometry imaging and its application in pharmaceutical research and development: A concise review,” *Int. J. Mass Spectrom.*, vol. 437, pp. 99–112, 2019.

[77] Y. Kim, S. R. Shanta, L. H. Zhou, and K. P. Kim, “Mass spectrometry based cellular phosphoinositides profiling and phospholipid analysis: A brief review,” *Exp. Mol. Med.*, vol. 42, no. 1, pp. 1–11, 2010.

[78] L. MacAleese, J. Stauber, and R. M. A. Heeren, “Perspectives for imaging mass spectrometry in the proteomics landscape,” *Proteomics*, vol. 9, no. 4, pp. 819–834, 2009.

[79] E. R. Amstalden van Hove, D. F. Smith, and R. M. A. Heeren, “A concise review of mass spectrometry imaging,” *J. Chromatogr. A*, vol. 1217, no. 25, pp. 3946–3954, 2010.

[80] D. F. Cobice, R. J. A. Goodwin, P. E. Andren, A. Nilsson, C. L. Mackay, and R. Andrew, “Future technology insight: mass spectrometry imaging as a tool in drug research and development,” *Br. J. Pharmacol.*, vol. 172, pp. 3266–3283, 2015.

[81] Y. Schober, S. Guenther, B. Spengler, and A. Römpp, “Single Cell Matrix-Assisted Laser Desorption/Ionization Mass Spectrometry Imaging,” *Anal. Chem.*, vol. 84, p. 6293−6297, 2012.

[82] D. M. G. Anderson, D. Mills, J. Spraggins, W. S. Lambert, D. J. Calkins, and K. L. Schey, “High-resolution matrix-assisted laser desorption ionization-imaging mass spectrometry of lipids in rodent optic nerve tissue.,” *Mol. Vis.*, vol. 19, pp. 581–92, 2013.

[83] M. Kompauer, S. Heiles, and B. Spengler, “Atmospheric pressure mAldi mass spectrometry imaging of tissues and cells at 1.4-mm lateral resolution,” *Nat. Methods*, vol. 14, no. 1, pp. 90–96, 2017.

[84] E. A. Jones, N. P. Lockyer, J. Kordys, and J. C. Vickerman, “Suppression and Enhancement of Secondary Ion Formation Due to the Chemical Environment in Static-Secondary Ion Mass Spectrometry,” *J Am Soc Mass Spectrom*, vol. 18, pp. 1559–1567, 2007.

[85] A. F. M. Altelaar, J. Van Minnen, C. R. Jiménez, R. M. A. Heeren, and S. R. Piersma, “Direct molecular imaging of Lymnaea stagnalis nervous tissue at subcellular spatial resolution by mass spectrometry,” *Anal. Chem.*, vol. 77, no. 3, pp. 735–741, 2005.

[86] A. F. M. Altelaar, S. L. Luxembourg, L. A. McDonnell, S. R. Piersma, and R. M. A. Heeren, “Imaging mass spectrometry at cellular length scales,” *Nat. Protoc.*, vol. 2, no. 5, pp. 1185–1196, 2007.

[87] Z. Takáts, J. M. Wiseman, B. Gologan, and R. G. Cooks, “Mass Spectrometry Sampling Under Ambient Conditions with Desorption Electrospray Ionization,” *Science (80-.).*, vol. 306, pp. 471–473, 2004.

[88] K. Y. Garza, C. L. Feider, D. R. Klein, J. A. Rosenberg, J. S. Brodbelt, and L. S. Eberlin, “Desorption Electrospray Ionization Mass Spectrometry Imaging of Proteins Directly from Biological Tissue Sections,” *Anal. Chem.*, vol. 90, pp. 7785–7789, 2018.

[89] C.-C. Hsu, P.-T. Chou, and R. N. Zare, “Imaging of Proteins in Tissue Samples Using Nanospray Desorption Electrospray Ionization Mass Spectrometry,” *Anal. Chem.*, vol. 87, pp. 11171–11175, 2015.

[90] M. W. Towers, T. Karancsi, E. A. Jones, S. D. Pringle, and E. Claude, “Optimised Desorption Electrospray Ionisation Mass Spectrometry Imaging (DESI-MSI) for the Analysis of Proteins/Peptides Directly from Tissue Sections on a Travelling Wave Ion Mobility Q-ToF,” *J. Am. Soc. Mass Spectrom.*, vol. 29, no. 12, pp. 2456–2466, 2018.

[91] S. Banerjee *et al.*, “Diagnosis of prostate cancer by desorption electrospray ionization mass spectrometric imaging of small metabolites and lipids,” *Proc. Natl. Acad. Sci.*, vol. 114, no. 13, pp. 3334–3339, 2017.

[92] A. K. Jarmusch, V. Pirro, Z. Baird, E. M. Hattab, A. A. Cohen-Gadol, and R. G. Cooks, “Lipid and metabolite profiles of human brain tumors by desorption electrospray ionization-MS,” *PNAS*, vol. 113, no. 6. pp. 1486–1491, 2016.

[93] A. L. Dill, D. R. Ifa, N. E. Manicke, Z. Ouyang, and R. G. Cooks, “Mass spectrometric imaging of lipids using desorption electrospray ionization,” *J. Chromatogr. B*, vol. 877, no. 26, pp. 2883–2889, 2009.

[94] I. Lanekoff, M. Thomas, and J. Laskin, “Shotgun Approach for Quantitative Imaging of Phospholipids Using Nanospray Desorption Electrospray Ionization Mass Spectrometry,” *Anal. Chem.*, vol. 86, pp. 1872–1880, 2014.

[95] D. R. Ifa, J. M. Wiseman, Q. Song, and R. G. Cooks, “Development of capabilities for imaging mass spectrometry under ambient conditions with desorption electrospray ionization (DESI),” *Int. J. Mass Spectrom.*, vol. 259, no. 1–3, pp. 8–15, 2007.

[96] T. Vallianatou *et al.*, “A mass spectrometry imaging approach for investigating how drug-drug interactions influence drug blood-brain barrier permeability,” *Neuroimage*, vol. 172, pp. 808–816, 2018.

[97] S. Okutan, H. S. Hansen, and C. Janfelt, “Cryo-sectioning of mice for whole-body imaging of drugs and metabolites with desorption electrospray ionization mass spectrometry imaging - a simplified approach,” *Proteomics*, vol. 16, no. 11–12. pp. 1633–1641, 2016.

[98] R. Vismeh, D. J. Waldon, Y. Teffera, and Z. Zhao, “Localization and Quantification of Drugs in Animal Tissues by Use of Desorption Electrospray Ionization Mass Spectrometry Imaging,” *Anal. Chem.*, vol. 84, pp. 5439–5445, 2012.

[99] F. M. Green, P. Stokes, C. Hopley, M. P. Seah, I. S. Gilmore, and G. O'Connor, "Developing Repeatable Measurements for Reliable Analysis of Molecules at Surfaces Using Desorption Electrospray Ionization," *Anal. Chem.*, vol. 81, pp. 2286–2293, 2009.

[100] D. R. Ifa, C. Wu, Z. Ouyang, and R. G. Cooks, "Desorption electrospray ionization and other ambient ionization methods: current progress and preview," *Analyst*, vol. 135, pp. 669–681, 2010.

[101] R. D. Addie, B. Balluff, J. V. M. G. Bovée, H. Morreau, and L. A. McDonnell, "Current State and Future Challenges of Mass Spectrometry Imaging for Clinical Research," *Anal. Chem.*, vol. 87, pp. 6426–6433, 2015.

[102] D. R. Ifa, L. M. Gumaelius, L. S. Eberlin, N. E. Manicke, and R. G. Cooks, "Forensic analysis of inks by imaging desorption electrospray ionization (DESI) mass spectrometry," *Analyst*, vol. 132, pp. 461–467, 2007.

[103] A. Bodzon-Kulakowska and P. Suder, "Imaging Mass Spectrometry: Instrumentation, Applications, and Combination with other Visualization Techniques," *Mass Spectrom. Rev.*, vol. 35, pp. 147–169, 2016.

[104] M. Shariatgorji *et al.*, "Simultaneous imaging of multiple neurotransmitters and neuroactive substances in the brain by desorption electrospray ionization mass spectrometry," *Neuroimage*, vol. 136, pp. 129–138, 2016.

[105] B. A. Boughton, D. Thinagaran, D. Sarabia, A. Bacic, and U. Roessner, "Mass spectrometry imaging for plant biology: a review," *Phytochem Rev*, vol. 15, pp. 445–488, 2016.

[106] D. Eikel *et al.*, "Liquid extraction surface analysis mass spectrometry (LESA-MS) as a novel profiling tool for drug distribution and metabolism analysis: The terfenadine example," *Rapid Commun. Mass Spectrom.*, vol. 25, no. 23, pp. 3587–3596, 2011.

[107] P. Nemes and A. Vertes, "Laser Ablation Electrospray Ionization for Atmospheric Pressure Molecular Imaging Mass Spectrometry," in *Mass Spectrometry Imaging-Principles and Protocols, Methods in Molecular Biology*, vol. 656, S. S. Rubakhin and J. V. Sweedler, Eds. Totowa N J-US: Humana Press, 2010, pp. 159–171.

[108] V. Kertesz and G. J. Van Berkel, "Fully automated liquid extraction-based surface sampling and ionization using a chip-based robotic nanoelectrospray platform," *J. Mass Spectrom.*, vol. 45, no. 3, pp. 252–260, 2010.

[109] J. G. Swales *et al.*, "Mapping Drug Distribution in Brain Tissue Using Liquid Extraction Surface Analysis Mass Spectrometry Imaging," *Anal. Chem.*, vol. 87, no. 19, pp. 10146–10152, 2015.

[110] J. G. Swales *et al.*, "Mass Spectrometry Imaging of Cassette-Dosed Drugs for Higher Throughput Pharmacokinetic and Biodistribution Analysis," *Anal. Chem.*, vol. 86, p. 8473−8480, 2014.

[111] R. L. Griffiths, E. K. Sisley, A. F. Lopez-Clavijo, A. L. Simmonds, I. B. Styles, and H. J. Cooper, "Native mass spectrometry imaging of intact proteins and protein complexes in thin tissue sections," *Int. J. Mass Spectrom.*, vol. 437, pp. 23–29, 2019.

[112] R. L. Griffiths, A. L. Simmonds, J. G. Swales, R. J. A. Goodwin, and H. J. Cooper, "LESA MS Imaging of Heat-Preserved and Frozen Tissue: Benefits of Multistep

Static FAIMS," *Anal. Chem.*, vol. 90, no. 22, pp. 13306–13314, 2018.

[113] Z. Hall, Y. Chu, and J. L. Griffin, "Liquid Extraction Surface Analysis Mass Spectrometry Method for Identifying the Presence and Severity of Nonalcoholic Fatty Liver Disease," *Anal. Chem.*, vol. 89, no. 9, pp. 5161–5170, 2017.

[114] J. G. Swales, G. Hamm, M. R. Clench, and R. J. A. Goodwin, "Mass spectrometry imaging and its application in pharmaceutical research and development: A concise review," *Int. J. Mass Spectrom.*, vol. 437, pp. 99–112, 2019.

[115] A. Arakawa *et al.*, "High-resolution laser ablation inductively coupled plasma mass spectrometry used to study transport of metallic nanoparticles through collagen-rich microstructures in fibroblast multicellular spheroids," *Anal. Bioanal. Chem.*, vol. 411, no. 16, pp. 3497–3506, 2019.

[116] T. Van Acker *et al.*, "High-resolution imaging and single-cell analysis via laser ablation-inductively coupled plasma-mass spectrometry for the determination of membranous receptor expression levels in breast cancer cell lines using receptor-specific hybrid tracers," *Anal. Chim. Acta*, vol. 1074, pp. 43–53, 2019.

[117] L. Lobo, R. Pereiro, and B. Fernández, "Opportunities and challenges of isotopic analysis by laser ablation ICP-MS in biological studies," *Trends Anal. Chem.*, vol. 105, pp. 380–390, 2018.

[118] O. B. Bauer, C. Köppen, M. Sperling, H. J. Schurek, G. Ciarimboli, and U. Karst, "Quantitative Bioimaging of Platinum via Online Isotope Dilution-Laser Ablation-Inductively Coupled Plasma Mass Spectrometry," *Anal. Chem.*, vol. 90, no. 11, pp. 7033–7039, 2018.

[119] D. Pozebon, G. L. Scheffler, and V. L. Dressler, "Recent applications of laser ablation inductively coupled plasma mass spectrometry (LA-ICP-MS) for biological sample analysis: A follow-up review," *J. Anal. At. Spectrom.*, vol. 32, no. 5, pp. 890–919, 2017.

[120] A. Sussulini, J. S. Becker, and J. S. Becker, "Laser ablation ICP-MS: Application in biomedical research," *Mass Spectrom. Rev.*, vol. 36, pp. 47–57, 2015.

[121] N. S. Mokgalaka and J. L. Gardea-Torresdey, "Laser ablation inductively coupled plasma mass spectrometry: Principles and applications," *Appl. Spectrosc. Rev.*, vol. 41, no. 2, pp. 131–150, 2006.

[122] R. Liu, P. Wu, L. Yang, X. Hou, and Y. Lv, "Inductively coupled plasma mass spectrometry-based immunoassay: A review," *Mass Spectrom. Rev.*, vol. 33, no. 5, pp. 373–393, 2014.

[123] Z. Qin, J. A. Caruso, B. Lai, A. Matusch, and J. S. Becker, "Trace metal imaging with high spatial resolution: Applications in biomedicine," *Metallomics*, vol. 3, no. 1, pp. 28–37, 2011.

[124] IONOPTIKA: ion beam technology, "Ion Beams and their Applications - Application Note | Ionoptika Ltd." [Online]. Available: https://www.ionoptika.com/application-note/ions-beams-their-applications/. [Accessed: 01-Aug-2018].

[125] O. Reifschneider *et al.*, "Quantitative bioimaging of p-boronophenylalanine in thin liver tissue sections as a tool for treatment planning in boron neutron capture therapy," *Anal. Bioanal. Chem.*, vol. 407, no. 9, pp. 2365–2371, 2015.

[126] P. Agüi-Gonzalez, S. Jähne, and N. T. N. Phan, “SIMS imaging in neurobiology and cell biology,” *J. Anal. At. Spectrom.*, vol. 34, pp. 1355–1368, 2019.

[127] M. K. Passarelli *et al.*, “The 3D OrbiSIMS—label-free metabolic imaging with subcellular lateral resolution and high mass-resolving power,” *Nat. Methods*, vol. 14, no. 12, pp. 1175–1183, 2017.

[128] Q. Hu, R. J. Noll, H. Li, A. Makarov, M. Hardman, and R. G. Cooks, “The Orbitrap: a new mass spectrometer,” *J. Mass Spectrom.*, vol. 40, pp. 430–443, 2005.

[129] G. L. Fisher *et al.*, “A New Method and Mass Spectrometer Design for TOF-SIMS Parallel Imaging MS/MS,” *Anal. Chem.*, vol. 88, no. 12, pp. 6433–6440, 2016.

[130] J. S. Fletcher *et al.*, “A new dynamic in mass spectral imaging of single biological cells,” *Anal. Chem.*, vol. 80, no. 23, pp. 9058–9064, 2008.

[131] D. F. Smith, A. Kiss, F. E. Leach III, E. W. Robinson, L. Paša-Tolić, and R. M. A. Heeren, “High mass accuracy and high mass resolving power FT-ICR secondary ion mass spectrometry for biological tissue imaging,” *Anal. Bioanal. Chem.*, vol. 405, no. 18, pp. 6069–6076, 2013.

[132] H. Liebl, “SIMS instrumentation and imaging techniques,” *Scanning*, vol. 3, no. 2, pp. 79–89, 1980.

[133] A. M. Piwowar and N. Winograd, “Application of SIMS to study of biological system,” in *TOF-SIMS: Materials analysis by mass spectrometry*, 2nd ed., J. C. and D. B. Vickerman, Ed. IM Publications, 2013, pp. 561–565.

[134] A. J. Eccles and J. C. Vickerman, “The characterization of an imaging time-of-flight secondary ion mass spectrometry instrument,” *J. Vac. Sci. Technol. A Vacuum, Surfaces, Film.*, vol. 7, no. 2, pp. 234–244, 1989.

[135] A. Brunelle, D. Touboul, and O. Laprévote, “Biological tissue imaging with time-of-flight secondary ion mass spectrometry and cluster ion sources,” *J. Mass Spectrom.*, vol. 40, no. 8, pp. 985–999, 2005.

[136] N. S. Smith, P. P. Tesch, N. P. Martin, and R. W. Boswell, “The Hyperion^{TM} ion probe for next generation FIB, SIMS and Nano-Ion implantation,” *Microsc. Microanal.*, vol. 15, no. Suppl 2, pp. 312–313, 2009.

[137] Oregon Physics, “Hyperion II Dual Polarity Ion Source,” *Oregon Physics*, 2015. [Online]. Available: http://www.oregon-physics.com/hyperion2.php. [Accessed: 15-Jul-2018].

[138] R. Levi-Setti *et al.*, “Critical issues in the application of a gallium probe to high resolution secondary ion imaging,” *Surf. Sci.*, vol. 246, pp. 94–106, 1991.

[139] F. M. Green, A. G. Shard, I. S. Gilmore, and M. P. Seah, “Analysis Of The Interface And Its Position In C_{60}^{n+} Secondary Ion Mass Spectrometry Depth Profiling,” *Anal. Chem.*, vol. 81, no. 1, pp. 75–79, 2009.

[140] A. G. Marshall and C. L. Hendrickson, “High-Resolution Mass Spectrometers,” *Annu. Rev. Anal. Chem.*, vol. 1, no. 1, pp. 579–599, 2008.

[141] D. McPhail and M. Dowsett, “Dynamic SIMS,” in *SurfaceAnalysis – ThePrincipal Techniques*, 2nd ed., A John Wiley and Sons, Ltd, 2009, p. 226.

[142] K. Downard, “The Mass Spectrum,” in *Mass Spectrometry: A Foundation Course*, Sydney: The Royal Society of Chemistry, 2004, pp. 18–19.

[143] R. M. Braun *et al.*, “Performance characteristics of a chemical imaging time-of-flight mass spectrometer,” *Rapid Commun. Mass Spectrom.*, vol. 12, no. 18, pp. 1246–1252, 1998.

[144] P. Hoppe, S. Cohen, and A. Meibom, “GGR Cutting-Edge Review NanoSIMS : Technical Aspects and Applications in Cosmochemistry and Biological Geochemistry,” *Geostand. Geoanalytical Res.*, vol. 37, pp. 111–154, 2013.

[145] P. L. Clode, R. A. Stern, and A. T. Marshall, “Subcellular Imaging of Isotopically Labeled Carbon Compounds in a Biological Sample by Ion Microprobe (NanoSIMS),” *Microsc. Res. Tech.*, vol. 70, no. 3, pp. 220–229, 2007.

[146] J. C. Vickerman, “Impact of Mass Spectrometry in Surface Analysis,” *Analyst*, vol. 119, 1994.

[147] E. A. Jones, N. P. Lockyer, and J. C. Vickerman, “Mass spectral analysis and imaging of tissue by ToF-SIMS-The role of buckminsterfullerene, C_{60}^{+}, primary ions,” *Int. J. Mass Spectrom.*, vol. 260, no. 2–3, pp. 146–157, 2007.

[148] L. Van Vaeck, A. Adriaens, and R. Gijbels, “Static secondary ion mass spectrometry (S-SIMS) Part 1: methodology and structural interpretation,” *Mass Spectrom. Rev.*, vol. 18, no. 1, pp. 1–47, 1999.

[149] K. L. Moore, “High resolution secondary ion mass spectrometry analysis of trace elements in cereal grain and roots,” PhD thesis, Oxford University, UK, 2011.

[150] J. J. D. Fitzgerald, P. Kunnath, and A. V Walker, “Matrix-Enhanced Secondary Ion Mass Spectrometry (ME SIMS) Using Room Temperature Ionic Liquid Matrices,” *Technology*, vol. 82, no. 11, pp. 4413–4419, 2010.

[151] J. C. Vickerman, “Molecular imaging and depth profiling by mass spectrometry—SIMS, MALDI or DESI?,” *Analyst*, vol. 136, no. 11, p. 2199, 2011.

[152] A. F. M. Altelaar, J. Van Minnen, C. R. Jiménez, R. M. A. Heeren, and S. R. Piersma, “Direct molecular imaging of Lymnaea stagnalis nervous tissue at subcellular spatial resolution by mass spectrometry,” *Anal. Chem.*, vol. 77, no. 3, pp. 735–741, 2005.

[153] A. Delcorte, N. Médard, and P. Bertrand, “Organic secondary ion mass spectrometry: Sensitivity enhancement by gold deposition,” *Anal. Chem.*, vol. 74, no. 19, pp. 4955–4968, 2002.

[154] A. Delcorte, “Matrix-enhanced secondary ion mass spectrometry: The Alchemist’s solution?,” *Appl. Surf. Sci.*, vol. 252, no. 19, pp. 6582–6587, 2006.

[155] M. S. Burns, “Biological microanalysis by secondary ion mass spectrometry: status and prospects,” *Ultramicroscopy*, vol. 24, no. 2–3, pp. 269–281, 1988.

[156] L. M. Jackson, J. J. Hue, and N. Winograd, “Quantitative Detection of Purines in Biologically-Relevant Films with TOF-Secondary Ion Mass Spectrometry.,” *Surf. Interface Anal.*, vol. 45, no. 1, pp. 237–239, 2013.

[157] U. Littmark and W. O. Hofer, “The influence of surface structures on sputtering: Angular distribution and yield from faceted surfaces,” *J. Mater. Sci.*, vol. 13, no. 12, pp. 2577–2586, 1978.

[158] R. Levi-Setti, “Structural and microanalytical imaging of biological materials by scanning microscopy with heavy-ion probes,” *Annu. Rev. Biophys. Biophys. Chem.*, vol. 17, pp. 325–347, 1988.

[159] P. A. W. Van der Heide, M. S. Lim, S. S. Perry, and J. Bennett, “A systematic study of the surface roughening and sputter rate variations occurring during SIMS ultrashallow depth profile analysis of Si with Cs^+,” *Nucl. Instruments Methods Phys. Res. Sect. B*, vol. 201, no. 2, pp. 413–425, 2003.

[160] H. W. Werner and N. Warmoltz, “The influence of selective sputtering on surface composition,” *Surf. Sci.*, vol. 57, no. 2, pp. 706–714, 1976.

[161] L. Adriaensen, F. Vangaever, and R. Gijbels, “Metal-assisted secondary ion mass spectrometry: Influence of Ag and Au deposition on molecular ion yields,” *Anal. Chem.*, vol. 76, no. 22, pp. 6777–6785, 2004.

[162] H. Nygren, P. Malmberg, C. Kriegeskotte, and H. F. Arlinghaus, “Bioimaging TOF-SIMS: Localization of cholesterol in rat kidney sections,” *FEBS Lett.*, vol. 566, no. 1–3, pp. 291–293, 2004.

[163] A. Benninghoven, J. Okano, R. Shimizu, and H. W. Werner, *Secondary Ion Mass Spectrometry, SIMS IV*. Germany: Springer-Verlag, 1984.

[164] M. L. Yu and N. D. Lang, “Mechanisms of atomic ion emission during sputtering,” *Nucl. Inst. Methods Phys. Res. B*, vol. 14, no. 4–6, pp. 403–413, 1986.

[165] N. Davies, D. E. Weibel, P. Blenkinsopp, N. Lockyer, R. Hill, and J. C. Vickerman, “Development and experimental application of a gold liquid metal ion source,” *Appl. Surf. Sci.*, vol. 203, pp. 223–227, 2003.

[166] M. J. Baker, J. S. Fletcher, H. Jungnickel, N. P. Lockyer, and J. C. Vickerman, “A comparative study of secondary ion yield from model biological membranes using Au_n^+ and C_{60}^+ primary ion sources,” *Appl. Surf. Sci.*, vol. 252, no. 19, pp. 6731–6733, 2006.

[167] G. Slodzian, B. Daigne, F. Girard, F. Boust, and F. Hillion, “Scanning secondary ion analytical microscopy with parallel detection,” *Biol. Cell*, vol. 74, no. C, pp. 43–50, 1992.

[168] A. Laufer *et al.*, “Determination of secondary ion mass spectrometry relative sensitivity factors for polar and non-polar ZnO,” *J. Appl. Phys.*, vol. 110, no. 9, pp. 1–5, 2011.

[169] EAG Laboratories, “SIMS Tutorial: Theory - Secondary ion yield,” *Evans Analytical Group Laboratories*. [Online]. Available: https://www.eag.com/resources/tutorials/sims-tutorial-theory/. [Accessed: 13-Aug-2017].

[170] R. G. Wilson and S. W. Novak, “Systematics of secondary-ion-mass spectrometry relative sensitivity factors versus electron affinity and ionization potential for a variety of matrices determined from implanted standards of more than 70 elements,” *J. Appl. Phys.*, vol. 69, no. 1, pp. 466–474, 1991.

[171] D. Phinney, “Quantitative Analysis of Microstructures by Secondary Ion Mass Spectrometry,” *Microsc. Microanal.*, vol. 12, pp. 352–355, 2006.

[172] S. Chandra, T. Ahmad, R. F. Barth, and G. W. Kabalka, “Quantitative evaluation of

boron neutron capture therapy (BNCT) drugs for boron delivery and retention at subcellular-scale resolution in human glioblastoma cells with imaging secondary ion mass spectrometry (SIMS)," *J. Microsc.*, vol. 254, no. 3, pp. 146–156, 2014.

[173] S. Chandra, W. Tjarks, D. R. Lorey, and R. F. Barth, "Quantitative subcellular imaging of boron compounds in individual mitotic and interphase human glioblastoma cells with imaging secondary ion mass spectrometry (SIMS)," *J. Microsc.*, vol. 229, no. 1, pp. 92–103, 2008.

[174] W. A. Ausserer, Y. C. Ling, S. Chandra, and G. H. Morrison, "Quantitative Imaging of Boron, Calcium, Magnesium, Potassium, and Sodium Distributions in Cultured Cells with Ion Microscopy," *Anal. Chem.*, vol. 61, no. 24, pp. 2690–2695, 1989.

[175] R. Hill and P. W. M. Blenkinsopp, "The development of C_{60} and gold cluster ion guns for static SIMS analysis," *Appl. Surf. Sci.*, vol. 231–232, pp. 936–939, 2004.

[176] M. Tajmar and A. Genovese, "Experimental validation of a mass- efficiency model for an indium liquid-metal ion source," *Appl. Phys. A Mater. Sci. Process.*, vol. 76, no. 6, pp. 1003–1006, 2003.

[177] J. C. Vickerman, D. Briggs, and R. Hill, "Chapter 10: Analysis beams used in ToF-SIMS," in *ToF-SIMS: Materials Analysis by Mass Spectrometry*, 2nd ed., IM Publications, 2013, pp. 271–275.

[178] A. V. Walker and N. Winograd, "Prospects for imaging with TOF-SIMS using gold liquid metal ion sources," *Appl. Surf. Sci.*, vol. 203–204, pp. 198–200, 2003.

[179] CAMECA, "NanoSIMS 50/ 50L," 2006. [Online]. Available: https://microscopie.univ-rennes1.fr/sites/microscopie.univ-rennes1.fr/files/field/image/publiNano/Instrumentation.pdf. [Accessed: 07-Jul-2015].

[180] EAG Laboratories, "SIMS Instrumentation Tutorial- History of SIMS," *Evans Analytical Group Laboratories*. [Online]. Available: https://www.eag.com/resources/tutorials/sims-tutorial-instrumentation/. [Accessed: 15-Jul-2018].

[181] W. E. Stephens, "A Pulsed Mass Spectrometer with Time Disaersion," *Phys. Rev*, vol. 69, p. 691, 1946.

[182] W. C. Wiley and I. H. McLaren, "Time-of-flight mass spectrometer with improved resolution," *Rev. Sci. Instrum.*, vol. 26, no. 12, pp. 1150–1157, 1955.

[183] R. J. Cotter, "The New Time-of-Flight Mass Spectrometry.," *Anal. Chem.*, vol. 71, no. 13, pp. 445A-451A, 1999.

[184] J. C. Vickerman and I. S. Gilmore, "Molecular Surface Mass Spectrometry by SIMS," in *Surface Analysis – The Principal Techniques*, 2nd ed., Chichester, 2009, pp. 113–198.

[185] A. Taamalli, D. Arráez Román, A. M. Gómez Caravaca, M. Zarrouk, and A. Segura Carretero, "Geographical Characterization of Tunisian Olive Tree Leaves (cv. Chemlali) Using HPLC-ESI-TOF and IT/MS Fingerprinting with Hierarchical Cluster Analysis," *J. Anal. Methods Chem.*, vol. 2018, pp. 1–10, 2018.

[186] T. Planck, B. Shahida, J. Malm, and J. Manjer, "Vitamin D in Graves Disease: Levels, Correlation with Laboratory and Clinical Parameters, and Genetics," *Eur. Thyroid J.*,

vol. 7, no. 1, pp. 27–33, 2018.

[187] K. M. Armbruster and T. C. Meredith, “Enrichment of Bacterial Lipoproteins and Preparation of N-terminal Lipopeptides for Structural Determination by Mass Spectrometry,” *J. Vis. Exp.*, vol. 135, pp. 1–9, 2018.

[188] B. A. Mamyrin, “Time-of-flight mass spectrometry (concepts, achievements, and prospects),” *Int. J. Mass Spectrom.*, vol. 206, no. 3, pp. 251–266, 2001.

[189] I. S. Gilmore and M. P. Seah, “Ion detection efficiency in SIMS: Dependencies on energy, mass and composition for microchannel plates used in mass spectrometry,” *Int. J. Mass Spectrom.*, vol. 202, no. 1–3, pp. 217–229, 2000.

[190] J. Ladislas Wiza, “Microchannel plate detectors,” *Nucl. Instruments Methods*, vol. 162, no. 1–3, pp. 587–601, 1979.

[191] B. G. West, “Time-to-digital converter,” US 6,501,706 B1, 2002.

[192] K. L. Moore, M. Schröder, and C. R. M. Grovenor, “Imaging secondary ion mass spectrometry,” in *Handb. Nanoscopy*, Weinheim:Wiley- VCH, 2012, pp. 709–744.

[193] G. D. Schilling *et al.*, “Characterization of a second-generation focal-plane camera coupled to an inductively coupled plasma Mattauch-Herzog geometry mass spectrograph,” *Anal. Chem.*, vol. 78, no. 13, pp. 4319–4325, 2006.

[194] K. Downard, “Chapter 3: The Mass spectrometer,” in *Mass Spectrometry: A Foundation Course*, Sydney: The Royal Society of Chemistry, 2004, pp. 39–48.

[195] K. L. Moore, E. Lombi, F. J. Zhao, and C. R. M. Grovenor, “Elemental imaging at the nanoscale: NanoSIMS and complementary techniques for element localisation in plants,” *Anal. Bioanal. Chem.*, vol. 402, no. 10, pp. 3263–3273, 2012.

[196] K. T. L. 2005, “Bio TOF: SIMS analysis for biological/biotech applications,” *Kore*, 2013. [Online]. Available: http://www.kore.co.uk/ms2000.htm. [Accessed: 03-Jul-2018].

[197] A. M. Piwowar *et al.*, “C_{60} ToF SIMS imaging of frozen hydrated HeLa cells,” *Surf. Interface Anal.*, vol. 45, no. 1, pp. 302–304, 2013.

[198] “CAMECA NanoSIMS 50L: ion microprobe for ultra fine feature analysis in materials, geology, planetary and life sciences.” [Online]. Available: https://www.cameca.com/products/sims/nanosims?requestedmedia=/-/media/ametekcameca/acameca/download library/sims/4_ns50_biology_application_booklet_24mar2017_web.pdf&EmailRequired=yes. [Accessed: 20-Oct-2019].

[199] Y. Takado *et al.*, “Imaging liver and brain glycogen metabolism at the nanometer scale,” *Nanomedicine Nanotechnology, Biol. Med.*, vol. 11, no. 1, pp. 239–245, 2015.

[200] S. Lozano-Perez, M. R. Kilburn, T. Yamada, T. Terachi, C. A. English, and C. R. M. Grovenor, “High-resolution imaging of complex crack chemistry in reactor steels by NanoSIMS,” vol. 374, no. 1–2, pp. 61–68, 2008.

[201] N. Musat, H. Stryhanyuk, P. Bombach, L. Adrian, J. Audinot, and H. H. Richnow, “The effect of FISH and CARD-FISH on the isotopic composition of $^{13}C^-$ and $^{15}N^-$ labeled Pseudomonas putida cells measured by NanoSIMS,” *Syst. Appl. Microbiol.*, vol. 37, no. 4, pp. 267–276, 2014.

[202] S. Behrens *et al.*, “Linking Microbial Phylogeny to Metabolic Activity at the Single-Cell Level by Using Enhanced Element Labeling-Catalyzed Reporter Deposition Fluorescence In Situ Hybridization (EL-FISH) and NanoSIMS,” *Appl. Environ. Microbiol.*, vol. 74, no. 10, pp. 3143–3150, 2008.

[203] M. Angelo *et al.*, “Multiplexed ion beam imaging of human breast tumors,” *Nat. Med.*, vol. 20, no. 4, pp. 436–442, 2014.

[204] M. Keiluweit, J. J. Bougoure, P. S. Nico, J. Pett-ridge, P. K. Weber, and M. Kleber, “Mineral protection of soil carbon counteracted by root exudates,” *Nat. Clim. Chang.*, vol. 5, pp. 588–595, 2015.

[205] P. L. Clode *et al.*, “In Situ Mapping of Nutrient Uptake in the Rhizosphere Using Nanoscale Secondary Ion Mass Spectrometry,” *Plant Phsiology*, vol. 151, no. 4, pp. 1751–1757, 2009.

[206] N. Tanji, M. Okamoto, Y. Katayama, M. Hosokawa, N. Takahata, and Y. Sano, “Investigation of the cosmetic ingredient distribution in the stratum corneum using NanoSIMS imaging,” *Appl. Surf. Sci.*, vol. 255, pp. 1116–1118, 2008.

[207] S. Messenger, L. P. Keller, F. J. Stadermann, R. M. Walker, and E. Zinner, “Samples of Stars Beyond the Solar System : Silicate Grains in Interplanetary Dust,” *Science (80-.).*, vol. 300, pp. 105–108, 2003.

[208] J. Pett-Ridge, “Nanosims Isotopic Imaging of C and N Assimilation in Complex Microbial Communities,” 2015. [Online]. Available: https://aaas.confex.com/aaas/2015/webprogram/Paper14606.html. [Accessed: 01-Aug-2018].

[209] D. Gao, X. Huang, and Y. Tao, “A critical review of NanoSIMS in analysis of microbial metabolic activities at single-cell level,” *Crit. Rev. Biotechnol.*, vol. 36, no. 5, pp. 884–890, 2016.

[210] J. Malherbe *et al.*, “A New Radio Frequency Plasma Oxygen Primary Ion Source on Nano Secondary Ion Mass Spectrometry for Improved Lateral Resolution and Detection of Electropositive Elements at Single Cell Level,” *Anal. Chem.*, vol. 88, no. 14, pp. 7130–7136, 2016.

[211] K. H. Lau, M. Christlieb, M. Schröder, H. Sheldon, A. L. Harris, and C. R. M. Grovenor, “Development of a new bimodal imaging methodology: A combination of fluorescence microscopy and high-resolution secondary ion mass spectrometry,” *J. Microsc.*, vol. 240, no. 1, pp. 21–31, 2010.

[212] J. Nuñez, R. Renslow, J. B. Cliff, and C. R. Anderton, “NanoSIMS for biological applications: Current practices and analyses,” *Biointerphases*, vol. 13, no. 3, p. 03B301, 2018.

[213] N. Winograd and A. Bloom, “Sample Preparation for 3D SIMS Chemical Imaging of Cells,” *Methods Mol Biol*, vol. 1203, pp. 9–19, 2015.

[214] T. Stephan, “TOF-SIMS in cosmochemistry,” *Planet. Space Sci.*, vol. 49, no. 9, pp. 859–906, Aug. 2001.

[215] J. C. Vickerman & D. Briggs, “ToF-SIMS: Materials Analysis by Mass Spectrometry,” 2nd Ed., IM Publications, 2013, pp. 271–273.

2 Literature review of the 10Boronophenylalanine drug (BPA) and SIMS in localisation studies

2.1 Introduction

The number of cancer cases increases annually [1]–[3] and arise because of a random error in the DNA composition for reasons that are often unknown [4][5]. This dysfunction in DNA leads to unlimited cell division and the formation of aggressive cells that invade other tissues and spread to form malignant tumours. There are multiple types of malignant tumours that infect various tissues in the human body, one of which is glioblastoma multiforme tumour (GBM).

GBM is a primary malignant tumour from central nervous system tumours which infects brain tissue, it is severe and fatal [6][7]. The reason for its occurrence is unknown. It is difficult to treat this type of tumour because it infects deep internal sites of the brain, proliferates quickly, and spreads to other parts of the brain. Patients with GBM do not live for a long time; treatment only helps to increase the duration of the patient's life for a few years (approximately 1-3 years) [8][6].

BNCT, referred to in Chapter 1, is a form of targeted radiotherapy that depends on the preferential accumulation of ^{10}B containing drugs, such as boronophenylalanine (BPA), in the tumour core and the tumour cells infiltrating adjacent normal tissue. Ideally ^{10}B should be highly concentrated in cell nuclei [9][10]. BNCT is also one of the most promising treatments for GBM tumour and other types of cancer [9]. Its mechanism is that patients are treated with a ^{10}B enriched BPA [10] and the tumour sites are then exposed to low-energy thermal neutrons, mostly En < 0.49 eV or up to En < 9.9 keV if the tissue is thick or if thermal neutrons are directed to the skull [10]. The ^{10}B in the locations of these tumours works by capturing the neutrons to give fission reactions and produce $^{11}B^*$ (unstable isotope) which decays in ~ 10^{-12} s to produce linear particles, which include ^{7}Li (recoil ion) and ^{4}He (α particle) [11], as in Equation 2.1 [12]. The outputs of ^{7}Li and ^{4}He can penetrate the tumour cells with a high linear radiant energy transfer at short distances, approximately equivalent to the width of a single cell (161 keV/μm -5μm and 195 keV/μm -9μm) respectively, leading to the killing of cancer cells but not healthy cells, which in turn do not attract boron atoms [6] [12]–[15].

$$^{10}B + n_{th} \rightarrow [^{11}B]^* \rightarrow {}^{4}He\ (\alpha\ -\ 195keV) + {}^{7}Li\ (161keV) + 2.79\ MeV \qquad \text{Equation 2.1}$$

The success of BNCT treatment depends on the use of drugs which enhance the localisation of boron (^{10}B) in enough quantity (~ 20 - 30 ppm or more) selectively in tumour cells to dispose of DNA unbalanced cells without causing damage to surrounding healthy cells [11][16][17]. BNCT is more successful when boron is centred in the nuclei of infected cells due to the short penetration distance of the BNCT outputs [13]. Preferably, the ratio of the boron concentration in tumour cells should be three or more times higher than that of normal cells (3:1) [11]. This means delivering a concentration of boron > 30 ppm in cancerous cells and <10 ppm in healthy cells [16][17].

Conventional bulk analytical methods provide quantitative information of the level of boron in blood and tissue but are not able to determine cellular distribution with lateral resolution [18]. For example, Detta and Cruickshank presented a study that measured BPA concentration using inductively coupled plasma mass spectrometry (ICP-MS), as explained in section 2.2.1 [19]. Basilico *et al.* reported the possibility of quantifying the ^{10}BPA compound in biological samples, such as the patient's blood and urine, using flow- injection electrospray tandem mass spectrometry (FI/ESI-MS/MS) with high sensitivity to measure concentrations up to 10,000 ppb [20], but this technique does not have the characteristics of resolution required to map the distribution of elements within the cell and tissue. Witting *et al.* [21] used direct current plasma atomic emission spectroscopy (DCP-AES) to measure the ^{10}B concentration of BPA in rat 9L gliosarcoma cells, for more details see section 2.2.1.

Therefore, it is important to develop and assess methods capable of determining the localisation and distribution of ^{10}B of BPA at the cellular level in tumour cells, as well as the concentration of BPA, in order to enhance the methods of success of BNCT treatment. SIMS is one such technique.

2.2 10Boronophenylalanine

Boron has two stable isotopes: ^{10}B and ^{11}B; their natural abundance is 19.9% and 80.1% respectively and the ratio of ^{10}B to ^{11}B is 1: 4 [22]. As the natural abundance of ^{10}B is low, the ^{10}B in BNCT agents is enhanced up to 95% versus 5% ^{11}B during the stage of synthetic preparations to achieve greater drug effectiveness [11][23].

BPA is prepared by adding the ^{10}B isotope to phenylalanine, one of the amino acids important for growth and protein metabolism, by means of isotopic labelling using 13 different chemical mechanisms [24][25]. In the drug form of BPA, L- phenylalanine type is used as a transporter of ^{10}B where this L-type is the same as human amino acid expression [21][26]. The L-type of phenylalanine is absorbed and upregulated by cancer cells where the absorption process is very active in tumours, allowing accumulation of BPA preferentially in the tumour tissue [27][28]. The L-BPA enantiomer has been proven to accumulate in high levels in tumour cells, making it a more effective clinical treatment compared with the D-BPA enantiomer [11][29]. **Figure 2.1** shows the chemical structures of both enantiomers, as well as phenylalanine and tyrosine [30]–[33], **Table 2.1** shows the chemical properties of the ^{10}BPA compound [34][35].

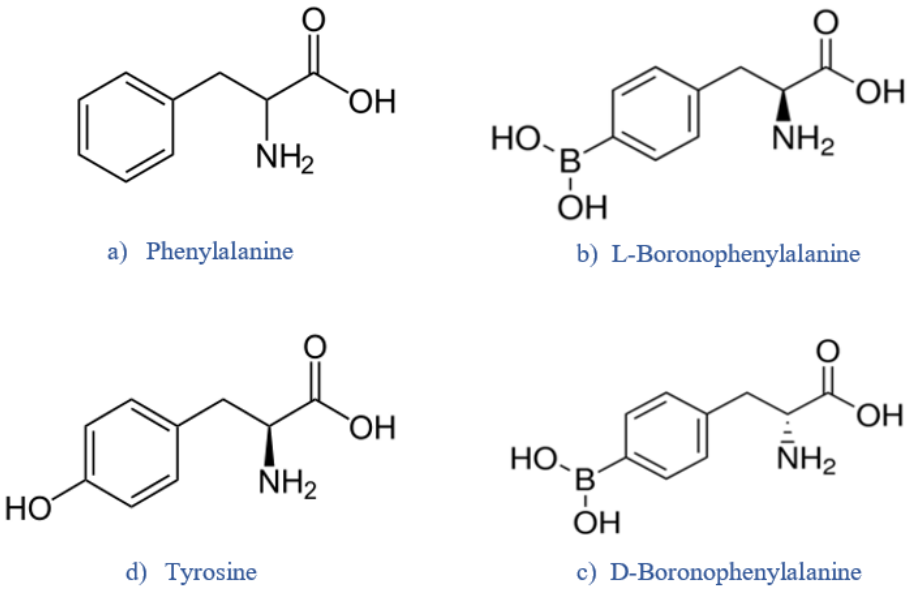

Figure 2.1: Structural formula of a) amino acid phenylalanine, b) L-BPA enantiomer of BNCT agents, c) D-BPA enantiomer, and d) tyrosine [30]–[33].

Table 2.1: Chemical properties of ^{10}BPA [23][34][35].

Chemical name	L-4-(2-Carboxy-2-aminoethyl) benzene boronic acid. 4-boronophenylalanine, 4-Borono-L-phenylalanine. (2s)-2-amino-3-(4-boronophenyl) propanoic acid (IUPAC name). P-Boronophenylalanine.
Molecular formula	$C_9H_{12}O_4N^{10}B$
Molecular weight	208.26 g/mol (95% ^{10}B, 5% ^{11}B) 209.00 g/mol (20% ^{10}B, 80% ^{11}B)
Physical description	White crystalline powder
Solubility	Fructose or Mannitol Can be solubilized in water at pH >8

BPA is weakly soluble in water and dissolves well in fructose or mannitol [23][34][35]. However, the shelf life of BPA - fructose after its preparation is short, which constitutes an obstacle in treatment management. Several attempts have been made to improve the solubility of BPA in water, these studies indicated that an increase in water solubility leads to reduced cytotoxicity and decreased cellular uptake of BPA, which reduces the effectiveness of the drug [11][36]. In an experiment administered to melanoma cells in hamsters, the results showed that after 18 days of thermal neutron treatment the melanoma tumour bulk decreased to ~18% of its original size using BPA-water while the tumour only decreased to ~50% when treated with BPA-fructose [36].

Various strategies have been used to improve the delivery of BPA to tumour tissue, which is based on the addition of small molecules of different amino acids to the tumour before starting treatment with BPA, such as L-tyrosine also called L-2-Amino-3(4-hydroxyphenyl) propanoic acid, and L-3, 4-dihydroxyphenylalanin (L- DOPA) [11]. The effect of L-tyrosine is reviewed below. The effect of the cell cycle on BPA uptake is also reviewed.

2.2.1 Effect of tyrosine on BPA uptake

Tyrosine is amino acid that enters the synthesis of most proteins and is used by the human body to form hormones [25][37]. The structural formula of L-tyrosine is given in **Figure 2.1** [33]. BPA is analogous in structure to tyrosine (but boronated), so BPA can be taken to cells using the same mechanism of transport of tyrosine, which is the L-system [21]. The L-system or L-amino acid transporter-1 (LAT-1) is a proteinic transporter situated in the cell

membrane which is responsible for the transport of L-type amino acids and has an important role in growth and proliferation in cells [38]–[40]. LAT-1 expression is often used in studies of malignant tumours due to its contribution to growth by increasing transport of L-amino acids to intracellular locations, therefore LAT-1 is likely to play an important role in the transport mechanism and selective accumulation of L-BPA in the tumour cells [41][42]. The L-system relies on an exchange mechanism between L-type amino acids for transport into and from cells. The L-type amino acids such as L-tyrosine are pre-accumulated at high levels in cells before being treated with L-BPA, leading to the stimulation of exchange and transport between L-tyrosine intracellularly and L-BPA extracellularly, which explains the high rate of accumulation of L-BPA when preloading with L- tyrosine compared with the absence of preloading [21][43]–[45]. Papaspyrou *et al.* [46] showed that pre-treatment of mouse melanoma cells with L-tyrosine stimulated BPA uptake and suggested that the L-system is responsible for the transport of BPA. Witting *et al.* [21] found that BPA uptake increased two-fold in rat 9L gliosarcoma cells when preloaded with L-tyrosine before L-BPA administration when compared with cells that were not preloaded with L-tyrosine. This result supports the assumption that the transport mechanism of BPA relies on the L-system, and that pre-accumulation of L-type amino acids enhances BPA uptake. Furthermore, the researchers showed that the efflux process, after treatment with BPA, in a medium containing only amino acid and another medium free of both amino acid and boron led to a clear and rapid reduction in BPA uptake, indicating that efflux is also an intracellular and extracellular exchange process [21]. Capuani *et al.* presented two studies explaining the possibility of enhancing BPA uptake by using L-DOPA with C6-glioma cells *in vitro* as well as *in vivo*, whereby glioma cells were implanted in rat brain. The study showed that *in vitro* and *in vivo* pre-treatment with L-DOPA resulted in an increased intracellular concentration of BPA [26][47]. Wingelhofer *et al.* also found that pre-treatment with L-tyrosine or L-DOPA enhanced the [18F]-FBPA (2-[18F] fluoro-4-borono-L-phenylalanine) intracellular concentration. This finding was reached during the study of the accumulation of FBPA, an analogue of BPA used to predict concentrations of BPA, in three different types of tumour cells [48].

In contrast, Detta and Cruickshank presented a study on brain tumour (BT) and brain around tumour (BAT) harvested from patients with glioblastoma [19]. The biopsy samples (*in vitro*) were treated in four groups: 1) BPA; 2) BCH (2-aminobicyclo-(2,2,1)-heptane-2-carboxylic acid) as an inhibitor then BPA; 3) phenylalanine as a competitor with BPA simultaneously; and 4) tyrosine as stimulator then BPA. The uptake of BPA was terminated after the following time periods: 0, 1, 2, 4, and 8 h. After drying the samples, the level of ^{10}B was

measured using ICP-MS. Both BT and BAT samples showed almost identical results in terms of ^{10}B accumulation, see **Figure 2.2**, the ^{10}B reached the highest level of accumulation in the treated samples after 4 hours, and then the boron levels began to decline. Both BCH and phenylalanine had an inhibitor effect during the first 2 hours and then showed a slight increase. Pre-loading with tyrosine did not show any improvement in BPA uptake [19]. It should be noted that the number of tumour cells that had infiltrated to areas of the brain around the tumour were fewer than the number of cells at the tumour core; however, the levels of BPA uptake were convergent in both areas of cells. This may be attributable to the activity of LAT-1 expression that contributes to the uptake of BPA to infiltrated cells [19][49].

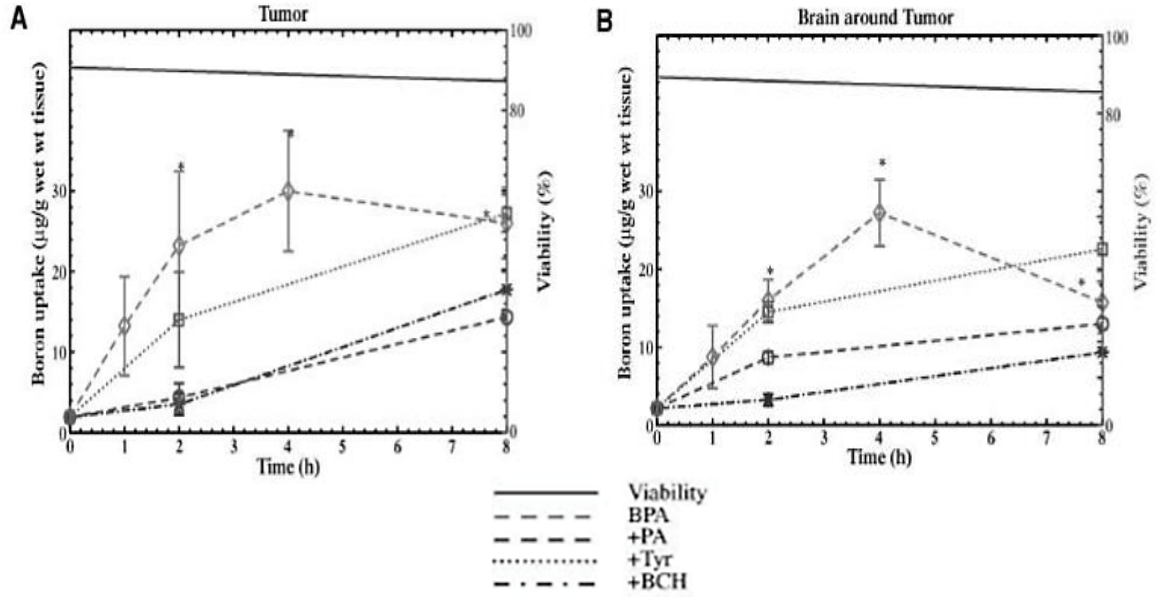

Figure 2.2: ^{10}B accumulation of BPA (μg/g) as a function of Time (0, 1, 2, 4 and 8 h) in two regions of glioblastoma tumours: (A) brain tumour and (B) brain around tumour. Tissue sections were incubated in four groups: BPA; phenylalanine as a competitor with BPA simultaneously; BCH as an inhibitor then BPA; and tyrosine as a stimulator then BPA. The number of glioblastoma tumour samples per time point ($n = 4$). Each type of line refers to a different uptake group as shown in the diagram. The topmost line represents the viability of the tissue. Measurements were performed using ICP-MS [19]. Reprinted with permission from American Association for Cancer Research.

Grunewald *et al.* [50] studied the effect of pre-treatment with L-tyrosine and L-DOPA on BPA absorption in different organelles of mice preinjected with a human hepatocellular carcinoma cell line. The results showed that neither L-tyrosine nor L-DOPA affected the BPA uptake in any of the samples, and the researchers attributed this outcome, which was contrary to previous results, to either LAT-1 expression varying from one patient to another or the effect of tyrosine varying from one tumour to another, as Yang *et al.* had pointed out. Yang *et al.* [51] had concluded that the effect of pre-treatment with L- amino acid as a stimulator of BPA uptake varies according to the histologic tumour type and the anatomic location of the tumour. They found that pre-treatment with L-DOPA in F98 glioma bearing rats (implanted in brain) led to increased uptake of BPA, while there was no effect on BPA uptake in B16 melanoma bearing mice (implanted subcutaneously). Therefore, the ability of L-amino acids to enhance the uptake of BPA cannot be conclusively determined.

2.2.2 Effect of the cell cycle on BPA uptake

The cell cycle also may affect the uptake of BPA. A cancer cell in interphase (G0) is subject to an initial active growth phase, called G1, in which there is no split of the nucleus, followed by the S-phase in which DNA begins to replicate inside the nucleus. Then the cell enters another more active growth phase, G2, followed by the mitotic-phase M, in which the cell begins to divide into two identical cells. However, the cell may enter a quiescent phase due to hypoxia or lack of nutrition resulting from weak vascularization or other causes [52][53].

Yoshida *et al.* measured the ^{10}B concentration of BPA in three different types of tumour cell lines *in vitro* using inductively coupled plasma atomic emission spectroscopy (ICP-AES). The cells were treated with BPA and then sorted by cell cycle into two groups: G0-G1 phase and G2-M phase. BPA uptake was then measured. The results showed that ^{10}B was more highly accumulated in G2-M phase than G0-G1 phase cells, indicating that the cell cycle affects the uptake of BPA where absorption increases with growth [54]. Ono *et al.* investigated the microdistribution of ^{10}B-enriched BPA in cell colonies in peripheral tumour in mice *in vitro* using γ-ray spectrometry. They found that ^{10}B is heterogeneously distributed in cells and may not accumulate in quiescent cells, which affects the effectiveness of BNCT [55]. Langen *et al.* tracked 123I-a-methyl-L-tyrosine (IMT) uptake in the human glioma cell line (86HG39) in different phases *in vitro* using single photon emission computed tomography (SPECT), and concluded that IMT transport is based on the cell proliferation phase, and the L-system is stimulated in proliferating cells, thus contributing mainly to increase the absorption of IMT [56]. Dahlstrom *et al.* incubated human glioma cell sub-

populations with BPA *in vitro* and then separated cell-associated boron of extracellular boron. The accumulation of boron was measured using ICP-AES. The results showed that ^{10}B accumulates at different and heterogeneous rates, indicating the importance of considering the differences in cell sub-populations during treatment with BNCT [57]. Carpano *et al.* showed a direct correlation between the proliferation and B uptake in the tumours when they studied three lines of human melanoma cells *in vitro*; as well as *in vivo* whereby mice containing pre-implanted melanoma cells were injected with BPA. Each *in vitro* cell line showed different patterns of B accumulation. *In vivo*, the accumulation level of B in the tumours was 25.9 ± 2.6 ppm, while in some individual tumour cells it was ranging between 12 and 52 ppm [58].

While some studies have shown that proliferation (cell cycle) is associated with high LAT-1 expressions in tumour cells, particularly in glioma cells, as mentioned previously [54]-[58], there are other studies that indicate that there is no correlation between proliferation and LAT-1 expressions. For example, Detta and Cruickshank [19] conducted a study on sections of brain tumour and brain around tumour (BAT) collected from patients with epilepsy (none of the samples were exposed to radiation or chemotherapy). The results showed that there was no correlation between proliferative activity and increased LAT-1 expression, and indicated the difficulty of comparing human cell samples *in vivo* with animal tumour models because human samples are heterogeneous and more complex. De Wolde *et al.* reached a similar conclusion during a study of the relationship between L-tyrosine and the state of proliferation in human brain tumours, pointing out that there is a lack of the correlation between them [59]. Sasajima *et al.* also inferred an inverse relationship between the absorption of the L-amino acid cycloleucine and proliferation status [60]. Chandra *et al.* also studied the distribution of ^{10}B (BPA) in human glioblastoma cells (T98G) *in vitro* using SIMS and measured the ^{10}B level in cells meta-phase and interphase. The results showed that ^{10}B accumulates at a higher level in the cytoplasm of interphase cells compared with meta-phase cells [61]. These studies [19][59] - [61] concluded that proliferation has no relation to the LAT system, although the latter seems to be responsible for increased BPA uptake.

2.3 SIMS analysis of biological samples

The scientific approach to the analysis of biological samples using dynamic SIMS began in 1982 in the life sciences with Burns [62]. There are a number of objectives behind analysing biological samples, most notably: identification of the chemical structures of cells and

tissues, determination of pathogenic chemical changes, and evaluation of the efficacy of pharmaceuticals to treat particular diseases and their localisation within specific cells. Moreover, there is a clear increase in the employment of SIMS techniques in biological studies because of their sensitivity, the ability to detect all elements in the periodic table (atoms, molecules, and isotopes) and to perform 2D and 3D imaging with high spatial and mass resolution [63][64].

SIMS techniques have been used to verify biological samples using two methods. The first method is by imaging the distribution and localisation of elements. For example, Lau *et al.* [65] compared NanoSIMS 50 with conventional fluorescent immunochemistry in imaging the localisation of BrdU (5-bromo-2-deoxyuridine), which is used in the treatment of cancerous cells, on the same HeLa cell. A NanoSIMS was used to measure the distribution of $^{16}O^-$, $^{12}C^{14}N^-$, $^{31}P^-$, $^{79}Br^-$ and $^{81}Br^-$. Both Br isotopes were measured to ensure the bromine distribution as there are interferences at both masses. **Figure 2.3** shows that both techniques gave the same result, where BrdU was strongly localised in the nucleus of the cell; however, the spatial resolution of fluorescent imaging is limited to, at best, 500 nm, whereas NanoSIMS images had much higher resolution.

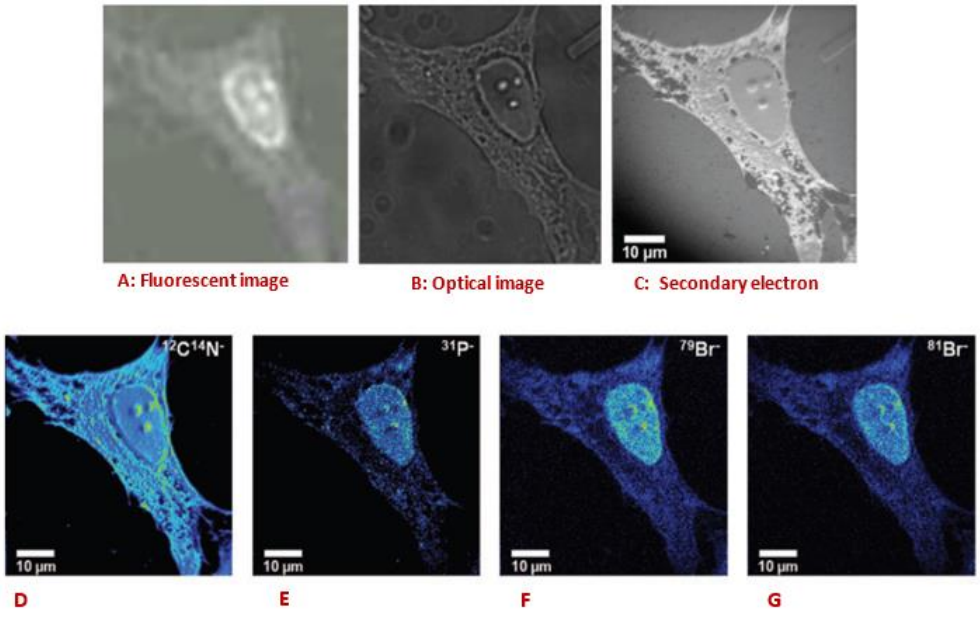

Figure 2.3: A single HeLa cell treated with 5-bromo-2-deoxyunidine (BrdU) analysed using a Cs^+ beam of a NanoSIMS 50 and fluorescent immunochemistry. A, B and C are fluorescent, optical, and NanoSIMS secondary electron images. D, E, F and G represent the distribution images of $^{12}C^{14}N^-$, $^{31}P^-$, $^{79}Br^-$ and $^{81}Br^-$ respectively. Br (BrdU) localised in the nucleus as shown in all images. The nucleoli features are also clear in all images. The NanoSIMS images (C-G) show much greater resolution detail than the fluorescent image [65]. Reprinted with permission from John Wiley and Sons.

The second method used in SIMS biological analysis is to measure the isotope ratio, whereby stable isotopes are used as labels by adding them to biological samples to understand different mechanisms, such as transport and sequestration [66][67]. The isotope method is usually studied using dynamic SIMS techniques because it is easier to separate mass interferences than with ToF-SIMS, which measures all ions in the sample, making it difficult to distinguish between masses. Examples of isotopes commonly used as labels are ^{2}H, ^{13}C, ^{15}N, ^{34}S, and ^{41}K [68]. Peteranderl and Lechene measured the isotopic ratio of C and N in rat fibroblast cells. Cells were either cultured in an unlabelled medium or in a medium supplemented with ^{13}C-glycine and ^{15}N-glycine, The NanoSIMS was set to detect $^{12}C^{-}$, $^{13}C^{-}$, $^{12}C^{14}N^{-}$, $^{12}C^{15}N^{-}$; the isotope ratios of $^{15}N/^{14}N$ and $^{13}C/^{12}C$ were determined and compared with the natural abundance. The unlabelled sample gave ratios very close to the natural abundance, while the samples supplemented with ^{13}C or ^{15}N-glycine had higher isotopic ratios. This study demonstrated the ability of the NanoSIMS to trace isotopes at a sub-cellular scale and the capability to distinguish between species with nominally the same mass. **Figure 2.4** shows the high mass resolution scans for these masses [69].

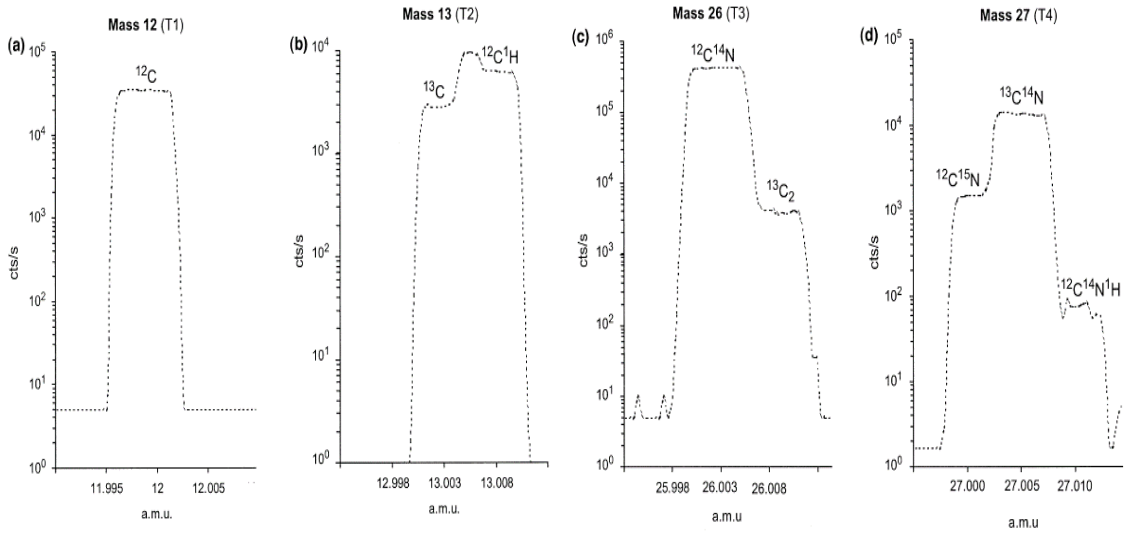

Figure 2.4: High mass resolution scans showing isobaric interferences in mass spectra of interest. The above shows the ability of the NanoSIMS to distinguish between convergent masses; a, b, c and d correspond to the nominal masses: 12, 13, 26 and 27 a.m.u, respectively [69]. Reprinted with permission from Springer Nature.

Lechene *et al.* presented a study to monitor the renewal of protein in the cochlea of mice at the sub-cellular scale. The cochlea contains tissues of different types of cells at a high level of organization, including stereocilia, the mechanosensing organelles. The study was performed on mice fed with ^{15}N-L-leucine and on a control sample (untreated). The experiment was conducted using NanoSIMS to map $^{12}C^-$, $^{13}C^-$, $^{12}C^{14}N^-$ and $^{12}C^{15}N^-$. The ratios $^{12}C^{15}N/^{12}C^{14}N$ and $^{13}C/^{12}C$ were calculated pixel by pixel by taking the ratios of the images. It was found that the untreated sample had isotopic ratios almost equal to the natural abundance of $^{15}N^-/^{14}N^-$ (0.368%) in the cochlea, whereas the ^{15}N-labelled samples had a high $^{15}N/^{14}N$ ratio due to the incorporation of ^{15}N into the proteins. The $^{12}C^{15}N^-/^{12}C^{14}N^-$ image shows strong contrast, whereas the $^{13}C/^{12}C$ image is homogeneous, as no additional ^{13}C was added. **Figure 2.5** shows these ratios in the stereocilia. The study demonstrated the ability of NanoSIMS to trace and measure isotopic ratios [70]. It should be noted that nitrogen cannot be detected as a monatomic negative ion due to difficulty in its ionization in SIMS, so it must be detected as CN^- ions [66]. CN^- is probably the best ion for tracing biological samples because it is a characteristic of amino acids and thus facilitates the determination of protein distribution [71]; cellular membranes also contain a high yield of CN, which is useful in determining the general morphology of samples [72].

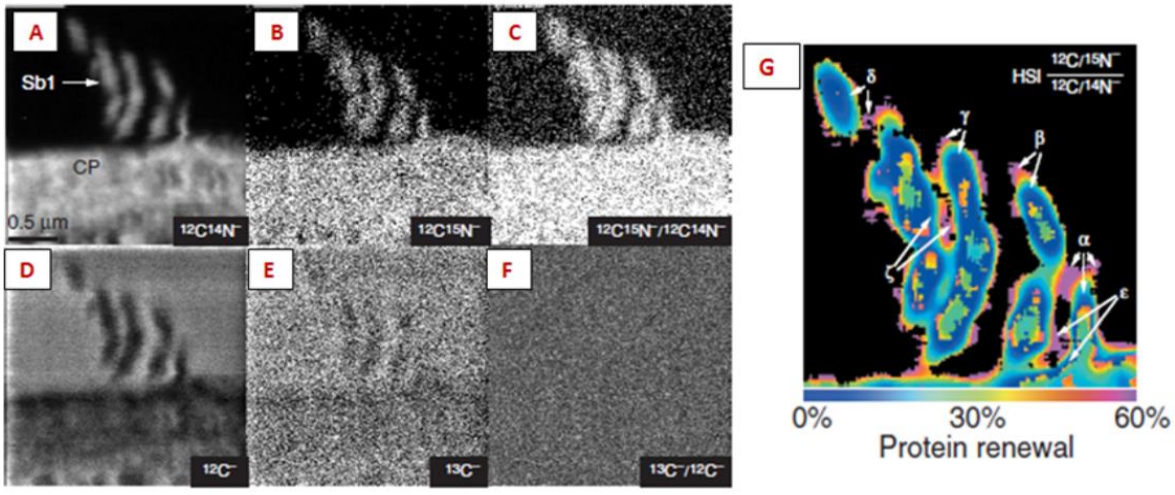

Figure 2.5: NanoSIMS maps of stereocilia (Sb1) from a cochlea treated for nine days with ^{15}N-L-leucine; (A–F) are high resolution maps of the Sb1 with 256×256 pixels; scale bar = 0.5 µm. G: Hue saturation intensity (HSI) map 3×3 µm of the $^{12}C^{15}N^-/^{12}C^{14}N^-$ ratio resulting from dividing image (B) by (A). Colours represent the excess amount of ^{15}N calculated from the $^{12}C^{15}N^-/^{12}C^{14}N^-$ ratio and thus represent protein renewal. The value scale is 0% (blue) to 60% (purple) [70]. Reprinted with permission from BioMed Central Ltd.

2.3.1 Localisation of BNCT agent using SIMS

It is important to understand the pharmacological distribution of ^{10}B (BPA) at the cellular level of the tumour as well as within infiltrating cells to the surrounding areas of the tumour. Therefore, studies have been carried out to evaluate the delivery of BPA and other BNCT agents and determine localisation in cell cultures and animal models using multiple analytical methods. Chandra undertook a large number of these SIMS studies, which began early in 1985 [73][74].

Lorey *et al.* presented a study of co-cultured cells from T98G human glioblastoma cells and LLCPKZ pig kidney epithelial cells. The cells were treated with 110 ppm 10Boronophenylalanin-Fructose (^{10}BPA-f) and prepared by freeze-fracturing and freeze-drying. The samples were analysed with an O_2^+ beam of a CAMECA IMS-3F ion microscope (Dynamic SIMS), which had a spatial resolution of 500 nm. The results showed that boron gave a comparable absorption in both types of cells and was located in cytoplasm to a slightly higher extent than in the nucleus, **Table 2.2** shows the concentrations. The outcomes were compared with T98G alone, which was treated with ^{10}BPA-f, and the results were similar, which suggests that the culture with other cells did not affect the T98G cells. This suggests that ^{10}BPA-f is selective to certain cells when studied *in vitro* [75].

Smith *et al.* compared the accumulation of ^{10}B from BPA between two brain tumour models of rats, 9L gliosarcoma and F98 glioma, using a CAMECA IMS-3F ion microscope with an O_2^+ beam. Both rat models were administered with BPA *in vivo* by continuous timed infusions (2, 3, 6, and 24 h). The results showed a similar pattern of $^{10}B^+$ distribution in both models, where $^{10}B^+$ accumulation in the tumour core was twice as high as that of the tumour cells infiltrating normal brain. Increased infusion time from 2h to 6h led to higher accumulation of $^{10}B^+$ in infiltrating tumour cells and it reached the same level of boron as the cells at the core of the tumour after dosing for 24 h (**Table 2.3**). **Figure 2.6** shows the distribution of $^{10}B^+$ in cells infiltrating a normal brain [76].

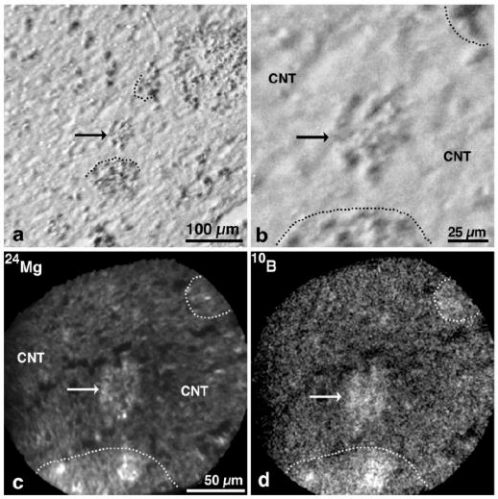

Figure 2.6: Images of a normal rat brain bearing a 9L gliosarcoma showing a cluster of tumour cells infiltrating the normal brain. (a) and (b) show an H&E-stained cryosection image and magnified Field of view (FoV) from the centre of the image respectively, the arrows refer to the site of the infiltrating tumour cells, the dotted lines refer to the edges of groups of infiltrating tumour cells; (c) and (d) show the distribution of $^{24}Mg^{+}$ and $^{10}B^{+}$ respectively in contiguous normal brain tissue (CNT). FoV is 250×250 μm^2 [76]. Reprinted with permission from American Association for Cancer Research.

Chandra *et al.* (2002) [77] studied the distribution of fluorine ($^{19}F^{-}$) and boron ($^{11}B^{+}$) from fluorinated p-boronophenylalanine (^{19}F-BPA) in T98G human glioblastoma cells using an O_2^{+} probe in a CAMECA IMS-3f ion microscope with 500 nm spatial resolution. **Figure 2.7** shows the SIMS imaging along with the reflected optical microscope image, and shows three subcellular regions, the nucleus (dotted line), mitochondria (arrows) and the cytoplasmic region. In terms of the distribution of ^{19}F-BPA, the $^{19}F^{-}$ and $^{11}B^{+}$ signals were found in the nucleus and cytoplasm and were relatively uniformly distributed across cells. The mitochondria contained low signals of $^{19}F^{-}$ and $^{11}B^{+}$. By comparing the distribution of $^{11}B^{+}$ of ^{19}F-BPA with the ^{10}B of BPA under the same experimental conditions, it was observed that there was no difference in the distribution and quantitative measurements between the two compounds. **Table 2.2** shows the subcellular concentration of $^{10}B^{+}$ from BPA. This supports the possibility of using ^{19}F-BPA in the distribution studies and boron delivery to tumour cells as the BPA. ^{19}F-BPA is a fluorinated positron emission tomography compound used to measure the concentration of boron in tumours for the purpose of determining the radiation dose, this study was reviewed in 2008 [78].

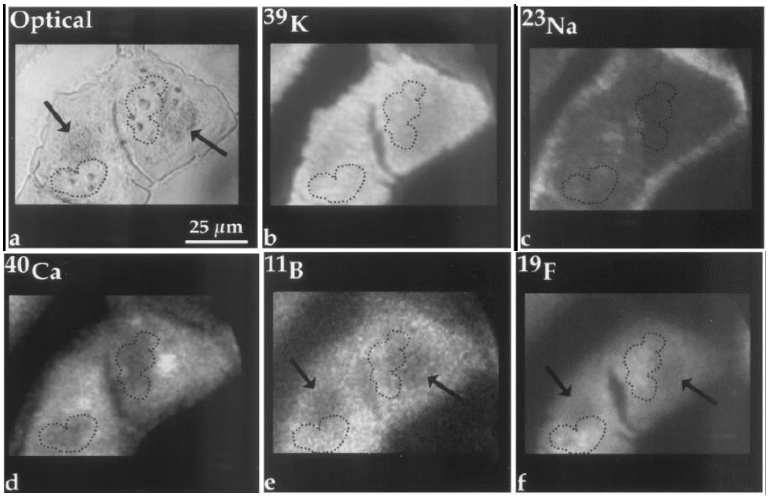

Figure 2.7: SIMS analysis of human glioblastoma cells (T98G) treated with F-BPA (110 µg/ml-6h). a) presents optical images of two fractured freeze dried T98G cells and shows the sub-cellular compartments: the nuclei with dotted lines, mitochondria with arrows, and the remaining cytoplasmic region. b-f) show the positive secondary ion distribution of ^{39}K, ^{23}Na, ^{40}Ca, ^{11}B, and ^{19}F respectively. FoV = 250×250 µm^2 [77]. Reprinted with permission from American Association for Cancer Research.

Chandra *et al.* (2002) determined the distribution of boron isotopes in the same T98G human glioblastoma cells when treated at the same time with a combination of ^{10}B-labelled BPA-f and ^{11}B-labelled BSH (sodium borocaptate) using an O_2^+ beam on a CAMECA IMS-3f ion microscope with a spatial resolution of 500 nm. BSH is one of BNCT drugs that is approved for clinical use. The BSH mechanism presumes that the boron is delivered to tumour tissue by crossing blood-brain barrier [79]. However, this mechanism is still unclear [80]. The analysis compared cells treated with each single-drug separately under the same experimental conditions. The results showed that the $^{10}B^+$ was heterogeneously distributed between the nucleus and cytoplasm with low signal intensity in the mitochondria. The concentrations of boron doubled in all compartments after 6h of ^{10}BPA-f exposure compared with 1h (**Table 2.2**). $^{11}B^+$ was homogeneously distributed throughout the cells, $^{11}B^+$ concentrations in all compartments were almost the same and not affected by the exposure time to BSH. The results of mixed-drug treatment corresponded to those of single-drug treatment, suggesting that there is no synergistic or competitive effect between the two compounds [79].

Oyedepo *et al.* published a study of gliosarcoma cells (GS9L) extracted from mouse brain treated with ^{10}BPA and analysed using a dynamic SIMS instrument (constructed in house) with an ion microprobe beam of Ga^+. This instrument provides spatial resolution of 100 nm for imaging applications and 300 nm for applications requiring high sensitivity. The ratio of $^{10}B^+/^{12}C^+$ was calculated in three regions: normal brain, border brain, and cancerous brain. In the first tumour section, the $^{10}B^+/^{12}C^+$ ratio was much higher in the tumour than in the normal part of the brain, while $^{10}B^+/^{12}C^+$ in the border region was half that found in the tumour area, which means that the $^{10}B^+/^{12}C^+$ ratios for the normal to border to tumour regions was 1: 5:10. In addition, the proportion of boron in the tumour tissue compared with normal tissue was 12:1 in the second tumour section. Furthermore, the distribution of $^{10}B^+$ in cultured mouse melanoma (B16) cells was limited to the nucleus of cells and the outer perimeter around the cells. K^+ was distributed inside and outside the nucleus and Na^+ appeared in the nuclei with high intensity, **Figure 2.8** [13].

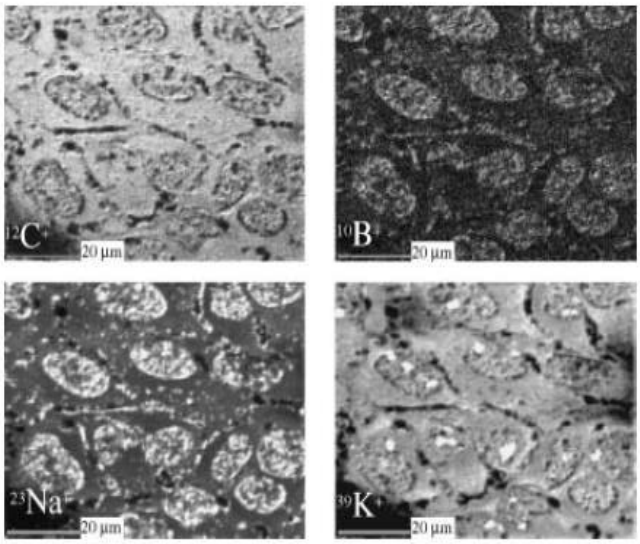

Figure 2.8: Secondary ion maps showing the distributions of $^{12}C^+$, $^{10}B^+$, $^{23}Na^+$ and $^{39}K^+$ in cultured mouse melanoma B16 cells treated with ^{10}BPA-f (50 ppm-2 days) analysed using a Ga^+ beam. In the maps, the white colour indicates high counts area, the black colour indicates no counts in the area (values are not mentioned in the reference). The cell size is 20 µm. $^{12}C^+$ distributed almost homogeneously; $^{10}B^+$ is concentrated in the nuclei and periphery of cells; $^{23}Na^+$ is distributed in a similar manner to boron; and $^{39}K^+$ is distributed in the nucleus and cytoplasm with some bright regions in the nuclei that indicate the presence of crystals of the nutrient medium [13]. Reprinted with permission from John Wiley and Sons.

Arlinghaus *et al.* (2006) used a 200 nm Ga^+ beam ToF-SIMS followed by laser post-ionization secondary neutral mass spectrometry (laser-SNMS) to image the distribution of ^{10}B in freeze-dried kidney tissues of rats. Mice were implanted with murine sarcoma tumour and treated *in vivo* in three groups: 2.5 h of 200 mg/kg BSH, 1.5 h of 700 mg/kg BPA and a combination of BPA and BSH. The results from the sarcoma tumour showed that ^{10}B was distributed inside and outside the cells with an uneven signal intensity, and had largely accumulated in the nucleus compared with the other regions, as shown in **Figure 2.9**. The CN signal resulted from proteins and DNA, with the higher concentration regions inferred as being nuclei sites. The C_3H_8N represented the choline headgroup of the L-adipalmitoylphosphatidylcholine (DPPC), which in turn showed the cellular structure surrounding the nuclei and is characteristic of the cell membrane. In addition, the study showed that treatment using BPA and a combination of BPA and BSH led to a higher accumulation of boron in the tumours (30 ± 4 ppm and 35 ± 12 ppm respectively) than treatment with BSH alone (15 ± 5 ppm). The use of laser-SNMS with ToF-SIMS helped to identify more clearly the cell structures and increased the sensitivity of imaging for low concentrations of boron [81]. This study was re-published with more detail by Wittig and Arlinghaus *et al.* in 2008 [82].

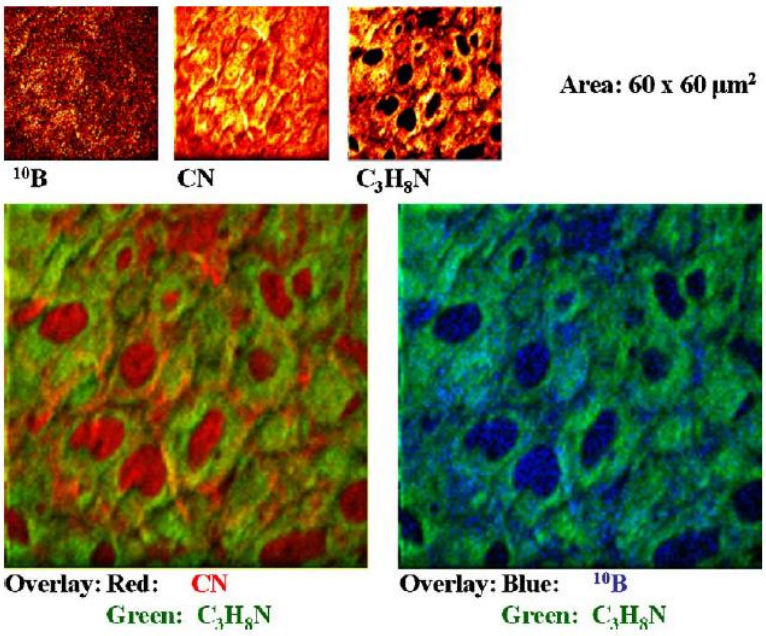

Figure 2.9: Images of sarcoma tumour section treated with BPA *in vivo* for NMRI nude mice which were analysed using ToF-SIMS and laser-SNMS. FoV = 60×60 µm^2 [81]. Reprinted with permission from Elsevier.

Chandra *et al.* (2007) measured boron in human glioblastoma cells (T98G) treated for different time periods with ^{10}BPA and $^{13}C^{15}N$ labelled phenylalanine using an O_2^+ beam. The samples were prepared by being fractured and freeze-dried. The samples were examined with an optical microscope; and it was found that all the samples prepared retained the form of the nucleus (multinuclei) and the cytoplasm and cytoplasmic region rich with mitochondria. The distribution of $^{10}B^+$ and $^{13}C^{15}N^-$ was determined using a CAMECA IMS-3f ion microscope (dynamic SIMS). It was observed that both $^{10}B^+$ and $^{13}C^{15}N^-$ had high accumulations in the samples treated for a long period of time (6 hours), which suggests that cells need amino acid and there is similarity in the mechanism of entry of amino acids through the cell membrane to tumour cells. The difference was that $^{10}B^+$ accumulates more in both the nucleus and cytoplasm in a somewhat heterogeneous manner, while $^{10}B^+$ was low in the cytoplasmic region rich in mitochondria (**Figure 2.10)**. In contrast, $^{13}C^{15}N^-$ was distributed homogeneously throughout the cells without being concentrated in a particular area. This difference in absorbance suggest that the intracellular processes associated with mitochondria are able to distinguish small differences in amino acid which refer to a difference in metabolism. **Table 2.2** shows the sub-cellular concentration of $^{10}B^+$ from BPA. The cell cycle effect on the uptake of ^{10}BPA was also investigated in the S-phase and non-S-phase of T98G cells, more detail about the phases of the cell cycle in 2.2.2 section. The S-phase was distinguished by determining the replicating DNA using Bromodeoxyuridine (BrdU) as a marker. BrdU was added with the BPA at same time during the preparation. The results showed that boron was distributed in cell nuclei in the S-phase to a greater extent than in the non-S-phase [6].

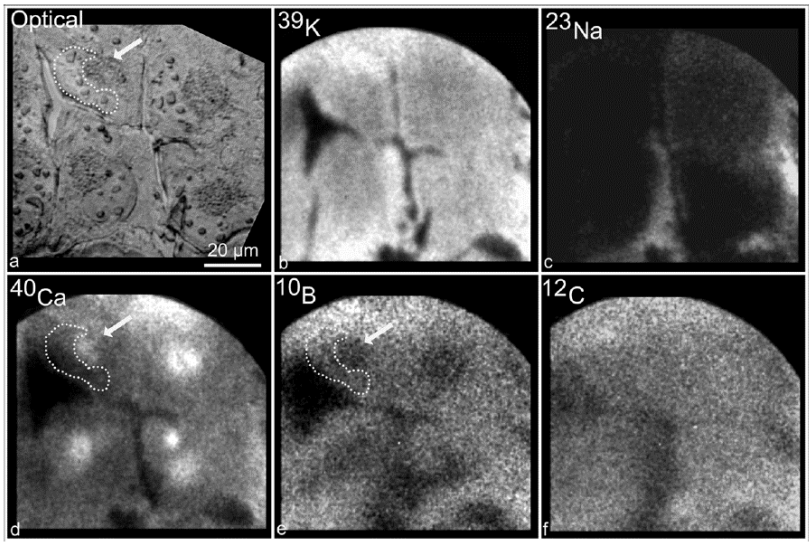

Figure 2.10: SIMS analysis of glioblastoma cells (T98G) treated for 2 h with 110 ppm of BPA. a) Optical microscope image showing a group of cells prepared by freeze-fracture. CAMECA IMS-3f images (b-f) show the distribution of positive secondary ions: $^{39}K^+$, $^{23}Na^+$, $^{40}Ca^+$, $^{10}B^+$ and $^{12}C^+$ respectively. The dotted line refers to the nucleus in one cell, while the arrow refers to cytoplasmic region rich in mitochondria. Bright areas indicate high counts of ions, while black areas refer to no counts. FoV = 250×250 μm^2 [6]. Reprinted with permission from Elsevier.

Yokoyama *et al.* used an IMS-6F dynamic SIMS instrument equipped with an O_2^+ beam and ~ 40 µm spatial resolution in the imaging of C6 glioma cells of rat's brains. The samples were prepared as freeze sectioned tissue then freeze dried. The study aimed to compare the ^{10}B accumulation of BSH and BPA agents of BNCT. BPA was accumulated heterogeneously in tumour area and only selectively in tumour cells that infiltrated into the normal brain tissue surrounding the tumour, **Figure 2.11**. In contrast, BSH was accumulated homogeneously in tumour but diffusely in both tumour and normal cells in the normal brain tissue surrounding the tumour [80]. They attributed the difference in the distribution mechanism between the two agents of BNCT to BPA preferring to accumulate in cells proliferating actively compared with quiescent cells and also being affected by the cell cycle. BSH tends to accumulate equally in individual tumour cells. This is in line with what Smith *et al.* had observed in a previous study [76].

Figure 2.11 has been removed due to Copyright restrictions. The original image can be found in the following reference:

Figure 1 from K. Yokoyama *et al.*, "Analysis of boron distribution *in vivo* for boron neutron capture therapy using two different boron compounds by secondary ion mass spectrometry.," *Radiat. Res.*, vol. 167, no. 1, pp. 102–109, 2007.

Figure 2.11: Images of C6 rat glioma sections after being treated with BPA (500 mg/kg). Light microscope images A-C represent sections stained by hematoxylin and eosin (H&E). A: main tumour mass showing a large pool of tumour cells (Purple); B: interface between tumour and normal brain; C: normal brain (Pink space) and some infiltrating cancer cells (Purple); images D-F using IMS-6F show the heterogeneous distribution of $^{10}B^+$ in tumour core, the interface between the tumour and normal brain area, and the normal brain area respectively. Scale bar = 6 µm [80].

Alkins *et al.* investigated BPA-f uptake, an analogue of BPA, *in vivo* in 9L gliosarcoma tumour sections of rat' brain (Fisher 344) using ToF–SIMS IV with a Bi_1^+ liquid metal ion beam and ICP-AES. The results, shown in **Figure 2.12,** were that both $^{23}Na^+$ and $^{39}K^+$ led to saturation of the detector and were of high signal intensity in the tumour area (lower left corner and dotted line) compared with adjacent normal brain tissues (upper right corner). $^{24}Mg^+$ was also highly localised in the tumour. $^{10}B^+$ accumulation was higher in the tumour area compared with normal brain area. However, $^{10}B^+$ showed no appreciable distribution pattern in the cellular structure. $^{12}C^+$ was uniform in both the tumour and normal brain tissue. The ICP-AES measurements confirmed that the $^{10}B^+$ concentration in the tumour was 3-fold higher than cells that had infiltrated the surrounding normal brain area (**Table 2.3**) [9].

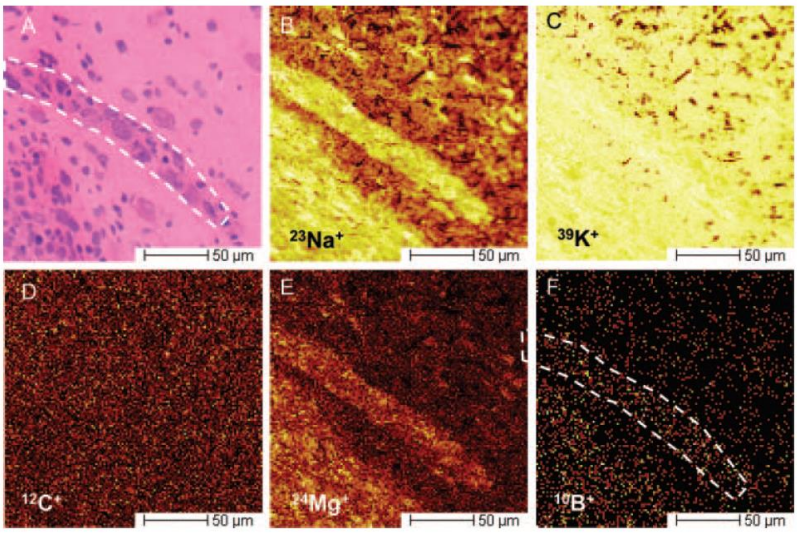

Figure 2.12: Images presenting 9L gliosarcoma tumour section of a Fisher rat brain treated *in vivo* with BPA-f. (A) The H&E-stained frozen section image shows the same area prepared for SIMS analysis. In the images of the tumour tissue in the lower left corner and normal brain tissue in the upper right corner, the dotted line refers to an island of tumour in the middle of the image. (B–F) ToF–SIMS IV images show the distribution of (B) $^{23}Na^+$, (C) $^{39}K^+$, (E) $^{24}Mg^+$ and (F) $^{10}B^+$ which all have higher localisation in the tumour tissue compared to normal brain tissue. (D) Shows $^{12}C^+$ uniformly distributed across the tissue section. The field of view in all images is 200×200 µm^2 with 128×128 pixels [9]. Reprinted with permission from Oxford University Press.

Chandra *et al.*'s (2008) research continued using the same instrument on T98G human glioblastoma cells, estimating the concentration of boron in different phases of the cell cycle: interphase and mitotic-phase. It was noted that there were differences between the phases in the absorption of boron, which has an impact on BNCT treatment. There was a lower concentration of boron in the mitotic phase (by two times) compared with the interphase, the reason being that in the interphase the nucleus prefers BPA to proteins which it needs to build DNA, while in the mitotic phase the chromosome does not need proteins. It was also noted that the cytoplasm in the interphase had higher boron ratios than in the mitotic phase, which shows the difference in absorption between cell stages; this increases the understanding of the mechanism of the arrival of boron in BNCT agents. In the interphase cells, ^{10}B was distributed relatively heterogeneously between the nucleus and the cytoplasm and with comparable concentrations (**Table 2.2**) [61].

Arlinghaus *et al.* compared imaging characteristics between a sputter-initiated resonance ionization microprobe (SIRIMP) and a laser atomization resonance ionization microprobe (LARIMP) in determining the localisation and quantification of boron concentrations in rat tissue sections. The difference between the two techniques was that SIRIMP uses a pulsed ion beam from a duoplasmatron ion gun, while LARIMP uses a pulsed laser for its atomization process. Mice were treated with a BSH dimer (BSSB - $^{10}B_{24}H_{22}S_2^{4-}$) *in vivo* prior to the harvesting of tissue from the brain, kidney and liver. In all tissues, both techniques provided highly sensitive imaging capabilities for determining the boron spatial distribution, as well as quantitative measurement. The LARIMP technique was deemed suitable for the analysis of large areas, whereas SIRIMP was more suited to studying variability in intracellular areas [83].

Chandra *et al.* (2014) [14] published a similar study to [61] which extended the work by measuring the concentrations of boron which are retained within the cell when exposed to a nutrient medium containing a quantity of phenylalanine equal to that of the BPA. The results showed that 25% – 70% of the boron concentration was retained within the cell compartments before exposed to a nutrient medium and ^{10}B was uniformly distributed between the nucleus and cytoplasm with similar concentrations (**Table 2.2**), and with less concentration in the mitochondrial-rich region, as shown in **Figure 2.13**. The presence of phenylalanine in the nutrient medium creates a competitive effect with BPA, which leads to a decrease in both the level of boron retained in the intracellular regions and the absorption rate of the BPA by 40- 50%. It is, therefore, suggested that patients are placed on a low phenylalanine diet before exposure to BNCT [14].

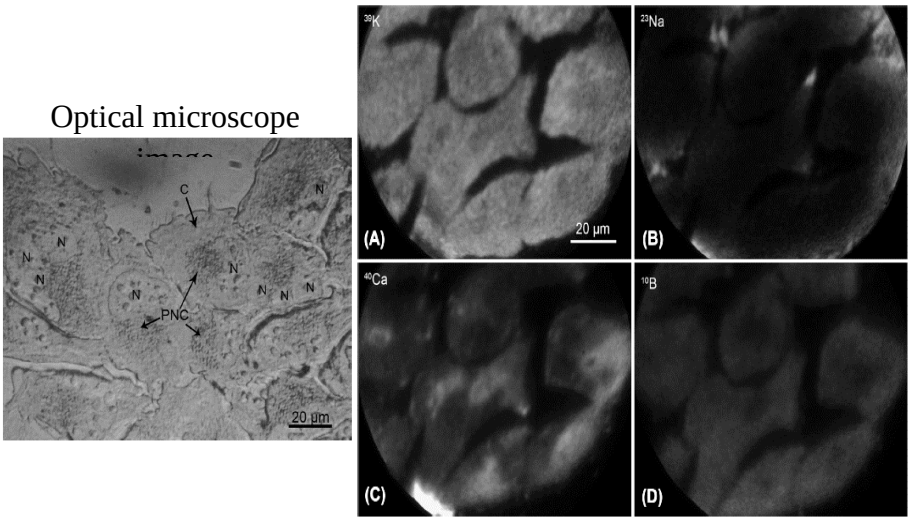

Figure 2.13: SIMS analysis of glioblastoma cells (T98G) treated for 6h with 110 µg/g BPA. a) The Nomarski microscope image on the left shows a group of cells prepared by being fractured freeze-dried: (N) nuclei, (C) cytoplasm and (PNC) mitochondria in the perinuclear cytoplasmic region. CAMECA IMS-3f images (A-D) show the distribution of positive secondary ion respectively ^{39}K, ^{23}Na, ^{40}Ca, ^{10}B. In A-D, the bright areas mean high counts of ions, while the black areas refer to no counts. Scale bar = 20 µm, FoV is 250×250 μm^2 [14]. Reprinted with permission from John Wiley and Sons.

Fartmann *et al.* identified the distribution of $^{10}B^+$ in cell cultures from human malignant melanoma that had been treated with different concentrations of sodium mercaptoundecahydro-closo-dodecaborate ($Na_2\ ^{10}B_{12}H_{11}SH$; BSH), using 200 nm Ga^+ of ToF-SIMS/laser-SNMS instrument. The images taken with both techniques showed that the intensity of the boron signals in the samples increased with greater concentrations of BSH, and that $^{10}B^+$ was distributed homogeneously at the cellular level with high extracellular accumulation. **Figure 2.14** shows the distribution of boron in human malignant melanoma cells treated with 480 ppm BSH [84].

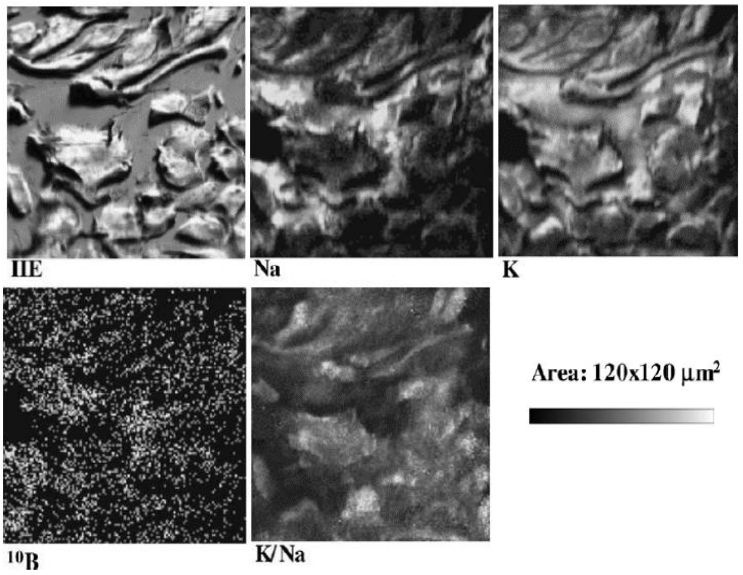

Figure 2.14: Ion-induced electron image (IIE) showing the general morphology of freeze-fractured and freeze-dried cell cultures of human malignant melanoma cancer incubated with 480 ppm BSH (24h). ToF-SIMS images show the distribution of $^{23}Na^+$, $^{39}K^+$ and $^{10}B^+$ at the cellular level. The overlay image (K/Na) shows low signals of Na and high signals of K in cells. The colour bar: white means high counts of ions, while the black refers to no counts (no values of counts given in original reference) [84]. Reprinted with permission from Elsevier.

Kabalka *et al.* investigated the $^{11}B^+$ delivery of cis and trans isomers of 1-amino-3-bronocyclopentanecarboxylic acid (ABCPC) in B16 melanoma tumour cells and compared the results with the accumulation of $^{10}B^+$ from BPA. These cells were incubated in mice and administered with compounds *in vivo* before they were harvested (from liver and kidneys) and fractionated to thin sections for analysis with a CAMECA IMS-3f ion microscope. The results showed that the three compounds had a similar pattern in the delivery of boron to melanoma cells and that the boron was distributed almost homogeneously between the nucleus and cytoplasm areas, **Figure 2.15** [85].

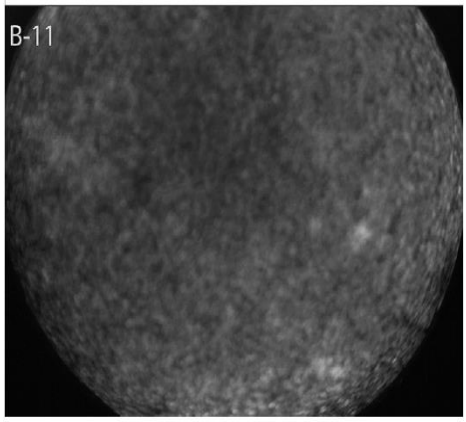

Figure 2.15: SIMS image showing almost homogeneous distribution of $^{11}B^{+}$ from trans-ABCPC in tissue section of a B16 mouse melanoma tumour. Scale bar in image is 40 µm [85]. Reprinted with permission from Elsevier.

2.3.1.1 Quantification of the ^{10}BPA localisation in SIMS studies

Quantitative measurements of ^{10}B concentrations from BPA from the SIMS studies presented in section 2.3.1, measured in sub-cellular compartments of the nucleus and cytoplasm as well as at the cellular level of tissue sections are summarised in **Table 2.2** and **Table 2.3** respectively.

^{10}B concentrations in sub-cellular compartments in **Table 2.2** revealed the following:

(i) the measured concentrations indicate that there is no significant difference in ^{10}B accumulations between the nucleus and cytoplasm [6][14][61][75][77][79] even though some studies in 2.3.1 show an apparent visible difference between the nucleus and cytoplasm.

(ii) increasing the exposure time of the BPA from 1 - 2 h to 6 h increased the accumulation of ^{10}B in all compartments by 1.5-2 fold, which indicates the cells' need for amino acids in their metabolism [6][14][79].

(iii) the standard deviation (SD) in each treatment shows the variability of uptake of BPA from cell to cell with high SD for samples exposed for 6 h, indicating that the BPA uptake may vary depending on the cell cycle [6][14][79].

The BPA uptake in the tissue sections in **Table 2.3** indicates that:

(i) ^{10}B concentrations in the tumour mass (T) were over 1.5-fold higher than that measured in cells infiltrating the normal brain around tumour (IT). This is because the tumour contains more malignant cells than those infiltrating the normal brain. This observation is consistent with high intensity of boron signals observed in the tumour areas compared to that accumulated in the IT areas as shown in **Figure 2.6** [76] and **Figure 2.12** [9].

(ii) increasing BPA exposure time to 6 h resulted in doubling of the accumulated ^{10}B in the infiltrating cells, but there was no large increase in ^{10}B concentration in the tumour when increasing from 2 – 3 h to 6 h. After 24 h of BPA exposure the concentration of ^{10}B in the infiltrating cells reached the same level of boron as in the tumour cells, which reduced compared to the 6h exposure [76]. This observation can be explained in light of the hypothesis that the activity of LAT-1 expression in infiltrating cells contributes to increased uptake of BPA and the probability of tumour recurrence at different locations [19][49].

(iii) in both references [9][76], very similar boron concentrations were obtained after 2 h exposure using different cells and SIMS instruments as shown in **Table 2.3**.

Table 2.2: Sub-cellular ^{10}B concentrations (mean ± SD) from ^{10}BPA-f in T98G human glioblastoma cells treated with 110 ppm ^{10}B equivalent of drug for different time durations. The boron concentrations were all measured using a CAMECA IMS-3F ion microscope. Data summarised from various references as shown in the table.

Reference no.	Treatment time (h)	Subcellular ^{10}B concentration (μg/g wet weight)	
		Nucleus	cytoplasm
[75]	1	141 ± 15	155 ± 33
[77]	6	281 ± 8	280 ± 10
[79]	1 6	132 ± 46 311 ± 118	164 ± 52 336 ± 132
[6]	1 2 6	136 ± 55 191 ± 68 295 ± 120	176 ± 57 141 ± 37 297 ± 140
[61]	1	145 ± 38	157 ± 45
[14]	2 6	252 ± 31 347 ± 88	269 ± 36 379 ± 71

Table 2.3: ^{10}B concentrations (mean ± SD) in tissue sections of 9L gliosarcoma tumour (T) and tumour cells infiltrating the normal rat brain around tumour (IT) treated with different doses of ^{10}BPA for different infusion times. The ^{10}B concentrations were measured from two different references as shown in the table.

Reference no.	Treatment dose (ppm)	Treatment time (h)	^{10}B concentration in tissue (μg/g)		Measured by
			T	IT	
[76]	250 250 250 125	2 3 6 24	83±23 75±30 90±14 53±10	31±12 37±7 65±11 52±14	IMS-3F ion microscope
[9]	250	2	85±29	25±11	ICP-AES

2.3.2 SIMS studies with other cancer drug treatments

Cisplatin plays the role of a chemical activator of tumour cell death, either through necrosis and destruction of the cell membrane by the use of high cisplatin concentrations, or apoptosis with low cisplatin concentrations where the drug is associated with DNA in nuclei and causes chromatin condensation [86]. Gulin *et al.* identified the distribution of platinum (Pt^+) in a human glioblastoma cell line (U87MG) treated with cisplatin using a 500 nm Bi_3^+ beam with ToF-SIMS. The results showed that Pt^+ is distributed in nuclei with a concentration ~ 1.5 times higher than the cytoplasmic regions [86].

Chandra (2010) investigated changes in the chemical composition of an LLC-PK1 pig kidney cell line resulting from cisplatin treatment, using an O_2^+ beam of a CAMECA IMS-3f SIMS ion microscope with a spatial resolution of 500 nm. The imaging results showed that individual cells differed in their response to cisplatin. $^{195}Pt^+$ of cisplatin accumulates in some cells without causing the chemical composition to change. In other cells, Ca^{2+} content decreased in the cytoplasm and this appeared in the initial response phase of cisplatin treatment. Another group of cells showed an increase in Ca^{2+} and Na^+ content and a decrease in K^+ with the accumulation of cisplatin, which indicates cell injury [87].

Legin *et al.* used NanoSIMS to determine the distribution of ^{15}N-labelled cisplatin in cancer cells from human colon. Cisplatin (a platinum containing drug) is one of the chemical treatments for cancer and requires cisplatin accumulation inside the cancer cell. The analysis

showed a high accumulation of platinum in the nucleus, platinum colocalised with high sulfur and phosphorus in the nucleolus, and accumulated in the cytoplasm where there were some strong signals, **Figure 2.16** [88].

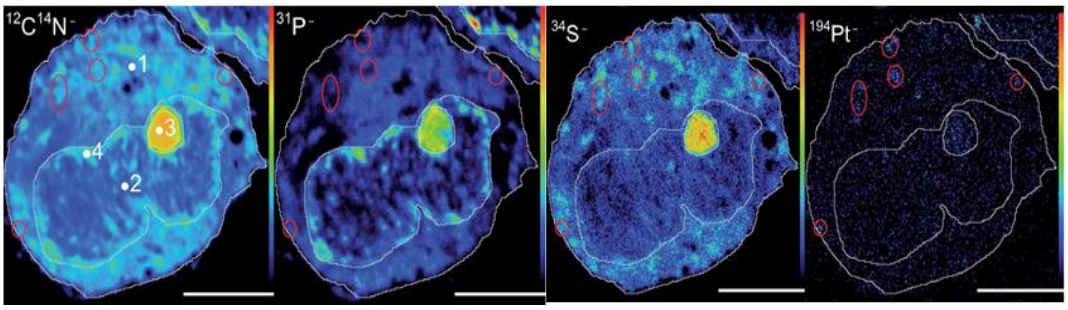

Figure 2.16: NanoSIMS 50L images of $^{12}C^{14}N^-$,$^{31}P^-$, $^{34}S^-$and $^{194}Pt^-$ respectively, in human colon cancer cell treated with cisplatin. 1, 2, 3 and 4 indicate the cytoplasm, nucleus, nucleolus and chromatin respectively. Pt^- signals show a high rate of accumulation in the nucleus, colocalisation with sulfur in the cytoplasm, colocalisation at the site with sulfur and phosphorus in the nucleolus at a high rate. The intensity of the signals is shown on a rainbow-scale, from black to red, indicating a scale from low to high signals. Scale bar = 5 µm [88]. Reproduced with permission from The Royal Society of Chemistry under creative comments license 3.0.

Wedlock *et al.* (2011) studied one of the most promising treatments for cancer cells: a gold (1) phosphine complex. The distribution of $^{197}Au^-$ in human breast cancer cells (MDA 123 - cell line) was determined and investigated to establish how it is toxic to cancer cells. The authors used the high resolution and sensitivity of the NanoSIMS with Cs^+ beam to map the distribution of the $^{197}Au^-$ in the cells, along with $^{31}P^-$ and $^{32}S^-$, which can be used to show the structure of cell. It was observed that the Au^- was distributed in the nucleus and cytoplasm areas which contain a high rate of sulfur, suggesting that these gold complexes work by inhibiting thiol-containing proteins, **Figure 2.17** [89].

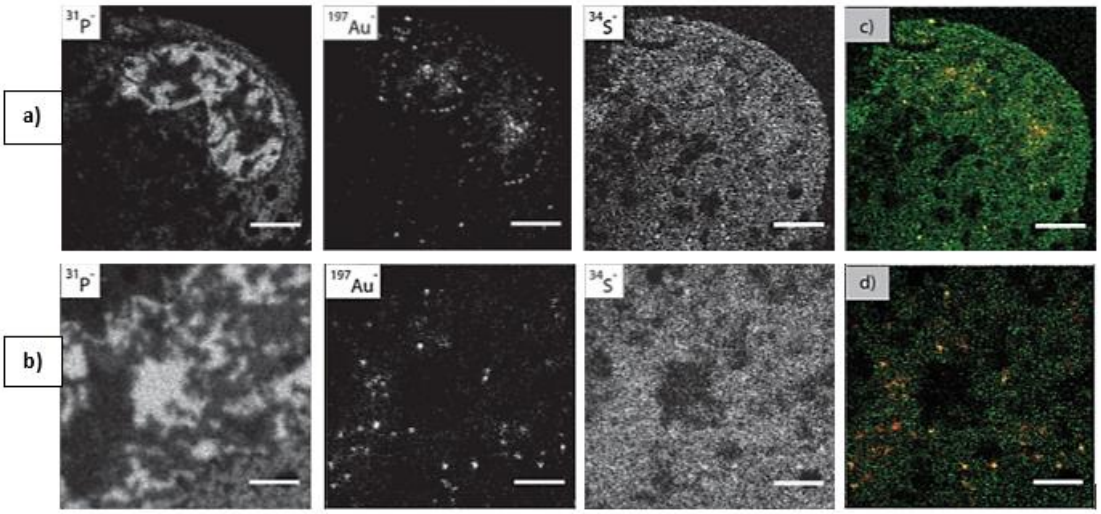

Figure 2.17: (a) and (b) show $^{31}P^-$, $^{197}Au^-$ and $^{34}S^-$ secondary ion maps of MDA cells (two different cells) treated with 100 mM of gold (1) for 2 h analysed by NanoSIMS; (c) and (d) are overlapping maps of the $^{34}S^-$ (green) and $^{197}Au^-$ (red) shown above in (a) and (b); sites shared between $^{34}S^-$ and $^{197}Au^-$ in the nuclear, perinuclear and cytoplasmic regions are shown in yellow. Scale bars: 2 µm in (a) and (c), 1 µm in (b) and (d) [89]. Reprinted with permission from The Royal Society of Chemistry.

Wedlock *et al.* (2013) used a Cs^+ beam of NanoSIMS to determine the localisation of both ^{15}N and ^{195}Pt-labelled triplatinNC and cisplatin compounds (anti-tumour agents) in single cells of human breast adenocarcinoma (MCF7). The results showed that $^{195}Pt^-$ of triplatinNC is highly localised in the cytoplasm and co-localises with ^{15}N ($^{12}C^{15}N^-$) in the nucleolus. Whereas $^{195}Pt^-$ of cisplatin was randomly distributed with lower $^{195}Pt^-$ counts than the triplatinNC. NanoSIMS did not detect any localisation of $^{15}N^-$ from cisplatin. This finding confirms the different uptake of the two anti-tumour agents in cells [90].

Proetto *et al.* used a Cs^+ beam NanoSIMS to determine the distribution of Pt (II) from the drug oxaliplatin in HT-1080 fibrosarcoma tumour tissue implanted in mice. The drug was delivered *in vivo* as a portable part of an enzyme-directed assembly of particle therapeutics (EDAPT) prepared by the authors. The results showed that the drug was released from the EDAPT nanocarrier and colocalised in ^{15}N-enriched areas in the tumour tissue sections, **Figure 2.18** [91].

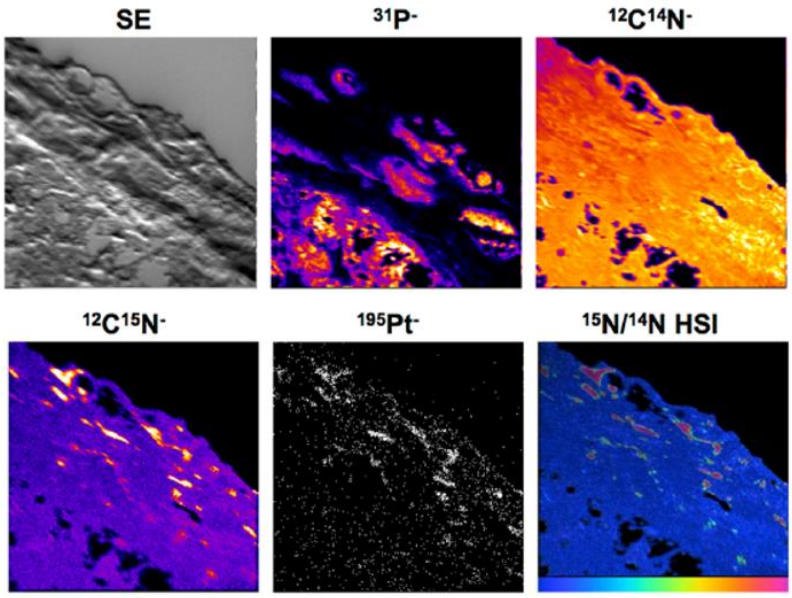

Figure 2.18: NanoSIMS imaging of fibrosarcoma tumour tissue section of mice treated with ^{195}Pt of oxaliplatin drug delivered using EDAPT *in vivo*. SE: Secondary electron map shows the morphology of the histological section. The maps of $^{31}P^-$, $^{12}C^{14}N^-$ and $^{12}C^{15}N^-$, shows the signals intensities in a fire scale, while the $^{195}Pt^-$ map in white/black scale. HSI: a hue-saturation-intensity map show the $^{12}C^{15}N/^{12}C^{14}N$ ratio and indicate to areas enriched with ^{15}N. FoV in all maps is 48×48 μm^2 [91]. Reprinted with permission from ACS Publications.

2.4 Biological sample preparation

SIMS instruments need to operate under ultra-high vacuum (UHV) (< 10^{-8} Pa) to protect the primary and secondary beams from deflection and defocusing as a result of a reaction or collision with the remaining gas molecules or contaminants that may be adsorbed from the sample surface, as well as to prevent contamination of the instruments and detector [92]. Biological samples contain about 80% water, which must be removed prior to analysis; otherwise, the water will rapidly be evaporated in UHV, which can cause cell rupture and changes to the elemental and molecular distribution. Thus, biological sample preparation should maintain both the sample structure as well as the chemical distribution of the elements. Therefore, biological sample preparation is extremely important and can be carried out by fixing the sample either chemically or cryogenically, as discussed in the following sub-sections [93]–[95].

2.4.1 Cryofixation process

Cryofixation has been widely used for the preparation of biological samples in SIMS analysis. This method involves a rapid freezing step to freeze cell components (molecules

and elements) in their *in vivo* locations by immersion in liquid nitrogen, ethane, propane or isopentane prior to the samples being stored, usually at -80 °C. The reason for the use of fast freezing is that it creates amorphous ice, whereas slower freezing creates ice crystals which can rupture the cells or result in the redistribution of small molecules and elements [96]. The cold-stored tissue is prepared by a cryo-sectioning method, whereby it is cut into slices using a microtome in a cryostat at a temperature of -20 °C. Each section is then deposited on a substrate. Cryosectioning offers the possibility of obtaining a flat tissue surface with different thicknesses (15–20 μm) and the possibility of obtaining sequential samples [97]–[99].

After fast freezing and sectioning, samples for SIMS analysis can be freeze-dried. The freeze-drying method involves transferring the frozen sample to a vacuum system for several hours until it warms to room temperature, so that the remaining water or ice can be removed by sublimation [96]. One of the experiments that used this method of preparation was carried out by Sjövall *et al.*, when they studied the distribution of fatty acids resulting from the intake of Omega-3 in the muscles and liver tissue of rats. The researchers took slices of tissue, immediately immersed them in liquid nitrogen, stored them at a temperature of -80 °C, then cut them to a thickness of 16 μm at -20 °C and stored them at that temperature. The samples were freeze dried in a vacuum overnight to prepare them for ToF-SIMS analysis [100].

Alternatively, frozen samples can be analysed in the hydrated state on SIMS instruments with a cryostage. In this process, the sample is fast frozen, as explained above, but instead of removing the water, the sample is transferred into vacuum and onto the cryostage at a temperature of ~ 166 K and a pressure of 1×10^{-8} mbar. This method protects the cell components from evaporation or ice condensation and prevents them from diffusion and thus keeps the sample in a state that is more similar to the *in vivo* condition, maintaining the distribution and morphology of its elements [101]. However, samples in the hydrated state are not suitable when quantitative measurements for ion yields are carried out because they increase the matrix effects [102][103]. Metzner *et al*. studied xylem vessels to transport macronutrients to the sub-cellular level in bean stem sections. The samples were kept frozen-hydrated and transported to the cryostage of a ToF-SIMS (cryo-ToF-SIMS). The results showed that $^{39}K^+$, and $^{41}K^+$ tend to be distributed in xylem vessels, whereas $^{23}Na^+$ tends to be distributed more in the xylem parenchyma surrounding the xylem vessels. These results agreed with the theory of nutrient transport in plants [104].

Samples can also be prepared for SIMS analysis by freeze-fracturing, whereby a hydrated sample is placed between two substrates; it can also be placed with spacer beads to protect

the sample from crushing, and is then plunge-frozen. The substrates are separated from each other, either simply by pulling them apart which leads to fracturing the sample [105], or the use of a cryo-knife. This process exposes the interior of the sample and allows sub-cellular analysis to be performed in the central regions of the cell without the need for depth profiling. Samples are then transferred to a vacuum, where they can be prepared for analysis by either being freeze dried or left frozen-hydrated [101]. Zha *et al.* used this method in their experiments [10]. Chandra and others have conducted many studies in which freeze fracturing was used for sample preparation [75][106][107].

Imprinting is another, less common, method of preparation for biological samples, in which a sample is provided in the form of an imprint on a substrate for SIMS imaging. The sample is pressed onto the substrate for a short amount of time with the aim of leaving material imprinted onto the surface. This method has been shown to increase the secondary ion yield compared with other means of preparation, thereby increasing the sensitivity of the measurement. Sjövall *et al.* demonstrated an improvement in ionic yields when blood cells were placed on a glass substrate and washed with a phosphate-buffered saline (PBS) buffer, then rinsed with 0.15 M NH_4CL, followed by freeze drying. The sample was then pressed against silver foil for 10 s. The results showed the localisation of cholesterol in the plasma membrane and phosphocholine in the nuclear membrane. In the case of a wet sample, it should be dried before making an imprint [108]. The Nygren group used this method to localise lipids in a membrane [109]. Therefore, the preparation of biological samples using both freeze fracturing and imprinting exposes the internal parts of a sample for analysis and thus increases secondary ion yield and creates clearer 3D images [101][108].

Sample washing can cause a redistribution of ions. Sample are normally washed for a short time (a few seconds) before freezing in order to remove any external contamination and salts present on the sample surface, thus preventing them from interfering in the spectrum or causing ionization suppression. The most common solutions used in washing are ammonium acetate ($CH_3CO_2NH_4$) and ammonium formate (NH_4HCO_2) due to the volatilization of their salts [101]. Sjövall *et al.* studied the localisation of lipids in the mouse brain. The tissue section mounted onto a substrate was frozen at -80 °C and washed by being plunged for 30 s in 0.15 M of NH_4HCO_2 solution to remove salt contamination, then stored at -78 °C. The section was then prepared for analysis by being freeze dried in a vacuum chamber. The results of the analysis at varying temperatures of between -130 °C and 60 °C show that the signal intensity of the lipid changed, which indicates lipid migration to different locations of the sample surface [110].

2.4.2 Chemical fixation process

Chemical fixation is another method of preparing biological samples, as an alternative to cryofixation. Chemical fixation is a simple method based on the addition of chemicals to a biological sample to preserve the internal structure of the cell, such as the membrane and DNA, which is fixed and then analysed at room temperature. The chemicals most commonly used in fixation are formaldehyde, formalin, and glutaraldehyde (GA). This method is only suitable for biological samples when studying structures, as it may lead to a change in the sample chemistry [101][105]. Typically, diffusible ions, such as K^+ and Na^+, and some small molecules will be completely redistributed from their *in vivo* locations, so this preparation method is not suitable for SIMS if ion distribution is to be studied [95][111]. It is however a useful and simple method of preparing biological samples for SIMS analysis when the elements to be studied are tightly bound such as studying protein formation [112].

Malm *et al.* studied the human cell fibroblast cell (hTERT) on silicon substrates, and a comparison was made between two cell preparation methods and analysis by ToF-SIMS. The first method was chemical fixation using GA for samples washed with deionized water and then freeze-dried. The second method was cryogenic fixation, which included washing with ammonium formate, followed by plunge freezing and finally freeze-dried. The results showed that cryogenic fixation was best for ToF-SIMS analysis for several reasons, such as maintaining the distribution of ions and lipids, providing high ion yields, and preserving the phospholipids in cell membranes. Washing with ammonium formate for 1 min caused sample swelling, which was observed when the sample was examined under reflection microscopy. The chemical fixation method using GA caused the removal of phospholipids from the cell membrane. Chemical fixation showed fine structures on the sample surface but changed the distribution of the ions [113].

2.5 Summary

Previous studies in pharmacological distribution analysis have offered a number of conclusions regarding BPA. The general impression is that ^{10}B from BPA is expected to be distributed heterogeneously among tumour cells at the tumour core and to accumulate selectively in the cancerous cells infiltrating the area around the tumour [6][14][61][75][76][79][82]. This suggests that BPA is able to distinguish tumour cells from the normal cells. The observed heterogeneity of the ^{10}B distribution may be due to one of two causes. The first is the difference in the cell cycle (or proliferating state) followed by different cell activity or the cell may be in a quiescent phase, leading to a difference in BPA

uptake between the cells [54]–[58]. The second is a rise in the activity of the LAT-1 transporter, which has been associated with an increase in the transfer of amino acid, although the LAT-1 transporter presented a difference of opinions regarding the extent of its association with the proliferating state of the cell [19][41][42][49][50][59]-[61]. Analysis of the brain around the tumour (BAT) area has shown very uneven levels of BPA uptake [19]. Although the pattern of ^{10}B distribution across cells is different, quantitative measurements indicate that there is no significant difference in the ^{10}B concentrations between the nucleus and the cytoplasm [6][14][61][75][77][79]. Moreover, tumour tissue sections showed a higher concentration of ^{10}B (~1.5-fold) compared to the BAT areas containing infiltrated tumour cells [9][76]. The diversity of SIMS possibilities in imaging makes it a valuable tool in quantitative bioanalytical applications provided the sample preparation can accurately represent the *in vivo* distribution of the elements.

The aim of preloading samples with L-tyrosine is to enhance the BPA uptake of cells [21][43]-[45]. However, while some studies showed a high accumulation of BPA with tyrosine [21][26][46]-[48], some demonstrated the opposite, suggesting that tumours may differ in their behaviour [19][50][51]. Furthermore, the vast majority of studies on BPA were focused on quantitative measurement using different analytical methods including ICP-MS, FI/ESI-MS/MS, DCP-AES, ICP-AES, radiowave dielectric spectroscopy (RDS), electrothermal atomic absorption spectrometry, gamma counter, inductively coupled plasma-optical emission spectroscopy (ICP-OES), and γ-ray spectrometry [19]-[21][26][46]-[48][54]–[60], whereas imaging studies to determine the localisation of BPA were limited [6][9][13][14][51][61][75]-[91]. In addition, the SIMS analytical instruments used in the localisation study of BPA showed differences in their ability and efficiency to detect ^{10}B at the cellular and sub-cellular level [84]-[91].

The majority of the samples studied by SIMS were *in vitro*, whether cell lines or animal models, and *in vivo* samples were limited to treatments in mice or rats. Hence, the uniqueness of the current thesis is its use of human brain tumour and brain-around-tumour biopsy samples pre-treated with BPA *in vivo* and primary cell cultures of human brain tumour and brain-around-tumour biopsies (from patients) processed *in vitro*. In addition, these samples have not been analysed previously with both NanoSIMS and ToF-SIMS in order to determine the localisation and distribution of BPA using the imaging method and none of the previous SIMS studies of BPA have been undertaken with NanoSIMS which should offer sub-cellular information.

2.6 References

[1] "Cancer Statistics for the UK." [Online]. Available: https://www.cancerresearchuk.org/health-professional/cancer-statistics-for-the-uk. [Accessed: 08-Mar-2019].

[2] "Worldwide cancer statistics | Cancer Research UK." [Online]. Available: https://www.cancerresearchuk.org/health-professional/cancer-statistics/worldwide-cancer. [Accessed: 08-Mar-2019].

[3] "Brain Tumor FAQs | ABTA." [Online]. Available: https://www.abta.org/about-brain-tumors/brain-tumor-education/#statistics. [Accessed: 08-Mar-2019].

[4] "What Is Cancer? - National Cancer Institute." [Online]. Available: https://www.cancer.gov/about-cancer/understanding/what-is-cancer. [Accessed: 08-Mar-2019].

[5] S. McGuire, "World Cancer Report 2014. Geneva, Switzerland: World Health Organization, International Agency for Research on Cancer, WHO Press, 2015," *Adv. Nutr.*, vol. 7, no. 2, pp. 418–419, 2016.

[6] S. Chandra and D. R. Lorey, "SIMS ion microscopy imaging of boronophenylalanine (BPA) and $^{13}C^{15}N$-labeled phenylalanine in human glioblastoma cells: Relevance of subcellular scale observations to BPA-mediated boron neutron capture therapy of cancer," *Int. J. Mass Spectrom.*, vol. 260, no. 2–3, pp. 90–101, 2007.

[7] D. N. Louis *et al.*, "The 2007 WHO classification of tumours of the central nervous system," *Acta Neuropathol.*, vol. 114, no. 2, pp. 97–109, 2007.

[8] A. Sarkar and E. A. Chiocca, "Glioblastoma and Malignant Astrocytoma," *Brain Tumors*, pp. 384–407, 2012.

[9] R. D. Alkins, P. M. Brodersen, R. N. S. Sodhi, and K. Hynynen, "Enhancing drug delivery for boron neutron Capture Therapy of Brain Tumors With Focused Ultrasound," *Neuro. Oncol.*, vol. 15, no. 9, pp. 1225–1235, 2013.

[10] X. Zha, W. A. Ausserer, and G. H. Morrison, "Quantitative imaging of a radiotherapeutic drug, $Na_2B_{12}H_{11}SH$, at subcellular resolution in tissue cultures using ion microscopy," *Cancer Res.*, vol. 52, no. 19, pp. 5219–5222, 1992.

[11] M. J. Luderer, P. De La Puente, and A. K. Azab, "Advancements in Tumor Targeting Strategies for Boron Neutron Capture Therapy," *Pharm. Res.*, vol. 32, no. 9, pp. 2824–2836, 2015.

[12] R. F. Barth, P. Mi, and W. Yang, "Boron delivery agents for neutron capture therapy of cancer," *Cancer Commun.*, vol. 38, no. 35, pp. 1–15, 2018.

[13] A. C. Oyedepo, S. L. Brooke, P. J. Heard, J. C. C. Day, G. C. Allen, and H. Patel, "Analysis of boron-10 in soft tissue by dynamic secondary ion mass spectrometry," *J. Microsc.*, vol. 213, no. 1, pp. 39–45, 2004.

[14] S. Chandra, T. Ahmad, R. F. Barth, and G. W. Kabalka, "Quantitative evaluation of boron neutron capture therapy (BNCT) drugs for boron delivery and retention at subcellular-scale resolution in human glioblastoma cells with imaging secondary ion mass spectrometry (SIMS)," *J. Microsc.*, vol. 254, no. 3, pp. 146–156, 2014.

[15] "Nuclear fusion against cancer-physics," 2016. [Online]. Available:

https://physicsgg.me/2016/03/20/πυρηνική-σύντηξη-εναντίον-καρκίνου/. [Accessed: 22-Aug-2018].

[16] S. Chandra, “SIMS ion microscopy as a novel, practical tool for subcellular chemical imaging in cancer research,” *Appl. Surf. Sci.*, vol. 203–204, pp. 679–683, 2003.

[17] A. Portu *et al.*, “Inter-comparison of boron concentration measurements at INFN-University of Pavia (Italy) and CNEA (Argentina),” *Appl. Radiat. Isot.*, vol. 106, pp. 171–175, 2015.

[18] C. L. Schütz *et al.*, “Intercomparison of inductively coupled plasma mass spectrometry, quantitative neutron capture radiography, and prompt gamma activation analysis for the determination of boron in biological samples,” *Anal. Bioanal. Chem.*, vol. 404, pp. 1887–1895, 2012.

[19] A. Detta and G. S. Cruickshank, “L-Amino Acid Transporter-1 and Boronophenylalanine-Based Boron Neutron Capture Therapy of Human Brain Tumors,” *Cancer Res.*, vol. 69, no. 5, pp. 2126–2132, 2009.

[20] F. Basilico, W. Sauerwein, F. Pozzi, A. Wattig, R. Moss, and P. L. Mauri, “Analysis of ^{10}B antitumoral compounds by means of flow-injection into ESI-MS/MS,” *J. Mass Spectrom*, vol. 40, pp. 1546–1549, 2005.

[21] A. Wittig, W. A. Sauerwein, and J. A. Coderre, “Mechanisms of Transport of p-Borono-Phenylalanine through the Cell Membrane In Vitro,” *Radiat. Res.*, vol. 153, no. 2, pp. 173–180, 2000.

[22] R. N. Sah and P. H. Brown, “Isotope ratio determination in Boron analysis,” *Biol. Trace Elem. Res.*, vol. 66, no. 1–3, pp. 39–53, 1998.

[23] W. A. Sauerwein, A. Wittig, R. Moss, and Y. Nakagawa, “Drugs for BNCT: BSH and BPA,” in *Neutron Capture Therapy - Principles and Applications*, Verlag Berlin Heidelberg: Springer, 2012, pp. 136–144.

[24] I. B. Sivaev and V. I. Bregadze, “L-4-Boronophenylalanine (all around the one molecule),” *Arkivoc*, vol. 2008, no. 4, pp. 47–61, 2008.

[25] N. V. Bhagavan and C. Ha, “Protein and Amino Acid Metabolism,” in *Essentials of Medical Biochemistry*, 2015, p. 256.

[26] S. Capuani *et al.*, “Boronophenylalanine uptake in C6 glioma model is dramatically increased by L-DOPA preloading,” *Appl. Radiat. Isot.*, vol. 67, pp. S34–S36, 2009.

[27] C. M. van. Rij, A. J. Wilhelm, W. A. G. Sauerwein, and A. C. van. Loenen, “Boron neutron capture therapy for glioblastoma multiforme,” *Pharm. World Sci.*, vol. 27, no. 2, pp. 92–95, 2005.

[28] B. C. Fuchs and B. P. Bode, “Amino acid transporters ASCT2 and LAT1 in cancer: Partners in crime?,” *Semin. Cancer Biol.*, vol. 15, no. 4, pp. 254–266, 2005.

[29] C. Malan and C. Morin, “A Concise Preparation of 4-Borono-L-phenylalanine (L-BPA) from L-Phenylalanine,” *J. Org. Chem.*, vol. 63, no. 18, pp. 8019–8020, 1998.

[30] “L-Phenylalanine | Sigma-Aldrich.” [Online]. Available: https://www.sigmaaldrich.com/catalog/substance/lphenylalanine165196391211?lang=en&region=GB. [Accessed: 24-Aug-2018].

[31] “4-Borono-L-phenylalanine ≥95.0% (HPLC) | Sigma-Aldrich.” [Online]. Available: https://www.sigmaaldrich.com/catalog/product/sial/17755?lang=en&region=GB. [Accessed: 24-Aug-2018].

[32] “4-Borono-D-phenylalanine ≥97.0% (HPLC) | Sigma-Aldrich.” [Online]. Available: https://www.sigmaaldrich.com/catalog/product/aldrich/68047?lang=en&region=GB. [Accessed: 24-Aug-2018].

[33] “L-Tyrosine reagent grade, ≥98% (HPLC) | Sigma-Aldrich.” [Online]. Available: https://www.sigmaaldrich.com/catalog/product/sial/t3754?lang=en&region=GB. [Accessed: 24-Aug-2018].

[34] Cancer Research UK, “‘Investigator Brochure, L-Boronophenylalanine’ [L-(4-10Borononphenyl) alanine, L-BPA, BPA-mannitol] and Mannitol (20% w/v),” *Brain Tumors*, vol. 4, p. 11, 2012.

[35] “Boronophenylalanine B-10 | $C_9H_{12}BNO_4$ - PubChem.” [Online]. Available: https://pubchem.ncbi.nlm.nih.gov/compound/25033700#section=Top. [Accessed: 24-Aug-2018].

[36] H. Nemoto, J. Cai, N. Asao, S. Iwamoto, and Y. Yamamoto, “Synthesis and Biological Properties of Water-Soluble p-Boronophenylalanine Derivatives. Relationship between Water Solubility, Cytotoxicity, and Cellular Uptake,” *J. Med. Chem.*, vol. 38, no. 10, pp. 1673–1678, 1995.

[37] R. M. B. Ferreira and A. R. N. Teixeira, “Metabolism,” *Amino Acids*, pp. 197–206, 1989.

[38] F. Verrey, “System L: Heteromeric exchangers of large, neutral amino acids involved in directional transport,” *Pflugers Arch. Eur. J. Physiol.*, vol. 445, no. 5, pp. 529–533, 2003.

[39] C. A. Wagner, F. Lang, and S. Bröer, “Function and structure of heterodimeric amino acid transporters,” *Am J Physiol Cell Physiol*, vol. 281, pp. C1077–C1093, 2001.

[40] Y. Liu and Q. He, “The Route of Nanomaterials Entering Brain,” in *Neurotoxicity of Nanomaterials and Nanomedicine*, X. Jiang and H. Gao, Eds. Elsevier Inc., 2017, pp. 33–57.

[41] W. A. Campbell, D. E. Sah, M. M. Medina, J. E. Albina, W. B. Coleman, and N. L. Thompson, “TA1/LAT-1/CD98 light chain and system L activity, but not 4F2/CD98 heavy chain, respond to arginine availability in rat hepatic cells. Loss of response in tumor cells,” *J. Biol. Chem.*, vol. 275, no. 8, pp. 5347–5354, 2000.

[42] D. A. Wolf, S. Wang, M. A. Panzica, N. H. Bassily, and N. L. Thompson, “Expression of a Highly Conserved Oncofetal Gene , TA1 / E16 , in Human Colon Carcinoma and Other Primary Cancers : Homology to Schistosoma Mansoni Amino Acid Permease and Caenorhabditis Elegans Gene Products,” *Cancer Res.*, vol. 56, pp. 5012–5022, 1996.

[43] J. R. Jara, J. H. Martinez-Liarte, F. Solano, and R. Peñafiel, “Transport of L-tyrosine by B16/F10 melanoma cells: the effect of the intracellular content of other amino acids.,” *J. Cell Sci.*, vol. 97, pp. 479–485, 1990.

[44] G. C. Gazzola, V. Dall’Asta, and G. G. Guidotti, “The transport of neutral amino acids in cultured human fibroblasts.,” *J. Biol. Chem.*, vol. 255, no. 3, pp. 929–936, 1980.

[45] T. Lahoutte *et al.*, "SPECT and PET amino acid tracer influx via system L (h4F2hc-hLAT1) and its transstimulation.," *J. Nucl. Med.*, vol. 45, pp. 1591–1596, 2004.

[46] M. Papaspyrou, L. E. Feinendegen, and H. W. Müller-Gärtner, "Preloading with L-Tyrosine Increases the Uptake of Boronophenylalanine in Mouse Melanoma Cells," *Cancer Res.*, vol. 54, no. 24, pp. 6311–6314, 1994.

[47] S. Capuani *et al.*, "L-DOPA Preloading Increases the Uptake of Borophenylalanine in C6 Glioma Rat Model: A New Strategy to Improve BNCT Efficacy," *Int. J. Radiat. Oncol. Biol. Phys.*, vol. 72, no. 2, pp. 562–567, 2008.

[48] B. Wingelhofer *et al.*, "Preloading with L-BPA, L-tyrosine and L-DOPA enhances the uptake of [^{18}F]FBPA in human and mouse tumour cell lines," *Appl. Radiat. Isot.*, vol. 118, pp. 67–72, 2016.

[49] H. Nawashiro *et al.*, "High expression of L-type amino acid transporter 1 in infiltrating glioma cells," *Brain Tumor Pathol.*, vol. 22, no. 2, pp. 89–91, 2005.

[50] C. Grunewald *et al.*, "On the applicability of [^{18}F]FBPA to predict L-BPA concentration after amino acid preloading in HuH-7 liver tumor model and the implication for liver boron neutron capture therapy," *Nucl. Med. Biol.*, vol. 44, pp. 83–89, 2017.

[51] W. Yang *et al.*, "Effects of L-DOPA pre-loading on the uptake of boronophenylalanine using the F98 glioma and B16 melanoma models," *Appl Radiat Isot*, vol. 88, pp. 69–73, 2014.

[52] Emory University, "The Cell Cycle | Cancer Quest," *Winship Cancer Institute*, 2017. [Online]. Available: https://www.cancerquest.org/index.php/cancer-biology/cell-cycle. [Accessed: 26-May-2018].

[53] R. C. Jackson, "The Problem of the Quiescent Cancer Cell," *Adv. Enzym. Regul*, vol. 29, no. 8, pp. 27–46, 1989.

[54] F. Yoshida *et al.*, "Cell cycle dependence of boron uptake from two boron compounds used for clinical neutron capture therapy," *Cancer Lett.*, vol. 187, no. 1–2, pp. 135–141, 2002.

[55] K. Ono *et al.*, "Radiobiological evidence suggesting heterogeneous microdistribution of boron compounds in tumors :its relation to quiescent cell population and tumor cure in neutron capture therapy," *Int. J. Radiat. Oncol. Biol. Phys.*, vol. 34, no. 5, pp. 1081–1086, 1996.

[56] K. Langen, H. Mühlensiepen, M. Holschbach, H. Hautzel, P. Jansen, and H. H. Coenen, "Transport Mechanisms of 3-[^{123}I]Iodo-a-Methyl-L-Tyrosine in a Human Glioma Cell Line : Comparison with [^{3}H-methy 1]-L-Methionine," *J. Nucl. Med.*, vol. 41, no. 7, pp. 1250–1255, 2000.

[57] M. Dahlström, J. Capala, P. Lindström, A. Wasteson, and A. Lindström, "Accumulation of boron in human malignant glioma cells in vitro is cell type dependent," *J. Neurooncol.*, vol. 68, no. 3, pp. 199–205, 2004.

[58] M. Carpano *et al.*, "Experimental studies of boronophenylalanine (^{10}BPA) biodistribution for the individual application of boron neutron capture therapy (BNCT) for malignant melanoma treatment," *Int. J. Radiat. Oncol. Biol. Phys.*, vol. 93, no. 2, pp. 344–352, 2015.

[59] H. De Wolde, J. Pruim, M. F. Mastik, J. Koudstaal, and W. M. Molenaar, “Proliferati ve Activity in Human Brain Tumors : Comparison of Histopathology and L-[1-^{11}C] Tyrosine PET,” *J. Nucl. Med.*, vol. 38, no. 9, pp. 1369–1374, 1997.

[60] T. Sasajima, T. Miyagawa, T. Oku, J. G. Gelovani, R. Finn, and R. Blasberg, “Proliferation-dependent changes in amino acid transport and glucose metabolism in glioma cell lines,” *Eur. J. Nucl. Med. Mol. Imaging*, vol. 31, no. 9, pp. 1244–1256, 2004.

[61] S. Chandra, W. Tjarks, D. R. Lorey, and R. F. Barth, “Quantitative subcellular imaging of boron compounds in individual mitotic and interphase human glioblastoma cells with imaging secondary ion mass spectrometry (SIMS),” *J. Microsc.*, vol. 229, no. 1, pp. 92–103, 2008.

[62] C. R. M. Grovenor *et al.*, “Specimen preparation for NanoSIMS analysis of biological materials,” *Appl. Surf. Sci.*, vol. 252, no. 19, pp. 6917–6924, 2006.

[63] S. Chandra, D. R. Smith, and G. H. Morrison, “Sub cellular image by dynamic SIMS ion microscop,” *Anal. Chem.*, pp. 104–114, 2000.

[64] M. S. Burns, “Applications of Secondary Ion Mass Spectrometry (SIMS) in biological research : a review,” *J. Microsc.*, vol. 127, pp. 237–258, 1982.

[65] K. H. Lau, M. Christlieb, M. Schröder, H. Sheldon, A. L. Harris, and C. R. M. Grovenor, “Development of a new bimodal imaging methodology : a combination of fluorescence microscopy and high-resolution secondary ion mass spectrometry,” *J. Microsc.*, vol. 240, pp. 21–31, 2010.

[66] P. L. Clode *et al.*, “In Situ Mapping of Nutrient Uptake in the Rhizosphere Using Nanoscale Secondary Ion Mass Spectrometry,” *Plant Phsiology*, vol. 151, no. 4, pp. 1751–1757, 2009.

[67] S. Behrens *et al.*, “Linking Microbial Phylogeny to Metabolic Activity at the Single-Cell Level by Using Enhanced Element Labeling-Catalyzed Reporter Deposition Fluorescence In Situ Hybridization (EL-FISH) and NanoSIMS,” *Appl. Environ. Microbiol.*, vol. 74, no. 10, pp. 3143–3150, 2008.

[68] P. L. Clode, R. A. Stern, and A. T. Marshall, “Subcellular Imaging of Isotopically Labeled Carbon Compounds in a Biological Sample by Ion Microprobe (NanoSIMS),” *Microsc. Res. Tech.*, vol. 70, no. 3, pp. 220–229, 2007.

[69] R. Peteranderl and C. Lechene, “Measure of carbon and nitrogen stable isotope ratios in cultured cells,” *J. Am. Soc. Mass Spectrom.*, vol. 15, no. 4, pp. 478–485, 2004.

[70] C. Lechene *et al.*, “High-resolution quantitative imaging of mammalian and bacterial cells using stable isotope mass spectrometry,” *J. Biol.*, vol. 5, pp. 1–30, 2006.

[71] R. Levi-Setti, “Structural and microanalytical imaging of biological materials by scanning microscopy with heavy-ion probes,” *Annu. Rev. Biophys. Biophys. Chem.*, vol. 17, pp. 325–347, 1988.

[72] N. Grignon, S. Halpern, A. Gojon, and P. Fragu, “^{14}N and ^{15}N imaging by SIMS microscopy in soybean leaves,” *Biol. Cell*, vol. 74, pp. 143–146, 1992.

[73] S. Chandra and G. H. Morrison, “Imaging Elemental Distribution and Ion Transport in Cultured Cells with Ion Microscopy,” *Science (80-.).*, vol. 228, pp. 1543–1544, 1985.

[74] W. A. Ausserer, Y. Ling, S. Chandra, and G. H. Morrison, “Quantitative Imaging of Boron, Calcium, Magnesium, Potassium, and Sodium Distributions in Cultured Cells with Ion Microscopy,” *Anal. Chem.*, vol. 61, pp. 2690–2695, 1989.

[75] D. R. Lorey, G. H. Morrison, and S. Chandra, “Dynamic secondary ion mass spectrometry analysis of boron from boron neutron capture therapy drugs in co-cultures: Single-cell imaging of two different cell types within the same ion microscopy field of imaging,” *Anal. Chem.*, vol. 73, no. 16, pp. 3947–3953, 2001.

[76] D. R. Smith, S. Chandra, R. F. Barth, W. Yang, D. D. Joel, and J. A. Coderre, “Quantitative imaging and microlocalization of boron-10 in brain tumors and infiltrating tumor cells by SIMS ion microscopy: Relevance to neutron capture therapy,” *Cancer Res.*, vol. 61, no. 22, pp. 8179–8187, 2001.

[77] S. Chandra, G. W. Kabalka, D. R. Lorey II, D. R. Smith, and J. A. Coderre, “Imaging of Fluorine and Boron from Fluorinated Boronophenylalanine in the Same Cell at Organelle Resolution by Correlative Ion Microscopy and Confocal Laser Scanning Microscopy,” *Clin. Cancer Res.*, vol. 8, pp. 2675–2683, 2002.

[78] S. Chandra, “Challenges of biological sample preparation for SIMS imaging of elements and molecules at subcellular resolution,” *Appl. Surf. Sci.*, vol. 255, pp. 1273–1284, 2008.

[79] S. Chandra, D. R. Lorey II, and D. R. Smith, “Quantitative Subcellular Secondary Ion Mass Spectrometry (SIMS) Imaging of Boron-10 and Boron-11 Isotopes in the Same Cell Delivered by Two Combined BNCT Drugs : In Vitro Studies on Human Glioblastoma T98G Cells,” *Radiat. Res.*, vol. 157, no. 6, pp. 700–710, 2002.

[80] K. Yokoyama *et al.*, “Analysis of boron distribution in vivo for boron neutron capture therapy using two different boron compounds by secondary ion mass spectrometry.,” *Radiat. Res.*, vol. 167, no. 1, pp. 102–109, 2007.

[81] H. F. Arlinghaus, C. Kriegeskotte, M. Fartmann, A. Wittig, W. Sauerwein, and D. Lipinsky, “Mass spectrometric characterization of elements and molecules in cell cultures and tissues,” *Appl. Surf. Sci.*, vol. 252, pp. 6941–6948, 2006.

[82] A. Wittig *et al.*, “Laser postionization secondary neutral mass spectrometry in tissue : a powerful tool for elemental and molecular imaging in the development of targeted drugs,” *Am. Assoc. Cancer Res.*, vol. 7, pp. 1763–1772, 2008.

[83] H. F. Arlinghaus, M. T. Spaar, R. C. Switzer, and G. W. Kabalka, “Imaging of Boron in Tissue at the Cellular Level for Boron Neutron Capture Therapy,” *Anal. Chem.*, vol. 69, no. 16, pp. 3169–3176, 1997.

[84] M. Fartmann, C. Kriegeskotte, S. Dambach, A. Wittig, W. Sauerwein, and H. F. Arlinghaus, “Quantitative imaging of atomic and molecular species in cancer cell cultures with TOF-SIMS and Laser-SNMS,” *Appl. Surf. Sci.*, vol. 231, no. 232, pp. 428–431, 2004.

[85] G. W. Kabalka *et al.*, “Boronated unnatural cyclic amino acids as potential delivery agents for neutron capture therapy,” *Appl. Radiat. Isot.*, vol. 69, no. 12, pp. 1778–1781, 2011.

[86] A. A. Gulin, M. S. Pavlyukov, S. K. Gularyan, and V. A. Nadtochenko, “Visualization of the Spatial Distribution of Pt^{+} Ions in Cisplatin-Treated Glioblastoma Cells by Time-of-Flight Secondary Ion Mass Spectrometry,” *Biol. Membr.*, vol. 32, no. 3, pp.

202–210, 2015.

[87] S. Chandra, “Quantitative Imaging of Chemical Composition in Single Cells by Secondary Ion Mass Spectrometry : Cisplatin Affects Calcium Stores in Renal Epithelial Cells,” in *Mass Spectrometry Imaging-Principles and Protocols*, New York: Springer science, 2010, pp. 113–130.

[88] A. A. Legin *et al.*, “NanoSIMS combined with fluorescence microscopy as a tool for subcellular imaging of isotopically labeled platinum-based anticancer drugs,” *Chem. Sci.*, vol. 5, no. 8, pp. 3135–3143, 2014.

[89] L. E. Wedlock, M. R. Kilburn, J. B. Cliff, L. Filgueira, M. Saunders, and S. J. Berners-Price, “Visualising gold inside tumour cells following treatment with an antitumour gold(I) complex,” *Metallomics*, vol. 3, no. 9, pp. 917–925, 2011.

[90] L. E. Wedlock, M. R. Kilburn, R. Liu, J. A. Shaw, S. J. Berners-Price, and N. P. Farrell, “NanoSIMS multi-element imaging reveals internalisation and nucleolar targeting for a highly-charged polynuclear platinum compound,” *Chem. Commun.*, vol. 49, pp. 6944–6947, 2013.

[91] M. T. Proetto *et al.*, “Tumor Retention of Enzyme-Responsive Pt (II) Drug-Loaded Nanoparticles Imaged by Nanoscale Secondary Ion Mass Spectrometry and Fluorescence Microscopy,” *ACS Cent. Sci.*, vol. 4, pp. 1477–1484, 2018.

[92] K. Downard, “The Mass Spectrometer,” in *Mass Spectrometry: A Foundation Course*, Sydney: The Royal Society of Chemistry, 2004, p. 61.

[93] J.-L. Guerquin-Kern, T. Wu, C. Quintana, and A. Croisy, “Progress in analytical imaging of the cell by dynamic secondary ion mass spectrometry (SIMS microscopy),” *Biochim. Biophys. Acta*, vol. 1724, pp. 228–238, 2005.

[94] R. Cooke and I. D. Kuntz, “The Properties of Water in Biological Systems,” *Annu. Rev. Biophys. Bioeng.*, vol. 3, no. 1, pp. 95–126, 1974.

[95] P. Mentré, “Preservation of the diffusible cations for SIMS microscopy. I. A problem related to the state of water in the cell,” *Bio. Cell*, vol. 74, pp. 19–30, 1992.

[96] N. Winograd and A. Bloom, “Sample Preparation for 3D SIMS Chemical Imaging of Cells,” *Methods Mol Biol*, vol. 1203, pp. 9–19, 2015.

[97] J. S. Fletcher, S. Rabbani, A. M. Barber, N. P. Lockyer, and J. C. Vickerman, “Comparison of C_{60} and GCIB primary ion beams for the analysis of cancer cells and tumour sections,” *Surf. Interface Anal.*, vol. 45, no. 1, pp. 273–276, 2013.

[98] D. Touboul, S. Roy, D. P. Germain, P. Chaminade, A. Brunelle, and O. Laprévote, “MALDI-TOF and cluster-TOF-SIMS imaging of Fabry disease biomarkers,” *Int. J. Mass Spectrom.*, vol. 260, no. 2–3, pp. 158–165, 2007.

[99] N. Tahallah, A. Brunelle, S. De La Porte, and O. Laprévote, “Lipid mapping in human dystrophic muscle by cluster-time-of-flight secondary ion mass spectrometry imaging,” *J. Lipid Res.*, vol. 49, no. 2, pp. 438–454, 2008.

[100] P. Sjövall, M. Rossmeisl, J. Hanrieder, O. Kuda, J. Kopecky, and M. Bryhn, “Dietary uptake of omega-3 fatty acids in mouse tissue studied by time-of-flight secondary ion mass spectrometry (TOF-SIMS),” *Anal. Bioanal. Chem.*, vol. 407, no. 17, pp. 5101–5111, 2015.

[101] A. M. Piwowar and N. Winograd, “Application of SIMS to study of biological system,” in *TOF-SIMS: Materials analysis by mass spectrometry*, 2nd ed., J. C. and D. B. Vickerman, Ed. IM Publications, 2013, pp. 561–565.

[102] S. Chandra, “Challenges of biological sample preparation for SIMS imaging of elements and molecules at subcellular resolution,” *Appl. Surf. Sci.*, vol. 255, no. 4, pp. 1273–1284, 2008.

[103] C. Dérue, D. Gibouin, F. Lefebvre, D. Studer, M. Thellier, and C. Ripoll, “Relative sensitivity factors of inorganic cations in frozen-hydrated standards in secondary ion MS analysis,” *Anal. Chem.*, vol. 78, no. 8, pp. 2471–2477, 2006.

[104] R. Metzner, H. U. Schneider, U. Breuer, and W. H. Schroeder, “Imaging Nutrient Distributions in Plant Tissue Using Time-of-Flight Secondary Ion Mass Spectrometry and Scanning Electron Microscopy,” *Plant Physiol.*, vol. 147, no. 4, pp. 1774–1787, 2008.

[105] J. C. Vickerman and N. Winograd, “Cluster TOF-SIMS imaging and the Cterization of Biological Materials,” in *Cluster Secondary ion mass spectrometry : Principles and Applications*, Canada: John Wiley & Sons Inc, 2013, pp. 273–274.

[106] S. Chandra and G. H. Morrison, “Evaluation of fracture planes and cell morphology in complementary fractures of cultured cells in the frozen-hydrated state by field-emission secondary electron microscopy: Feasibility for ion localization and fluorescence imaging studies,” *J. Microsc.*, vol. 186, no. 3, pp. 232–245, 1997.

[107] S. Chandra and D. R. Lorey, “SIMS ion microscopy imaging of boronophenylalanine (BPA) and $^{13}C^{15}N$-labeled phenylalanine in human glioblastoma cells: Relevance of subcellular scale observations to BPA-mediated boron neutron capture therapy of cancer,” *Int. J. Mass Spectrom.*, vol. 260, no. 2–3, pp. 90–101, 2007.

[108] P. Sjövall, J. Lausmaa, H. Nygren, L. Carlsson, and P. Malmberg, “Imaging of Memabrane Lipids in Single Cells by Imprint-Imaging Time-of-Flight Secondary Ion Mass Spectrometry,” *Anal Chem*, vol. 75, no. 14, pp. 3429–3434, 2003.

[109] H. Nygren *et al.*, “A cell preparation method allowing subcellular localization of cholesterol and phosphocholine with imaging TOF-SIMS,” *Colloids Surfaces B Biointerfaces*, vol. 30, no. 1–2, pp. 87–92, 2003.

[110] P. Sjövall, B. Johansson, and J. Lausmaa, “Localization of lipids in freeze-dried mouse brain sections by imaging TOF-SIMS,” *Appl. Surf. Sci.*, vol. 252, no. 19, pp. 6966–6974, 2006.

[111] S. Chandra and G. H. Morrison, “Sample preparation of animal tissues and cell cultures for secondary ion mass spectrometry (SIMS) microscopy,” *Biol Cell*, vol. 74, no. 1, pp. 31–42, 1992.

[112] K. L. Moore, M. Schröder, and C. R. M. Grovenor, “Imaging secondary ion mass spectrometry,” in *Handb. Nanoscopy*, Weinheim:Wiley- VCH, 2012, pp. 709–744.

[113] J. Malm, D. Giannaras, M. O. Riehle, N. Gadegaard, and P. Sjövall, “Fixation and drying protocols for the preparation of cell samples for time-of-flight secondary ion mass spectrometry analysis,” *Anal. Chem.*, vol. 81, no. 17, pp. 7197–7205, 2009.

3 Experimental Methods and Preliminary experiments

3.1 Introduction

This chapter describes the preliminary experiments that were conducted to determine the appropriate analytical conditions for the methodology used in the analysis of biological samples in Chapters 4 and 5 with both NanoSIMS and BioToF instruments. Sample preparation for all the samples used in this thesis and the data processing for both instruments are also discussed.

3.2 Sample preparation

3.2.1 Standard solutions

A set of ^{11}BPA standards (Sigma Aldrich, UK) were prepared in 125 mM trehalose dehydrate solution (Sigma Aldrich, UK) at the following concentrations: 1, 10, 30, 50,100, 300, 500, 1000 ppm. The BPA used for standard solutions was commercially available at low cost and contains 20% ^{10}B and 80% ^{11}B. This is different from the ^{10}B-labelled BPA (see **Table 2.1**) used in clinical treatment and preparation of the real samples in section 3.2.2, which is very expensive. Trehalose was used as a matrix to mimic tissue in the standard solutions. 100 µl from each BPA concentration was deposited individually onto 5×5 mm^2 silicon wafers (IDB Technologies Ltd., UK) using a spin coater device (Laurell Technologies Corporation, USA) at a speed of 5900 rpm for 2 minutes. Silicon wafers were cleaned before use in hexane, methanol, then H_2O (HPLC) for 15 minutes in ultra-sonication, respectively, then were rinsed with deionized water and dried under clean compressed air, (all these solvents from Sigma Aldrich, UK). The samples were then transferred for SIMS analysis.

3.2.2 Biological samples

All biological samples were provided from the Molecular Neuro-oncology Laboratory in the Queen Elizabeth Neuroscience Centre, The University of Birmingham - UK. These samples were prepared in order to study the pharmacokinetics of 10-Boron Phenylalanine (BPA) in clinical trials with patients that have a high degree of brain tumours to optimize uptake parameters for Boron Neutron Capture Therapy (BNCT), reference LREC no. 05/Q2704/61.

3.2.2.1 Primary cell cultures

The cell cultures were prepared in six stages as described below to ensure the removal of any contamination or other cell types such as blood cells, fibroblast cells, stromal cells and glial cells [1].

1-Tissue harvesting: From the operating theatre, fresh unfixed brain tumour (GBM) and brain-around-tumour (BAT) tissues were collected from patients undergoing craniotomies. Around 1 cm^3 of tumour tissue (and a lesser amount of BAT tissue) was placed promptly in ice-cold medium dedicated for tissue. The collection medium contains: 100 µg/ml gentamicin, 200 µg/ml streptomycin, Ham's F12 medium complemented with 20 mM HEPES buffer, 2.5 µg/ml Fungizone and 200 U/ml penicillin (all from ThermoFisher, UK). The remaining tissue parts were kept routinely in formal-saline to use them in other diagnostic and histopathological studies. This harvesting was done according to the ethical guidelines for research and development in the hospital at the Birmingham Institute [2].

2-Tissue dispersion: Within an hour of harvesting, the remaining blood in tissue was washed three times with ice-cold HBSS, and any blood clots were peeled off. The tissue was divided into slices of about 1 mm^3 size using crossed scalpels, and then washed again with ice-cold HBSS. After washing the slices were re-suspended in 30 mL of HBSS and exposed to digestion at 37 °C and 4 °C respectively for 30 min in the following enzymes mixture: 0.25 mg/ml collagenase (Invitrogen, Life Technologies), 0.4 mg/ml DNase, and 0.5 mg/ml pronase (both from Sigma Aldrich, UK). The slices were filtered from the enzyme mixture to remove undigested materials using nylon mesh (100 µm pore) and then were placed upon 2 × 12 ml of Ficoll-paque intensity gradient media (Amersham Pharmacia, UK). Centrifugation was performed for 30 min at 400 g at room temperature resulting in dispersion and separation of tumour cells on the surface, while the red blood cells were sedimented at the bottom of tube. Finally, HBSS was used to wash the cells once and then they were re-suspended in the same solution for viability test [2]. This method of dispersing tissue was modified from the original one by Farr-Jones *et al.* [3].

3- Viability: Dispersed cells showed high degrees of viability، this was verified using the Trypan blue exclusion method [4].

4- Cell plating: The following medium was used for seeding tissue biopsies and forming cultures: 2×10^5 /cm^2 in 1:1 of DMEM/F12 (Invitrogen, Life Technologies) complemented with 10% pooled human plasma (Patricell Ltd, UK), 2 mM of L-glutamine, 0.05 mM of non-essential amino acids, 100 µM of sodium pyruvate (all from Invitrogen, Life Technologies), 2.5 µg/ml of Fungizone, 100 U/ml of penicillin and 100 µg/ml of streptomycin onto 5 × 7 mm^2 sterile silicon wafers placed in 12-well plates in duplicates, then incubated overnight with 99% humidity and 5% CO_2 at 37 °C. The next day, the medium was renewed after the unattached cells removed by aspiration method. Cells were left to grow for 7 days and then transferred to the treatment step [2].

5- Cell treatment: There were 4 different biopsies: 2 of GBM tumour (A & B) and 2 of BAT tissue (C & D) respectively; and 4 treatment groups for B and D biopsies:

1. Control (no drugs).
2. 10 mM ^{10}BPA-mannitol for 4 h (^{10}BPA-mannitol was gifted from Cancer Research, UK).
3. 10 mM Tyrosine-mannitol for 4 h (Sigma Aldrich, UK) followed by a wash and then 4 h incubation with 10 mM ^{10}BPA-mannitol.
4. 4 h ^{10}BPA-mannitol (10 mM) followed by 4 h efflux.

For the remainder of the thesis ^{10}BPA-mannitol will be referred to as ^{10}BPA.

For the A and C biopsies, there was only one sample from each type without treatment (1=control). After treatment the silicon wafers were washed with ice-cold physiological pH saline and were immediately flash-frozen in isopentane/liquid nitrogen and stored at -80 °C until analysis [2].

6- Preparing for SIMS analysis: Prior to analysis with SIMS the samples were prepared by freeze-drying at Manchester. Samples were transferred to the surface analysis research lab in a solid carbon dioxide ice basin at -78 °C, then mounted on a pre-cooled copper stub under N_2 gas flow and left in a vacuum chamber overnight and under a pressure of 1×10^{-8} mbar. After 24 hours, the samples were ready for SIMS analysis.

3.2.2.2 Biopsies imprints

Patients received the pharmacological doses of ^{10}BPA *in vivo*, the amount of these doses was not disclosed for patient confidentiality. During 1- 2 hours of infusion ^{10}BPA doses into the patient's body, the tissue biopsies were harvested from the operating theatre in the manner described in section 3.2.2.1 according to the ethical guidelines for research and development in the Birmingham hospital [2]. Bulk ^{10}B concentrations in biopsies were measured using ICP-MS.

Harvested biopsies of GBM tumour and BAT tissue were cut into $5\times5\times1$ mm^3 sections. The sections were then washed with ice-cold physiological saline, blotted dry, and pressed onto 5×7 mm^2 sterile silicon wafers to leave an imprint of the cut surface on the wafer. Silicon wafers were promptly flash-frozen in isopentane/liquid nitrogen and stored at -80 °C until analysis time [5]. Prior to analysis with SIMS, the samples were prepared by freeze-drying as described in section 3.2.2.1 in the surface analysis research lab in the University of Manchester.

The preparation this type of primary samples, biopsies imprints, in the operating theatre immediately after removal from patients has placed considerable restrictions on the selected method for sample preparation. Neither the cryo-sectioning [6] nor the freeze-fracturing [7] methods were possible to use as they required relatively long procedures not available in the operating theatre. The freeze-fracturing method is more common with cell lines where the conditions of sample preparation can be controlled, as Chandra *et al.* [8][9] have done in many studies as well as Zha *et al.* [10]. The chemical fixation method also was not a suitable solution for samples preparation because it can cause the redistribution of ions and small molecules from their *in vivo* sites as demonstrated by Malm *et al.* [11] and other studies [12]–[14]. Thus, an imprint method was the appropriate quick option to prepare the samples for this study. An imprint method on a metal surface can be effective in increasing ion yields and the sensitivity of measurement, as indicated by Sjövall *et al.* [15] and Nygren *et al.* [16]. Since the study aimed to determine the distribution of boron in primary samples, the imprint steps included rapid freezing to ensure that the components of the samples are kept in place. All preparation methods mentioned above have been reviewed with more detail in section 2.4.

In addition, one sample of biopsy imprint was coated with 10 nm platinum to increase the electrical conduction of the sample and verify the effectiveness of the coating before making the decision whether or not to cover the rest of the samples, more details in section 5.2.3.1.3.

During SIMS analysis of the primary cell cultures, very few artefacts were observed, any that were present will be discussed during interpretation of the images in Chapter 4. The artefacts are related to deposits on the cell surface, freezing damage and elemental redistribution due to freeze-drying.

For imprints of biopsies, optical microscopy images, for example **Figure 3.1**, showed that they are not completely flat, some areas appear thicker or rougher compared to others. This may be because the imprints have various levels from transferred material such as other cell types and/or some blood clots, which necessitated avoiding some of these areas during the analysis so as not to affect the signal intensity and image contrast. Further detail on the morphology of the samples and their artefacts of cracks and necrosis is given in section 5.2.3.1. The nature of the samples also added other obstacles that were inferred during the SIMS analysis of the samples and are presented in 5.2.3.2.

In both types of samples, freeze-drying may change morphology and may lead to cell shrinkage, but it is still possible to identify the nucleus versus cytoplasm in cell cultures and

whole cells in tissue imprints. Other cellular components will not be interpreted, and no interpretation will be given on cell size or shape. Only the chemical distribution between cell compartments and cellular level will be explained. Each type of samples is treated similarly, and interpretation is based on the difference between these samples in each chapter separately.

Scanning electron microscope (SEM) imaging can be conducted before SIMS imaging to identify areas containing cells, but when conducting NanoSIMS analysis, it may be found that these areas do not contain any boron or the SEM electron beam has caused redistribution of the most mobile ions such as Na and K.

Based on the above observations, there was no other viable option for sample preparation so it was necessary to try to find well-preserved areas suitable for analysis as best as possible. The primary cell cultures treated *in vitro* were used as a model system to help interpret the more heterogeneous tissue biopsy samples. Furthermore, SIMS analysis for samples similar in type and preparation had not previously been conducted, making this a novel study.

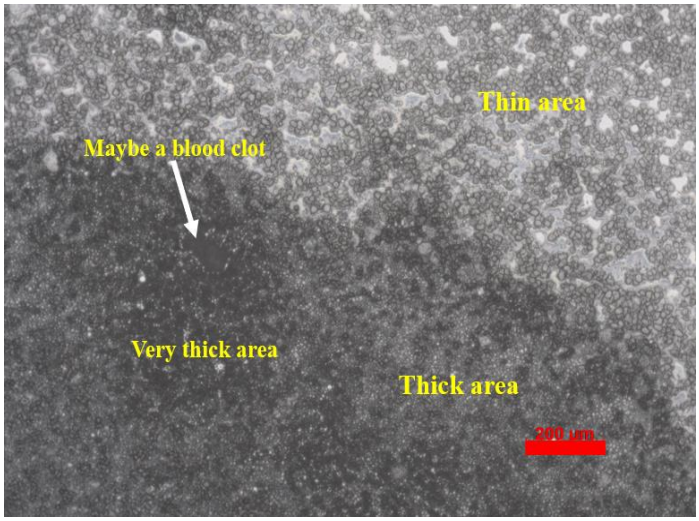

Figure 3.1: Optical microscope image captured from one of biopsy imprints showing the general morphology of the sample in terms of thickness, and that the sample surface not completely flat. Scale bar = 200 µm.

3.3 Optical Microscopy

Biopsy imprint samples were imaged using a reflective light microscope before loading them into the SIMS instruments to identify appropriate regions for SIMS analysis in terms of a thin or thick area and to avoid areas which have more topography. Two types of light microscope were used: the Zeiss Lab. A1 microscope equipped with an AxioCam ERc 5s camera and connected to AxioVision SE64 Rel.4.9 software - edition 2012; and a KEYENCE- VHX-5000 Digital Microscope.

3.4 Investigations with NanoSIMS

3.4.1 Data acquisition

At the beginning of each NanoSIMS session, the instrument must be fully tuned for this experiment, as described below.

Each analysis session starts by measuring the Cs^+ current intensity from the source (FCp), and the current that actually reaches the sample (FCo) with all D1 aperture sizes. The D1 aperture is used to select the size of the primary ion beam to achieve the required spatial resolution, whereby it is possible, with D1 = 5 and with L1>7000 V, to obtain the highest spatial resolution (50 nm). An example of D1 values from one of the experiments is shown in **Table 3.1**.

The detector trolleys are then aligned to the sites of the required masses. The magnetic field is then adjusted to find the highest counts of each mass using suitable standards and then fixed and verified using a high mass resolution (HMR) scan. Secondary ion extraction optics (P2, P3, Cy and EOS) are also aligned and tuned to achieve the maximum transmission of signals on each region of interest. The ES and AS slits are used to shape the secondary ion beam further, improve mass resolving power and give flat top peaks (necessary for long term stability of the measurement).

Regions of interest (ROI) were selected using a charge-coupled device (CCD) which generates optical images of the sample surface. The focus of the image in the CCD camera was optimized by moving the stage in Z, this also optimises sample position for the extraction of the secondary ions. The ROI was implanted with a defocused Cs^+ beam with D1 = 0 (in which the aperture is completely removed) and a high L1 value to increase the primary beam current; the dose required (Equation 3.1) for the sample to reach steady state was added to the ROI (more details in 3.6.1 and 3.6.2.3). The implantation process was

carried out on a larger raster than those specified for analysis in order to avoid the influence of a crater edge during imaging.

Dose per image plane is calculated using Equation 3.1 [17][18]:

$$Dose\ (ions.cm^{-2}) = \frac{Time(s) \times current(A)}{area(cm^2)\ \times 1.6 \times 10^{-19}} \qquad \text{Equation 3.1}$$

After implantation, the NanoSIMS was reverted to the normal mode of data acquisition (L1 = 0 V) and the D1 aperture was changed to a smaller probe size (D1 = 2) for all the experiments. The P2, P3 and Cy deflector plates and EOS lens were checked again and modified for the sample if needed. Then HMR scans for all trolleys were checked again on the sample by comparison with HMR scans obtained from the standards.

Image clarity was improved by refocusing the primary ion beam using the EOP lens and adjusting the astigmatism. The secondary ion images were then acquired in a series of successive planes (depth profiling). In addition, a secondary electron (SE) detector is used to show the topography of the sample surface; the ion-induced secondary electrons can be mapped simultaneously with the secondary ions. Image acquisition took from 3 to 20 hours or more (overnight), depending on the size of the area under study (raster) and the dwell times of the primary ion beam (1000 or 2000 µs/px).

Table 3.1: Different sizes of D1 aperture with the currents measured from one of the experimental sessions.

Aperture position	**D1 diameter (µm)**	**FCo Cs^+ current (pA)**
D1 = 0	-	100
D1 = 1	750	14
D1 = 2	300	2.3
D1 = 3	200	1.2
D1 = 4	150	0.6
D1 = 5	100	0.3

3.4.2 NanoSIMS data processing

Image processing was performed using Fiji (an updated version of ImageJ 1.51a-Rasband, activated in 2015) with the OpenMIMS (multi-isotope imaging mass spectrometry) v2.5 plugin from the National Resource for imaging Mass Spectrometry (NRIMS) Analysis-Harvard. Image processing included aligning planes, data summing, selecting the ROIs, measuring ion intensities, statistical processing, and adding the scale and calibration bars.

Depth profiling curves were extracted using both Fiji and Excel software. Data (the quantification and the graphs) were managed using Microsoft Excel and OriginPro Lab software, the signals of interest extracted from the areas defined on the images were normalised to the highest intensity ions and the most homogenously distributed across the samples in images. These ratios of each sample (including several areas) were presented separately in box plots showing the mean, median, the interquartile range, and the maximum and minimum values of the signals.

In the quantitative measurement of isotopes, the isotope ratios were calculated in each sample separately (includes several areas) and were presented in box plots. The mean and the SD values were then calculated from the set of ratios represented for each sample.

It was decided not to do a full t-test (P- probability value) on the data for two reasons. The first is because of the relatively small number of areas that were run for each sample, the inability to run enough samples due to the nature of the experiment and difficulty to acquire the data. The second reason is that the cells may be in different phases of the cell cycle, which may cause the cells to differ in the uptake of the treatment, thus cause a wide spread in the data. This spread in the data and the small size of the sample conflicts with the criteria for t-test [19][20].

3.5 Investigations with BioToF-SIMS

3.5.1 Data acquisition

In this project, the LMIG was run to generate a Au^+ primary ion beam, the latter being directed to the samples by an extraction system in the LMIG gun column that is described in [21][22]. The BioToF-SIMS instrument is tuned to analyse samples by three controllers. An independent control unit (from Ionoptika Ltd) associated with the ion gun, which is, in turn, connected to a computer. The benefit of this unit is that it improves the performance of the ion gun by controlling and monitoring its operational parameters such as lenses to focus the primary ion beam; X and Y alignment to correct any deviation from the beam path; Wien

filter (WF) to select the *m/z* ratio required for the primary ions of choice (Au^+) and stigmator deflectors to improve the shape of ion beam [23]. At the beginning of each lab session, the primary ion beam current arriving at the sample stub is measured using a picoameter (Keithly- Tektronix UK Ltd.).

In addition, the raster controller unit is used to select the field of view (FoV) required for analysis, not exceeding $2700 \times 2700\ \mu m^2$, and to adjust the position of the ion beam rastering in directions X and Y to ensure its presence within the optical gate area. The optical gate refers to the position in which the analysed area, ToF mass analyser, and ion detector FoV are compatible with each other. Due to the non-normal incidence of the primary beam, the sample height affects the position of the optical gate; therefore, when moving from one sample to another, the raster area should be checked or the sample stage height adjusted along the Z-axis. Furthermore, the raster controller unit enables the running of two modes: a TV mode, in which the beam is rastered automatically in the specific FoV to produce the spectrum, and an EXTERNAL mode which is used for imaging applications (spectrum and image).

Secondary ion acquisition and extraction is controlled by a digital delay generator (BNC 700, Berkley Nucleonics Corporation, USA). This unit allows the timing to be changed in four channels for each experimental cycle. Using the C channel, it is possible to control the trigger timing of the primary ion gun, which is associated with the pulser unit and thus defines the pulse width of the primary ion beam. Channel B represents the extraction pulse in the sample stage after bombardment, and an extraction potential of +2500 V when the SIMS is run in the positive ion mode and -2500 V in the negative ion mode. The delay for the B and C channels is determined by monitoring the mass spectra in real time before starting analysis; the delay time is kept constant throughout the experiment to ensure that mass calibration is not changed in the spectra. In the non-delayed extraction mode, the primary ion pulse width will determine the mass resolution. Channel D is used to set the pulse in the electron flood gun when needed for charge compensation and to neutralize the charged sample that is affected by the primary ion beam [24]. Finally, Channel A is used when ion suppression is required *e.g.* for post-ionization mode.

In the *delayed extraction mode,* a voltage pulse is applied on the sample stage to compensate the variation in ion formation time during a long primary ion beam pulse. The extraction potential (+ 2500 V) is applied a few ns after the end of the primary ion impact, accelerating all secondary ions into the ToF extraction lens during the rise time of this extraction pulse (~5 ns). The extraction lens potential is usually set at - 4300 V and ensures efficient

collection of secondary ions into the ToF analyser [25][26]. In this research, the B and C channels were both tuned, while there was no need to use an electron flood gun or ion suppression.

Moreover, the software interface on the host computer allows some instrument parameters and data acquisition to be managed within a large set of commands, such as:

- Selecting the desired ion mode as positive or negative. In this work, BioToF-SIMS analysis was acquired in the positive ion mode only.

- Adjusting the voltages in high voltage supply units depending on the ion mode selected for detection. **Table 3.2** summarizes the values used for the voltages in the positive ion mode.

- Determining the acquisition range of mass which is to be measured.
- Choosing the desired analysis process type as imaging or depth profiling.
- Selecting the experimental conditions, such as the number of pixels, repetitions and summing the results of the layers.
- The possibility of calibrating the spectra as well as processing images resulting from the analysis.

Table 3.2: Summary of the operational voltages during BioToF-SIMS analysis in the positive ion mode.

Component voltage	Source	Voltage value (V)
Reflect	ToF mass analyser	~+2540
Retard	ToF mass analyser	~+1100
Extraction lens	Lens between analyser and sample stage	-4300
Stage (+ve)	Channel B in BNC unit	+2500
Stage (-ve)	Channel A in BNC unit	0

3.5.2 BioToF-SIMS data processing

In this research, the resulting total spectra and image were processed using in-house BioToF software. The region of interest (ROI) in an image was first identified to obtain the spectrum, then the ions of interest (peak areas) were selected to create an image of each ion separately. In some images, the Fiji software (more information is provided in 3.4.2) was used only to illustrate the identification of the ROI. The spectra were plotted using OriginPro Lab 2015-

2017. Data was managed by OriginPro Lab and Microsoft Excel software, as explained in 3.4.2.

3.6 Preliminary NanoSIMS experiments

3.6.1 Experimental section

First stage: The sensitivity of the instrument with 16 keV (+8 kV on source, -8 kV on sample) Cs^+ beam was investigated on 100 and 1000 ppm ^{11}BPA standards. The mass detectors were set to detect the following negative secondary ions ^{10}B, $^{10}B^{12}C$, $^{10}B^{14}N$, $^{10}B^{16}O$, $^{10}B^{16}O^{1}H$, ^{30}Si and $^{10}B^{16}O_2$ simultaneously. It was ascertained that there were no mass interferences between the ions by calibrating the peak locations using a reference standard for each ion, then checked by HMR scans using similar way to that explained in 3.4.1 and 3.6.2.2 The analysis area was determined using the CCD camera. The samples were implanted using a Cs^+ dose of 1×10^{17} ions/cm^2 with D1 = 2 and a FoV 20×20 µm^2. Data were then acquired using NanoSIMS depth-profiling software by adding a total dose of 7×10^{17} ions/cm^2 of Cs^+ with D1 = 1 and a beam current of 9.4 pA to 10×10 µm^2 FoV with 256×256 pixels, the dwell time was 1000 µs/pixel. The resulting intensities were normalised to beam current to make the comparison possible between the two concentrations. Depth profiling curves were extracted using Microsoft Excel.

The sensitivity of ^{10}B from ^{11}BPA to the type of primary ion beam used was also investigated by analysing the 1000 ppm ^{11}BPA standard with a 16 keV O^- beam from a duoplasmatron ion source, more detail about this source is given in [27][28]. The mass detectors were adjusted to detect the following positive secondary ions ^{10}B, ^{11}B, $^{11}B^{1}H$, $^{11}B_2$, $^{11}B^{12}C$, $^{11}B^{12}C^{1}H$ and ^{30}Si simultaneously. Ion peak locations were verified using HMR scans and the analysis area was determined using the CCD camera. Depth profiling was then performed with D = 1 and a total dose 5×10^{17} ions/cm^2 and a beam current of 182 pA, rastered on a 10×10 µm^2 FOV of sample. The data was processed and extracted as mentioned above with a Cs^+ beam. The ion yields of ^{10}B with both sources were then compared.

The second stage (1st step): at the beginning of each NanoSIMS session, after measuring the current of the Cs^+ beam with all D1 apertures, the 7 detectors were set to detect the following ion species in cell cultures: $^{10}B^-$, $^{12}C^-$, $^{10}B^{12}C^-$, $^{12}C^{14}N^-$, $^{29}Si^-$, $^{31}P^-$ and $^{32}S^-$ respectively. In biopsy imprint samples the position of the seven detectors was tuned to detect the following secondary ions: $^{10}B^-$, $^{10}B^{12}C^-$, $^{12}C^{14}N^-$, $^{29}Si^-$, $^{31}P^-$, $^{32}S^-$ and $^{10}B^{16}O_2^-$. For some imprint samples: $^{10}B^{14}N^-$ or $^{12}C^-$ were tuned instead of $^{10}B^{16}O_2^-$. A range of B-

containing secondary ions previously studied by SIMS were investigated to determine the highest signal intensity which did not have mass interferences. The mass spectrometer tuning was verified using HMR scans on appropriate standards as well as on the sample under study with a 16 keV Cs^+ beam, DI = 1 and FoV 10×10 μm^2, more details about setting the instrument and HMR scanning are explained in section 3.4.1. The standard materials used to generate HMR scans are: solid pure nature isotopic ratio boron to calibrate B ions species (as well as ^{32}S and ^{12}C from the surface); silicon wafer for ^{29}Si and $^{12}C^{14}N$; solid gallium phosphide for ^{31}P.

The second stage (2nd step): depth profiling was performed using the NanoSIMS imaging software in three samples of cell cultures: B2, D2 and B3 in order to determine the dose required to achieve the maximum ion signal intensity before the cells were sputtered away. In each sample, one cell was selected using the built-in CCD camera and analysed without exposing it to any implantation dose so that the ion signals could be monitored from the top surface. The beam was focused on an adjacent cell before moving to the target cell for the depth profiling process. The 16 keV Cs^+ beam was rastered over 40×40 μm^2 area in B2 and D2, and 25×25 μm^2 in B3. Primary ion beam current in FCo with D1 = 1 was 29.5 pA for B2 and D2 and 13.9 pA for B3 (experiments conducted on different days). All analyses were conducted with a dwell time of 1000 µs per pixel and an image resolution of 128×128 pixel. The intensity of the negative ions from ^{10}B, ^{12}C, $^{10}B^{12}C$, $^{12}C^{14}N$, ^{29}Si, ^{31}P and ^{32}S were extracted from regions of interest within the scanned cell and measured as a function of depth. 1000 image layers (planes) were acquired for the B2 and D2 samples and 250 layers for the B3 sample. This depth profiling was performed only once before starting the analysis of the samples but it allowed determination of the appropriate Cs^+ beam dose required for implantation in cells and showed how the cells were sputtered.

For the biopsy imprints, depth profiling was not conducted, and a standard implantation dose (1×10^{17} ions/cm^2) for biological tissue samples was used [29][30].

3.6.2 NanoSIMS Results and Discussion

3.6.2.1 Sensitivity - first stage

Numerous studies have shown the high sensitivity of NanoSIMS in detecting concentrations down to the ppb level and distinguishing between ions of almost equal mass such as $^{13}C^-$and $^{12}C^1H^-$ [31]–[33]. In this regard, NanoSIMS sensitivity with Cs^+ beam was checked on 1000 and 100 ppm from BPA as described in 3.6.1.

Figure 3.2 shows the depth profiling curve of the intensity of the secondary ions mentioned in 3.6.1 (first stage) as a function of sputter time (s) for both concentrations. **Figure 3.2 -a** shows that the secondary ion yields of 1000 ppm increased with time and reached a stable plateau at 1800 sec except for the Si signal which continued to increase as a result of the continuous sputtering process, the curve also showed the intensity obtained for each ion. The same trend was observed in the profiled 100 ppm of BPA (**Figure 3.2 -b**), but the plateau began at a time of 2700 sec with lower ion yields than that resulted in **Figure 3.2 -a**. **Figure 3.2** also shows that BC^- signals are 6 times more intense than B^- signals for both concentrations, for that reason BC^- was used as additional indication of the boron distribution in the cells during imaging. Both B^- and BC^- signals in the 1000 ppm standard are ~ 10 times higher than 100 ppm, so it is expected that the10 ppm should be detectable with NanoSIMS especially with the BC^- signal and maybe with the B^- signal because depth profiling in **Figure 3.2** showed a clear step above noise when the sample was sputtered. These results show the sensitivity of NanoSIMS with Cs^+ beam as well as the stability of the measurement and homogeneity of the standard. It should be noted that the negative ions $^{10}B^{14}N$, $^{10}B^{16}O$, $^{10}B^{16}O^1H$ and $^{10}B^{16}O_2$ were not detected in the real samples due to their absence, low intensity or presence of mass interferences in the samples, so these ions are not mentioned when presenting HMR scans.

The analysis of the 1000 ppm ^{11}BPA standard using an O^- beam (**Figure 3.3**) did not record any intensities for $^{11}B^1H^+$ and $^{11}B^{12}C^1H^+$, and did not provide high secondary yields for other selected ions mentioned in 3.6.1, especially $^{10}B^+$, compared to those resulting from using Cs^+ beam in the analysis (**Figure 3.2 -a**).

To achieve the aim of the thesis with NanoSIMS: boron can be verified using both Cs^+ (to generate negative ions) and O^- (to generate positive ions). However, the ionization energy of boron is high, which means that the sensitivity when detecting boron as a positive ion will not be very good [34][35]. Furthermore, there are many ways B can be detected as a negative ion [36]–[38]. In addition, for this thesis the accurate determination of the cellular structure of the cells requires the detection of P^-, S^- and CN^-, ions that cannot be detected using the O^- beam. Therefore, all the analysis with the CAMECA NanoSIMS 50L in this thesis was carried out using a Cs^+ ion beam because the ions under study, ^{10}B and $^{10}B^{12}C$, are sputtered with the highest yields as negative ions. The Cs^+ beam is capable of imaging with a spatial resolution of at best 50 nm, while an O^- beam from a duoplasmatron source provides resolution of at best 200 nm [33].

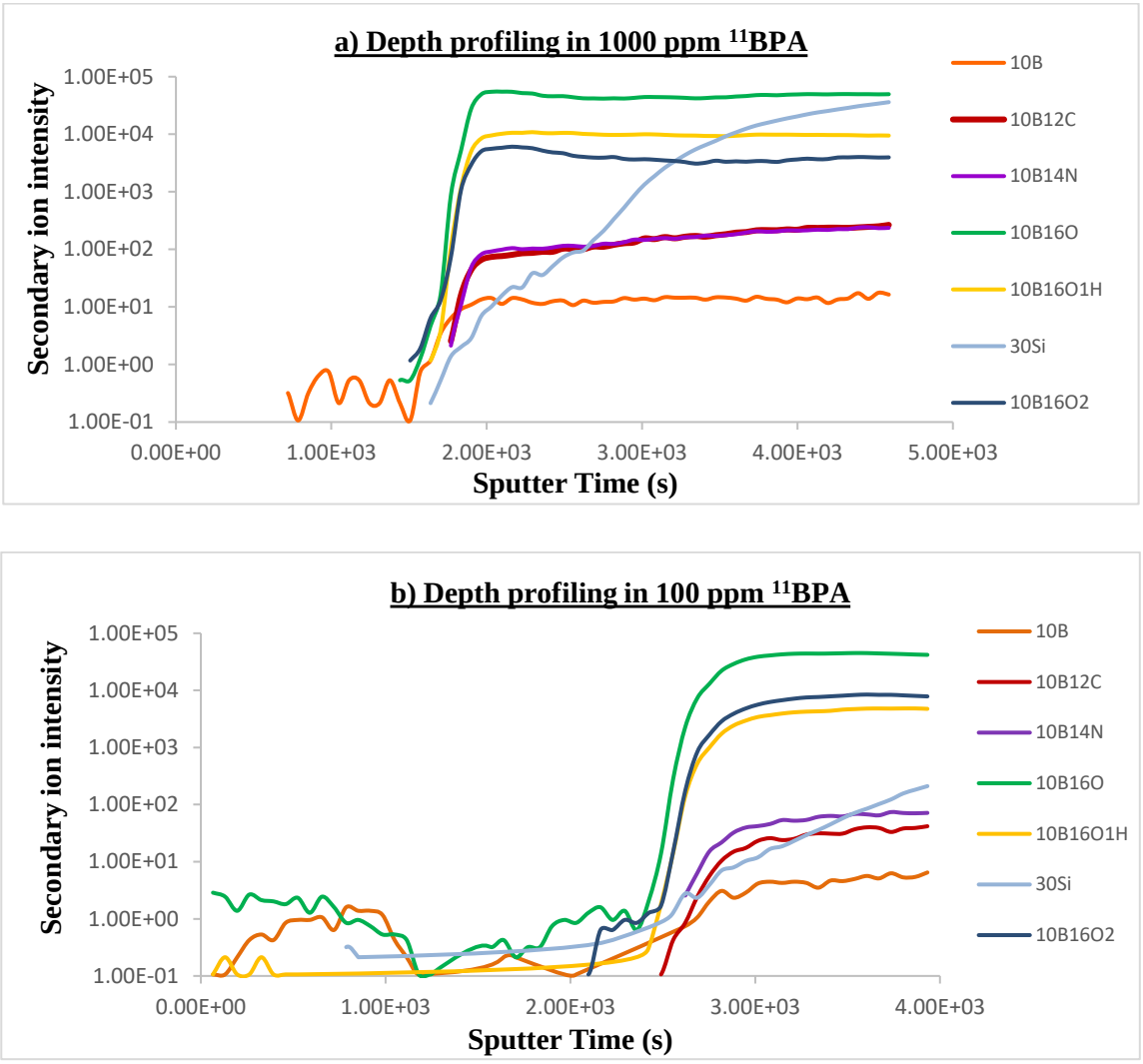

Figure 3.2: Depth profiles curves for **(a)** 1000 ppm and **(b)** 100 ppm of ^{11}BPA, acquired using the NanoSIMS Cs^+ beam. Secondary ion intensities were normalised to beam current.

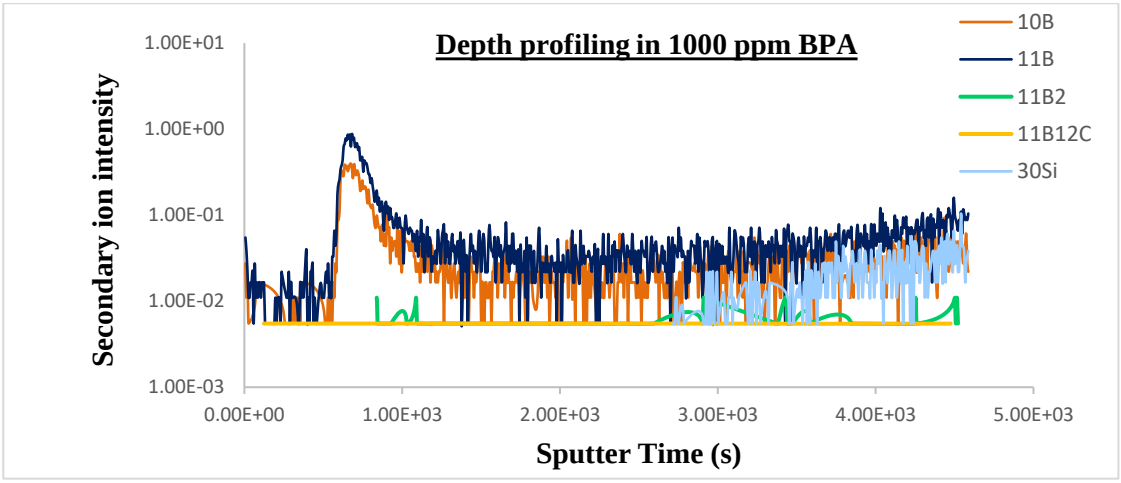

Figure 3.3: Depth profiles curves for 1000 ppm of ^{11}BPA, acquired using the NanoSIMS O^- beam. Secondary ion intensities were normalised to beam current.

It should be noted that at the beginning of 2018, the duoplasmatron source on the Manchester NanoSIMS 50L instrument was replaced with a new source called a Hyperion^{TM}. This non-thermal source provides a primary high-density ion beam that demonstrates ultra-high brightness, low energy spread, a long lifetime, and high primary beam current [39][40]. Recently studies show how an oxygen (O^-) Hyperion source was used for surface analysis with a resolution of 20 nm at 30 keV and a brightness 30 times greater than the duoplasmatron source with a resolution of < 200 nm. The analysis duration was also reduced by 20 times compared with the old source [39][41]. This ion source was not available for use for the duration of this study, which therefore focused on negative ion analysis using the Cs^+ beam.

3.6.2.2 High mass resolution curves (HMR) - second stage - 1st step

The objective of the HMR scanning is to determine the location (in the mass spectrometer) of the ion mass of interest from the sample (blue line) compared to the same ion mass from a suitable standard as previously described (green line) and to ensure that there is no mass interference with any other potential ions. The high mass resolution of the NanoSIMS and the use of AS and ES slits improve the separation of ions and peak shape, thus the spectra are produced with steep sides and flat top peaks making it possible to distinguish between the interfering ions. The ion species were distinguished from each other by reading the mass at the middle of each peak, then calculating the mass difference between each two adjacent peaks and comparing them with the recorded differences between the exact masses of these ions, as shown in **Table 3.3** (for cell culture) and **Table 3.4** (for biopsies imprints).

For cell cultures, the mass spectral curves in **Figure 3.4** were obtained by HMR scanning of the ions listed in **Table 3.3**. The $^{10}B^-$ and $^{12}C^-$ peaks are free of interference with any other ion as shown in **Figure 3.4 -a &b** respectively, while the $^{10}B^{12}C^-$ ion has an adjacent $^{11}B_2^-$ peak, both are strong peaks on the standard and overlap slightly leading to the emergence of the protrusion in the middle between them, which falsely looks like a third peak (**Figure 3.4 -c)**. Therefore, when selecting the detector position for the $^{10}B^{12}C^-$ peak, a point to the left of the centre of this peak should be selected to avoid the $^{11}B_2^-$ peak and any tails. The $^{11}B_2^-$ peak is absent from the sample (blue line) because it is only present at natural levels and the ^{10}BPA drug only contains ^{10}B. $^{12}C^{14}N^-$ overlaps slightly with $^{12}C_2{}^1H_2^-$ and $^{29}Si^-$ with $^{28}Si^1H^-$, but these adjacent peaks are sufficiently separated so they can be distinguished from each other with careful detector positioning (**Figure 3.4 -d & e** respectively).

The $^{31}P^-$ and $^{30}Si^1H^-$ peaks are often completely resolved from each other in both the standard and sample, **Figure 3.4 -f**. Sometimes a small peak, like a shoulder, appears to the right of the $^{31}P^-$ peak in the HMR spectrum of sample (blue line), this unknown shoulder may be an overlap of the low mass tail of $^{31}P^-$ peak with a very low peak of an unknown ion, so the small shoulder is avoided by positioning the detector to the left of the centre of the $^{31}P^-$ peak. The $^{32}S^-$ and $^{16}O_2^-$ peaks are completely resolved from each other in the standard (green line), while on the sample (blue line) two peaks are observed on the right of the $^{32}S^-$ peak, one of them, labelled unknown, could be $^{31}P\ ^1H^-$ and the other is the $^{16}O_2^-$ peak, however, the $^{32}S^-$ peak remains clear and distinctive, thus the detector was almost positioned in the middle of the $^{32}S^-$ peak, **Figure 3.4 -g.** The detector positioning for all masses is indicated by the black vertical line on the HMR curves. Thus, all these ions $^{10}B^-$, $^{12}C^-$, $^{10}B^{12}C^-$, $^{12}C^{14}N^-$, $^{29}Si^-$, $^{31}P^-$ and $^{32}S^-$ were used to image cell cultures because they could be distinguished from neighbouring peaks.

Table 3.3: The exact masses of negative secondary ions observed in mass spectra that were used to distinguish between overlapping peaks by calculating the difference between them, tuned in cell cultures.

Negative ions	Exact Masses/u	Mass difference/u	Negative ions	Exact Masses/u	Mass difference/u
^{10}B	10.0129	-	^{29}Si	28.9765	0.00826
^{12}C	12.000	-	$^{28}Si^1H$	28.9848	
$^{10}B^{12}C$	22.0129	0.00567	^{31}P	30.9738	0.00783
$^{11}B_2$	22.0186		$^{30}Si^1H$	30.9816	
$^{10}B^{11}B^1H$	22.0301	0.01146	^{32}S	31.9721	0.01776
$^{12}C^{14}N$	26.0031	0.011	$^{16}O_2$	31.9898	
$^{12}C_2{}^1H_2$	26.0157		-	-	-

For the biopsy imprint samples, HMR scans of ions $^{10}B^-$, $^{12}C^-$, $^{10}B^{12}C^-$, $^{12}C^{14}N^-$, $^{29}Si^-$, $^{31}P^-$ and $^{32}S^-$ were very similar to those obtained in cell cultures (**Figure 3.4** and **Table 3.3**). The HMR scans of the ions $^{10}B^{14}N^-$ and $^{10}B^{16}O_2^-$ are shown in **Figure 3.5** The ions masses shown on the curves are listed in **Table 3.4**, and were used to distinguish the different peaks from each other by finding the difference between two adjacent masses. In **Figure 3.5** -a, the curve from the standard, solid boron shown with a green line, shows the $^{10}B^{14}N^-$ peak overlapping with an unknown peak on the left (small shoulder). In a biopsy sample (blue line), the $^{10}B^{14}N^-$ ion signal is very weak and sometimes the signal is not detectable when using a FoV less than 50×50 µm2. Therefore, the $^{10}B^{14}N^-$ cannot be clearly resolved from the unknown mass interference in the sample and was therefore deemed unreliable when interpreting the results. When considering the $^{10}B^{16}O_2^-$ signal from the boron standard (green line), shown in **Figure 3.5** -b, the ion appears with high intensity but is accompanied by mass interferences from both the right and left sides (identified in red). On the biopsy sample, the $^{10}B^{16}O_2^-$ peak only appears as a small shoulder at the far right of the blue curve (identified in black) and overlaps strongly with the neighboring ion $^{12}C^{14}N^{16}O^-$, which gives high counts, making it difficult to resolve the $^{10}B^{16}O_2^-$. Therefore, both ions $^{10}B^{14}N^-$ and $^{10}B^{16}O_2^-$ will not be considered during the interpretation of images as they are unreliable due to very close mass interferences. Similar to cell cultures, all these ions $^{10}B^-$, $^{10}B^{12}C^-$, $^{12}C^{14}N^-$, $^{29}Si^-$, $^{31}P^-$ and $^{32}S^-$ were used to image biopsy imprints alongside $^{12}C^-$ in some samples. This detector alignment was repeated at the beginning of each session, and the HMR scans were checked every time a new area or another sample was analysed to ensure there was no movement of the peaks.

Table 3.4: The exact masses of negative secondary ions observed in HMR spectra of biopsy imprints that were used to distinguish between overlapping peaks by calculating the difference between them.

Negative ions	Exact Masses/u	Mass difference/u	Negative ions	Exact Masses/u	Mass difference/u
$^{12}C_2$	24.000	0.01601	$^{28}Si^{14}N$	41.9800	0.00501
$^{10}B^{14}N$	24.0160		$^{32}S^{10}B$	41.9850	0.00952
$^{11}B^{12}C^{1}H$	24.0171	0.00112	$^{31}P^{10}B^{1}H$	41.9945	0.00346
			$^{12}C^{14}N^{16}O$	41.9980	0.00478
			$^{10}B^{16}O_2$	42.0028	0.01235
			$^{11}B^{16}O^{14}N^{1}H$	42.0151	

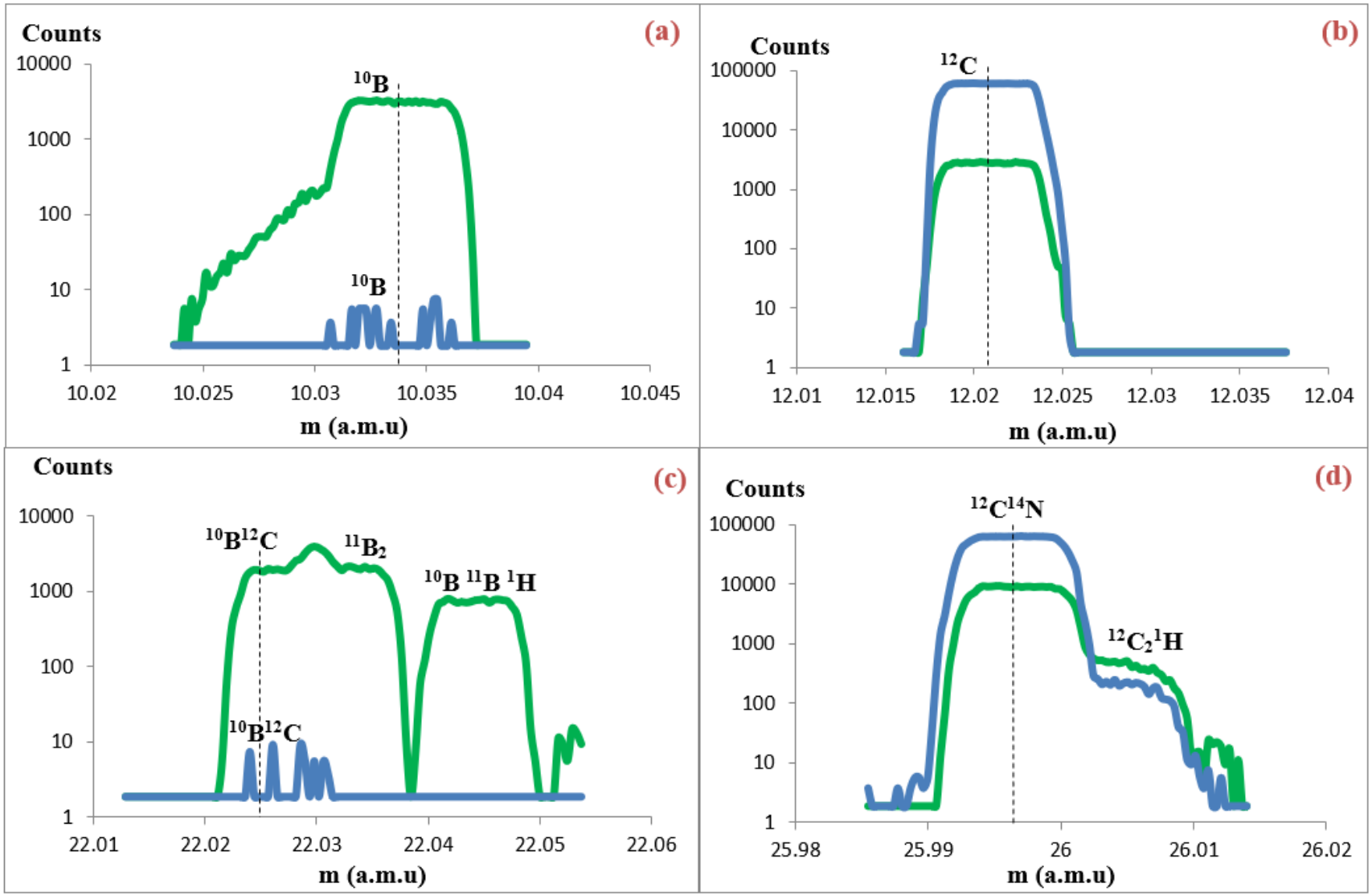
(a)
Counts
10000
1000
100
10
1
^{10}B
^{10}B
10.02
10.025
10.03
10.035
10.04
10.045
m (a.m.u)
(b)
Counts
100000
10000
1000
100
10
1
^{12}C
12.01
12.015
12.02
12.025
12.03
12.035
12.04
m (a.m.u)
(c)
Counts
10000
1000
100
10
1
^{10}B^{12}C
^{11}B$_2$
^{10}B ^{11}B ^{1}H
^{10}B^{12}C
22.01
22.02
22.03
22.04
22.05
22.06
m (a.m.u)
(d)
Counts
100000
10000
1000
100
10
1
^{12}C^{14}N
^{12}C$_2$^{1}H
25.98
25.99
26
26.01
26.02
m (a.m.u)

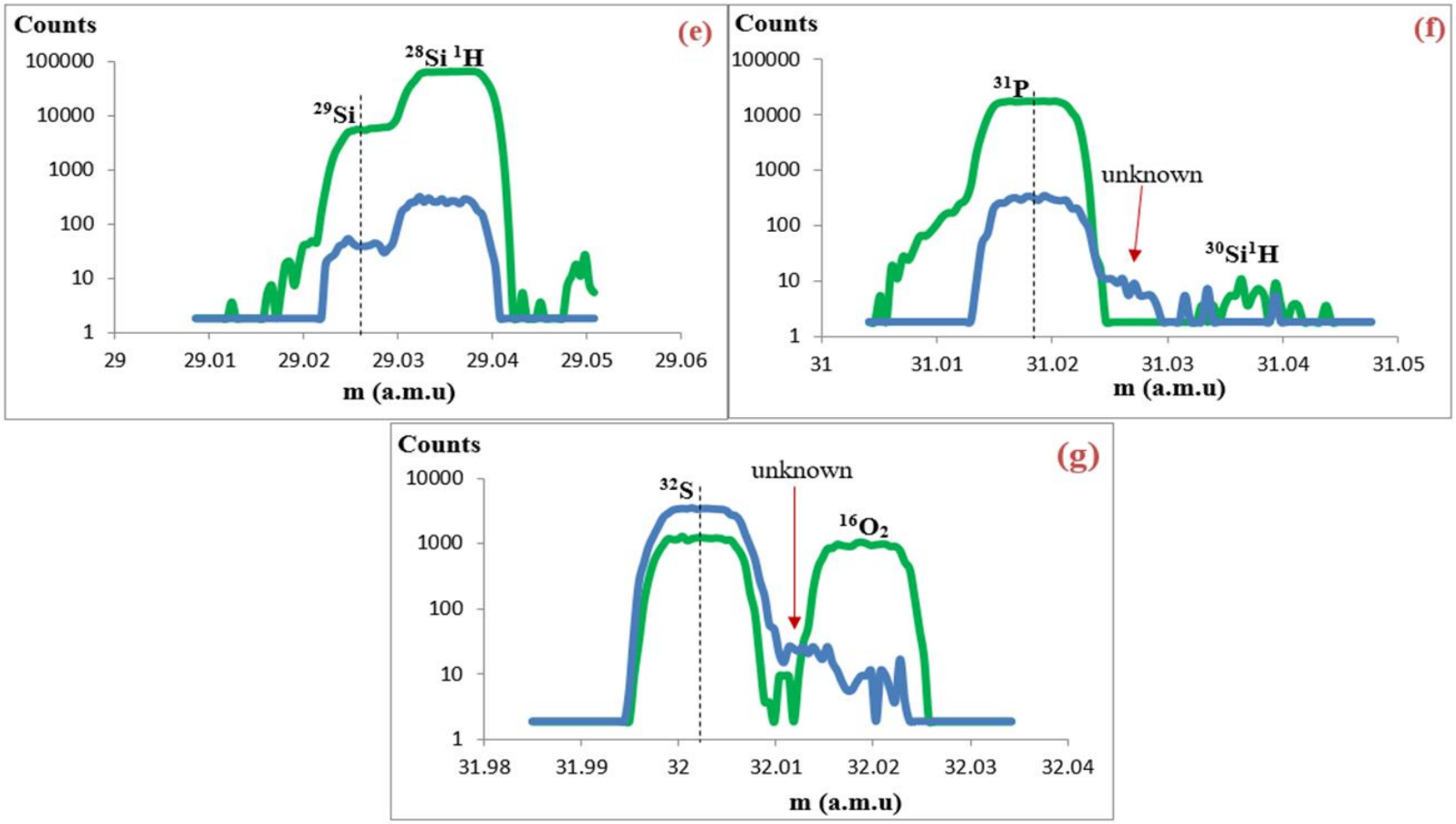

Figure 3.4: High Mass Resolution spectra from the NanoSIMS 50L of the standard (green line) and cell culture sample (blue line). The detectors were tuned to the following negative secondary ions with the standard used given in brackets: **a)** ^{10}B (pure boron), **b)** ^{12}C (pure boron), **c)** $^{10}B^{12}C$ (pure boron), **d)** $^{12}C^{14}N$ (silicon wafer), **e)** ^{29}Si (silicon wafer), **f)** ^{31}P (gallium phosphate fixed), and **g)** ^{32}S (pure boron).

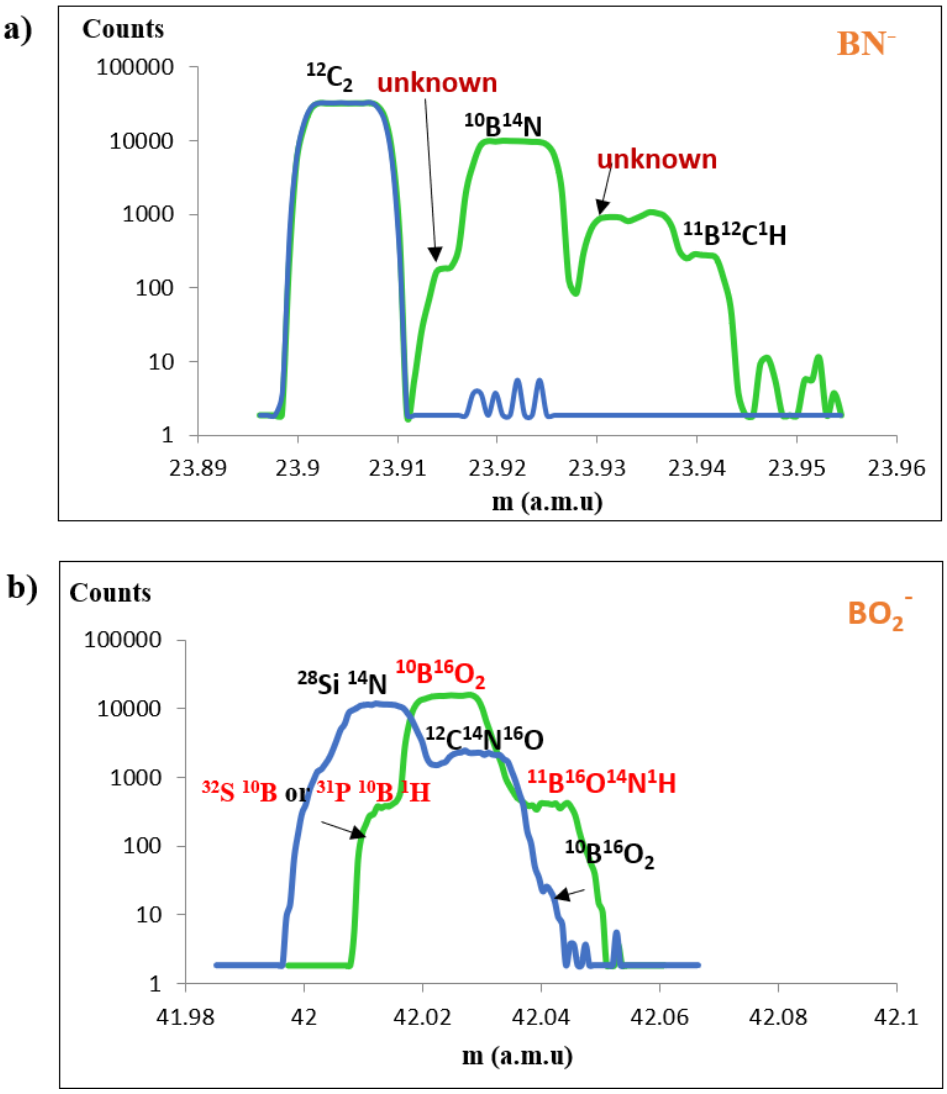

Figure 3.5: High Mass Resolution scans from the NanoSIMS 50L of the pure boron standard (green line) and tissue biopsy sample (blue line). (**a**) and (**b**) shows the interference of the ions $^{10}B^{14}N^-$ and $^{10}B^{16}O_2^-$ respectively with the other adjacent ions obtained from a FoV 50×50 µm^2.

3.6.2.3 Depth profiling curves - second stage-2nd step

Depth profiling was performed to determine the appropriate Cs^+ dose to ensure the sample was at steady state, also called the implantation dose. Depth profiling allowed determination of the optimum implantation dose while still leaving sufficient sample left to accumulate enough counts from the boron ion signals before the sample was completely sputtered away. Depth profile curves monitor the intensity of secondary ion signals over time and from this the implantation, and steady state doses can be calculated. This test was conducted using the imaging mode so that disappearance (sputtering rate differences / thickness differences) of different parts of the sample, e.g. nucleus and cytoplasm, could be monitored and signals

from different parts of the cell distinguished. The analysis was stopped when the images showed that the sample was completely sputtered away. The B2 and D2 samples were selected for this test to investigate whether different types of cells, GBM tumour or BAT, give similar results in terms of Cs^+ doses. In addition, these samples were treated with somewhat low concentrations of the BPA and thus the depth profile curves will allow the tracking of lower signals of ^{10}B and $^{10}B^{12}C$ (ions of interest) and determine when these signals reach steady state. A third sample, B3, was treated with tyrosine before treating with BPA which may affect the point at which steady state is achieved so it was also tested.

Raster areas of respectively 40×40 μm^2 and 25×25 μm^2 for the B2-D2 and B3 samples were selected depending on the size of the cell under examination. In general, cells were selected so that the whole cell could be imaged and smaller cells were chosen to perform the measurement within 4 hours. The dwell time was set at 1000 µs per pixel and 1000 or 250 layers per area for B2-D2 and B3 respectively were acquired to ensure the sample was completely sputtered away. The D1 aperture was set to D1-1 to allow a fast sputtering rate and the current measured with this aperture was used to calculate doses.

When the depth profiling experiment was completed, the resulting image series was processed using the FIJI (ImageJ) software. Layers were aligned to correct for drift and then the layers were summed to allow identification of regions of interest. Drift correction caused part of the images to be lost, but the remaining image was sufficiently large enough to extract results. Focusing of the primary beam had to be conducted on an adjacent cell so that the depth profile could be acquired from zero dose. This, along with using a large D1 aperture, meant that the analysed cell was not perfectly in focus. Nevertheless, the location of the nucleus and cytoplasm, which are the main areas of interest in the cells, could still be determined. **Figures 3.6**, **3.7** and **3.8** shows the cells analysed for the B2, D2 and B3 samples respectively, the green line outlines the nucleus and part of the cytoplasm is outlined in red.

To verify of the sputtering behaviour in different parts of the samples, depth profile curves from the nucleus and the cytoplasm were extracted from the individual layers. While steady state might be reached in the thickest part, the same dose might result in complete sputtering of the thin part, so it is necessary to choose a primary ion beam dose that is suitable for both regions and accept that performing analysis at steady state may not be possible in these samples. The total number (sum) of counts from each selected area of each layer in the image was extracted for all ions and plotted against the calculated accumulated dose. The measured current was 29.5 pA for samples B2-D2 and 13.9 pA for the B3 sample so the dose for each

layer was 1.89×10^{14} and 2.29×10^{14} ions/cm^2 respectively calculated using Equation 3.1. **Figures 3.9, 3.10** and **3.11** show the depth profile curves for the three samples.

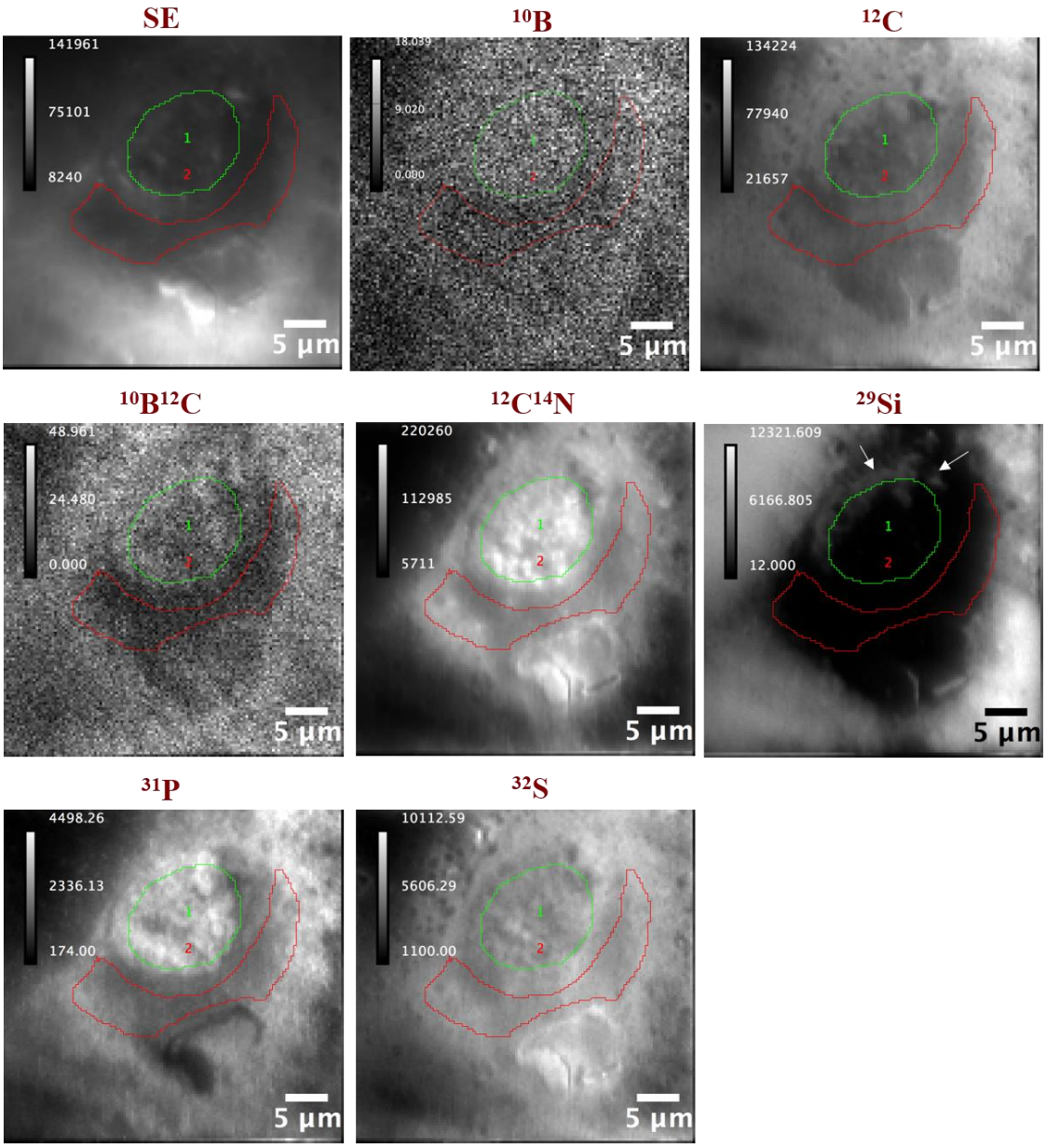

Figure 3.6: NanoSIMS 50L images of $^{10}B^-$, $^{12}C^-$, $^{10}B^{12}C^-$, $^{12}C^{14}N^-$, $^{29}Si^-$, $^{31}P^-$ and $^{32}S^-$ and the secondary electron image (SE) from B2 sample of GBM tumour cell cultures showing the distribution of negative ions in cell and selected areas of interest; **1)** nucleus area (green line) and **2)** cytoplasm area (red line). Images were acquired from depth profiling a 40×40 µm^2 area with 128×128 pixel and stacking 1000 layers giving a total dose of 1.89×10^{17} ions/cm^2. The arrows in the Si image points to where the nucleus begins to disappear as indicated by the Si counts which originate from the substrate. A calibration bar is shown for each ion separately and indicates the minimum and maximum values for counts in the image, the black colour indicates the absence of counts from area while the bright white colour indicates areas of high signal intensity.

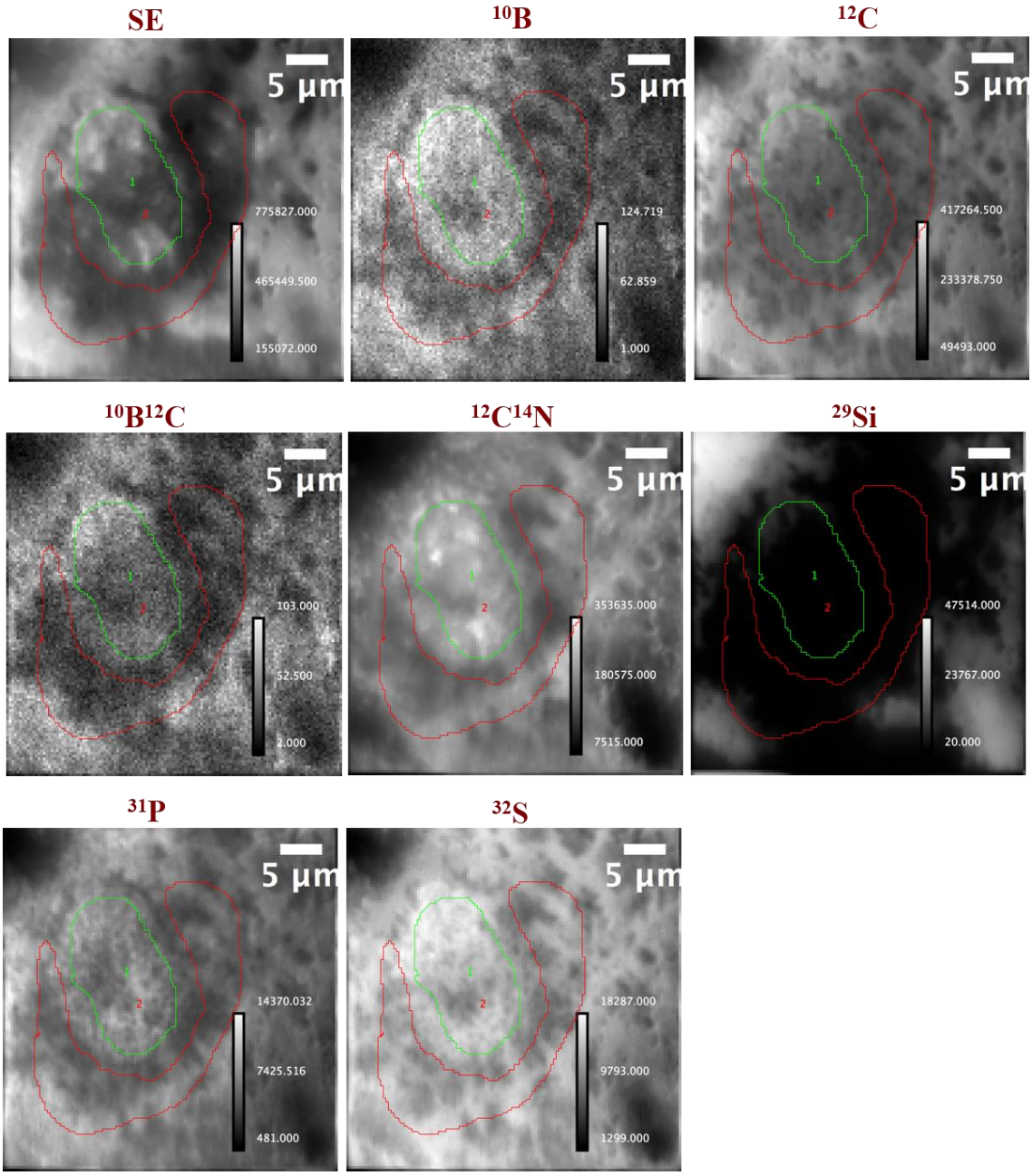

Figure 3.7: NanoSIMS 50L images of $^{10}B^-$, $^{12}C^-$, $^{10}B^{12}C^-$, $^{12}C^{14}N^-$, $^{29}Si^-$, $^{31}P^-$ and $^{32}S^-$ and SE image showing the cell analysed in D2 sample of BAT cell cultures. Each map shows the negative ion distribution, scale bar, calibration bar of minimum and maximum counts (colour bar) and selected areas of interest;**1-** nucleus area (green line) and **2-**cytoplasm area (red line). The images represent a depth profiling measurement over an area of 40×40 µm^2 with 128×128 pixel and sum 1000 layers giving a total dose of 1.89×10^{17} ions/cm^2.

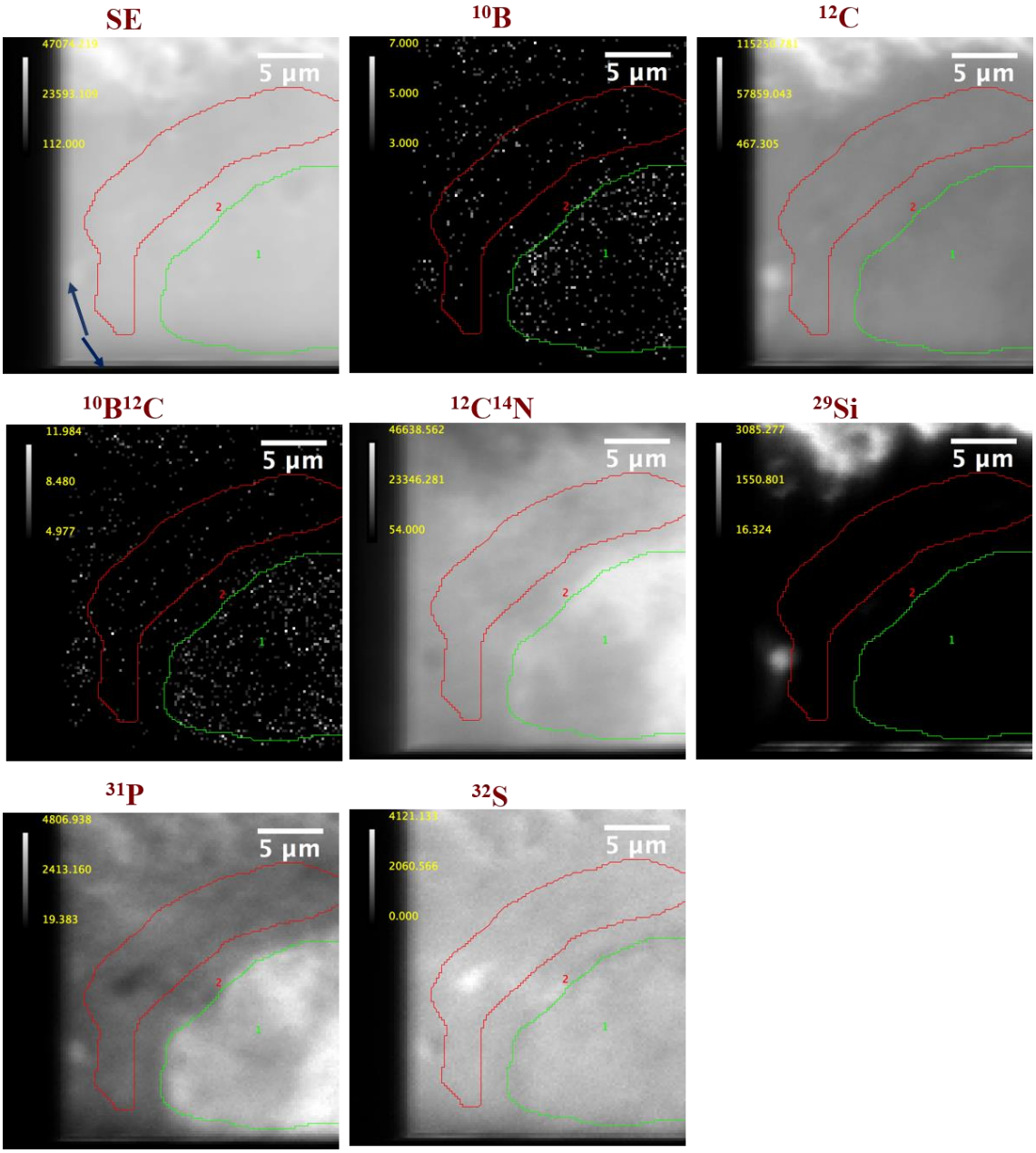

Figure 3.8: Images of $^{10}B^-$, $^{12}C^-$, $^{10}B^{12}C^-$, $^{12}C^{14}N^-$, $^{29}Si^-$, $^{31}P^-$ and $^{32}S^-$ and SE image using NanoSIMS 50L from B3 of GBM cell culture sample. The images were obtained from an area of 25×25 µm^2, 128×128 pixels and 250 layers giving a total dose of 5.72×10^{16} ions/cm^2. The images show the distribution of negative ions in two selected regions; **1**-nucleus area (green line) and **2**-cytoplasm area (red line). The black area located the left and bottom side of the images (blue arrows in SE image) shows the missing parts of the images as a result of aligning the layers and correcting the drift. The scale and the calibration bars for each ion are shown on each image.

In the following section, the depth profile curves are explained alongside the image (layer by layer). Depth profiling in the nucleus area of the B2 cell (**Figure 3.9 -a**) showed that Si began to rise gradually from the beginning. In **Figure 3.6** a small number of counts were observed around the edge of the nucleus as a result of preferential sputtering at the interface with the cytoplasm. The Si signal started to increase significantly at a dose of 5×10^{16} ions/cm^2, this is where the nucleus starts to disappear more rapidly starting from the upper left-hand side as indicated by the arrow in the silicon map in **Figure 3.6.** The Si signal continued to increase throughout the depth profile with the continued demise of the nucleus. The Si signal reached steady state when the cell was completely sputtered away and only the silicon substrate remained. Depth profiling was performed using silicon 29 isotope with a natural abundance 4.67% instead of silicon 28 that has abundance 92.23% in order to protect the detector from damage resulting from receiving a large number of ions when reaching the substrate, which in turn causes the detector to saturate and switch off.

The P and S signals show a steady increase in the nucleus and reached steady state at a dose of 1.9×10^{16} ions/cm^2 then showed a slight and gradual decrease in signal intensity to a dose of 1.09×10^{17} ions/cm^2, this may be due to the early disappearance of part of the nucleus, after this the decline became more pronounced. The $^{12}C^{14}N$ signal shows high intensity right from the start and is essentially at steady state by 1.89×10^{14} ions/cm^2 with a slight increase at the beginning of the curve and a gradual decrease in the middle at a dose of 1.09×10^{17} ions/cm^2, then the decrease is clearly noticeable with the full sputtering of the nucleus. The C signal also reached steady state at 1.9×10^{16} ions/cm^2. Although there is a slight decrease in the middle of the steady state, the carbon signal seems more stable than the other ions. This stability in the C signal is expected as carbon is the most homogenously distributed element in the cells. Both ^{10}B and $^{10}B^{12}C$ have the same behaviour and reached steady state at 1.9×10^{16} ions/cm^2 and decreased at 1.09×10^{17} ions/cm^2. The decreases in intensity that occur for all ions throughout the profile are linked to the rises in Si signal, which is due to the nucleus slowly disappearing.

Based on the observations of the nucleus, it is clear that the most appropriate dose for most ion signals to reach steady state is 1.9×10^{16} ions/cm^2, and analysis should be stopped at 1.09×10^{17} ions/cm^2, however, due to rapid sputtering of the nucleus and increased silicon signal, it was decided to stop the analysis at 8.69×10^{16} ions/cm^2 to achieve a balance between the disappearance of the nucleus and to ensure that sufficient counts are obtained for all ions from the analysed areas. When determining the area of the nucleus in the studied samples

during imaging (later), any area that begins to disappear early (sputters faster) is avoided to achieve greater reliability in the results.

In terms of depth profiling of the cytoplasmic area in this cell B2 (**Figure 3.9 -b**) it was observed from the images that the cell disappearance began in the nucleus first and after a very short time the disappearance expanded into the cytoplasm, so the silicon signal appeared semi-constant in the cytoplasm for a period of time slightly longer than in the nucleus with a slight rise starting at a dose of 1.9×10^{16} ions/cm^2. The silicon ion intensity then gradually increased at a dose of 6.14×10^{16} ions/cm^2. The nucleus was expected to be thicker than the cytoplasm and thus the cytoplasm expected to be sputtered away fully before the nucleus, but the opposite was observed with the nucleus disappearing before the cytoplasm as observed from the Si behaviour above in the depth profile. The curves of ions B, BC, C, P and S have a similar behaviour to what occurred in the nucleus and all of them reached steady state at a dose of 1.9×10^{16} ions/cm^2 and began to decrease clearly at a dose of 1.32×10^{17} ions/cm^2, and the carbon signal is the most stable. Similarly, CN ion gave the same behaviour that appeared in the nucleus and reached steady state at 1.89×10^{14} and decreased at 1.32×10^{17} ions/cm^2. All ions showed a slight decrease during the steady state region at the point corresponding to the beginning of the cytoplasm disappearance as indicated by the increasing silicon signal. From the depth profile in the cytoplasm it is clear that the most appropriate dose for implantation for all ions is 1.9×10^{16} ions/cm^2 and the analysis should be stopped at a dose is of 1.32×10^{17} ions/cm^2. As the cytoplasm begins to disappear at a dose of 6×10^{16} ions/cm^2, the dose 8.69×10^{16} ions/cm^2 was chosen as a compromise so areas that begin to sputter away early are avoided when determining signal intensities from the cytoplasm.

In the D2 cell of BAT sample in both the nucleus and the cytoplasm (**Figure 3.10 - a** and **b**), it is observed that the signal of all ions rises gradually at the beginning of curves, suggesting that the ions are heading towards steady state however a drop in signals intensity was observed after this initial rise. When returning to the images to verify the cause of the drop, it was observed that there was charging in layers 244 (4.61×10^{16} ions/cm^2) to 388 (7.33×10^{16} ions/cm^2). After this the charging subsided and the images returned to normal, which explains the drop of the counts and then its return to a steady state.

In the nucleus (**Figure 3.10 -a**), the intensity of ions B, BC, P and S decrease at 1.2×10^{17} ions/cm^2. The behaviour of these ions during this profile is similar to that of the nucleus of the sample B2. The CN signal began to decrease at dose 1.05×10^{17} ions/cm^2. The Si signal increased rapidly at 8.26×10^{16} ions/cm^2 where the images show that the nucleus has begun

to disappear. From this curve, 1.9×10^{16} ions/cm^2 was chosen as the dose for implantation, and analysis stopped at 1.11×10^{17} ions/cm^2 by the same method that was followed with the B2 sample. Similarly, in the cytoplasm (**Figure 3.10 -b**) at the dose 1.15×10^{17} ions/cm^2 the signals of B, BC, P and S decrease, while CN ion drops early at 1.02×10^{17} ions/cm^2 because the signal for CN is lower in cytoplasm than the nucleus. The silicon starts to increase gradually immediately after the charging at 6.18×10^{16} ions/cm^2 until the whole sample disappeared. It was decided to stop the analysis at 1.11×10^{17} ions/com^2 and the implantation dose was chosen to be 1.9×10^{16} ions/cm^2.

Depth profiling in the nucleus of the B3 sample (**Figure 3.11 -a**) was different from the previous samples. The ions curves of B, BC, C, P and S show a gradual increase from the beginning of the profiling, while the CN signal starts high and decreases slightly before reaching steady state. All the ions except CN reach a plateau from 1.89×10^{16} ions/cm^2 to 3.57×10^{16} ions/cm^2 and then begin to decrease gradually. The nucleus begins to be sputtered at 4.81×10^{16} ions/cm^2 as indicated by the Si signal. This depth profiling was done with only 250 layers and the sample did not completely disappear, as the experiment was stopped as soon as the nucleus was removed. CN signal appears to be different here than the other ions, it reaches a high intensity at 1.89×10^{16} ions/cm^2 until it reaches the dose 4.81×10^{16} ions/cm^2. This is the typical behaviour of CN in the analysis of biological samples where it is often used in SIMS imaging and to focus images [42]–[44]. The dose 1.89×10^{16} ions/cm^2 was chosen for primary beam implantation and 3.5×10^{16} ions/cm^2 to stop the analysis since most of the ions did not reach the steady state completely. In the cytoplasm (**Figure 3.11 -b**), the ions behaved similarly to the nucleus, except that silicon took a slight upward trend from the beginning of the depth profile to the end. The images showed that the majority of silicon ions originated from the substrate originating from holes in the sample, also the cytoplasm's demise began at the dose 4.17×10^{16} ions/cm^2. Therefore, from this cytoplasm the dose 1.89×10^{16} ions/cm^2 for implantation and 3.57×10^{16} ions/cm^2 to stop analysis was determined.

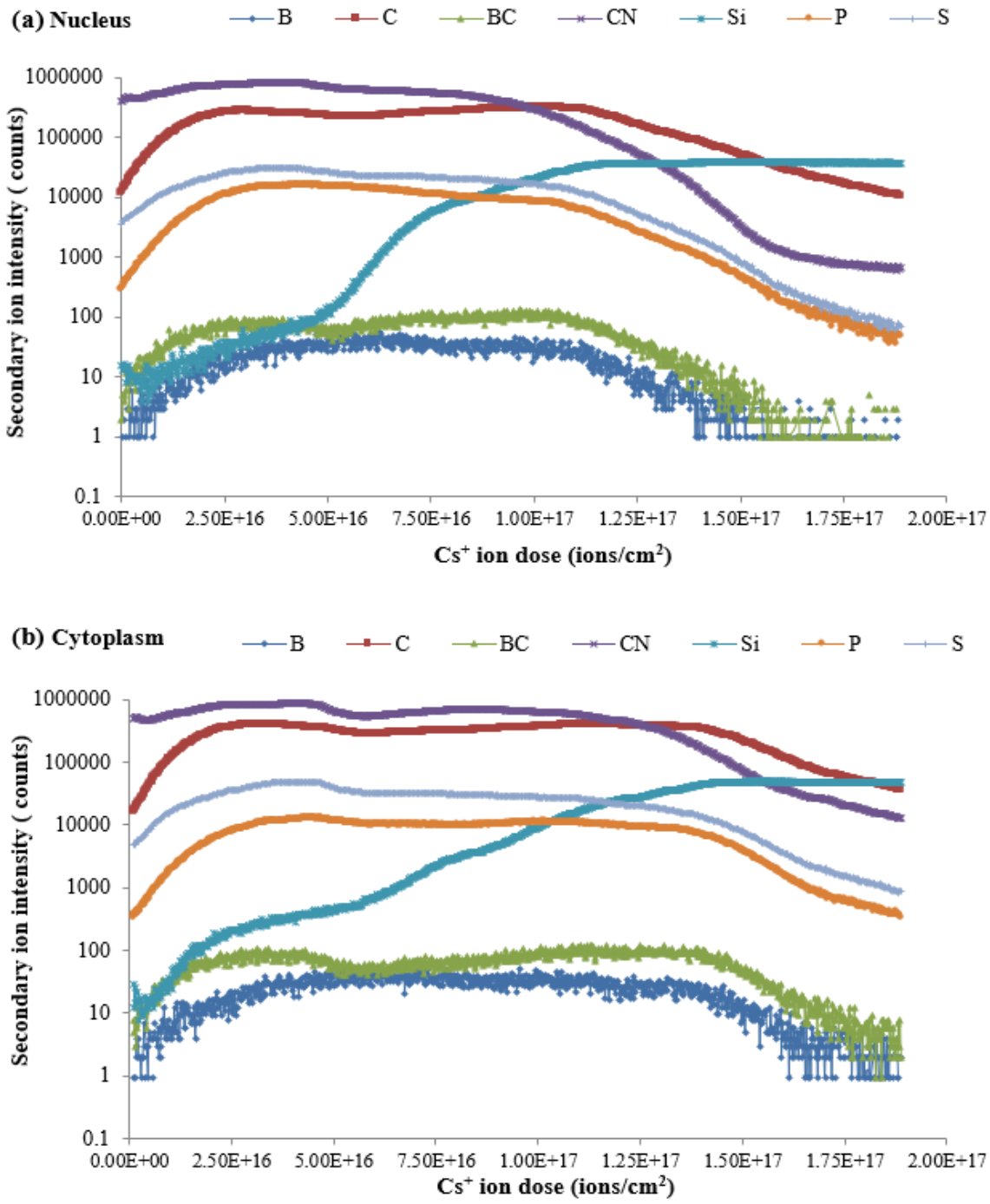

Figure 3.9: Depth profiles from a 40×40 µm^2 FoV of the B2 sample shows the changes in the intensity of negative secondary ions of ^{10}B, ^{12}C, $^{10}B^{12}C$, $^{12}C^{14}N$, ^{29}Si, ^{31}P and ^{32}S with Cs^+ ion beam dose. **(a)** and **(b)** depth profiling curves extracted from the nucleus-area 1 and cytoplasm-area 2 respectively that was selected in Figure 3.6

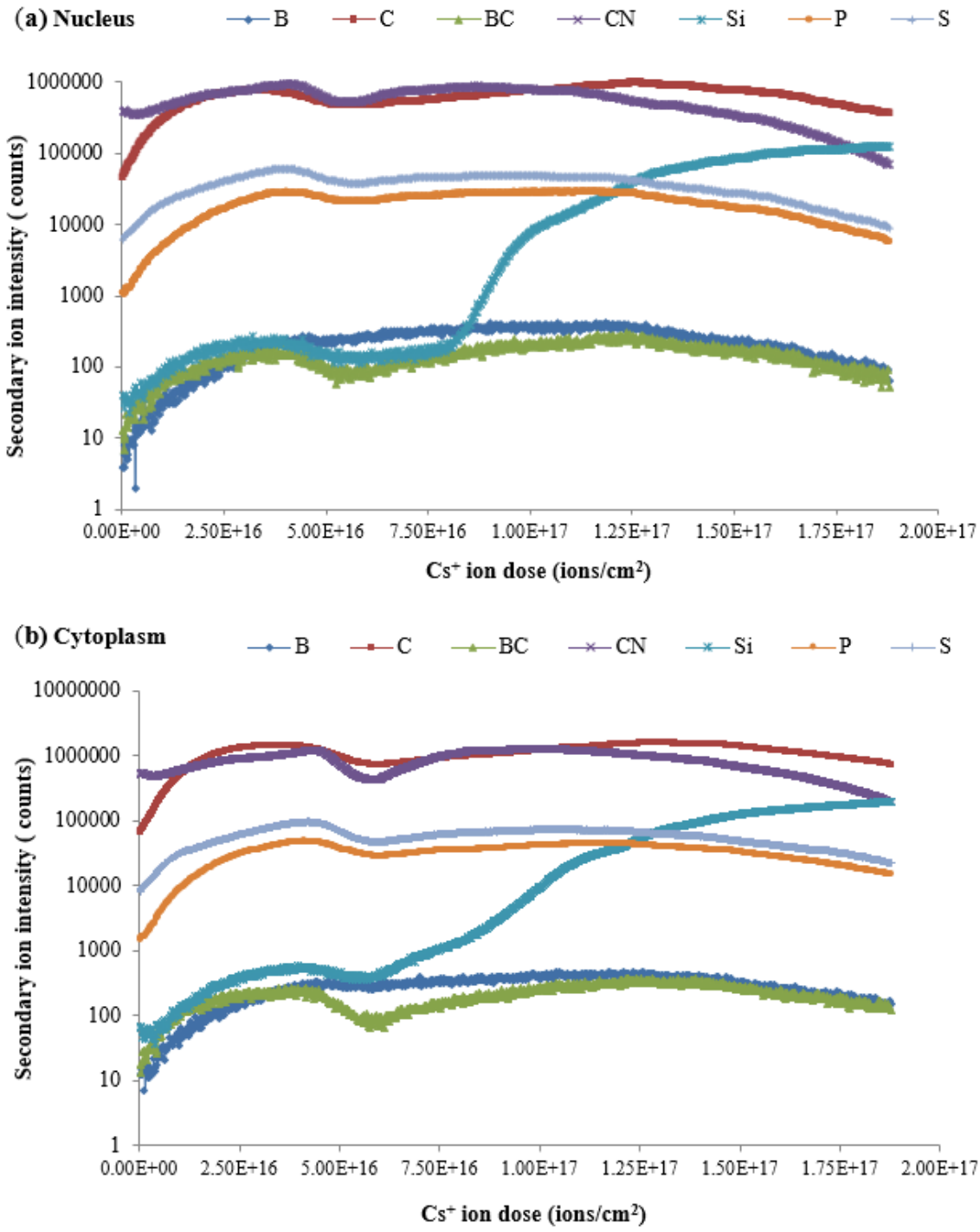

Figure 3.10: NanoSIMS 50L depth profiles of **a)** nucleus-area1 and **b)** cytoplasm-area 2 as selected in Figure 3.7 when analyse D2 sample with 40×40 µm^2 FoV. The intensity of negative secondary ions ^{10}B, ^{12}C, $^{10}B^{12}C$, $^{12}C^{14}N$, ^{29}Si, ^{31}P and ^{32}S were plotted as a function of Cs^+ ion beam dose.

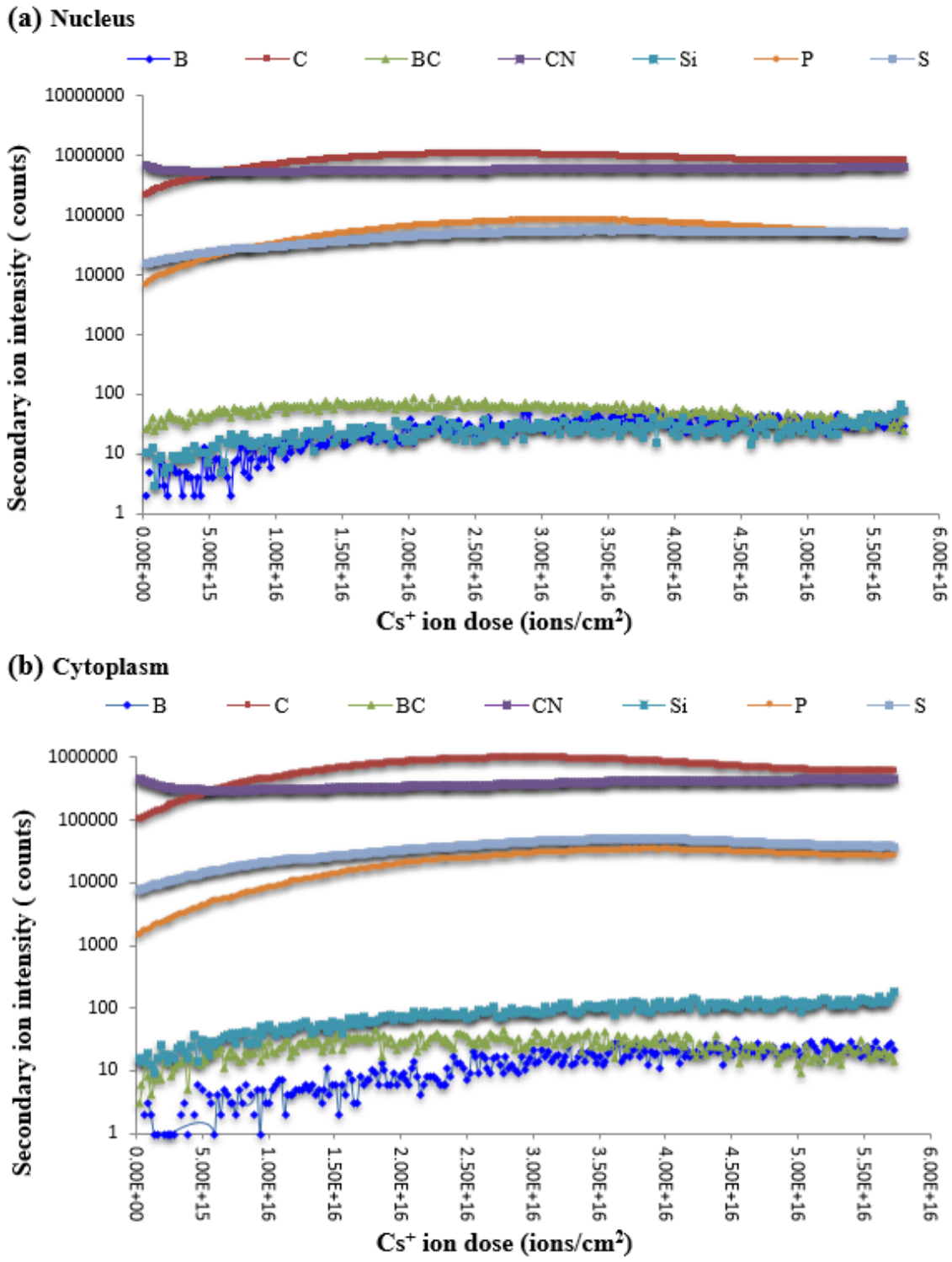

Figure 3.11: Depth profiles of negative secondary ions: ^{10}B, ^{12}C, $^{10}B^{12}C$, $^{12}C^{14}N$, ^{29}Si, ^{31}P and ^{32}S, obtained from a 25×25 μm^2 FoV in B3 sample, plotted against the Cs^+ dose. The **(a)** and **(b)** curves were extracted from nucleus-area 1 and cytoplasm-area 2 respectively as illustrated in Figure 3.8. These depth profiles were used to indicate the approximate dose required, but the dose will vary from cell to cell depending on thickness, holes, and cellular features.

From the graphs, it is clear that numerous reasons such as charging, early disappearance of the nucleus, holes, thickness and cellular features present mean that steady state may not be reached. This makes the precise determination of the beginning and end of the analysis slightly different from one cell to another, but performing depth profiling for each cell of interest to determine these doses is impractical and time consuming. Therefore, it was necessary to make a compromise in determining the implantation dose in order to start the analysis at a point where the sample was at, or almost at, steady state, as well as the determine the point at which the analysis should be stopped so that sufficient counts could be detected, especially from ions that have low concentration such as B, before the cell was sputtered away. Thus, the average of the implantation doses was calculated from areas depth profiled above and is shown in **Table 3.5**. An implantation dose of 1.9×10^{16} ions/cm^2 in the analysis of all cell cultures samples was used. A dose of 5.89×10^{16} ions/cm^2 was added during imaging after implantation, which meant that imaging was stopped before significant cell disappearance. This dose was calculated by averaging the doses found in **Table 3.5**.

Table 3.5: Summary of the doses (ions/cm^2) determined during the depth profiling of B2, D2 and B3 samples, the calculation of the average of implantation dose and the appropriate dose for analysis.

Samples	**areas**	**Implantation dose (ID)** (ions/cm^2)	**Analysis dose (AD)** (ions/cm^2)	**The added dose of the image (AD - ID)** (ions/cm^2)
B2	Nucleus	1.9×10^{16}	8.69×10^{16}	6.8×10^{16}
	Cytoplasm	1.9×10^{16}	8.69×10^{16}	6.8×10^{16}
D2	Nucleus	1.9×10^{16}	1.11×10^{17}	9.2×10^{16}
	Cytoplasm	1.9×10^{16}	1.11×10^{17}	9.2×10^{16}
B3	Nucleus	1.89×10^{16}	3.57×10^{16}	1.68×10^{16}
	Cytoplasm	1.89×10^{16}	3.57×10^{16}	1.68×10^{16}
Average		1.895×10^{16}		5.89×10^{16}

It was found that adding 5.89×10^{16} ions/cm^2 to an area of 40×40 μm^2 using D1 = 2, 256×256 pixels and a dwell time of 2000 μs/pixel took 1 day to complete, increasing the raster size to

60×60 µm^2 took over two days, making the sample throughput very slow, so the added dose was reduced to 1.44×10^{16} ions/cm^2. This dose was selected during the analysis of the first samples, where during each image it was verified that sufficient amounts of all ions were obtained when this dose was added. This methodology allowed the analysis of all samples in the same way with the possibility of comparing them to each other. In addition, C ion appears to be the most stable in behaviour compared to other ions, so it was used as an internal standard to normalise the other ions to account for ion beam current drift or sample charging.

3.6.2.4 Spatial resolution

Spatial resolution of the NanoSIMS Cs^+ beam was determined using the L'image software (LR Nittler, Carnegie Institution of Washington). To achieve this, ion images with high-contrast (i.e. the $^{29}Si^-$ image) were used to draw a line profile over the edge of the cell, and create a line profile of distance (µm) vs $^{29}Si^-$ signal intensity as shown in **Figure 3.12 -a** and **b** respectively, further detail about image acquisition is given in Chapter 4. By using the 16–84% resolution measurement, the distance between the vertical lines in **Figure 3.12 -b** corresponds to a spatial resolution of 400 nm.

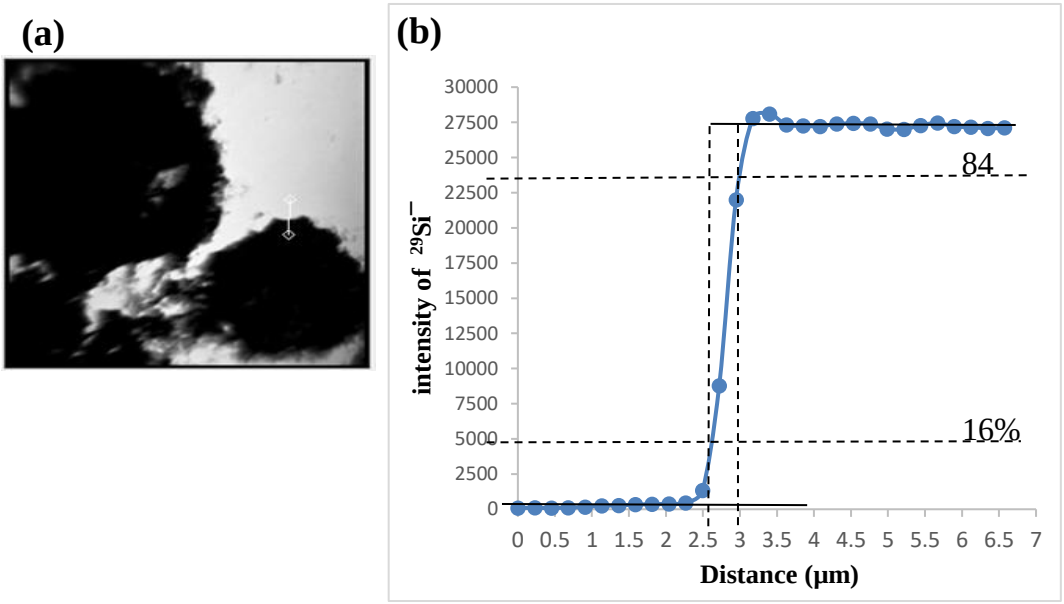

Figure 3.12: a) $^{29}Si^-$ map of the B3 GBM-tumour cell culture imaged by NanoSIMS Cs^+ beam with D1=2, FoV 60×60 µm^2 and 256×256 pixels. The map shows two cells (dark areas) on the Si substrate (bright areas) and line profile over the edge of right cell. **b)** shows the graph of distance (µm) vs the $^{29}Si^-$ intensity with a spatial resolution of 400 nm determined using the 16-84% resolution measurement.

3.7 Preliminary BioToF-SIMS experiments

3.7.1 Experimental Section

1-Sensitivity test: The set of ^{11}BPA standards were analysed in positive mode using a dose of 2×10^{11} ions/cm^2 of Au^+ beam at 20 keV, rastered in pulsed mode over a FoV of 300×300 μm^2 to acquire a spectrum from the sample surface. The area then underwent a single etch using a dose 1×10^{14} ions/cm^2 of Au^+ beam with 600×600 μm^2 FoV in DC mode. FoV for etching was always bigger than FoV for analysis to avoid crater edge effects. The intensities were collected again from the sample surface after etching. The analysis was repeated at 3 different locations for each sample. BioToF-IMS software was used to select the spectrum area from 1 to 150 Da and extract the intensities from the peak areas for the secondary ions of interest $^{10}B^+$, $^{11}B^+$ and $^{12}C^+$. The $^{10}B^+$ intensity was normalised to $^{12}C^+$ intensity to correct differences in sputter yields, also the mean and SD of the data were calculated at each concentration.

In addition, depth profiling of several layers (5-13) on the 100 and 1000 ppm samples was continued at the same conditions above. The intensity was then extracted from the $^{10}B^+$ and $^{11}B^+$ peaks and normalised to the highest intensity of each ion. $^{10}B^+/^{11}B^+$ ratios were also calculated from all ^{11}BPA standards. All graphs of results were plotted using Microsoft Excel.

2-Depth profiling: the samples were depth profiled in order to determine the number of layers (cycles) appropriate to obtain high secondary ion signals before the cells began to damage, this is a similar process to that described previously for NanoSIMS analysis (the second stage-2nd step). The results were verified on two samples, D3 of BAT and B3 of GBM using 20 keV Au^+ primary beam with 6 nA current and 256×256 pixels in positive mode. With the D3 sample: the intensity of secondary ions were collected from 21 layers of the cell surface with FoV 74×74 μm^2, subsequently the first etch was performed using a dose similar to that in the NanoSIMS experiment of 1.9×10^{16} ions/cm^2 of Au^+ with 200×200 μm^2 FoV in DC mode. The intensities were collected again from 20 layers-three consecutive times, each time intensity was summed to the previous 21 layers of the surface to get a final number 41, 61 and 81 layers of the cell. A second etching with the same dose was then performed and the intensities were obtained from 20, 40 and 60 layers respectively-separately from previous layers. The third etching and analysis were conducted under the same conditions of the second step. The 4th to 11th etchings were carried out as previously but the intensities were only measured from 20 layers. The time taken to complete this verification was 15

hours. With B3 sample: the acquisition of ions was performed with 60×60 μm^2 FoV in the same way as the D3 sample. The 2^{nd} to 4^{th} etchings were carried out under the same conditions as the first etch and intensities were obtained after 20 consecutive layers. The analysis was stopped after the fourth etching as the result was already clear. The results were extracted using the BioToF software to determine the number of layers which are needed to achieve high signal intensity.

3.7.2 BioToF-SIMS Results and Discussion

3.7.2.1 Sensitivity and spatial resolution

An increase in spatial resolution in SIMS is always coupled with decrease in sensitivity, which may affect the measurement of elements with low concentrations in samples [10]. Due to the difficulty of detecting boron intensities ($^{10}B^+$ and $^{11}B^+$) in the ^{11}BPA standards observed with BioToF-SIMS, sensitivity was maximized by controlling a digital delay generator (channel C and B) as described in 3.5.1, and also sacrificing spatial resolution by increasing the size of the primary ion beam spot to allow the passage of high ion current into the sample through apertures with multiple sizes in the column of the LMIG, until maximum sensitivity was achieved. This setting was kept constant throughout the experiments along with the parameters in **Table 3.2**.

In order to verify the sensitivity of BioToF-SIMS the series of ^{11}BPA standards were analysed in different concentrations ranging from 1-1000 ppm as explained in 3.7.13.7.1 (sensitivity test). **Figure 3.13** shows a good linear correlation between ^{11}BPA concentrations and $^{10}B^+/^{12}C^+$ ratios detected from the surface and the first depth of each sample. It is clear from **Figure 3.13** that a decrease in the $^{10}B^+/^{12}C^+$ ratios between each two consecutive concentrations is a factor ~1.5. However, the $^{10}B^+/^{12}C^+$ ratios at the lower concentration 1ppm can be detected using BioToF-SIMS, which means the possibility of providing acceptable quantitative results. In addition, $^{10}B^+/^{12}C^+$ ratios measured from the surface are ~ 2 times more intense than $^{10}B^+/^{12}C^+$ ratios measured after first depth profile in all concentrations. Depth profiling results of 100 and 1000 ppm samples in **Figure 3.14 -a** and **b** indicate the replicability of the analysis for several layers.

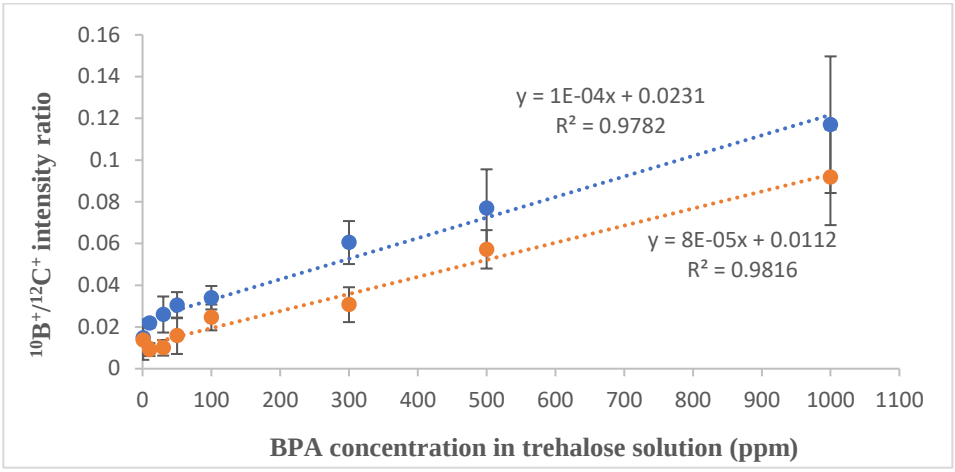

Figure 3.13: $^{10}B^+/^{12}C^+$ ratios obtained from BioToF-SIMS as a function of the B concentration in ^{11}BPA standards; ratios acquired from the surface (blue line) and after the first depth profile (orange line). Each data point represents the mean ± SD of three independent measurements.

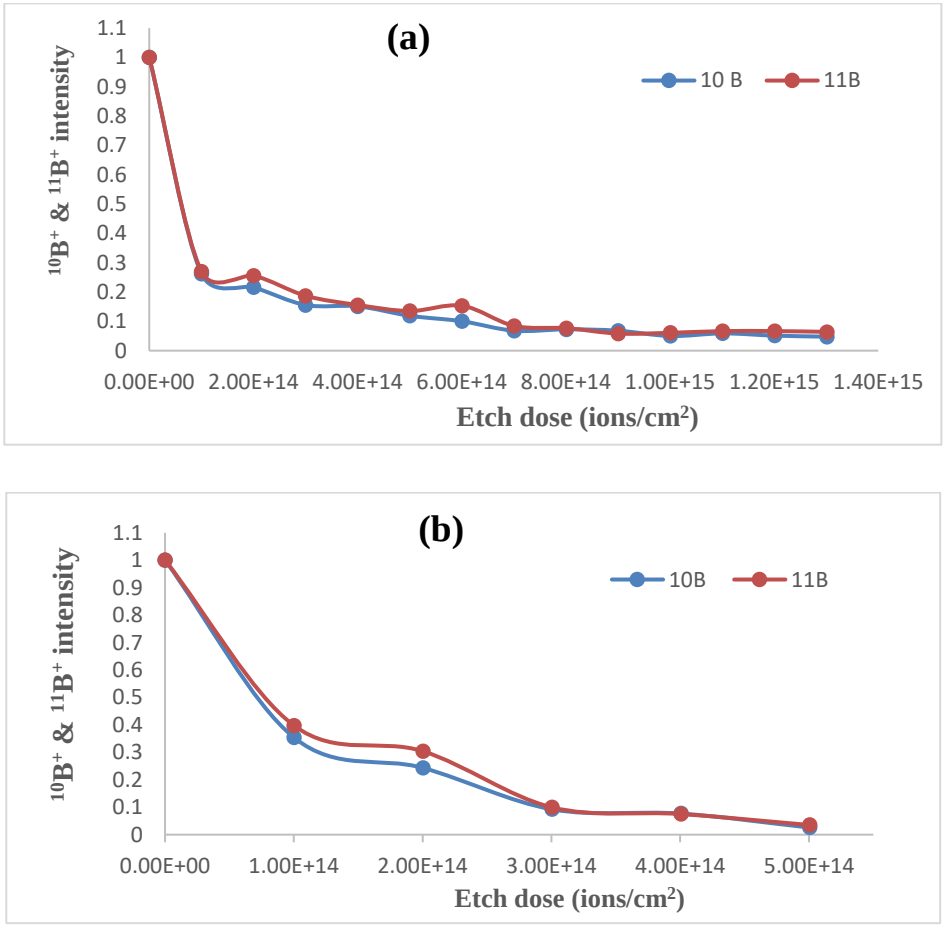

Figure 3.14: Depth profiles curves for **(a)** 1000 ppm and **(b)** 100 ppm of ^{11}BPA. $^{10}B^+$ and $^{11}B^+$ intensities were normalised to the higher intensity value of each ion.

In addition, $^{10}B^{+}/^{11}B^{+}$ ratios calculated as a function of the concentrations in **Figure 3.15** show a horizontal straight-line correlation of similar ratios values around 0.33. This ratio (0.33) is higher than the natural ratio (0.247) and may be due to the contribution of noise to the measurement. These $^{10}B^{+}$ /$^{11}B^{+}$ ratios are not an important parameter for the measurement that will conducted in Chapters 4 and 5 because there is less than the natural isotopic abundance of ^{11}B in the ^{10}BPA drug used in the preparation of cell cultures and imprints samples. Measurements will focus on the $^{10}B^{+}$ signals.

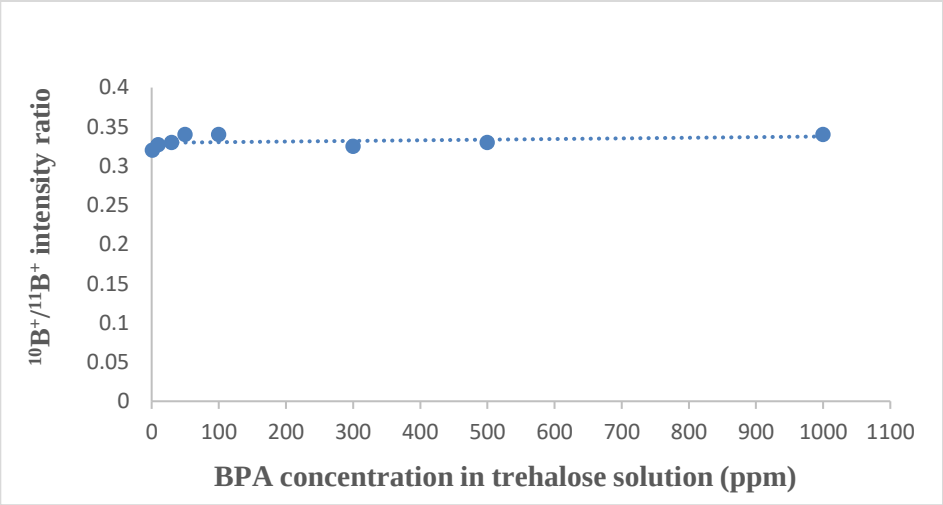

Figure 3.15: $^{10}B^{+}/^{11}B^{+}$ ratios as a function of ^{11}BPA concentrations obtained from BioToF-SIMS; ratios were acquired from the surface. Each data point represents the mean of three independent measurements.

Under the conditions described above for the sensitivity measurements, the spatial resolution of the Au^{+} beam was determined by a line profile in the BioToF-SIMS software using the 16-84% resolution measurement on a 300 square copper mesh (3.05 mm - 83 µm pitch - Agar Scientific Ltd, UK). The latter was imaged with a FoV of 1082×1082 μm^2 with 256×256 pixels, **Figure 3.16 -a**. **Figure 3.16 -b** shows the graph of distance (µm) vs $^{63}Cu^{+}$ intensity creating from line profile in **Figure 3.16 -a**. The distance between the red vertical doted lines in **Figure 3.16 -b** corresponds to a spatial resolution of 1-2 µm.

Thus, in this work the compromise between sensitivity for boron intensity and spatial resolution was achieved by using a 1-2 µm Au^{+} beam which in turn was used for all BioToF-SIMS experiments to determine the localisation of boron in the real samples from cellular cultures and biopsies.

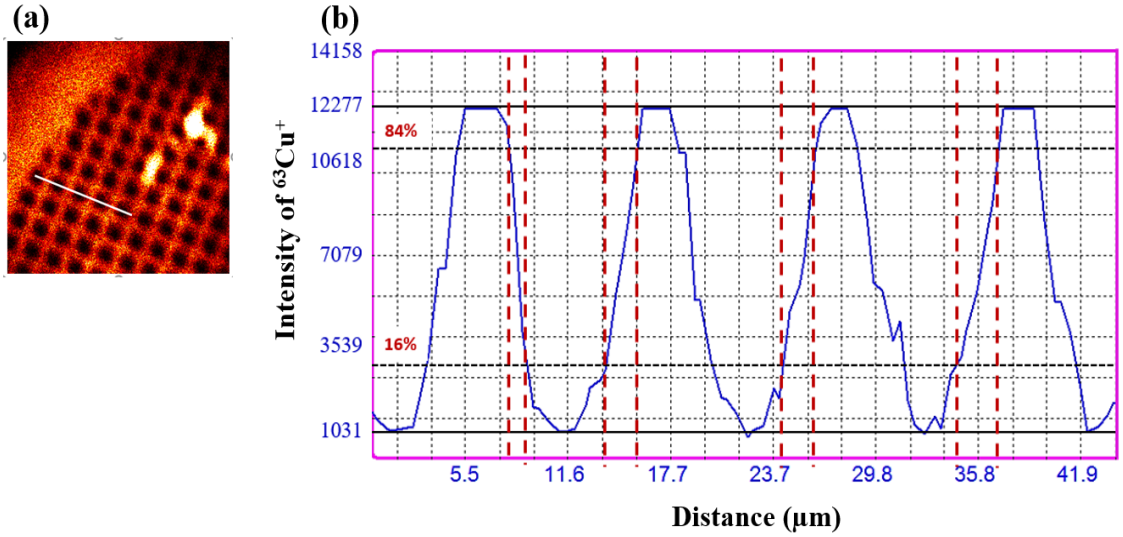

Figure 3.16: a) $^{63}Cu^{+}$ image of the copper mesh obtained by an Au^{+} beam-BioToF-SIMS with FoV 1082×1082 µm^2 and 256×256 pixels. The image shows white line profile over the mesh. **b)** shows the graph of distance (µm) vs the $^{63}Cu^{+}$ intensity with a spatial resolution of 1-2 µm determined using 16-84% resolution measurement.

3.7.2.2 Study of B3 and D3 samples in depth

The second step for ToF-SIMS analysis was to determine the primary ion dose and corresponding number of layers in depth appropriate for the acquisition of secondary ion images from the cells before loss of intensities. The D3 of BAT and B3 of GBM samples were selected because they were treated with tyrosine and BPA respectively and this also ensured that the same result was obtained in both types of cells. After summing the data from the layers at each time point as explained in the section 3.7.1 (depth profiling), the cell of interest is determined using BioToF software to extract the mass spectrum. From the mass spectrum, the intensities are extracted from the peak area for the positive ions of interest: ^{12}C, ^{23}Na, ^{28}Si and ^{39}K, all secondary intensities have been normalised for the higher intensity value for each ion.

In the D3 sample of BAT, the highest-intensity ions in the cell,$^{12}C^{+}$, $^{23}Na^{+}$ and $^{32}K^{+}$, were traced across the layers as a function of the etch dose in **Figure 3.17**. **Figure 3.18** shows that the highest intensities of ions were obtained from 81 layers after the 1st etching, while the 2nd and 3rd etch showed a decrease in the intensities after summing from 20 layers to 61 layers, indicating probable loss of parts of the cell. After the 4th etching, the drop in intensity was very clear indicating a significant loss in cell structure. To make sure, $^{12}C^{+}$ and $^{28}Si^{+}$ intensities were represented as images for each sum of layers in each etch and are shown in

Figure 3.18, where the site of the cell on the substrate is inferred from the $^{12}C^{+}$ signal and the absence of the $^{28}Si^{+}$ signal. By observing the ion images across the layers in **Figure 3.18 -a**, it is noticed that the intensity of the C^{+} signal in the cell's body gradually increases until it reaches layer 81 after the 1st etching, then the signal intensity decreases after the 2nd and 3rd etching accompanied by a decrease in the area of the cell, indicating the beginning of cell removal. From the 4th etching to the 7th etching, the cell continued to decrease in size. From the 8th to the 11th etching, the vast majority of the cell structure has faded and the C^{+} signal has disappeared.

Conversely, the Si^{+} signal behavior in **Figure 3.18 -b** is opposite to that of the C^{+} signal, the Si^{+} signal was absent from the site of the cell until the analysis reached layer 81. After the 2nd and 3rd etching, the cell size decreased and the Si^{+} signal increased in the cell perimeter. From the 4th to the 7th etch, the Si^{+} signal increased at the site of the cell in conjunction with the decrease in cell area. From the 8th to the 11th etching, Si^{+} was detected across the location of the cell, confirming the disappearance of the cell structure.

In sample B3 of the GBM, in a similar manner to sample D3, the tracing of $^{12}C^{+}$, $^{23}Na^{+}$ and $^{32}K^{+}$ ions in **Figure 3.19** showed that the highest signal of ion intensities was at 81 layers of the 1st etching, then decreased after the 2nd etching and continued to decline after the 3rd etching with minimal intensities after the 4th etching. Furthermore, the C^{+} and Si^{+} ion images in **Figure 3.20 -a &b** showed that the C^{+} signal intensity increased at layer 81 after the 1st etching with the absence of silicon signal from the cell site. After the 2nd etching, the size of the cell decreased significantly in conjunction with the decrease in the intensity of the C^{+} signal and the increase of the Si^{+} signal at the site of the cell. In the 3rd and 4th etching, the cell had disappeared.

Thus, it is concluded that both cell types behave similarly and that the number of layers suitable for data collection and obtaining the highest number of ion intensities before the cell begins to be significantly eroded is 81 layers, from surface to after the 1st etching, so all cell cultures samples were analyzed at this number of layers in depth.

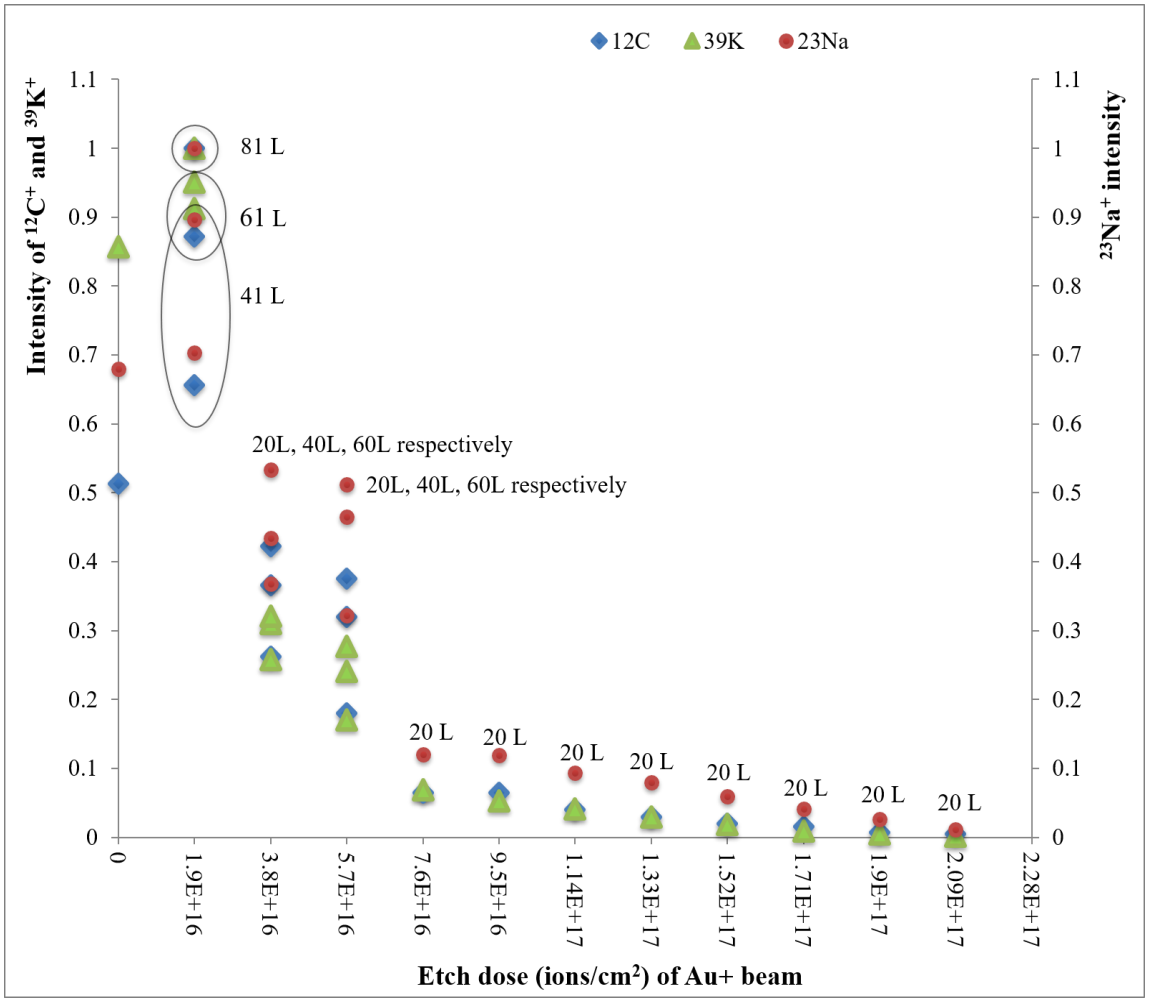

Figure 3.17: Positive secondary ion intensities of ^{12}C, ^{23}Na and ^{32}K resulting of D3 cell of BAT from different layers (L) in depth plotted as a function of etch dose using a 20 keV Au^+ beam. The intensities have been normalised for the higher intensity value for each ion.

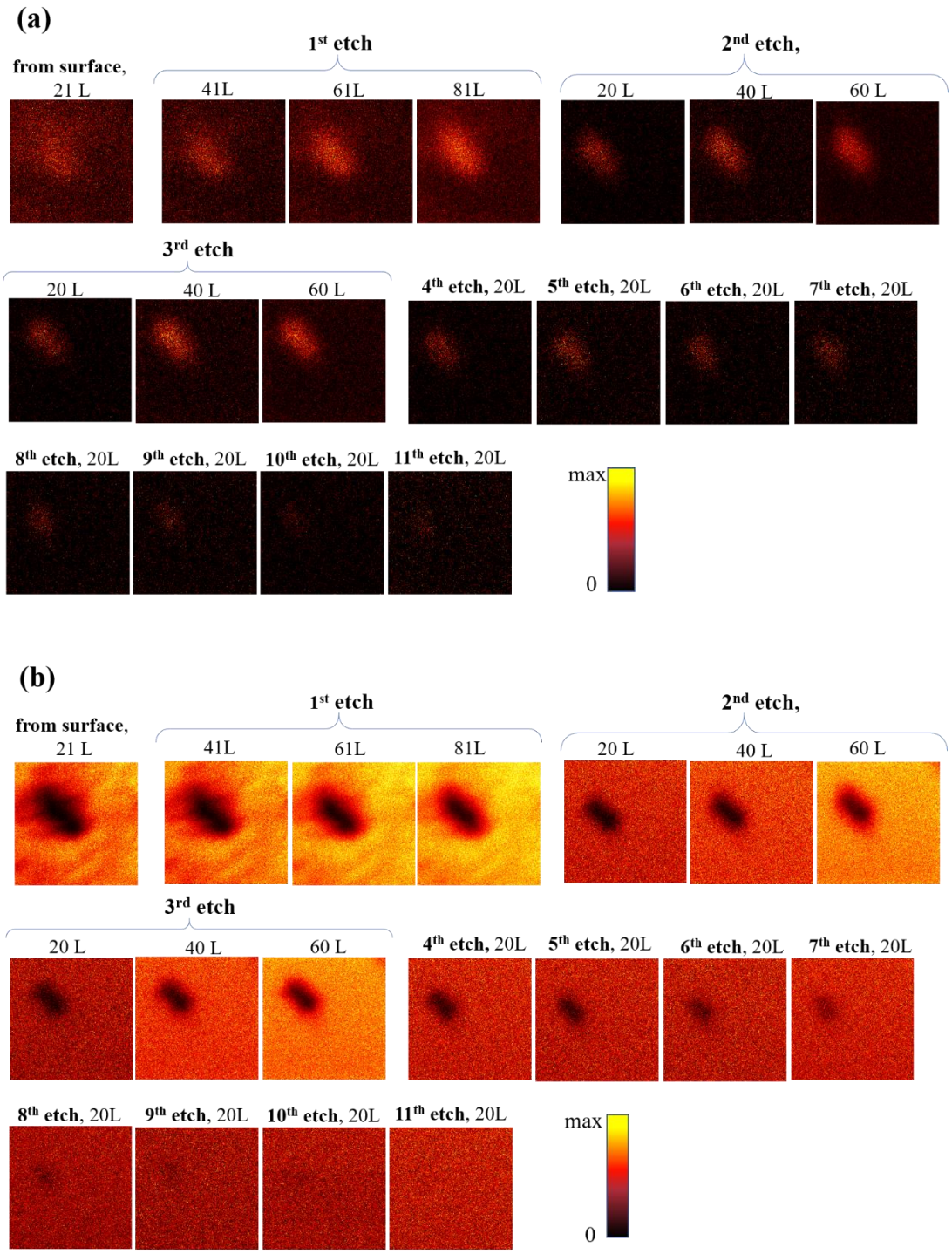

Figure 3.18: BioToF-SIMS images of D3-cell of BAT-biopsy culture in positive mode obtained using 20 keV Au^+. Images are 256×256 pixels, FoV 74×74 µm^2, etching dose was 1.9×10^{16} ions/cm^2 with FoV 200×200 µm^2. The analysis dose in the images is 1.6×10^{15} ions/cm^2. The images show the C^+ signal: *m/z* 12 in (a) and the Si^+ signal: *m/z* 28 in (b) through layers in depth from the 1st to the 11th etching. L: the number of layers summed after each etching.

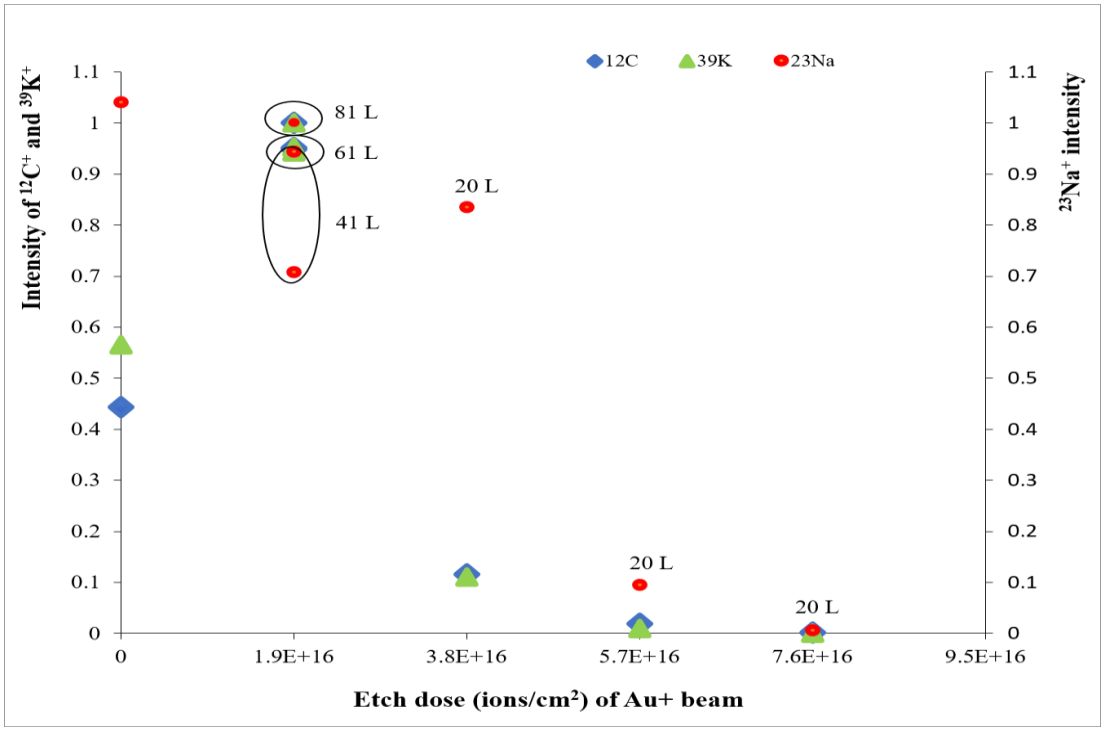

Figure 3.19: Secondary ion intensity of the following ions $^{12}C^+$, $^{23}Na^+$ and $^{32}K^+$ resulting from different layers (L) in depth of a B3 cell of GBM plotted as a function of etch dose using a Au^+ beam (20 keV). The intensities have been normalised for the higher intensity value for each ion.

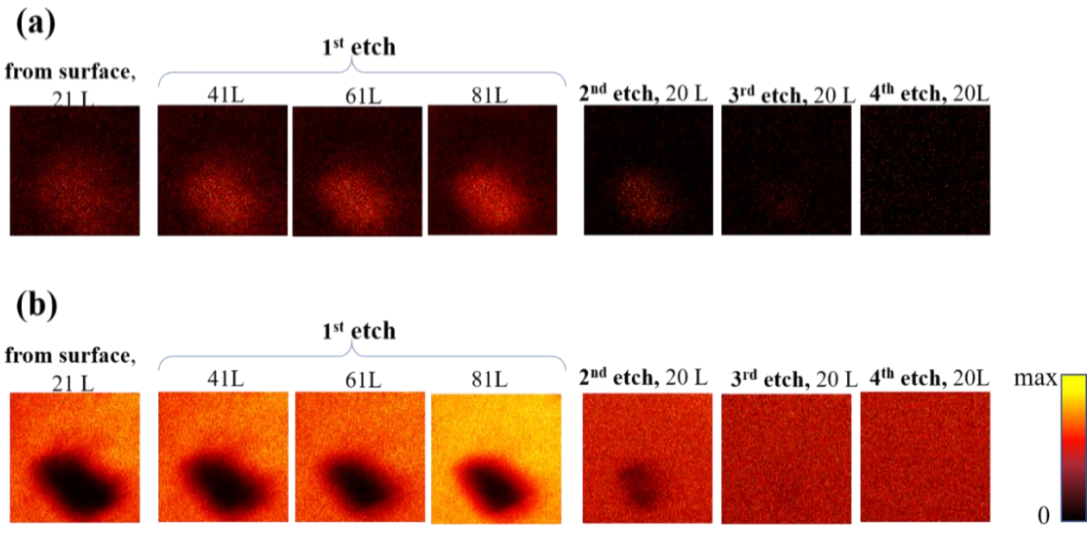

Figure 3.20: Positive ion BioToF-SIMS images of B3-cell of GBM biopsy cultures exposed to 20 keV $Au^{+\cdot}$ Analysis area 60×60 µm^2 with 256×256 pixels, etch FoV 200×200 µm^2 with dose 1.9 × 10^{16} ions/cm^2. The analysis dose in the images is 6.4×10^{14} ions/cm^2. (a) & (b) show the images of C^+ and Si^+ signals intensities at *m/z* 12 and 28 respectively from a cell in depth by summing the layers from the 1st to the 4th etching. L represent the layers number after each etching process.

3.8 References

[1] A. Detta, “personal communication,” 2018.

[2] A. Detta, J. Harland, I. Hanif, S. M. Brown, and G. Cruickshank, “Proliferative activity and in vitro replication of HSV1716 in human metastatic brain tumours,” *J. Gene Med.*, vol. 5, no. 8, pp. 681–689, 2003.

[3] M. A. Farr-Jones, I. F. Parney, and K. C. Petruk, “Improved technique for establishing short term human brain tumor cultures,” *J. Neurooncol.*, vol. 43, pp. 1–10, 1999.

[4] R. I. Freshney, *Culture of Animal Cells: A Manual of Basic Techniques*, 3rd ed. New York: Wiley-Liss, 1994.

[5] A. Detta and G. S. Cruickshank, “L-Amino Acid Transporter-1 and Boronophenylalanine-Based Boron Neutron Capture Therapy of Human Brain Tumors,” *Cancer Res.*, vol. 69, no. 5, pp. 2126–2132, 2009.

[6] N. Tahallah, A. Brunelle, S. De La Porte, and O. Laprévote, “Lipid mapping in human dystrophic muscle by cluster-time-of-flight secondary ion mass spectrometry imaging,” *J. Lipid Res.*, vol. 49, no. 2, pp. 438–454, 2008.

[7] J. C. Vickerman and N. Winograd, “Cluster TOF-SIMS imaging and the Cterization of Biological Materials,” in *Cluster Secondary ion mass spectrometry : Principles and Applications*, Canada: John Wiley & Sons Inc, 2013, pp. 273–274.

[8] D. R. Lorey, G. H. Morrison, and S. Chandra, “Dynamic secondary ion mass spectrometry analysis of boron from boron neutron capture therapy drugs in co-cultures: Single-cell imaging of two different cell types within the same ion microscopy field of imaging,” *Anal. Chem.*, vol. 73, no. 16, pp. 3947–3953, 2001.

[9] S. Chandra and G. H. Morrison, “Evaluation of fracture planes and cell morphology in complementary fractures of cultured cells in the frozen-hydrated state by field-emission secondary electron microscopy: Feasibility for ion localization and fluorescence imaging studies,” *J. Microsc.*, vol. 186, no. 3, pp. 232–245, 1997.

[10] X. Zha, W. A. Ausserer, and G. H. Morrison, “Quantitative Imaging of a Radiotherapeutic Drug, $Na_2B_{12}H_{11}SH$, at Subcellular Resolution in Tissue Cultures Using Ion Microscopy,” *Cancer Res.*, vol. 52, no. 19, pp. 5219–5222, 1992.

[11] J. Malm, D. Giannaras, M. O. Riehle, N. Gadegaard, and P. Sjövall, “Fixation and drying protocols for the preparation of cell samples for time-of-flight secondary ion mass spectrometry analysis,” *Anal. Chem.*, vol. 81, no. 17, pp. 7197–7205, 2009.

[12] P. Mentré, “Preservation of the diffusible cations for SIMS microscopy. I. A problem related to the state of water in the cell,” *Bio. Cell*, vol. 74, pp. 19–30, 1992.

[13] S. Chandra and G. H. Morrison, “Sample preparation of animal tissues and cell cultures for secondary ion mass spectrometry (SIMS) microscopy,” *Biol Cell*, vol. 74, no. 1, pp. 31–42, 1992.

[14] K. L. Moore, M. Schröder, and C. R. M. Grovenor, “Imaging secondary ion mass spectrometry,” in *Handb. Nanoscopy*, Weinheim:Wiley- VCH, 2012, pp. 709–744.

[15] P. Sjövall, J. Lausmaa, H. Nygren, L. Carlsson, and P. Malmberg, “Imaging of Memabrane Lipids in Single Cells by Imprint-Imaging Time-of-Flight Secondary Ion Mass Spectrometry,” *Anal Chem*, vol. 75, no. 14, pp. 3429–3434, 2003.

[16] H. Nygren *et al.*, "A cell preparation method allowing subcellular localization of cholesterol and phosphocholine with imaging TOF-SIMS," *Colloids Surfaces B Biointerfaces*, vol. 30, no. 1–2, pp. 87–92, 2003.

[17] D. M. Jamba, *Semiconductor Measurement Technology: Some Aspects of Dose Measurement for Accurate Ion Implantation*. Washington: National Bureau of Standards special publication, 1977.

[18] N. Cheung, "Ion Implantation," *University of California*, 2010. [Online]. Available: http://www-inst.eecs.berkeley.edu/~ee143/fa10/lectures/Lec_08.pdf. [Accessed: 08-Oct-2019].

[19] K. Yeager, "SPSS Tutorials: Independent Samples t Test," *Kent State University*. [Online]. Available: https://libguides.library.kent.edu/spss/independentttest. [Accessed: 14-Jan-2019].

[20] INVESTOPEDIA, "What assumptions are made when conducting a t-test?" [Online]. Available: https://www.investopedia.com/ask/answers/073115/what-assumptions-are-made-when-conducting-ttest.asp. [Accessed: 14-Jan-2019].

[21] R. Hill and P. W. M. Blenkinsopp, "The development of C_{60} and gold cluster ion guns for static SIMS analysis," *Appl. Surf. Sci.*, vol. 231–232, pp. 936–939, 2004.

[22] N. Davies, D. E. Weibel, P. Blenkinsopp, N. Lockyer, R. Hill, and J. C. Vickerman, "Development and experimental application of a gold liquid metal ion source," *Appl. Surf. Sci.*, vol. 203–204, pp. 223–227, 2003.

[23] R. M. Braun *et al.*, "Performance characteristics of a chemical imaging time-of-flight mass spectrometer," *Rapid Commun. Mass Spectrom.*, vol. 12, no. 18, pp. 1246–1252, 1998.

[24] M. G. Ponomarev, B. J. Garrison, J. C. Vickerman, and R. P. Webb, "A molecular dynamics study of a 5 keV C_{60} fullerene impact on a two-component organic molecular sample," *Surf. Interface Anal.*, vol. 43, no. 1–2, pp. 107–111, 2011.

[25] E. De Hoffmann and V. Stroobant, *Mass Spectrometry: Principles and Applications*, 3rd ed. England: John Wiley & Sons Ltd, 2007.

[26] R. J. Cotter, "The New Time-of-Flight Mass Spectrometry.," *Anal. Chem.*, vol. 71, no. 13, pp. 445A-451A, 1999.

[27] J. C. Vickerman and I. S. Gilmore, *Surface Analysis – The Principal Techniques*, 2nd ed. 2009.

[28] J. C. Vickerman, D. Briggs, and R. Hill, "Analysis beams used in ToF-SIMS," in *ToF-SIMS: Materials Analysis by Mass Spectrometry*, 2nd ed., IM Publications, 2013, pp. 271–275.

[29] H. Jiang, "Exploiting Stable Isotope Imaging with High Resolution Secondary Ion Mass Spectrometry for Applications in Biology," PhD thesis, Oxford University, UK, 2014.

[30] D. K. Schroder, *Semiconductor Material and Device Characterization*, 3rd ed. United States of America: John Wiley & Sons Inc, 2006.

[31] D. Gao, X. Huang, and Y. Tao, "A critical review of NanoSIMS in analysis of microbial metabolic activities at single-cell level," *Crit. Rev. Biotechnol.*, vol. 36, no.

5, pp. 884–890, 2016.

[32] K. H. Lau, M. Christlieb, M. Schröder, H. Sheldon, A. L. Harris, and C. R. M. Grovenor, “Development of a new bimodal imaging methodology : a combination of fluorescence microscopy and high-resolution secondary ion mass spectrometry,” *J. Microsc.*, vol. 240, no. January, pp. 21–31, 2010.

[33] J.-L. Guerquin-Kern, T. Wu, C. Quintana, and A. Croisy, “Progress in analytical imaging of the cell by dynamic secondary ion mass spectrometry (SIMS microscopy),” *Biochim. Biophys. Acta*, vol. 1724, pp. 228–238, 2005.

[34] M. Thellier *et al.*, “Methodological developments for application to the study of physiological boron and to boron neutron capture therapy,” *J. Trace Microprobe Tech.*, vol. 19, no. 4, pp. 623–657, 2001.

[35] A. R. Spurr and P. Galle, “Localization of Elements in Botanical Materials by Secondary Ion Mass Spectrometry,” in *Secondary Ion Mass Spectrometry SIMS II*, A. Benninghoven, C. A. EvansJr, R. A. Powell, R. ShimizuH., and H. A. Storms, Eds. Verlag New York: Springer, 1979, pp. 252–255.

[36] S. K. Aggarwal, B. S. Wang, C. F. You, and C. H. Chung, “Fractionation Correction Methodology for Precise and Accurate Isotopic Analysis of Boron by Negative Thermal Ionization Mass Spectrometry Based on BO_2 Ions and Using the $^{18}O/^{16}O$ Ratio from ReO_4 for Internal Norm,” *Anal. Chem.*, vol. 81, no. 17, pp. 7420–7427, 2009.

[37] V. A. Arslambekov, V. S. Petrov, and M. V. Ivanov, “Sublimation of volatile components of electrolessly reduced Ni - B alloys: Kinetics and mass spectrometry,” *Prot. Met.*, vol. 37, no. 4, pp. 327–330, 2001.

[38] R. N. Sah and P. H. Brown, “Isotope ratio determination in Boron analysis,” *Biol. Trace Elem. Res.*, vol. 66, no. 1–3, pp. 39–53, 1998.

[39] J. Malherbe *et al.*, “A New Radio Frequency Plasma Oxygen Primary Ion Source on Nano Secondary Ion Mass Spectrometry for Improved Lateral Resolution and Detection of Electropositive Elements at Single Cell Level,” *Anal. Chem.*, vol. 88, no. 14, pp. 7130–7136, 2016.

[40] N. S. Smith, P. P. Tesch, N. P. Martin, and R. W. Boswell, “The Hyperion™ ion probe for next generation FIB, SIMS and Nano-Ion implantation,” *Microsc. Microanal.*, vol. 15, no. Suppl 2, pp. 312–313, 2009.

[41] Oregon Physics, “Hyperion II Dual Polarity Ion Source,” *Oregon Physics*, 2015. [Online]. Available: http://www.oregon-physics.com/hyperion2.php. [Accessed: 15-Jul-2018].

[42] J. P. Berry, P. Galle, D. Chassoux, F. Escaig, L. G. Linarez-Cruz, and G. Lespinats, “Mapping of intracellular halogenous molecules by low and high resolution SIMS microscopy,” *Biol. Cell*, vol. 74, no. C, pp. 93–98, 1992.

[43] R. Peteranderl and C. Lechene, “Measure of carbon and nitrogen stable isotope ratios in cultured cells,” *J. Am. Soc. Mass Spectrom.*, vol. 15, no. 4, pp. 478–485, 2004.

[44] C. Lechene *et al.*, “High-resolution quantitative imaging of mammalian and bacterial cells using stable isotope mass spectrometry,” *J. Biol.*, vol. 5, pp. 1–30, 2006.

4 Determining the Uptake and the Subcellular Distribution of 10-Boron in Cell culture samples of Glioblastoma Multiform Tumours (GBM) and Brain around Tumour (BAT) Treated with ^{10}B Phenylalanine (BPA)[1]

4.1 Introduction

2D and 3D imaging studies on biological samples have received considerable attention in chemical and pharmacological analyses because of their ability to provide maps that determine the distribution and localisation of elements and molecules at the subcellular level in tissues and cells. These studies contribute to the improvement of analysis applications using chemical imaging as well as understanding many of the therapeutic aspects in different diseases. ^{10}BPA is one of the most important agents of the BNCT treatment used to treat malignant tumours as has been explained in Chapter 2. The success of BNCT relies on the precise localisation of ^{10}B of the BPA inside the tumour cells, especially in the nuclei, hence the need to use imaging techniques able to identify drug distribution sites. Imaging experiments require spatial resolution in the acquisition of images, which in turn vary from one instrument to another according to the type, energy and focus of analysis beam used.

In this study, the capabilities of two SIMS instruments were evaluated in the determination of the ^{10}B distribution of BPA treatment at the cellular level of biological samples using the microprobe imaging approach. The NanoSIMS with a ~ 400 nm diameter Cs^+ beam and the BioToF-SIMS with a 1-2 µm diameter Au^+ beam was used for this work; the instruments are described in Chapter 1. The analysed samples were primary cell cultures grown from GMB tumour and BAT tissue biopsies of patients with a high degree of tumour. The difference between the two biopsies is that the GBM was taken from tumour core and is expected to contain many tumour cells, while BAT was taken from the surrounding areas of the tumour (brain around tumour, BAT) and contains a few infiltrating tumour cells. This is the first time that drug uptake in primary human brain tumour cell cultures have been studied with SIMS giving spatial distribution. Both types of samples were treated *in vitro* in three groups: with BPA, addition of tyrosine then BPA, addition of BPA and followed by an efflux process. The samples were imaged and the quantitative measurements of the secondary ion yields from the boron counts were extracted for the different treatments and compared

[1] The main results from this Chapter have now been published. S. Aldossari, G. McMahon, N. P. Lockyer, and K. L. Moore, "Microdistribution and quantification of the boron neutron capture therapy drug BPA in primary cell cultures of human glioblastoma tumour by NanoSIMS," *Analyst*, vol. 144, pp. 6214–6224, 2019. DOI: 10.1039/C9AN01336A.

between the samples. The results from the two instruments were then compared in terms of spatial resolution of imaging and quantification.

4.2 Experimental section

4.2.1 Sample preparation

The preparation of primary cell cultures samples of GBM and BAT was explained in section 3.2.2.1. There were 4 different biopsies: 2 of GBM tumour (A & B) and 2 of BAT tissue (C & D) respectively; and 4 treatment groups for B and D biopsies:

1. Control (no drugs).
2. 10 mM ^{10}BPA-mannitol for 4 h (^{10}BPA-mannitol was gifted from Cancer Research, UK).
3. 10 mM Tyrosine-mannitol for 4 h (Sigma Aldrich, UK) followed by a wash and then 4 h incubation with 10 mM ^{10}BPA-mannitol.
4. 4 h ^{10}BPA-mannitol (10 mM) followed by 4 h efflux.

For the remainder of the thesis ^{10}BPA-mannitol will be referred to as ^{10}BPA.

For the A and C biopsies, there was only one sample from each type without treatment (1=control). After treatment the silicon wafers were washed with ice-cold physiological pH saline and were immediately flash-frozen in isopentane/liquid nitrogen and stored at -80 °C until analysis [1].

Prior to analysis with SIMS the samples were prepared by freeze-drying at Manchester. Samples were transferred to the surface analysis research lab in a solid carbon dioxide ice basin at -78 °C, then mounted on a pre-cooled copper stub under N_2 gas flow and left in a vacuum chamber overnight and under a pressure of 1×10^{-8} mbar. After 24 hours, the samples were ready for SIMS analysis.

4.2.2 SIMS analysis

4.2.2.1 NanoSIMS analysis

The NanoSIMS 50L instrument is discussed in Chapter 1. For each NanoSIMS session and before beginning the analysis of each sample, the current of the Cs^+ beam was measured in FCo with all D1 apertures. Based on the results of the preliminary experiments in Chapter 3, the samples were analysed with NanoSIMS in two stages as follows.

The first stage: The natural boron isotope ratios in the control samples of cell cultures (A1-B1 of GBM and C1-D1 of BAT) and the increase in boron isotopes signals for the treated samples of cell cultures (B2 of GBM and D2 of BAT) were verified. The mass detectors were tuned to detect the following negative secondary ions ^{10}B, ^{11}B, ^{12}C, $^{10}B^{12}C$, $^{12}C^{14}N$, ^{29}Si and ^{31}P simultaneously. The positions of the isotopic peaks were calibrated using a reference standard suitable for each ion to avoid any interferences between ions, and checked by HMR scans as explained previously in sections 3.6.1 (the second stage-1st step) and 3.6.2.2. The CCD camera in the NanoSIMS instrument was used to choose ROIs of cells to perform detailed analysis. The samples were implanted using a Cs^+ dose of 1.9×10^{16} ions/cm^2 (as determined in section 3.6.2.3) with D1=0 (unfocused beam) and rastering over an area of 100×100 µm^2. Images were then acquired adding a further dose of 1.44×10^{16} ions/cm^2 to the ROIs with D1 = 2 with a beam current ranging from 2-3.4 pA. During imaging, the Cs^+ ion beam was rastered on an area between 35×35 and 75×75 µm^2 depending on the single cell size or 75×75 and 80×80 µm^2 when imaging more than one cell together in the same frame. In all images the dwell time was 2000 µs/pixel with 256×256 pixels. Under these imaging conditions, the Cs^+ beam provides a spatial resolution of 400 nm as described in section 3.6.2.4. The images were processed using the Fiji -ImageJ software with Open MIMS plugin, the software details were mentioned in Chapter 3. The graphs of results and quantification were carried out using Origin and Microsoft Excel.

The second stage (The main experiment): The aim was to study and compare the distribution of ^{10}B from BPA drug at the cellular level in cell cultures, the GBM samples (B2, B3, B4) and BAT samples (D2, D3, D4) and compare the amount of ^{10}B between treatments. The ion detectors were tuned to collect the following negative ions ^{10}B, ^{12}C, $^{10}B^{12}C$, $^{12}C^{14}N$, ^{29}Si, ^{31}P and ^{32}S simultaneously. Cells were selected using the CCD and analysed in the same way as in the first stage above using the same Cs^+ doses for implantation and image acquisition. The beam current intensity ranged from 1.9-5.3 pA. The FoV of primary ion beam during imaging ranged from 35×35 - 60×60 µm^2 with a single cell or 56×56 - 80×80 µm^2 for areas

containing more than one cell. All NanoSIMS images were acquired with D1=2, 256×256 pixels and a dwell time of 2000 µs/pixel. The processing of images and the graphs of results and quantification were performed using the same software mentioned above.

4.2.2.2 BioToF-SIMS analysis

The BioToF-SIMS instrument was previously discussed in Chapter 1. All GBM tumour and BAT samples were analysed (etching and imaging) with a Au^+ primary beam (LMIG: Ionoptika Ltd., UK) at 20 keV and 4-9 nA current in positive mode with 256×256 pixels. The pulse width of the Au^+ beam was 100 ns for acquisitions in order to increase measurement sensitivity. A Au^+ beam in imaging mode provides a spatial resolution of 1-2 µm using the instrument setting conditions as described in sections 3.7.1 and 3.7.2.1.

The main experiment to study the distribution and amount of the drug in the samples is described as follows. Data were acquired from 21 layers of cell surface in pulse mode with a variable FoV depending on the cell size under study, between 60×60 μm^2 to 252×252 μm^2. The area was then exposed one etching using a dose of 1.9×10^{16} ions/cm^2 of Au^+ beam in DC mode with a FoV 350×350 μm^2 to 600×600 μm^2, the etched area was selected to be at least twice the size of the image FoV to avoid the crater edge effects. After etching data was collected again using the pulsed beam from 60 extra layers and added them to the data of the first 21 layers. Finally, data was processed from the total 81 layers, where accumulated doses of primary ions were $2\text{-}5\times10^{14}$ ions/cm^2. BioToF software was used to select the spectral region from 1 to 150 Da and generate maps of relevant ions $^{10}B^+$, $^{11}B^+$, $^{12}C^+$, $^{23}Na^+$, $^{28}Si^+$ and $^{39}K^+$. The time taken to complete one experiment was approximately 3-5 hours. The analysis was repeated 3-5 times on different cells for each sample. The processing of images and the graphs of results and quantification were performed as described in section 3.5.2.

4.2.3 NanoSIMS results and discussion

4.2.3.1 Chemical imaging of boron isotopes (First stage)

In this step, the ratios of boron isotopes ($^{10}B/^{11}B$) and their comparison with natural ratio were verified to check the source of the boron in the treated samples compared to the control samples. All control samples (A1, B1, C1 and D1) and treated cell samples (B2 and D2) with BPA for 4h were analysed under the same analytical conditions and compared quantitatively.

4.2.3.1.1 Control samples imaging

The negative secondary ion maps from the area indicated with an arrow in the CCD image in A1 of GBM control sample (Cell Culture), which was not pre-treated with BPA drug, are presented in **Figure 4.1**. It is clear from the maps that there is a significant difference in the distribution of ions, which helps to distinguish the cell morphology (nucleus and cytoplasm). SE maps show the general structure of the cell. The Si map also shows that the cell completely covered the silicon substrate and was free of holes. The carbon map shows high intensity of the C ion across the cell with a slight contrast between the nucleus and cytoplasm, while the CN map showed lower signal intensity than the C with more contrast between the parts of the cell. The P indicated the position of the nucleus where it was much more intense than the cytoplasm. The most important thing here is that the NanoSIMS detected very weak signals for each of the ^{10}B, ^{11}B and $^{10}B^{12}C$, which were distributed across the cell in similar pattern. This is to be expected because this sample was not pre-treated with BPA. Despite the low counts of these ions, they accumulate heavily outside of the cell, specifically around the cell. The entire cell was selected with the avoidance of some features, specifically in the top right part of the cell, which gave a high signal with CN, low signal with C, and no P signal. These features do not appear as holes in the Si map, so it is likely to be a contaminant on the surface. The area around the edge of the cell, where the P and C signals are high, has not been determined to be within the cell because of the uncertainty of the identity of this area. This has been discussed in more detail in section 4.2.3.2.4. **Figure 4.2** shows another control cell, B1, from a different GBM tumour biopsy (cell culture). In boron isotopes maps, the ions showed a similar distribution pattern to cell A1. In the B1 cell there are small features uniformly distributed across the cell which give varying signal intensities of C, CN and P, these are likely to be crystals from the sample preparation medium.

Figure 4.3 & 4.4 shows the imaging of C1 and D1 control cell cultures from two different BAT biopsies. It is observed from the images that all ions were distributed across the cell in a pattern similar to that of the A1 cell. Looking at the maps of boron isotopes, ^{10}B and ^{11}B signals accumulate in the outer perimeter of the cell more than inside the cell, where high signals of P and C appear. On the surface of cell D1 in **Figure 4.4**, there are features that look like branches. Wherever these features are found, a slight decrease in the ion signal intensity was observed which may indicate that these are crystals that originate from the medium of preparation. Analysis was repeated on different cells for each sample at least three times. All control sample images, although different in origin (different patients) and type (BAT or GBM), showed similar results for the distribution of boron isotopes in terms of localisation. The total counts of ^{11}B summed from the cell is four times the total ^{10}B counts consistent with the natural isotope ratio. The primary ion beam settings in this experiment provided sufficient spatial resolution, as shown in the images of C, CN and P, to allow cell morphology to be distinguished from features on the cell surface.

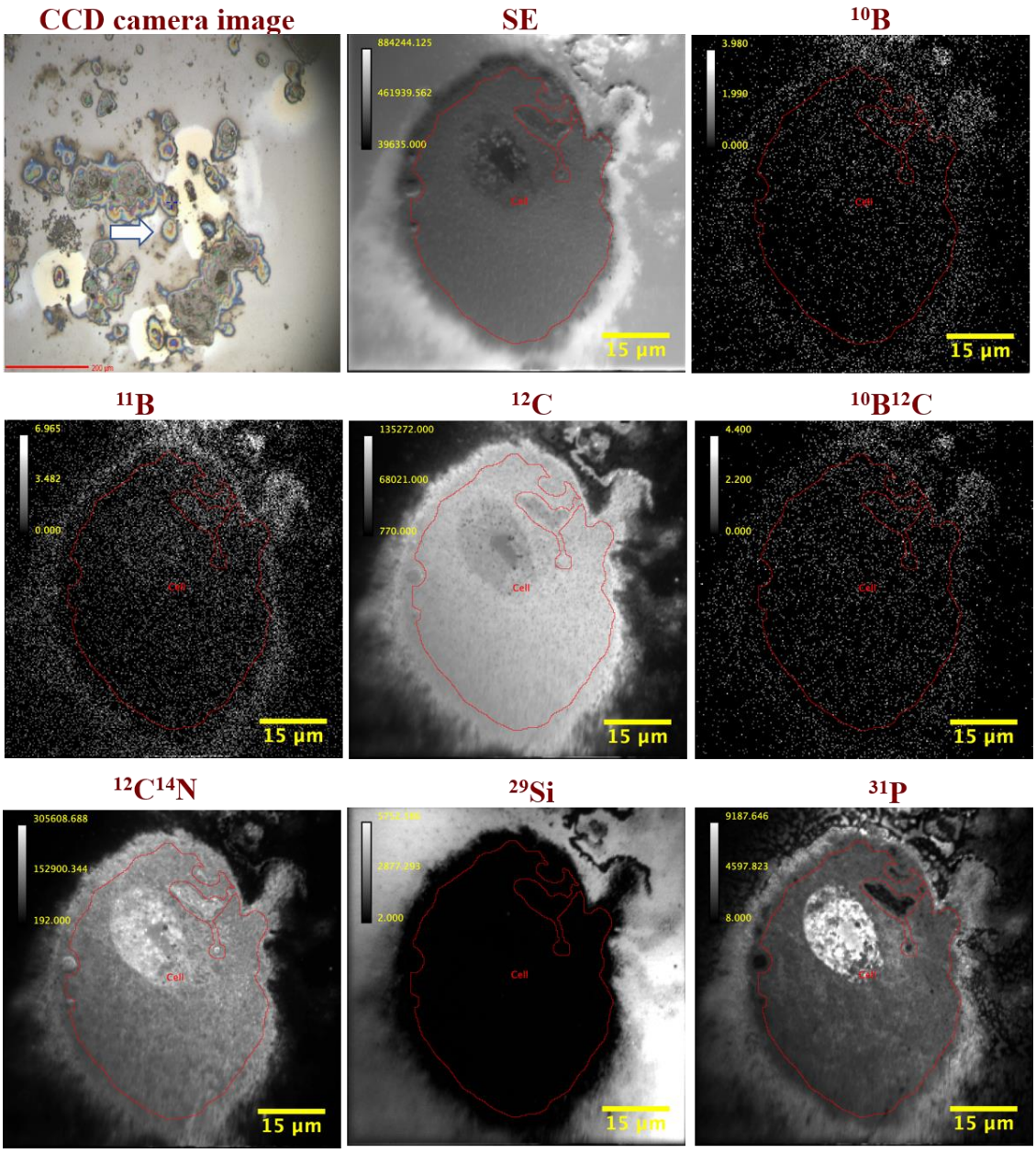

Figure 4.1: NanoSIMS analysis for cell A1 of GBM control sample with FoV 75×75 µm^2. The arrow in the CCD camera image indicates the chosen cell (scale bar 200 µm). SE: secondary electron image shows the total structure of the cell. Images of the following negative secondary ions: ^{10}B, ^{11}B, ^{12}C, ^{10}B^{12}C, ^{12}C^{14}N, ^{29}Si and ^{31}P show the ion distribution across the cell.

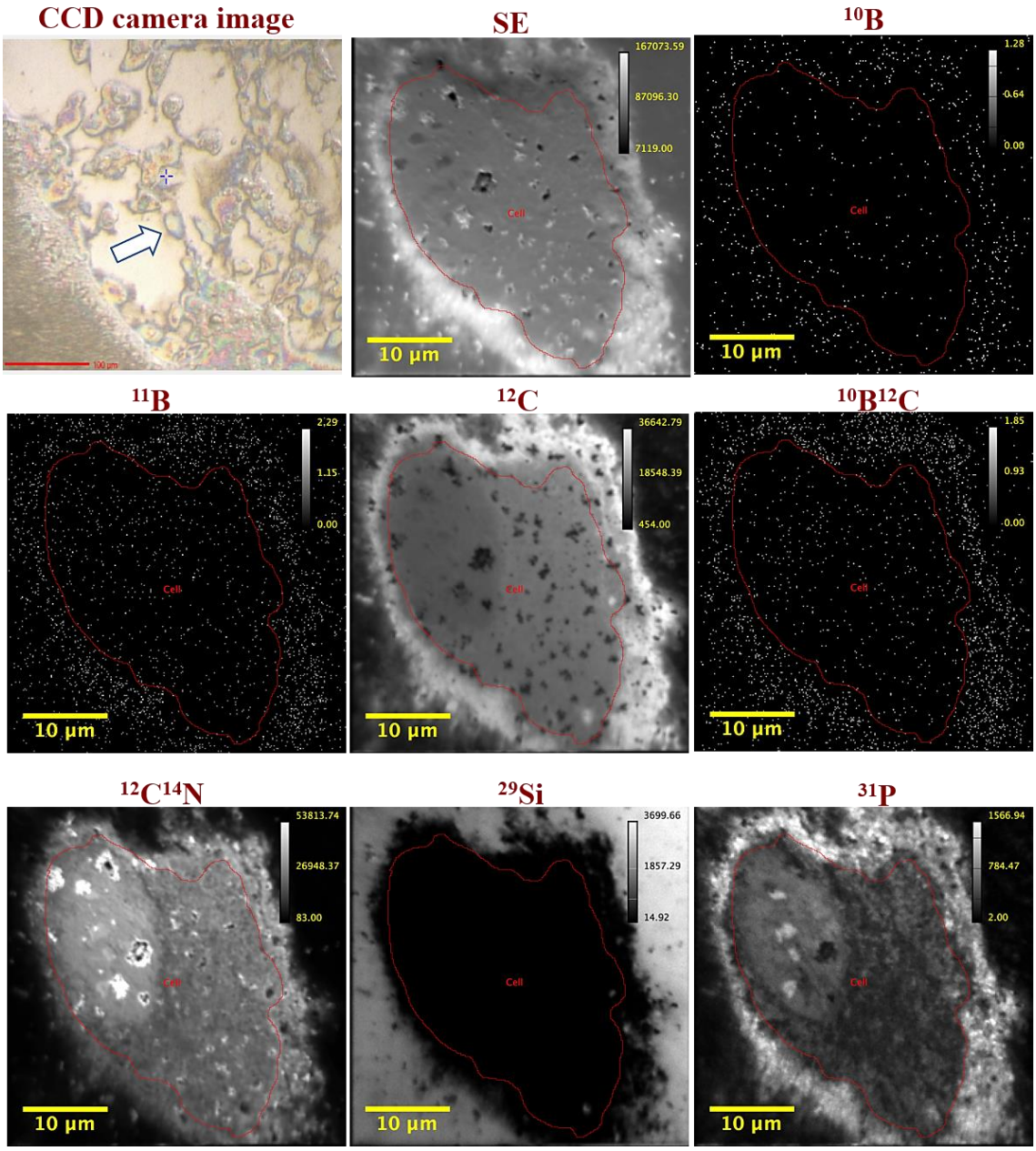

Figure 4.2: The analysis of cell B1 of GBM control sample with FoV 40×40 µm^2 by NanoSIMS. The selected cell for analysis is shown in the CCD camera image (scale bar 100 µm). SE: secondary electron image shows the total cell structure. Images of the following negative secondary ions: ^{10}B, ^{11}B, ^{12}C, ^{10}B^{12}C, ^{12}C^{14}N, ^{29}Si and ^{31}P show the ion distribution across the cell.

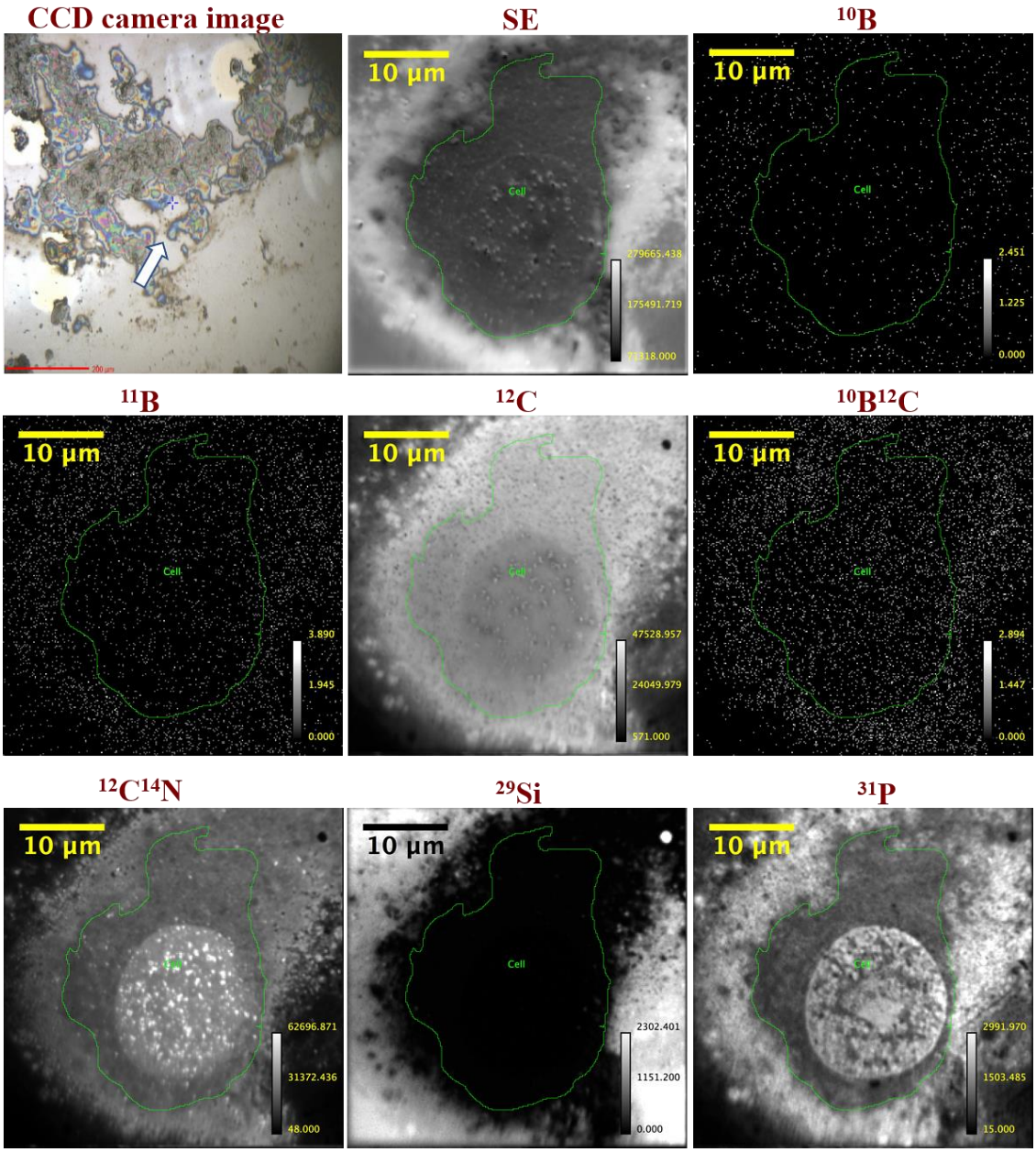

Figure 4.3: NanoSIMS analysis of a C1 cell of BAT control sample with FoV 40×40 µm^2. CCD camera image (scale bar 200 µm) indicating selected cell for analysis by arrow. SE: secondary electron image shows the general shape of the cell. Images of the following negative secondary ions: ^{10}B, ^{11}B, ^{12}C, ^{10}B^{12}C, ^{12}C^{14}N, ^{29}Si and ^{31}P show the ion distribution across the cell.

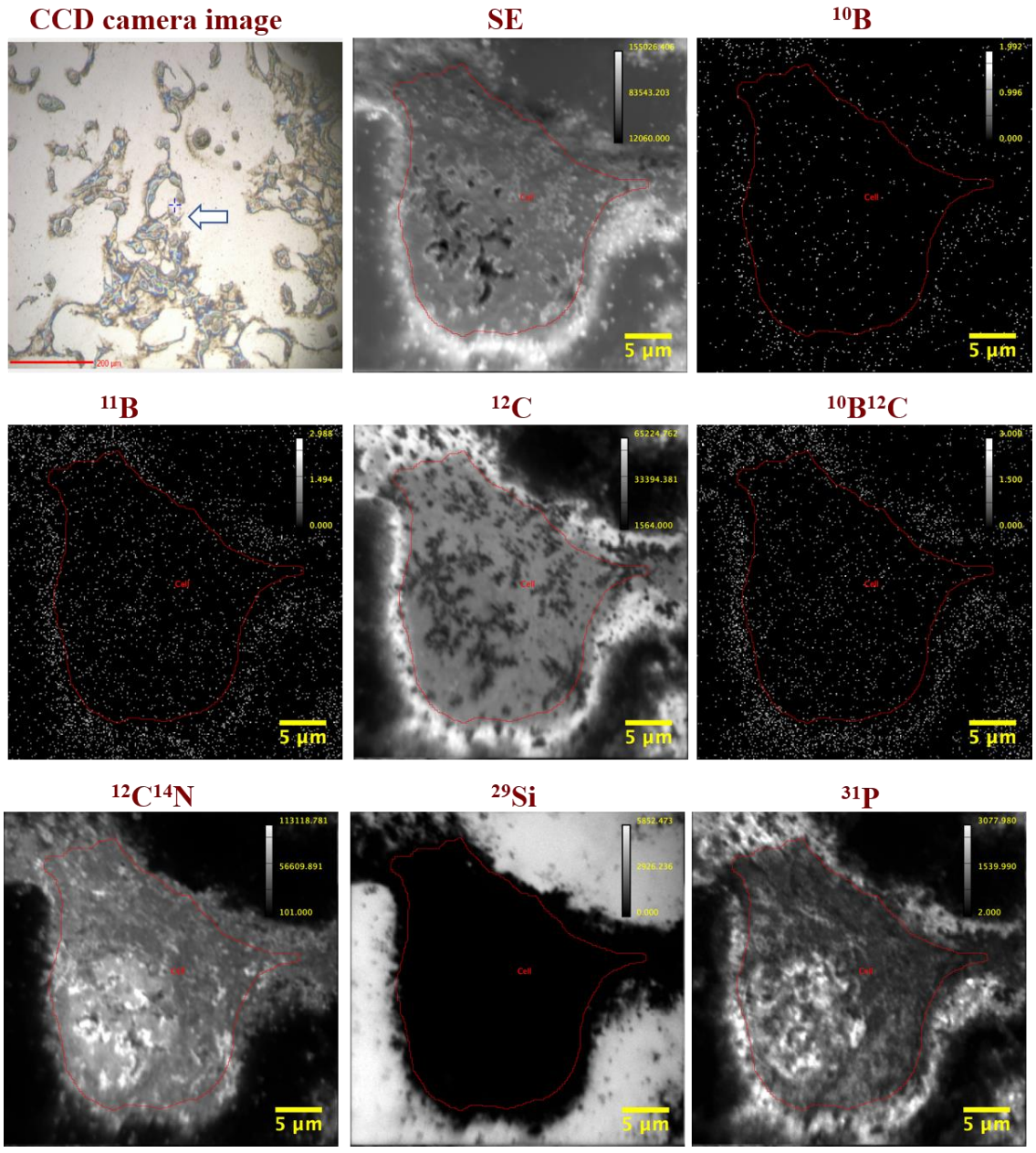

Figure 4.4: NanoSIMS analysis of cell culture D1 of BAT control sample with FoV 35×35 µm^2. The chosen cell for analysis is marked by an arrow in the CCD camera image (scale bar 200 µm). SE: secondary electron image displays the total cell structure. Images of the following negative secondary ions: ^{10}B, ^{11}B, ^{12}C, ^{10}B^{12}C, ^{12}C^{14}N, ^{29}Si and ^{31}P show the ion distribution across the cell.

4.2.3.1.2 B2 of GBM and D2 of BAT imaging

Images of the cell culture B2 sample, which was pre-treated with BPA for 4 hours, are shown in **Figure 4.5**. Cell morphology was evident from the distribution of C, CN and P ions with the same features as shown for sample A1. The SE image showed the general shape and location of the cells, while the Si map showed no holes in the cell body. In terms of the distribution of the boron isotopes, it is noted that both ^{10}B and ^{11}B are distributed in a pattern very similar to sample A1, but the ^{10}B and the $^{10}B^{12}C$ signals in this sample are higher than the control samples. The ^{10}B map shows that there is greater accumulation of ^{10}B in the nuclei and areas surrounding the cell compared to the ^{11}B. Despite the weakness of the ^{11}B signals, the localisation of ^{11}B was more around the cell than inside it. The ^{10}B is in an active form (in BPA) to promote its uptake into the cell, while any contamination from ^{11}B is not likely to be in an active form and remains outside the cell. The cytoplasmic region of the B2 cell exhibited accumulation of ^{10}B in contrast to the control samples.

Figure 4.6 shows the images of D2 sample of cell culture which was also incubated with BPA drug for 4-hours. C, CN and P ions images are localised to specific cell morphology and are distributed across the nucleus and cytoplasm in a manner similar to all previous cells. Boron isotope maps again showed that the signal intensity of ^{10}B was higher than ^{11}B. ^{10}B accumulates in the nucleus and the area surrounding the cell, as well as in the cytoplasm at a lower level. The ^{11}B signal was low and does not show preferential accumulation within the cell.

This analysis was repeated at least three times on other cells for each sample.

It is clear in both B2 and D2 samples that the pre-treatment with the BPA resulted in a clear accumulation of ^{10}B in cells which was different between the parts of the cell, whereas the boron isotope signals in the control samples represented the natural background level of boron where ^{11}B signal was more intense than that of ^{10}B. Thus, the difference in the distribution of boron isotopes and signal intensity between the control samples and the treated samples with low concentrations of BPA is evident from the imaging of samples. In addition, in both samples B2 and D2 the total counts of ^{10}B summed from cell is ~ 6-fold higher than the ^{11}B counts, which is completely opposite to the control samples. This indicates that the B2 and D2 samples absorbed the BPA enriched in ^{10}B.

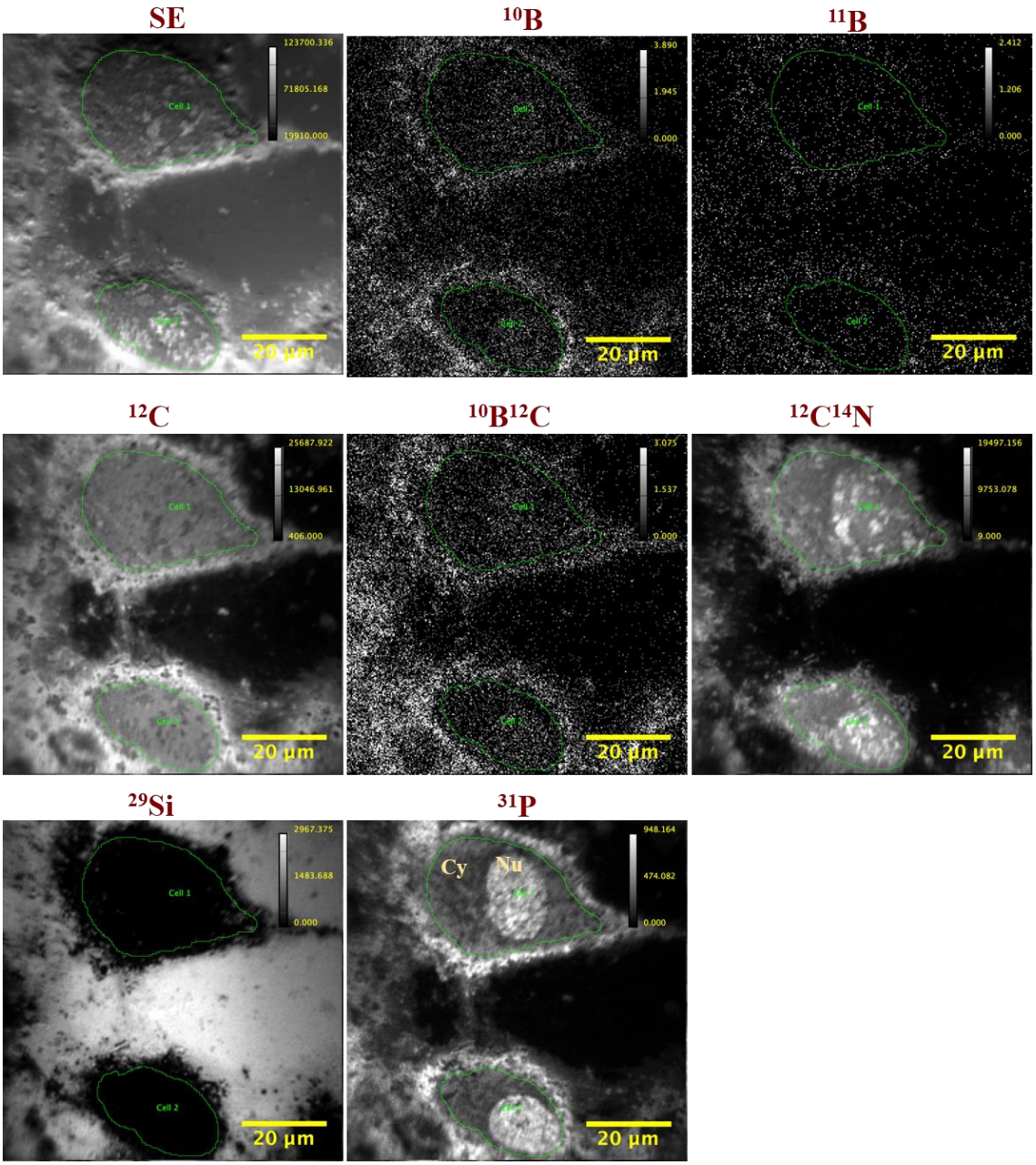

Figure 4.5: NanoSIMS analysis of cell B2 of pre-treated GBM sample with BPA for 4 hours in a FoV of 80×80 µm^2. SE map shows the total cells structures. The maps of negative secondary ions: ^{10}B, ^{11}B, ^{12}C, $^{10}B^{12}C$, $^{12}C^{14}N$, ^{29}Si and ^{31}P show the ion distribution across the cell. (Nu) refers to nucleus and (Cy) refers to cytoplasm.

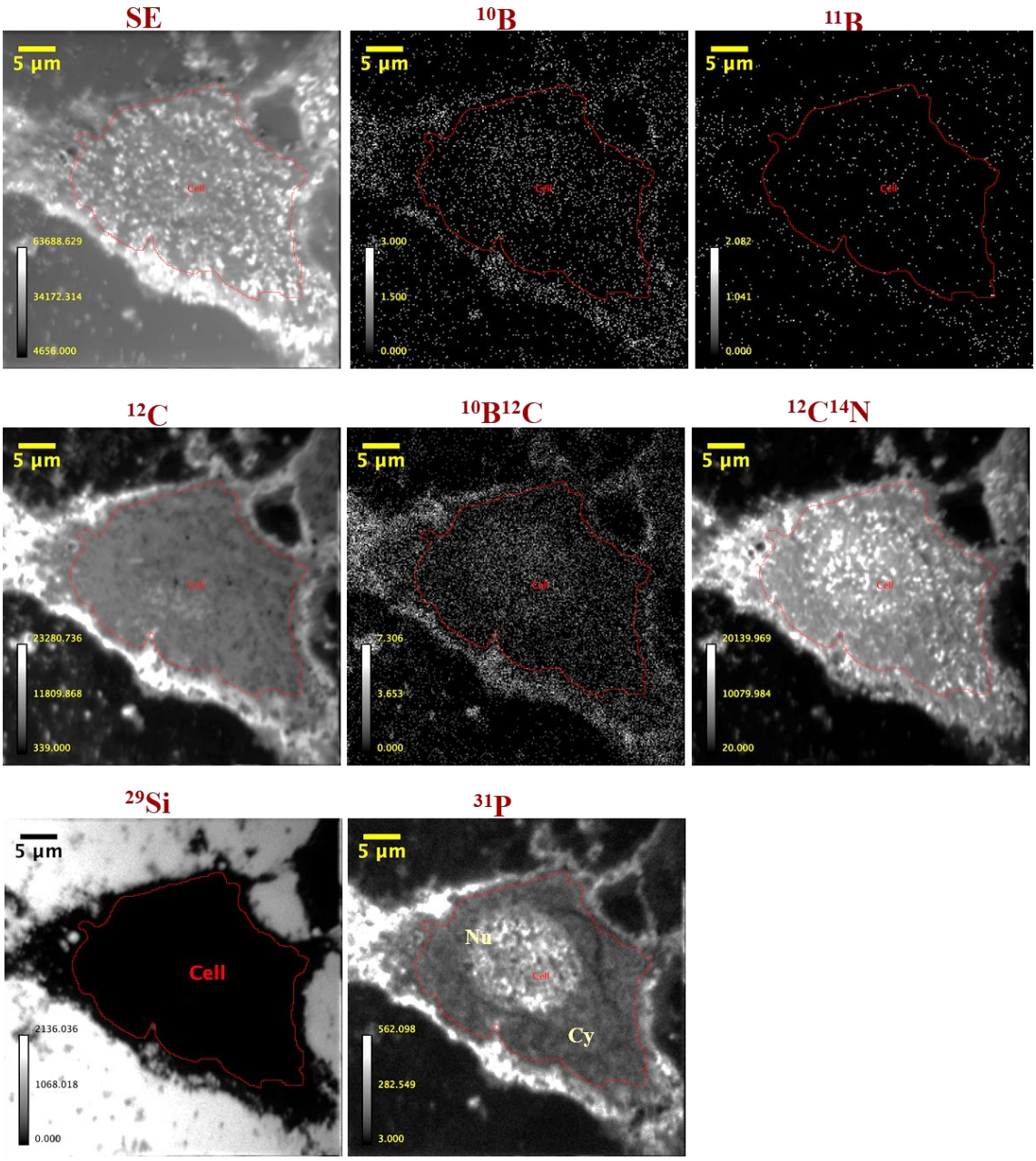

Figure 4.6: NanoSIMS analysis of cell D2 of pre-treated BAT sample with BPA drug (4 h) in a FoV of 45×45 µm^2. Secondary electron map shows the cell structure. The maps of negative secondary ions: ^{10}B, ^{11}B, ^{12}C, ^{10}B^{12}C, ^{12}C^{14}N, ^{29}Si and ^{31}P show the ion distribution across the cell. (Nu) refers to nucleus and (Cy) refers to cytoplasm.

4.2.3.1.3 Quantitative determination of boron isotope ratios

The ratios of stable boron isotopes, $^{10}B/^{11}B$, from identified cells in the NanoSIMS maps for all control samples as well as B2 and D2 samples, which were pre-treated with BPA, were calculated to compare between them as well as to compare them with the natural ratio. The results are shown in **Figure 4.7**. In the A1 and B1 samples of GBM control samples, **Figure 4.7-a**, the $^{10}B/^{11}B$ ratios were 0.26 ± 0.02 and 0.27 ± 0.02 (mean ± SD) respectively with a median value of 0.27. In addition, the $^{10}B/^{11}B$ counts ratios in C1 and D1 of BAT control sample, **Figure 4.7 -a**, were 0.26 ± 0.02 and 0.25 ± 0.03 respectively with a median value of 0.25. These values agree well with the natural ratio of B isotopes ($^{10}B/^{11}B$) which is 0.247 i.e. roughly 1:4 of ^{10}B:^{11}B [2][3].

In contrast, the boron isotope ratios were significantly higher in the B2 and D2 samples, **Figure 4.7 -b.** $^{10}B/^{11}B$ ratios were 4.7 ± 0.6 in B2 with median 4.6, and 6.4 ± 0.7 in the D2 with median value of 6.6, which means that the $^{10}B/^{11}B$ ratio in treated samples is ~ 18-26 times higher than natural level.

The box plot schematic shows the values represented: the maximum and minimum values of the counts, first quarter (Q1), median, mean (X), third quarter (Q3) and the interquartile range (IQR) as in **Figure 4.7 -c**.

These results demonstrate that the control samples have the natural isotope ratio giving a higher ^{11}B signal than ^{10}B, as is apparent in **Figures 4.1-4.4**. Treated samples showed a large increase in the boron isotope ratio with ^{10}B significantly higher than ^{11}B, which confirms that the samples took the BPA into cell bodies where potentially it can be activated by radiotherapy and that the NanoSIMS can detect an increase in ^{10}B signal over background levels.

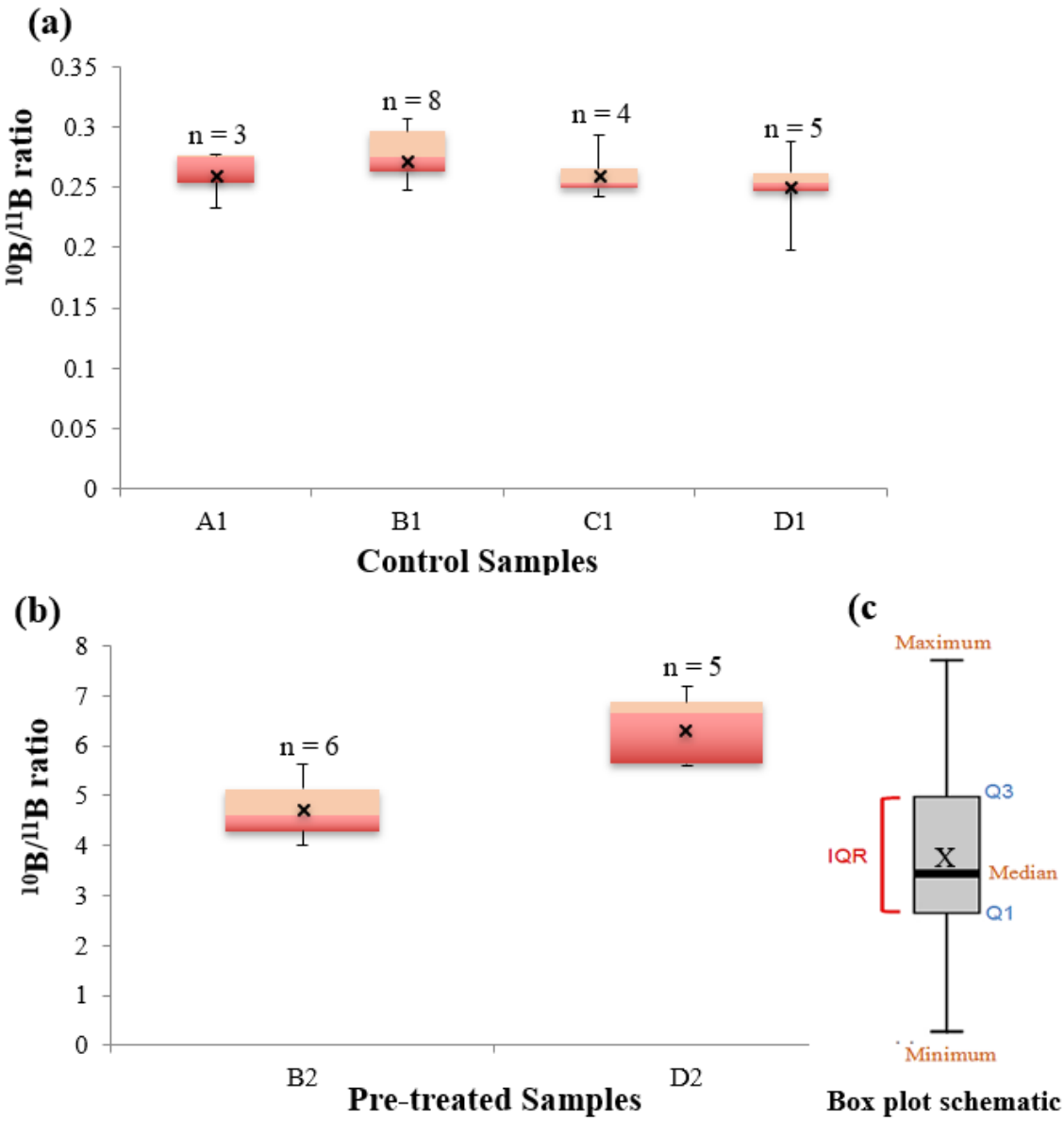

Figure 4.7: A comparison of the boron isotope ratios determined by NanoSIMS in the control samples and pre-treated samples with BPA. **Panel a**: The $^{10}B/^{11}B$ ratios in the control samples, A1 and B1 cultured cells of different GBM biopsies, C1 and D1 cultured cells of different BAT biopsies. All control samples gave ratios values ranging from 0.25-0.27 similar to the value of natural ratio of 0.25. **Panel b**: The ratios of $^{10}B/^{11}B$ in the pre-treated samples (cells cultures) with 4h of BPA, B2 cells of GBM biopsy, D2 cells of BAT biopsy. B2 and D2 gave high ratios of $^{10}B/^{11}B$ ranging from 4.6-6.6. There was significant difference in $^{10}B/^{11}B$ ratio between control samples and pre-treated samples. ***n*:** number of cells analysed. **Panel c**: The box plot schematic explains the meaning of the data in panels **a** and **b**; the maximum and minimum values of the counts, Q1: first quarter, median, X: mean, Q3: third quarter, IQR: the interquartile range.

4.2.3.2 Cellular imaging analysis of ^{10}B distribution from BPA drug in GBM (B group) and BAT (D group) samples of cells cultures (Second stage)

In this step, which represents the main experiment to achieve the objective of the research, the distribution and localisation of ^{10}B from BPA drug at the cellular level in the cell cultures was studied in order to assess the NanoSIMS imaging capabilities in terms of spatial resolution and sensitivity. To achieve the quantitative comparison, all GBM samples (B group) and BAT samples (D group) were analysed under the same analytical conditions, **Table 4.1** summarizes the treated groups in the cultured cells. B1 and D1 control samples were previously discussed in section 4.2.3.1.1 and **Figures 4.2 and 4.4.**

In the experimental set-up, the D1 aperture was set to position number 2 in order to generate a good secondary ion yield of the selected ions within a reasonable time period with good spatial resolution for the acquisition of clear images. The dwell time was selected to be 2000 µs to make the analysis possible across many layers before holes started appearing in the sample. The image resolution was set to 256×256 pixels to acquire the data in a reasonable time frame.

Table 4.1: Summary of the treated groups in the cultured cells.

B group		D group	
B1	GBM control	D1	BAT control
B2	GBM + BPA (4h)	D2	BAT + BPA (4h)
B3	GBM + Tyrosine (4h) + BPA (4h)	D3	BAT + Tyrosine (4h) + BPA (4h)
B4	GBM + BPA (4h) +efflux (4h)	D4	BAT + BPA (4h) +efflux (4h)

4.2.3.2.1 B2 maps

The B2 cell culture sample of GBM tumour was treated with a 10 mM BPA for 4 hours. The CCD camera in the NanoSIMS was used to select a cell for analysis as shown in **Figure 4.8** which displays the optical image of the cell before and after NanoSIMS analysis.

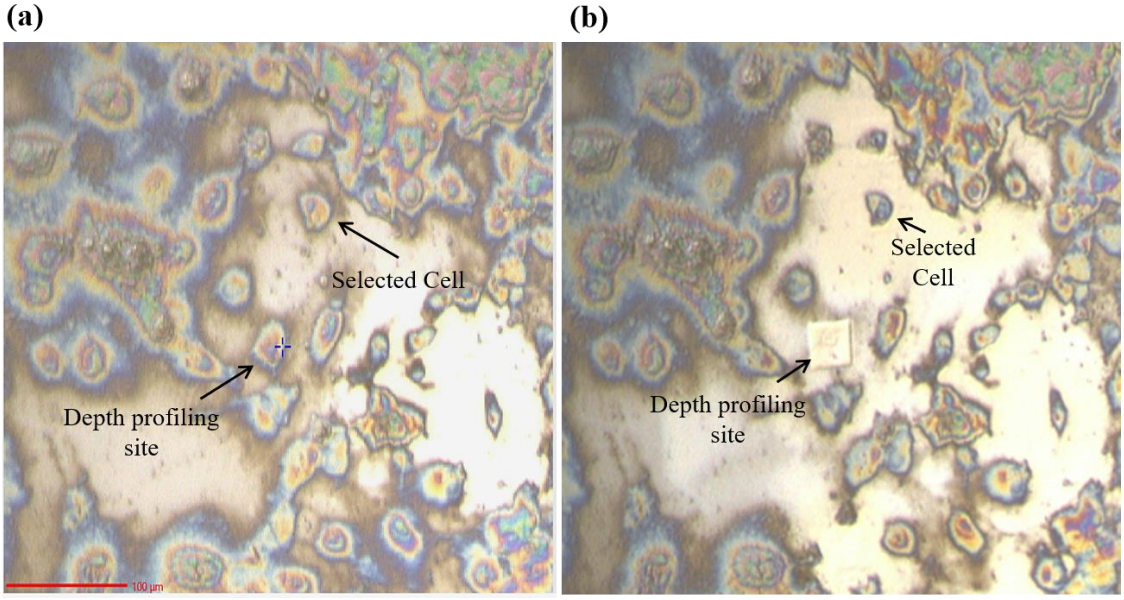

Figure 4.8: Images from the CCD camera showing the B2 cell chosen for NanoSIMS imaging before (a) and after (b) analysis. The images (a & b) also show the location of a depth profiling crater discussed in the section 3.6.2.3 and Figure 3.6. Scale bar = 100 µm.

The NanoSIMS maps of the secondary ions of the selected area are shown in **Figure 4.9**. The maps show contrast in the distribution of ions between cell compartments which have been separated into nucleus (region 1- green line) and cytoplasm (region 2- red line). The SE map shows the general morphological features of the cell where the nucleus and cytoplasm regions of the cell can be clearly distinguished, as well as the outer area around the cell and small features on the surface. The Si map shows the area covered by the cell and confirms that there are no holes in the cell and that the cell has not been completely sputtered away during the acquisition of images (adding a dose of 1.44×10^{16} ions/cm^2). The Si map is used during the identification of ROIs from the cell to avoid areas where the Si signal appears high such as around the outer edge of the cell.

The C map shows that carbon is distributed relatively uniformly between cellular parts, and is highly concentrated around the edge of the cell. The C ion signal intensity is higher than the rest of the ions signals as found by comparing the total counts of ions summed from cell. CN also has a high signal intensity but CN is more localised in the nucleus than cytoplasm, this is because the nucleus contains proteins and DNA, and the latter contains many nitrogenous bases [4]–[6]. The high intensity of the CN signal and the clear difference in intensity and localisation in different cellular parts makes it an important and commonly used ion for imaging biological samples and is easy to detect using the NanoSIMS [7]–[9].

The distribution of CN in the B2 sample is similar to its distribution in human breast adenocarcinoma (MDA) cells that reported by Wedlock *et al.* [10], and in the tissue sections of mouse cochlea [9]. The cell structure is rich in C and CN ions, this is due to the cell composition which is rich in many substances such as carbohydrates, proteins, lipids and amino acids [11]–[13].

Phosphorous was more concentrated in the nucleus region than the cytoplasm. This is consistent with many imaging studies that used phosphorus to infer the nucleus site because the nucleus contains the chromosomes which in turn are rich in phosphate groups in the DNA synthesis [10][14]–[16]. In addition, one study identified chromatin locations in the nucleus by imaging the distribution of phosphorus ions in semi-thin sections of human colon cancer cells line [17]. The S ion map shows a higher intensity in the cytoplasm with localised regions of high-intensity observed on the nucleus, this is similar to the distribution of sulfur in human colon cancer cells where it was co-localised with P generally in the cytoplasm and specifically in the nucleolus and chromatin inside the nucleus [17]. The sulfur ion can also be used to trace the lysosomes sites in the cytoplasm of cells [14][18]. The source of sulfur is usually sulfur -containing amino acids such as methionine and glutathione which in turn are involved in different biological processes in cells, the most important of which is protein synthesis [19][20].

In the middle and slightly towards the bottom of the nucleus there is a small oval feature in the SE map with higher accumulation of CN, P and S as indicated by the maps. This feature may indicate a nucleolus and this is consistent with the result of Legin *et al.* which showed co-localisation of CN, P and S ions in the nucleoli of a human colon cancer cells line [17]. In the SE map, the apparent change in surface morphology outside the nucleus in the lower left side of cytoplasm where the CN and P signal is weak and the S signal is high, may indicate the presence of lysosomes. This is similar to what Lau *et al.* found during the study of ATN-224 treatment distribution in Human umbilical cord endothelial cells line [14].

The bright white area surrounding the outer edge of the cell was discussed separately in section 4.2.3.2.4.

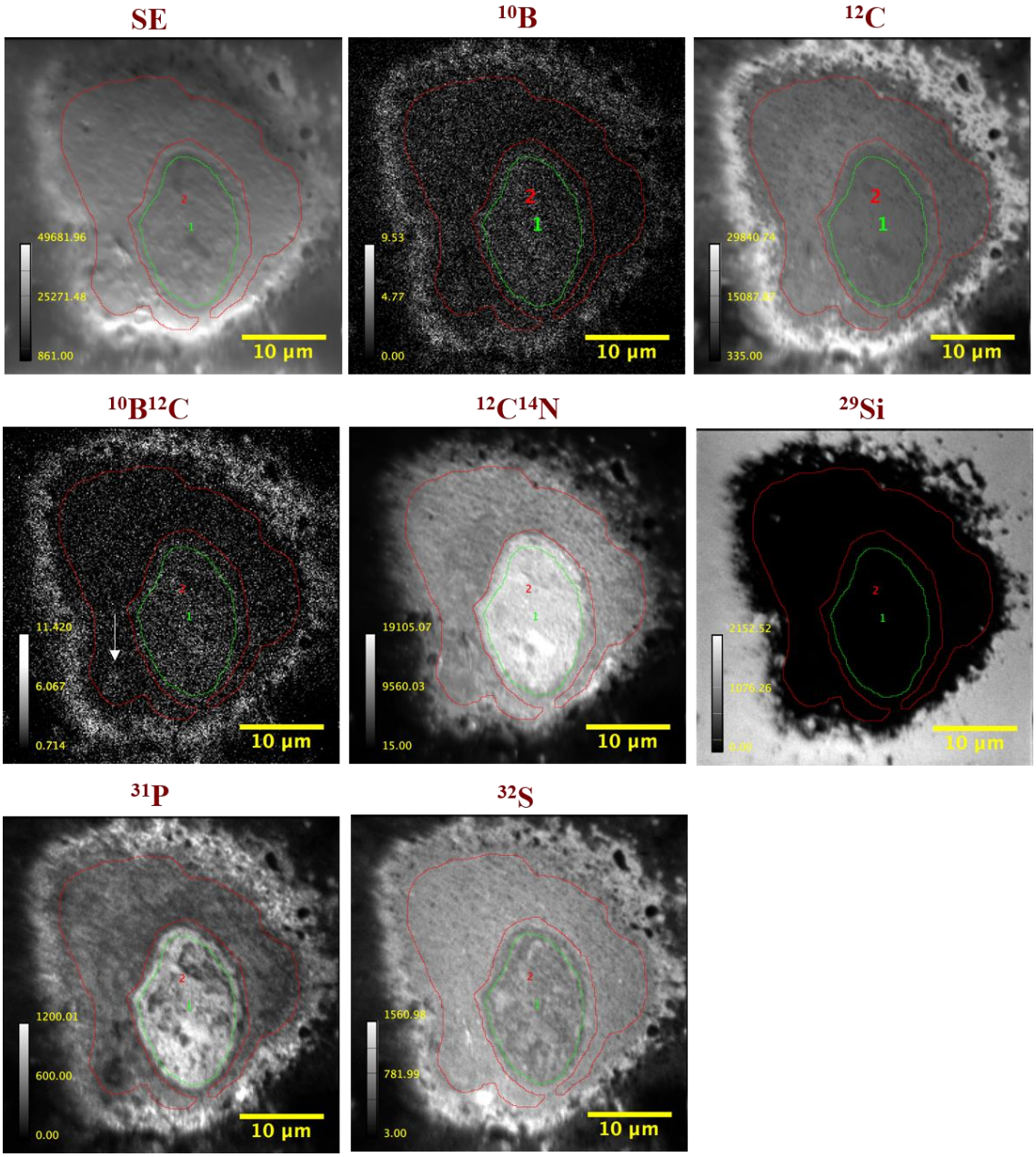

Figure 4.9: NanoSIMS maps for B2 sample of GBM-cell culture incubated in 10 mM of ^{10}BPA for 4h and was imaged in FoV 40×40 µm^2 with 256×256 pixels. SE: secondary electron map shows the structure of the cell. The maps of negative secondary ions: ^{10}B, ^{12}C, ^{10}B^{12}C, ^{12}C^{14}N, ^{29}Si, ^{31}P and ^{32}S respectively display the ions distribution across the cell compartments; ROI1- Nucleus (green line) and ROI2- Cytoplasm (red line). Arrow in ^{10}B^{12}C map refers to a feature concentrated in boron.

What is important here is that the ^{10}B signal shows that the accumulation of boron of the BPA is heterogeneous between the nuclear and cytoplasmic compartments. The accumulation of ^{10}B in the nucleus and the area surrounding the cell was clearly higher than the cytoplasm. The $^{10}B^{12}C$ signal shows an identical distribution to ^{10}B, with a higher signal in the nucleus than the cytoplasm. The distribution pattern of ^{10}B and $^{10}B^{12}C$ was similar in the all analysed cells of the B2 sample (n = 3). It is also noted in the ^{10}B and $^{10}B^{12}C$ maps that boron is detected across the cytoplasm and shows a small concentrated feature in the lower left corner of the cytoplasm (arrow in $^{10}B^{12}C$ map) which corresponded with a reduced P signal. This increase in boron signal is unlikely to be due to the topography as other signals did not have a corresponding increase in signal. The accumulation may be related to unknown organelles which are not visible with the ions being detected by the NanoSIMS.

When comparing the B2 cell shown in **Figure 4.9** with the B1-control cell in **Figure 4.2** the B2 cell confirms the accumulation of ^{10}B and $^{10}B^{12}C$ of BPA drug in the cell compartments in contrast to the untreated B1-control cell that only shows natural ratios of boron isotopes as explained in section 4.2.3.1. 1and a lower intensity of boron species.

The preferential accumulation of ^{10}B and $^{10}B^{12}C$ ions in the cell nucleus (which was not observed in the control samples) increases the chances of successful tumour cell destruction if it is exposed to a fission reaction by low-energy thermal neutrons. The resulting high energy linear particles only penetrate the cells a short distance and lead to the elimination of tumour cells [21]–[24], preferential localisation of ^{10}B in the nucleus is therefore preferential.

4.2.3.2.2 B3 maps

The B3 of GBM tumour cell culture sample was treated with tyrosine at a concentration of 10 mM for 4h and then incubated with 10 mM of BPA for 4h. The purpose of pre-treatment with tyrosine is to investigate of extent to which tyrosine enhances BPA uptake in tumour cells as indicated by previous studies [25]–[27]. **Figure 4.11** shows the maps of the ion distributions obtained from the NanoSIMS from the selected region in the CCD-image in **Figure 4.10**. Two cells were imaged, so the nuclei represent areas 1 & 2 (green lines) while the cytoplasmic regions represent areas 3 & 4 (red lines).

The SE map provides a clear image of the surface features, the whole shape of the cells and the surrounding outer area of the cells. The Si map shows the area of substrate covered by

the cells and confirms that the cell structure is relatively intact. In nucleus 2 there are holes through which the silicon signal appears, so they were avoided during selection of the ROI in the cells and extraction of quantitative data.

The maps show that C, CN, P, and S ions are distributed among cell compartments with a similar distribution to the B2 sample. The C map shows a relatively uniform distribution across cell compartments, with high signal intensity in the area surrounding the cells. The CN map also gives high ion signals in all cells and is more concentrated in the nuclei than in the cytoplasm regions because of the presence of protein and DNA which is, in turn, rich in nitrogenous bases. CN does not show a higher intensity around the edge of the cell unlike carbon. P ions were distributed differently between cell compartments and accumulated in the nuclei more than in the cytoplasm due to the nuclei containing the chromatin which in turn contains phosphate groups. The phosphorus signals showed high intensity in the outer edge surrounding the cells and the area between the cells. The distribution of S ions is similar to the carbon distribution pattern where it is distributed relatively uniformly across cells with a slightly elevated localisation at the outer edge of the cells.

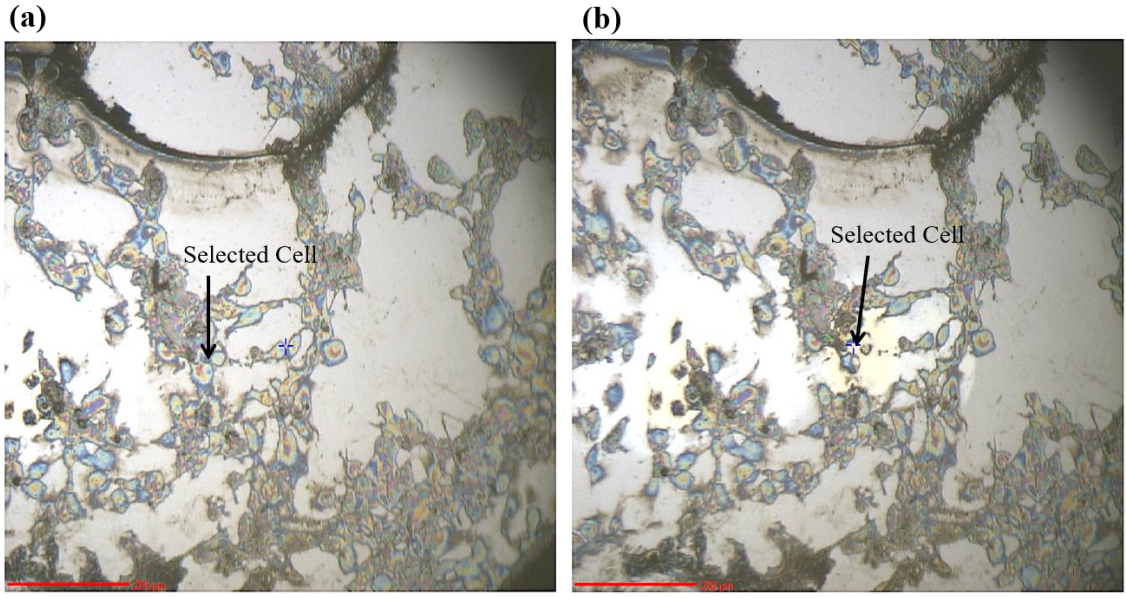

Figure 4.10: Images from the CCD camera showing the B3 cell chosen before (a) and after (b) analysis with the NanoSIMS (arrow). Scale bar = 200 µm.

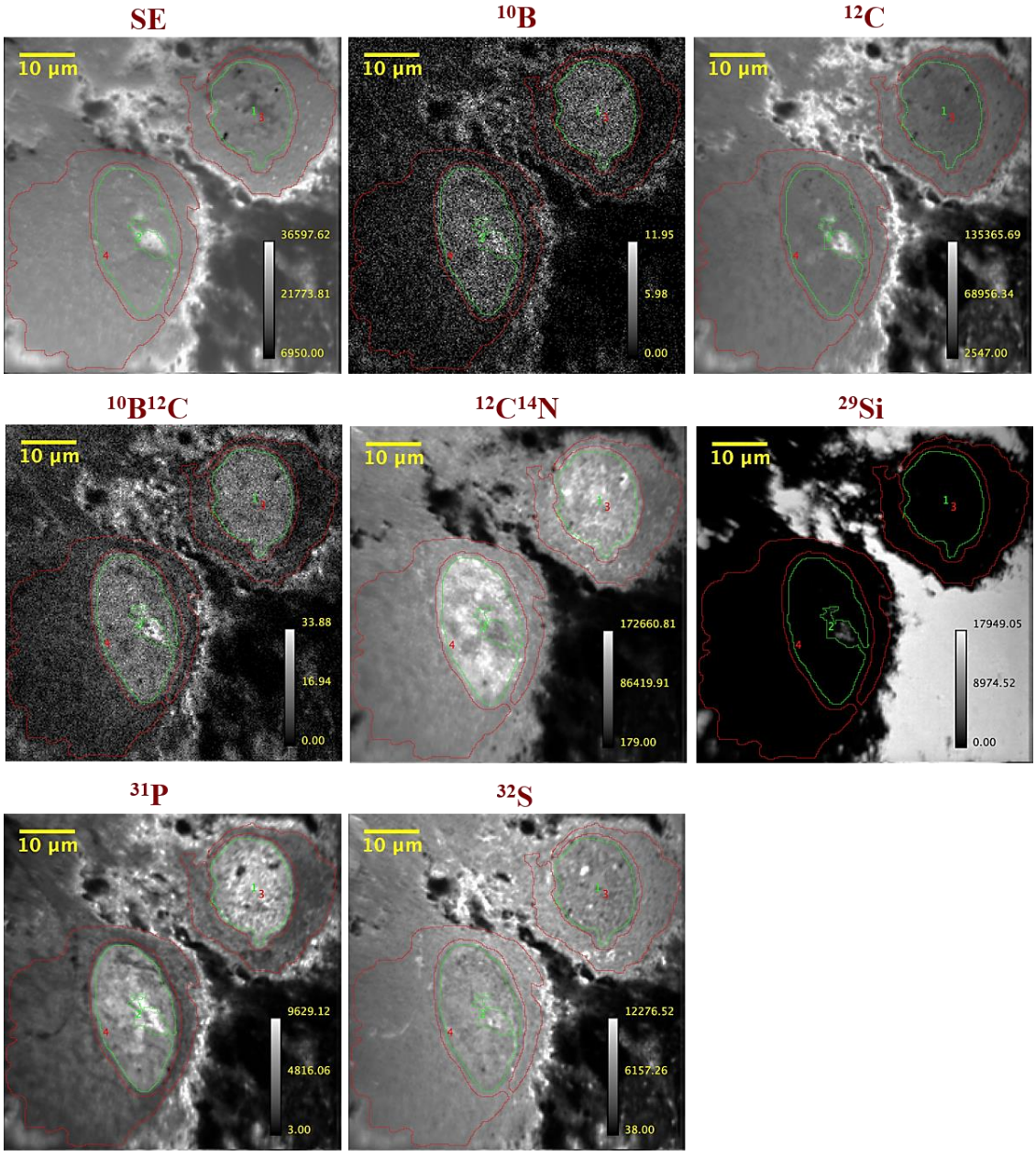

Figure 4.11: NanoSIMS maps from the B3 GBM-tumour cell culture treated with 10 mM of tyrosine (4h) then 10 mM of BPA (4h). SE: secondary electron map shows the general shape of the cells. The maps show the subcellular distribution of negative ions of ^{10}B, ^{12}C, $^{10}B^{12}C$, $^{12}C^{14}N$, ^{29}Si, ^{31}P and ^{32}S respectively in the cell compartments. The areas within the green lines (1&2) display the position of the nuclei and red lines (3&4) indicate the cytoplasm. The FoV was 60×60 µm^2 with 256×256 pixels.

In the phosphorus map, the nucleus of cell-1 shows the existence of two unknown features where the P signal is absent, while showing a high S signal and signals of C and CN which are similar to surrounding areas of nucleus. In the same cell-1 nucleus from left and right edges some features which look like holes in the SE map have appeared. Within these features, which are likely to be contaminants on the surface, the signals of all measured ions disappear, but Si is not detected indicating these are not holes.

In terms of localisation of boron, the maps indicate that ^{10}B and $^{10}B^{12}C$ ions accumulate strongly in the nuclei with lower signals in the cytoplasm and high signals at the outer edge and the area between the cells, which is a pattern similar to the boron distribution in the B2 sample which confirms the BPA uptake by the samples. All the analysed cells in the B3 sample (n = 3) showed similar accumulation of ^{10}B and $^{10}B^{12}C$ ions.

By analysing the counts of ^{10}B and $^{10}B^{12}C$ in samples B2 (**Figure 4.9**) and B3 (**Figure 4.11**), it was observed that for the B3 samples the $^{10}B^{12}C$ ion is more intense, while the ^{10}B ion signal intensity was ~ 3 times lower than the summed signals in the B2 cells, possibly indicating that tyrosine did not induce an increase in BPA absorption in the B3 sample. It is also evident from the analysis of the B3 sample that $^{10}B^{12}C$ signal was ~ 4 times higher than the ^{10}B signal. More details on $^{10}B/^{12}C$ and $^{10}B^{12}C/^{12}C$ ratios are discussed in 4.2.3.2.5.

4.2.3.2.3 B4 maps

The B4 cell culture of GBM sample was incubated with 10 mM of BPA and was then exposed to an efflux process. Both uptake and efflux mechanisms of the drug were performed for 4h to ensure the highest level of BPA uptake was achieved and then returned to the minimum level of treatment in the cell *via* efflux at the same speed (two counteractive processes). The purpose of this step is to verify the effect of the efflux process on the level of boron in the cell. **Figure 4.12** and **Figure 4.13** shows the CCD images of the cell selected for analysis and the ion distribution maps obtained from the NanoSIMS respectively. The cell of interest was determined in the maps so that the nucleus represented area 1 (the green line) while the cytoplasm represented area 2 (the red line).

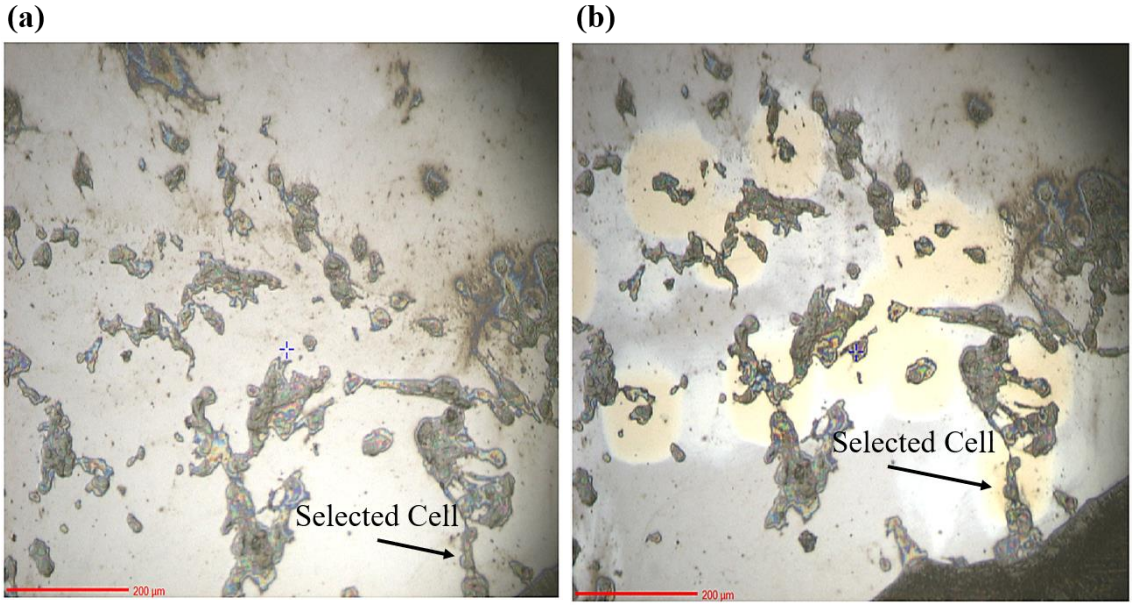

Figure 4.12: The CCD camera images refers to (a) the selected cell in B4 for NanoSIMS analysis and (b) the shape of cell after analysis (arrows). Other bright spots in the image (b) show the locations of other cells analysed. Scale bar = 200 µm.

In **Figure 4.13** the SE map shows the full structure of the cell and that it is connected to other cells in the upper and lower parts of the image. The Si map confirmed the integrity of the cell structure during the acquisition of the images with a dose 1.44×10^{16} ions/cm^2. The ion maps show that C, CN, P and S were distributed between the cell parts in a similar way to the maps of the B2 and B3 samples. Both C and CN ions provided high ion signal intensity across the cell. The distribution of the C ion was relatively uniform with high intensity at the outer edge, whereas the CN ion was higher in the nucleus than in the cytoplasm and showed no clear localisation to the outer edge. The P map shows the very high accumulation of ions in the nucleus compared to the cytoplasm, also P is co-localised with C at the outer edge. The S map shows the distribution of ions is roughly uniform with a higher concentration in the outer edge of the cell, like the C ion. This pattern in the distribution of C, CN, P and S was explained in more detail during in the discussion of B2 sample maps.

The bottom right corner of the image out of cell shows a high ion signal of S and CN, while the C and P signals were low. This area completely covered the Si substrate so may indicate that this is a part of the tissue that binds this cell with the neighbouring cell. Topography may have affected the intensity of the ion signals as is evident in the SE map in **Figure 4.13**.

The distribution maps of boron signals detected as ^{10}B and ^{10}B^{12}C showed that the intensity in the nucleus was higher than the cytoplasm and that the ions showed an accumulation in

the outer edge surrounding the cell, which was discussed separately in section 4.2.3.2.4. The localisation of the boron between the cell compartments in this sample is similar to that of the B2 and B3 samples. All cells analysed in the B4 sample (n = 5) gave a similar distribution of boron.

By comparing the normalised intensities of the boron signals summed from cells in B4 and previous samples B1, B2 and B3 in **Figure 4.13, 4.2, 4.9** and **4.11**, it is clear that the signal intensity of ^{10}B and $^{10}B^{12}C$ in sample B4 is lower than the B2 and B3 samples by a factor of ~ 9 and 4 respectively, which suggests the efflux process resulted in a clear reduction in the BPA uptake. However, the normalised intensities of ^{10}B and $^{10}B^{12}C$ signals in B4 remained higher than the B1 by a factor of ~12, this indicates that a portion of the ions remained in the cell which in turn proves that the efflux process is slower than the uptake process and there is not a complete loss of all absorbed ions within 4h. In addition, the normalised intensity of $^{10}B^{12}C$ signal in B4 sample was ~ 6 times higher than the ^{10}B signal. More details on $^{10}B/^{12}C$ and $^{10}B^{12}C/^{12}C$ ratios are discussed in 4.2.3.2.5.

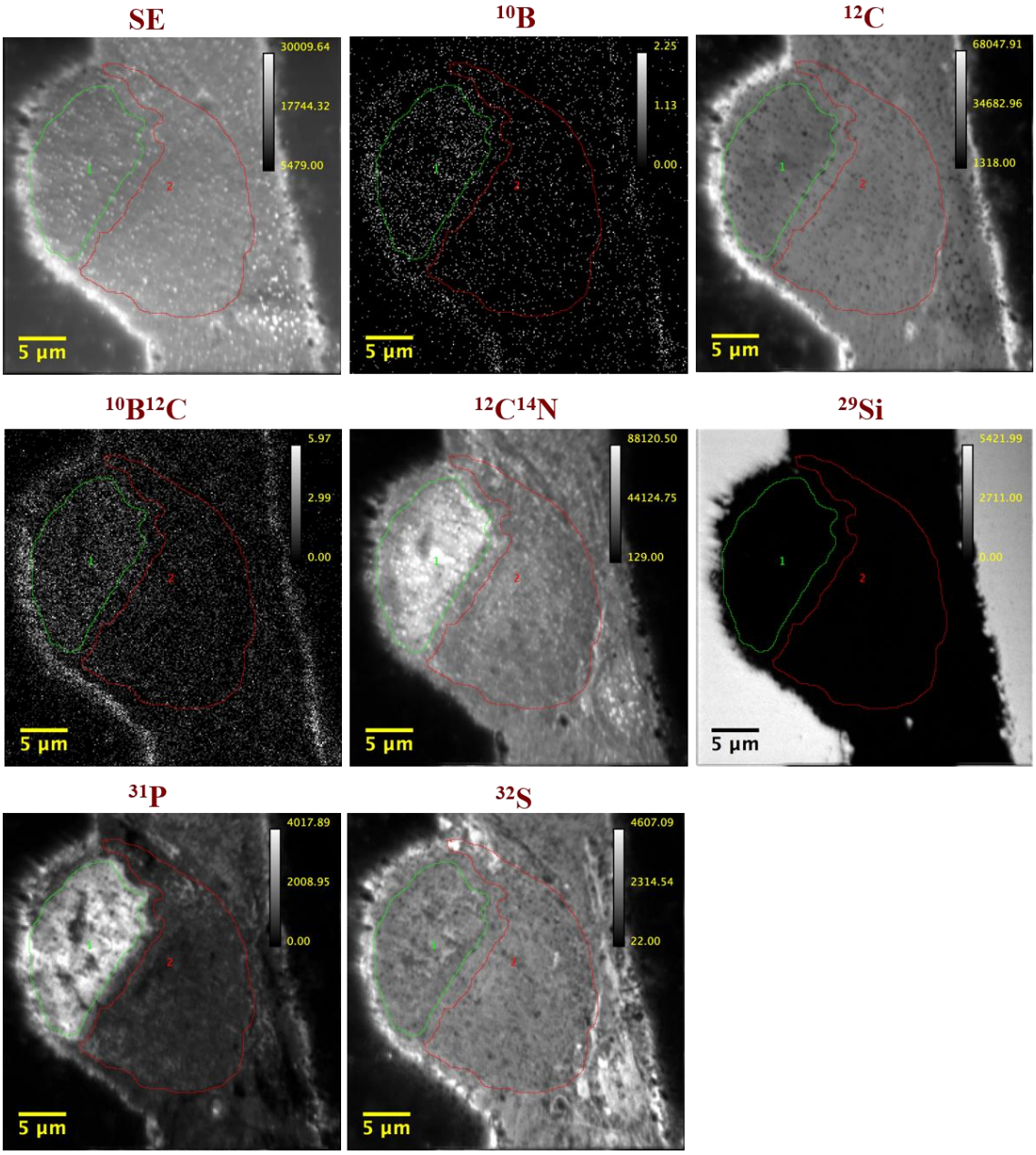

Figure 4.13: NanoSIMS analysis for B4 of GBM cell culture treated with 10mM of BPA (4h) then exposed to an efflux process (4h). SE: map of secondary electrons shows the overall structure of the cell. SIMS maps reveal the distribution of negative ions respectively ^{10}B, ^{12}C, ^{10}B^{12}C, ^{12}C^{14}N, ^{29}Si, ^{31}P and ^{32}S within cellular parts; nucleus (green line) and cytoplasm (red line) with a FoV of 35×35 µm^2 and 256×256 pixels.

4.2.3.2.4 The outer edge of cells

The bright white area around the outer edge of the cell shows high signal intensities of B, C, BC, P and S ions while the CN signal is low. The Si signal shows that this area around the edge of the cell has numerous holes. It is difficult to interpret the area around the edge of the cell for several reasons.

First, in the prepared cultures, cells may be connected to each other rather than isolated [28][1]. Looking at the CCD image of the B2 sample in **Figure 4.8 -a**, as well as all the CCD images and maps of the analyzed cells, the area surrounding the cell sometimes appears to be a connection between cells, but this connection does not appear on all sides of the cell. In these unconnected regions the sample may have shrunk during sample preparation or during preparation for SIMS analysis in vacuum, or this area was removed during the primary ion beam implantation process before NanoSIMS analysis. For further illustration, in **Figure 4.6** the area around the cell shows a connection between the displayed cell and the adjacent cell in the top right corner of the maps where the Si signal is low and the signal intensity of all other ions is high. In addition, the connection in **Figure 4.5** is shown on the left side of the maps with high signals of Si, it is also possible to observe possible remnants of links between the two cells in the middle of the maps which may have been removed during the implantation process, where the signal of all ions except for silicon appears to be weak, while there is almost no CN signal. The area surrounding the cell in **Figure 4.3** shows a connection from the upper right corner with high ion signal intensity for both C and P and a reasonable intensity of the CN ion.

Secondly, a part of the area around the cell edge probably represents the cell membrane with reasonable signal of S, and a high signals of P and C due to the presence of phospholipids, proteins, lipids and carbohydrates in the membrane composition [12][13][29]. Furthermore, the studies [30]–[32] indicated that the cell membrane contains LAT-1 transporters, channels of protein [33], responsible for the transfer of L-amino acids such as BPA into the cell through an active uptake process. At the same time the efflux process occurs, which is less active than the uptake process, where BPA goes out of cell [30]–[32]. Both processes indicate that the boron will be present in the cell membrane, this may explain the high signal intensity of B and BC around the edge of the cell as shown in all previous figures of BPA treated cells. However, the activity of the LAT-1 transporters may vary depending on the cell cycle [34]–[36], which indicates a probability that the intensity of the boron signal in this region will vary. However, the literature is not in agreement about how the cell cycle will affect the BPA uptake as discussed in section 2.2.2. In addition, investigating

distribution as a function of cell cycle is challenging in this cell culture as they are primary cells not cell lines. The thickness of the cell membrane ranges approximately between 4 - 10 nm [37][38], but it is noted from the maps of the analyzed cells that this bright white region sometimes appears as much as ~ 2µm thick around the cell as in **Figure 4.6** and **4.9**, while it looks ~ 18 µm thick in other cells. This would suggest that the membrane is spread out or flat on the substrate as in **Figure 4.3**. Most often, the thickness of white area varies around a cell as shown in **Figure 4.2, 4.4, 4.5**, and **4.9**. This variation in the thickness of the surrounding area is not consistent with this area being interpreted only as a cellular membrane.

Finally, part of the area around the cell may show a high intensity of B and BC signals because it is from the preparation medium containing the BPA, as in **Figure 4.5, 4.6** and **4.9**. Moreover, in the control samples untreated with BPA a natural ratio of ^{10}B and ^{11}B and $^{10}B^{12}C$ was observed in the surrounding area, which may indicate the presence of the connecting tissue between cells or cell membranes or both, **Figures 4.1-4.4**. When the cells were treated with the BPA, ^{10}B and $^{10}B^{12}C$ signals increased in the area surrounding the cell, indicating either the area absorbed the BPA (as mentioned above) or that the preparation medium was accumulated in this area or both possibilities occurred together, **Figure 4.5, 4.6, 4.9, 4.11** and **4.13**.

As a result of the uncertainty of the nature of the area surrounding the cell edge for the reasons mentioned above, the decision was made not to include this area during the determination of ROIs in cells and was excluded from the quantitative calculations of the boron distribution.

4.2.3.2.5 Quantification of ^{10}B in B group samples

Quantitative determination of the therapeutic boron distribution between cell compartments in the GBM-cell culture samples of B2, B3 and B4 were calculated. The measurements of ^{10}B and $^{10}B^{12}C$ were normalised to ^{12}C, which has the highest intensity and is the most homogenously distributed ion across the cell. Normalising two ions acquired simultaneously accounts for different image sizes and minimises the effect of any variations in primary ion beam current, total sputter yield and ion transmission, between different ROIs and images acquired across different NanoSIMS sessions. The secondary ion intensity ratios $^{10}B/^{12}C$ and $^{10}B^{12}C/^{12}C$ from nuclei and cytoplasm of each sample are represented separately in box plots in **Figure 4.14**, an explanation of how to interpret the box plot graph was previously shown

in **Figure 4.7 -c**. **Table 4.2** shows the mean values of $^{10}B/^{12}C$ and $^{10}B^{12}C/^{12}C$ ratios from all the samples of group B in the box plots shown in **Figure 4.14**, where the difference can be observed between them. At least three cells were analysed for each sample.

The B2, B3, and B4 samples showed a similar boron distribution pattern in terms of the NanoSIMS images. The results from the NanoSIMS in **Figure 4.14** shows that $^{10}B^{12}C/^{12}C$ ratio is always higher than the $^{10}B/^{12}C$ ratio form in both the nucleus and cytoplasm, indicating the relative stability of the $^{10}B^{12}C$ fragment and/or its higher ionization probability compared to atomic ^{10}B. In B2 and B3 samples, both $^{10}B/^{12}C$ and $^{10}B^{12}C/^{12}C$ ratios indicate an increased level of BPA uptake in cell nuclei compared to cytoplasm. For samples B2 and B3 the mean $^{10}B/^{12}C$ and $^{10}B^{12}C/^{12}C$ ratios indicate nuclear : cytoplasm BPA distribution are 2.6 ± 0.3 and 2.5 ± 0.2 respectively. The data clearly indicate a ~ 2-fold excess of BPA in the nucleus compared to the cytoplasm under the treatments used in B2 and B3. This accumulation of boron in the nucleus is desirable for the success of BNCT treatment if the cells are exposed to low-energy thermal neutrons, because the linear particles resulting from the neutron fission reaction have high energy and penetrate the cells in short distances which leads to the destruction of tumour cells, as indicated by previous studies [21][22][39].

Table 4.2: The mean values of $^{10}B/^{12}C$ and $^{10}B^{12}C/^{12}C$ ratios from the B group samples (shown in **Figure 4.14**).

Ratio	**$^{10}B/^{12}C$**			
Mean ($\times 10^{-4}$) ± SD of	B1	B2	B3	B4
Nuclei	0.009 ± 0.004	1.1 ± 0.4	0.35 ± 0.2	0.075 ± 0.01
Cytoplasm	0.006 ± 0.002	0.45 ± 0.3	0.12 ± 0.06	0.027 ± 0.004
Ratio	**$^{10}B^{12}C/^{12}C$**			
Mean ($\times 10^{-4}$) ± SD of	B1	B2	B3	B4
Nuclei	0.016 ± 0.003	1.49 ± 0.03	1.55 ± 0.6	0.36 ± 0.07
Cytoplasm	0.01 ± 0.002	0.59 ± 0.01	0.6 ± 0.3	0.17 ± 0.02

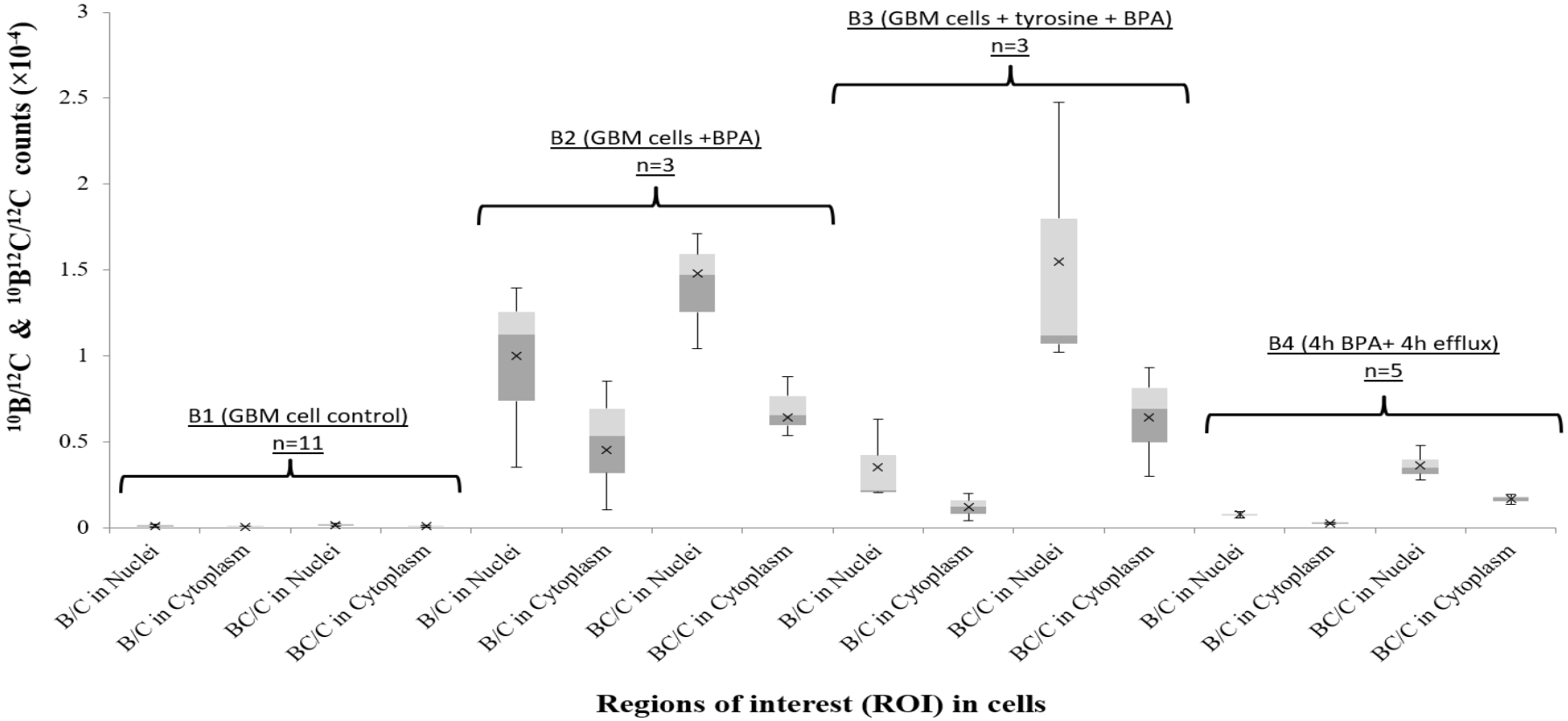

Figure 4.14: Comparison between the GBM-cell culture samples: B1, B2, B3 and B4 in terms of $^{10}B/^{12}C$ and $^{10}B^{12}C/^{12}C$ ratios in the nuclei and cytoplasm regions measured by NanoSIMS. The $^{10}B/^{12}C$ and $^{10}B^{12}C/^{12}C$ ratios in nuclei areas were significantly higher than cytoplasmic areas in all samples. The $^{10}B^{12}C/^{12}C$ ratios in both cell compartments were usually higher than $^{10}B/^{12}C$ ratios. The distribution of boron in the B2 sample is higher than B3 sample with some overlap. The boron accumulation in B4 lower than B2 and B3 but still higher than B1. ***n***: represents the number of cells analysed for each sample.

A 4 h BPA treatment in sample B2 resulted in a 40-70 fold increase in $^{10}B/^{12}C$ ratio and a 60-80 fold increase in $^{10}B^{12}C/^{12}C$ ratio in nucleus and cytoplasm compared to the control. In B3 sample, adding tyrosine resulted in a ~ 50 % decrease in $^{10}B/^{12}C$ ratio compared to BPA-alone (B2), indicating that tyrosine did not enhance the accumulation of boron in the cells. With regards to the $^{10}B^{12}C/^{12}C$ ratios in B3 sample, they gave more spread in IQR values and significantly overlapped with those in the B2 sample. This overlap in the values of $^{10}B^{12}C$ levels between the two samples, also suggests that tyrosine did not enhance intracellular BPA uptake.

In the B4 sample, the ratios of $^{10}B/^{12}C$ and $^{10}B^{12}C/^{12}C$ in both cell compartments decreased significantly in comparison with samples B2 and B3, proving that the 4h efflux process allowed the escape of ions to the outside of the cell. However, the $^{10}B/^{12}C$ and $^{10}B^{12}C/^{12}C$ ratios following the efflux treatment have not returned to the baseline levels and are approximately an order of magnitude greater than in the control sample B1 (**Figure 4.22**). This proves that the efflux is an exchange process between the cell and surrounding medium and is slower than the BPA uptake process which in turn was conducted over 4h as well. Pharmacokinetic profiles are key parameters in determining the optimum radiotherapy timepoint and dosage – ideally the boron agent should be cleared from healthy tissues and blood but retained in tumour cells at the time of irradiation.

Absolute subcellular concentrations of ^{10}B can be determined from the $^{10}B/^{12}C$ ion ratios and the relative sensitivity for B^- in an appropriate matrix. The RSF value (RSF_B) used here is that obtained by Wilson *et al.* on a PMMA sample implanted with boron [40]. Although not an exact match for the freeze-dried cell sample, the polymer reference is a close analogue to the biological sample. The dry-weight concentration c_B(dry) of ^{10}B is given by Equation 4.1:

$$c_B(\text{dry}) = c_C(\text{dry}) \cdot (I_B/I_C) \cdot \text{RSF}_B \qquad \text{Equation 4.1}$$

where c_C(dry) is the dry weight carbon concentration (assumed 100%), and I_B/I_C is the ionic intensity ratio $^{10}B/^{12}C$. From the dry-weight concentration the wet-weight concentration c_B can be determined assuming the water-content of live cells (85%) and average cell density (1 g cm^{-3}). Using this approach, the equivalent wet-weight concentrations of ^{10}B in measured regions of interest were estimated in **Table 4.3**, noting the therapeutic threshold of ~15–30 μg g^{-1} [41].

Example calculation:

- The $^{10}B/^{12}C$ ratio in one of the nuclei of sample B2 cells was 1.09×10^{-4}.

- By applying Equation 4.1 using RSF_B of 1×10^{24} cm^{-3}, and $^{10}B/^{12}C$ ratio, the c_B(dry) concentration is 1.09×10^{20} atoms/cm^3.
- By multiplying the previous number by $10\times1.6\times10^{-27}$ kg/atom (for ^{10}B), this is equivalent to 1.75×10^{-6} kg/cm^3, which in turn converts to 1.75×10^{-3} g/cm^3 (in dry cell).
- Assuming the water-content of live cells is 85%, the result is 2.62×10^{-4} g/cm^3.
- Assuming cell density 1g/cm^3 then the wet weight is 2.62×10^{-4} g/g.
- By converting g/g to µg/g, the concentration is 262 µg/g (in wet cell).

The concentration is calculated in nucleus and cytoplasm for each cell and then the mean and standard deviation are taken to obtain the results shown in **Table 4.3**.

Table 4.3: Estimated ^{10}B concentration in sub-cellular regions of interest measured in GBM tumour cell culture samples (group B).

Sample	^{10}B µg per g (wet wt) (mean ± SD)	
	Nucleus	Cytoplasm
B1 (*n* = 11) Tumour control	2.4 ±0.9	1.4 ± 0.5
B2 (*n* = 3) Tumour BPA	240 ± 130	120 ± 93
B3 (*n* = 3) Tumour Tyr + BPA	86 ± 61	30 ± 20
B4 (*n* = 5) Tumour BPA + efflux	19 ± 3.7	6.5 ±1.1

Currently it is not possible to estimate absolute concentration levels from the $^{10}B^{12}C/^{12}C$ ion ratios without a relative sensitivity factor for the $^{10}B^{12}C$ ion. This requires further calibration work using a more closely-matched matrix standard.

Thus, the statistical summary of these results above is that the level of boron distribution in the nuclei is higher than the cytoplasm in B2, B3, and B4. The localisation of ^{10}B ion in the sample B2 is higher than the B3 and the latter is higher than the B4. All BPA treated samples show higher boron levels than the B1 control sample.

4.2.3.2.6 D2 maps

The D2 sample is a cell culture of BAT-biopsy treated with 10 mM of BPA for 4h. Selection of a cell for analysis was done *via* the CCD camera in the NanoSIMS instrument as shown in **Figure 4.15**.

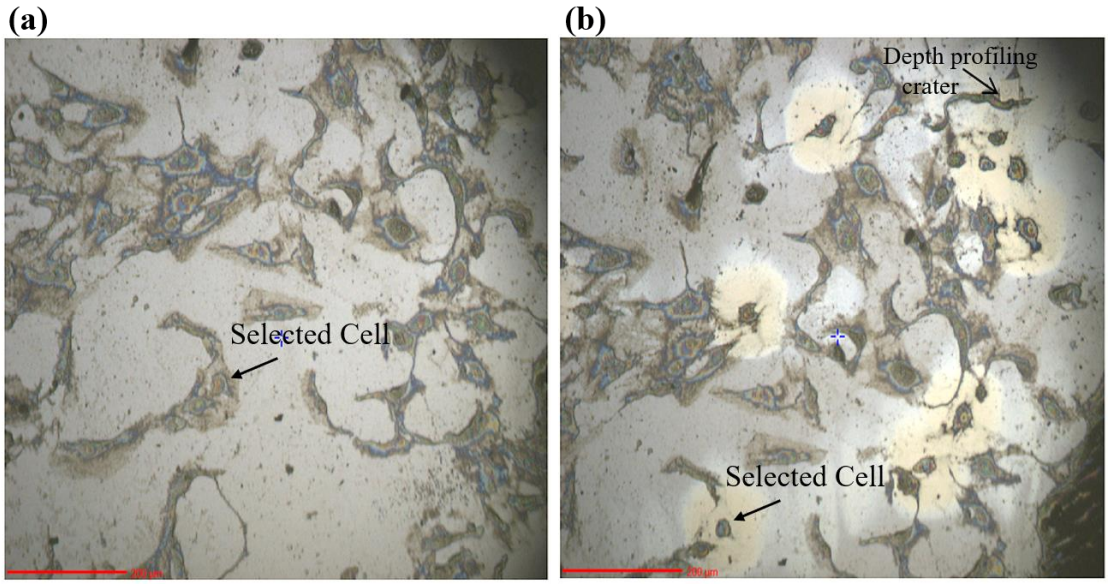

Figure 4.15: The CCD camera images (a) show the selected cell of D2 for NanoSIMS analysis, (b) reveals the shape of cell after analysis (arrow) and several cells analysed (bright spots - not shown). The image (b) shows also the depth profiling crater discussed in section 3.6.2.3 and Figure 3.7, indicated by an arrow. Scale bar = 200 µm.

The secondary ion images resulting from analysis are shown in **Figure 4.16** with the cell compartments identified on the images, nucleus (area 1-green line) and cytoplasm (area 2-red line). From the SE image, the general morphology of the cell, the area surrounding the cell and the features spread on the cell surface can be clearly distinguished. The Si image confirms the integrity of the cell structure. The Si image is also useful to avoid areas with high Si signal during the identification of ROI's in the cell. **Figure 4.16** shows that the distribution of C, CN, P and S ions between the cellular parts is similar to that in the sample B2 which was previously explained in section 4.2.3.2.1 in more detail. The bright white rim surrounding the cell shows high ion signals of B, C, BC, P and S, while the CN signal does not show a difference between this rim and cytoplasm area, further details are given in section 4.2.3.2.4.

The SE image shows branch-like features on the cell surface, especially around the edge of the nucleus and extending into the cytoplasmic region, as well as small bright dots grouped on the nucleus surface. These features display a low intensity of C, P and S ions and uneven signal intensity of CN. Moreover, the Si image does not show any cracks, voids or holes in the cell structure, suggesting that there may be salt crystals on the surface originating from the saline solution used in the sample washing. Some of these features may be a freezing artefact (ice crystals) created during preparation for analysis. In the SE, C, CN, P and S images there are small black spots at the bottom of the nucleus as well as on the left side of the cytoplasm while Si map confirms that there are no holes in the location of these black spots, indicating the possibility of contaminants on the surface with signals not pre-tuned for detection with NanoSIMS.

With regards to the accumulation of boron from the BPA, it is clear from the images that both the ^{10}B and $^{10}B^{12}C$ ions are distributed in the nucleus and the rim surrounding the cell more than the cytoplasm. This high accumulation of boron ions in the nucleus would increase the success rate of BNCT in the destruction of tumour cells infiltrating to BAT area when exposed to low-energy thermal neutron interaction as indicated by previous studies [21][22]. The summed counts of $^{10}B^{12}C$ ions is higher than that of the ^{10}B ions- this is evident from the intensity of the ion signals obvious through the images. All the analysed cells in sample D2 (n = 3) gave a similar distribution pattern of the boron. The behaviour of the boron distribution in sample D2 is similar to that obtained during the analysis of the B group samples. The signal intensity of ^{10}B and $^{10}B^{12}C$ ions in **Figure 4.16** confirmed that sample D2 absorbed the BPA compared to the control sample cells D1 in **Figure 4.4** which showed natural ratios of boron isotope, the latter being detailed in section 4.2.3.1.1. When comparing D2 with B2 images, both samples gave a similar number of summed ^{10}B counts, while the summed $^{10}B^{12}C$ counts in sample D2 were ~ 3 times higher than the B2 sample, more detail was shown in quantitative comparisons in 4.2.3.3. High resolution imaging of NanoSIMS at the subcellular level with Cs^+ beam in the D2 sample showed the slight differences in the distribution of ion signals between cell compartments and the sample preparation artefacts on the surface.

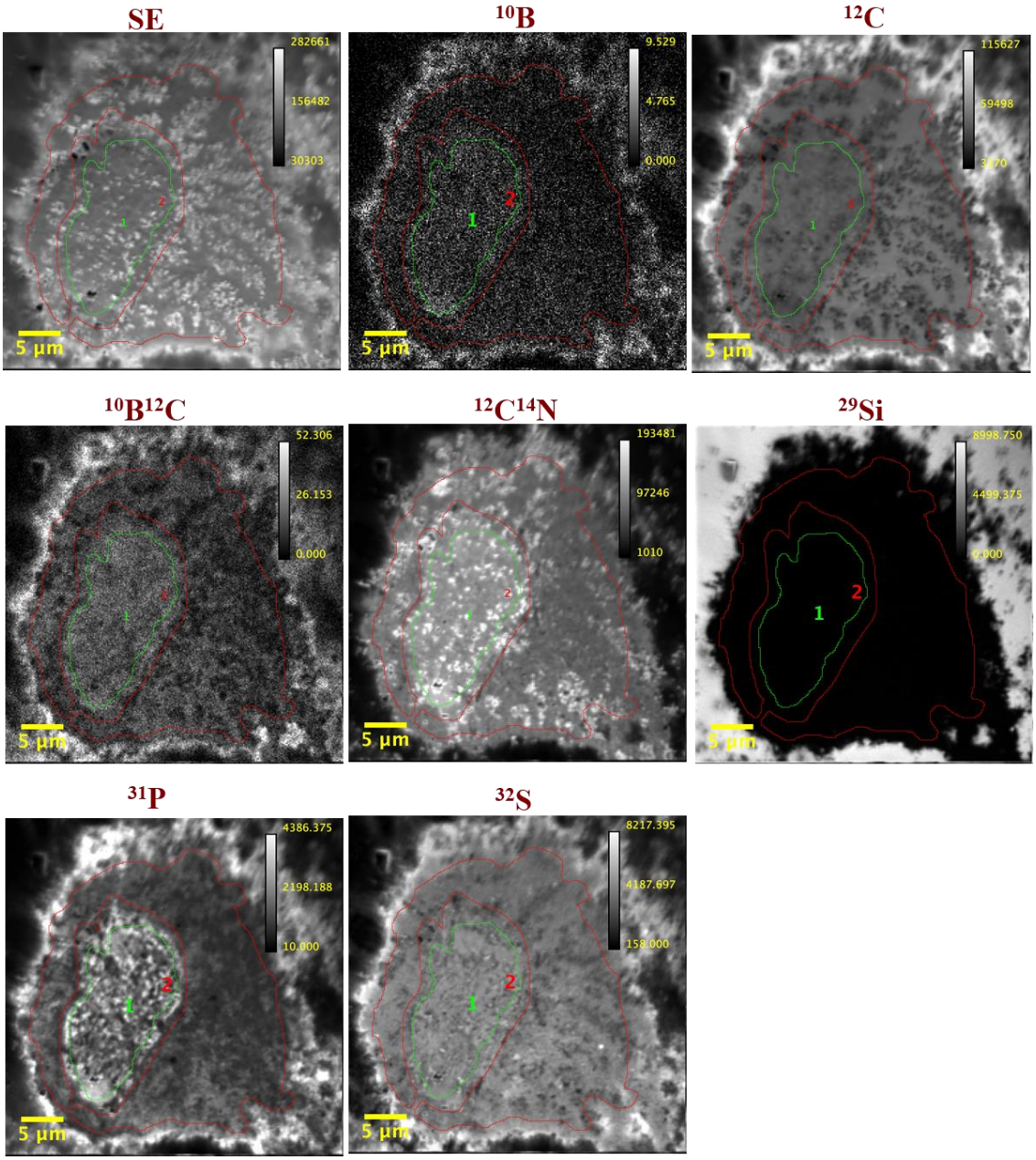

Figure 4.16: NanoSIMS images for the D2 sample of BAT-cell culture treated with10 mM of ^{10}BPA (4h), FoV 40×40 µm^2 with 256×256 pixels. SE image displays the overall cell structure and branch-like features on the surface. The images of negative secondary ions: ^{10}B, ^{12}C, ^{10}B^{12}C, ^{12}C^{14}N, ^{29}Si, ^{31}P and ^{32}S respectively shows the ion distribution across the cellular parts; Nucleus (1)- green line and Cytoplasm (2)- red line.

4.2.3.2.7 D3 maps

The D3 cell culture was pre-incubated with tyrosine before treatment with BPA for 4h with 10 mM concentration to explore the role of tyrosine in improving BPA uptake in tumour cells infiltrating to BAT area. **Figure 4.17** and **Figure 4.18** shows the CCD image of the selected cell and the distribution images of the secondary ions respectively using NanoSIMS.

Cell compartments; nucleus (region 1) and cytoplasm (region 2); were identified on the ion images.

The SE and Si images show the cell morphology and the substrate region covered by the cell. As for the distribution of C, CN, P and S ions between the cellular parts it is similar to the sample D2 as well as the B group samples and the descriptions in section 4.2.3.2.1 are valid for these samples as well.

Like all previous samples, ^{10}B and $^{10}B^{12}C$ ions of the BPA are distributed with high signals in the nucleus and outer rim around cell while the signals are lower in the cytoplasm. The same distribution was obtained in all cells analysed in the D3 sample (n = 3).

By comparing the summed counts of D3 (**Figure 4.18**) with D2 (**Figure 4.16**), it was observed that the ^{10}B ion signal in sample D3 is close to the D2 sample while the sum of $^{10}B^{12}C$ signals in sample D3 was ~2 times lower than that summed in the D2. This observation indicates that preloading with tyrosine did not improve BPA uptake in D3, and this is similar to what was indicated during the discussion of sample B3 compared to sample B2. The analysis also shows that $^{10}B^{12}C$ signal in D3 sample was ~ 6 times higher than the ^{10}B signal. More details on $^{10}B/^{12}C$ and $^{10}B^{12}C/^{12}C$ ratios of D samples are discussed in 4.2.3.2.9.

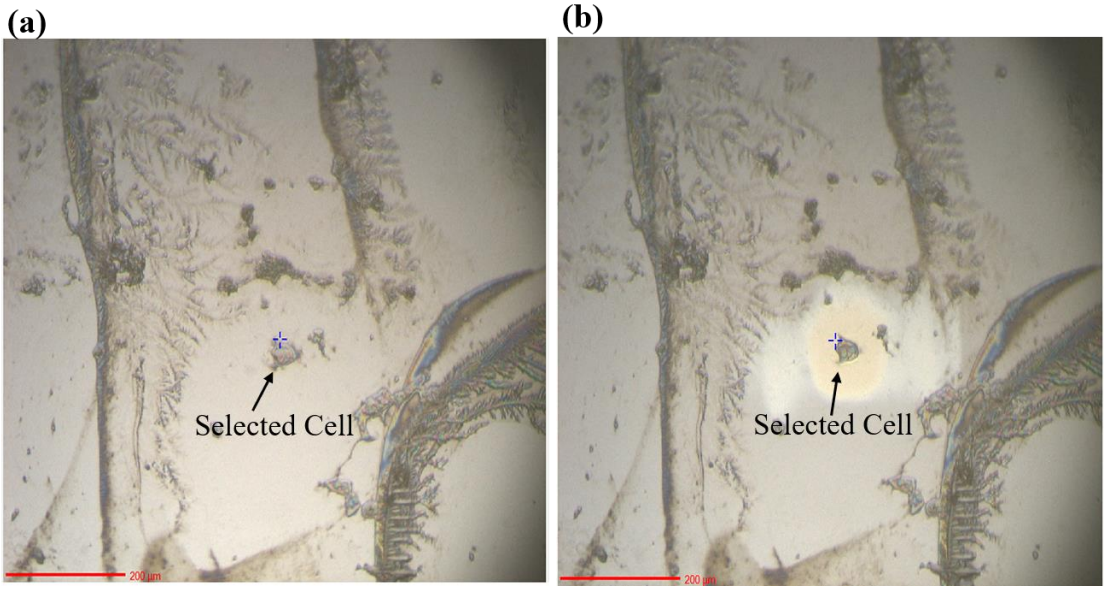

Figure 4.17: D3-selected cell images were captured before(a) and after (b) analysis using the NanoSIMS-CCD camera (arrows). Scale bar = 200 µm.

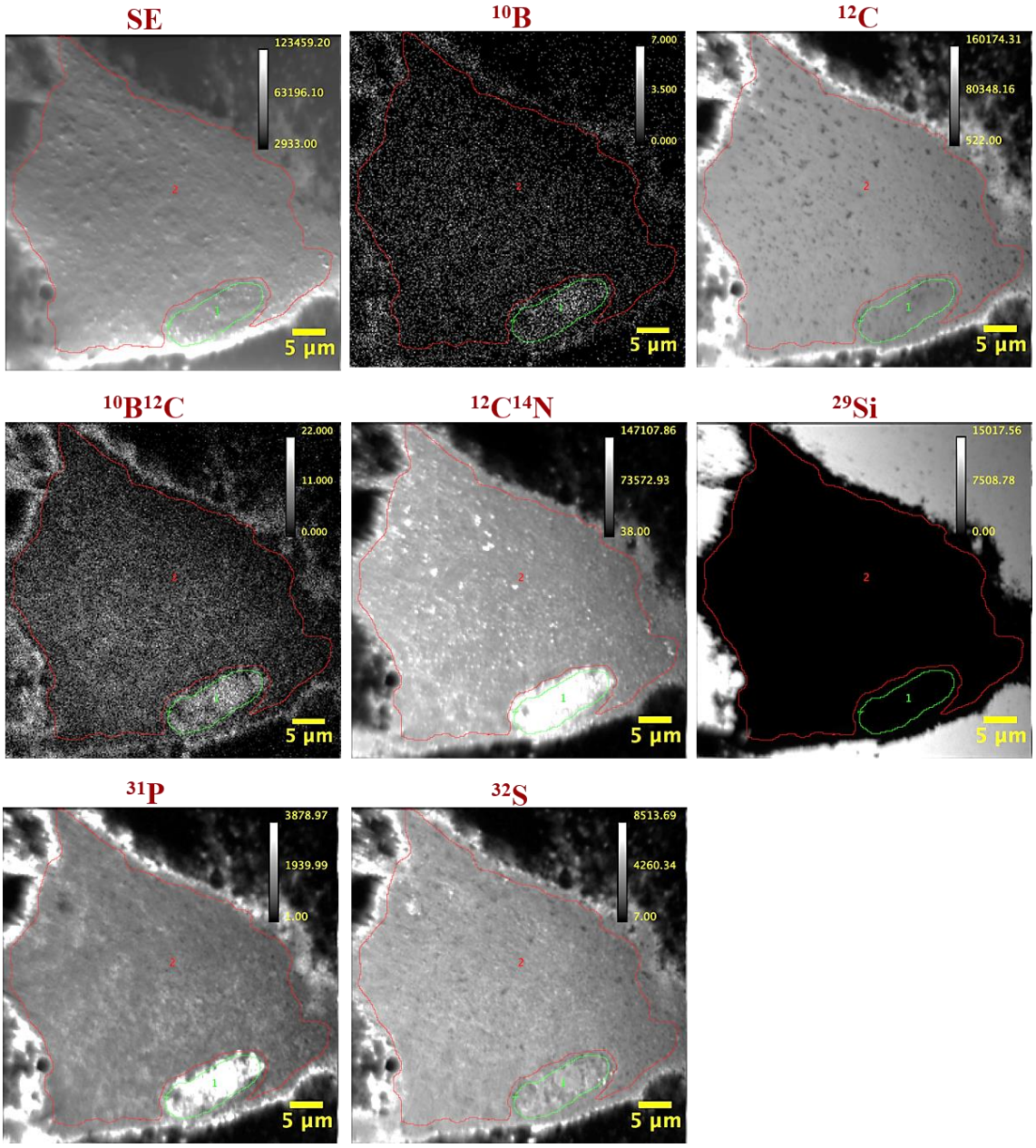

Figure 4.18: NanoSIMS images for D3 of BAT-cell culture preloaded with tyrosine (10 mM - 4h) then treated with BPA (10 mM - 4h). SE images shows the structure of the cell. The images of $^{10}B^-$, $^{12}C^-$, $^{10}B^{12}C^-$, $^{12}C^{14}N^-$, $^{29}Si^-$, $^{31}P^-$ and $^{32}S^-$ respectively show the subcellular distribution of negative ions in the cellular compartments; (1) Nucleus in green line and (2) Cytoplasm in red line. The FoV is 50×50 µm^2 with 256×256 pixels.

4.2.3.2.8 D4 maps

The D4 sample was subjected to two consecutive processes with the same duration (4 hours), the same as for the B group samples. The first was an uptake process by incubation with 10 mM BPA followed by the second step which is an efflux process where the ions were allowed to escape from the sample. Thus, the effect of efflux process on therapeutic boron levels in cells here was determined.

The CCD image and the ion distribution maps of the analysed cell are presented in **Figures 4.19** and **4.20** respectively. ROI's in the cell were determined to indicate the nucleus in region 1 (green line) and cytoplasm in region 2 (red line). The SE image shows the general shape of the cell and the surrounding area while the Si image shows the area of the substrate covered by the sample. The images of ion distributions of C, CN, P and S at the cellular level are similar to that shown in all previous samples.

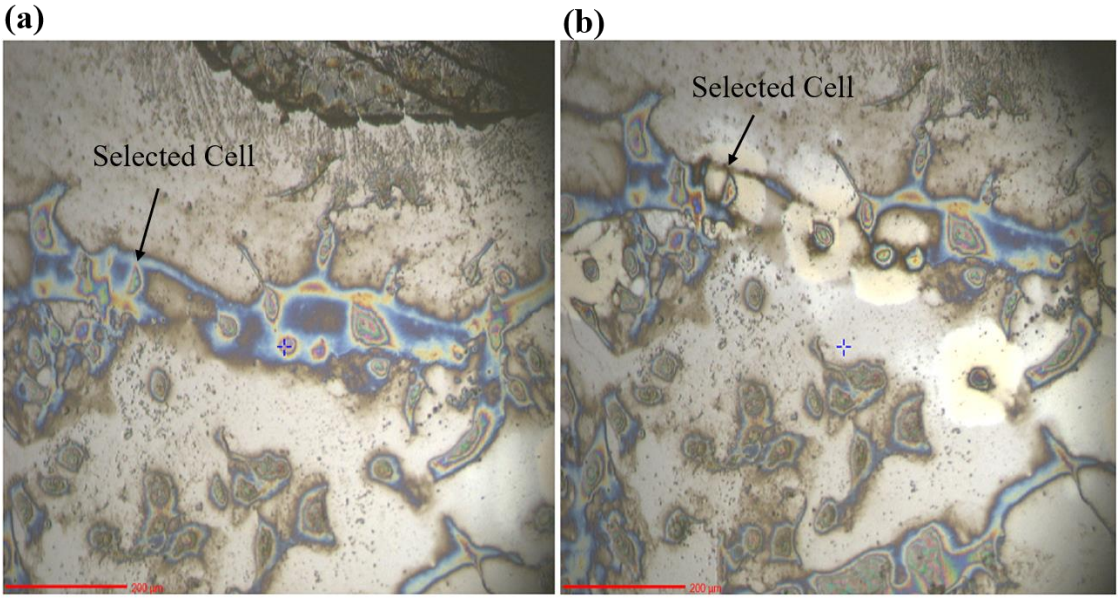

Figure 4.19: The images of the selected D4 cell chosen before (a) and after (b) analysis were captured using the CCD camera in NanoSIMS (arrows). (b) shows bright spots for other cells analysed (not shown). Scale bar = 200 µm.

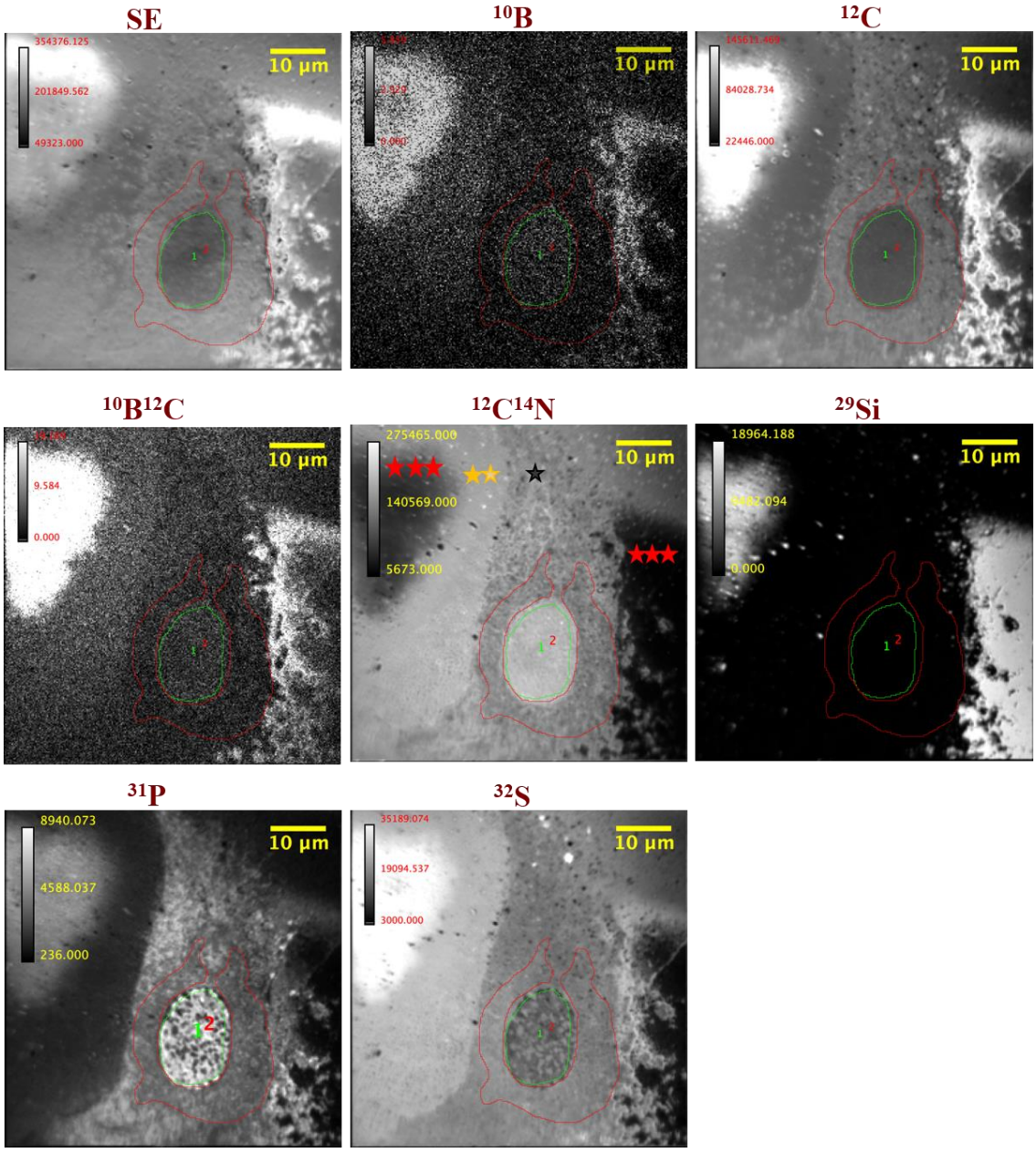

Figure 4.20: Images of NanoSIMS analysis for D4 of BAT cell culture exposed to an efflux process (4h) after treatment with BPA (10mM - 4h). SE: secondary electron image showing the general shape of the cell. SIMS images reveal the distribution of negative ions: ^{10}B, ^{12}C, ^{10}B^{12}C, ^{12}C^{14}N, ^{29}Si, ^{31}P and ^{32}S respectively within cell compartments; nucleus (green line-1) and cytoplasm (red line-2); FoV 60×60 µm^2 and 256×256 pixels. The stars in the CN image refer to three different regions in the distribution of ions around the cell.

It is noted in the images that the cell is surrounded by three regions which differ in the intensity of ion signals. The first area around the cell directly, indicated (* in the CN image), is where there is a reasonable intensity of C, CN, P and S signals while the B and BC signals are higher than those in the cell cytoplasm. This area extends both towards the top and bottom of the image and could be connections between cells, or it might be the cell membrane diffusing outwards, or both as was explained in section 4.2.3.2.4. The second area (**) shows a high signal intensity of CN and S ions, a low signal of C and an absence of P signal, while the absence of Si signal confirms the existence of material covering the substrate it is a different type to that in the first area (*). The signal of B and BC in the second area is higher than that in the first area and the cytoplasm area, which may indicate the presence of the sample preparation medium. The third area, referred to by (***) on the right side of the image and on the upper left side, gave high signal intensity with all ions except CN which appeared with low intensity, indicating the substrate location which often contain the preparation medium and remnant of cellular material.

As for the distribution of boron at the cellular level, both ^{10}B and $^{10}B^{12}C$ ions accumulate more in the nucleus than the cytoplasm. The distribution of boron ions between cellular parts in this D4 sample is quite similar to that obtained in D2 and D3 samples as well as B group samples. The same results were obtained for the distribution of boron in all analysed cells in the D4 sample (n = 5).

By comparing the total intensities of the boron signals summed from cells in the D samples as seen in the **Figures 4.4, 4.16, 4.18** and **4.20**, it is noted that the ion signal intensity of ^{10}B and $^{10}B^{12}C$ in D4 is less than D2 and D3 by factor of ~ 4 and 3 respectively, indicating a decrease in the level of accumulated ions of BPA during the efflux process. However, the total intensities of ^{10}B and $^{10}B^{12}C$ signals in D4 remained ~ 50 % higher than D1, which confirms that the sample still retained some BPA ions and that the efflux process is slow compared to the uptake process during the 4h, this result is similar to what was obtained with the sample B4 of Group B. In addition, the total signal intensity of $^{10}B^{12}C$ in D4 sample was ~ 5 times higher than the ^{10}B signal. More details on $^{10}B/^{12}C$ and $^{10}B^{12}C/^{12}C$ ratios of D samples are discussed in 4.2.3.2.9.

4.2.3.2.9 Quantification of ^{10}B in D group samples

The amount of boron from the BPA in the cellular parts for the BAT-cell cultures samples D1, D2, D3 and D4 was quantified. Boron signals were normalised to carbon and was represented in the same manner used with the B group samples. **Figure 4.21** shows the $^{10}B/^{12}C$ and $^{10}B^{12}C/^{12}C$ ratios in both nuclear and cytoplasmic areas while the **Figure 4.7 -c** explains how to interpret the graph. **Table 4.4** shows the mean values of $^{10}B/^{12}C$ and $^{10}B^{12}C/^{12}C$ ratios from all D group samples in the box plots shown in **Figure 4.21**, where the difference can be observed between them. At least three cells were analysed for each sample.

Group D samples showed a distribution pattern of BPA similar to the B group samples that were shown previously in **Figure 4.14**. The ratios of $^{10}B/^{12}C$ and $^{10}B^{12}C/^{12}C$ were higher in nuclear areas compared to cytoplasmic areas. For samples D2 and D3 the mean of $^{10}B/^{12}C$ and $^{10}B^{12}C/^{12}C$ ratios indicate nuclear : cytoplasm BPA distribution are 2.1± 0.1 and 1.8 ± 0.6 respectively, indicating a ~ 2-fold excess of BPA in the nucleus compared to the cytoplasm under the treatment used in D2 and D3. These statistical measurements match with the ionic distributions of boron shown in D samples images (**Figures 4.16, 4.18** and **4.20)**.

Table 4.4: The mean values of $^{10}B/^{12}C$ and $^{10}B^{12}C/^{12}C$ ratios from the D group samples (shown in **Figure 4.21**).

Ratios	**$^{10}B/^{12}C$**			
Mean ($\times 10^{-4}$) ± SD of	D1	D2	D3	D4
Nuclei	0.01 ± 0.005	0.66 ± 0.14	0.64 ± 0.3	0.16 ± 0.05
Cytoplasm	0.006 ± 0.002	0.33 ± 0.03	0.3 ± 0.2	0.13 ± 0.018
Ratios	**$^{10}B^{12}C/^{12}C$**			
Mean ($\times 10^{-4}$) ± SD of	D1	D2	D3	D4
Nuclei	0.012 ± 0.006	4.5 ± 0.15	3.17 ± 1.4	0.93 ± 0.27
Cytoplasm	0.008 ± 0.004	2.7 ± 0.03	1.7 ± 0.9	0.8 ± 0.23

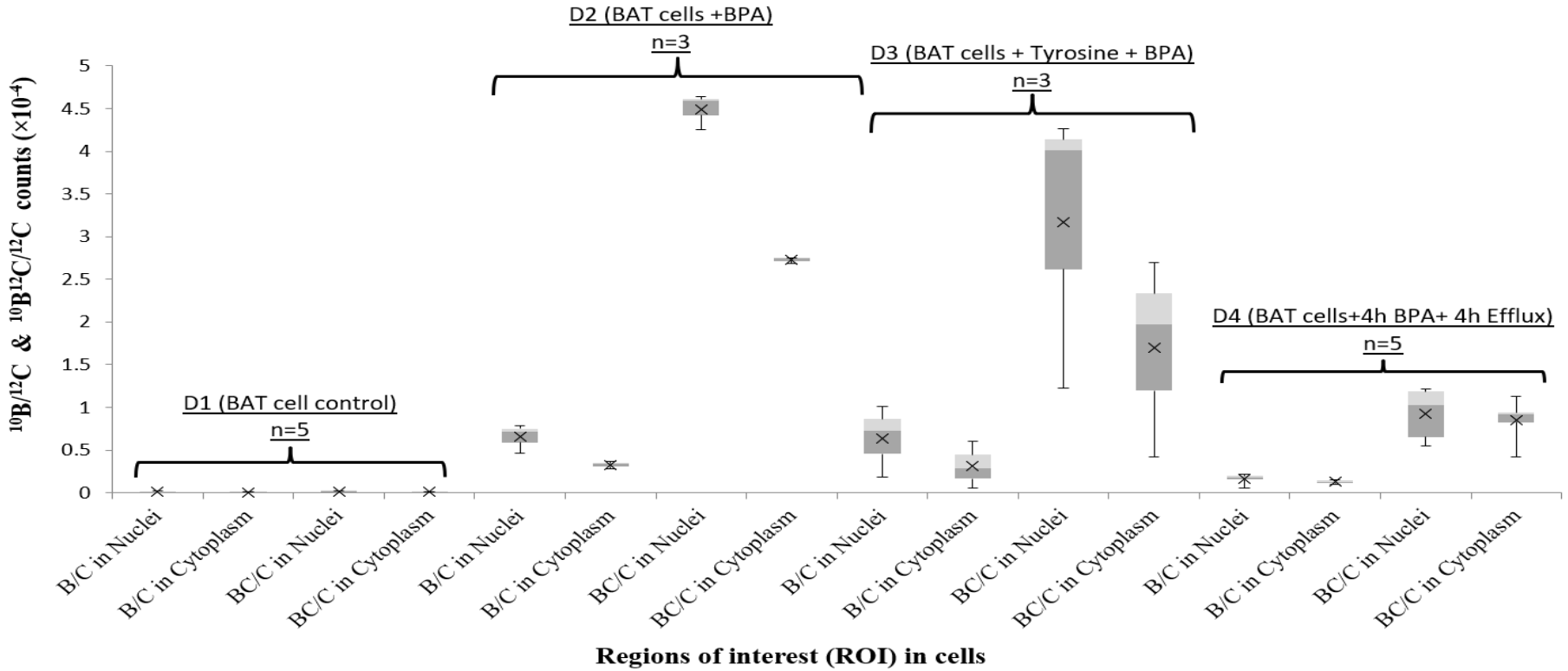

Figure 4.21: Comparison of the BAT-cell culture samples: D1, D2, D3 and D4 in terms of $^{10}B/^{12}C$ and $^{10}B^{12}C/^{12}C$ ratios accumulated in cell compartments determined by NanoSIMS. In all samples, nuclei regions show $^{10}B/^{12}C$ and $^{10}B^{12}C/^{12}C$ ratios higher than cytoplasmic regions. The $^{10}B^{12}C/^{12}C$ ratios in both cellular parts are significantly higher than $^{10}B/^{12}C$ ratios. The accumulation of boron in the D2 sample is higher than the D3 sample with some overlap in $^{10}B/^{12}C$ ratios. The boron distribution in both D2 and D3 higher than D4, the latter still higher than D1. ***n***: represents the number of cells analysed for each sample.

In D2 sample, treatment with BPA- 4h resulted in a 50 - 70 fold increase in $^{10}B/^{12}C$ ratio and a ~ 300-fold in $^{10}B^{12}C/^{12}C$ ratio in both compartments compared to the D1 control. In the D3 sample, the tyrosine has no significant effect in BPA uptake that measured by $^{10}B/^{12}C$ ratio compared with D2. In terms of the $^{10}B^{12}C/^{12}C$ ratios in both subcellular parts of the D3 sample, they were ~ 30% lower than those in the D2 sample but with wide IQR (discussed below in 4.2.3.3). This observation of the D3 may indicate that tyrosine did not stimulate the BPA uptake in BAT cells. In the D4 sample, the effect of the efflux process resulted in a decrease by a factor 2-4 in $^{10}B/^{12}C$ and $^{10}B^{12}C/^{12}C$ ratios in both subcellular parts compared to D2 and D3. However, the $^{10}B/^{12}C$ and $^{10}B^{12}C/^{12}C$ ratios in D4 are an order of magnitude higher than in the control sample D1 (**Figure 4.22**), indicating that the cell compartments retain a portion of the boron ions, which in turn demonstrate that the efflux process is a slower process than the uptake process.

In all D samples, the wet weight concentrations of ^{10}B in the nucleus and the cytoplasm from $^{10}B/^{12}C$ ratios were estimated (**Table 4.5**) using the same approach described in the calculation of B group sample concentration in the section 4.2.3.2.5. The quantitative comparison showed that there is no significant difference in ^{10}B levels between D2 and D3. The levels of ^{10}B and $^{10}B^{12}C$ ions in D4 are less than D2 and D3 but higher than in the control sample D1.

Table 4.5: Estimated ^{10}B concentration in sub-cellular regions of interest measured in BAT cell culture samples (group D).

Sample	^{10}B µg per g (wet wt) (mean ± SD)	
	Nucleus	Cytoplasm
D1 (*n* = 5) BAT control	2.5 ±1.4	1.4 ± 0.6
D2 (*n* = 3) BAT BPA	160 ± 43	79 ± 10
D3 (*n* = 3) BAT Tyr + BPA	160 ± 100	77 ± 69
D4 (*n* = 5) BAT BPA + efflux	39 ± 16	31 ± 5

4.2.3.3 Quantitative comparisons of ^{10}B distribution from BPA drug between B and D groups samples

Figure 4.22 shows normalised intensities of ^{10}B and $^{10}B^{12}C$ from the control samples B1 and D1. For both boron-related signals, the normalised levels in these control samples are within experimental uncertainty (similar standard deviation) when comparing nuclei to cytoplasm or GBM tumour to BAT samples and have very similar boron levels, see also **Tables 4.2** and **4.4**. The normalised intensities of the control samples are very low compared to the BPA-treated samples (**Figure 4.23**) which is consistent with them not having been exposed to the ^{10}B-enriched BPA formulation. The concentrations of ^{10}B in B1 (**Table 4.3**) and D1 (**Table 4.5**) are within the physiological levels of total boron in human soft tissues that range from 0.1–10 ppm [42].

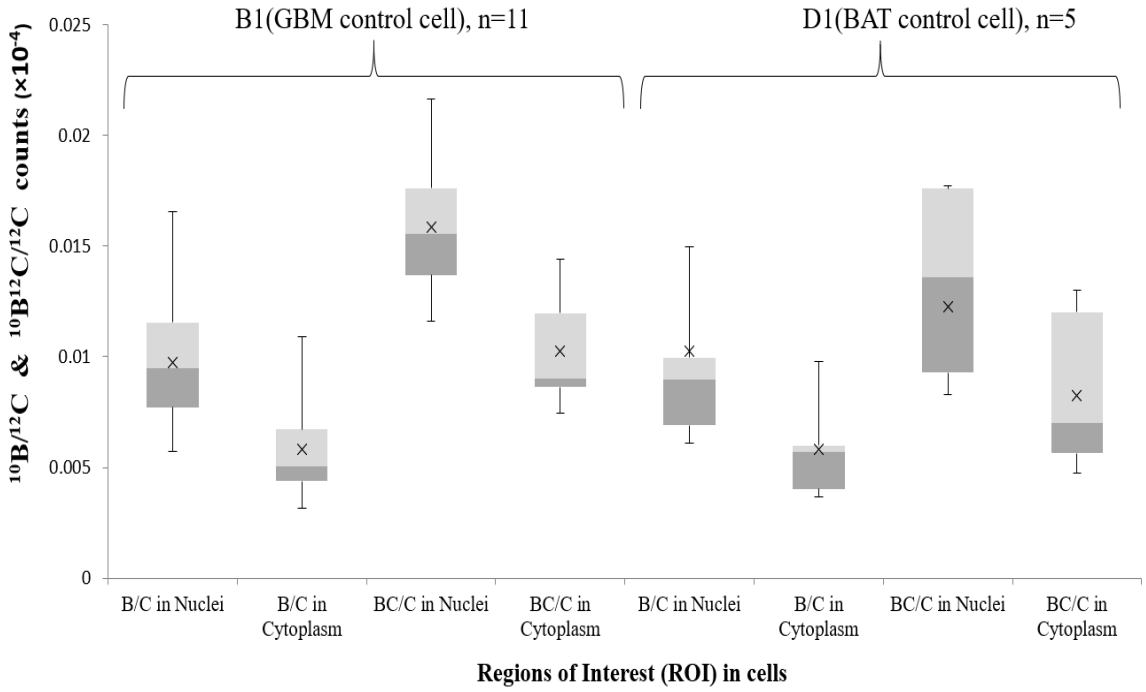

Figure 4.22: Comparison between the GBM (B group) and BAT (D group) control samples untreated with BPA in terms of $^{10}B/^{12}C$ and $^{10}B^{12}C/^{12}C$ ratios in the nuclei and cytoplasm regions measured by NanoSIMS. ***n*** = number of cells analysed for each sample.

The BPA treated samples of GBM (group B) and BAT (group D) were compared in **Figure 4.23**. The boron levels in the treated B and D samples confirm that the cells have taken up the BPA compared to control samples B1 and D1 in **Figure 4.22.** The results (**Figure 4.23**)

are consistent in that $^{10}B/^{12}C$ and $^{10}B^{12}C$ $/^{12}C$ ratios are ~ 2-fold higher in nuclei areas compared to cytoplasmic areas, and that $^{10}B^{12}C$ $/^{12}C$ ratios in both compartments are higher than $^{10}B/^{12}C$ ratios in all samples. Interestingly, the $^{10}B^{12}C$ $/^{12}C$ ratios are significantly higher in BAT cells (D2, D3 and D4) than in tumour core cells under the corresponding treatment.

In sample D3, a significant variation is observed in the values of the $^{10}B^{12}C$ $/^{12}C$ ratio, the B3 sample also showed a large scatter but less than for D3. This is due to three possible causes. First, that the addition of tyrosine has played a role in changing the chemistry of the sample. Second, that the effect of tyrosine may vary depending on the cell cycle, this is what Langen *et. al*. concluded, the uptake of IM-tyrosine in the human glioma cells line was increased in the proliferating cells [43]. Yoshida *et. al*. also explained that the uptake of L-amino acids is affected by cell cycle [34]. Third, that the effect of tyrosine was based on the activity of LAT-1 expression, which in turn may vary from cell to another without dependence on the proliferation state as noted by De Wolde *et. al*., Sasajima *et. al*., and Detta *et al*. [44]–[46] and Grunewald *et al*.[47]. To provide further information on cell cycle, histological stains could be used or cells could be sorted in suspension. However, neither of these approaches is compatible directly with SIMS imaging so would not provide answers regarding the phase of a specific cell in relation to its boron level. High resolution SEM could provide insights based on cell morphology before/after SIMS imaging e.g. dividing cells identified. This could be an area of future study.

Since an important goal of BNCT is to kill tumour cells invading the healthy tissue around the tumour core, it is interesting to compare the estimated BPA levels in cells from tumour (B) and BAT (D) samples of **Tables 4.3** and **4.5** respectively. Of measured relative boron levels in individual cells it was found that considering experimental uncertainty and/or cell-to-cell variations, the mean ^{10}B concentrations are not significantly different in samples B2 and D2. This result is consistent with the findings of Detta and Cruickshank, where they explained that tumour cells that infiltrated tissues around the tumour (BAT) showed uptake levels of BPA close to the GBM tumour cells. This is despite the number of BAT cells being less than those in the core of the GBM tumour as showed in **Figure 2.2**, suggesting that the LAT-1 expression in BAT cells is more active than the GBM cells. This activity, in turn, contributes to the selective localisation of the BPA in the tumour cells infiltrating into healthy tissue [46]. Nawashiro *et al.* also reached the same conclusion during the study of LAT-1 expression in the GBM tumour cells at edges between tumour and normal brain tissues from 68 patients [48]. Additionally, the nuclear concentrations of ^{10}B measured for sample B2 and D2 in this work (~200 μg per g wet wt) are very similar to those reported in

literature on cell lines or in animal models using different primary ion beams and mass analysers [49]–[54] as shown in the 2.3.1.1 and **Table 2.2**. Cytoplasm ^{10}B concentrations for B2/D2 samples are approximately 50% of those measured in previous studies. This may be due to differences in cell type or cell cycle stage at the point of fixation. As mentioned previously in **Tables 4.3** and **4.5**, with tyrosine pre-treatment the mean boron level is significantly reduced in B3 samples but not in D3 samples. The concentrations of ^{10}B in B4 and D4 confirms that BPA uptake levels have decreased compared to other treatments but did not reach those concentrations calculated in the control samples B1 and D1. The mean boron level in both samples D3 and D4 are higher than those corresponding in B group as shown from **Figure 4.23**, **Tables 4.2** and **4.4**.

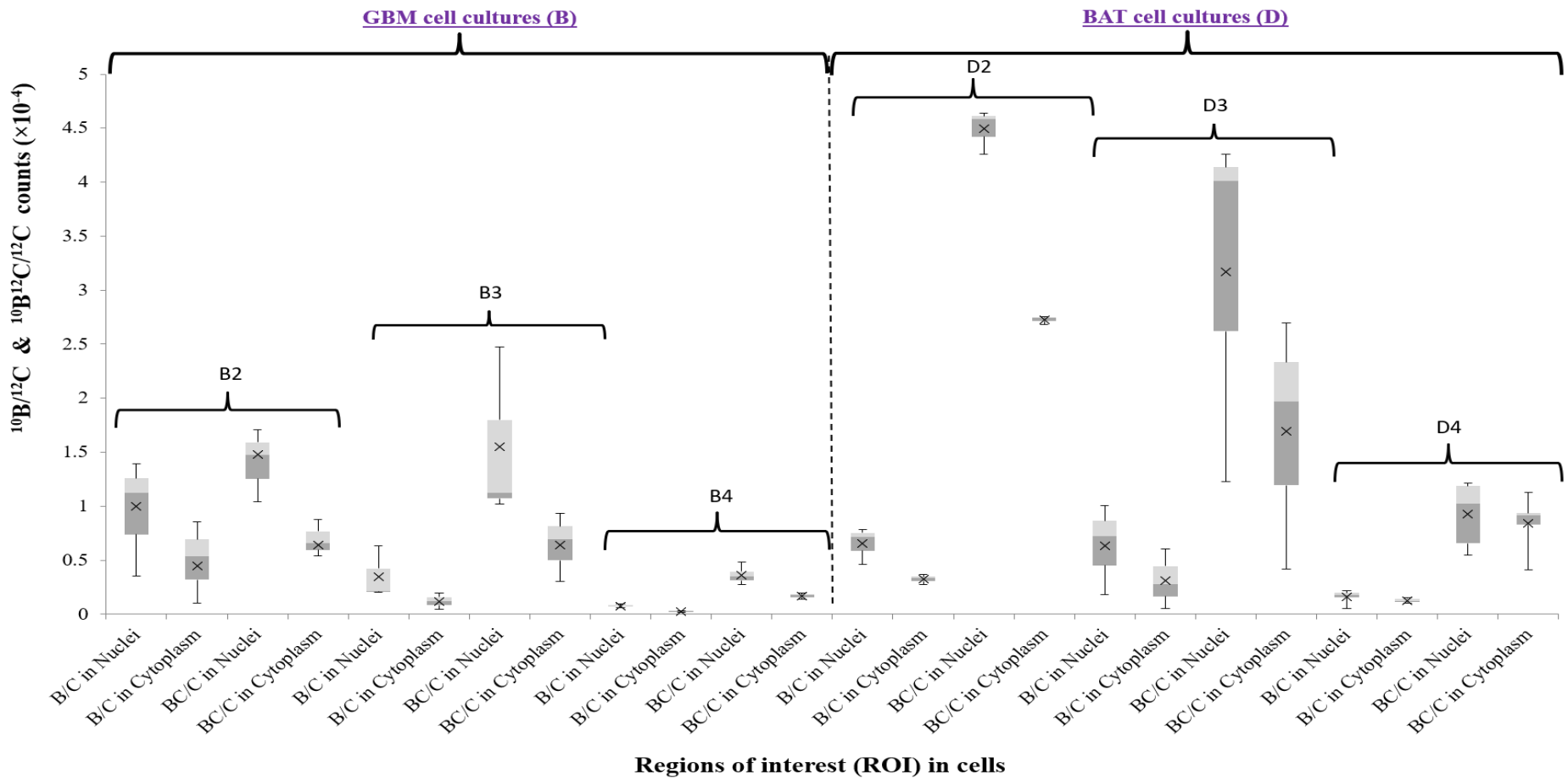

Figure 4.23: Comparison between GBM cells (B group) and BAT cells (D group) in terms of $^{10}B/^{12}C$ and $^{10}B^{12}C/^{12}C$ ratios accumulated of BPA in nuclei and cytoplasmic areas of cells measured by NanoSIMS.

4.2.4 BioToF-SIMS results and discussion

4.2.4.1 Imaging of boron isotopes in control samples

In the control cell-culture samples A1, B1, C1 and D1, the ratios of boron isotopes were measured to determine naturally existing boron in the samples and thus ensure any observed increase in the ratios of boron in the samples treated with BPA, that were discussed later. None of the control samples were pre-treated with BPA and were analysed under the same analytical conditions. After the completion of the automated analysis the data was processed as explained in section 3.5.2.

In the control sample A1 of GBM, the total ion image, shown in **Figure 4.24 -a**, was used to select the area of the cell for data extraction (shown in green). The total Si^+ image, shown in **Figure 4.24 -b**, was used to ensure the Si^+ signal was absent from the area selected. The resulting mass spectrum in **Figure 4.25 -a &b** that was extracted from the selected cells clearly shows a high signal intensity of Na^+ at *m/z* 23 compared to the K^+ signal intensity at *m/z* 39. The intensities of the C^+ signal and boron isotopes were verified by magnification of the mass spectrum, as shown in **Figure 4.25 -c** and **Figure 4.25 -d**. This latter figure shows that the signals of boron isotopes at *m/z* 10 and 11 do not appear as clear peaks, the signals are so weak that they interfere with the level of background noise from the instrument. This suggests the concentration is at the limit of detection for boron.

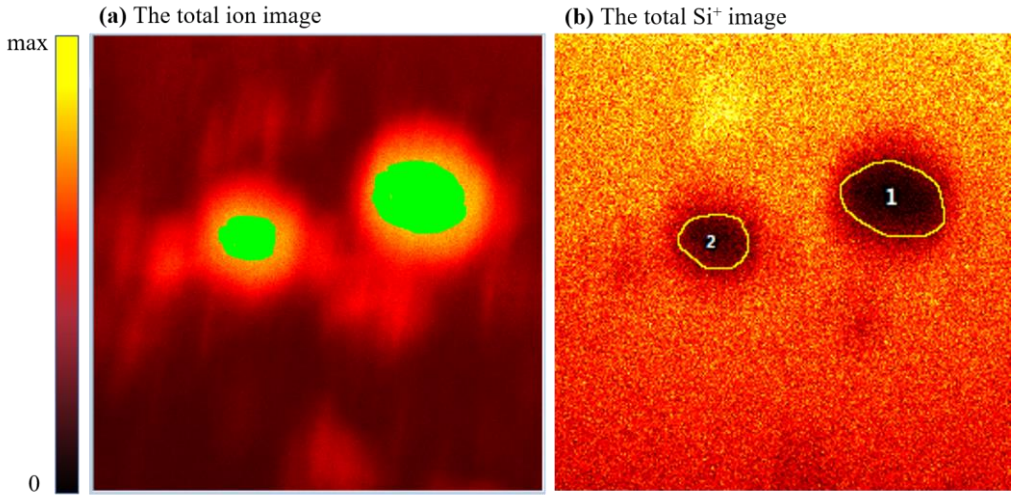

Figure 4.24: BioToF analysis for A1 sample showing (a) the cells chosen on the total ion image to extract the data (spectra and images). (b) The total Si^+ image showing the location of the cells 1&2 on the substrate (black areas). FoV is 153×153 μm^2.

The positive secondary ion images, ^{12}C, ^{23}Na, ^{28}Si and ^{39}K were generated from the signal intensity in the mass spectra while images of ^{11}B and ^{10}B were generated from the spikes along with the noise. The distribution of all these ions within cells is shown in **Figure 4.26**. The silicon signal is again absent where the cells cover the substrate, but appears clearly from the exposed substrate around the cells. The sodium image shows high signal intensity and approximately uniform distribution of Na across the bulk of the cell, less intensity is observed in some areas surrounding the cells as indicated by arrows which may be the remnants of tissue parts between cells or perhaps the preparation medium. The ^{39}K image shows a very similar distribution to that of the Na but with lower signal intensity than Na in the centre of the cells. A higher signal intensity of ^{39}K was observed on the right side of cell 1 (indicated by arrow) but it is not possible to identify if this is a nucleus or other cellular feature as the resolution of the image is too low. The carbon is distributed in the cells fairly homogenously but with less signal intensity than the sodium and potassium ions. The BioToF- SIMS detected very weak signals in the mass range of both boron isotopes. Although the images did not accurately determine the localisation of these isotopes, the intensity in the ^{11}B image appears higher than ^{10}B. The very low level of boron signals in the cells is expected considering boron is at natural abundance levels as these samples were not pre-treated with the BPA.

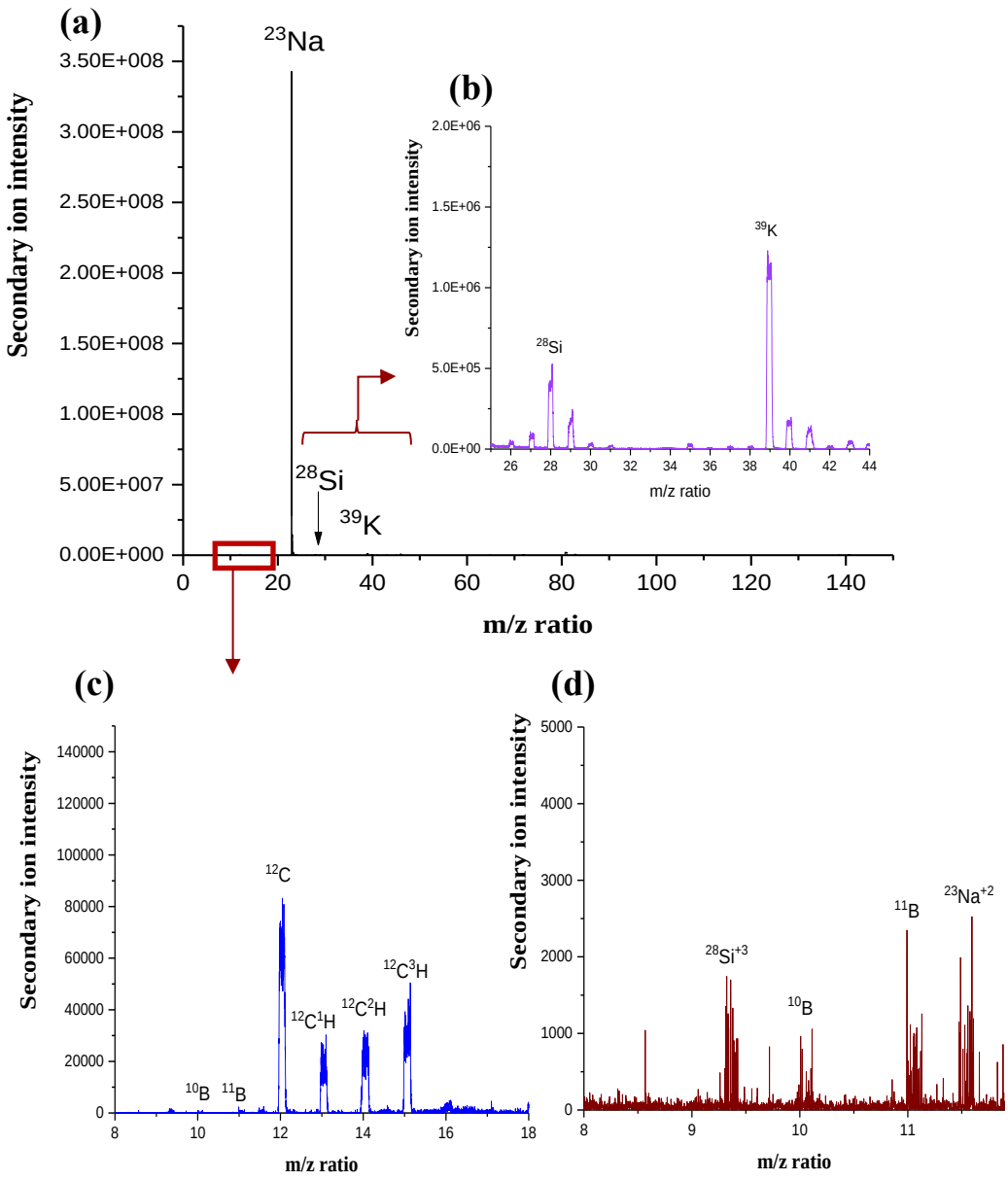

Figure 4.25: Positive secondary ion mass spectra of A1 cells from GBM control sample, obtained after exposure to a dose of 1.34×10^{14} ions/cm^2 of the Au^+ beam at 20 keV. (a) shows the full spectrum. (b), (c) and (d) show the magnification of the *m/z* range from 25-44, 8-18 and 8-12 respectively.

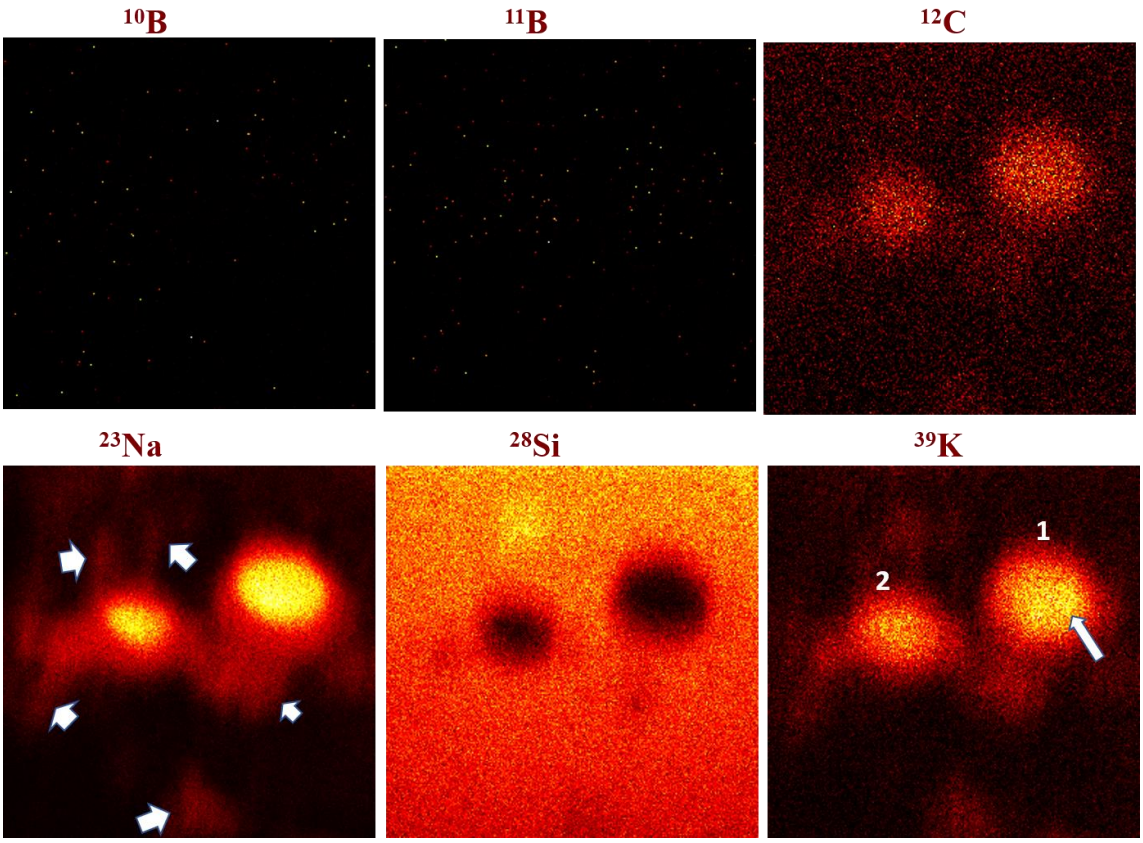

Figure 4.26: BioToF-SIMS analysis for A1 control cells of GBM sample with FoV 153×153 µm^2. The positive secondary ion images of ^{10}B, ^{11}B, ^{12}C, ^{23}Na, ^{28}Si, and ^{39}K respectively show the ion distributions within the cell. The arrow in the ^{39}K image shows the location of the high intensity in cell 1. The arrows in the ^{23}Na image indicate the lower intensity regions of Na^+ around the cell. The analysis dose in the images is 1.34×10^{14} ions/cm^2. The colour gradient from black to yellow shows the signal intensity from zero to the maximum values.

Figure 4.27 -a shows the selected cell from another control sample B1 cultured from a different GBM biopsy. The region coloured green on the total ion image, as well as outlined on the total silicon ion image in **Figure 4.27 -b** was where data was extracted from. The presence of another cell that has not been selected (marked with a star) can also be seen in the Si image. The mass spectrum extracted from the selected cell is shown in **Figure 4.28 - a, b, c & d** and presents similar results to the spectrum of sample A1. Although boron isotopic signals are low and interfered with the noise signals, the intensity of the ^{11}B signal is still higher than the ^{10}B signal. **Figure 4.29** shows the positive secondary ion images generated from the peaks of interest. The images show that the ions were distributed across the cell in a pattern similar to the A1 cell sample. The images of Na and K showed that there is co-accumulation with high intensity of both ions on the left side of the cell (indicated by the arrow). There are more ^{11}B signals compared to the ^{10}B but the images do not show the localisation of these signals, this is similar to the A1 sample.

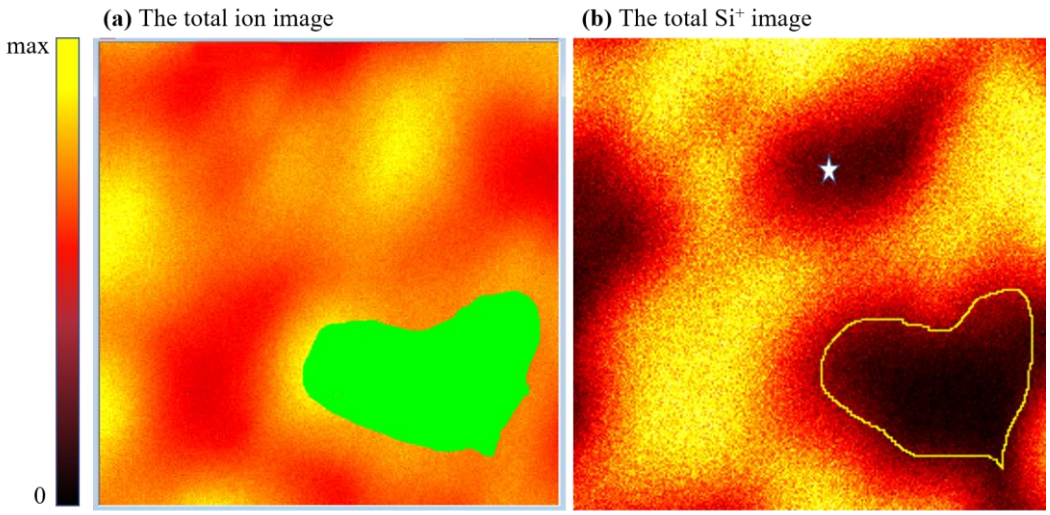

Figure 4.27: The total ion image obtained from the BioToF analysis shows (a) the cell selected in the B1 sample from which data of spectra and images were extracted, (b) the total Si^+ image confirming the location of the cell on the substrate (black area). The star refers to the location of another cell apparent in Si image. FoV in images is 100×100 μm^2.

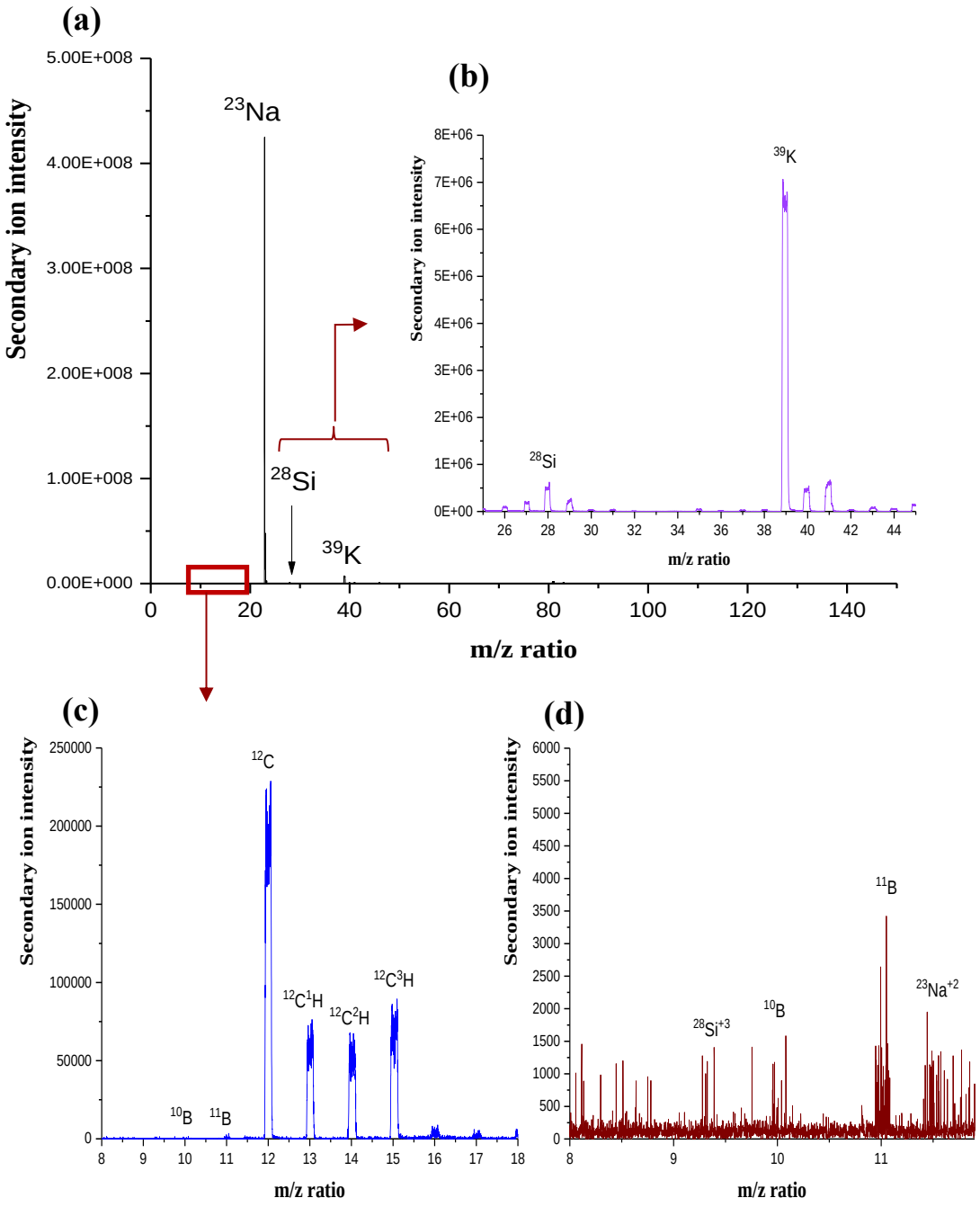

Figure 4.28: Positive secondary ion mass spectra of B1 cell from GBM control sample, obtained after a dose of 2.05×10^{14} ions/cm^2 from the 20 keV Au^+ beam. (a) shows the full spectrum. (b), (c) and (d) show the magnification of the *m/z* range from 25-45, 8-18 and 8-12 respectively.

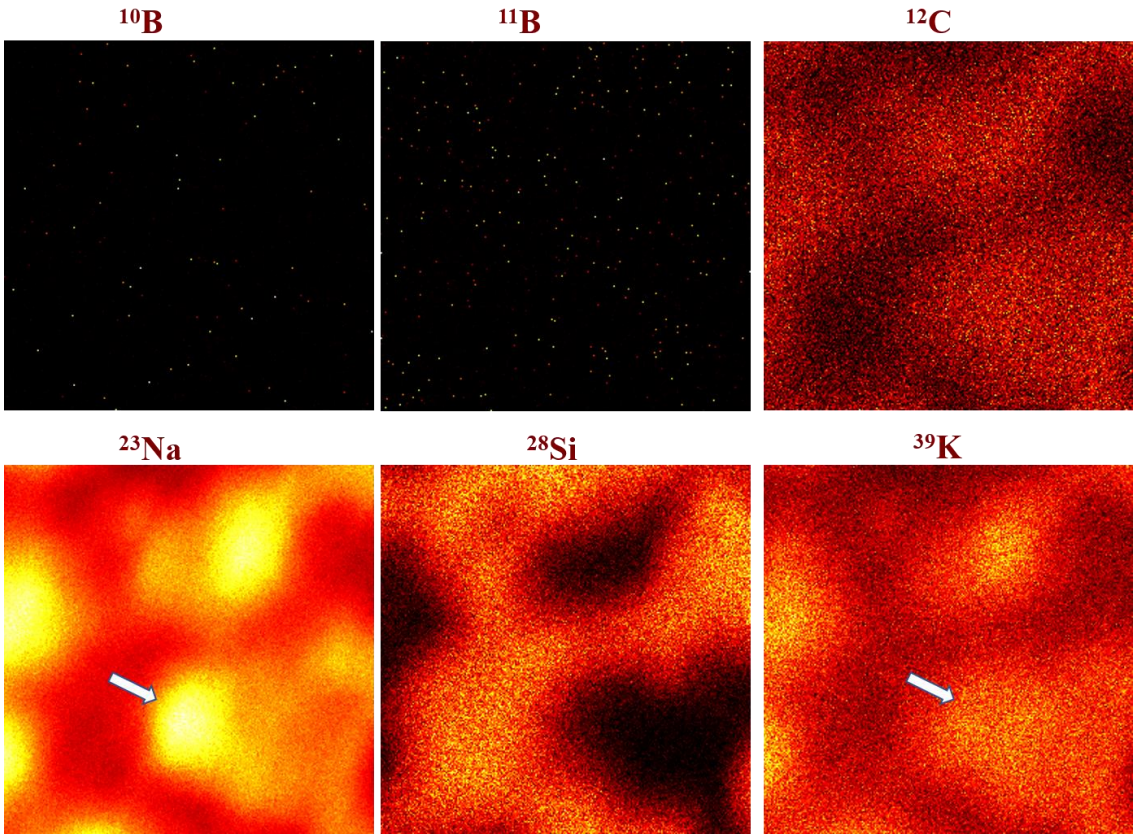

Figure 4.29: B1 control cell from GBM sample with FoV 100×100 µm^2 using BioToF-SIMS. The positive secondary ion images of ^{10}B, ^{11}B, ^{12}C, ^{23}Na, ^{28}Si, and ^{39}K respectively show the distribution of ions across the cell. The arrows in the Na and K images indicate to the location of co-accumulation with high intensity of Na^+ and K^+ in the cell. The analysis dose in the images was 2.05×10^{14} ions/cm^2. The colour gradient from black to yellow shows the signal intensity from zero to the maximum values.

In the C1 control sample cultured from BAT biopsy, the data were extracted from the cell selected in **Figure 4.30**. The acquired spectrum is shown in **Figure 4.31** and presents similar results to the samples A1 and B1. The images in **Figure 4.32** show distribution of secondary ions in the cell similar to those of A1 and B1, localisation of boron could not be seen.

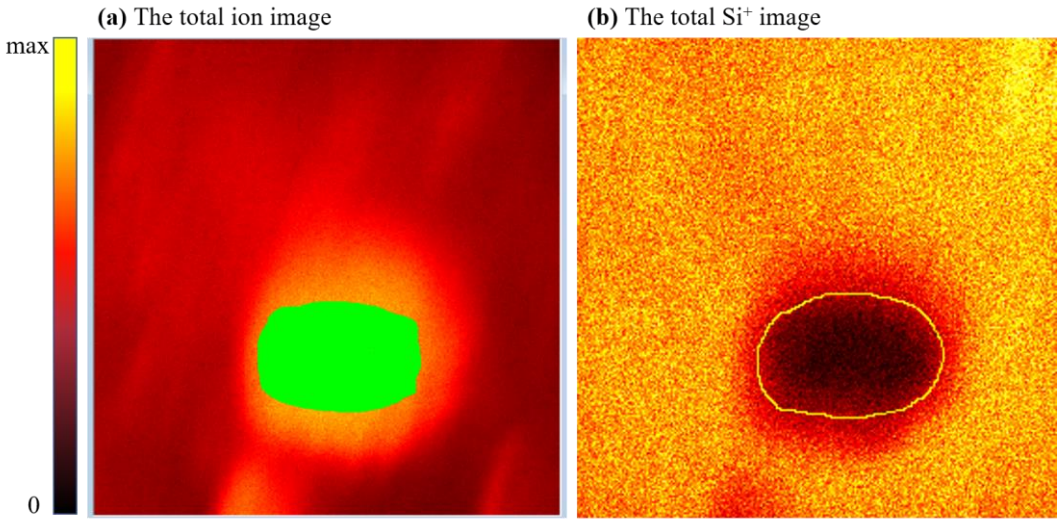

Figure 4.30: The images of BioToF analysis for C1 sample showing (a) the selected cell on the total ion image to extract the spectra and ions images, and (b) The total Si^+ image showing the cell site on the substrate (black area). FoV in images is 90×90 μm^2.

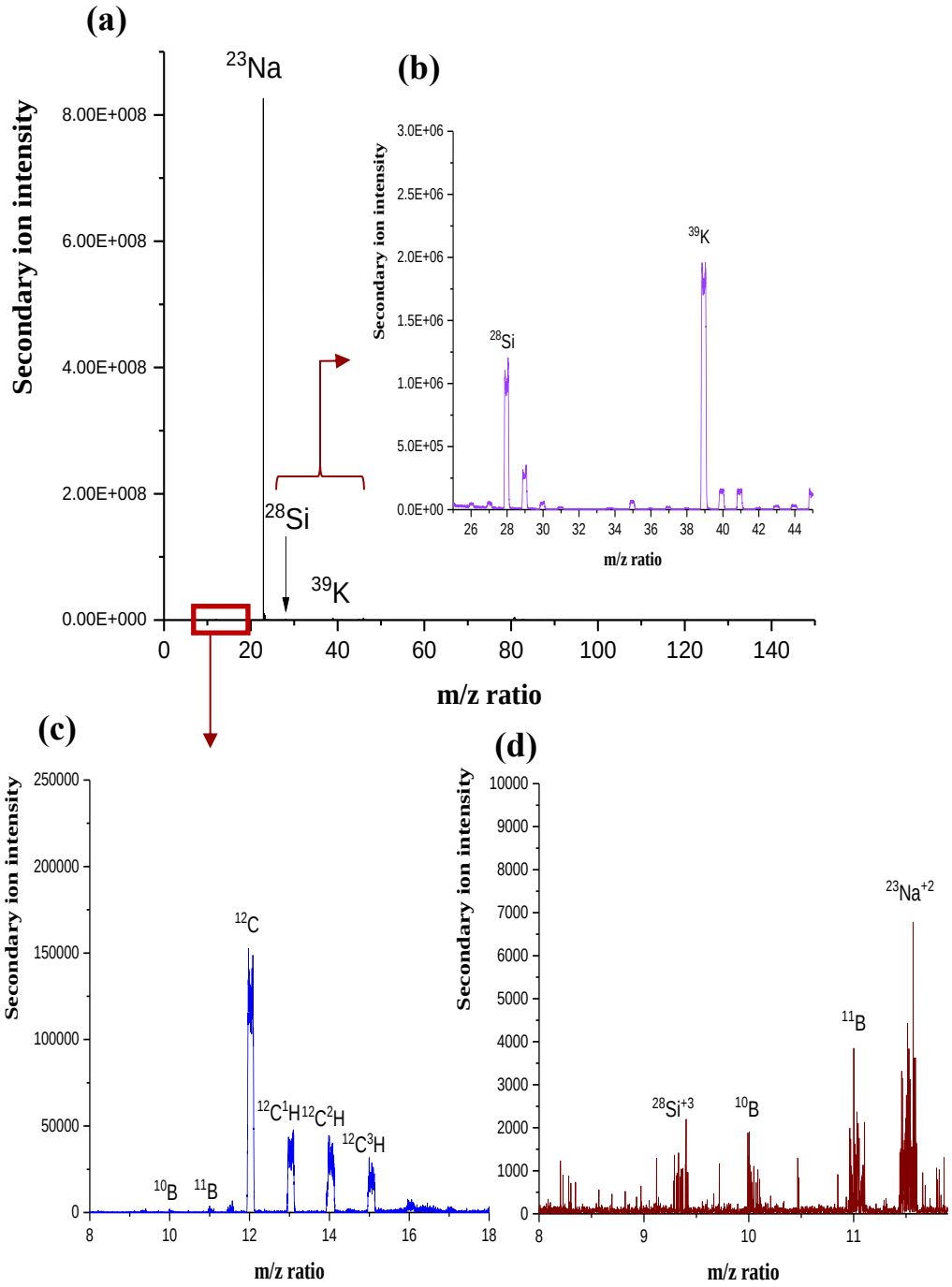

Figure 4.31: Positive secondary ion mass spectra of C1 cell from BAT control sample, acquired after a dose 2.86×10^{14} ions/cm^2 of the 20 keV Au^+ beam. (a) shows the full spectrum. (b), (c) and (d) show the magnification of the *m/z* range from 25-45, 8-18 and 8-12 respectively.

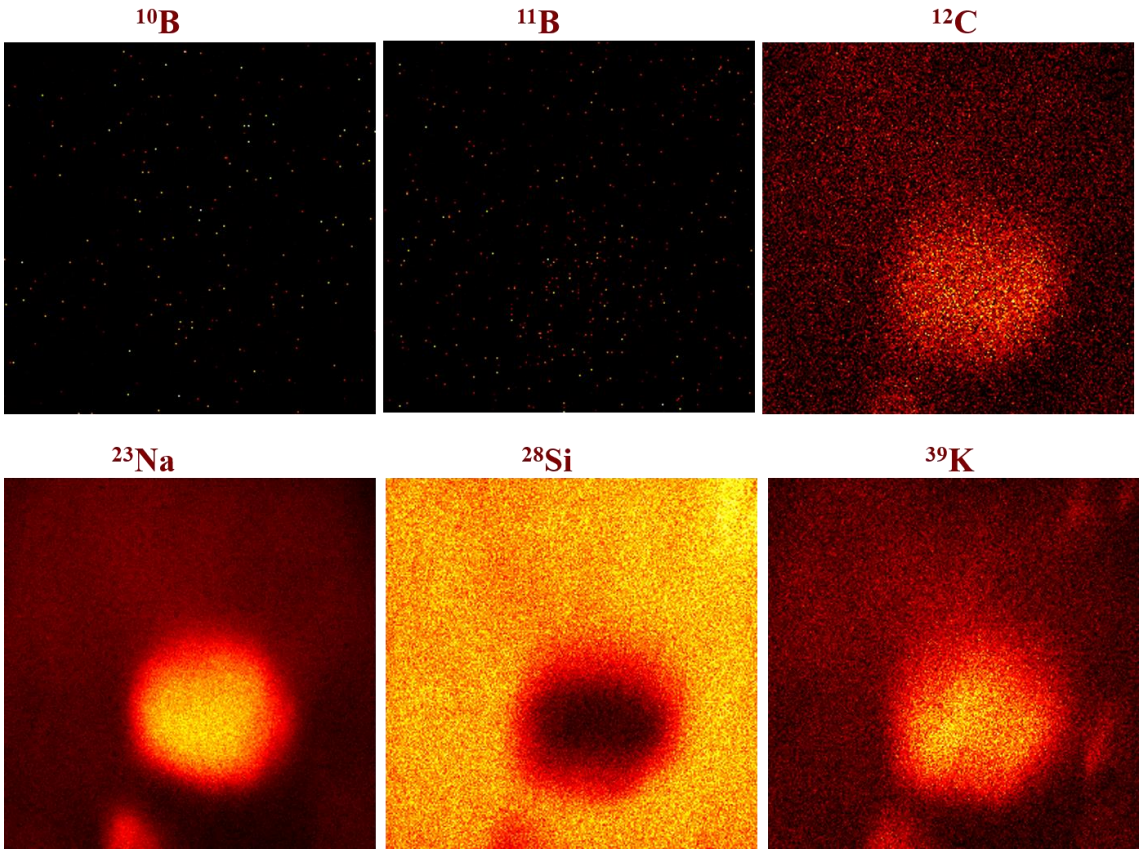

Figure 4.32: BioToF-SIMS analysis for C1 control cell of BAT sample with FoV 90×90 µm^2. Images of the following positive secondary ions: ^{10}B, ^{11}B, ^{12}C, ^{23}Na, ^{28}Si, and ^{39}K within the cell. The analysis dose in the images 2.86×10^{14} ions/cm^2. The colour gradient from black to yellow shows the signal intensity from zero to the maximum values.

Figure 4.33 -a & b shows the selected cell in another control sample, D1, from a different BAT biopsy (cell culture) and the total silicon image of the cell location respectively. **Figure 4.34** shows mass spectrum of the cell, which is similar to the spectra of the control samples mentioned above. From the images in **Figure 4.35** it was observed that ions were distributed across the cell with an intensity similar to the A1, B1 and C1 control cells. The images show high potassium intensity but low sodium intensity at the top of the cell within a feature which extends to the centre (arrows) but this cellular feature could not be identified. Boron isotope images show a similar result to the control samples above.

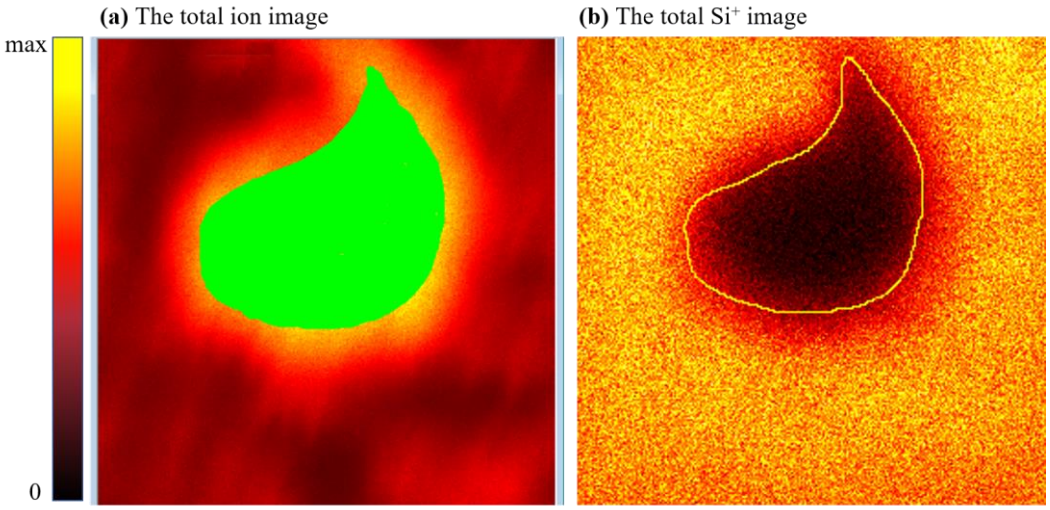

Figure 4.33: The total ion image resulting from the BioToF analysis for D1 sample showing (a) the chosen cell to extract the data. (b) shows the location of the cell (black area) on the total Si^+ image. FoV in images is $65 \times 65\ \mu m^2$.

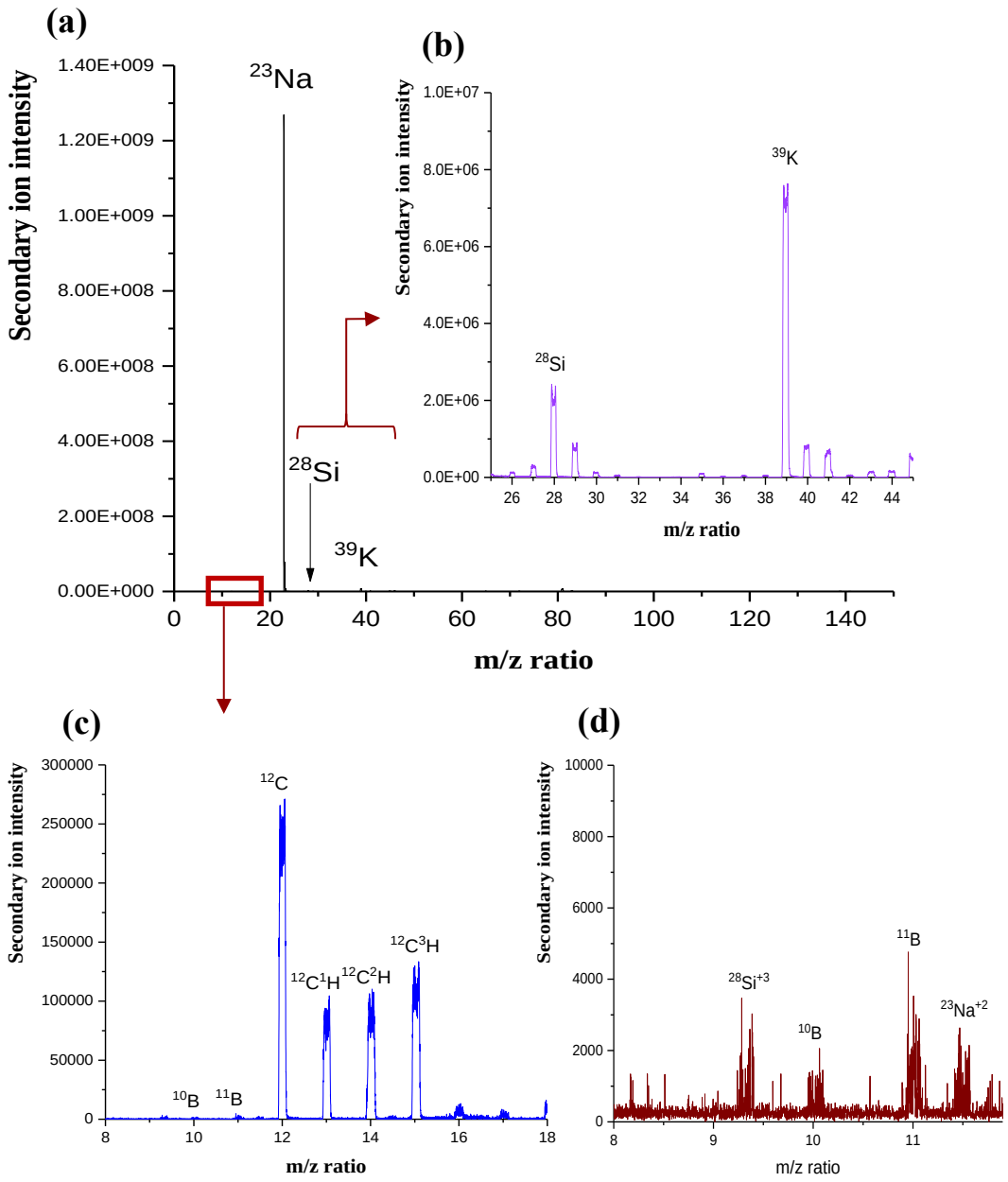

Figure 4.34: Positive secondary ion mass spectra of D1 cell from BAT control sample, acquired after a dose of 5.18×10^{14} ions/cm^2 of the 20 keV Au^+ beam. (a) shows the full spectrum. (b), (c) and (d) show the magnification of the *m/z* range from 25-45, 8-18 and 8-12 respectively.

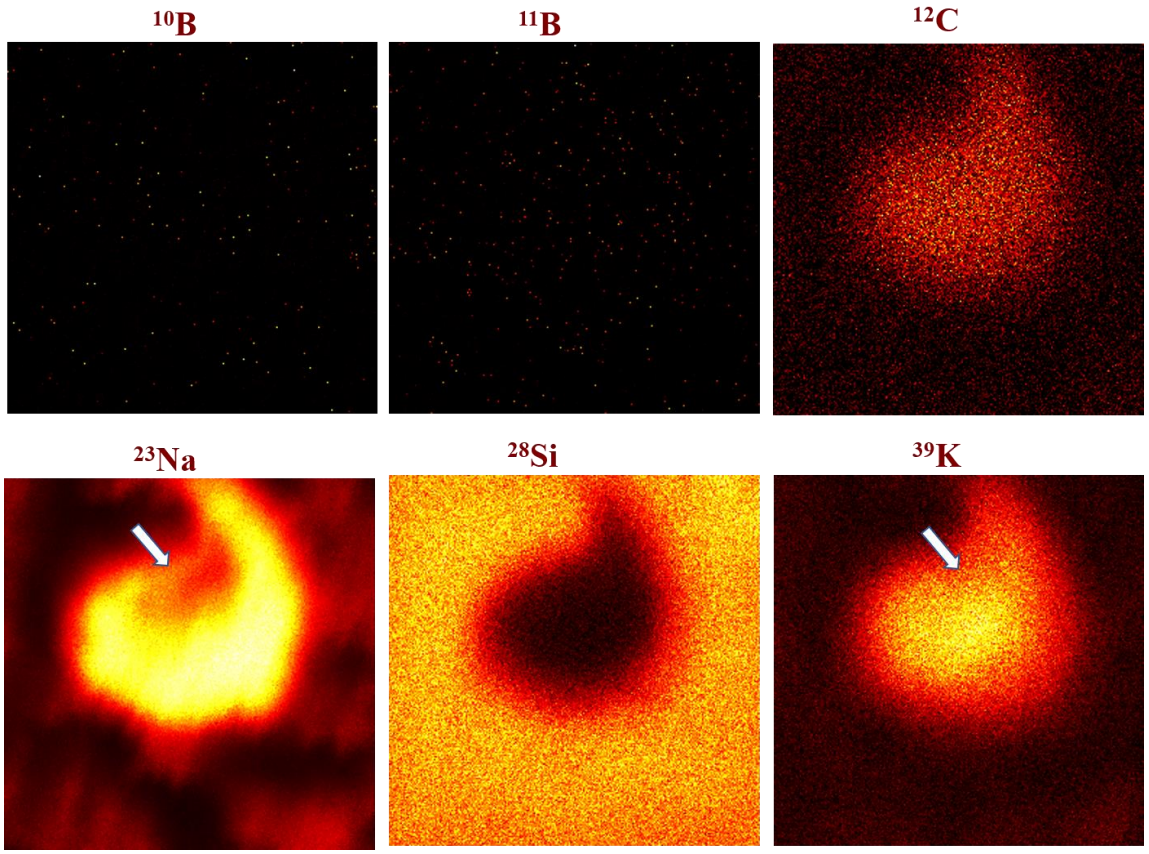

Figure 4.35: The analysis of D1 cell from BAT control sample with FoV 65×65 μm^2 by BioToF-SIMS. The images show the distribution of the following positive secondary ions in the cells: ^{10}B, ^{11}B, ^{12}C, ^{23}Na, ^{28}Si, and ^{39}K. The arrows indicate the site of the high intensity of K^+ with a low intensity of Na^+ at the top of the cell extending to the center of cell. The analysis dose in the images was 5.18×10^{14} ions/cm^2. The colour gradient from black to yellow shows the signal intensity from zero to the maximum values.

BioToF-SIMS analysis was repeated on new cells for each sample at least three times. All control samples produced very similar mass spectra as well as a similar distribution of boron isotopes in terms of low signal intensity and the accumulation of more signal from the ^{11}B region compared with ^{10}B region with no obvious localisation. Although this result is similar to the results of the control samples in the NanoSIMS in terms of the low intensity of boron isotopes, the NanoSIMS was able to measure and localise low levels of boron in images more accurately than BioToF-SIMS. Furthermore, it is clear from the BioToF-SIMS images that there is no significant contrast in the distribution of ions ^{12}C, ^{23}Na and ^{39}K across the cells, which means that the 1-2 μm Au^+ primary ion beam (operated in high-current mode to maximise sensitivity) did not provide adequate spatial resolution to distinguish cell compartments, nor the features on the surface of the cell or surrounding area unlike the resulting images with the 400 nm Cs^+ beam in the NanoSIMS.

4.2.4.1.1 Quantification of boron isotope ratios

From the spectra of the cells identified in BioToF-SIMS images, the ratios of the boron isotopes for all the control samples were calculated from the signal intensity corresponding to *m/z* 10 and 11 (as explained in 3.5.2) even though there were background noise signals at the same mass. The boron isotope ratios are shown in **Figure 4.36**, the box plot schematic was shown in **Figure 4.7 -c.** These ratios were compared between control samples, as well as with natural ratio, and were later used to verify the level of boron in pre-treated samples with BPA.

In the A1 and B1 control samples of the GBM cell cultures, the ratios of $^{10}B/^{11}B$ (mean ± SD) were respectively 0.45±0.04 (median 0.47) and 0.44±0.03 (median 0.43). The $^{10}B/^{11}B$ ratios in C1 and D1 control samples of the BAT cell cultures were 0.45±0.035 (median 0.45) and 0.38±0.14 (median 0.32) respectively.

It is noted that the ratios of $^{10}B/^{11}B$ in samples A1, B1 and C1 are similar, but these ratios are ~ 2 times higher than the natural ratio 0.247 [2][3]. This discrepancy is due to relative low boron signals and interference with the noise signals which are more significant for the lower signal of ^{10}B. There is a possible mass interference from $^{10}B^{1}H$, that cannot be resolved and would reduce the apparent $^{10}B/^{11}B$ ratio. The $^{10}B/^{11}B$ ratio in sample D1 was lower than the other control samples and closer to the natural ratio of B isotopes but with a larger scatter. For sample D1 in **Figure 4.34** the ^{10}B and ^{11}B signals were higher than the noise signals and more intense compared to the other control samples (**Figures 4.25**, **4.28** and **4.31**) and so the error in D1 is smaller.

The results here show that it is difficult to accurately measure very low signals of boron in control samples with BioToF-SIMS.

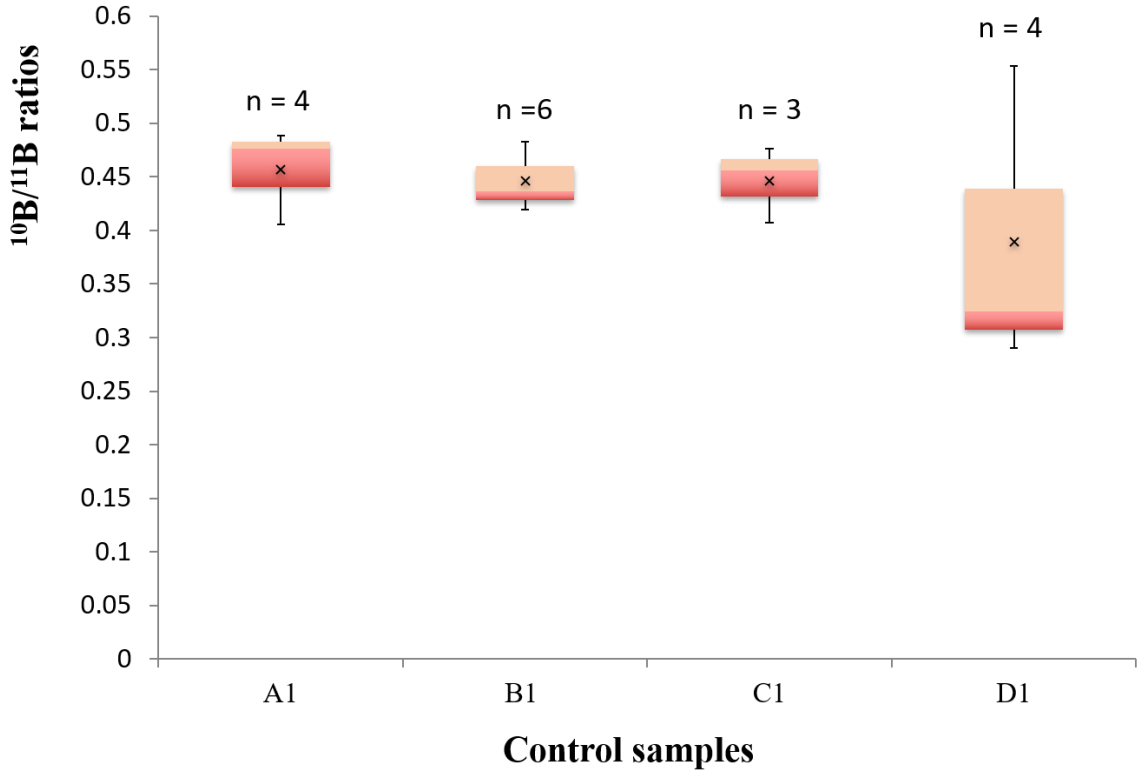

Figure 4.36: A comparison between the boron isotope ratios in control samples measured by BioToF-SIMS. A1 and B1 represent cultured cells from different biopsies of GBM, C1 and D1 cultured cells from different biopsies of BAT. A1, B1 and C1 samples gave $^{10}B/^{11}B$ ratios values ranging from 0.44-0.45, ~ 2 times higher than the natural ratio of B isotopes of 0.25. D1 samples gave a $^{10}B/^{11}B$ ratio of 0.34, closer to the natural ratio value than the other control samples but with a larger scatter. The number of areas analyzed in each sample was 3, while the number of cells used to extract the results is (***n***) on the graph. The box plot schematic is displayed in **Figure 4.7 -c**.

4.2.4.2 Imaging of cellular distributions of ^{10}B-BPA drug in GBM (B group) and BAT (D group) samples

The use of BioToF-SIMS with the Au^+ primary beam in the analysis of the control samples in the section 4.2.4.1 was simply to determine the natural ratios and intensity of ^{10}B in the samples, it was concluded that the spatial resolution is not sufficient to localise ^{10}B to cellular components. Therefore, in this section, BioToF-SIMS imaging capabilities are assessed on the measurement and distribution of ^{10}B at the general cellular level only in the samples of cell cultures pre-treated with BPA. The analyzed samples are B group and D group of GBM and BAT cell cultures respectively, **Table 4.1** provides a summary of the treated groups. All samples were analyzed under the same conditions and then were compared quantitatively.

4.2.4.2.1 B2 images

After analysis of sample B2, which was treated with 10 mM BPA (4h), the resulting total ion image and the total silicon image, shown in **Figure 4.37**, were used to determine the perimeter of the cell of interest and then extract the mass spectrum from within this region as shown in **Figure 4.38**.

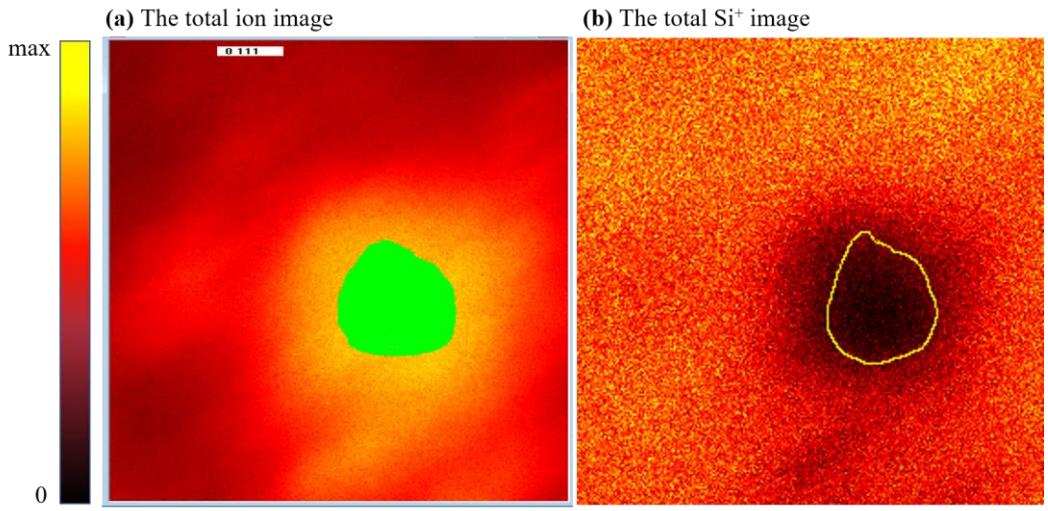

Figure 4.37: BioToF analysis for the B2 sample showing (a) the selected cell on the total ion image used to extract the spectrum and ion images, and (b) The total Si^+ image showing the location of the cell on the substrate (black area). FoV is 60×60 μm^2.

In the resulting positive ion spectrum (**Figure 4.38**), it is clear that the Na^+ peak at *m/z* 23 has the highest intensity in the cell, followed by the K^+ peak at *m/z* 39 and the C^+ peak at *m/z* 12 respectively. The Si^+ signal intensity in the spectrum represents those ions from around the edge of the cell and may also include signals within the cell due to the presence of cracks or holes. It is also apparent from the spectrum that the secondary ion yield of ^{10}B signal intensity is three times higher than ^{11}B intensity. This is unlike the intensity of the boron isotopes shown in the B1 control sample discussed earlier in **Figure 4.28**, thus this observation confirms the uptake of BPA (with ^{10}B) in the B2 sample.

BioToF-SIMS images of secondary ions of interest ^{10}B, ^{11}B, ^{12}C, ^{23}Na, ^{28}Si and ^{39}K are presented in **Figure 4.39**. The images show the intensity of ion signals across the cell. The use of the Si image was limited to locating the cell and did not provide further information on the integrity of the cell throughout the analysis. The Si map in the NanoSIMS provided

more details that enabled more accurate determination of the cell boundary and meant strange features or damaged sites in the cell structure could be avoided in the data analysis.

The Na image shows the highest signal intensity and is distributed almost uniformly across the cell. K has the next highest ion intensity, and shows that the K is distributed in the cell with more contrast than Na. Furthermore, K appears to be accumulating with highly ion intensity in the lower right corner of the cell, which may indicate the location of the nucleus or other features on the surface. The nucleus cannot be confirmed due to the low spatial resolution in the image and thus the chemical distribution sites in the cell structure are not sufficiently clear. Sodium and potassium ions are important cofactors for regulating the activity of proteins and contribute to many interactions and activities within cells such as growth, metabolism, transfer of amino acids and nucleotides across the nuclear membrane [55]–[58]. The results of sodium and potassium in terms of signal intensity pattern are similar to those resulting from freeze-fractured, freeze-dried thyroid tumours biopsies [59] , as well as of invasive urogenital cancers [60] using energy-dispersive X-ray microanalysis. Both studies [59][60] revealed that the sodium content compared to potassium increases in cancer cells biopsies.

The C image showed a homogeneous distribution with a high accumulation of signals towards the middle of the cell compared the region surrounding the cell, but the signal intensity of C ion is much less than the signals intensity of the Na and K ion. The C ions will originate from parts of the cell rich in proteins, lipids, amino acids and carbohydrates [11]–[13].

As for the distribution of the boron isotopes, the ^{10}B image showed a nearly homogeneous accumulation of ^{10}B ions from the BPA in the cell structure with a reasonable signal intensity. The extracellular region showed low and diffused ^{10}B intensity, indicating either the presence of the preparation medium or parts of tissue that acquired boron from the sample preparation medium or both. The ^{11}B image revealed a nearly homogeneous accumulation with very weak signal intensity in the cell. The normalised boron isotope intensity to ^{12}C intensity shows that the accumulated signals of ^{10}B in the cell is ~ 4 times higher than ^{11}B. The distribution of ^{10}B and ^{11}B was similar in all cells (n = 3) analysed in the B2 sample. When comparing the B2 cell image in **Figure 4.39** with the control cell B1 in **Figure 4.29**, cell B2 confirms the accumulation of ^{10}B of BPA in the cell structure unlike the untreated B1 control cell as was discussed in section 4.2.4.1.

The BioToF-SIMS images in **Figure 4.39**, with a Au^+ spot size of ~ 1 - 2 µm, did not show the internal cell compartments (the nucleus and cytoplasm) and did not explain the contrast in the distribution of ions between these compartments, nor show the morphological features on the cell surface, nor the details of the outer area surrounding the cell as accurately as in the images from the NanoSIMS in **Figure 4.9**. However, the BioToF-SIMS images provide general information on the distribution and intensity of ion signals across the cell. Therefore, it is not possible to distinguish the presence of any preferential accumulation of ^{10}B from the BPA in the sub-cellular structure, which is an important sign for the success of BNCT treatment in the destruction of cancer cells as explained in section 2.1 [21]–[24].

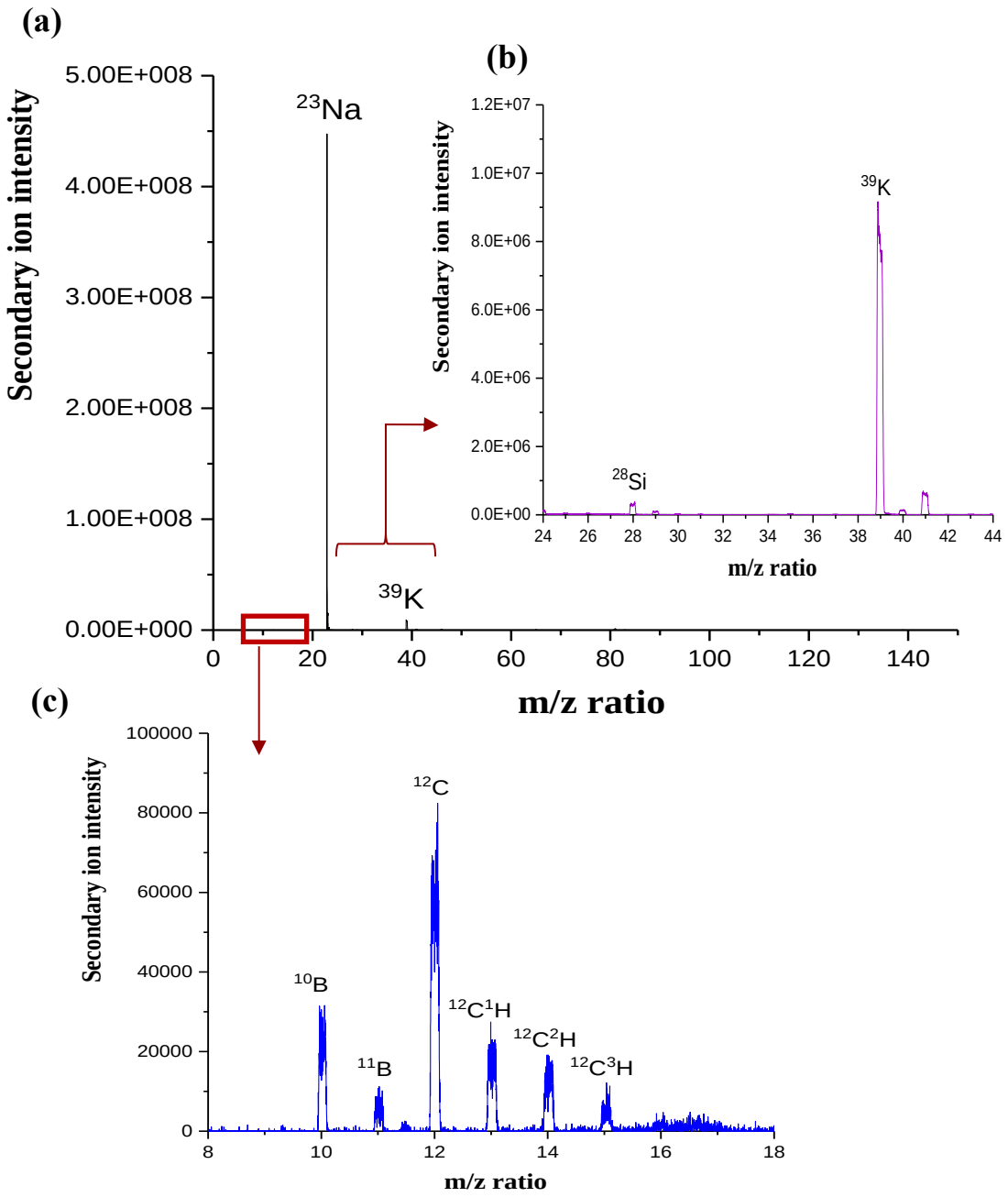

Figure 4.38: Positive secondary ion mass spectra of B2 cell from GBM, obtained after a dose of 3.68×10^{14} ions/cm^2 of the 20 keV Au^+ beam. (a) shows the full spectrum. (b) and (c) show the magnification of the *m/z* range from 24-44 and 8-18 respectively.

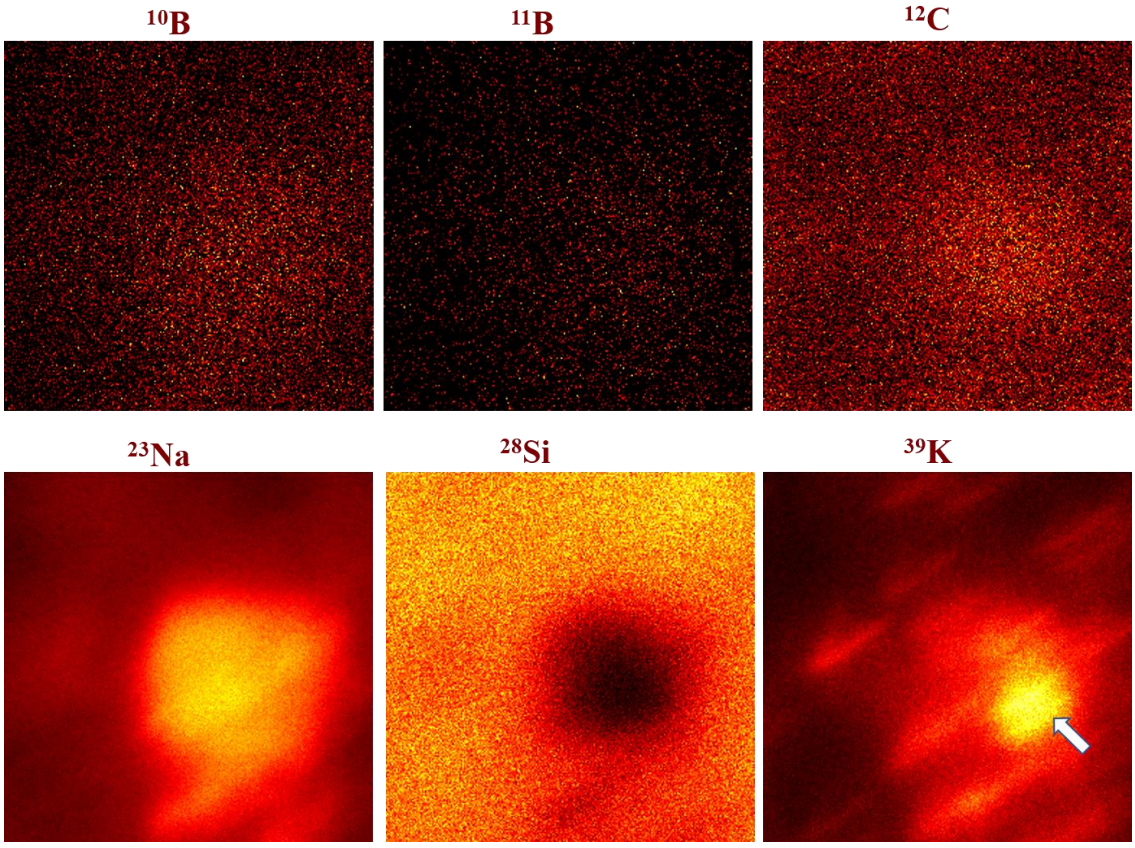

Figure 4.39: BioToF-SIMS analysis for the B2 cell culture from GBM biopsy incubated in 10 mM of ^{10}BPA for 4h. The FoV is 60×60 µm^2. The positive secondary ion images of ^{10}B, ^{11}B, ^{12}C, ^{23}Na, ^{28}Si, and ^{39}K show the distributions within the cell. The arrow in the ^{39}K image shows the site of the high intensity in cell which may indicate the nucleus. The analysis dose in images is 3.68×10^{14} ions/cm^2. The colour gradient from black to yellow shows the signal intensity from zero to the maximum values.

4.2.4.2.2 B3 images

In order to obtain distributional and quantitative information about the effect of tyrosine on the uptake of BPA in tumour cells, the B3 sample, which was pre-loaded with tyrosine (10 mM - 4h) and subsequently loaded with BPA (10 mM-4h), was analysed with BioToF-SIMS under the same conditions explained previously in section 4.2.2.2. **Figure 4.40** shows the total ion and the total silicon ions images resulting from the analysis showing the location of the cell. The cell was determined on total images to extract the mass spectrum shown in **Figure 4.41**. The secondary ion signal of ^{10}B is approximately ~ 5 times higher than the ^{11}B signal intensity. The ion yield of the ^{10}B in sample B3 indicates higher accumulation of BPA in the cell structure compared to the B1 control sample in **Figure 4.28**.

To verify the distribution of ion signals across the cell, BioToF-SIMS images were generated from the spectral peaks of ^{10}B, ^{11}B, ^{12}C, ^{23}Na, ^{28}Si, and ^{39}K and presented in **Figure 4.42**. Similarly to sample B2, the K image shows a differential distribution across the cell with high accumulation in the bottom, middle region of the cell. The identity of this accumulation of K cannot be determined due to the poor spatial resolution in the K image but is likely to be a nucleus. In terms of boron localisation, the images show that the ^{10}B of the BPA is distributed quite homogeneously in the cell with lower signal intensity compared to intensity of ^{12}C, whereas the ^{11}B appears to be randomly distributed across the image with the low signal intensity. The normalised boron isotope intensities from images show that the intensity of ^{10}B was ~ 8 times higher than ^{11}B. All the analysed cells (n = 4) in the B3 sample yielded similar results for boron distribution. In addition, the distribution pattern of ^{10}B and ^{11}B in sample B3 were similar to sample B2. For all analysed regions in B3 and B2, the normalised ^{10}B signal was higher in the B2 cells compared to B3, these data are treated quantitatively in section 4.2.4.2.4.

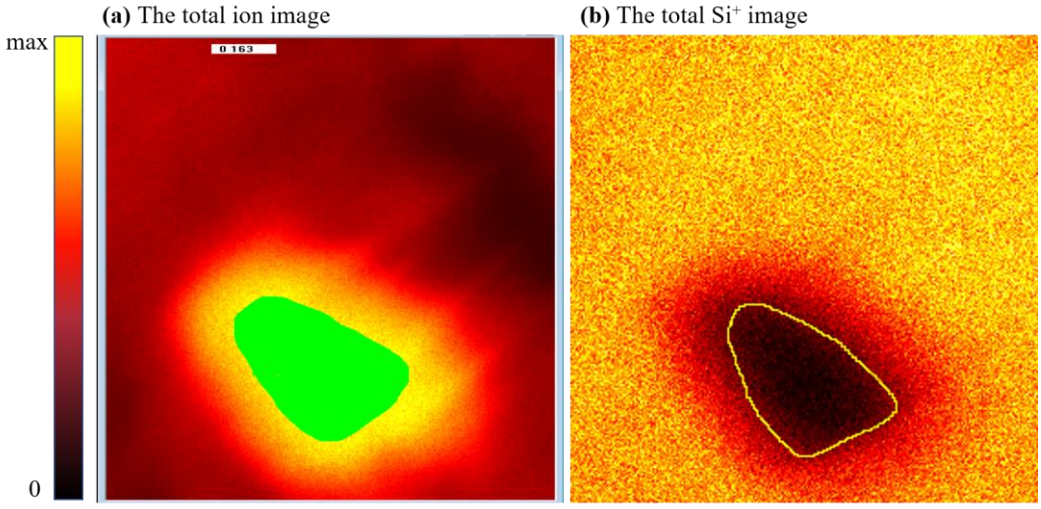

Figure 4.40: The BioToF analysis for the B3 sample showing (a) the selected cell on the total ion image used to extract the spectrum and ion images, and (b) The total Si^+ image showing the location of the cell on the substrate (black area). FoV is 60×60 μm^2.

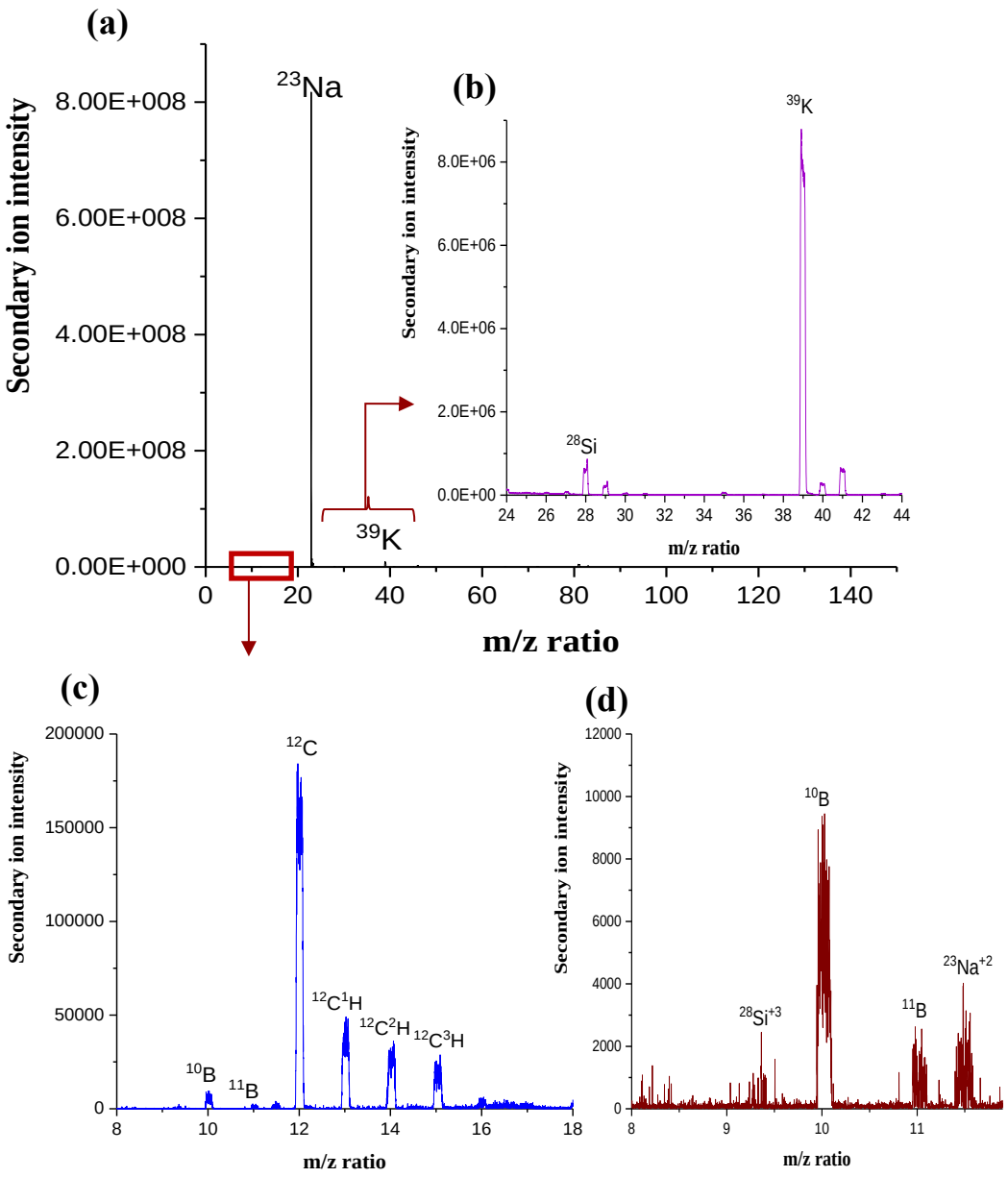

Figure 4.41: Positive secondary ion mass spectra of B3 cell from GBM, obtained after a dose of 6.4×10^{14} ions/cm^2 from the 20 keV Au^+ beam. (a) shows the full spectrum. (b), (c) and (d) show the magnification of the *m/z* range from 24-44, 8-18 and 8-12 respectively.

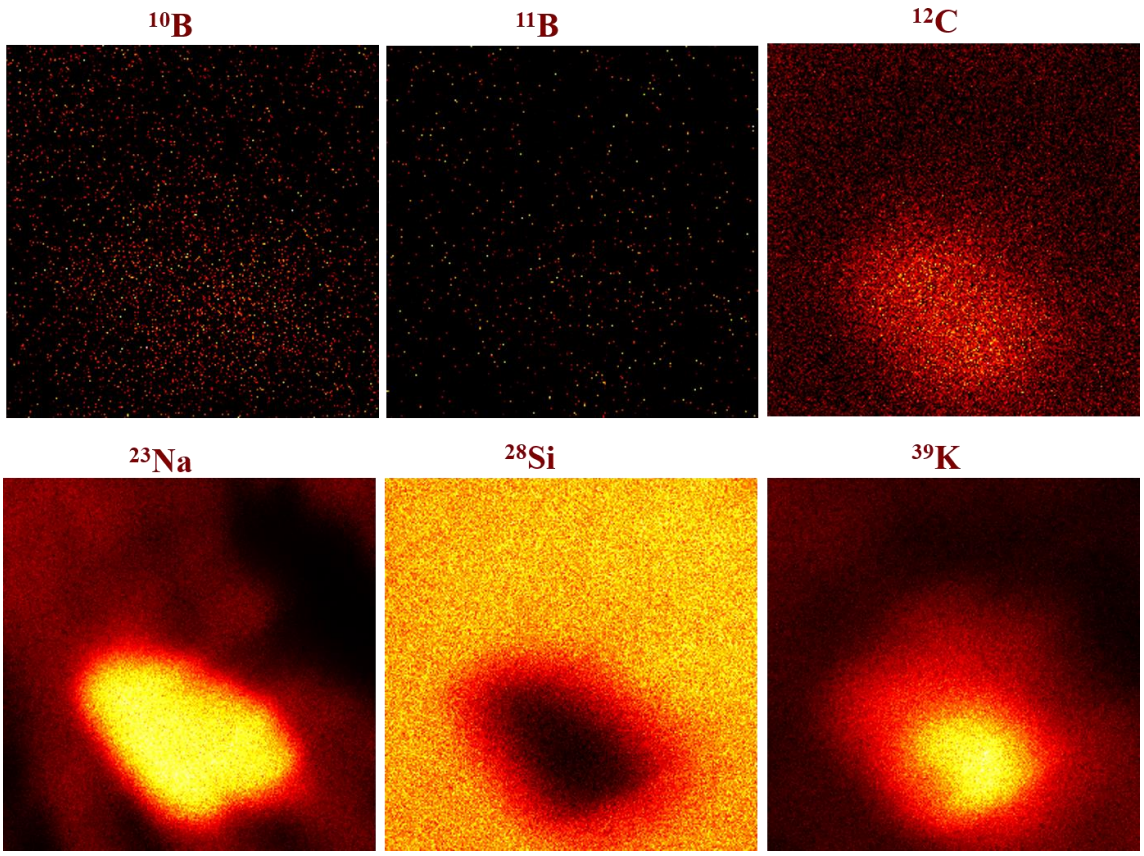

Figure 4.42: BioToF-SIMS analysis for the B3 cell culture from GBM biopsy treated with 10 mM of tyrosine (4h) then 10 mM of BPA (4h). The FoV is 60×60 µm^2. The positive secondary ion images of ^{10}B, ^{11}B, ^{12}C, ^{23}Na, ^{28}Si, and ^{39}K show the ion distributions within the cell. The analysis dose in the images was 6.4×10^{14} ions/cm^2. The colour gradient from black to yellow shows the signal intensity from zero to the maximum values.

4.2.4.2.3 B4 images

The B4 sample was investigated to verify the effect of the efflux process on the boron level in the cell. B4 was prepared with two contrasting processes, uptake process by incubation with 10 mM BPA (4 h) followed by efflux process (4 h) to allow ions to escape. **Figure 4.43** shows the cell of interest on the images of the total ions and total Si ion. **Figure 4.44** shows the mass spectrum extracted from the selected cell. The mass spectrum of B4 sample in **Figure 4.44** shows a similar behaviour to the B2 and B3 spectra in **Figure 4.38** and **4.41** respectively. It is also apparent from the spectrum that the secondary ion intensity of ^{10}B is ~ 2 times higher than the ^{11}B intensity. **Figure 4.45** shows images of ion distributions generated from the mass spectrum, similar to those of B2 and B3 samples. The K ion varied in its distribution across the cell where it showed higher intensity on the right and left sides of the cell as indicated by arrows in **Figure 4.45**, C ions were almost homogeneously distributed, and showed slight variation with slightly higher accumulation in the right side of the cell (arrow). Both ^{10}B and ^{11}B ions appeared to be diffusely distributed across the cell with a slight concentration of the ^{10}B at the left side of the cell (arrow). The normalised ^{10}B intensity across the cell is ~ 2 times higher than the ^{11}B - more detail is given in the quantification section 4.2.4.2.4. All the analysed cells (n = 3) in the B4 sample gave similar distribution of boron.

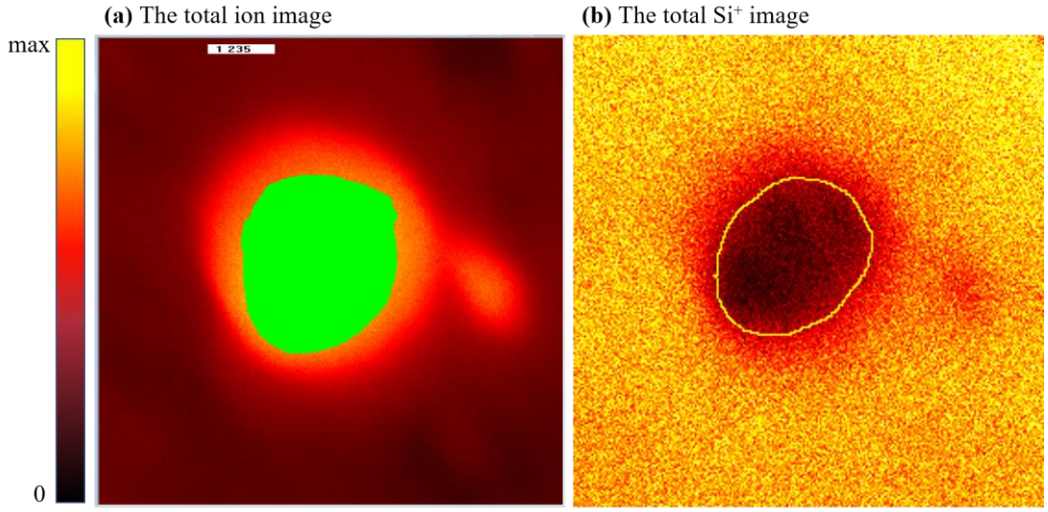

Figure 4.43: BioToF analysis for the B4 sample showing (a) the selected cell on the total ion image used to extract the spectrum and ion images, and (b) the total Si^+ image showing the location of the cell on the substrate (black area). FoV is 90×90 µm^2.

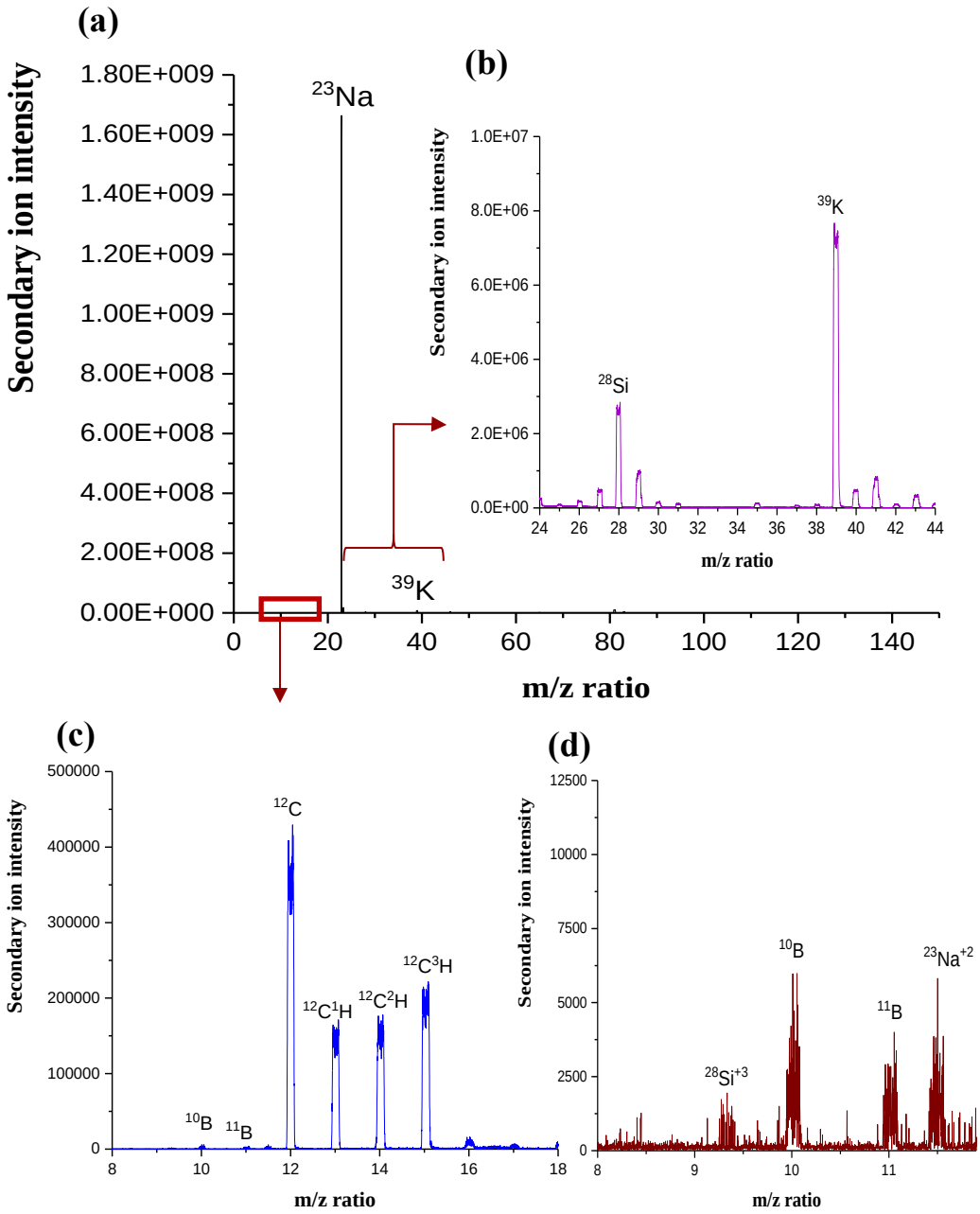

Figure 4.44: Positive secondary ion mass spectra of B4 cell from GBM, obtained after a dose of 2×10^{14} ions/cm^2 of the 20 keV Au^+ beam. (a) shows the full spectrum. (b), (c) and (d) show the magnification of the *m/z* range from 24-44, 8-18 and 8-12 respectively.

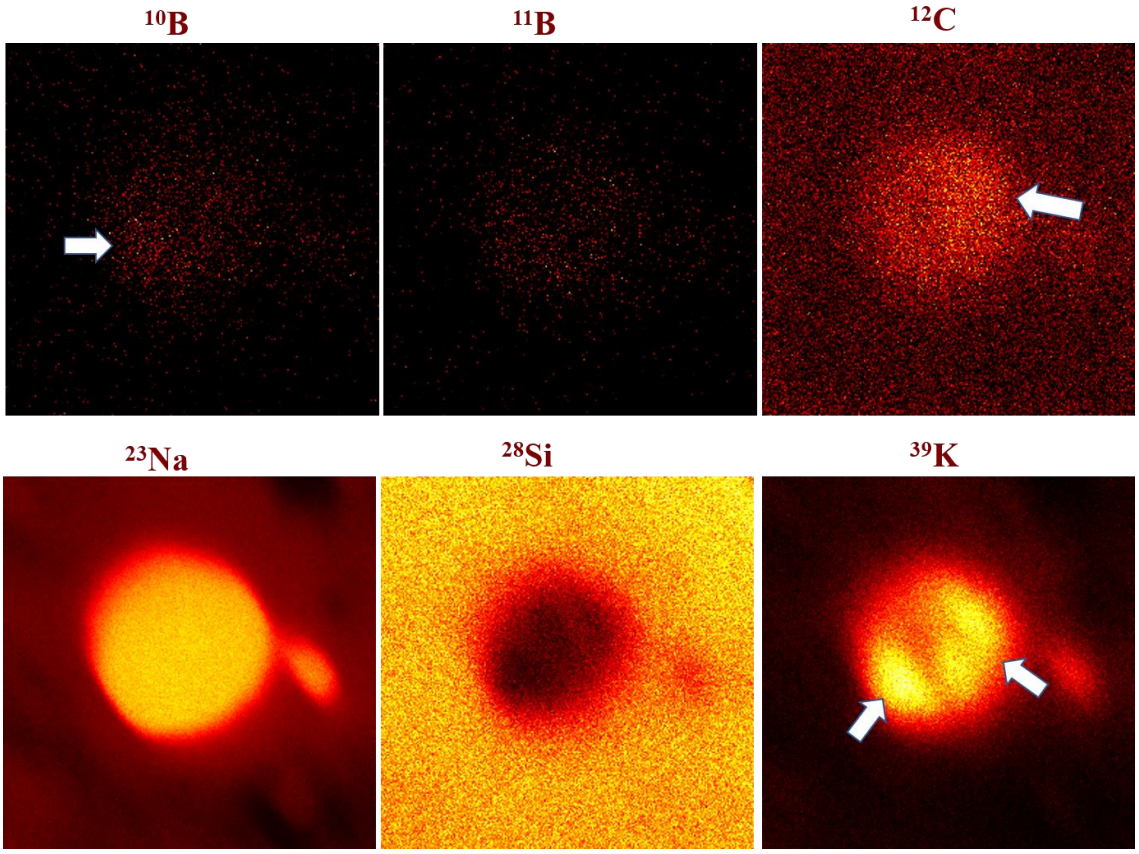

Figure 4.45: BioToF-SIMS analysis for the B4 cell culture from the GBM biopsy treated with 10mM of BPA (4h) then exposed to an efflux process (4h). The FoV is 90×90 µm^2. The positive secondary ion images of ^{10}B, ^{11}B, ^{12}C, ^{23}Na, ^{28}Si, and ^{39}K show the ion distribution within the cell. The arrows in the ^{10}B, ^{12}C and ^{39}K images show the site of highest signal intensity in the cell. The analysis dose in the images is 2×10^{14} ions/cm^2. The colour gradient from black to yellow shows the signal intensity from zero to the maximum values.

4.2.4.2.4 Quantitative measurement of ^{10}B in B group samples

Quantitative measurements at the cellular level of ^{10}B of BPA were calculated in the B group samples of the GBM tumour biopsy. For each cell, the ^{10}B were normalised to the ^{12}C intensities as there was an almost constant carbon distribution across the cell, as well as to make comparison possible later with the statistical results of the NanoSIMS. The results are shown in **Figure 4.46 -a**. The ratio of ^{10}B/^{11}B was also determined, as shown in **Figure 4.46 -b**. The boron isotope ratio was determined because the lack of resolution in the images meant it was difficult to determine whether the carbon signal originated only from the cell or included signals from the background or the preparation medium or another source. **Table 4.6** shows the mean values of the ratios of ^{10}B/^{12}C and ^{10}B/^{11}B for all the samples of group B.

The BioToF-SIMS results in **Figure 4.46 -a** and **Table 4.6** show that the B2 sample gave the highest $^{10}B/^{12}C$ ratio indicating high accumulation of BPA. The reduction of the $^{10}B/^{12}C$ ratio in the pre-loaded B3 sample with tyrosine by factor 20 compared to B2 would suggest that tyrosine did not stimulate ^{10}B uptake into intracellular B3.

For the B4 sample, the $^{10}B/^{12}C$ ratio was significantly lower than the B2 and B3 by factor 80 and 4 respectively, indicating that the ions were lost from the cells within 4h of the efflux process. However, the $^{10}B/^{12}C$ ratio in B4 is still ~5 times higher than that of the control, B1, which proves that the BPA was not completely lost from the cell. This confirms that the efflux process from cell to the surrounding medium is slower than the uptake process. This observation is important in the field of clinical therapy to determining the optimum radiotherapy time point and dosage for BNCT treatment [41] as explained previously in the section 4.2.3.2.5.

When normalising the measurements of ^{10}B to ^{11}B in **Figure 4.46 -b**, the results of BioToF-SIMS showed that the $^{10}B/^{11}B$ ratio at the cellular level in B3 is higher than the rest of the samples, opposite to the result of normalising to ^{12}C, which would indicate that the preloading of the tyrosine in the B3 has enhanced the BPA-uptake. The B2 sample gave the ratio of $^{10}B/^{11}B$ in the cell higher than B1 and B4 by factor of 9 and 3 respectively, confirming the uptake of the B2 sample for BPA. The reduction of the $^{10}B/^{11}B$ ratio in B4 compared with B2 and B3 gives a similar result to that observed when calculating the$^{10}B/^{12}C$ ratio in the B4.

To summarise, the level of $^{10}B^+/^{12}C^+$ in sample B2 is higher than B3 and the latter is higher than B4, this is a similar trend to the NanoSIMS results ($^{10}B^-/^{12}C^-$) in section 4.2.3.2.5 although the ionization probability is different between both instruments due to the different primary ion, and secondary ion polarity. In contrast, B3 was higher than B2 when normalised with ^{11}B but due to the very low signals of ^{11}B and the fact that it often interferes with the background noise signals this normalisation method gives less reliability compared to the normalisation to the very high signals of ^{12}C. Cellular wet-weight concentrations of ^{10}B cannot be determined from the $^{10}B^+/^{12}C^+$ ratios measured with BioToF-SIMS using the same method used for NanoSIMS results in section 4.2.3.2.5 due to the lack of a relative sensitivity factor value on the BioToF-SIMS from a reference identical or close to the freeze-dried cell sample. An attempt was made to calculate ^{10}B concentrations with BioToF-SIMS, $^{10}B^+/^{12}C^+$ mean values measured in **Table 4.6** were used with the calibration curve of different BPA concentrations in trehalose in **Figure 3.13**, but that did not work because the values in **Table 4.6** are out of linear correlation in **Figure 3.13**, this may be because trehalose dihydrate

matrix differs from the cell. Therefore, it is not possible to extract absolute quantification values from the data. Instead ion ratios were discussed for relative quantification above.

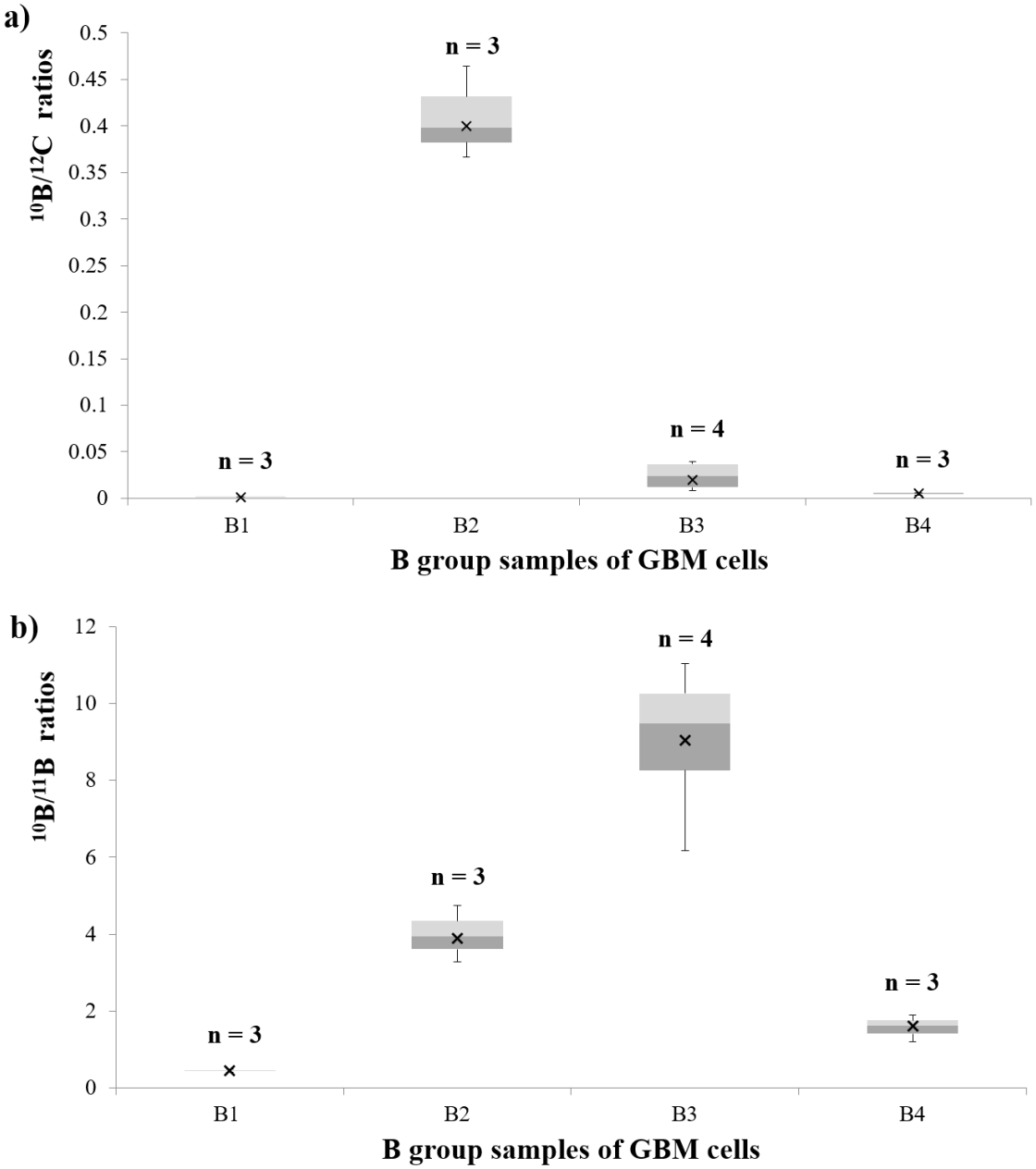

Figure 4.46: Comparison between the GBM-cell culture samples: B1, B2, B3 and B4 in terms of $^{10}B/^{12}C$ and $^{10}B/^{11}B$ ratios at the cellular level measured by BioToF-SIMS. (a) shows that the $^{10}B/^{12}C$ ratio in the B2 was significantly higher than the B3 and the latter was higher than the B4. (b) showed that the $^{10}B/^{11}B$ ratio was higher in B3 followed by B2 then B4. In (a) & (b) the B4 remained higher than the control sample B1. (***n***) refers to the number of cells analysed for each sample.

Table 4.6: The mean values of $^{10}B/^{12}C$ and $^{10}B/^{11}B$ ratios from the B group samples (shown in **Figure 4.46**).

Ratios	**$^{10}B/^{12}C$**			
Mean ± SD values of whole cell	B1	B2	B3	B4
	0.001 ± 0.00	0.4 ± 0.04	0.02 ± 0.01	0.005 ± 0.001
Ratios	**$^{10}B/^{11}B$**			
Mean ± SD values of whole cell	B1	B2	B3	B4
	0.45 ± 0.03	3.9 ± 0.5	9.04 ± 1.8	1.6 ± 0.3

4.2.4.2.5 D2 images

The D2 sample represents cultured cells from a BAT biopsy and treated for 4h with 10 mM BPA. The total ion and the total Si ion images, as shown in **Figure 4.47**, were used to determine the cell location and extract the mass spectrum shown in **Figure 4.48**.

The intensity of the boron isotopes in **Figure 4.48** indicates that the ^{10}B signal is four times higher than the ^{11}B signal. Thus, the ^{10}B peak confirms the accumulation of BPA in the D2 sample as opposed to that shown in the D1 control sample in **Figure 4.34**.

The images of the secondary ions of interest from the cell's BioToF-SIMS spectrum are shown in **Figure 4.49**. The location of the target cell on the substrate can be clearly distinguished where the silicon signal is absent. In Si image, two other parts of cells appear on the left and right sides (indicated by arrows). The ion images also show that the distribution of Na, K and C in the cell structure is similar to that in the sample B2, which has been previously explained in section 4.2.4.2.1.

The ^{10}B is distributed in the cell almost homogeneously with signal intensity lower than ^{12}C intensity and showed accumulation in a small area below the cell as indicated by the arrow. The image of ^{11}B has low signal intensity compared to ^{10}B image. The images of ^{10}B and ^{11}B for sample D2 in **Figure 4.49** show that the normalised signal intensity of ^{10}B to ^{12}C intensity in the cell is ~ 5 times higher than ^{11}B normalised to ^{12}C intensity, and thus confirm the uptake of BPA in the D2 cell compared to the D1 control cell in **Figure 4.35**. The distribution of ^{10}B in sample D2 is very similar to that of sample B2 in **Figure 4.39**. The same results

were obtained for the distribution of ^{10}B and ^{11}B in all analysed D2 cells (n = 5) with BioToF-SIMS.

When comparing the quality of the resulting D2 images of the BioToF-SIMS in **Figure 4.49** with NanoSIMS in **Figure 4.16**, the NanoSIMS images reveal many details in the cell structure such as nuclei sites, and slight variations in the distribution of the ions. In contrast, BioToF-SIMS images were limited to showing the general level of the intensity of ion signals across the cell.

All ions images in the **Figure 4.49** except silicon image showed a low signal intensity in the outer region around the cell, which may indicate that there is cellular material between cells or the sample preparation medium or both.

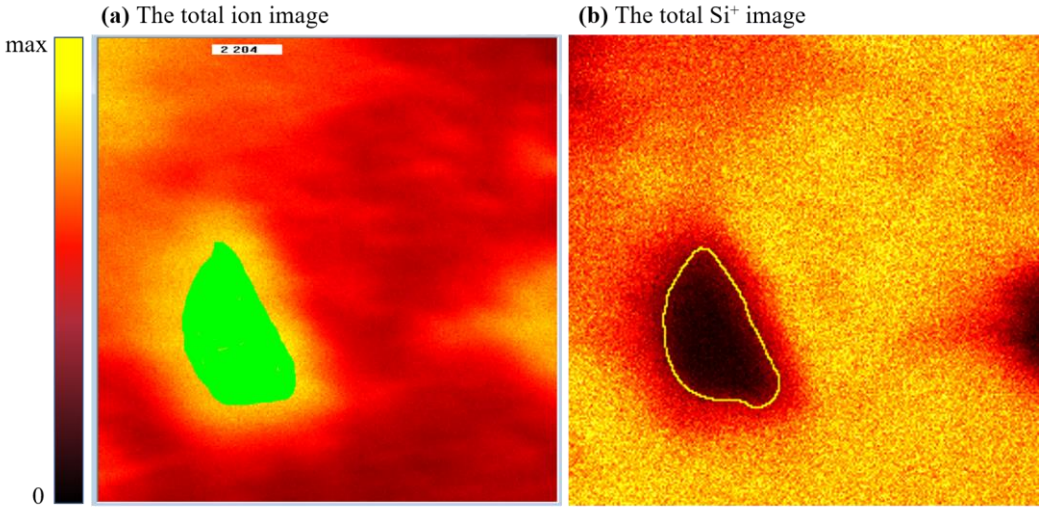

Figure 4.47: BioToF analysis for D2 sample showing (a) the selected cell on the total ion image used to extract the spectrum and ion images, and (b) the total Si^+ image showing the location of the cell on the substrate (black area). FoV is 100×100 μm^2.

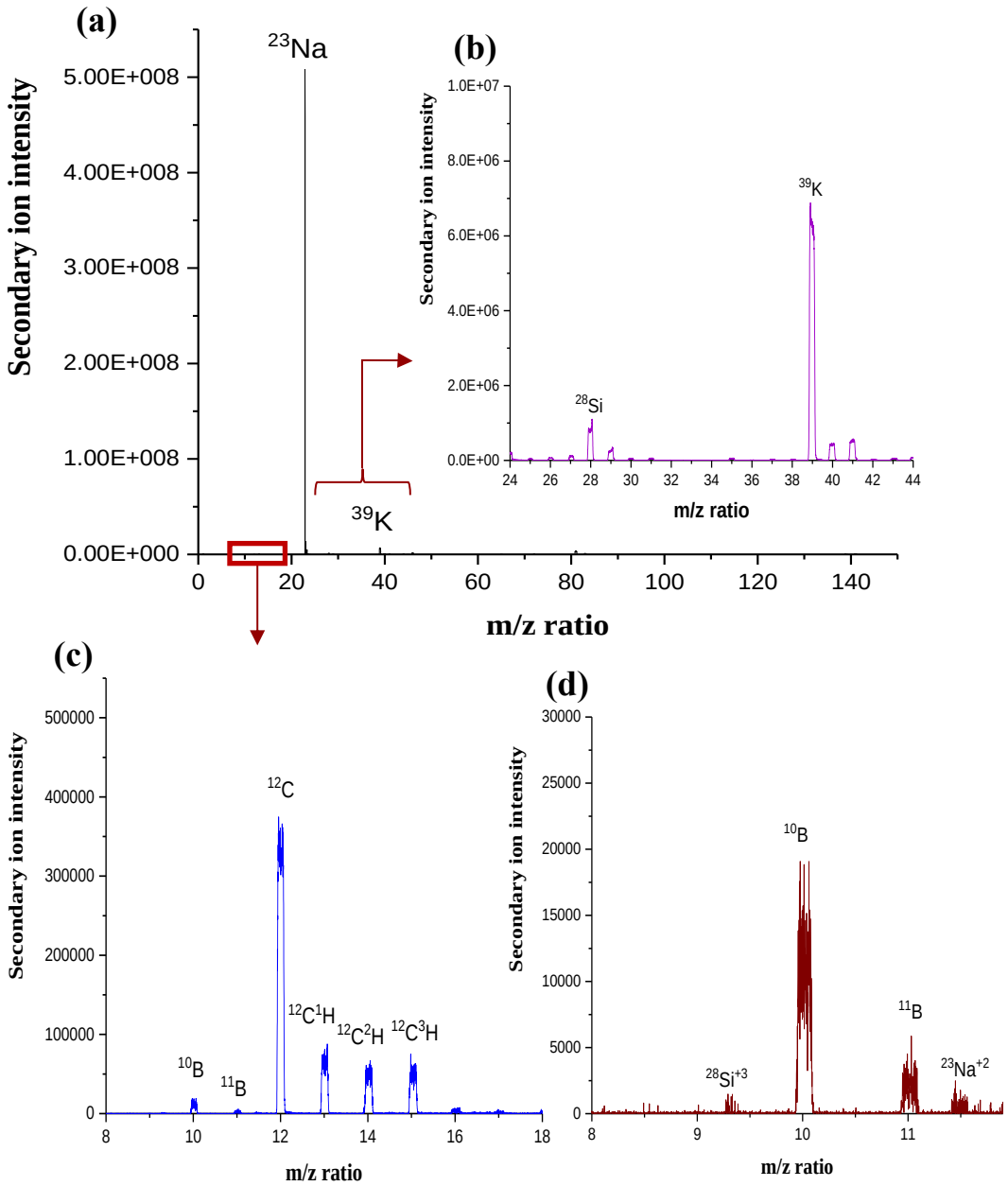

Figure 4.48: Positive secondary ion mass spectra of D2 cell from BAT, obtained after a dose of 1.79×10^{14} ions/cm^2 of the 20 keV Au^+ beam. (a) shows the full spectrum. (b), (c) and (d) show the magnification of the *m/z* range from 24-44, 8-18 and 8-12 respectively.

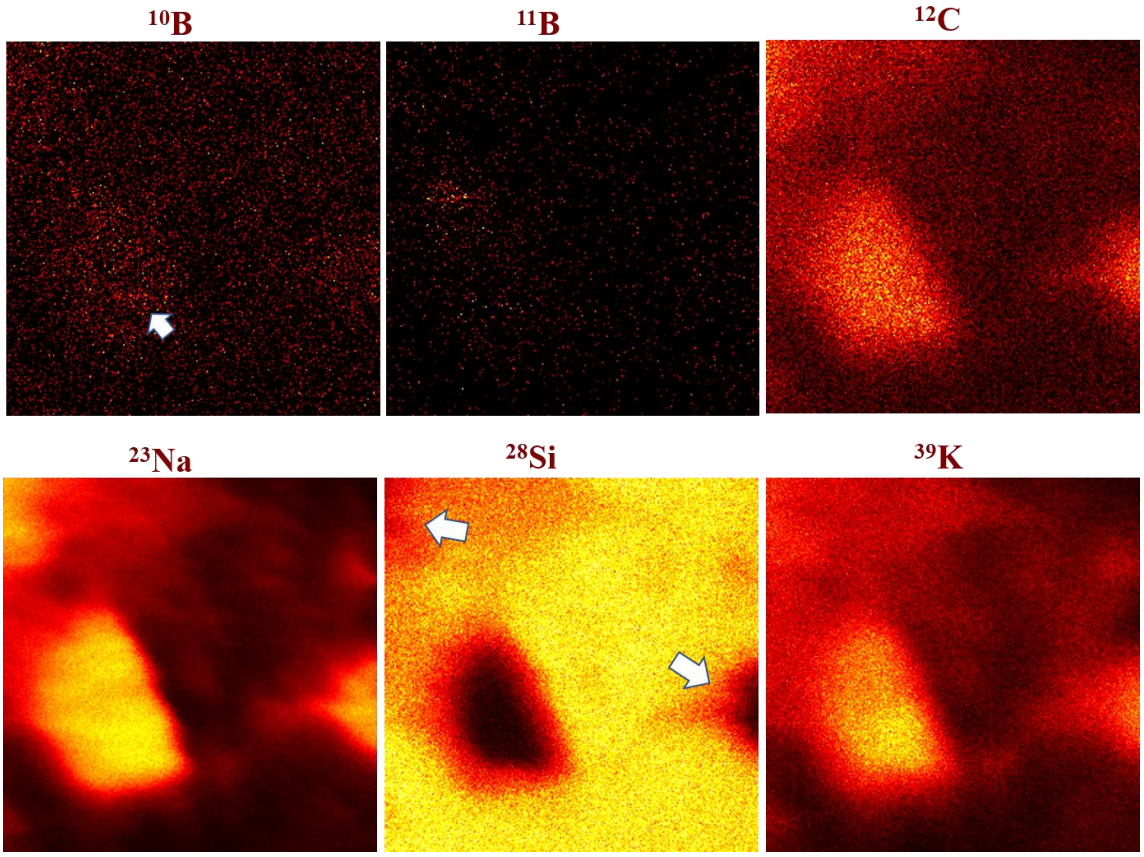

Figure 4.49: BioToF-SIMS analysis for D2 cell culture from BAT biopsy incubated in 10 mM of ^{10}BPA for 4h. The FoV is 100×100 µm^2. The positive secondary ion images of ^{10}B, ^{11}B, ^{12}C, ^{23}Na, ^{28}Si, and ^{39}K show the ion distributions within the cell. The arrows in the ^{10}B and ^{11}B images shows the sites of small accumulations of signal in the image. The arrows in the ^{28}Si refer to two other cellular parts in the image frame. The analysis dose in the images was 1.79×10^{14} ions/cm^2. The colour gradient from black to yellow shows the signal intensity from zero to the maximum values.

4.2.4.2.6 D3 images

In the D3 sample of BAT, which was pre-treated with tyrosine and then treated with the BPA with a concentration of 10 mM for 4h each, the effect of tyrosine on the uptake level of ^{10}B in infiltrating cells to the surrounding areas of the tumour was investigated using BioToF-SIMS. **Figure 4.51** shows the mass spectrum extracted from the selected cell on the total ion and the total silicon ion images in **Figure 4.50**. The resulting mass spectrum shows peaks similar to those of B group samples as well as D2 spectrum unlike the spectrum of D1 control sample in **Figure 4.34**. **Figure 4.51** shows that the ^{10}B intensity is approximately 12 times higher than the ^{11}B signal intensity, indicating that the uptake of the D3 sample for BPA is greater than the D2 sample in **Figure 4.49**.

Figure 4.52 shows the distribution images of secondary ions extracted from the cell BioToF-SIMS spectrum. The ion distribution of Na, K and C ions in the cell is similar to the D2 as well as the B group samples, and explained in more detail in section 4.2.4.2.1. With regard to the distribution of boron isotopes, the image of the ^{10}B from BPA reveals lower signal intensity compared to ^{12}C image, with a fairly homogeneous distribution of ^{10}B across the cell and a higher accumulation in the same region where the K intensity is higher as indicated by an arrow. The ^{11}B appears to be homogeneous in the cell. The normalised boron isotope intensity to ^{12}C intensity from images show that the ^{10}B signal in the cell is ~ 8 times higher than ^{11}B. All the analysed D3 cells (n = 3) provided similar images for the boron distribution. By comparing D3 with D2, the distribution pattern of ^{10}B and ^{11}B were similar in both samples. Furthermore, the normalised intensity of ^{10}B signal in the D3 was 10 times higher and sometimes close to the D2 sample signal, indicating that pre-treatment with tyrosine may have enhanced BPA uptake in the D3 sample, more detail in the quantification section 4.2.4.2.8. All ion images in **Figure 4.52**, except Si, gave low signal intensity in the outer region around the cell compared to the inside of the cell.

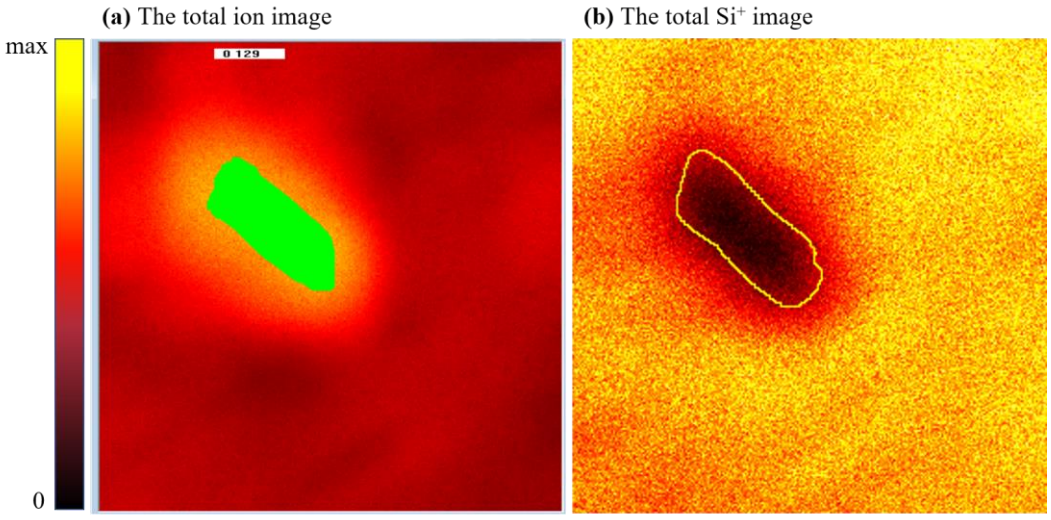

Figure 4.50: BioToF analysis for D3 sample showing (a) the selected cell on the total ion image used to extract the spectrum and ions images, and (b) the total Si^+ image showing the location of the cell on the substrate (black area). FoV is 74×74 μm^2.

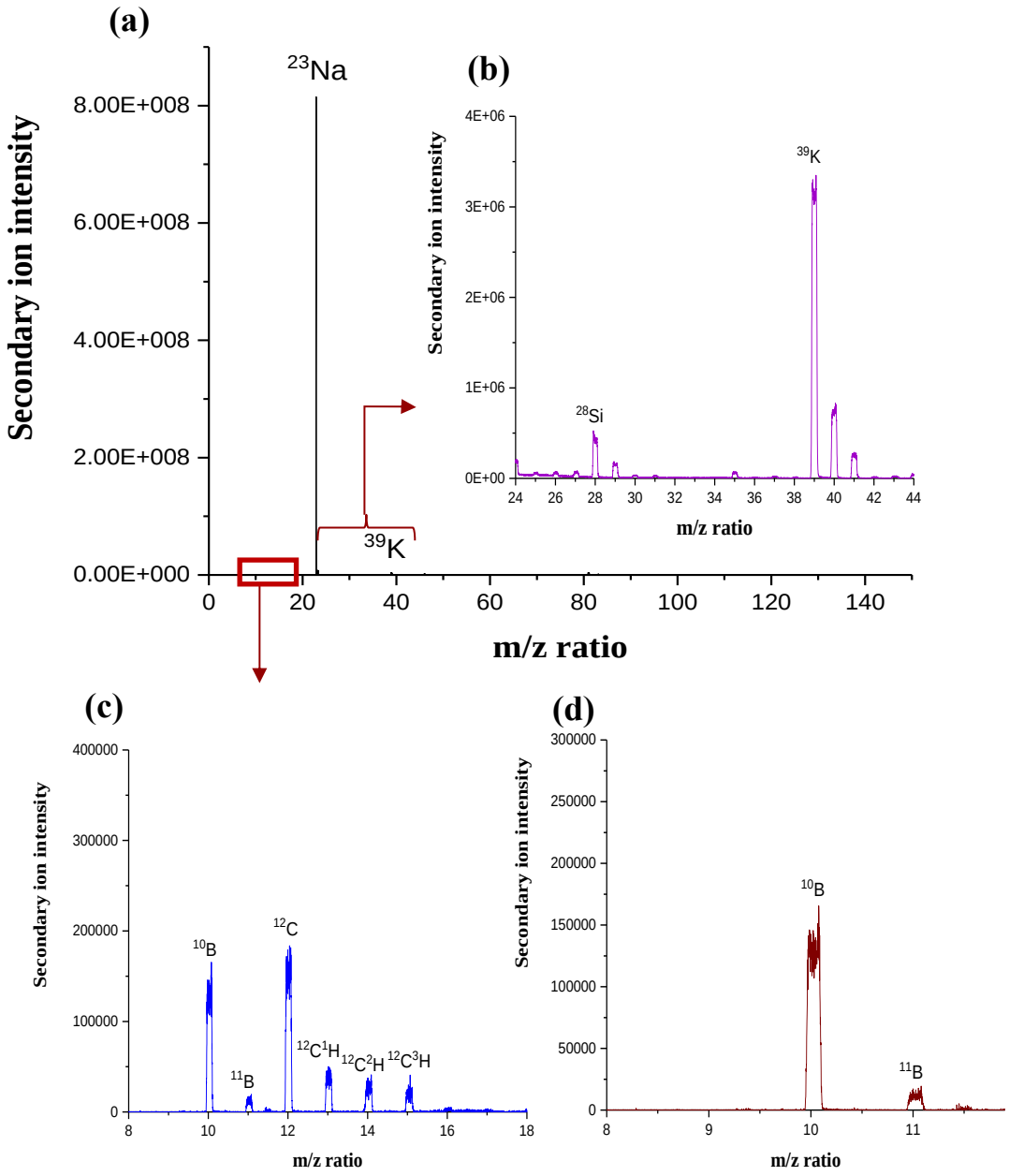

Figure 4.51: Positive secondary ion mass spectra of D3 cell from BAT, obtained after a dose of 3.57×10^{14} ions/cm^2 of the 20 keV Au^+ beam. (a) shows the full spectrum. (b), (c) and (d) show the magnification of the *m/z* range from 24-44, 8-18 and 8-12 respectively.

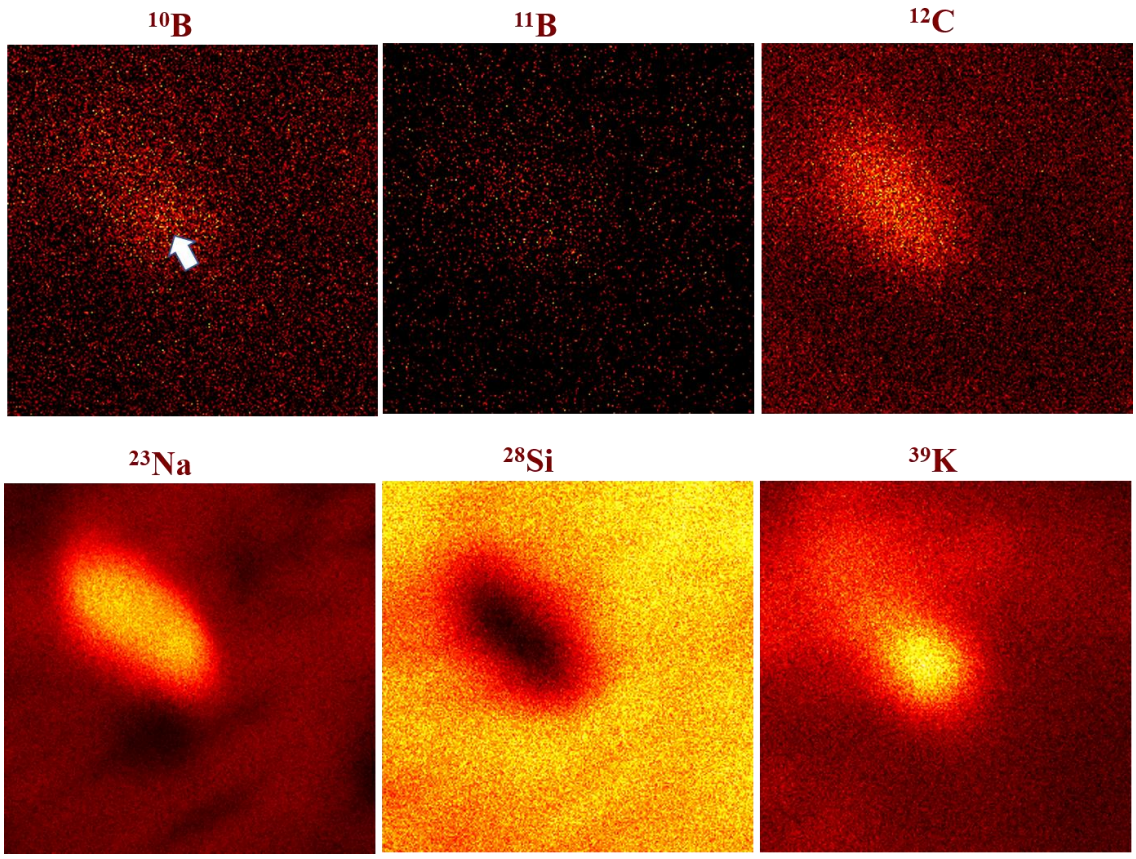

Figure 4.52: BioToF-SIMS analysis for D3 cell culture from BAT biopsy treated with 10 mM of tyrosine (4h) then 10 mM of BPA (4h). The FoV is 74×74 µm^2. The positive secondary ion images of ^{10}B, ^{11}B, ^{12}C, ^{23}Na, ^{28}Si, and ^{39}K show the ion distributions within the cell. The arrow in the ^{10}B refers to the site of higher accumulation. The analysis dose in the images was 3.57×10^{14} ions/cm^2. The colour gradient from black to yellow shows the signal intensity from zero to the maximum values.

4.2.4.2.7 D4 images

The D4 sample was analysed with BioToF-SIMS for the purpose of investigating the effect of the efflux process on the ^{10}B therapeutic levels of the BPA in cultured cells from a BAT biopsy. The mass spectrum was extracted in **Figure 4.54** from cells of interest using the total ion and total Si^+ images in **Figure4.53**.

In the positive mass spectrum **Figure 4.54**, the ^{10}B signal intensity is close to the ^{11}B signal intensity. **Figure 4.55** shows the images of ion distributions generated from mass spectrum peaks. Both ^{10}B and ^{11}B signals appear to be diffused across cellular structures. The normalised boron isotope intensity to ^{12}C intensity shows that the ^{10}B signal across the cells in images is close to the ^{11}B. All the analysed cells (n = 3) in the D4 sample gave a similar distribution pattern of the boron ions.

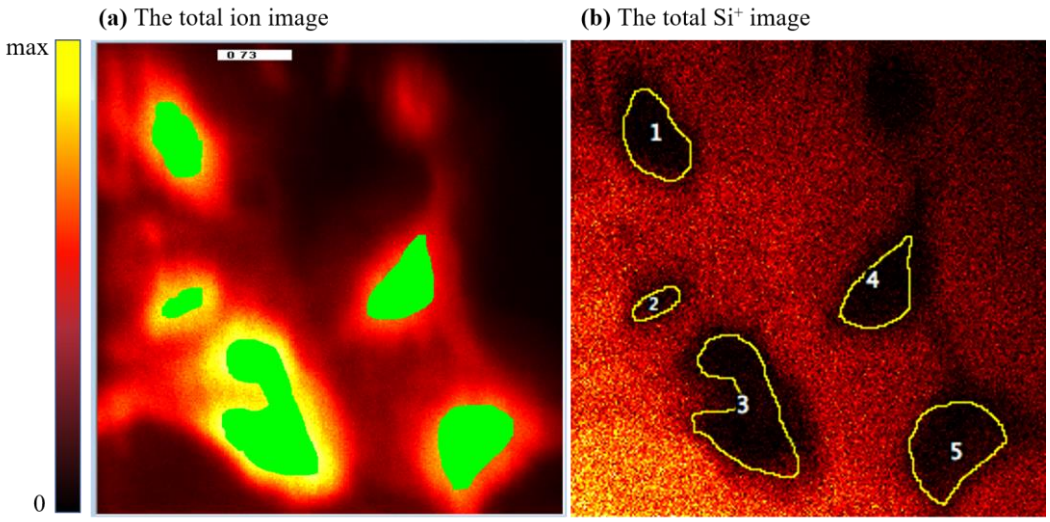

Figure4.53: BioToF analysis for D4 sample showing (a) the selected cells on the total ion image used to extract the spectrum and ion images, and (b) the total Si^+ image showing the location of the cells on the substrate (black areas), five numbered cells appear in the image frame. FoV is 252×252 μm^2.

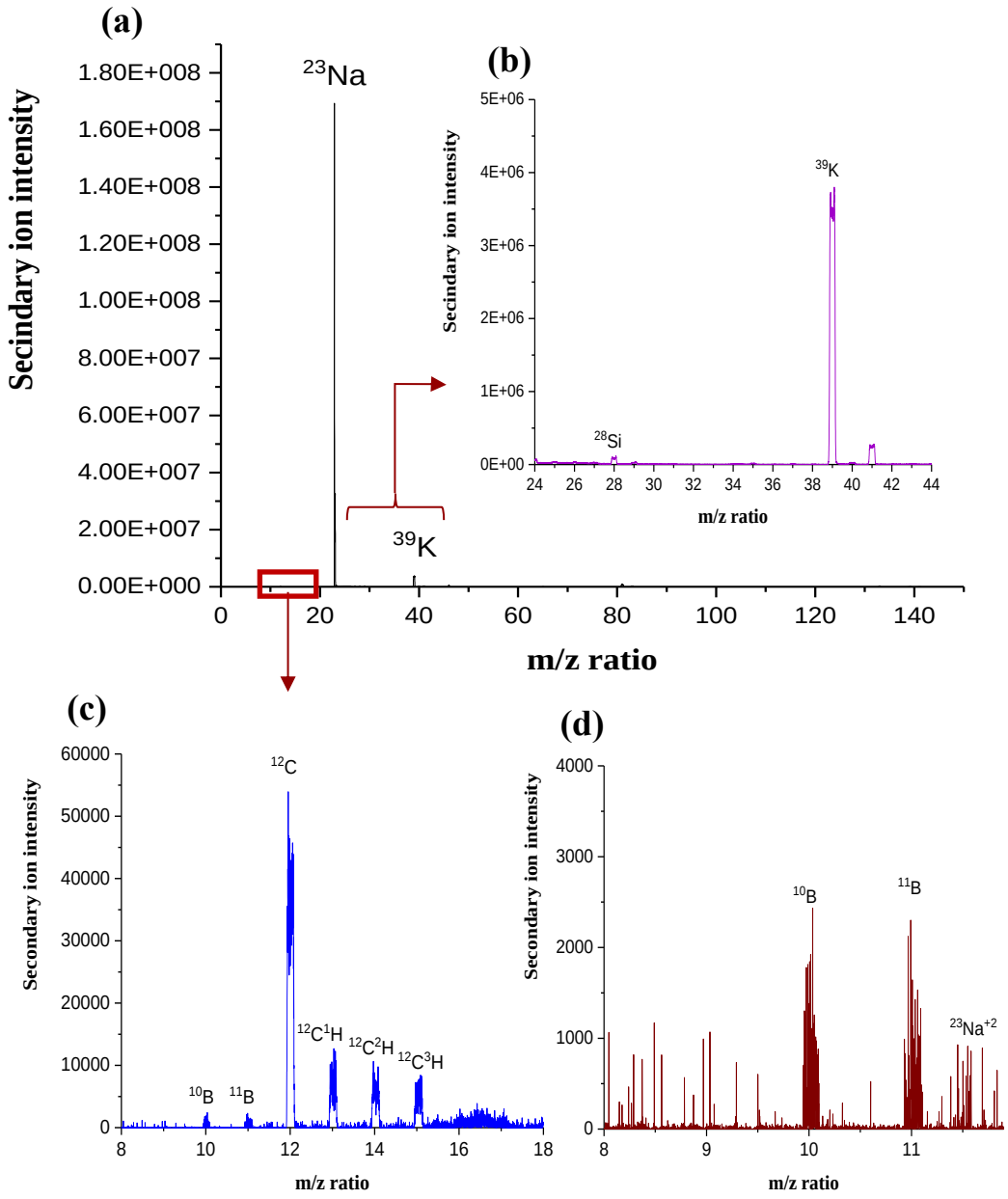

Figure 4.54: Positive secondary ion mass spectra of D4 cell from BAT, obtained after a dose of 2.61×10^{13} ions/cm^2 of the 20 keV Au^+ beam. (a) shows the full spectrum. (b), (c) and (d) show the magnification of the *m/z* range from 24-44, 8-18 and 8-12 respectively.

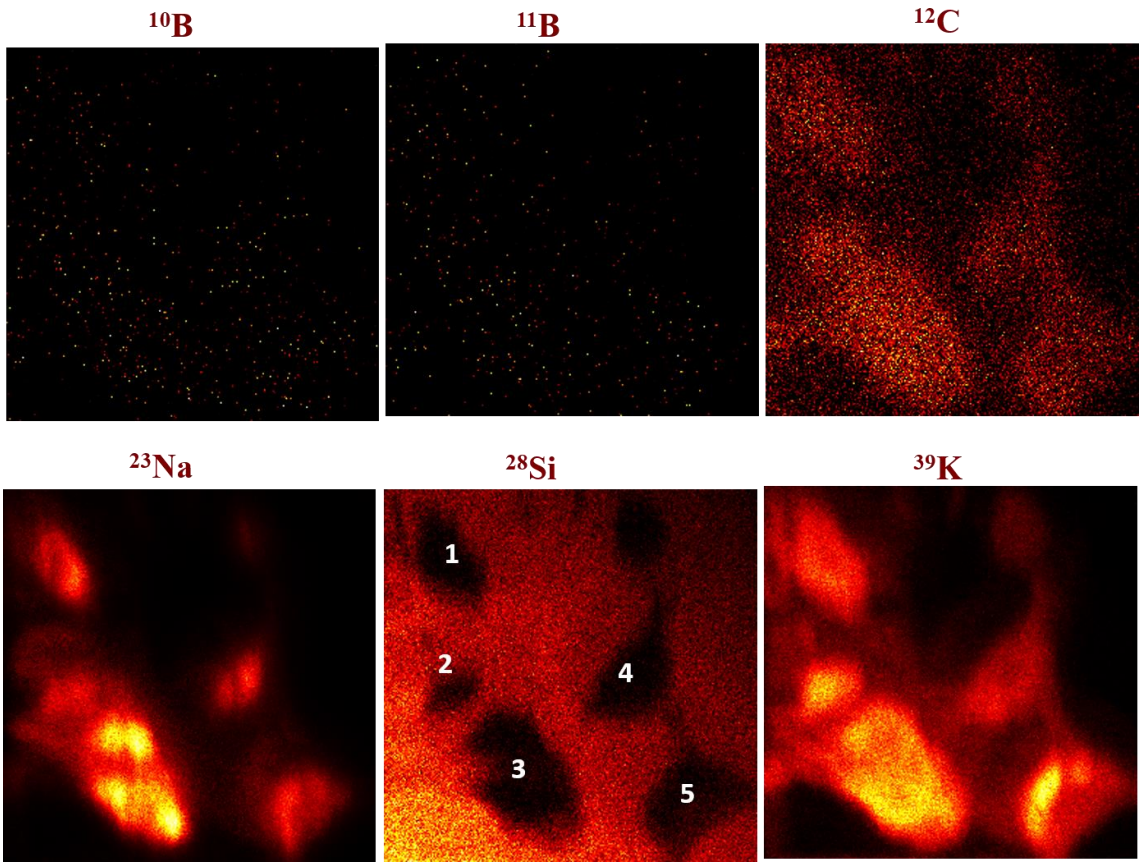

Figure 4.55: BioToF-SIMS analysis for D4 cells cultured from a BAT biopsy treated with 10 mM of BPA (4h) then exposed to the efflux process (4h). The FoV is 252×252 µm^2. The positive secondary ion images of ^{10}B, ^{11}B, ^{12}C, ^{23}Na, ^{28}Si, and ^{39}K show the ion distributions within the cells. The Si image shows the location of five cells of interest in the image frame. The analysis dose in the images was 2.6×10^{13} ions/cm^2. The colour gradient from black to yellow shows the signal intensity from zero to the maximum values.

4.2.4.2.8 Quantitative measurement of ^{10}B in D group samples

Quantitative measurements of ^{10}B of the BPA were made at the cellular level in the D group samples of BAT biopsy. The measurements were normalised to the ^{12}C in **Figure 4.56 -a**, and ^{11}B in **Figure 4.56 -b**. This normalisation was justified during the discussion of quantitative measurement in B group samples in section 4.2.4.2.4. **Table 4.7** shows the mean values for all samples of group D for both ratios, ^{10}B/^{12}C and ^{10}B/^{11}B, where the difference can be observed between them. Quantitative measurements of the ^{10}B/^{12}C ratios in **Figure 4.56 -a** and **Table 4.7** showed that the ratios in the D3 (pre-treated tyrosine) were highest, followed by the D2 and then the D4 samples.

In the $^{10}B/^{12}C$ graph (**Figure 4.56 -a**), the data did not show any overlap in the box plots between the samples, the values in the D3 sample were more variable in the third part of IQR (Q3). The dispersion in IQR of D3 can be explained by three possible causes already mentioned in the section 5.2.3.3, which in turn may also be the reason for the difference of the sample D3 results with the BioToF-SIMS than those obtained with NanoSIMS in section 4.2.3.2.9.

In the $^{10}B/^{11}B$ graph (**Figure 4.56 -b**), the D2 values were overlapping with the D3 sample and the mean value in D2 sample was close to the D3 mean, but the D3 remained with a greater dispersion in the Q3 part of IQR compared to the sample D2. However, the results of normalisation to ^{11}B is less reliable than normalising ^{12}C due to the variation and decrease in ^{11}B signals, and the contribution of the background noise signals. In addition, the sample D4 provided in both **Figure 4.56 -a** and **b** gave a similar result that showed a decrease in the ratios of ^{10}B accumulated in the cells due to exposure to the efflux process. The $^{10}B/^{12}C$ ratios in D4 were ~ 4 times and 40 times lower than the D2 and D3 respectively, but 2 times higher than D1. Whereas the $^{10}B/^{11}B$ ratios in D4 were lower by a factor of ~ 5 than the D2 and D3 respectively, but 3 times higher than D1. Therefore, this decrease of ^{10}B in D4 did not reach the level of the control samples, which confirms that some BPA has remained in the cells and that the efflux process in 4h is slow compared with the uptake process in 4 h.

It was not possible to calculate the concentrations of ^{10}B in D group samples with BioToF-SIMS using $^{10}B^{+}/^{12}C^{+}$ ratios in **Table 4.7** for the same reasons explained previously in section 4.2.4.2.4.

Table 4.7: The median values of the $^{10}B/^{12}C$ and $^{10}B/^{11}B$ ratios from the D group samples (shown in **Figure 4.56**).

Ratios	**$^{10}B/^{12}C$**			
Mean ± SD values of whole cell	D1	D2	D3	D4
	0.007 ± 0.01	0.04 ± 0.013	0.4 ± 0.3	0.01 ± 0.00
Ratios	**$^{10}B/^{11}B$**			
Mean ± SD values of whole cell	D1	D2	D3	D4
	0.4 ± 0.12	5.5 ± 0.7	7 ± 2.6	1.2 ± 0.13

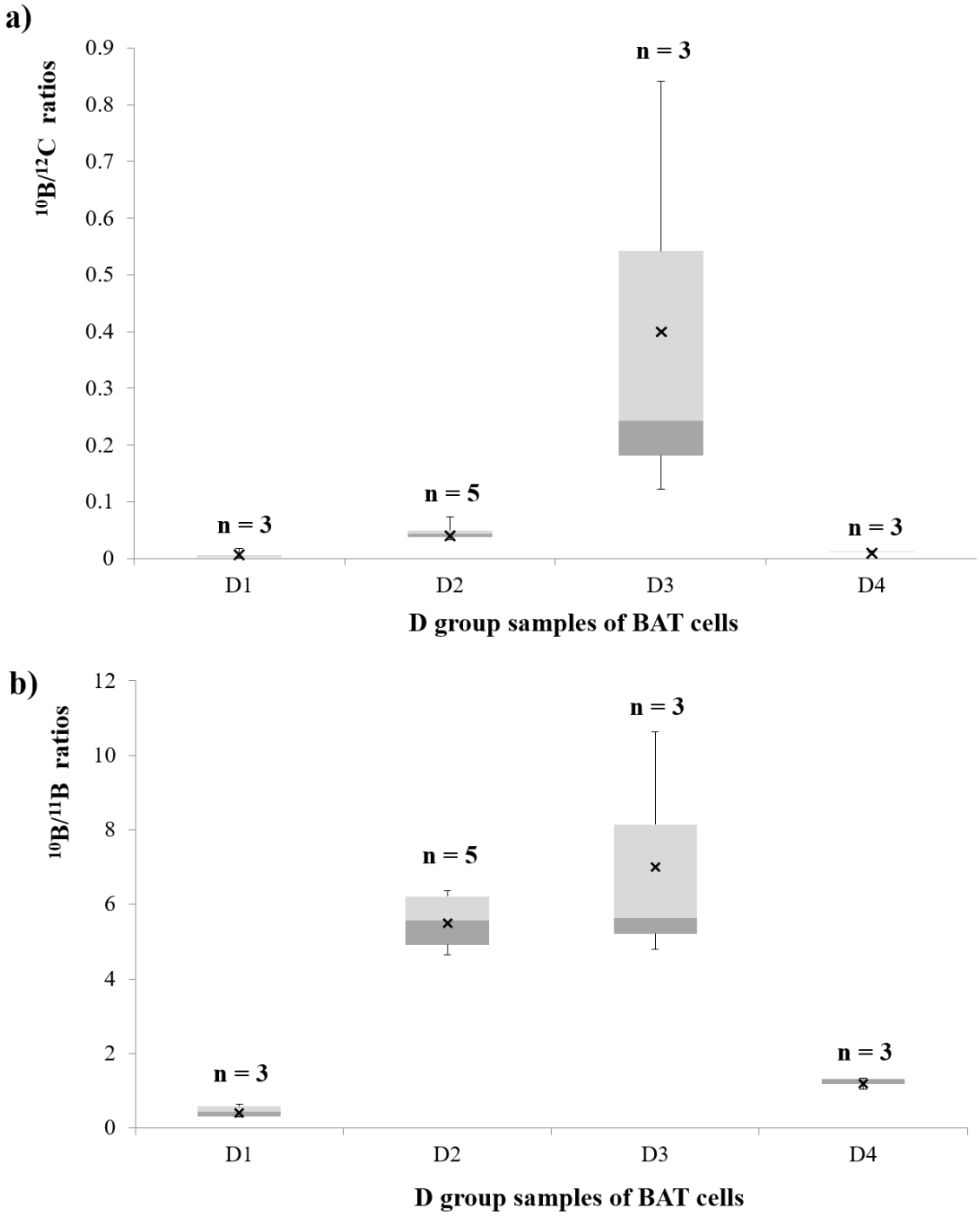

Figure 4.56: Comparison of the BAT cell culture samples: D1, D2, D3 and D4 in terms of $^{10}B/^{12}C$ and $^{10}B/^{11}B$ ratios accumulated at a cellular level determined by BioToF-SIMS. (a) shows that $^{10}B/^{12}C$ ratio was higher in D3 followed by D2 then D4. (b) shows that the $^{10}B/^{11}B$ ratio is slightly higher in D3 than D2 and both of them are higher than D4. In (a) & (b) the D4 remained higher than the control sample D1. ***n***: represents the number of cells analysed for each sample.

4.2.4.3 Comparison of the quantitative measurement of the ^{10}B distribution of BPA between B and D groups samples

Quantitative measurements of the ^{10}B distribution of BPA between cell cultures of the GBM (group B) and the BAT (group D) were compared using the results of BioToF-SIMS analysis in **Figure 4.57** for the $^{10}B/^{12}C$ ratios and **Figure 4.58** for the $^{10}B/^{11}B$ ratios.

Quantitatively comparing between the mean values of the $^{10}B/^{12}C$ ratios at the cellular level in **Figure 4.57** with **Tables 4.6 and 4.7**, the sample B2 was ~10 times higher than the sample D2. In the D3 sample, the mean was an order of magnitude higher than the mean of sample B3. The D4 mean was ~ 2 times higher than the mean of B4 sample. The B1 and D1 control samples were overlapping with mean values close together. In all of these comparisons, there is no overlap between each GMB box-plot and the corresponding one in the BAT samples group. Therefore, the D3 and D4 samples gave higher $^{10}B/^{12}C$ ratios than B3 and B4 while the ratio in D2 was lower than B2. This result of $^{10}B/^{12}C$ ratios using BioToF-SIMS at the cellular level is similar to that obtained from quantitative measurements at the sub-cellular level using NanoSIMS in **Figure 4.23**. The difference in BPA uptake between the two groups of GBM (group B) and BAT (group D) cells can be attributed to the explanation described by Detta and Cruickshank [46] which was discussed in greater detail in the quantitative comparison between the two groups with NanoSIMS in section 5.2.3.3.

In terms of comparison of the mean values of the $^{10}B/^{11}B$ ratios at the cellular level between the two groups B and D in **Figure 4.58** with **Tables 4.6 and 4.7**, it was shown that the mean of D2 sample was ~ 2 times higher than the mean in the sample B2 and there is no overlap between the values of the box plots. The mean of sample D3 was close to the mean of the sample B3 and the overlap was significant between the two samples. In sample D4, the mean was also close to the B4 mean and overlapped with the minimum value of sample B4. The control samples B1 and D1 were overlapping with a similar mean value. Therefore, the D3 and D4 samples gave close ratios of $^{10}B/^{11}B$ to B3 and B4, while the ratio in D2 was higher than B2 and the latter was similar to that obtained with NanoSIMS in **Figure 4.7 -b**.

For the $^{10}B/^{11}B$ ratios in samples D3 and B3 (**Figure 4.58**), as well as in the $^{10}B/^{12}C$ ratio in the sample D3 (**Figure 4.57**) the ratio values were more variable compared to other samples in the same measurement, the same result was observed in the NanoSIMS results on the same samples and gave a wide dispersion in the values of $^{10}B^{12}C/^{12}C$ (**Figure 4.23**), this observation can be interpreted in three ways as explained previously in section 4.2.3.3.

From this comparison between B and D groups, it is concluded that the results of the normalisation of ^{10}B to ^{12}C are similar from both instruments although the absolute ratios are different because the polarity of the ions is different and the instrument sensitivity is also different. The low counts of ^{11}B make quantification using normalisation with ^{11}B more unreliable. This means that both instruments provided a similar result in quantitative measurement although spatial resolution was lower in the BioToF-SIMS images compared to NanoSIMS.

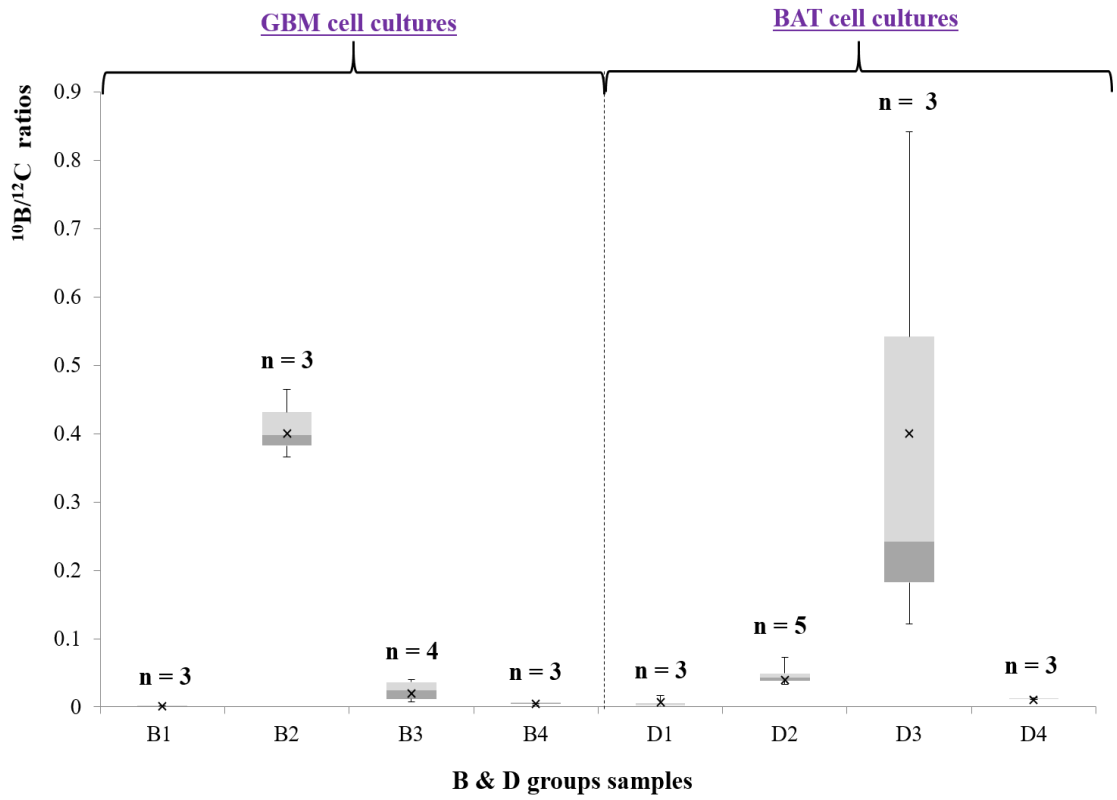

Figure 4.57: Comparison between GBM cells (B group) and BAT cells (D group) in terms of $^{10}B/^{12}C$ ratios indicating accumulation of BPA in the whole cell as measured by BioToF-SIMS. ***n***: represents the number of cells analysed for each sample.

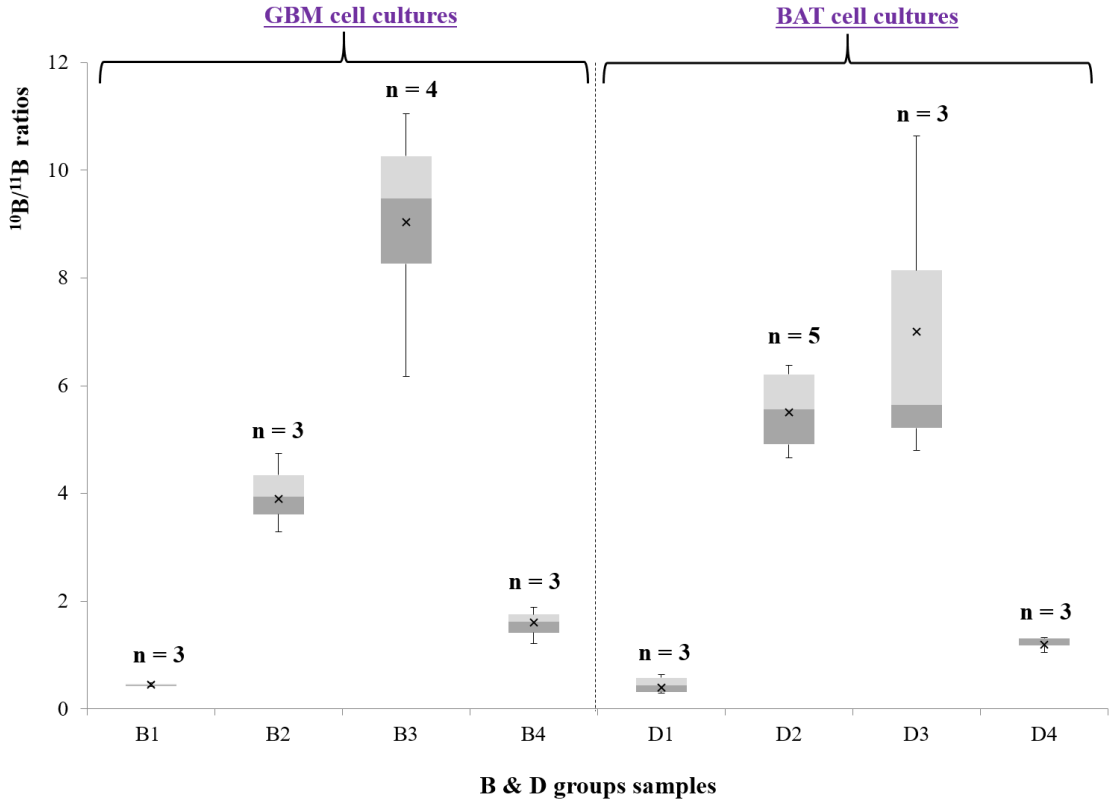

Figure 4.58: Comparison between GBM cells (B group) and BAT cells (D group) in terms of $^{10}B/^{11}B$ ratios indicating accumulation of BPA in the whole cell as measured by BioToF-SIMS. ***n***: represents the number of cells analysed for each sample.

4.3 Summary of the results of the analysis of cell culture samples with both NanoSIMS and BioToF-SIMS instruments

In this chapter, the quantitative imaging capabilities of NanoSIMS and BioToF-SIMS were assessed to determine the localisation and distribution of ^{10}B from the BPA in cellular cultures from the biopsies GBM (group B) and BAT (group D).

4.3.1 Summary of NanoSIMS results

The results of NanoSIMS imaging using a ~ 400 nm Cs^+ beam in all cell cultures of group B and D showed sub-cellular features, surface morphology, the area around the cells, and showed contrast in the distribution of different ions between cellular compartments. All control samples, whether of GBM (A1 and B1) or BAT (C1 and D1), showed a similar distribution of boron isotopes even though they were cultured from biopsies of different patients. This can be seen in **Figures 4.1- 4.4** where the B isotopes accumulated in the extracellular region. The ratios of $^{10}B/^{11}B$ in cells were between 0.25 – 0.27, and corresponds

with the level of natural ratio of $^{10}B/^{11}B$ (0.247) [2][3], as is clear from the measurement in **Figure 4.7**, confirming that control cells contained natural ratios of boron isotope.

The distribution of BPA in NanoSIMS images in all samples in the B and D groups, except control samples, showed a heterogeneous distribution of $^{10}B^-$ and $^{10}B^{12}C^-$ ions between cell compartments. Both ions accumulate to a greater level (~ 2-fold) in nuclei regions than cytoplasmic regions but the normalised counts of $^{10}B^{12}C^-$ was higher than that of atomic form, $^{10}B^-$. The higher ^{10}B signals in the cells of the BPA treated D and B samples, in comparison to the control samples B1 and D1, confirms that the samples absorbed the BPA and this is evident from the quantitative measurements in **Figures 4.14** and **4.21**. This preferential accumulation of $^{10}B^-$ and $^{10}B^{12}C^-$ ions in the nuclei of the cells is desirable to increase the chances of success of the BNCT treatment for the tumours, where the exposure of tumours to a fission reaction using low-energy thermal neutrons generates linear particles that penetrate cells for short distances with high energy, leading to the destruction of tumour cells [21]–[24].

The heterogeneous ^{10}B distribution between cell compartments in all B and D groups samples is very similar to the ^{10}B distribution in Mouse melanoma cells (B16) *in vitro* where Oyedepo *et al.* explained that the localisation of boron of BPA was limited in the nucleus and outer edge of the cell as in **Figure 2.8** and did not refer to any localisation in the cytoplasm [39]. Chandra *et al.* also presented a study on human glioblastoma cells (T98G) *in vitro* which indicated the difference in the ^{10}B distribution of BPA drug from cell to cell, while some cells gave a boron distribution pattern similar to those of B and D groups samples, other cells were completely opposite where the boron was concentrated in the cytoplasm more than the nucleus, **Figure 2.10** [61]. The difference in the distribution of ^{10}B signals between the B2 (as example from thesis samples), mouse melanoma [39] and human glioblastoma [61] cells may be due to the difference in treatment dosage and time of exposure to the dose, which were respectively 100 p.p.m for 4 h, 50 p.p.m for 2 days and 110 p.p.m for 2h. Although the treatment BPA concentration in the three samples differed, increasing the incubation time with the BPA may have allowed enough time for the boron ions to concentrate in the nucleus and improve intracellular accumulation, Table 2.2 shows that the incubation time has an effect on BPA uptake. In addition, the uptake of BPA (level and location) may be different between cell types and organism e.g. Human vs Mouse, emphasising the importance of making these measurements in primary cell cultures from Humans as well as in primary tissue for patients.

By comparing the quality of the images of the three samples in **Figures 4.9, 2.8** and **2.10** it was found that the intensity of the boron ion signals when using a ~ 400 nm Cs^+ beam (in this thesis) and 300 nm Ga^+ beam [39] in the analysis of samples B2 and melanoma cells respectively were better than 500 nm spatial resolution obtained with an O_2^+ beam used to analyse glioblastoma cells [61]. Chandra had to use reflected light microscopy in imaging the glioblastoma cells to determine the location and boundaries of the nuclei and cells prior to initiation of the study of the BPA distribution, as other ion maps did not clearly distinguish the internal or surface features of the cells. In contrast, the high sensitivity of Cs^+ (in this thesis) and Ga^+ [39] beams in the analysis of B2 and melanoma samples respectively showed the features and boundaries of cells and the varying distribution between cell compartments without the need for reflected light microscopy imaging. The Ga^+ beam was optimised for sample current (sensitivity) rather than spot size [39] so the smaller Cs^+ beam showed more details, for example the slight variations in the distribution of low signals for $^{10}B^-$ and $^{10}B^{12}C^-$ ions in the cytoplasm (B2) indicate higher resolution imaging for NanoSIMS at the sub-cellular level.

In the pre-treated samples with tyrosine where the aim was to increase BPA uptake, the NanoSIMS imaging and quantitative measurement results of sample B3 in **Figures 4.11** and **4.14** respectively indicated that the accumulation of ^{10}B was lower than in sample B2 (**Figures 4.9** and **4.14)**. The D3 sample results in **Figures 4.18 and 4.21**show that the ^{10}B signals in D3 were close to D2 (**Figures 4.16 and 4.21**)**,** also the $^{10}B^{12}C$ signals were lower than the D2. Thus, the results of the B3 and D3 indicate that pre-treatment with tyrosine does not enhance the uptake of BPA in either sample. This finding is inconsistent with some previous studies that have demonstrated that preloading with L-amino acids increases the BPA uptake in tumour cells [23][27][30][31]. Wingelhofer *et. al.* illustrated that pre-treatment with L-tyrosine and L-DOPA improve the uptake of FBPA, an analogue of BPA used to predict concentrations of BPA, in three cell lines *in vitro*, which are the mouse melanoma, the human colorectal adenocarcinoma and the human hepatocellular carcinoma [62]. Capuani *et al.* reported that pre-loading of L-DOPA in rat C6-glioma cells *in vitro* and *in vivo* increased the accumulation of intracellular BPA [63][64]. Witting et.al. [30] and Papaspyrou *et al.* [65] proved that preloading of tyrosine increased the BPA uptake in rat gliosarcoma and mouse melanoma cells respectively. Most of these studies were conducted on animal cells whether *in vitro* or *in vivo* and only one study on the lines of human cells [62], which in turn differed from the type and nature of human samples used in this thesis. This difference in sample type may be the reason why the results of preloading of tyrosine in B3 and D3 is not consistent with these studies. Primary human cells are heterogeneous

and more complex, making a comparison between animal models and human cell lines difficult [46].

In contrast, our results are consistent with the Grunewald's *et al.* conclusion, which showed that pre-loading with L-tyrosine and L-DOPA did not affect the BPA uptake in all organelles of the mice carrying the human hepatocellular carcinoma cells line because either the effect of tyrosine varies from tumour to tumour or the activity of LAT-1 expression in transfer L-amino acid is different from patient to patient [47].Yang *et. al.* stated that the effect of tyrosine could not be determined definitively in a study conducted on F98 glioma bearing rats with L-DOPA and B16 melanoma bearing mice with L-tyrosine [66] because the preloading with the amino acid is different depending on the anatomic location of the tumour and histologic tumour. Detta and Cruickshank also demonstrated that pre-treatment with tyrosine did not improve BPA uptake in the GBM brain tumour and brain around tumour biopsies as showed in **Figure 2.2** [46]. The samples, analysed by Detta and Cruickshank are the closest in nature and type to the cultured cells samples used in this thesis as was explained in 3.2.2.

In the samples exposed to the efflux process (4h) after incubation with BPA (4h), B4 maps in **Figure 4.13** and the quantitative measurement in **Figure 4.14** showed a decrease in the intensity of ^{10}B and $^{10}B^{12}C$ accumulated in the cell compartments compared to B2 and B3. The D4 maps in **Figure 4.20** and the quantitative measurement in **Figure 4.21** showed a similar behaviour to sample B4 where the ^{10}B and $^{10}B^{12}C$ intensity in the cells also decreased compared with D2 and D3 samples. However, boron levels in B4 and D4 samples remained higher than the B1 and D1 control samples, indicating that the boron ions are not completely lost from cells during the efflux process. Results of B4 and D4 are compatible with Witting *et.al.* study, which showed that the efflux process in a medium containing amino acid and another medium that does not contain amino acid will lead in both cases to a clear and rapid reduction in BPA uptake in gliosarcoma cells of rat, confirming that the efflux process is an exchange between the inside and outside the cell and slower than the uptake process [30].

The wet weight concentrations of ^{10}B determined using the $^{10}B^-/^{12}C^-$ ratios that measured from the B samples in **Table 4.3** and D samples in **Table 4.5** using the NanoSIMS confirms an increased drug concentration in cellular nuclei compared to the cytoplasm. This is an important finding that has implications for the efficacy of BNCT treatment considering the short range of radiant energy transfer from irradiated ^{10}B atoms as explained earlier in section 4.2.3.2.5. There was no statistically significant difference in mean ^{10}B concentrations between the B2 and D2, and this is similar to the findings of Detta and Cruickshank [46]

explained extensively in the section 4.2.3.3. Tyrosine was found to result in a significant decrease in cellular BPA uptake in B3 cells from the tumour core, but not from the D3 of BAT, this is identical with some studies [46][47][66] and is inconsistent with other studies [30][62][65] discussed above. The concentrations also suggest that the BPA efflux process is slower than the uptake process and is not complete within 4 h. Residual levels of ^{10}B in B4 and D4 cells derived from GBM tumour and BAT respectively are above the lethal BNCT threshold, ~15–30 μg g^{-1} [41], following 4 h efflux treatment. The concentration of $^{10}B^{12}C^{-}/^{12}C^{-}$ ratios were not estimated due to the lack of a relative sensitivity factor for the $^{10}B^{12}C^{-}$ from an appropriate standard.

4.3.2 Summary of BioToF-SIMS results

The results of BioToF-SIMS imaging using a 1 – 2 μm Au^{+} beam in all samples of the two groups B and D provided general information on the distribution and intensity of ion signals at the cellular level, and did not distinguish cell compartments compared to the images from the NanoSIMS. All control samples from BAT and GBM provided similar results for the distribution of boron isotopes in **Figures 4.25 – 4.35**, The quantitative measurement in **Figure 4.36** shows that the ratio of $^{10}B/^{11}B$ was approximately 0.38 – 0.45 which is higher than the natural ratio 0.247 [2][3] due to interference with the noise signals which reduced the accuracy.

The pharmacological distribution of BPA in BioToF-SIMS images in all samples of the B group from GBM and the D group from BAT, with the exception of the control samples, showed a fairly homogeneous distribution of ^{10}B at the cellular level without showing any clear localisation in the cell structure. The difference between the images of the samples was in the number of ion signals accumulated in the cells. The quantitative measurements in **Figure 4.46** and **4.56** confirm that the ^{10}B from the BPA was localised within the cells of all B and D samples with the exception of the B1 and D1 control samples. The BioToF-SIMS images cannot determine the preferred accumulation sites for ^{10}B from BPA in cells unlike NanoSIMS images, which showed the preferential accumulation sites at the subcellular level. Knowing the location of the BPA is necessary to determine the success of the BNCT treatment in destroy cancer cells as described in section 2.1 [21]–[24].

The homogeneous ^{10}B distribution in all B and D groups samples treated with BPA is somewhat similar to the ^{10}B distribution between the nucleus and the cytoplasm indicated by Chandra *et. al.* during the study of the human glioblastoma cells line (T98G) and the extent of the effect of exposure to a nutrient medium containing phenylalanine at the level

of internal boron in cells as in **Figure 2.13** [67]. However, Chandra *et. al.* showed in a previous study that the distribution of boron is uneven between T98G cell compartments as discussed in **Figure 2.10** [61]. In addition, the distribution of Na, K, C and ^{10}B ions for all samples of the B and D groups are similar to that obtained by Alkins *et al.* when analysing 9L gliosarcoma tumour sections model of Fisher 344 rats treated with BPA-f *in vivo* using ToF–SIMS IV with Bi_1^+ beam, the similarity is that the ions did not show any clear pattern of localisation within the cellular structure as shown in **Figure 2. 12**[21]. By comparing the image quality of samples B2 imaged with NanoSIMS, B2 imaged with BioToF-SIMS, glioblastoma cells line (T98G) [67] and 9L gliosarcoma tumour [21] in **Figures 4.9, 4.39, 2.13, and 2.12** respectively, which were analysed using ~ 400 nm Cs^+, 1-2µm Au^+, stigmatic-imaging with O_2^+, and Bi_1^+ (probe size not given) respectively, it is clear that the Cs^+ beam was better than the other beams in providing high spatial resolution images for localising boron and other ions to features in the cell structure. The O_2^+ beam is the next best at showing boron signals but with the need to use a reflection light microscope to determine the location of the cell compartments before the analysis of the sample. The Au^+ and Bi^+ were close in performance, showing the difference in the intensity of the ion signal in general without localisation to the cellular compartments.

In terms of pre-loaded samples with tyrosine, the imaging results for ^{10}B in the B3 sample in **Figure 4.42** and the quantitative measurement made by normalisation with ^{12}C in **Figure 4.46 -a** showed that the ^{10}B ion signals in the cell structure was ~ 20 times lower than the B2 sample in **Figure 4.39** and **4.46 -a**. The result of the B3 sample indicates that pre-treatment with tyrosine has not improved the uptake of BPA in sample. This result is similar to that obtained when analysing the B3 using the NanoSIMS which is already mentioned above. Accordingly, the result of B3 contradicts some of the earlier investigations in the literature that indicated that pre-treatment with L-tyrosine improves BPA uptake in tumour cells [30][62]–[65], while corresponding with other studies that showed that the effect of tyrosine varies depending on the type and location of the tumour or that the activity of LAT-1 expressions in transfer L-amino acids is different among patients [46][47][66]. These consistent and conflicting studies were reviewed in greater detail during the summary of the B3 sample results with the NanoSIMS above. The D3 sample results (**Figure 4.52** and **Figure 4.56**) show a opposite result to those in B3, where the ^{10}B signals in D3 were ~ 10 times higher than D2 (**Figure 4.49** and **4.56**).

In the B4 and D4 samples exposed to the efflux process, the images in **Figure 4.45** and **4.55** as well as quantitative measurements normalised by ^{12}C and in **Figure 4.46** and **4.56** showed

a similar result. The ^{10}B signal in the cell structure decreased compared with other B and D groups samples, but remained higher than the control samples B1 and D1. Results of B4 and D4 are compatible with Witting's et.al. results, which was reviewed in the summary of NanoSIMS results [30].

4.3.3 Conclusions

In the comparison between the B and D groups, the $^{10}B/^{12}C$ ratios results using NanoSIMS in **Figure 4.23** and BioToF-SIMS in **Figure 4.57** showed a similar result, which is that the accumulation of ^{10}B of BPA in D group samples was higher than the B group samples, except that D2 was less than B2 in BioToF-SIMS measurements, while D2 and B2 were close to each other in NanoSIMS measurements. Moreover, the results of comparing the $^{10}B/^{11}B$ ratios between the two groups using NanoSIMS in **Figure 4.7 -b** and BioToF-SIMS in **Figure 4.58** gave a similar result in that the intensity of ^{10}B of BPA in D2 was higher than B2 which in turn reversed the results of $^{10}B/^{12}C$ ratios. This means that both instruments provided a similar performance in quantitative measurement although spatial resolution decreased in the BioToF-SIMS images compared to NanoSIMS.

In addition, measured ^{10}B concentrations (μg/g) in nuclei and cytoplasm using NanoSIMS (**Tables 4.3** and **4.5)** are similar to literature, with a nuclear : cytoplasmic concentration ratio which is preferable to the success of BNCT. Analyses with NanoSIMS have demonstrated cellular heterogeneity which bulk techniques cannot address. On the other hand, it was not possible to calculate the ^{10}B concentrations from the $^{10}B^+/^{12}C^+$ ratios in **Tables 4.6** and **4.7** with BioToF-SIMS due to the absence of a RSF value from a suitable reference to the freeze-dried cells samples. The use of a calibration curve for different BPA concentrations in trehalose (**Figure 3.13**) was also not useful for determining ^{10}B concentrations with BioToF-SIMS.

Thus, the NanoSIMS was able to map and quantify ^{10}B distribution in cells. Together these observations represent the first intracellular study of BPA uptake and L-tyrosine pre-treatment in human cells. Although the sample numbers are small in this proof-of-principle study, due to the low throughput of the NanoSIMS and BioToF-SIMS techniques, the results are still important for determining the success of BNCT in patients.

4.4 References

[1] A. Detta, J. Harland, I. Hanif, S. M. Brown, and G. Cruickshank, "Proliferative activity and in vitro replication of HSV1716 in human metastatic brain tumours," *J. Gene Med.*, vol. 5, no. 8, pp. 681–689, 2003.

[2] M. F. L'Annunziata, *Handbook of Radioactivity Analysis*, 3rd ed. Elsevier, 2012.

[3] R. N. Sah and P. H. Brown, "Isotope ratio determination in boron analysis.," *Biol. Trace Elem. Res.*, vol. 66, no. 1–3, pp. 39–53, 1998.

[4] H. F. Arlinghaus, C. Kriegeskotte, M. Fartmann, A. Wittig, W. Sauerwein, and D. Lipinsky, "Mass spectrometric characterization of elements and molecules in cell cultures and tissues," *Appl. Surf. Sci.*, vol. 252, no. 19, pp. 6941–6948, 2006.

[5] P. Yakovchuk, E. Protozanova, and M. D. Frank-Kamenetskii, "Base-stacking and base-pairing contributions into thermal stability of the DNA double helix," *Nucleic Acids Res.*, vol. 34, no. 2, pp. 564–574, 2006.

[6] J. M. Berg, J. L. Tymoczko, and L. Stryer, *Biochemistry*, 5th ed. New York: W H Freeman, 2002.

[7] J. P. Berry, P. Galle, D. Chassoux, F. Escaig, L. G. Linarez-Cruz, and G. Lespinats, "Mapping of intracellular halogenous molecules by low and high resolution SIMS microscopy," *Biol. Cell*, vol. 74, no. C, pp. 93–98, 1992.

[8] R. Peteranderl and C. Lechene, "Measure of carbon and nitrogen stable isotope ratios in cultured cells," *J. Am. Soc. Mass Spectrom.*, vol. 15, no. 4, pp. 478–485, 2004.

[9] C. Lechene *et al.*, "High-resolution quantitative imaging of mammalian and bacterial cells using stable isotope mass spectrometry," *J. Biol.*, vol. 5, pp. 1–30, 2006.

[10] L. E. Wedlock, M. R. Kilburn, J. B. Cliff, L. Filgueira, M. Saunders, and S. J. Berners-Price, "Visualising gold inside tumour cells following treatment with an antitumour gold(I) complex," *Metallomics*, vol. 3, no. 9, pp. 917–925, 2011.

[11] G. Karp, *Cell and molecular biology : concepts and experiments*, 6th ed. United States of America: John Wiley and Sons, 2010.

[12] G. J. Doherty and H. T. McMahon, "Mediation, Modulation, and Consequences of Membrane-Cytoskeleton Interactions," *Annu. Rev. Biophys.*, vol. 37, no. 1, pp. 65–95, 2008.

[13] I. Budin and N. K. Devaraj, "Membrane assembly driven by a biomimetic coupling reaction," *J. Am. Chem. Soc.*, vol. 134, no. 2, pp. 751–753, 2012.

[14] K. H. Lau, M. Christlieb, M. Schröder, H. Sheldon, A. L. Harris, and C. R. M. Grovenor, "Development of a new bimodal imaging methodology : a combination of fluorescence microscopy and high-resolution secondary ion mass spectrometry," *J. Microsc.*, vol. 240, no. January, pp. 21–31, 2010.

[15] A. Ghosh and M. Bansal, "A glossary of DNA structures from A to Z," *Acta Crystallographica - Section D*, vol. 59, no. 4. pp. 620–626, 2003.

[16] B. Alberts, A. Johnson, J. Lewis, M. Raff, K. Roberts, and P. Walter, "Chapter 4: DNA, Chromosomes and Genomes," in *Molecular Biology of the Cell*, 6th ed., New York: Garland Science, 2014.

[17] A. A. Legin *et al.*, “NanoSIMS combined with fluorescence microscopy as a tool for subcellular imaging of isotopically labeled platinum-based anticancer drugs,” *Chem. Sci.*, vol. 5, no. 8, pp. 3135–3143, 2014.

[18] M. C. Mony and E. Larras-Regard, “Imaging of subcellular structures by scanning ion microscopy and mass spectrometry. Advantage of cryofixation and freeze substitution procedure over chemical preparation,” *Biol. Cell*, vol. 89, no. 3, pp. 199–210, 1997.

[19] T. Ubuka, “Assay methods and biological roles of labile sulfur in animal tissues,” *J. Chromatogr. B*, vol. 781, no. 1–2, pp. 227–249, 2002.

[20] T. R. Sutton *et al.*, “A robust and versatile mass spectrometry platform for comprehensive assessment of the thiol redox metabolome,” *Redox Biol.*, vol. 16, no. 1, pp. 359–380, 2018.

[21] R. D. Alkins, P. M. Brodersen, R. N. S. Sodhi, and K. Hynynen, “Enhancing drug delivery for boron neutron Capture Therapy of Brain Tumors With Focused Ultrasound,” *Neuro. Oncol.*, vol. 15, no. 9, pp. 1225–1235, 2013.

[22] X. Zha, W. A. Ausserer, and G. H. Morrison, “Quantitative imaging of a radiotherapeutic drug, $Na_2B_{12}H_{11}SH$, at subcellular resolution in tissue cultures using ion microscopy,” *Cancer Res.*, vol. 52, no. 19, pp. 5219–5222, 1992.

[23] M. J. Luderer, P. De La Puente, and A. K. Azab, “Advancements in Tumor Targeting Strategies for Boron Neutron Capture Therapy,” *Pharm. Res.*, vol. 32, no. 9, pp. 2824–2836, 2015.

[24] R. F. Barth, P. Mi, and W. Yang, “Boron delivery agents for neutron capture therapy of cancer,” *Cancer Commun.*, vol. 38, no. 35, pp. 1–15, 2018.

[25] J. R. Jara, J. H. Martinez-Liarte, F. Solano, and R. Peñafiel, “Transport of L-tyrosine by B16/F10 melanoma cells: the effect of the intracellular content of other amino acids.,” *J. Cell Sci.*, vol. 97, pp. 479–485, 1990.

[26] G. C. Gazzola, V. Dall’Asta, and G. G. Guidotti, “The transport of neutral amino acids in cultured human fibroblasts.,” *J. Biol. Chem.*, vol. 255, no. 3, pp. 929–936, 1980.

[27] T. Lahoutte *et al.*, “SPECT and PET amino acid tracer influx via system L (h4F2hc-hLAT1) and its transstimulation.,” *J. Nucl. Med.*, vol. 45, pp. 1591–1596, 2004.

[28] A. Detta, “personal communication,” 2018.

[29] J. W. Kimball, “Cell Membranes,” *Kimball’s Biology Pages*. [Online]. Available: http://www.biology-pages.info/C/CellMembranes.html. [Accessed: 23-Oct-2018].

[30] A. Wittig, W. A. Sauerwein, and J. A. Coderre, “Mechanisms of Transport of p-Borono-Phenylalanine through the Cell Membrane In Vitro Linked references are available on JSTOR for this article : Mechanisms of Transport of p-Borono-Phenylalanine through the Cell Membrane In Vitro,” *Radiat. Res.*, vol. 153, no. 2, pp. 173–180, 2000.

[31] W. A. Campbell, D. E. Sah, M. M. Medina, J. E. Albina, W. B. Coleman, and N. L. Thompson, “TA1/LAT-1/CD98 light chain and system L activity, but not 4F2/CD98 heavy chain, respond to arginine availability in rat hepatic cells. Loss of response in tumor cells,” *J. Biol. Chem.*, vol. 275, no. 8, pp. 5347–5354, 2000.

[32] F. Verrey, “System L: Heteromeric exchangers of large, neutral amino acids involved in directional transport,” *Pflugers Arch. Eur. J. Physiol.*, vol. 445, no. 5, pp. 529–533, 2003.

[33] R. J. Boado, J. Y. Li, M. Nagaya, C. Zhang, and W. M. Pardridge, “Selective expression of the large neutral amino acid transporter at the blood – brain barrier,” *PNAS*, vol. 96, no. 21, pp. 12079–12084, 1999.

[34] F. Yoshida *et al.*, “Cell cycle dependence of boron uptake from two boron compounds used for clinical neutron capture therapy,” *Cancer Lett.*, vol. 187, no. 1–2, pp. 135–141, 2002.

[35] K. Ono *et al.*, “Radiobiological evidence suggesting heterogeneous microdistribution of boron compounds in tumors :its relation to quiescent cell population and tumor cure in neutron capture therapy,” *Int. J. Radiat. Oncol. Biol. Phys.*, vol. 34, no. 5, pp. 1081–1086, 1996.

[36] M. Dahlström, J. Capala, P. Lindström, A. Wasteson, and A. Lindström, “Accumulation of boron in human malignant glioma cells in vitro is cell type dependent,” *J. Neurooncol.*, vol. 68, no. 3, pp. 199–205, 2004.

[37] H. Curtis and N. S. Barnes, *Invitation to biology*, 5th ed. New York: N.Y. : Worth Publishers, 1994.

[38] “What is the thickness of the cell membrane?” [Online]. Available: http://book.bionumbers.org/what-is-the-thickness-of-the-cell-membrane/. [Accessed: 23-Oct-2018].

[39] A. C. Oyedepo, S. L. Brooke, P. J. Heard, J. C. C. Day, G. C. Allen, and H. Patel, “Analysis of boron-10 in soft tissue by dynamic secondary ion mass spectrometry,” *J. Microsc.*, vol. 213, no. 1, pp. 39–45, 2004.

[40] R. G. Wilson, G. E. Lux, and C. L. Kirschbaum, “Depth profiling and secondary ion mass spectrometry relative sensitivity factors and systematics for polymers/organics,” *J. Appl. Phys.*, vol. 73, no. 5, p. 2524, 1993.

[41] M. J. Luderer, P. De La Puente, and A. K. Azab, “Advancements in Tumor Targeting Strategies for Boron Neutron Capture Therapy,” *Pharm. Res.*, vol. 32, no. 9, pp. 2824–2836, 2015.

[42] T. A. Devirian and S. L. Volpe, “The Physiological Effects of Dietary Boron,” *Crit. Rev. Food Sci. Nutr.*, vol. 43, no. 2, pp. 219–231, 2003.

[43] K. Langen, H. Mühlensiepen, M. Holschbach, H. Hautzel, P. Jansen, and H. H. Coenen, “Transport Mechanisms of 3-[^{123}I]Iodo-a-Methyl-L-Tyrosine in a Human Glioma Cell Line : Comparison with [^{3}H-methy 1]-L-Methionine,” *J. Nucl. Med.*, vol. 41, no. 7, pp. 1250–1255, 2000.

[44] H. De Wolde, J. Pruim, M. F. Mastik, J. Koudstaal, and W. M. Molenaar, “Proliferati ve Activity in Human Brain Tumors : Comparison of Histopathology and L-[1-^{11}C] Tyrosine PET,” *J. Nucl. Med.*, vol. 38, no. 9, pp. 1369–1374, 1997.

[45] T. Sasajima, T. Miyagawa, T. Oku, J. G. Gelovani, R. Finn, and R. Blasberg, “Proliferation-dependent changes in amino acid transport and glucose metabolism in glioma cell lines,” *Eur. J. Nucl. Med. Mol. Imaging*, vol. 31, no. 9, pp. 1244–1256, 2004.

[46] A. Detta and G. S. Cruickshank, “L-Amino Acid Transporter-1 and Boronophenylalanine-Based Boron Neutron Capture Therapy of Human Brain Tumors,” *Cancer Res.*, vol. 69, no. 5, pp. 2126–2132, 2009.

[47] C. Grunewald *et al.*, “On the applicability of [^{18}F]FBPA to predict L-BPA concentration after amino acid preloading in HuH-7 liver tumor model and the implication for liver boron neutron capture therapy,” *Nucl. Med. Biol.*, vol. 44, pp. 83–89, 2017.

[48] H. Nawashiro *et al.*, “High expression of L-type amino acid transporter 1 in infiltrating glioma cells,” *Brain Tumor Pathol.*, vol. 22, pp. 89–91, 2005.

[49] S. Chandra and D. R. Lorey, “SIMS ion microscopy imaging of boronophenylalanine (BPA) and $^{13}C^{15}N$-labeled phenylalanine in human glioblastoma cells: Relevance of subcellular scale observations to BPA-mediated boron neutron capture therapy of cancer,” *Int. J. Mass Spectrom.*, vol. 260, no. 2–3, pp. 90–101, 2007.

[50] S. Chandra, T. Ahmad, R. F. Barth, and G. W. Kabalka, “Quantitative evaluation of boron neutron capture therapy (BNCT) drugs for boron delivery and retention at subcellular-scale resolution in human glioblastoma cells with imaging secondary ion mass spectrometry (SIMS),” *J. Microsc.*, vol. 254, no. 3, pp. 146–156, 2014.

[51] S. Chandra, W. Tjarks, D. R. Lorey, and R. F. Barth, “Quantitative subcellular imaging of boron compounds in individual mitotic and interphase human glioblastoma cells with imaging secondary ion mass spectrometry (SIMS),” *J. Microsc.*, vol. 229, no. 1, pp. 92–103, 2008.

[52] D. R. Lorey, G. H. Morrison, and S. Chandra, “Dynamic secondary ion mass spectrometry analysis of boron from boron neutron capture therapy drugs in co-cultures: Single-cell imaging of two different cell types within the same ion microscopy field of imaging,” *Anal. Chem.*, vol. 73, no. 16, pp. 3947–3953, 2001.

[53] S. Chandra, G. W. Kabalka, D. R. Lorey, D. R. Smith, and J. A. Coderre, “Imaging of fluorine and boron from fluorinated boronophenylalanine in the same cell at organelle resolution by correlative ion microscopy and confocal laser scanning microscopy,” *Clin. Cancer Res.*, vol. 8, no. 8, pp. 2675–2683, 2002.

[54] S. Chandra, D. R. Lorey II, and D. R. Smith, “Quantitative Subcellular Secondary Ion Mass Spectrometry (SIMS) Imaging of Boron-10 and Boron-11 Isotopes in the Same Cell Delivered by Two Combined BNCT Drugs: In Vitro Studies on Human Glioblastoma T98G Cells,” *Radiat. Res.*, vol. 157, no. 6, pp. 700–710, 2002.

[55] D. J. Hare, E. J. New, M. D. De Jonge, and G. McColl, “Imaging metals in biology: Balancing sensitivity, selectivity and spatial resolution,” *Chem. Soc. Rev.*, vol. 44, no. 17, pp. 5941–5958, 2015.

[56] Z. Qin, J. A. Caruso, B. Lai, A. Matusch, and J. S. Becker, “Trace metal imaging with high spatial resolution: Applications in biomedicine,” *Metallomics*, vol. 3, no. 1, pp. 28–37, 2011.

[57] H. Sediqi, A. Wray, C. Jones, and M. Jones, “Application of Spectral Phasor analysis to sodium microenvironments in myoblast progenitor cells,” *PLoS One*, vol. 13, no. 10, p. e0204611, 2018.

[58] L. G. Palmer and M. M. Civan, “Distribution of Na^+, K^+ and Cl^- between nucleus and cytoplasm in Chironomus salivary gland cells,” *J. Membr. Biol.*, vol. 33, no. 1, pp.

41–61, 1977.

[59] I. Zs.-Nagy, G. Lustyik, V. Zs.-Nagy, G. Lukacs, and G. Balazs, “Correlation of Malignancy with the Intracellular Na^+:K^+ Ratio in Human Thyroid Tumors,” *Cancer Res.*, vol. 43, no. 11, pp. 5395–5402, 1983.

[60] I. Z. Nagy, G. Lustyik, V. Z. Nagy, B. Zarándi, and C. Bertoni-Freddari, “Intracellular Na^+:K^+ ratios in human cancer cells as revealed by energy dispersive X-ray microanalysis,” *J. Cell Biol.*, vol. 90, no. 3, pp. 769–777, 1981.

[61] S. Chandra and D. R. Lorey, “SIMS ion microscopy imaging of boronophenylalanine (BPA) and $^{13}C^{15}N$-labeled phenylalanine in human glioblastoma cells: Relevance of subcellular scale observations to BPA-mediated boron neutron capture therapy of cancer,” *Int. J. Mass Spectrom.*, vol. 260, no. 2–3, pp. 90–101, 2007.

[62] B. Wingelhofer *et al.*, “Preloading with L-BPA, L-tyrosine and L-DOPA enhances the uptake of [^{18}F]FBPA in human and mouse tumour cell lines,” *Appl. Radiat. Isot.*, vol. 118, pp. 67–72, 2016.

[63] S. Capuani *et al.*, “L-DOPA Preloading Increases the Uptake of Borophenylalanine in C6 Glioma Rat Model: A New Strategy to Improve BNCT Efficacy,” *Int. J. Radiat. Oncol. Biol. Phys.*, vol. 72, no. 2, pp. 562–567, 2008.

[64] S. Capuani *et al.*, “Boronophenylalanine uptake in C6 glioma model is dramatically increased by L-DOPA preloading,” *Appl. Radiat. Isot.*, vol. 67, pp. S34–S36, 2009.

[65] M. Papaspyrou, L. E. Feinendegen, and H. W. Müller-Gärtner, “Preloading with L-Tyrosine Increases the Uptake of Boronophenylalanine in Mouse Melanoma Cells,” *Cancer Res.*, vol. 54, no. 24, pp. 6311–6314, 1994.

[66] W. Yang *et al.*, “Effects of L-DOPA pre-loading on the uptake of boronophenylalanine using the F98 glioma and B16 melanoma models,” *Appl Radiat Isot*, vol. 88, pp. 69–73, 2014.

[67] S. Chandra, T. Ahmad, R. F. Barth, and G. W. Kabalka, “Quantitative evaluation of boron neutron capture therapy (BNCT) drugs for boron delivery and retention at subcellular-scale resolution in human glioblastoma cells with imaging secondary ion mass spectrometry (SIMS),” *J. Microsc.*, vol. 254, no. 3, pp. 146–156, 2014.

5 Determining the Uptake and Subcellular Distribution of 10-Boron in Glioblastoma Multiform Tumours (GBM) and Brain around Tumour (BAT) Tissue Biopsies Treated with ^{10}B Phenylalanine (BPA)

5.1 Introduction

In this Chapter, the bio-distribution of boron from BPA treatment at the cellular level in tissue imprint samples was explored using SIMS imaging. The instruments used were NanoSIMS and BioToF-SIMS with primary ion beams of Cs^+ (~ 400 nm diameter) and Au^+ (approximately 1 – 2 µm diameter) respectively, the instrumentation was described in Chapter 1.

The analysed samples were histological biopsy imprints from the GBM tumour and BAT tissues taken from patients with a high degree of brain tumour. Patients were administered with the ^{10}BPA drug *in vivo*. GBM biopsies were harvested from the tumour core where they are expected to contain many tumour cells, while BAT biopsies are not completely healthy tissue from the surrounding area of the tumour, containing very few infiltrated tumour cells. It is important that the ^{10}BPA reaches the infiltrating tumour cells in BAT that are responsible for the spread of the disease without accumulating in the adjacent healthy brain cells in order to preserve the latter from damage during BNCT radiotherapy.

The distribution of boron was imaged in samples, then the quantitative measurements of the secondary ion signals from the boron were extracted. The pharmacological accumulation was quantitatively compared between different tissue types. The results from the two instruments were compared in terms of imaging capabilities and quantification.

Note that the imprint samples were analysed before the cell culture samples presented in Chapter 4. There is a difference in the ion species measured between the samples of Chapter 5 and Chapter 4, as explained in section 5.2.2.1, and it is this difference which makes the normalisation method different between Chapters 4 and 5, as will be seen during this chapter. The results of Chapter 4 were presented before Chapter 5 as the primary cell cultures treated *in vitro* were used as a model system to help interpret the more heterogeneous tissue biopsy samples.

5.2 Experimental section

5.2.1 Sample preparation

The preparation of the imprint samples of GBM and BAT tissues biopsies which were administered with the ^{10}BPA drug *in vivo* was explained in section 3.2.2.2. Both types of imprints were prepared from two patients and summarized in **Table 5.1**.

5.2.2 SIMS analysis

5.2.2.1 NanoSIMS analysis

The NanoSIMS 50L instrument was explained in Chapter 1. At the beginning of each NanoSIMS session, the current of the 16 keV Cs^+ beam was measured in FCo with all D1 aperture sizes, then the samples were analysed in a manner almost identical to the cell culture samples in Chapter 4. The position of the seven detectors was tuned to detect the following secondary ions: $^{10}B^-$, $^{10}B^{12}C^-$, $^{12}C^{14}N^-$, $^{29}Si^-$, $^{31}P^-$, $^{32}S^-$ and $^{10}B^{16}O_2^-$. For some samples $^{10}B^{14}N^-$or $^{12}C^-$ were imaged instead of $^{10}B^{16}O_2^-$. The reason for choosing these species was explained previously in section 3.6.1 (the second stage -1st step). The instrument settings and HMR scans ensured no mass interferences between ions of interest and are shown in sections 3.4.1 and 3.6.2.2 respectively.

The imprint samples of GBM tumour and BAT tissues biopsies were analysed to determine the distribution of ^{10}B from the BPA drug at the cellular level as follows. ROI's of tissues were selected using the CCD camera in the NanoSIMS instrument alongside optical images of the samples captured before the experiment started using a reflective light microscope (see section 3.3). The ROI's were implanted using a dose 1×10^{17} Cs^+ ions/cm^2 of 16 keV with D1 = 0 (defocused beam) and rastered over an area of 100×100 µm^2. The reason for choosing implantation dose of 1×10^{17} ions/cm^2 was explained in section 3.6.1. After implantation, images were acquired by adding doses which ranged between 1.2×10^{15} and 2.7×10^{17} ions/cm^2 to the implanted ROI's with D1= 2, the beam current intensity ranged between 1 – 5 pA. The Cs^+ ion beam was rastered over an area ranging from 25×25 to 75×75 with 512 × 512 or 256×256 pixels and the dwell time per pixel was 1000, 2000 or 5000 µs. The analysis was stopped when a total of 100 counts of $^{10}B^-$ were measured when summing all the images to ensure sufficient signal for analysis of regions of interest. The resulting images were processed using the Fiji -ImageJ software, the software details were illustrated in section 3.4.2. The quantification and the graphs of results were created using OriginPro and Microsoft Excel software as illustrated in section 3.4.2.

5.2.2.2 BioToF-SIMS analysis

Imprint samples of GBM tumour and BAT tissue biopsies were analyzed by following the same methodology used in the analysis of cell culture samples in Chapter 4 with the BioToF-SIMS instrument. Further detail about the instrument was described in Chapter 1.

LMIG - Au^+ primary ion beam (Ionoptika Ltd., UK) at 20 keV with 5–9 nA current was used for analysis in pulsed mode and etching in DC mode. All the experiments were performed with 256×256 pixels, positive mode, and 100 ns pulse width of Au^+ beam to increase measurement sensitivity during image acquisition. The etching process was done once with a Au^+ beam with an ion dose of 1.9×10^{16} ions/cm^2 over a FoV of 400×400 μm^2 which was three times bigger than the FoV during imaging to avoid crater edge effects. During the imaging process secondary ion signals were collected from 21 layers of the surface before etching and then collected from 60 layers after etching. The imaging FoV was variable between 52×52 μm^2 and 150×150 μm^2, depending on the size of the area under study. The final result of spectrum and images were acquired from summing all 81 layers. The analysis took ~ 3 h 45 min with an ion dose accumulation of $2 - 6 \times 10^{14}$ ions/cm^2. The signals of $^{10}B^+$, $^{11}B^+$, $^{12}C^+$, $^{23}Na^+$, $^{28}Si^+$ and $^{39}K^+$ were selected from 1–150 Da spectral region to create two dimensional images using the BioToF software. All image sizes were calibrated using a 300 square copper mesh (3.05 mm – 83 μm pitch – Agar Scientific Ltd, UK). Each sample was analyzed 3–8 times with a new area every time. The graphs and quantification were made using OriginPro and Microsoft Excel as explained in the section 3.5.2.

5.2.3 NanoSIMS results and discussion

5.2.3.1 Cellular imaging of ^{10}B distribution from BPA drug in the imprint samples of GBM tumour and BAT tissue biopsies

This step represents the main experiment to achieve the objective of the research in assessing the imaging capabilities (spatial resolution and sensitivity) for the NanoSIMS instrument in determining the distribution of ^{10}B from the BPA drug at the cellular level in the tissue biopsy imprint samples and quantitative measurements of ^{10}B. **Table 5.1** summarizes the tissue biopsies studied and shows the symbolic abbreviation for each sample.

Table 5.1: Summary of the studied samples of the tissue biopsies and the abbreviation for each sample.

The imprints samples from the first patient (pt.1)	
Border around tumour tissue biopsy	BAT-pt.1
First tissue biopsy of GBM tumour	GBM-pt.1-1
First tissue biopsy of GBM tumour coated with Pt	GBM-pt.1-1-Pt
Second tissue biopsy of GBM tumour	GBM-pt.1-2
The imprints samples from the second patient (pt.2)	
Border around tumour tissue biopsy	BAT-pt.2
tissue biopsy of GBM tumour	GBM-pt.2

Before discussing the results of the analysis of the samples listed in **Table 5.1**, it is necessary to clarify the morphological differences between the brain tissue infected with GBM tumour and BAT tissues. **Figure 5.1** shows images of frozen sections of GBM tumour and BAT biopsies harvested from both patients and stained with haematoxylin and eosin (H&E), provided from the Molecular Neuro-oncology Laboratory in the Queen Elizabeth Neuroscience Centre, The University of Birmingham - UK. Tumour cells acquire purple colour due to nuclei dysfunction and chromatin condensation while healthy cells appear light pink due to protein balance in the cells, red blood cells show a dark pink colour, more detail about the H and E dyes in references [1][2].

Figure 5.1 -a shows the morphology of one of the sections of the BAT-pt.1 sample, where some tumour cells appear in the rim of the large, thick clumps and a few within the thinner clumps (purple colour), while the centre of the thick clumps is bloody (dark pink areas). **Figure 5.1 -b** shows one of the sections of the GBM-pt.1-1 sample that showed that all clumps have tumour cells (purple colour). Larger and thicker clumps are bloody in the centre (dark pink areas) but have tumour cells in the rim. In **Figure 5.1 -c** a thin imprint of the sample GBM-pt.1-2, contained sparsely spread individual tumour cells, and a reasonable number of tumour cells in the peripheral clumps (purple colour). **Figure 5.1 -d** shows one of the sections of BAT-pt.2, that appear as a thin imprint containing a few tumour cells spread in through the sample, as well as within the large clumps (purple colour). **Figure 5.1-e** shows a thin imprint of the GBM-pt.2 sample, containing tumour cells in all clumps, and a few tumour cells (purple colour) in the areas around the clumps.

Both images **5.1 - a** and **d** show that BAT tissues contain very few tumour cells that are difficult to distinguish from a large number of adjacent healthy cells. On the other hand, **5.1 b**, **c**, and **e** images show that GBM tumour tissues contain larger number of tumour cells compared to the BAT tissues (**a** and **d** images). The BAT and GBM tissues of patient-1 (**a - c** images) contain many cracks and necrosis, which are artefacts of the freezing process. Whereas the BAT and GBM samples of patient-2 appear to be better in terms of fewer cracks. All images in **Figure 5.1** show different thicknesses across the sample. The size of the tumour cells in tissues is approximately less than 10 μm [3].

It should be noted that the sections shown in **Figure 5.1** were not those analysed with NanoSIMS, which were analysed without H&E staining. Since the samples have different thicknesses based on the colour, the dwell time was selected to be 1000 μs/pixel for thin areas, 2000 μs/pixel in most sample areas, and 5000 μs/pixel for thick areas. The number of pixels used was mostly 512×512, but was changed to 256×256 when using 5000 μs/pixel to maintain a reasonable analysis time.

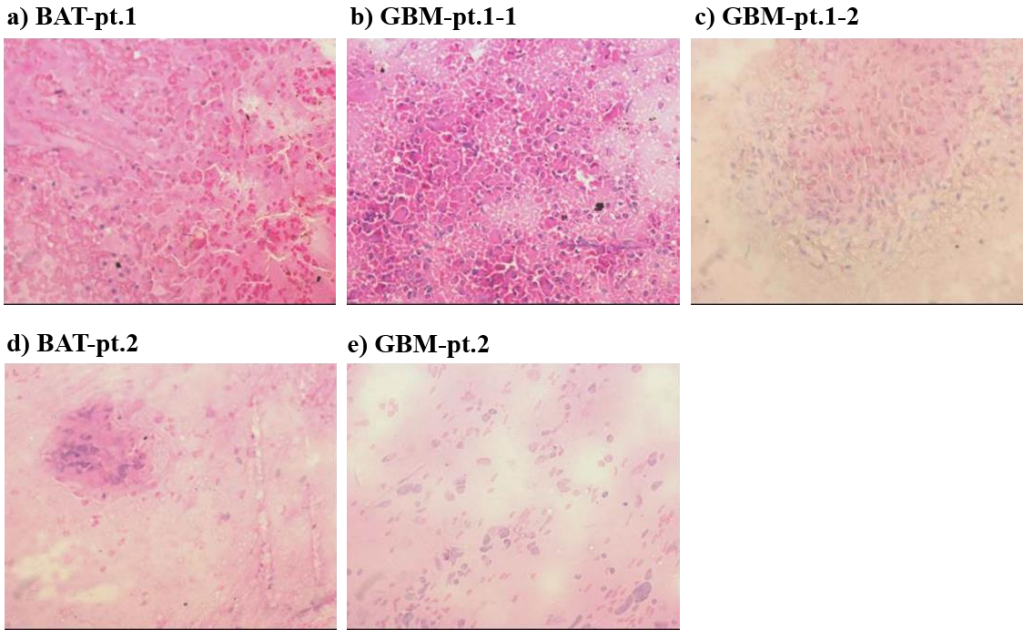

Figure 5.1: H&E-stained sections of brain tumour biopsies from patient-1 in panels **a-c** and patient-2 in panels **d-c**, more details about each imprint in the text.

5.2.3.1.1 BAT-pt.1 maps

The BAT-pt.1 sample is an imprint of border around tumour tissue biopsy harvested from the Patient-1. The sample is expected to contain very few infiltrating cells in healthy brain tissue in a similar manner to those shown in **Figure 5.1 -a**. ^{10}BPA treatment was delivered

to the patient *in vivo* during two hours. The concentration of ^{10}BPA in the entire biopsy after removal from patient-1 is 27.9 mg/kg measured by ICP-MS [3], this concentration is within the lethal BNCT dose of ~15–30 mg/kg [4]. A comprehensive image of the sample was captured on the silicon substrate using a reflective light microscope and presented in **Figure 5.2**. The captured image shows 12 different areas analysed within coloured squares. Seven areas (black squares) were excluded from the results for various reasons explained in section 5.2.3.2, results were extracted from only 5 regions (blue squares). Following is a discussion of the results of one of the areas, indicated with a red arrow, for illustrative purposes. All areas were included in quantitative data analysis in section 5.2.3.3.

The CCD camera in the NanoSIMS was used side by side with **Figure 5.2** to select the analysis area. The analysed areas were selected based on the following criteria; they must be flat, containing cells, essentially free from cracks and areas were selected from both thin and thick parts in an attempt to find tumour cells and obtain a successful analysis. The secondary ion maps resulting from NanoSIMS analysis of the selected area are shown in **Figure 5.3**. Maps show contrast in the distribution of ions across the tissue imprint.

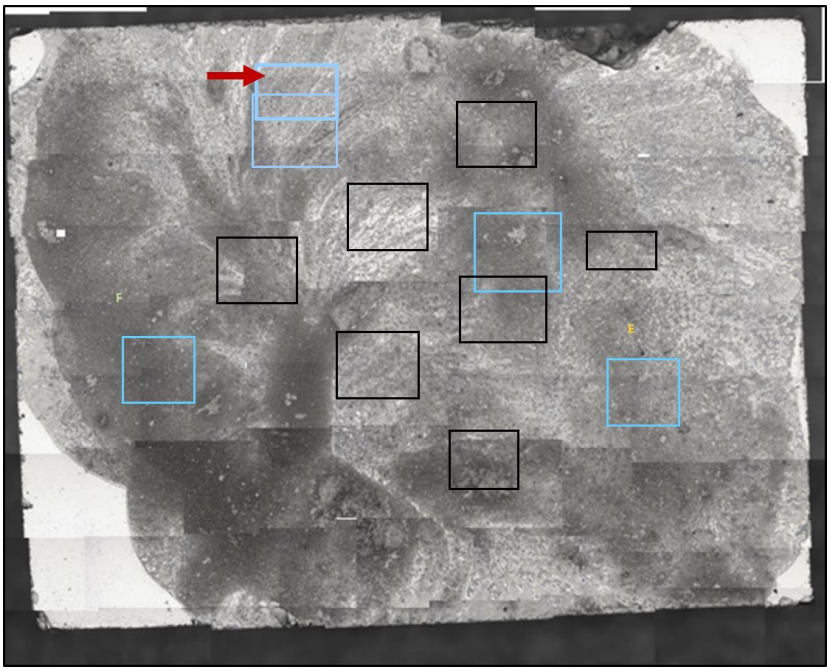

Figure 5.2: Image of freeze-dried BAT-pt.1 sample on the 5×7 mm^2 Si substrate captured using a reflective light microscope, a sequence of snapshots for sample were taken and then aligned to form a complete image of the sample. The image showing 12 areas analysed within the coloured squares. Results were extracted only from the 5 blue squares. Arrow refers to the area presented in the discussion.

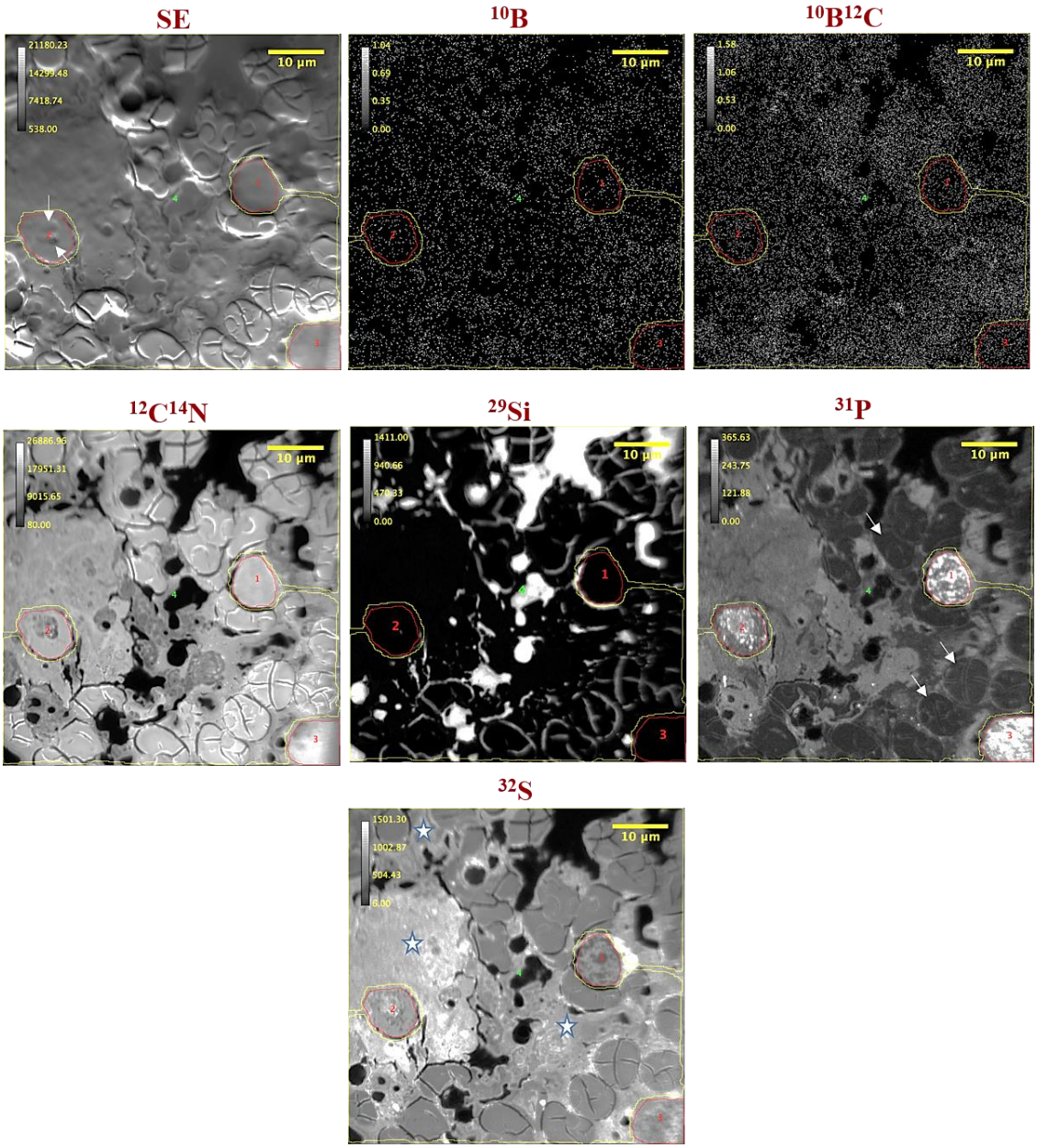

Figure 5.3: NanoSIMS maps for the imprint sample of BAT-pt.1 biopsy that was administered with ^{10}BPA *in vivo*. SE: secondary electron map shows the general morphology of the analysed area. The maps of negative secondary ions: ^{10}B, ^{10}B^{12}C, ^{12}C^{14}N, ^{29}Si, ^{31}P and ^{32}S respectively show the ion distributions across the sample. $^{10}B^{16}O_2^-$ was also mapped but not presented due to uncertainty of the peak due to mass interferences. ROI's 1, 2, and 3 identify cells (red lines). ROI 4 shows the rest of the sample parts (yellow line). The arrows in the SE map point to the topography in the cell-2. The arrows in P map indicate some unknown features. The stars (*) on the S map distinguish the connective tissue areas. The FoV is 60×60 µm^2 with 512×512 pixels. Analysis dose in images = 3.23×10^{15} ions/cm^2.

The SE map shows the general morphology of the area where the different features can be distinguished in the sample and exposed areas of silicon substrate, and also shows that the analysis area is almost flat. The Si map shows the areas of the substrate covered by the sample, and the locations of the cracks and holes in the sample where the high signal intensity of the Si is shown. These cracks and holes are mostly resulted from the freezing process, and have also been observed in the stained sections with H&E in **Figure 5.1 -a** Therefore, the Si map is used as an auxiliary guide to avoid open areas of the sample on Si substrate during the identification of the ROIs. Furthermore, the silicon map confirms that the cells of interest did not sputter away completely during image acquisition by adding a dose of 3.23×10^{15} ions/cm^2 of Cs^+ in this area.

The CN^-, P^- and S^- are commonly used in biological imaging to locate cells as described below. As observed in **Figure 5.3**, the CN^- is distributed almost uniformly across the imprint with very low contrast compared to other ion maps. The CN^- signal intensity is higher than the rest of the ions signals, as found by comparing the total summed intensities from the image for all ions. The high signal of CN^- from biological samples typically means it can be used to show features at the cellular and subcellular level in cell cultures samples, making it important and frequently used when imaging biological samples [5]–[7]. The CN^- distribution in the sample BAT-pt.1 is somewhat similar to the pattern of its distribution in the fibrosarcoma tumour tissue sections from mice shown in **Figure 2.18** that were studied by Proetto *et al.* [8]. CN^- signals originate mainly from proteins and amino acids existing in the cell structure and tissues between cells [9]–[11].

The P^- map shows the localisation of phosphorus-containing molecules such as phospholipids, phosphorylated-proteins and nucleic acids rich in phosphate groups [12]–[14]. Therefore, the high signal intensity of the P^- is an indicator of cell location and the nuclei at the subcellular level, this is consistent with many imaging studies that used the P signal for the same purpose [8][12][15][16]. The size of the tumour cells in the tissue is less than approximately 10 µm, as explained in section 5.2.3.1. Accordingly, the P map shows three cells (and not just nuclei) in the imprint sample numbered of 1-3 (red lines).

The sulfur ion map shows a heterogeneous distribution of S^- signals across the imprint. In most areas of the sample, the intensity of S^- signals is higher than P^- and less than CN^-. The S signal is usually generated from sulfur-containing amino acids such as methionine and glutathione, which in turn are necessary for the protein synthesis [17][18].

In both the P and S ion maps, the three highlighted cells appear somewhat different in their P^- and S^- distribution pattern. In Cell-1, Phosphorus ion was more concentrated in the upper left inner edge of the cell and extended to the right edge, which may indicate the cell membrane or some topography originating from the cracks around the cell or both. The high signal intensity of the P^- also appears as a bright spot in the centre of cell-1, which may refer to the nucleus site (under marker 1). The rest of the cell structure contained less intensity of P^- and possibly refers to cell cytoplasm. The S^- signal also localised within cell-1 with the P^- signal, but the distribution is reversed, where the S^- signals are lower in intensity in sites of high P^- intensity at the edge surrounding the cell and nucleus, while the S^- signal intensity is higher than the P^- in the cytoplasmic regions. The distribution pattern of the phosphorus-sulfur ions signals in what appears to be the nucleus and cytoplasm in cell-1 is similar to their distribution between cells compartments in the cell culture samples which were discussed in Chapter 4, for example **Figure 4.9**. In addition, Legin's *et al.* study showed co-localisation between P^- and S^- in a human colon cancer cell line, which is somewhat similar to the distribution pattern of P^- and S^- signals in cell-1, **Figure 2.16** [15].

Cell-2 in the P^- map appears at first glance to have a large nucleus of high P^- signals intensity, but this nucleus contains some topography that can be observed on the SE map (arrow), the low CN^- signal and high S^- signal were also observed at the site of this topography. The differing distribution of P^- in cell-2 compared with that in cell-1 makes it difficult to identify from the phosphorus in cell-2 weather it was one nucleus or several nuclei in the case of the proliferating cell, while the area surrounding the P^- signals in cell-2 maintains a similar appearance to cell-1 in terms of CN and S ions signals intensity which in turn refer to the cytoplasm. Moreover, the P^- signal in cell-2 may represent a nucleus with a distorted membrane and blobby shape, which means that cell-2 may be one of the apoptotic cells.

The characteristics of the apoptotic cells are: an irregular nuclear membrane, DNA fragmentation and a condensed nucleus [19], membranes with blobby shape [20], loss of nucleus due to DNA degradation of the nucleus and decay to several separated chromatin bodies or small nuclear units [19]. Sometimes the cells appear as a fragmented area of the nuclear membrane [21], the internal general features become quite unclear as a result of the collapse of the proteinaceous cytoskeleton while cells maintain a relatively circular general shape [22]. All the BAT and GBM tumour tissues contain a large number of apoptotic cells due to very rapid cell growth with hypoxia and nutrient deficiency leading to cell stress and then apoptosis [3][23].

Cell-3 also looks like an apoptotic cell where a high signal of P^- accumulated with a lower signal of S^- in an irregular form indicating the possibility of a distorted nucleus.

The CN, S and P ions maps show that the area surrounding the cells (within the yellow line) has cracks and holes resulting from the freezing process, also includes two features. The first, unknown features are phosphorus ion depleted, but show high signal intensity of CN^- (indicated by arrows in the P^- map). The second is a tissue that connects the contents of the imprint, showing a weak P^- signal in grey and high signals of CN^- and S^- with some contrast in intensity from one side to another in the S^- map (stars in S^- map), this tissue is composed mainly of proteins such as collagen [24][25].

As for the distribution of ^{10}B from BPA in the tumour cells (active and apoptotic) infiltrating to the BAT tissue, the $^{10}B^-$ map showed signals of $^{10}B^-$ in the three cells. However, it is difficult to determine localisation of $^{10}B^-$ signals due to the small size of cells in FoV 50×50 μm^2, subcellular detail is not sufficiently clear or reliable, and there is a low intensity of $^{10}B^-$ signal detected in the sample compared with other ions intensities. The accumulation of ^{10}B in the unknown features in the outer region surrounding the cells (within the yellow line) was higher than in the tumour cells but it is not clear why this is the case. The $^{10}B^{12}C^-$ signal shows a similar distribution pattern to $^{10}B^-$ in the imprint (inside and outside the cells). The summed intensities of $^{10}B^{12}C^-$ signal from cells were ~ 2 times higher than summed intensities of $^{10}B^-$ as is evident from the analysis of normalised intensities in BAT-pt.1 sample, this means that the $^{10}B^{12}C$ fragment has relative stability and/or a higher ionization probability than the atomic ^{10}B. Hence the $^{10}B^{12}C^-$ gives a clearer image than B^-, more details on $^{10}B^-/^{12}C^{14}N^-$ and $^{10}B^{12}C^-/^{12}C^{14}N^-$ ratios are discussed in 5.2.3.3. The distribution pattern of ^{10}B and $^{10}B^{12}C$ ions was similar in all analysed areas (n = 5) of BAT-pt.1 sample. Most of analysed areas contained apoptotic cells only.

It is clear that the BAT-pt.1 sample morphology is more complicated than the BAT cell cultures samples (D group) because of cellular variety in the tissue imprint, the small size of the cells, and the small number of infiltrating cells to BAT-pt.1 tissue, makes it difficult to find tumour cells and distinguish cell compartments accurately. It was therefore not possible to determine any preferential accumulation of ^{10}B and $^{10}B^{12}C$ ions to subcellular features. The preferential accumulation for ^{10}B of BPA in tumour cells, especially in nuclei areas, is an important factor for increasing the chances of success of BNCT radiotherapy in the elimination of tumour cells with minimizing damage on adjacent healthy cells [4], [26]–[28] but this could not be determined in this sample.

5.2.3.1.2 GBM-pt.1-1 maps

The GBM-pt.1-1 sample is an imprint of the tissue biopsy of the glioblastoma multiforme tumour core harvested from patient-1, and is expected to contain a large number of tumour cells as explained in section 5.2.3.1 and **Figure 5.1 -b**. This sample was administered with BPA by *in vivo* treatment for 2 hours. The concentration of BPA in the entire biopsy after removal from patient-1 is 33.4 mg/kg as measured by ICP-MS [3], which is higher than the lethal BNC threshold (~15–30 mg/kg) [4]. **Figure 5.4** shows an overview image of the sample on the silicon substrate that was captured using a reflective light microscope, the image shows 11 different areas analysed within coloured squares. 10 areas (black squares) were excluded from results for different reasons mentioned in section 5.2.3.2, and the result was extracted from only one successfully imaged area (within the blue square) and discussed below.

Figure 5.5 shows the secondary ion distribution maps produced by the NanoSIMS analysis of the area within the blue square, chosen prior to NanoSIMS analysis using the CCD camera in the NanoSIMS alongside with **Figure 5.4**.

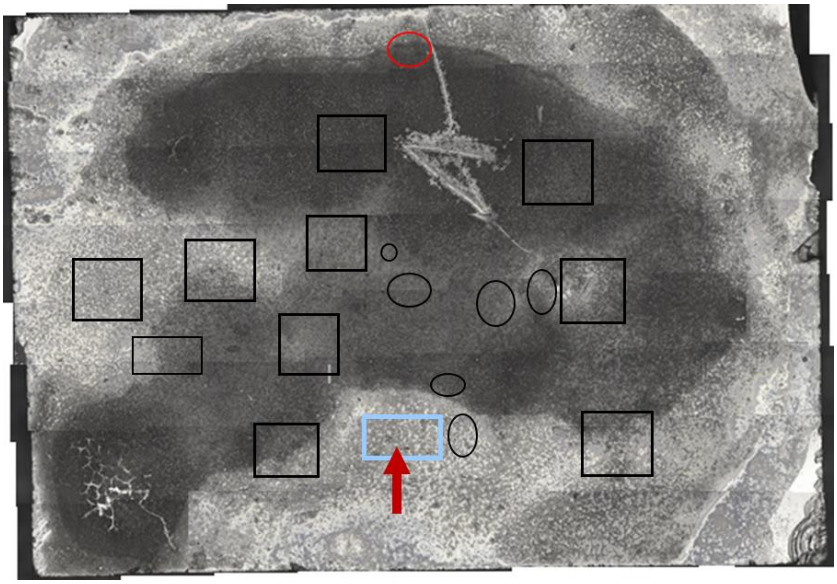

Figure 5.4: Image of freeze-dried GBM-pt.1-1 sample on the 5×7 mm^2 Si substrate captured using a reflective light microscope. A sequence of images were taken and then aligned to form a complete image of the sample. The image shows 11 areas analysed within the coloured squares. The NanoSIMS result presented for GBM-pt.1-1 was extracted from the blue square. The 7 areas highlighted with black circles were analysed after covering the sample with a 10 nm layer of Pt, the result extracted from the red circle is presented in the GBM-pt.1-1-Pt discussion.

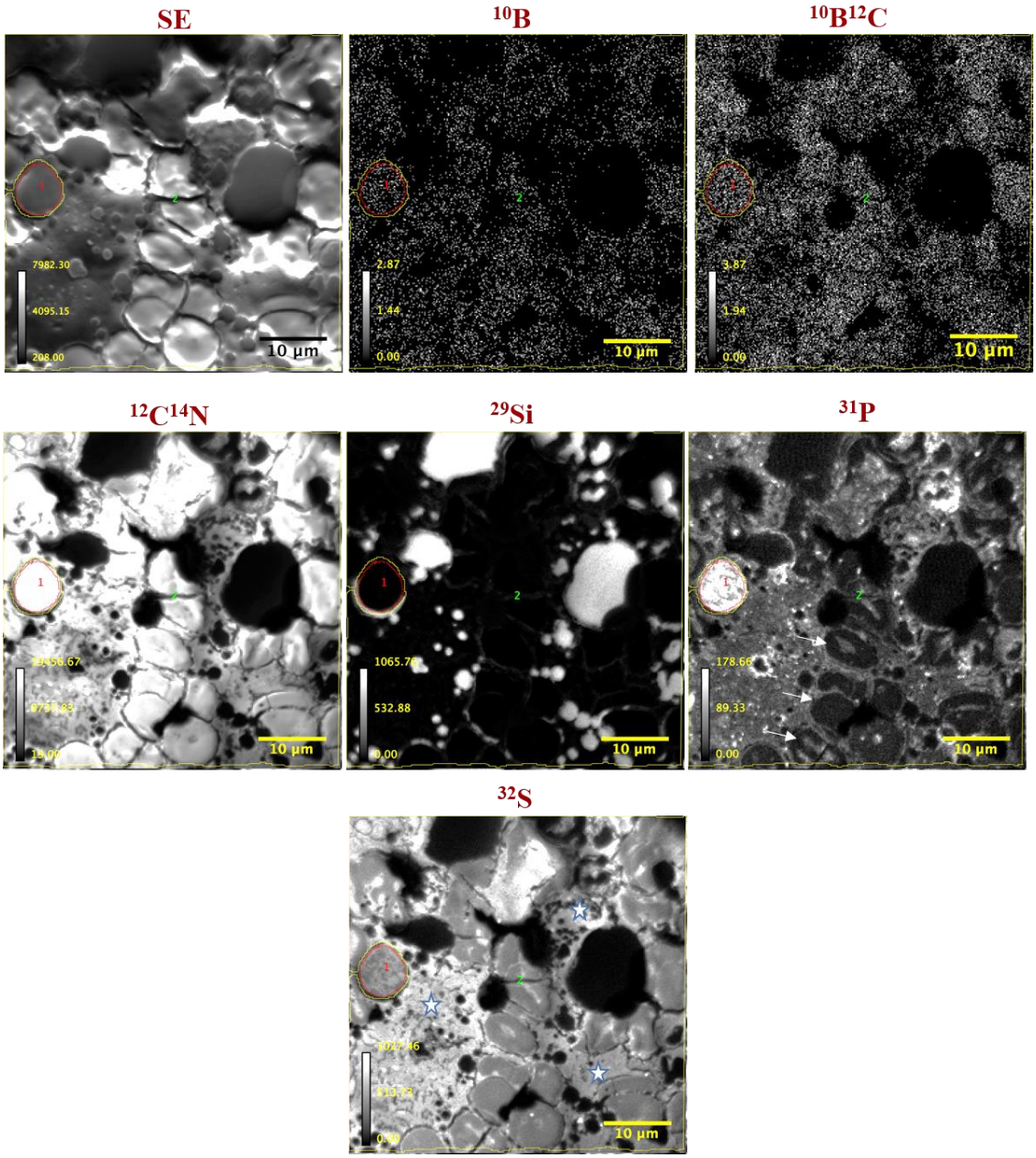

Figure 5.5: NanoSIMS maps for the imprint sample of GBM-pt.1-1 biopsy that was administered with ^{10}BPA *in vivo*. SE: secondary electron map showing the general surface features of the analysed area. The maps show the cellular distribution of negative ions: ^{10}B, ^{10}B^{12}C, ^{12}C^{14}N, ^{29}Si, ^{31}P and ^{32}S respectively across the sample. ^{10}B^{16}O$_2^-$ was also mapped but not presented due to uncertainty of the peak due to mass interferences. ROI1-cell (red line) and ROI2- the rest of the sample parts (yellow line). The arrows in the P map indicate unknown features. The stars (*) on the S map distinguish the connective tissue areas. The FoV is 50×50µm^2 with 256×256 pixels. Analysis dose in images = 1.23×10^{15} ions/cm^2.

The SE map shows the general shape of the analysed area, the different surface features, and confirms that the analysis area is almost flat. The Si map shows the substrate area covered by the sample where the silicon signal disappears, and shows that the area has holes and cracks where the high silicon signals appear, helping to avoid undesirable features during selection of ROIs in the imprint and extraction of quantitative measurements. The cracks in the imprints of GBM-pt.1-1 sample were also observed in sections stained using H&E in **Figure 5.1 -b**. The silicon map also confirms that the cell of interest was not sputtered away during the acquisition of the images by adding a dose of 1.23×10^{15} ions/cm^2 of Cs^+ beam to this area.

The ion maps of CN, P and S provide a distribution pattern across the imprint that is almost identical to the BAT-pt.1 sample. The CN^- map shows almost uniform distribution across the imprint with higher signal intensity than the rest of the ions signals as is evident from comparing the total intensities of ions summed from cells. The source of the high signal intensity of CN^- is the cell structure and tissues between cells rich in proteins and amino acids [9]–[11], and the CN^- signals follow the general features of the imprint at the cellular level.

The P ions were distributed heterogeneously across the sample. The high accumulation of P^- signal shows the location of cell-1 (red line) at the cellular level because the cell structure contains phosphorus-rich molecules such as phospholipids and DNA [12]–[14]. The S^- map shows higher signal intensity than P in most sample areas, with a heterogeneous distribution of S^- signals across the sample. The source of S signals is usually the sulfur-containing proteins [17][18].

In cell-1 (red line), P^- signals are randomly distributed with high intensity within the cell structure. S^- signal has a similar overall distribution to P^- signal but appears to be less intense at high intensity sites of P^- which in turn confirms the location of the cell. The unclear localisation pattern of P^- and S^- signals inside the cell does not allow one to distinguish cell compartments (nucleus and cytoplasm), indicating a possible fragmentation of the nucleus into several separate chromatin units due to DNA degradation, however the cell maintains a round shape. The features shown in cell-1 may indicate an apoptotic cell, the characteristics of the apoptotic cells were illustrated in section 5.2.3.1.1.

The area around cell-1 (yellow line) consists of: cracks, holes and unknown features. These unknown features have a high signal of CN^- and low P^- signals (the arrows in the P map).

There is also extracellular tissue which appears with low signal intensity of P^- and high signal intensity of the CN^- followed by the varying signal of S^- (stars on the S map).

In terms of boron localisation, maps show that $^{10}B^-$ and $^{10}B^{12}C^-$ ions are quite homogenously distributed within cell-1 as well as in the area surrounding cell from the outside (yellow line) similarly to the BAT-pt.1 sample. $^{10}B^-$ and $^{10}B^{12}C^-$ ions do not show any preferential accumulation within the cell structure, which may be due to the nucleus fragmentation into several chromatin bodies scattered in the cytoplasm. The total signal intensity of $^{10}B^{12}C^-$ is ~ 3 times more than total $^{10}B^-$ intensity in the cell as is evident from the analysis of normalised intensities in GBM-pt.1-1 sample, more details on $^{10}B^-/^{12}C^{14}N^-$ and $^{10}B^{12}C^-/^{12}C^{14}N^-$ ratios are discussed in 5.2.3.3.

In comparison to BAT-pt.1, it was observed that cell-1 in the GBM-pt.1-1 sample in **Figure 5.5** has normalised total intensities of $^{10}B^-$ and $^{10}B^{12}C^-$ signals that are ~ 7 times higher than the cells in the BAT-pt.1 sample in **Figure 5.3**, which indicates that for the studied cells BPA uptake in tumour core was higher than the border tissue surrounding the tumour. The measured bulk concentrations in both biopsies using ICP-MS was 33.4 mg /kg in GBM-pt.1-1 sample and 27.9 mg /kg in the BAT-1 sample of the same patient, these bulk values are very similar but only give bulk values whereas the NanoSIMS data is specific for tumour cells and hence can explain the difference. Despite differences in the detected signals intensity of $^{10}B^-$ and $^{10}B^{12}C^-$ between the GBM-pt.1-1 and BAT-pt.1 samples, they were similar in not showing a specific accumulation site for boron ion signals within the cell and $^{10}B^-$ and $^{10}B^{12}C^-$ signals were also detected outside the cells.

5.2.3.1.3 GBM-pt.1-1-Pt maps

In an attempt to improve the electrical conductivity of the GBM-pt.1-1 sample and overcome the charging that happened in some areas, a thin layer of 10 nm platinum was coated over the sample before further SIMS analysis, which may help to better determine sites of ion distribution by improving signal intensity. **Figure 5.4** shows 7 areas analysed, marked with circles that were selected before analysis using the CCD camera. 6 areas (black circles) were excluded from the results for various reasons as mentioned in section 5.2.3.2, and the result was extracted from only one successful area (red circle) and discussed below.

In **Figure 5.6**, the SE map shows a clear image of the general surface features and that the sample is almost flat. The Si map shows the locations of the holes and the cracks in the imprint sample, as well as the substrate area covered by the sample, which useful in identifying the cells of interest while avoiding undesirable features. The silicon map also

confirms the integrity of the cell structures of interest during image acquisition with a dose of 1.83×10^{16} ions/cm^2 in this area.

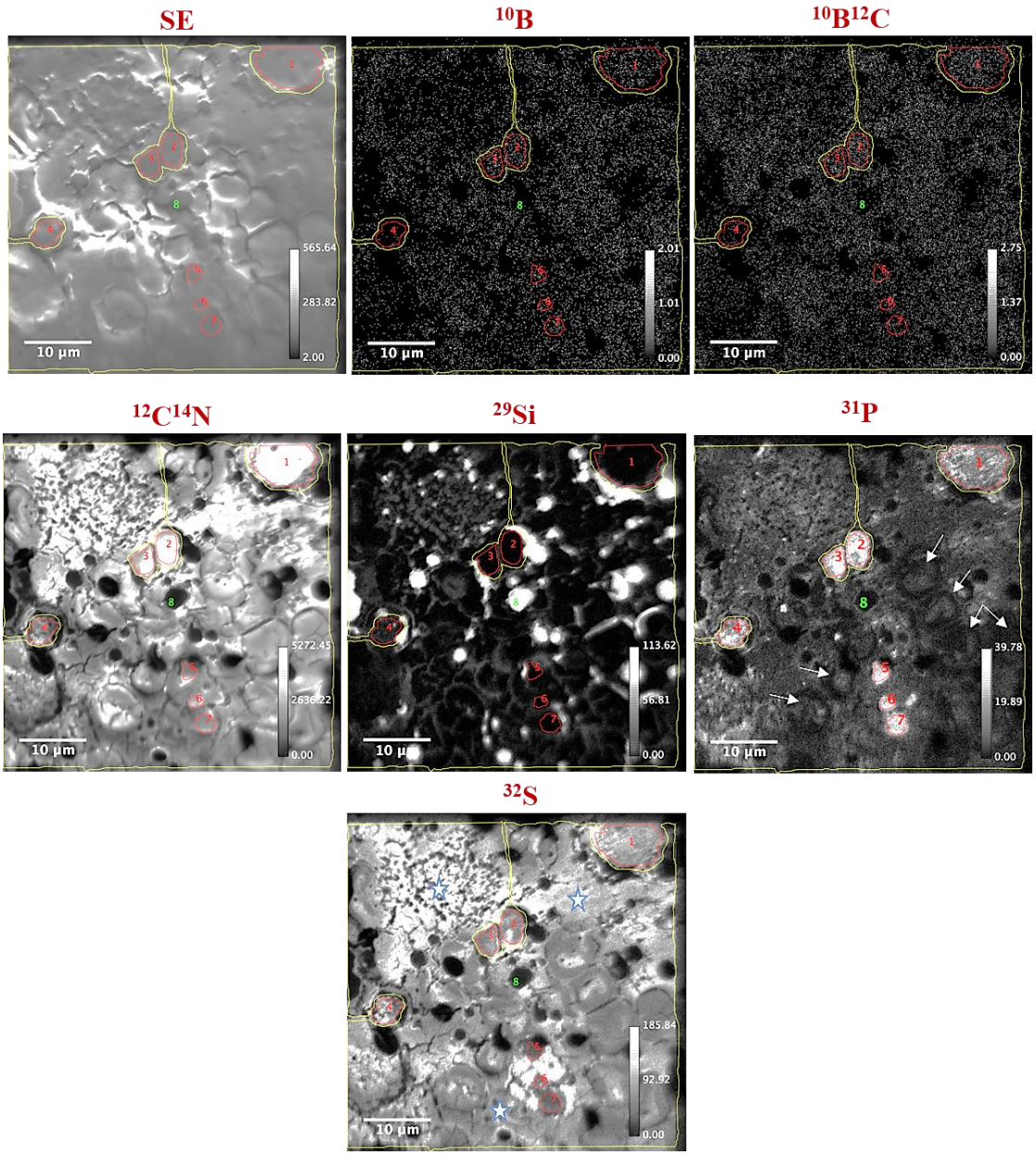

Figure 5.6: NanoSIMS analysis for the imprint sample of GBM-pt.1-1-Pt. SE: secondary electron map shows the general shape of the analysed area. SIMS maps reveal the distribution of negative ions respectively: ^{10}B, ^{10}B^{12}C, ^{12}C^{14}N, ^{29}Si, ^{31}P and ^{32}S within the sample. ^{10}B^{14}N$^-$ was also mapped but not presented due to uncertainty of the peak due to mass interferences. ROI's 1, 2, 3 and 4-cells (red lines), ROI's 5, 6, and 7 - unknown features (red lines). ROI8- the rest of the imprint (yellow line). The arrows in P map point to some unknown features. The stars (*) on the S map distinguish the connective tissue areas. The FoV is 50×50 µm^2 with 512×512 pixels. Analysis dose in images = 1.83×10^{16} ions/cm^2.

Ion maps show that CN^-, P^- and S^- were distributed across the imprint in a manner similar to the maps of the BAT-pt.1-1 and GBM-pt.1-1 samples. The CN^- map had high ion signal intensity compared with other ions and was distributed almost uniformly across the imprint. The P^- map shows a high accumulation of ions in specific areas of the sample numbered from 1-7 (red lines), which in turn may refer to the locations of the cells. S^- signals are distributed heterogeneously across the imprint. This pattern in the distribution of CN^-, P^- and S^- was illustrated in further detail during the BAT-pt.1 sample discussion.

Regarding areas numbered 1-7; area-1 appears to be an apoptotic cell because P^- signals are distributed irregularly with varying signal intensity throughout the cell structure, and no features are shown distinguishing the cell compartments from each other, indicating the loss of the nucleus and its degradation to several separate chromatin bodies. Moreover, cell-1 maintains a round general shape. More detail about the characteristics of the apoptotic cell is given in the section 5.2.3.1.1. Areas 2 and 3 may originally have been one cell which has divided into two parts under the effect of the freezing process and emergence of cracks, or a cell that has been subjected to fragmentation during a proliferation stage for tumour cell or a disassembly phase for apoptotic cell to apoptotic bodies. In all cases, it is difficult to determine the identity of these cells reliably. In area 4, the cell identity also cannot be determined due to the small size of the cell and cracks in its surrounding edges. The high signal intensity of P^- in area 4 may indicate the site of the nucleus in a tumour cell or nucleus with irregular membrane in apoptotic cell. Areas 5-7, although containing high P^- signals and very low S^- signals, do not appear as cellular structures in the CN^- and SE maps, and differ in their form compared with cells1-4, so they were considered as unknown features. The quantitative data for the accumulation of $^{10}B^-$ and $^{10}B^{12}C^-$ were obtained from cell 1-4, although the cells identity was not strictly defined in 2-4, while the unknown features in areas 5-7 were excluded from results.

The area outside the cells has holes, cracks, and connective tissue showing a high signal of CN^- while P^- signals are very low (* on the S map). In addition, unknown features containing CN^- and S^- but an absence of P^- signals (arrows in the P map) are present.

Maps of the boron ions showed a semi-homogeneous distribution of $^{10}B^-$ and $^{10}B^{12}C^-$ signals within cells 1-4 and also in the surrounding area of the cells (within the yellow line). The lack of clear cell compartments does not allow determination of the preferred accumulation sites of boron ions in cellular structures. The total intensity of the $^{10}B^{12}C^-$ signals accumulated in the cells is ~2 times higher than the total $^{10}B^-$ signal intensity as found from the analysis of normalised intensities in GBM-pt.1-1-pt sample, which are discussed in more

detail in section 5.2.3.3. Therefore, the $^{10}B^{12}C^-$ could provide a clearer image than $^{10}B^-$. However, the intensity of boron signals in the **Figure 5.6** is close to those from the same sample before being covered with 10 nm Pt in **Figure 5.5**, which in turn indicates that coating with platinum did not have a significant and clear effect in improving ion yield of boron from the sample, nor increase the number of successful areas of analysis. The distribution pattern of boron signals at the cellular level in the sample GBM-pt.1-1 before and after platinum coverage was similar. By comparing the normalised total intensities of the boron signals summed from cells between the GBM-pt.1-1-Pt and the BAT-pt.1 samples in **Figures 5.6 and 5.3** respectively, it is clear that the intensity of the $^{10}B^-$ and $^{10}B^{12}C^-$ signals in GBM-pt.1-1-Pt is ~ 9 times higher than BAT-pt.1, confirming again that the uptake of BPA in cells of tumour area is higher than the tumour cells infiltrating to BAT area.

5.2.3.1.4 GBM-pt.1-2 maps

GBM-pt.1-2 sample is an imprint of a different biopsy taken from another site of the brain tumour for the same patient-1 which was administered with BPA *in vivo* for one hour. The concentration of BPA in the bulk biopsy after harvest is 48.1 mg/kg measured by ICP-MS [3], which is much higher than the lethal BNC threshold (~ 30 mg/kg) [4] and from those measured in GBM-pt.1-1 and BAT-pt.1, indicating that the BPA uptake may vary depending to the anatomical location of the biopsy. An image of the sample on the Si substrate in Figure 5.7, showing the location of 16 analysed areas within the coloured squares, 12 areas (black squares) were excluded from the results for reasons explained in the section 5.2.3.2. Results were extracted from only 4 areas (blue squares), the following is a discussion of the results of one of these areas shown in **Figure 5.8**, from the blue square marked with a red arrow in **Figure 5.7**. The SE map shows the general morphological features of the imprint and confirms that the analysis area is flat, while the Si map shows the area of the substrate covered by the imprint, and the cracks locations in the analysis area. These cracks were previously observed in another imprint of the same sample stained with H&E in **Figure 5.1 -c**. The Si map also showed that the areas of interest (red lines) were not completely sputtered away during the acquisition of images by adding a dose of 2.72×10^{17} ions/cm^2 in this area.

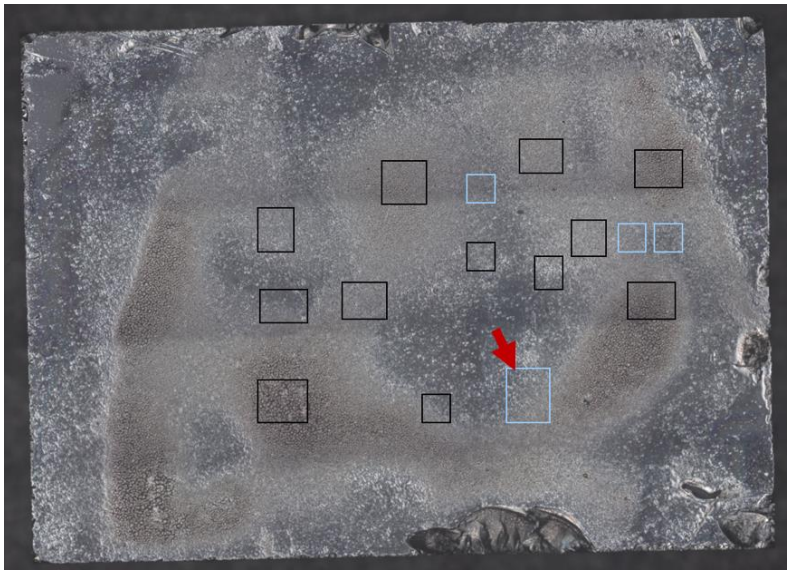

Figure 5.7: Image of freeze-dried GBM-pt.1-2 sample on the 5×7 mm^2 Si substrate captured using a reflective light microscope. The image shows 16 areas analysed within the squares. The results were extracted only from the 4 blue squares. Arrow refers to the area presented in the discussion.

Ion distribution maps for CN^-, P^- and S^- at the cellular level are similar to that in all previous imprint samples. The CN^- map shows a relatively uniform distribution across the imprint with higher signal intensity than the rest of the ions as found by comparing the total intensities of ions that summed from cell. P^- signals were heterogeneously distributed across the imprint and were highly accumulated in areas 1 and 2 (red lines) and indicate the structures of cells rich in phosphorus-molecules. S^- signal intensity appears higher than P^- and less CN^- in most imprint sample areas. Further details on the CN^-, P^- and S^- distribution pattern are described in section 5.2.3.1.1.

The cell-1 (red line) appears to have characteristics of an apoptotic cell in that it is not possible to distinguish the features of the nucleus within the cell, indicating a possible fragmentation of the nucleus into multiple chromatin bodies that then spread in the cytoplasm. This is confirmed by phosphorus signals that are distributed unevenly with high signal intensity throughout the cell structure. Despite the collapse of the proteinaceous cytoskeleton, the overall shape of the cell remains round. Area 2 (red line) shows part of another nearby cell where high and varying signals of phosphorus accumulated, but it is not possible to determine whether this is a tumour cell or apoptotic cell because the visible part of cell in the FoV is too small.

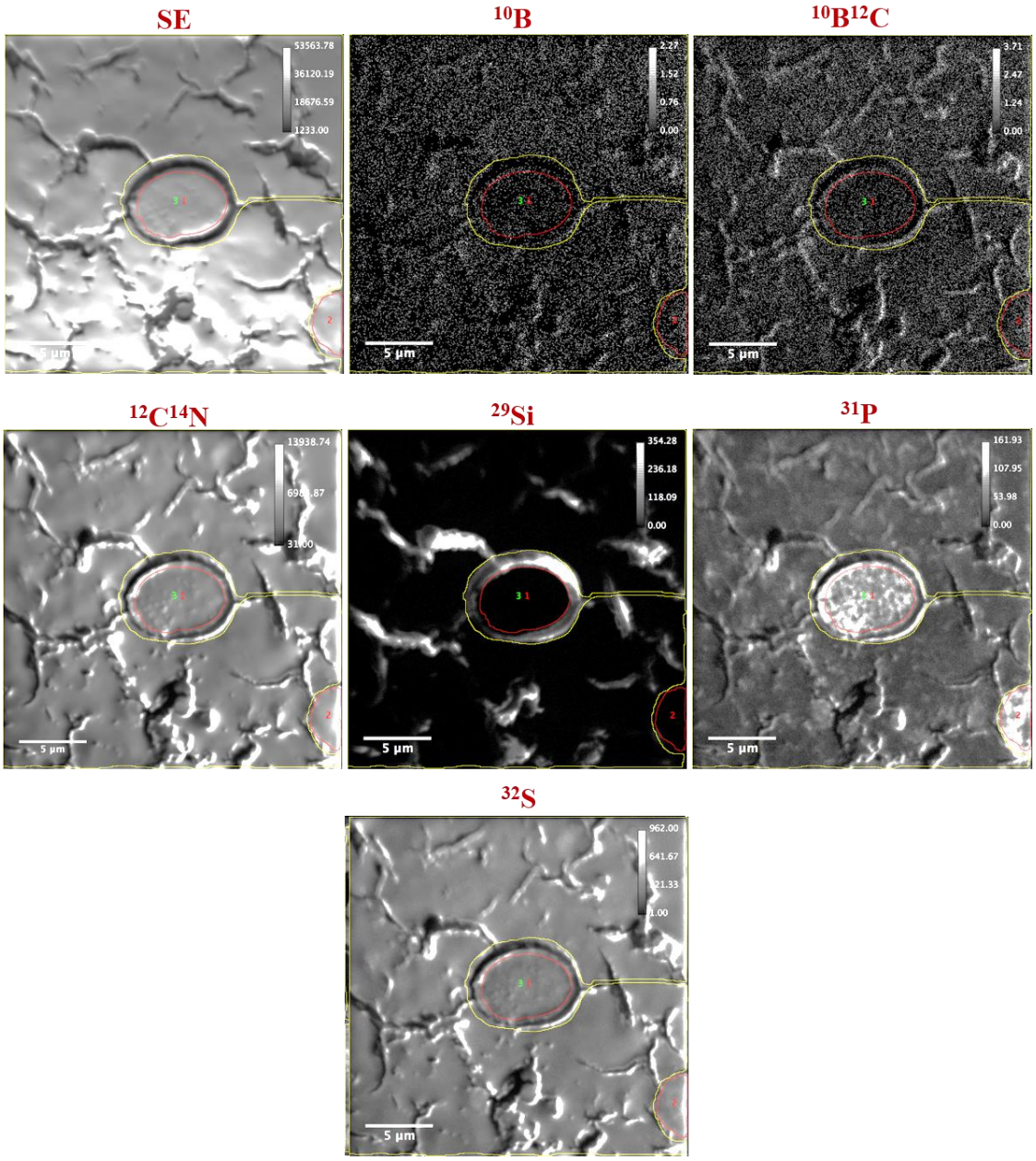

Figure 5.8: NanoSIMS maps for the imprint sample of GBM-pt.1-2 biopsy. SE: secondary electron map shows the general surface features of the analysed area. The maps show the cellular distribution of negative ions: ^{10}B, $^{10}B^{12}C$, $^{12}C^{14}N$, ^{29}Si, ^{31}P and ^{32}S respectively within the sample. $^{10}B^{14}N^-$ was also mapped but not presented due to uncertainty of the peak due to mass interferences. ROI's 1&2-cells (red line) and ROI3- the rest of the imprint (yellow line). The FoV is 25×25 µm^2 with 512×512 pixels. Analysis dose in images = 2.72×10^{17} ions/cm^2.

The area surrounding the cells (within yellow line) represents the tissue that binds the contents of the sample where high CN^-, S^- and low P^- signals are localised. This area contains also cracks resulting from the freezing process. In the area around the cells in sample GBM-pt.1-2, the holes and unknown features that were present in the previous imprint samples were absent, indicating that the sample morphology may be vary depending to the anatomical location of the biopsy.

As for the distribution of boron at the cellular level, both $^{10}B^-$ and $^{10}B^{12}C^-$ ions are distributed semi-homogeneously within cells-1 and 2, as well as in the surrounding area of the cells (yellow line). The total intensity of $^{10}B^{12}C^-$ signals across the cells is ~ 2 times higher than total intensity of $^{10}B^-$ signals as evident from the analysis of normalised intensities from GBM-pt.1-2 sample in 5.2.3.3. All areas (n = 4) analysed in the sample GBM-pt.1-2 gave a similar distribution of $^{10}B^-$ and $^{10}B^{12}C^-$. The distribution pattern of boron ions across the imprint GBM-pt.1-2 is similar to that obtained from the GBM-pt.1-1 sample before and after platinum coverage in **Figures 5.5** and **5.6**.

By comparing the normalised total intensities of the boron ions summed from cells in the samples GBM-pt.1 as seen in the **Figures 5.5, 5.6** and **5.8** with the BAT-pt.1 sample in **Figure 5.3**, It was observed that the signal intensity of $^{10}B^-$ and $^{10}B^{12}C^-$ in GBM-pt.1-2 is close to the GBM-pt.1-1 and the GBM-pt.1-1-pt.. All the GBM-pt.1 samples showed signal intensities of boron ions higher than BAT-pt.1 by a factor of ~ 8, which confirms that the uptake of boron ions from BPA in cells of tumour tissue was higher than tumour cells in BAT tissue, these observations in turn follow the same trend as the ICP-MS concentrations measured in the biopsies mentioned at the beginning discussion of each sample. More details on $^{10}B^-/^{12}C^{14}N^-$ and $^{10}B^{12}C^-/^{12}C^{14}N^-$ ratios are discussed in 5.2.3.3.

5.2.3.1.5 BAT-pt.2 maps

The BAT-pt.2 sample is an imprint of border around tumour tissue biopsy obtained from a patient-2 receiving the BPA *in vivo* within an hour. This sample is expected to contain very few tumour cells infiltrating healthy tissue in the brain as shown in section 5.2.3.1 and **Figure 5.1 -d**. The concentration of BPA in the entire biopsy was 6 mg/kg measured by ICP-MS [3], this is much lower than measured in all previous samples and below the lethal BNC threshold (~15–30 mg/kg) [4]. **Figure 5.9** presents an overview of the sample on the silicon substrate taken using a reflective light microscope. The image displays 20 analysed areas within the coloured squares. 18 of 20 areas (black squares) were excluded for multiple reasons explained in section 5.2.3.2, and results were extracted from only two areas (blue

squares). The results of one area are discussed below, indicate with a red arrow in **Figure 5.9**.

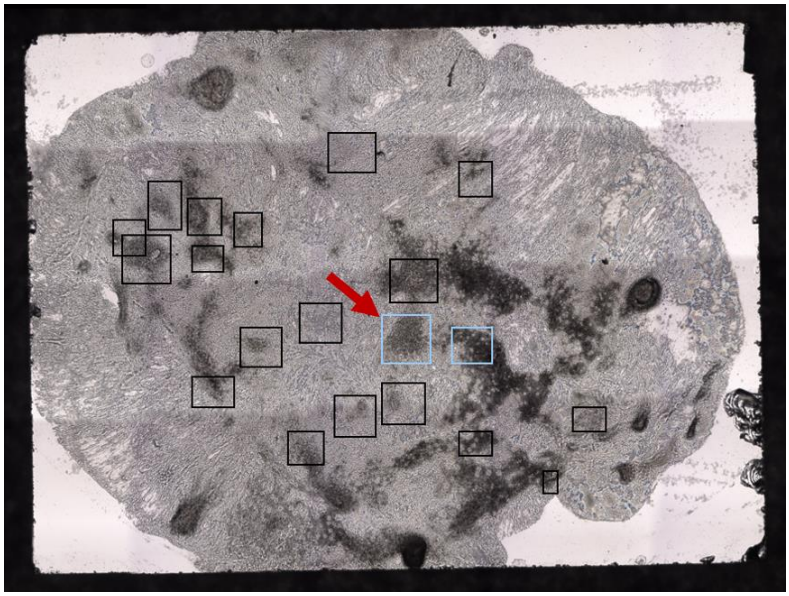

Figure 5.9: Image of freeze-dried BAT-pt.2 sample on the 5×7 mm^2 Si substrate captured using a reflective light microscope. The image showing 20 areas analysed within the coloured squares. Results were only extracted from the 2 blue squares. Arrow refers to the area presented in the discussion.

The selection of the analysis area was performed with the CCD camera in NanoSIMS instrument alongside **Figure 5.9**. The secondary ion maps resulting from the NanoSIMS analysis are shown in **Figure 5.10** that illustrate the variation in the distribution of ions across the imprint. From the SE map, the general shape of the analysed area and the features on the surface can be distinguished. The Si map shows that most of the substrate surface is covered by the sample which in turn has holes showing high intensity of silicon signals. Therefore, the silicon map is used to avoid undesirable areas during identification of the cells of interest. Furthermore, the silicon map confirms the integrity of the analysed area after imaging with a dose of 3.57×10^{16} ions /cm^2 in this area.

Distribution maps for CN^-, P^- and S^- are almost identical to those of the patient-1 samples. The CN map shows a semi uniform distribution of CN^- signals in the imprint with higher signal intensity than the rest of the ions as found by comparing the total intensities of ions summed from cells. Both the P^- and S^- maps show a heterogeneous distribution of signals across the imprint. The P^- map shows the accumulation of signals with high intensity in specific areas of the sample numbered of 1 and 2 (red lines) which may indicate the locations

of the cells. S^- signal with low intensity is anticorrelated with high intensity signals of P^- in regions 1 and 2 which in turn confirms the location of the cells. More details on the distribution of CN^-, S^- and P^- signals has been explained in the section 5.2.3.1.1.

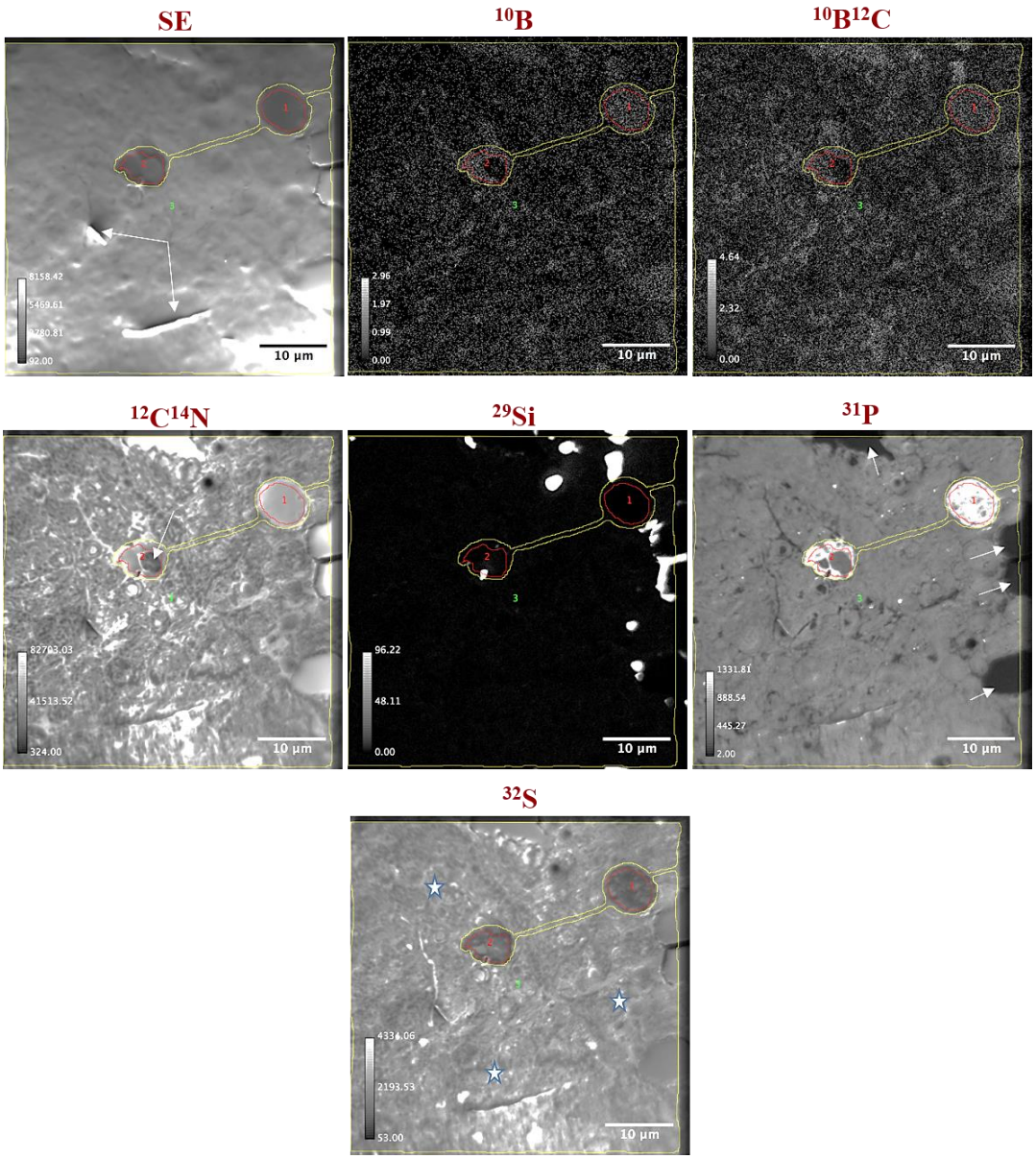

Figure 5.10: NanoSIMS maps for the imprint sample of BAT-pt.2 biopsy that was administered with ^{10}BPA *in vivo*. SE: secondary electron map shows the general morphology of the analysed area. The maps of negative secondary ions: ^{10}B, $^{10}B^{12}C$, $^{12}C^{14}N$, ^{29}Si, ^{31}P and ^{32}S respectively show the ion distribution across the imprint. $^{10}B^{14}N^-$ was also mapped but not presented due to uncertainty of the peak due to mass interferences. ROI 1-Cell (red line) and ROI 2-Excluded cell. ROI 3 represent the rest of the sample (yellow line). The arrows in the CN map and P map point to the hole in the cell-2 and some unknown features respectively. The stars (*) on the S map distinguish the connective tissue areas. The FoV is 50×50 µm^2 with 512×512 pixels. Analysis dose in images = 3.57×10^{16} ions/cm^2.

In area 1 (red line), no features of the nucleus can be distinguished, indicating possible degradation of the nucleus to multiple chromatin units, which may in turn explain the presence of P^- signals throughout the cell structure with high signal intensity. The absence of the nucleus features along with the preservation of the cell in a general round shape are traits that indicate an apoptotic cell in area-1.

Area 2 is predominantly an apoptotic cell. However, to the right of the cell (the arrow in the CN^- map), there is a spot with different CN^- and P^- signal from the rest of the cell structure in area-2, and is closer in its nature to the shape of outer tissue, indicating that the cell may be in partial demise or the cell is in a phase of fragmentation into smaller units called apoptotic bodies. Furthermore, the silicon ion map shows a hole in the bottom edge of cell-2. Due to the lack of confidence in area-2, it was excluded from quantitative measurements.

The outer area surrounding cells -1 and 2 (yellow line) is the tissue that binds the contents of the sample and has high CN^- signals and low intensity P^- signals (the stars on the S map). The outer area contains unknown features with the absence of P^- signal (arrows in the phosphorus ion map), while these features accumulate high signal intensity of CN^- and low intensity of S^-. The imprint also contains holes and cracks, where the CN^-, P^- and S^- signals are absent, less than those apparent in the patient-1 samples and this is similar to the observations on stained sections with H&E from the same sample in **Figure 5.1 -d**. The SE map shows two bright longitudinal features indicated by arrows. The intensity of CN^-, P^- and S^- signals from these features is not significantly different from the outer area surrounding the cells, whereas the Si^- map confirms that there are no cracks, voids or holes in the location of these features. Therefore, these features may have formed from the outer tissue or contaminants on the surface.

With regards to the distribution of boron from BPA, $^{10}B^-$ and $^{10}B^{12}C^-$ signals in the maps showed a semi-homogeneous distribution within the cell-1 as well as in the area surrounding the cells (yellow line). ^{10}B and $^{10}B^{12}C$ ions did not show any preferential accumulation within cell-1. The total intensity of $^{10}B^{12}C^-$ signals in the cell is ~ 2 times higher than the total signal intensity of $^{10}B^-$ as is evident from the analysis of normalised intensities of BAT-pt. 2 sample in 5.2.3.3. All areas (n = 2) analysed in the BAT-pt.2 sample showed a similar distribution of boron ion in both forms. The behaviour of the distribution of $^{10}B^-$ and $^{10}B^{12}C^-$ signals in the BAT-pt.2 sample in **Figure 5.10** is similar to the distribution in the samples GBM-pt.1 in **Figures 5.5, 5.6** and **5.8**.

By comparing the normalised total intensities of the boron signals that are summed from cells in BAT-pt.2 with BAT-pt.1 samples, the signal intensity of ^{10}B and $^{10}B^{12}C$ ions in **Figure 5.10** confirms that the BAT-pt.2 cells uptake the BPA ~ 2 times more than the BAT-pt.1 cells in **Figure 5.3.**, although bulk concentration in the BAT-pt.2 biopsy (6 mg/kg after 1 hour of BPA infusion) is significantly less than the concentration in BAT-pt.1 biopsy (27.9 mg/kg after 2 hours of BPA infusion). This difference is due to the fact that ICP-MS measurements represent the concentration of BPA in the entire biopsy including the remaining blood and connective tissues. While the boron signals intensity measured using NanoSIMS represents the level of BPA in specific cellular areas, this in turn shows the advantage of SIMS approach in distinguishing differences in localisation within tissue sections as the measurements are not affected by tumour cell density.

In addition, the difference in bulk concentrations and the signal intensity in the cells of both the BAT-pt.2 and BAT-pt.1 samples may be due to the difference in the activity of the LAT-1 expression in the tumour cells infiltrated into the BAT tissue before the cells enter the apoptosis phase. This reason is consistent with Nawashiro's *et al.* study, which concluded that the activity of LAT-1 expression in the infiltrating cells to the border zone of the tumour differed in 10 tissue sections taken from human primary glioma in brain from 10 different patients [29]. Grunewald *et al.* 's study also summarized a similar result that although pre-loading of L-amino acids acts as a stimulator for BPA uptake, the accumulation of BPA was different in all mice organelles carrying a human hepatocellular carcinoma cells, indicating that the activity of the LAT-1 expression in the cells may be different from one patient to another or from one tumour to another [30]. Detta and Cruickshank concluded that although there were few tumour cells in BAT the level of BPA uptake *in vitro* in cell infiltrating BAT was close to the level of *in vitro* BPA uptake in the cells of GBM, indicating that LAT-1 expression activity contributed in the passage of BPA to infiltrating cells [31]. Yang *et al.* also highlighted the difference in the accumulation of amino acids and the BPA according to the anatomical site of tumour and the type of histological tumour [32]. Another reason behind the difference in the normalised signal intensity of ^{10}B and $^{10}B^{12}C$ between the cells of BAT-pt.2 and BAT-pt.1 samples may be the proliferation phase for the tumour cell before it is transformed into the apoptotic cell. Yoshida *et al.* concluded that the accumulation of ^{10}B of BPA in several tumour cell lines (*in vitro*) was high in the G2-M phases compared to the G0-G1 phases [33]. Ono *et al.* showed that ^{10}B of BPA was accumulated in cell colonies in peripheral tumour in mice *in vitro* without any accumulation in the quiescent cells [34]. Dahlstrom *et al.* reported a heterogeneous accumulation of ^{10}B of BPA in the human glioma cell sub-populations, indicating the presence of the cells in different stages [35].

5.2.3.1.6 GBM-pt.2 maps

GBM-pt.2 sample is an imprint of tissue biopsy of the glioblastoma multiforme tumour core harvested from patient-2 and administered with BPA *in vivo* for an hour. GBM-pt.2 sample is expected to contain a larger number of tumour cells compared to sample BAT-pt.2 as illustrated in section 5.2.3.1 and **Figure 5.1 -e**. The bulk concentration of BPA in the entire biopsy after harvest is 17.8 mg/kg measured by ICP-MS [3], which is within the lethal BNCT dose (~15–30 mg/kg) [4] and higher than measured in BAT-pt.2 but lower than those in GBM-pt.1 samples. The number of analysed areas is 13. The results were extracted from only 4 areas - 9 areas were excluded from the results for reasons explained in the section 5.2.3.2. The following is a discussion of the results of one of the areas for illustrative purposes. The CCD camera in the NanoSIMS was used to select area for analysis as shown in **Figure 5.11**. All areas were included in quantitative data analysis in section 5.2.3.3.

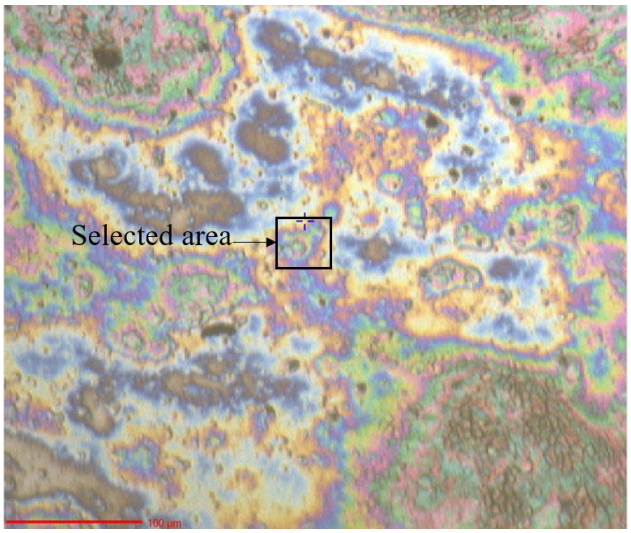

Figure 5.11: The image of the CCD camera shows the area chosen in GBM-pt.2 sample for NanoSIMS imaging. Scale bar =100 µm.

The distribution maps of the secondary ions from the NanoSIMS analysis were shown in **Figure 5.12**. SE and Si maps show the general morphology of the imprint and the substrate area covered by the sample, respectively. The Si map also shows the location of holes in the imprint and confirms the integrity of the area of interest after implantation and image acquisition with a total dose of 2.29×10^{15} ions/cm^2. The C^- map shows that the carbon is distributed semi-homogenously across most of the imprint but is highly concentrated around the edge of the imprint. The distribution of the CN, P and S ions in the imprint are similar to

that obtained in BAT-pt.2, as well as for the patient-1 samples. The distribution of CN, P and S signals were explained in more detail in section 5.2.3.1.1. The CN^- has an almost uniform distribution across the imprint with higher signal intensity than the rest of the ions, while the P^- and S^- signals are heterogeneously distributed in the sample. The S^- signal maintains a higher intensity than the P signal and less than the CN^- signal in most of the imprint areas, except for areas marked with red lines numbered 1-2. The P^- map shows a different accumulation pattern of P^- signals in areas-1 and 2 (red line) which may indicate the locations of the cells. The localisation of low S^- signal intensity with high P^- signals in areas-1 and 2 confirms the location of the cells. The P^- signals appear to accumulate less in cell-1 compared to the high signal's intensity in cell-2, this difference in the intensity of P^- signals may be due to the sample being not completely flat, which makes the signal intensity appear less in the right side of the image in general and for the cell-1 in particular, thus the variation in signal intensity is not sufficiently clear. Cell-1 was excluded from quantitative measurements due to the lack of confidence in the measured boron signals from it. Cell-2 shows the characteristics of apoptotic cell due to the absence of nucleus features, and the presence of high signal intensity of P^- with some contrast throughout the cell structure. In addition, cell-2 appears as a fragmented area of the cell membrane with the cell retaining its components.

In terms of the boron distribution of the BPA, both the ^{10}B and $^{10}B^{12}C$ ions were distributed semi-homogenously within cells-1 and 2, as well as in the external tissues surrounding the cells (the yellow line). The ions of $^{10}B^-$ and $^{10}B^{12}C^-$ did not show any preferential accumulation pattern within cells-1 and 2. The total intensity of signals accumulated from the $^{10}B^{12}C^-$ across the cell-1 is close to the total intensity of ^{10}B signals as is evident from the analysis of normalised intensities of GBM-pt.2 in 5.2.3.3. All areas (n = 4) analysed in the sample GBM-pt.2 showed a similar distribution of $^{10}B^-$ and $^{10}B^{12}C^-$. The distribution pattern of boron ion signals in both forms in the sample GBM-pt.2 is similar to the BAT-pt.2 sample maps as well as the GBM-pt.1 samples.

In comparison with the BAT-pt.2 in terms of normalised total intensity of boron signals summed from cells, it was observed that the intensity of the $^{10}B^-$ and $^{10}B^{12}C^-$ signals in the GBM-pt.2 sample is higher than the BAT-pt.2 by a factor of 4 and 2, respectively, which in turn confirms that the absorption of BPA in the tumour area was higher than the BAT area. This observation is consistent with the measured concentrations in both biopsies samples after one hour of harvesting, which was 17.8 mg/kg in GBM-pt.2 and 6 mg/kg in BAT-pt.2. More details on $^{10}B^-/^{12}C^{14}N^-$ and $^{10}B^{12}C^-/^{12}C^{14}N^-$ ratios are discussed in 5.2.3.3.

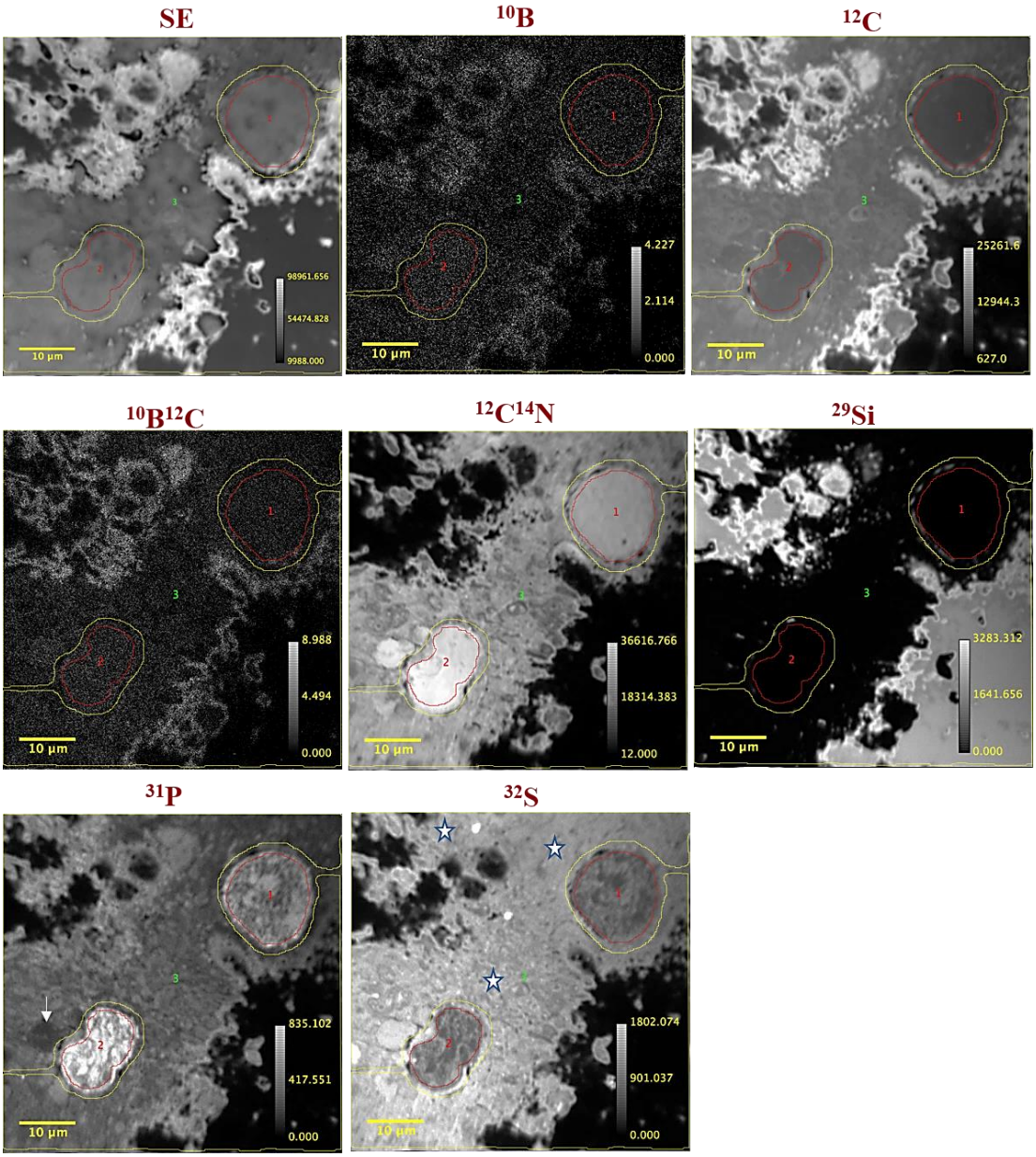

Figure 5.12: NanoSIMS maps for the imprint sample of GBM-pt.2 biopsy that was administered with ^{10}BPA *in vivo*. SE: secondary electron map shows the general shape of the analysed area. The maps show the cellular distribution of negative ions: ^{10}B, ^{12}C, ^{10}B^{12}C, ^{12}C^{14}N, ^{29}Si, ^{31}P and ^{32}S respectively across the sample. ROI 1-Excluded cell (red line) and ROI 2- Cell. ROI 3- the rest of the sample parts (yellow line). The arrow in P map indicates an unknown feature. The stars (*) on the S map distinguish the connective tissue areas. The FoV is 75×75 µm^2 with 512×512 pixels. Analysis dose in images = 2.29×10^{15} ions/cm^2.

Relatively high signal intensity of ^{10}B and $^{10}B^{12}C$ ions were observed at the edges of the external tissue, which may be due to accumulations of BPA flowing from inside the tissue to the tissue edges as a result of a natural efflux process during preparation of samples in the period from harvest, the concentration measurement, division of biopsies, and then the freezing process, before reaching the analysis stage in SIMS. Another possibility is that parts of tissue have been damaged and removed partially after implantation process using Cs^+ beam, making ions appear to be accumulated high intensity with a lot of morphology. The intensity of the CN^- and S^- signals in the edges did not differ from the nature of the internal tissues, whereas the P^- signal was higher than the interior of the tissue.

5.2.3.2 Challenges in biopsy sample analysis by NanoSIMS

Analysis of the imprint samples from tissue biopsies using NanoSIMS encountered a number of obstacles that limited the number of areas where reliable results could be extracted. These obstacles are mostly due to the nature of the sample. The thickness of the imprint is different across one sample as shown previously in **Figure 3.1**, which makes the fixed implantation dose insufficient to reach steady state for the thick areas, therefore these areas remain dark after the implantation process. In several areas the signal intensities for all ions was progressively lost from the outer edges of the analysed region. The image area starts with high and uniform signal intensity however during analysis one corner gets progressively darker and then this loss of intensity spreads over the entire analysis area, this may have been a charging effect as shown in CN^- images in **Figure 5.13 - a** taken from the GBM-pt.1 and GBM-pt.2 samples, respectively. Some areas lack the presence of obvious features, as well as the difficulty of finding tumour cells especially those infiltrating the BAT tissues. For example, images of CN^- and P^- from one of the sample areas BAT-pt.1 in **Figure 5.13 - b** shows no clear identifiable cellular features. Some parts of the samples are not completely flat, and this results in topographical enhancements of signal intensity so the images don't show purely compositional contrast. The tissue morphology was affected by cracks and necrosis that in turn destroys the structure of some tumour cells, making it difficult to obtain suitable areas for analysis. The tissues contain other cell types along with tumour cells such as fibroblast cells, apoptotic cells and necrotic cells that may be deceptive when selecting the desired area for analysis. For example, **Figure 5.13 - c** shows images of CN^-, Si^- and P^- resulting from the analysis of an area in the GBM-pt.1 sample, this area contains: cracks and necrosis as evidenced by Si^- signals, the presence of unknown cell types from which P^- signals are absent, and the sample is not completely flat with a variation of contrast. Often this situation can only be discovered after analysis and image processing using the Fiji

software is completed. When one of these obstacles occurs, the analysed area is excluded from the sample results.

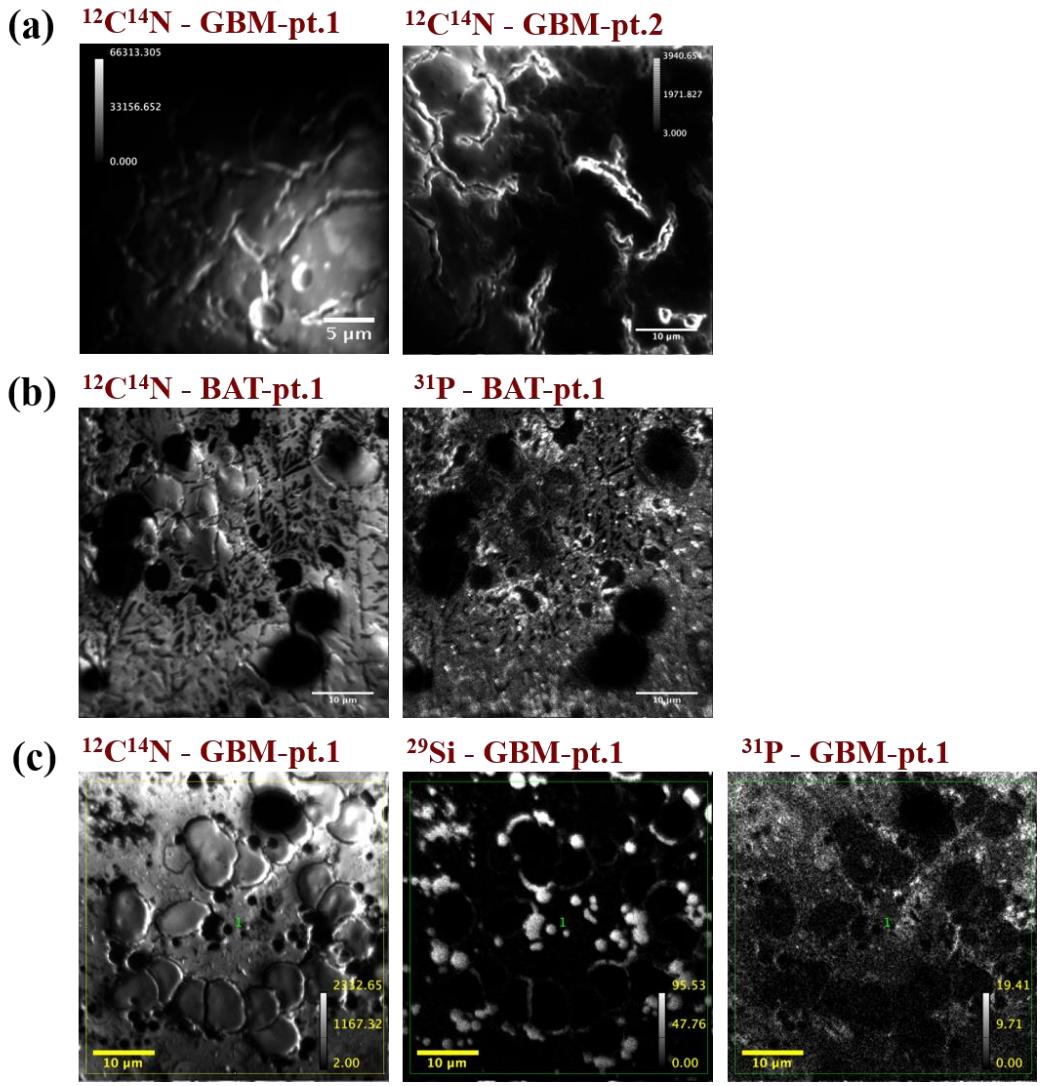

Figure 5.13: A selection of images from the imprint samples showing the obstacles encountered by NanoSIMS analysis. (a) $^{12}C^{14}N^-$ images from the GBM-pt.1 and GBM-pt.2, respectively, showing the loss of signal intensity which potentially occurs due to charging. The image area starts with high and uniform signal intensity however during analysis one corner gets progressively darker and then this loss of intensity spreads over the entire analysis area. (b) $^{12}C^{14}N^-$ and $^{31}P^-$ images from BAT-pt.1 showing no identifiable cellular features. (c) $^{12}C^{14}N^-$, $^{29}Si^-$ and $^{31}P^-$ images of GBM-pt.1 showing cracks and necrosis where a high intensity of $^{29}Si^-$ signals appears, unknown cell types where the $^{31}P^-$ signal is absent, and the sample is not completely flat with the signal intensity varying across the sample as shown from the $^{12}C^{14}N^-$ signals.

5.2.3.3 Quantitative comparisons of ^{10}B distribution from BPA drug between imprint samples of BAT and GBM tissue biopsies

Quantitative determination of the boron accumulated from BPA in the cells, whether tumour or apoptotic, identified in maps of the BAT and GBM tumour biopsy imprints was performed. The measurements of $^{10}B^-$ and $^{10}B^{12}C^-$ were normalised to $^{12}C^{14}N^-$, which is the highest signal intensity and the most uniformly distributed ion across the imprint compared to the other signals. $^{12}C^{14}N^-$ is a commonly reported negative ion in NanoSIMS cellular imaging and is relatively uniform in distribution [5]–[7]. Normalising two ions acquired simultaneously accounts for different image sizes and minimizes the effect of any variations in primary ion beam current, total sputter yield and ion transmission, between different ROIs and images acquired across different NanoSIMS sessions. The reason for not normalising with $^{12}C^-$ was given at the start of this chapter in section 5.1. The negative secondary intensity ratios of $^{10}B/^{12}C^{14}N$ and $^{10}B^{12}C/^{12}C^{14}N$, number of analyzed areas (n) and total number of cells in each sample were presented in box plot **Figure 5.14**. The box plot schematic to interpret the graphs was previously shown in **Figure 4.7 -c**. **Table 5.2** displays the mean values for all the samples in the box plot **Figure 5.14** for both $^{10}B/^{12}C^{14}N$ and $^{10}B^{12}C/^{12}C^{14}N$ ratios where the difference between them can be observed.

The imprint samples of tissue biopsies of patient-1 and patient-2 showed a similar boron distribution pattern in the NanoSIMS images. Quantitative results of NanoSIMS in **Figure 5.14** confirm that the cells in all the samples absorbed the BPA. The data show that the ratio of $^{10}B^{12}C/^{12}C^{14}N$ in the cells is always higher than the $^{10}B/^{12}C^{14}N$ ratio with some overlaps between the data, this means that the $^{10}B^{12}C$ fragment has relative stability and/or a higher ionization probability than atomic ^{10}B, which in turn is a behavior similar to that observed in the results of quantitative measurements in the cell cultures in **Figure 4.23**.

In imprint samples of the patient-1 biopsies, $^{10}B/^{12}C^{14}N$ and $^{10}B^{12}C/^{12}C^{14}N$ ratios are higher in the samples GBM-pt.1-1, GBM-pt.1-1-Pt, and GBM-pt.1-2 than those measured in BAT-pt.1. This is evident from the 7-9 fold increase in $^{10}B/^{12}C^{14}N$ and $^{10}B^{12}C/^{12}C^{14}N$ ratios in GBM-pt.1 samples compared with BAT-pt.1 without overlap between them.

In the sample GBM-pt.1-1-Pt, coated with 10 nm Pt the difference in mean values of the $^{10}B/^{12}C^{14}N$ and $^{10}B^{12}C/^{12}C^{14}N$ ratios were only 9% and 4% respectively of those single values obtained of the GBM-pt.1-1 sample as shown in the **Table 5.2**. This approximation between the mean values and the overlap in $^{10}B^{12}C/^{12}C^{14}N$ ratios between the two samples confirms that the Pt coverage did not significantly change the measured ratios.

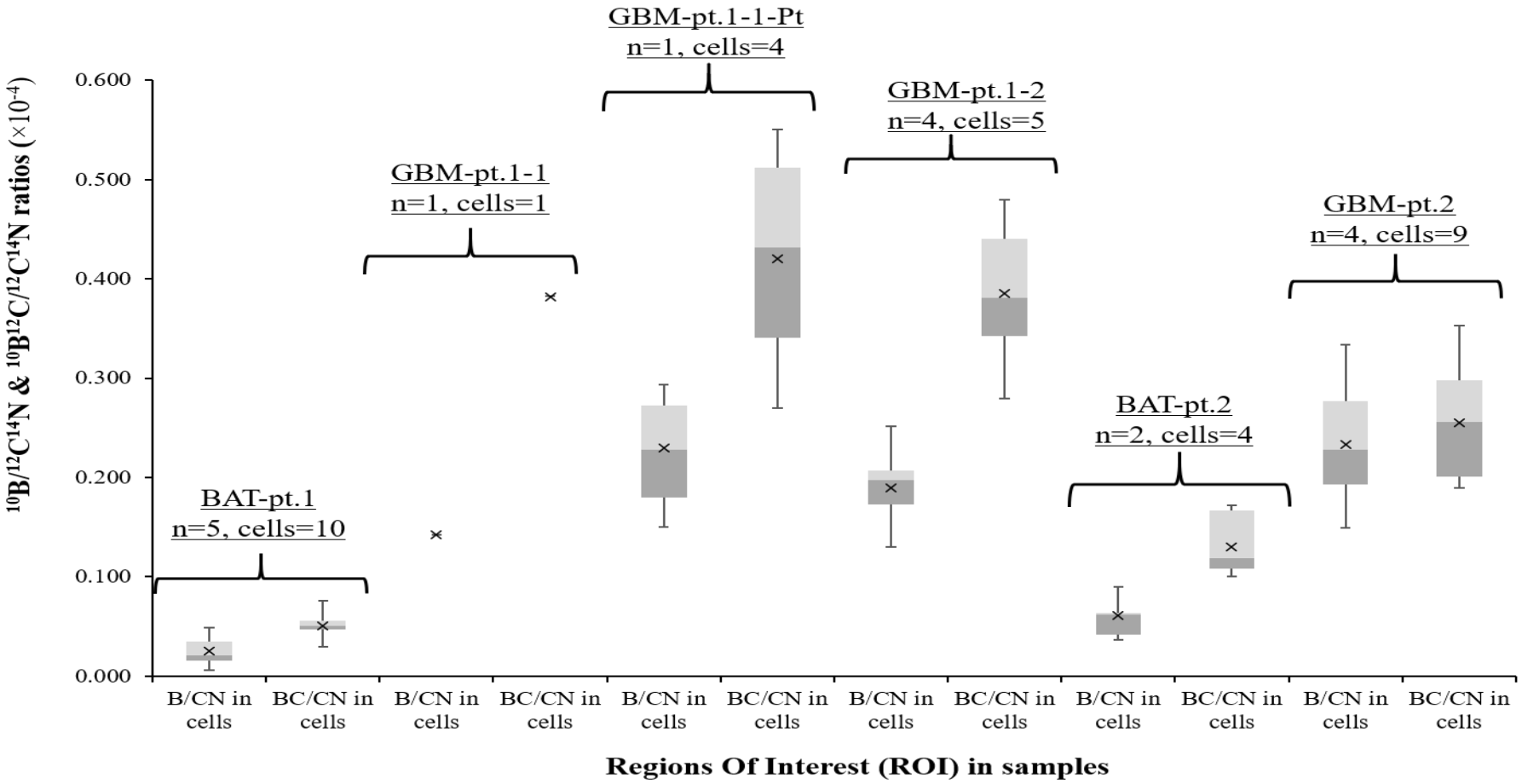

Figure 5.14: Comparison between the imprint samples from BAT and GBM tumour tissue biopsies in terms of $^{10}B^{-}/^{12}C^{14}N^{-}$ and $^{10}B^{12}C^{-}/^{12}C^{14}N^{-}$ ratios accumulated from BPA in cells areas measured by NanoSIMS.

Table 5.2: The mean values of the $^{10}B/^{12}C^{14}N$ and $^{10}B^{12}C/^{12}C^{14}N$ ratios in the imprint samples from BAT and GBM tumour tissue biopsies presented in the box plots **Figure 5.14**.

Ratios Mean ($\times10^{-4}$) ± SD	**Samples of**			
	first patient (pt.1)			
	BAT-pt.1	GBM-pt.1-1	GBM-pt.1-1-Pt	GBM-pt.1-2
$^{10}B^{-}/^{12}C^{14}N^{-}$	0.025 ± 0.012	0.14 ± 0.00	0.23 ± 0.06	0.19 ± 0.04
$^{10}B^{12}C^{-}/^{12}C^{14}N^{-}$	0.05 ± 0.012	0.38 ± 0.00	0.42 ± 0.11	0.38 ± 0.07
Ratios Mean ($\times10^{-4}$) ± SD	Second patient (pt.2)			
	BAT-pt.2	GBM-pt.2		
$^{10}B^{-}/^{12}C^{14}N^{-}$	0.06 ± 0.06	0.23 ± 0.06		
$^{10}B^{12}C^{-}/^{12}C^{14}N^{-}$	0.13 ± 0.03	0.25 ± 0.06		

In the sample GBM-pt.1-2, the ratios of $^{10}B/^{12}C^{14}N$ and $^{10}B^{12}C/^{12}C^{14}N$ were close to those ratios in both GBM-pt.1-1 and GBM-pt.1-1-Pt samples as shown in **Table 5.2**. The difference in mean values between the samples of the GBM-pt.1 did not exceed 9%. The interquartile range for $^{10}B/^{12}C^{14}N$ and $^{10}B^{12}C/^{12}C^{14}N$ for the samples GBM-pt.1-1-Pt and GBM-pt.1-2 were almost completely overlapping and therefore the two biopsy samples were considered to behave very similarly in terms of their BPA uptake.

In terms of imprint samples of biopsies from the patient-2, the mean values of the $^{10}B/^{12}C^{14}N$ and $^{10}B^{12}C/^{12}C^{14}N$ ratios in cells of the GBM-pt.2 were 4-fold and 2-fold respectively, higher than the mean values in the BAT-pt.2 sample, which confirms the high accumulation of the BPA in the GBM-pt.2 compared to the BAT-pt.2 sample. Furthermore, there is no overlap in the box plots between the two samples ratios, while the box plots of $^{10}B/^{12}C^{14}N$ $^{10}B^{12}C/^{12}C^{14}N$ ratios in sample GBM-pt.2 were highly overlapped and the mean values were close.

In comparison between the two types of samples from both patients, the mean values of the $^{10}B/^{12}C^{14}N$ and $^{10}B^{12}C/^{12}C^{14}N$ ratios in the BAT-pt.2 sample were ~ 2-fold higher than those in the BAT-pt.1 sample. The first and second quartile range of $^{10}B/^{12}C^{14}N$ ratios in BAT-pt.2 overlaps with the third and fourth quartile range of in BAT-pt.1 ratio, while there is no overlap in $^{10}B^{12}C/^{12}C^{14}N$ ratios between the two samples. This difference in the $^{10}B/^{12}C^{14}N$ and $^{10}B^{12}C/^{12}C^{14}N$ ratios between the samples BAT-pt.1 and BAT-pt.2 may be due to the difference in the activity of LAT-1 expression in the tumour cells infiltrating into BAT tissue, or that the distribution of boron was affected by the proliferation phase of the cell or site of the anatomical tumour and type of histological tumour, these reasons have been

discussed in detail in section 5.2.3.1.5. The mean value of $^{10}B/^{12}C^{14}N$ in the GBM-pt.2 was 9% higher than the mean in GBM-pt.1-1 and close to means in the GBM-pt.1-1-Pt and GBM-pt.1-2. $^{10}B/^{12}C^{14}N$ ratios were overlapping between all samples. In terms of the mean values of $^{10}B^{12}C/^{12}C^{14}N$ in GBM-pt.2 was 2-fold less than the means values in the samples of GBM-pt.1. The third and fourth quartile range of the box plot $^{10}B^{12}C/^{12}C^{14}N$ ratio in GBM-pt.2 overlapping with the first and second quartile range of samples GBM-pt.1-1-Pt and GBM-pt.1-2. Thus, all tumour samples showed close $^{10}B/^{12}C^{14}N$ ratios and the difference between them was 0.2-9%, while the $^{10}B^{12}C/^{12}C^{14}N$ ratios in GBM-pt.2 was slightly lower than GBM-pt.1 samples at 13-17%.

The statistical comparison of these results concluded that the level of cellular boron in all samples of GBM tumour was higher than the BAT samples. This higher accumulation of boron in the tumour sample cells and its accumulation in cells infiltrating into tissues surrounding the tumour contributes to the success of the BNCT therapy that is based on generating high-energy linear particles from a neutron fission reaction. These particles in turn penetrate the cells in short distances leading to the destruction of tumour cells [26][27][36]. The high spatial resolution for NanoSIMS imaging allowed the extraction of quantitative measurements from cellular areas of interest, comparing them and observing simple differences between them.

Cellular wet-weight concentrations of ^{10}B cannot be determined from the $^{10}B^{-}/^{12}C^{14}N^{-}$ ratios measured with NanoSIMS using the same method as in section 4.2.3.2.5 due to the lack of a $^{12}C^{14}N^{-}$ RSF value from a reference identical or close to the freeze-dried cell samples.

5.2.4 BioToF-SIMS results and discussion

In this section, the imaging capabilities of BioToF-SIMS instrument were assessed to determine the ^{10}B distribution at the cellular level in the imprint samples from GBM tumour and BAT tissues biopsies administered with BPA *in vivo* (the same samples that were analysed by NanoSIMS). **Table 5.1** shows a summary of the studied samples and the abbreviation for each sample. All samples were analyzed under the same analytical conditions and then were compared quantitatively.

5.2.4.1 Imaging of ion cellular distributions of ^{10}B from BPA drug in the imprint samples of GBM tumour and BAT tissue biopsies

In the imprint sample of tissue biopsy BAT-pt.1, 6 areas were selected and analyzed (different from those analyzed with NanoSIMS) in **Figure 5.2**. After completion of the analysis, the results were extracted and data was processed as explained in section 3.5.2, only one of these areas is discussed below for illustrative purposes. All areas were included in quantitative data analysis in section 5.2.4.2.

Figure 5.15 -a shows the positive ion mass spectrum resulting from one analysis area, which shows the high signal intensities of the Na at *m/z* 23 and the K at *m/z* 39. In **Figure 5.15 -b**, the signal intensity of the C at *m/z* 12 is relatively intense. **Figure 5.15 -c** shows the ion yields of the boron isotopes ^{10}B and ^{11}B.

To verify the distribution of ion signals of interest across the imprint, BioToF-SIMS images were generated for the positive ions ^{10}B, ^{11}B, ^{12}C, ^{23}Na, ^{28}Si and ^{39}K and presented in **Figure 5.16**. The Si^+ image shows that the majority of the substrate is covered with the imprint except the upper right corner where high silicon signals are shown. The few Si signals shown across the imprint may have resulted from the presence of cracks or holes in the imprint and that were previously observed in the NanoSIMS maps in the **Figure 5.3**.The image of H&E-stained section of brain tumour biopsy in **Figure 5.1** -a confirmed the presence of these cracks.

The pattern of signal intensity in Na^+ and K^+ images is similar to that obtained from energy-dispersive X-ray microanalysis of human biopsies of thyroid tumours [37] and invasive urogenital cancers [38]. Both studies [37] and [38] show that Na content increases in cancer biopsies compared to K due to increased proliferation rate and cell division, which in turn stimulates continuous polarization of the cell membrane. Sodium and potassium ions are

involved in many interactions and activities within cells such as growth, regulation of protein activity, metabolism, transfer of amino acids and nucleotides through cellular membranes [39]–[42]. Thus, the Na^+ and K^+ intensity confirms the identity of the sample and that it contains unbalanced cells.

The C^+ image shows a homogeneous distribution of C signals in the imprint with lower signal intensity than Na^+ and K^+ images. Carbon ion signals result from proteins, lipids, amino acids, and carbohydrates in the imprint structure [10][11][43]. As for boron isotope images, both $^{10}B^+$ and $^{11}B^+$ are distributed almost homogeneously in the sample. The signal intensity of all ions was low in the upper right corner where the high signal intensity of the silicon ion in the exposed area of the substrate was observed. The total ion image represents a comprehensive image for all ions apparent in the mass spectrum **Figure 5.15**.

None of the images in **Figure 5.16** showed the morphology of the imprint and did not distinguish the locations of the cells. The images did not show the variation in the distribution of signals between the different parts of the imprint as in the NanoSIMS maps of BAT-pt.1 in **Figure 5.3**, confirming the relatively low spatial resolution in the resulting images of BioToF-SIMS using primary beam Au^+ in imaging under the high-current settings to maximize sensitivity. Thus, it is not possible to determine the sites of accumulation of ^{10}B of BPA accurately in the images. However, the BioToF-SIMS images gave the intensity of the ion signals at the level of BAT-pt.1 imprint at a larger scale than was possible with the NanoSIMS. By comparing BioToF-SIMS images, the distribution pattern of all ions was similar in all areas analyzed (n = 6) in the BAT-pt.1 sample.

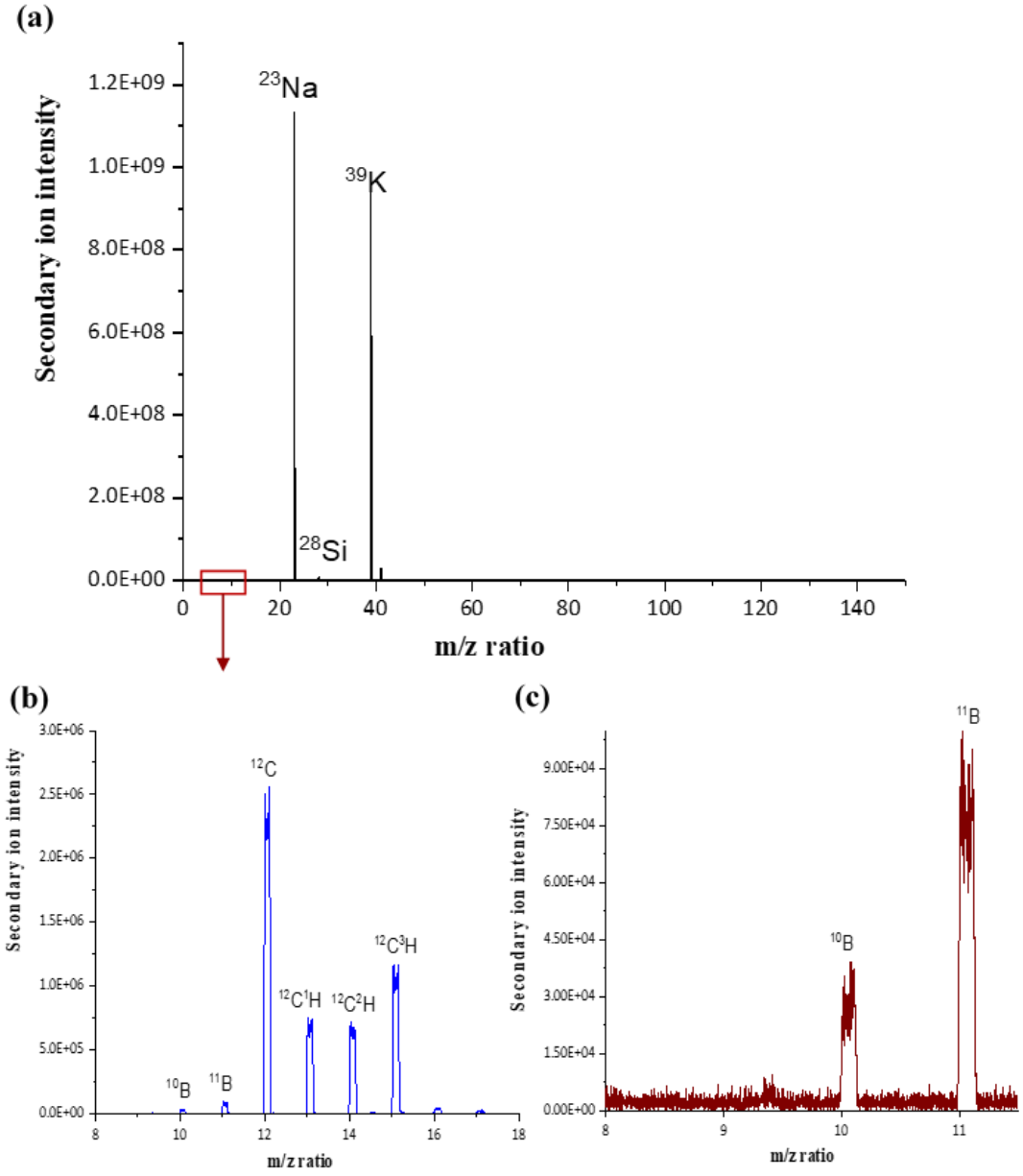

Figure 5.15: Positive secondary ion mass spectra from the imprint sample from BAT-pt.1, obtained after a dose of 2.65×10^{14} ions/cm^2 of the 20 keV Au^+ beam. (a) shows the full spectrum. (b) and (c) show the magnification of the *m/z* range from 8-18 and 8-12 respectively.

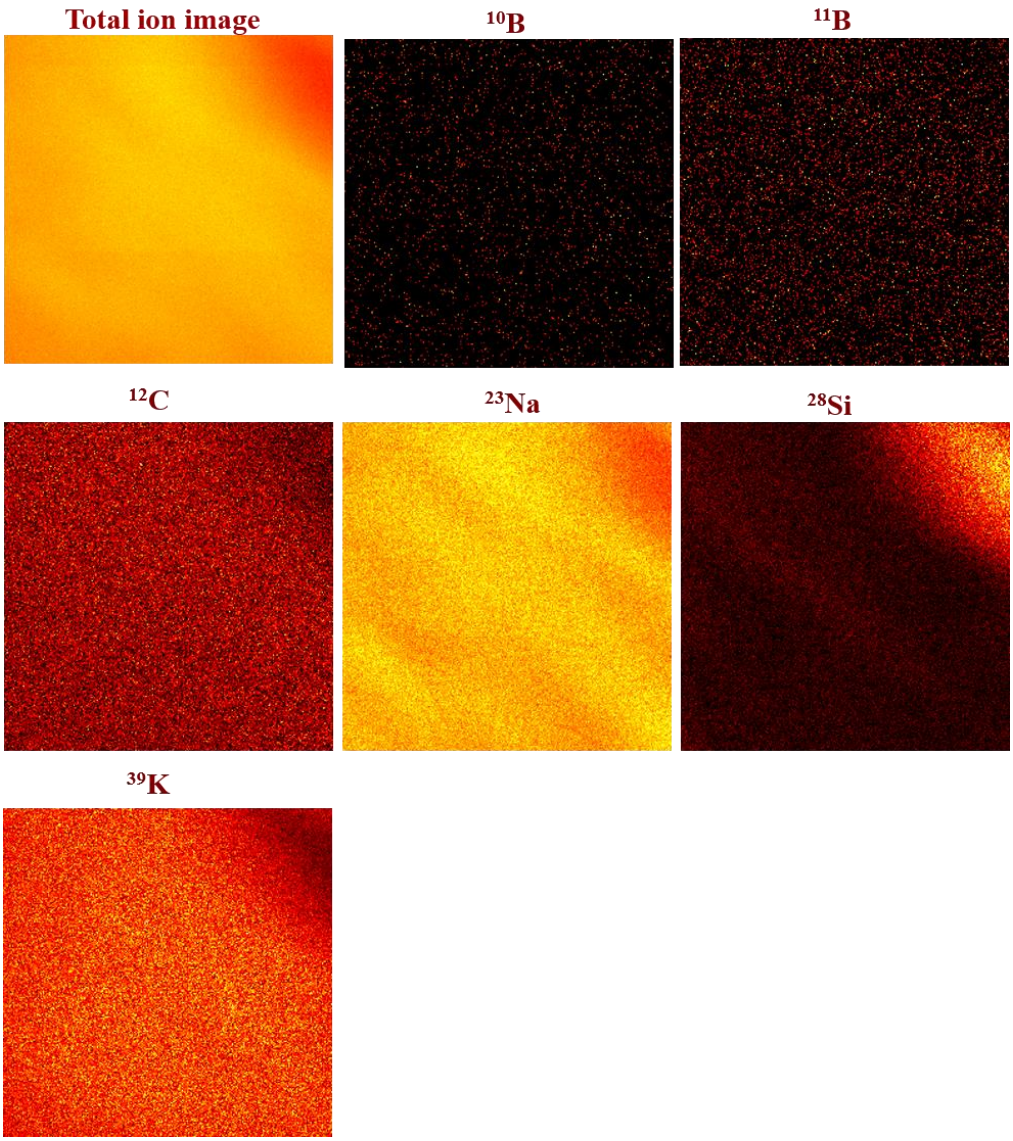

Figure 5.16: BioToF-SIMS analysis from the imprint sample from BAT-pt.1 treated with ^{10}BPA *in vivo*. The FoV is 100×100 µm^2. The total ion image represents all the ions visible in the mass spectrum presented in **Figure 5.15.** The positive secondary ion images of ^{10}B, ^{11}B, ^{12}C, ^{23}Na, ^{28}Si, and ^{39}K respectively show the ion distributions within the sample. The analysis dose in the images was 2.65×10^{14} ions/cm^2. The colour gradient from black to yellow shows the signal intensity from zero to the maximum values.

All other samples of BAT and GBM tumour listed in **Table 5.1** generated results very similar to images of the sample BAT-pt.1(**Figure 5.16**) in terms of unclear sample morphology and a similar general pattern of the distribution of ions. Since no information on the cellular distribution for ions in the images can be obtained on this image scale, only the spectra of these samples have been presented below. In the imprint sample of GBM-pt.1-1, 3 different

areas were analyzed and **Figure 5.17** shows the mass spectrum resulting from one of these areas, which in turn shows the signal intensity of $^{10}B^{+}$ and $^{11}B^{+}$. In comparison to BAT-pt.1, the normalised $^{10}B^{+}$ signal intensity to $^{12}C^{+}$ in sample GBM-pt.1-1 is ~ 3 times higher than the BAT-pt.1 sample, confirming that the BPA accumulation in sample GBM-pt.1-1 was more than accumulated in BAT-pt.1, more detail is given in the quantification section 5.2.4.2.

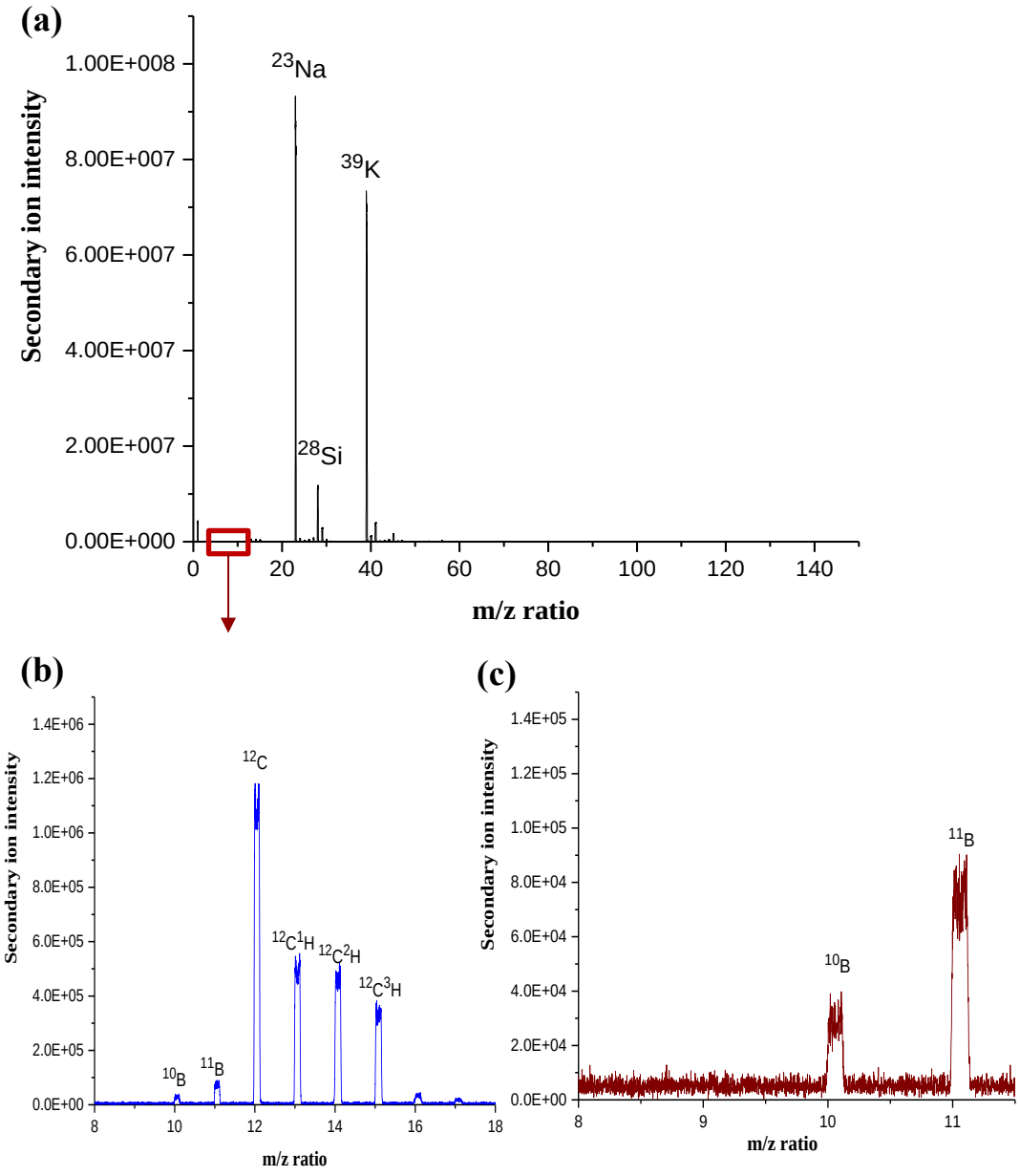

Figure 5.17: Positive secondary ion mass spectra from the imprint sample from GBM-pt.1-1, obtained after a dose of 2.98×10^{14} ions/cm^2 from the 20 keV Au^{+} beam. (a) shows the full spectrum. (b) and (c) show the magnification of the *m/z* range from 8-18 and 8-12 respectively.

In the sample GBM-pt.1-1-Pt, which is coated with 10 nm Pt, four different areas were analyzed and **Figure 5.18** shows the resulting mass spectrum from one of these areas. The normalised intensity of $^{10}B^{+}$ signal to $^{12}C^{+}$ intensity in GBM-pt.1-1-Pt is ~3 times higher than those in the samples BAT-pt.1 and close to GBM-pt.1-1, more detail is given in the quantification section 5.2.4.2. This finding indicates that coating the sample surface with platinum to reduce any sample charging issues did not have a significant effect on increasing the signal intensity from the sample GBM-pt.1-1-Pt, a result which agrees with the NanoSIMS analysis and did not change the measured ratios.

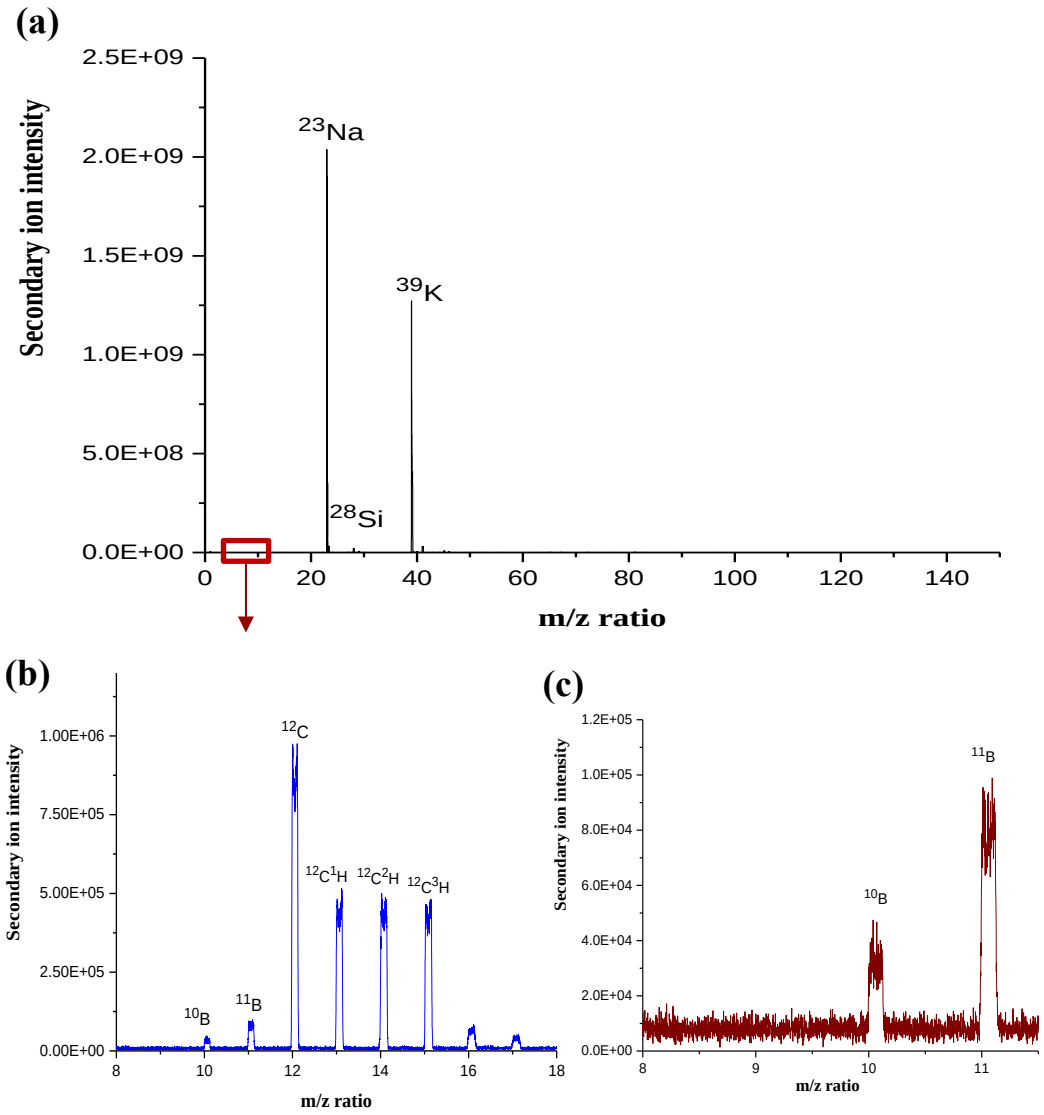

Figure 5.18: Positive secondary ion mass spectra from the imprint sample from GBM-pt.1-1-Pt, obtained after a dose of 2.75×10^{14} ions/cm^2 from the 20 keV Au^{+} beam. (a) shows the full spectrum. (b) and (c) show the magnification of the *m/z* range from 8-18 and 8-12 respectively.

Figure 5.19 shows the mass spectrum resulting from one of the seven areas analyzed in the GBM-pt.1-2 sample. From the spectrum it is clear that the intensities of the K^+ signal at *m/z* 39 and the Na^+ signal at *m/z* 23 are opposite to what was observed in the samples above. This may be because the area is free of cancer cells or contains a large number of other, non-tumour, cells with high potassium content, which in turn may affect the K^+ and Na^+ signal intensities.

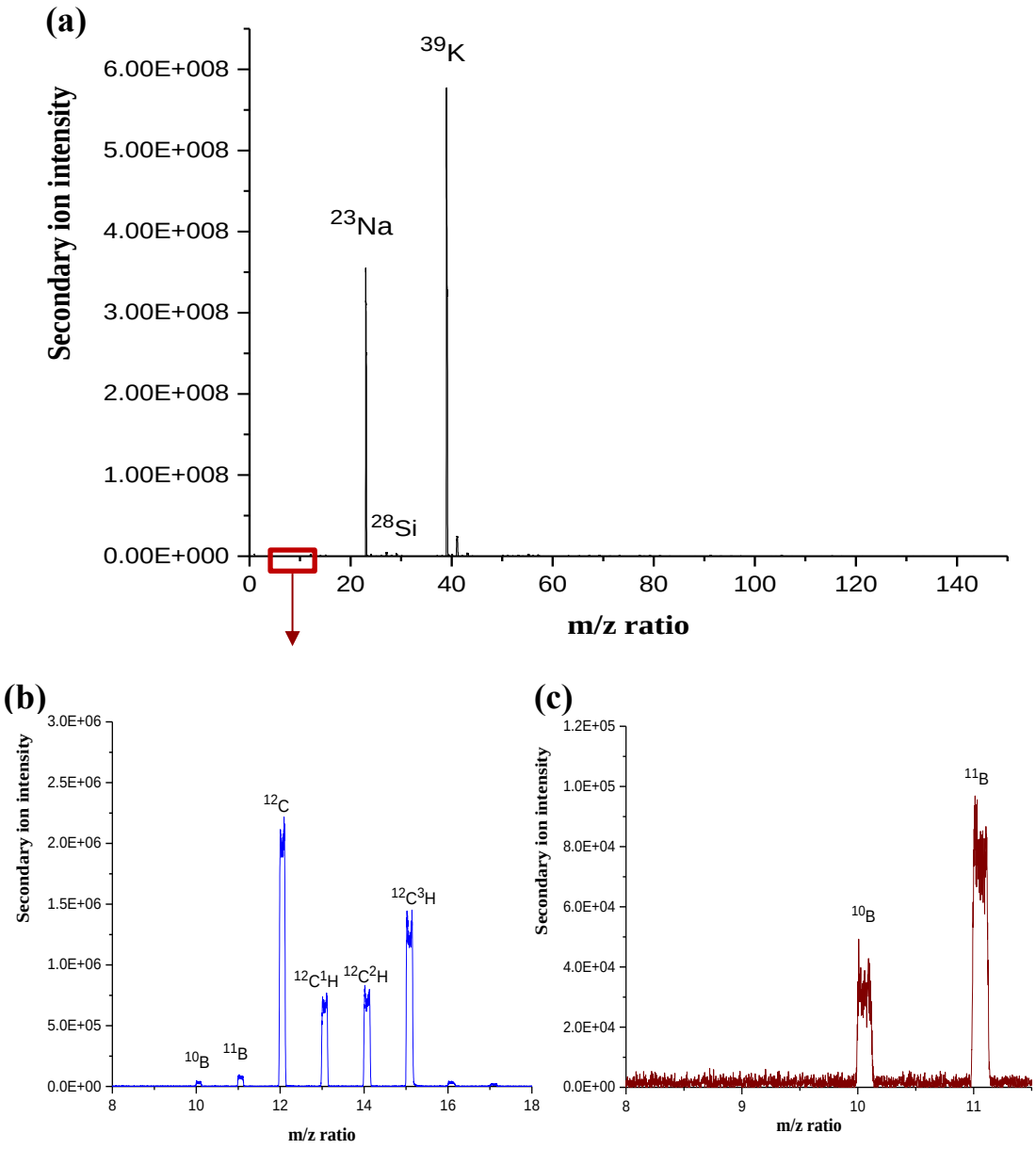

Figure 5.19: Positive secondary ion mass spectra from the imprint sample from GBM-pt.1-2, obtained after a dose of 2.65×10^{14} ions/cm^2 from the 20 keV Au^+ beam. (a) shows the full spectrum. (b) and (c) show the magnification of the *m/z* range from 8-18 and 8-12 respectively.

The resulting images of NanoSIMS of the same sample GBM-pt.1-2 in **Figure 5.8** show the presence of unknown cells in the phosphor map (arrows). The different harvest site of this sample may have a role in the difference in signal intensity (K^+ and Na^+). This difference in the intensity of K^+ and Na^+ signals was observed in all analyzed areas (n =7) of this sample GBM-pt.1-2. The normalised intensity of the $^{10}B^+$ signal to $^{12}C^+$ intensity in the sample GBM-pt.1-2 is ~ 2 times lower than the GBM-pt.1-1-Pt and GBM-pt.1-1 samples.

In terms of distribution and quantitative information for boron from BPA in the imprints of BAT and GBM tumour biopsies from the patient-2, the samples provided similar results to biopsy imprints of patient-1.

Figure 5.20 shows the mass spectrum that resulted from one of the 6 areas analyzed in the BAT-pt.2 sample, which shows the intensity pattern of signals similar to BAT-pt.1, GBM-pt.1-1, and GBM-pt.1-1-Pt. Compared to BAT-1, the normalised intensity of $^{10}B^+$ to $^{12}C^+$ intensity in BAT-pt.2 is ~ 2 times higher than the BAT-pt.1 sample. This difference in $^{10}B^+$ intensity between BAT-pt.1 and BAT-pt.2 may be due to several reasons and have been discussed the section 5.2.3.1.5. In the sample GBM-pt.2, the mass spectrum in **Figure 5.21** shows an intensity pattern for the ions similar to that in the previous samples. The spectrum also shows that the intensity of $^{10}B^+$ signal is higher than the $^{10}B^+$ signals in other samples by a factor of 2-4 when comparing normalised intensities, indicating a very high accumulation of BPA in sample GBM-pt.2 compared to all the imprint samples of BAT and GBM tumour, more detail is given in the quantification section 5.2.4.2.

The $^{10}B^+/^{11}B^+$ ratios were calculated of the boron isotopes in all the spectra shown in the **Figures 5.15-5.21** and discussed in section 5.2.4.2.

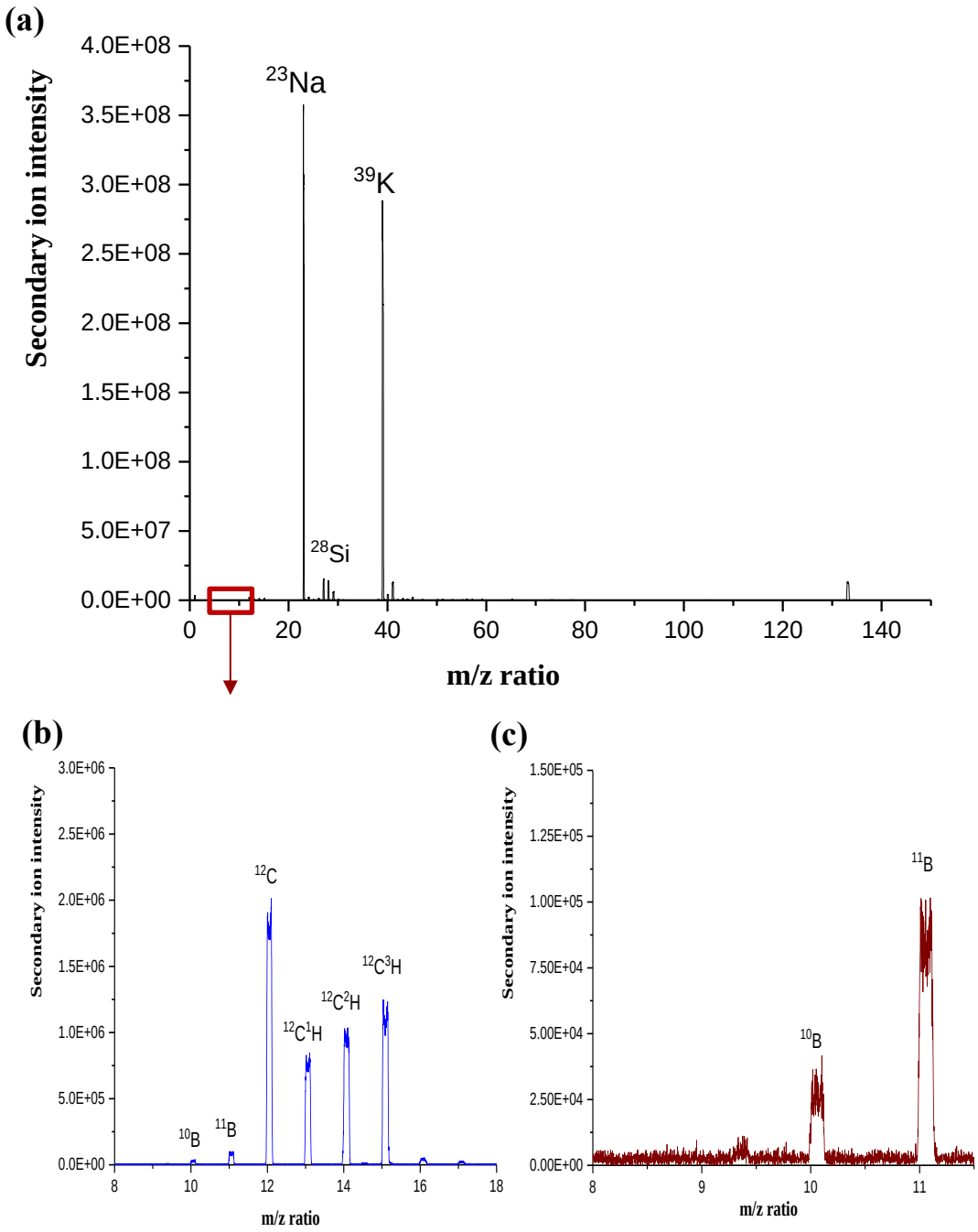

Figure 5.20: Positive secondary ion mass spectra of imprint sample from BAT-pt.2, obtained after a dose of 2.65×10^{14} ions/cm^2 from the 20 keV Au^+ beam. (a) shows the full spectrum. (b) and (c) show the magnification of the *m/z* range from 8-18 and 8-12 respectively.

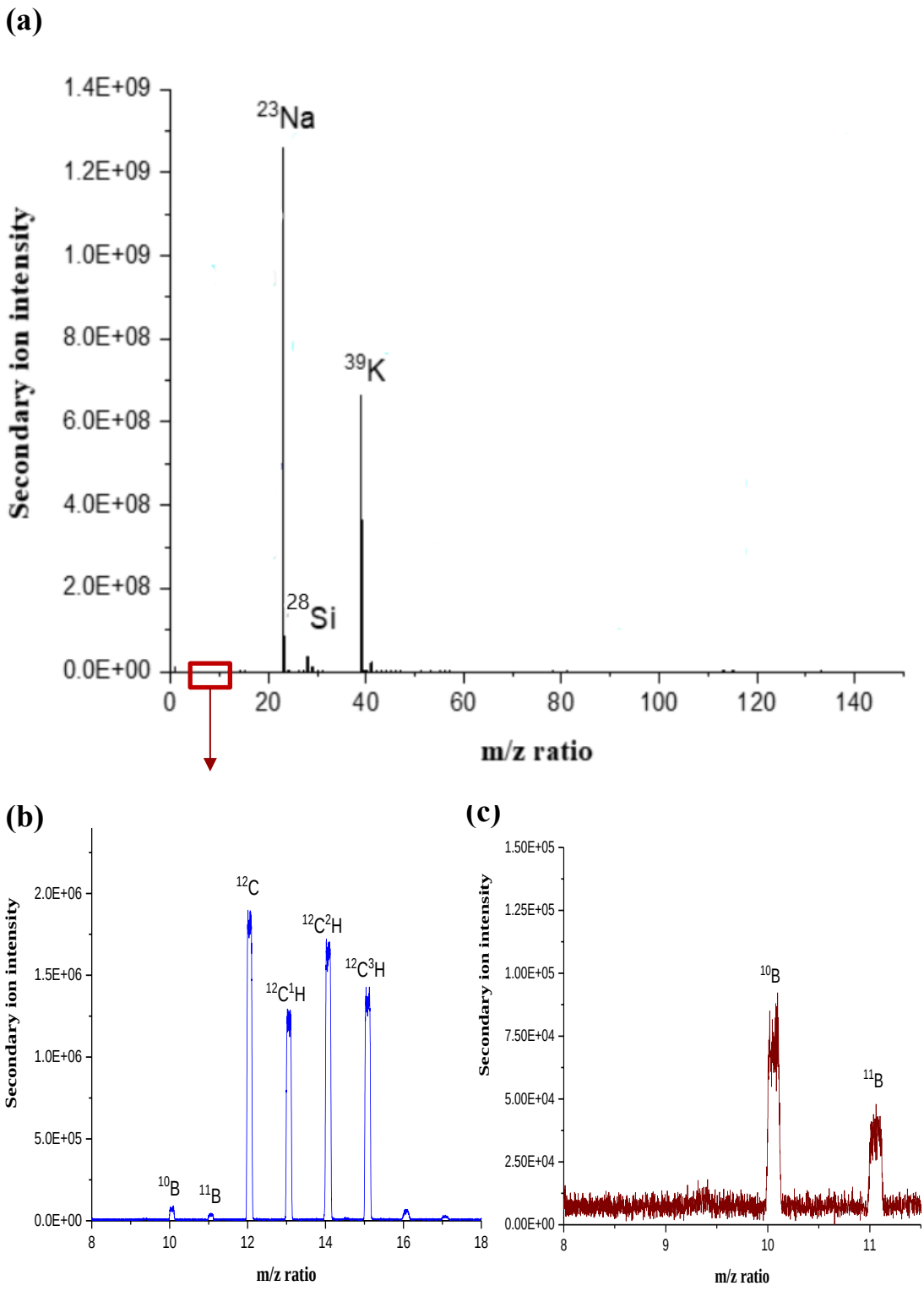

Figure 5.21: Positive secondary ion mass spectra of imprint sample from GBM-pt.2, obtained after a dose of 2.00×10^{14} ions/cm^2 from the 20 keV Au^+ beam. (a) shows the full spectrum. (b) and (c) show the magnification of the *m/z* range from 8-18 and 8-12 respectively.

5.2.4.2 Comparison of the quantitative measurement of the ^{10}B uptake between imprint samples of BAT and GBM tissue biopsies using BioToF-SIMS

Quantitative measurements of ^{10}B accumulated from BPA at the imprint level from biopsy samples of BAT and GBM tumour were calculated from the BioToF-SIMS results. The measurements of $^{10}B^+$ intensities were normalised to $^{12}C^+$ intensities in **Figure 5.22** -a.$^{12}C^+$ signal was selected for normalisation due to its relatively uniform distribution across the imprints. Moreover, $^{10}B^+$ signals were normalised to $^{11}B^+$ signals in **Figure 5.22** -b for further verification of ^{10}B accumulation in samples. The box plot schematic to interpret the graphs was shown in **Figure 4.7 -c**. The number of analyzed areas (*n*) in each sample is shown on **Figure 5.22**. **Table 5.3** shows the mean values of all BAT and GBM tumour samples in **Figure 5.22** for both $^{10}B/^{12}C$ and $^{10}B/^{11}B$, where the difference between them can be observed.

The BioToF-SIMS results in the box plot of **Figure 5.22 -a** and the mean values in **Table 5.3** show that the $^{10}B^+/^{12}C^+$ ratio in the sample GBM-pt.1-1 is ~ 3 times higher than the sample BAT-pt.1 without any overlap between them. The GBM-pt.1-1-Pt sample gave a $^{10}B^+/^{12}C^+$ ratio at the imprint level very close to that of the uncoated GBM-pt.1-1 and therefore coating had a negligible effect in improving the signal intensity from $^{10}B^+$ and did not change the normalisation. The sample GBM-pt.1-2 is ~ 2 times less than GBM-pt.1-1-Pt and GBM-pt.1-1 samples, while is still ~ 2 times higher than the BAT-pt.1 sample, the overlap between GBM-pt.1-2 and BAT-pt.1 is simple and confined in the upper whisker of the BAT-pt.1. The differences in the $^{10}B^+/^{12}C^+$ ratios between the GBM tumour samples of the patient-1 did not exceed 2%. Thus, all the imprint samples of GBM tumour biopsies from patient-1 gave $^{10}B^+/^{12}C^+$ ratios higher than the BAT-pt.1 sample.

A similar result was also obtained from the samples of patient-2. The ratio of $^{10}B^+/^{12}C^+$ in the sample GBM-pt.2 was 3 times higher than the BAT-pt.2 without overlap between samples.

By comparing the results of the samples from patient-1 and patient-2 the results confirm the higher accumulation of BPA in the tissue biopsies of GBM tumour compared with BAT biopsies. In addition, the accumulation of ^{10}B of BPA in the samples of patient-2 was higher by a factor of 2-3 than the samples of the patient-1. The results of the $^{10}B^+/^{12}C^+$ ratios using BioToF-SIMS is generally similar to that resulting from the quantitative measurement using NanoSIMS in **Figure 5.14**, while the lower imaging resolution in BioToF-SIMS analysis means conclusions regarding cellular accumulations cannot be made.

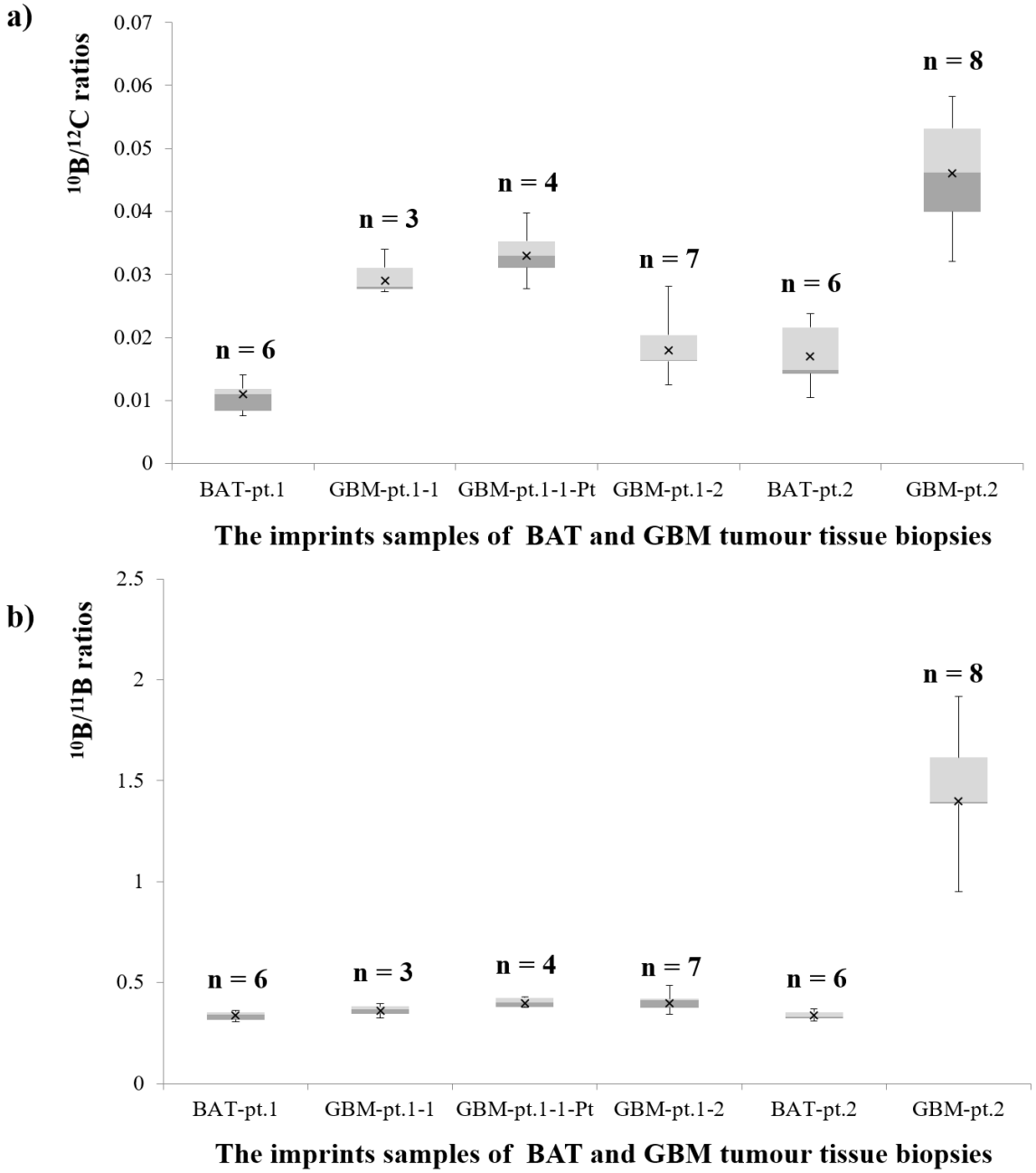

Figure 5.22: Comparison between the imprint samples from BAT and GBM tumour tissue biopsies in terms of **(a)** $^{10}B^{+}/^{12}C^{+}$ and **(b)** $^{10}B^{+}/^{11}B^{+}$ ratios showing accumulation of BPA measured by BioToF-SIMS. **(a)** showed that $^{10}B^{+}/^{12}C^{+}$ ratios were higher in GBM tumour imprints than BAT imprints samples and the accumulation of ^{10}B in patient-2 samples were more than the patient-1 samples. The only similarity between the $^{10}B^{+}/^{11}B^{+}$ ratios and the $^{10}B^{+}/^{12}C^{+}$ ratios is that the GBM-pt.2 sample contains more ^{10}B than the other samples. ***n***: represents the number of areas analyzed for each sample.

Table 5.3: The mean values of $^{10}B/^{12}C$ and $^{10}B/^{11}B$ ratios in the imprint samples from GBM tumour and BAT tissue biopsies presented in the box plots **Figure 5.22**.

Ratios - Mean ± SD values of whole area	Samples of first patient (pt.1)			
	BAT-pt.1	GBM-pt.1-1	GBM-pt.1-1-Pt	GBM-pt.1-2
$^{10}B^+/^{12}C^+$	0.011 ± 0.002	0.029 ± 0.003	0.033 ± 0.004	0.018 ± 0.004
$^{10}B^+/^{11}B^+$	0.34 ± 0.02	0.36 ± 0.03	0.4 ± 0.04	0.4 ± 0.02
Ratios - Mean ± SD values of whole area	Second patient (pt.2)			
	BAT-pt.2	GBM-pt.2		
$^{10}B^+/^{12}C^+$	0.017 ± 0.005	0.046 ± 0.009		
$^{10}B^+/^{11}B^+$	0.34 ± 0.02	1.4 ± 0.3		

In terms of quantitative measurements in **Figure 5.22 -b** and the mean values in **Table 5.3**, the results show that $^{10}B^+/^{11}B^+$ ratio in the samples of patient-1 were very close to each other with overlap with GBM-pt.1-1 in the upper-whisker from the BAT-pt.1, and with the lower-whisker for the GBM-pt.1-1-Pt and GBM-pt.1-2. The sample GBM-pt.1-1-Pt was fully overlapped with the IQR of sample GBM-pt.1-2. The latter in turn overlap in the upper whisker area of BAT-pt.1. The difference in mean values between the samples of the patient-1 did not exceed 4%. The samples of the patient-2 show that $^{10}B^+/^{11}B^+$ ratio in GBM-pt.2 was 4 times higher than the BAT-pt. 2 sample without any overlap between the samples.

The differences in $^{10}B^+/^{11}B^+$ ratios were small and carried a large uncertainty given the small number of data points. The Pt coating did not improve the signal intensity of the ion signals. Both ratios $^{10}B^+/^{12}C^+$ and $^{10}B^+/^{11}B^+$ showed that the GBM-pt.2 absorbed more BPA than samples from GBM-pt.1.

The wet-weight concentrations of ^{10}B at the imprint level cannot be determined from the $^{10}B^+/^{12}C^+$ ratios from BioToF-SIMS for the same reasons as previously mentioned in section 4.2.4.2.4.

5.3 Summary of the results of the analysis of imprint samples of BAT and GBM tumour biopsies using NanoSIMS and BioToF-SIMS instruments

This chapter includes an assessment of the imaging capabilities of the NanoSIMS and BioToF-SIMS instruments in determination of the drug distribution of BPA in the imprint samples of BAT and GBM tumour biopsies, which were removed from two different patients.

The resulting ion maps from NanoSIMS analysis using a ~ 400 nm Cs^+ beam showed the general morphology of the samples, the contrast in the distribution of different ions across the imprint, and identified the site of the cells and the surrounding area. The morphology of all imprint samples from BAT and GBM tumour tissue biopsies was more complex than cell cultures samples in Chapter 4 due to cellular diversity in tissue imprints, small cell size (~ <10 μm), the few numbers of tumour cells in imprints and the difficulty in finding them, and the existence of cracks and holes in the imprints.

From the NanoSIMS maps, it is clear that the boron distribution in all samples in **Figures 5.5- 5.12**, with the exception of BAT-pt.1 in **Figure 5.3**, was similar where $^{10}B^-$ and $^{10}B^{12}C^-$ were distributed almost homogenously within the tumour cells. The distribution of $^{10}B^-$ and $^{10}B^{12}C^-$ in BAT-pt.1 sample were not sufficiently clear due to the low level of signal accumulated in the cells. In addition, the higher accumulation of boron inside the cells of GBM tumour samples compared to cells of BAT samples of the same patient confirms that the uptake of BPA in the GBM tumour areas is higher than the areas surrounding the tumour BAT and this is also evident from the quantitative measurement in **Figure 5.14**. The distribution pattern of P^- and S^- in the cells showed absence of cell compartments features in all cells, except cell-1 in the BAT-pt.1 sample, indicating possibly the degradation of the nuclei into chromatin units scattered in the cytoplasm and collapse of proteinaceous cytoskeleton inside cells. However, the cells remain in a general round shape and reveal accumulations of $^{10}B^-$ and $^{10}B^{12}C^-$ signals inside cells. These features of the cells often indicate that tumour cells have undergone apoptosis as a result of the rapid growth of the cells under hypoxia and lack of nutrients, leading to cell stress and then apoptosis [23][3] The characteristics of the apoptotic cells were explained in more detail in section 5.2.3.1.1 [19]–[22]. In the light of the nature of the complex samples studied and the type of cells observed, it was not possible to distinguish the preferential accumulation of ^{10}B from BPA between cell compartments, which in turn is an important factor for the success of BNCT

therapy in the elimination of tumour cells with minimal damage to neighbouring health cells [4], [26]–[28].

On the other hand, the images resulting from BioToF-SIMS analysis using ~ 1-2 µm Au^+ beam in all imprint samples of the BAT and GBM tumour biopsies showed only general information about the ion signal intensity and the semi-homogeneous distribution of $^{10}B^+$ at the imprint level. Under the conditions used, the images did not show the morphology of the sample surface nor the contrast in the distribution of different ions across the imprint parts compared to the maps from the NanoSIMS. The Au^+ beam can be focussed to ~200 nm but with a significant loss in primary ion current. Given that the levels of $^{10}B^+$ were already approaching the limit of detection it was not expected that using a more focused primary beam would result in improved data quality. This is part of the challenge when working with drug treatments at therapeutic dose-levels. Therefore, it is impossible to distinguish the cell sites of imprints and to determine the preferential accumulation of ^{10}B from BPA at the cellular level in the BioToF-SIMS images. The difference between the BAT and GBM tumour samples was in the level of normalised ion intensities of $^{10}B^+$ measured from the signals in the mass spectra presented **in Figures 5.15 and 5.17-5.21.**

The homogenous distribution of ^{10}B within cells and in the surrounding areas of cells apparent in NanoSIMS maps as well as at the imprint level in BioToF-SIMS images is similar to the distribution of ^{11}B from cis- and trans-isomers of ABCPC and $^{10}B^+$ of BPA in the tissue sections of B16 melanoma tumour cells *in vivo* of mice that are referred to by Kabalka *et al.* as shown in **Figure 2.15** [44]. Fartmann *et al*. also conducted a study on cell cultures of human malignant melanoma *in vitro* and showed that $^{10}B^+$ from BSH in **Figure 2.14** is distributed in a pattern similar to all samples of GBM tumour and BAT-pt.2 sample [45] . Although the detected boron signal intensity was different between BAT and GBM tumour samples, all samples did not show specific accumulation sites for the ^{10}B signals within the cells structures or across the imprint. This observation is similar to the result of Alkins *et al.* in the study of the distribution of BPA-f in the 9L gliosarcoma tumour sections of rat's brain (Fisher 344) *in vivo* which indicated high localisation in the tumour regions of the BPA-f without an appreciable distribution pattern of $^{10}B^+$ in cells, **Figure 2.12-f** [26].

In contrast, Yokoyama *et al.* presented a study on tissue sections of C6 glioma cells of rat's brains *in vitro* showed that ^{10}B of the BPA accumulated heterogeneously in tumour regions, while accumulation was limited in infiltrating tumour cells to the area surrounding the tumour as in **Figure 2.11** [46]. In addition, in a study of kidney tissue sections of rats implanted with five types of tumours and treated with BPA *in vivo*, Arlinghaus *et al.*

illustrated that ^{10}B accumulated inside and outside of cells with varying signal intensity and high localisation of signals in nuclei areas as in **Figure 2.9** [9].

The difference in the distribution pattern of ^{10}B signals, whether at the cellular level in NanoSIMS maps or at the imprint level in the BioToF-SIMS images, between BAT and GBM tumour samples in this thesis and the different tissue sections mentioned above from the literature maybe due to several reasons. One reason might be differences in BPA dose and its delivery method to the tissue sections whether *in vitro* or *in vivo*. Secondly, the presence in tissue sections of various cell types such as tumour cells, apoptotic cell and other unknown cells may also affect the distribution pattern of BPA at the single cell level. Thirdly, differences in tumour type and the anatomic location of the tumour, this is a similar explanation to what Yang *et al.* have conclude during the study of the effect of pre-loading of amino acids on the BPA uptake [32]. Furthermore, LAT-1 expression activity in cells may differ from one tumour to another, which may play a role in differences in the accumulation pattern- this was concluded by Grunewald *et al.* during his study of the effect of pre-loading of tyrosine on the uptake of BPA in different organelles of mice preinjected with a human hepatocellular carcinoma cell line [30]. The third and fourth reasoning are given because BPA is transferred to the cells using the same transfer mechanism as L-amino acids, and thus uptake and accumulation of BPA and L-amino acids are likely to be affected by the same factors [47][48].

The results from BioToF images in this thesis, Kabalka *et al.* [44], and Yokoyama *et al.* [46] showed the distribution of ^{10}B at the level of the tissue sections without showing the distribution at the level of the single cell, whereas the results of NanoSIMS maps, Fartmann *et al.* [45] and Arlinghaus *et al.* [9] showed the distribution of ^{10}B at the cellular level, while Alkins *et al.* [26] did not distinguish any specific accumulation pattern in the cells. The difference in the ability to distinguish the ^{10}B accumulation sites is often due to the difference in the primary ion beam type used to image the ion distributions in the samples, as explained below, as well as the transmission of the system.

By comparing the quality of the images, it is clear that the intensity of ^{10}B signals and the sample morphology when using ~ 400 nm Cs^+ beam in the analysis of BAT and GBM tumour samples as example GBM-pt.1-1 in **Figure 5.5**, and also when using 200 nm Ga^+ beam in the analysis of cell cultures of human malignant melanoma cancer in **Figure 2.14** [45] and rat kidney tissues sections in **Figure 2.9** [9] were better than the Bi^+ beam (probe size not mentioned) used by Alkins *et al.* to analyse the 9L gliosarcoma tumour sections of rat brain in **Figure 2.12** [26]. Alkins *et al.* used H & E dye to locate cells in the gliosarcoma

sections before starting to study the distribution of BPA-f. The resulting ion images using Bi^+ beam did not clearly show the internal or surface characteristics of the cells. On the other hand, the high spatial resolution of Cs^+ and Ga^+ beams in imaging the samples presented in this thesis, human malignant melanoma cancer [45], and kidney tissues sections [9] respectively led to the appearance of the general features of cells and the contrast in the secondary ions distribution at cellular levels without the need for staining with H&E dyes. Furthermore, NanoSIMS analysis with a Cs^+ beam shows more accurate details across the cells in the images compared to the Ga^+ beam used in a ToF-SIMS system. Signals in the NanoSIMS were enhanced as the Cs^+ enhances ionization during implantation and analysis, this demonstrates that NanoSIMS has high imaging capabilities at the cellular level.

As for the 300 and 500 nm spatial resolution in the ion microscope analysis of C6 glioma cells of rat brains in **Figure 2.11** [46] and tissue sections of B16 melanoma tumour cells in **Figure 2.15** [44] respectively, the low spatial resolution using O_2^+ beam compared with Cs^+ and Ga^+ did not allow determination of sample morphology accurately nor localisation at the cellular level. The O_2^+ beam performance was limited to showing the intensity of the ion signals at the tissue section level. However, the ability of the O_2^+ beam to show the locations of ion accumulations in general in the samples was better than the 1-2 µm Au^+ beam used in imaging of BAT and GBM tumour samples as evident from the BAT-pt.1 images in **Figure 5.16**.

In addition, boron concentration in the sample plays an important role in determining the primary ion beam current (probe size) required to obtain a measurable signal. ^{10}B concentrations in the samples of the above studies were as follows: 480 ppm in human malignant melanoma cell cultures [45] and ~ 33 ppm in kidney tissues sections with five types of tumours [9], both samples were analysed with 200 nm Ga^+. While the ^{10}B concentration was 25 ppm in tissue sections of C6 glioma cells [46] and 20 ppm in tissue sections of B16 melanoma tumour cells [44] and its analysis required 300 – 500 nm of O_2^+ respectively. The bulk levels of ^{10}B measured by ICP-MS in thesis samples were 48.1 ppm as a maximum to 6 ppm as a minimum, which in turn required the use of 1 - 2 µm Au^+ beam to increase the sensitivity in the measurement of low signals.

The results of the quantitative measurement by NanoSIMS in **Figure 5.14** confirmed BPA uptake in all GBM tumour samples is higher than BAT samples, and that the $^{10}B^{12}C^-/^{12}C^{14}N^-$ ratios are always 2-3 times higher than $^{10}B^-/^{12}C^{14}N^-$ ratios in all samples, indicating that the $^{10}B^{12}C$ fragment has relative stability and/or a higher ionization probability than the atomic ^{10}B. Therefore, $^{10}B^{12}C^-$ could provide clearer images than $^{10}B^-$. $^{10}B^-/^{12}C^{14}N^-$ and

$^{10}B^{12}C^{-}/^{12}C^{14}N^{-}$ ratios in cells of GBM tumour samples of the patient-1 were 7 - 9 times higher than those measured in BAT-pt.1 sample, while those ratios were 2 - 4 times higher in the sample GBM-pt.2 of the patient-2 compared to the BAT-pt.2 sample. In addition, the quantitative measurement of the BioToF-SIMS in **Figure 5.22 -a & b** confirms that ^{10}B of BPA was accumulated in the GBM tumour samples more than the BAT samples. The $^{10}B^{+}/^{12}C^{+}$ ratios measured in the GBM tumour samples of the patient-1 were ~3 times higher than the BAT-pt.1 sample, and these also were 3 times higher in the sample GBM-pt.2 of the patient-2 compared with the BAT-pt.2 sample. Moreover, the samples of BAT and GBM tumour of the patient-2 showed 2 - 3 times higher BPA uptake than the samples of the patient-1. The quantitative results of $^{10}B^{+}/^{12}C^{+}$ using BioToF-SIMS are similar to those of $^{10}B/^{12}C^{14}N$ resulting from the measurement of NanoSIMS.

The quantitative results of NanoSIMS and BioToF-SIMS were consistent with Smith's findings showing that the ^{10}B accumulated in cells of tumour core was twice as high as those accumulated in tumour cells infiltrating normal brain tissue, in a study conducted on two tissue sections of 9L gliosarcoma and F98 glioma tumours of rats which were administered with BPA *in vivo* [49]. In addition, Oyedepo *et al.* provided similar results showed that the ^{10}B ratio of BPA accumulated in the tumour areas of the GS9L gliosarcoma tissue to the border areas surrounding tumour to the normal tissues of the brain was 10: 5: 1 respectively, which means that the accumulation of ^{10}B in the tumour parts was twice that of the border area , these samples of mouse were treated with the BPA *in vivo* [36]. Alkins *et al.* reported a similar trend during study of BPA uptake in 9L gliosarcoma tumour sections of rat brain (Fisher 344), where infiltrating cells contained ^{10}B equal 106 ± 25 (signal intensity level ± SD) compared with that in tumour cells, which was 123 ± 25 [26].

In addition, the results of NanoSIMS and BioToF-SIMS illustrated further detail as follows. The $^{10}B^{-}/^{12}C^{14}N^{-}$ and $^{10}B^{12}C^{-}/^{12}C^{14}N^{-}$ ratios in NanoSIMS, as well as $^{10}B^{+}/^{12}C^{+}$ ratios in BioToF-SIMS, were convergent in all GBM tumour samples of the patient-1, and that coating the sample surface with Pt did not significantly improve boron signals. The comparison of the two types of samples in the **Figure 5.14** and **Figure 5.22** revealed that $^{10}B^{-}/^{12}C^{14}N^{-}$ and $^{10}B^{12}C^{-}/^{12}C^{14}N^{-}$ ratios, as well as $^{10}B^{+}/^{12}C^{+}$ ratios, in the sample BAT-pt.2 were 2-fold higher than those obtained in the sample BAT-pt.1. In NanoSIMS, the $^{10}B^{-}/^{12}C^{14}N^{-}$ ratio in the GBM-pt.2 sample was close to that measured in GBM-pt.1 samples of the patient-1, whereas $^{10}B^{12}C^{-}/^{12}C^{14}N^{-}$ ratio in the GBM-pt.2 sample was ~2-fold lower than GBM-pt.1 samples of the patient-1. It is probable that differences in the uptake of boron are influenced by the location of the anatomical tumour and the histologic tumour type as

reported by Yang *et al.* [32], or may be affected by the proliferation state for cells, according to studies by Yoshida *et al.* [33], Ono *et al*. [34], and Dahlstrom *et al.* [35]. Furthermore, the difference in the boron ratios between BAT-pt.1 and BAT-pt.2 may be due to the difference in the activity of the LAT-1 expression in the tumour cells infiltrated to BAT tissue, as indicated by Nawashiro *et al.* [29], Grunewald *et al.* [30] and Detta and Cruickshank [31] in their studies. All these studies were discussed in detail in the section 5.2.3.1.5 and also in Chapter 2.

It was not possible to determine the wet-weight concentrations of ^{10}B at the cellular level with NanoSIMS and at imprint level with BioToF-SIMS using $^{10}B^{-}/^{12}C^{14}N^{-}$ and $^{10}B^{+}/^{12}C^{+}$ ratios respectively as previously explained in the sections 5.2.3.3 and 5.2.4.2.

5.4 References

[1] S. Paxton, M. Peckham, and A. Knibbs, "The Histology Guide | What is Histology," *The University of Leeds*, 2003. [Online]. Available: https://www.histology.leeds.ac.uk/what-is-histology/H_and_E.php. [Accessed: 05-Nov-2019].

[2] C. Sampias, "H&E Basics Part 4: Troubleshooting H&E," 2018. [Online]. Available: https://www.leicabiosystems.com/pathologyleaders/he-basics-part-4-troubleshooting-he/. [Accessed: 05-Nov-2019].

[3] A. Detta, "personal communication," 2018.

[4] M. J. Luderer, P. De La Puente, and A. K. Azab, "Advancements in Tumor Targeting Strategies for Boron Neutron Capture Therapy," *Pharm. Res.*, vol. 32, no. 9, pp. 2824–2836, 2015.

[5] H. Jiang *et al.*, "High-resolution imaging of dietary lipids in cells and tissues by NanoSIMS analysis," *Lipid Res.*, vol. 10, no. 55, pp. 2156–2166, 2014.

[6] R. Peteranderl and C. Lechene, "Measure of carbon and nitrogen stable isotope ratios in cultured cells," *J. Am. Soc. Mass Spectrom.*, vol. 15, no. 4, pp. 478–485, 2004.

[7] L. Claude *et al.*, "High-resolution quantitative imaging of mammalian and bacterial cells using stable isotope mass spectrometry," *J. Biol.*, vol. 5, pp. 1–30, 2006.

[8] M. T. Proetto *et al.*, "Tumor Retention of Enzyme-Responsive Pt (II) Drug-Loaded Nanoparticles Imaged by Nanoscale Secondary Ion Mass Spectrometry and Fluorescence Microscopy," *ACS Cent. Sci.*, vol. 4, no. 11, pp. 1477–1484, 2018.

[9] H. F. Arlinghaus, C. Kriegeskotte, M. Fartmann, A. Wittig, W. Sauerwein, and D. Lipinsky, "Mass spectrometric characterization of elements and molecules in cell cultures and tissues," *Appl. Surf. Sci.*, vol. 252, no. 19, pp. 6941–6948, 2006.

[10] G. Karp, *Cell and Molecular Biology: Concepts and Experiments*, 6th ed. John Wiley & Sons Ltd, 2009.

[11] G. J. Doherty and H. T. McMahon, “Mediation, Modulation, and Consequences of Membrane-Cytoskeleton Interactions,” *Annu. Rev. Biophys.*, vol. 37, no. 1, pp. 65–95, 2008.

[12] C. Quintana, T. Wu, B. Delatour, M. Dhenain, J. L. Guerquin-Kern, and A. Croisy, “Morphological and Chemical Studies of Pathological Human and Mice Brain at the Subcellular Level: Correlation Between Light, Electron, and NanoSIMS Microscopies,” *Microsc. Res. Tech.*, vol. 70, pp. 281–295, 2007.

[13] B. Alberts, A. Johnson, J. Lewis, M. Raff, K. Roberts, and P. Walter, “Chapter 4: DNA, Chromosomes and Genomes,” in *Molecular Biology of the Cell*, 6th ed., New York: Garland Science, 2014.

[14] A. Ghosh and M. Bansal, “A glossary of DNA structures from A to Z,” *Acta Crystallographica - Section D*, vol. 59, no. 4. pp. 620–626, 2003.

[15] A. A. Legin *et al.*, “NanoSIMS combined with fluorescence microscopy as a tool for subcellular imaging of isotopically labeled platinum-based anticancer drugs,” *Chem. Sci.*, vol. 5, no. 8, pp. 3135–3143, 2014.

[16] L. E. Wedlock, M. R. Kilburn, J. B. Cliff, L. Filgueira, M. Saunders, and S. J. Berners-Price, “Visualising gold inside tumour cells following treatment with an antitumour gold(I) complex,” *Metallomics*, vol. 3, no. 9, pp. 917–925, 2011.

[17] T. Ubuka, “Assay methods and biological roles of labile sulfur in animal tissues,” *J. Chromatogr. B*, vol. 781, no. 1–2, pp. 227–249, 2002.

[18] T. R. Sutton *et al.*, “A robust and versatile mass spectrometry platform for comprehensive assessment of the thiol redox metabolome,” *Redox Biol.*, vol. 16, no. 1, pp. 359–380, 2018.

[19] N. Kim-campbell, H. Gomez, and H. Bayir, “Cell Death Pathways : Apoptosis and Regulated Necrosis,” in *Critical Care Nephrology*, Third Edit., 2019, pp. 113-121.e2.

[20] R. Tixeira *et al.*, “Defining the morphologic features and products of cell disassembly during apoptosis,” *Apoptosis*, vol. 22, no. 3, pp. 475–477, 2017.

[21] N. Zamzami and G. Kroemer, “Condensed matter in cell death,” *Nature*, vol. 401, no. September, pp. 127–128, 1999.

[22] I. Böhm, “Disruption of the Cytoskeleton After Apoptosis Induction with Autoantibodies,” *healthsciences*, vol. 36, no. February, pp. 183–189, 2003.

[23] S. Elmore, “Apoptosis: A Review of Programmed Cell Death,” *Toxicol Pathol.*, vol. 35, no. 4, pp. 495–516, 2007.

[24] J. Rinn, C. Bondre, H. Gladstone, H. Brown, and P. Chang, “Anatomic Demarcation by Positional Variation in Fibroblast Gene Expression Programs,” *SIU School of Medicine*, 2006. [Online]. Available: http://www.siumed.edu/~dking2/intro/ct.htm#collagen. [Accessed: 20-Feb-2019].

[25] G. A. Di Lullo, S. M. Sweeney, J. Ko, L. Ala-kokko, and J. D. S. Antonio, “Mapping the Ligand-binding Sites and Disease-associated Mutations on the Most Abundant Protein in the Human , Type I Collagen,” vol. 277, no. 6, pp. 4223–4231, 2002.

[26] R. D. Alkins, P. M. Brodersen, R. N. S. Sodhi, and K. Hynynen, “Enhancing drug delivery for boron neutron capture therapy of brain tumors with focused ultrasound,”

Neuro. Oncol., pp. 1–11, 2013.

[27] X. Zha, W. A. Ausserer, and G. H. Morrison, "Quantitative imaging of a radiotherapeutic drug, $Na_2B_{12}H_{11}SH$, at subcellular resolution in tissue cultures using ion microscopy," *Cancer Res.*, vol. 52, no. 19, pp. 5219–5222, 1992.

[28] R. F. Barth, P. Mi, and W. Yang, "Boron delivery agents for neutron capture therapy of cancer," *Cancer Commun.*, vol. 38, no. 35, pp. 1–15, 2018.

[29] H. Nawashiro *et al.*, "High expression of L-type amino acid transporter 1 in infiltrating glioma cells," *Brain Tumor Pathol.*, vol. 22, pp. 89–91, 2005.

[30] C. Grunewald *et al.*, "On the applicability of [^{18}F] FBPA to predict L-BPA concentration after amino acid preloading in HuH-7 liver tumor model and the implication for liver boron neutron capture therapy," *Nucl. Med. Biol.*, vol. 44, pp. 83–89, 2017.

[31] A. Detta and G. S. Cruickshank, "L-Amino Acid Transporter-1 and Boronophenylalanine-Based Boron Neutron Capture Therapy of Human Brain Tumors," *Cancer Res.*, vol. 69, no. 5, pp. 2126–2132, 2009.

[32] W. Yang *et al.*, "Effects of L-DOPA pre-loading on the uptake of boronophenylalanine using the F98 glioma and B16 melanoma models," *Appl Radiat Isot*, vol. 88, pp. 69–73, 2014.

[33] F. Yoshida *et al.*, "Cell cycle dependence of boron uptake from two boron compounds used for clinical neutron capture therapy," *Cancer Lett.*, vol. 187, no. 1–2, pp. 135–141, 2002.

[34] K. Ono *et al.*, "Radiobiological evidence suggesting heterogeneous microdistribution of boron compounds in tumors :its relation to quiescent cell population and tumor cure in neutron capture therapy," *Int. J. Radiat. Oncol. Biol. Phys.*, vol. 34, no. 5, pp. 1081–1086, 1996.

[35] M. Dahlström, J. Capala, P. Lindström, A. Wasteson, and A. Lindström, "Accumulation of boron in human malignant glioma cells in vitro is cell type dependent," *J. Neurooncol.*, vol. 68, no. 3, pp. 199–205, 2004.

[36] A. C. Oyedepo, S. L. Brooke, P. J. Heard, J. C. C. Day, G. C. Allen, and H. Patel, "Analysis of boron-10 in soft tissue by dynamic secondary ion mass spectrometry," *J. Microsc.*, vol. 213, no. August 2003, pp. 39–45, 2004.

[37] I. Z. Nagy, G. Lustyik, G. Lukács, V. Z. Nagy, and G. Balázs, "Correlation of Malignancy with the Intracellular Na^+:K^+ Ratio in Human Thyroid Tumors," *Cancer Res.*, vol. 43, no. 11, pp. 5395–5402, 1983.

[38] I. Z. Nagy, G. Lustyik, V. Z. Nagy, B. Zarándi, and C. Bertoni-Freddari, "Intracellular Na^+:K^+ ratios in human cancer cells as revealed by energy dispersive X-ray microanalysis," *J. Cell Biol.*, vol. 90, no. 3, pp. 769–777, 1981.

[39] D. J. Hare, E. J. New, M. D. De Jongee, and G. McColl, "Imaging metals in biology: balancing sensitivity, selectivity and spatial resolution," *Chem. Soc. Rev.*, vol. 44, pp. 5941–5958, 2015.

[40] Z. Qin, J. A. Caruso, B. Lai, A. Matusch, and J. S. Becker, "Trace metal imaging with high spatial resolution: Applications in biomedicine," *Metallomics*, vol. 3, no. 1, pp. 28–37, 2011.

[41] H. Sediqi, A. Wray, C. Jones, and M. Jones, “Application of Spectral Phasor analysis to sodium microenvironments in myoblast progenitor cells,” *PLoS One*, vol. 13, no. 10, p. e0204611, 2018.

[42] L. G. Palmer and M. M. Civan, “Distribution of Na^+, K^+ and Cl^- between nucleus and cytoplasm in Chironomus salivary gland cells,” *J. Membr. Biol.*, vol. 33, no. 1, pp. 41–61, 1977.

[43] I. Budin and N. K. Devaraj, “Membrane assembly driven by a biomimetic coupling reaction,” *J. Am. Chem. Soc.*, vol. 134, no. 2, pp. 751–753, 2012.

[44] G. W. Kabalka *et al.*, “Boronated unnatural cyclic amino acids as potential delivery agents for neutron capture therapy,” *Appl. Radiat. Isot.*, vol. 69, no. 12, pp. 1778–1781, 2011.

[45] M. Fartmann, C. Kriegeskotte, S. Dambach, A. Wittig, W. Sauerwein, and H. F. Arlinghaus, “Quantitative imaging of atomic and molecular species in cancer cell cultures with TOF-SIMS and Laser-SNMS,” *Appl. Surf. Sci.*, vol. 231, no. 232, pp. 428–431, 2004.

[46] K. Yokoyama *et al.*, “Analysis of Boron Distribution In Vivo for Boron Neutron Capture Therapy using Two Different Boron Compounds by Secondary Ion Mass Spectrometry Analysis of Boron Distribution In Vivo for Boron Neutron Capture Therapy using Two Different Boron Compounds by,” *Radiat. Res.*, vol. 167, no. 1, pp. 102–109, 2007.

[47] W. A. Campbell, D. E. Sah, M. M. Medina, J. E. Albina, W. B. Coleman, and N. L. Thompson, “TA1/LAT-1/CD98 light chain and system L activity, but not 4F2/CD98 heavy chain, respond to arginine availability in rat hepatic cells. Loss of response in tumor cells,” *J. Biol. Chem.*, vol. 275, no. 8, pp. 5347–5354, 2000.

[48] D. A. Wolf, S. Wang, M. A. Panzica, N. H. Bassily, and N. L. Thompson, “Expression of a Highly Conserved Oncofetal Gene , TA1 / E16 , in Human Colon Carcinoma and Other Primary Cancers : Homology to Schistosoma Mansoni Amino Acid Permease and Caenorhabditis Elegans Gene Products,” *Cancer Res.*, vol. 56, pp. 5012–5022, 1996.

[49] D. R. Smith, S. Chandra, R. F. Barth, W. Yang, D. D. Joel, and J. A. Coderre, “Quantitative Imaging and Microlocalization of Boron-10 in Brain Tumors and Infiltrating Tumor Cells by SIMS Ion Microscopy : Relevance to Neutron Capture Therapy 1,” *Cancer Res.*, vol. 61, pp. 8179–8187, 2001.

6 Conclusion and Future Work

6.1 Conclusion

The NanoSIMS and BioToF-SIMS results in this thesis are a new and novel addition to the literature, as this is the first time that BPA uptake in primary human cell cultures (Chapter 4) and imprints of human brain tumour biopsies (Chapter 5) have been studied using SIMS imaging. Additionally, this is the first study to investigate the effect of pre-treatment with tyrosine and the efflux process on BPA uptake in primary glioblastoma cells cultures. ^{10}B distribution and quantification of the BPA were determined in different treatment regimes.

The importance of the study of the ^{10}B distribution lies in understanding the differential BPA uptake in the brain-around-tumour cells (BAT) compared to the main tumour mass (GBM) depending on the duration and formulation of drug dosing as reported in previous studies [1]–[3]. These factors affect the success of BNCT treatment as success depends on the preferential accumulation of ^{10}B within tumour cells, especially in nuclei due to the limited lethal range of the $^{10}B(n,\alpha)\ ^{7}Li$ reaction [4]–[6].

Bulk analytical methods can provide quantitative information of the level of boron in blood and tissue to determine if the required levels of ^{10}B have been achieved [7]–[11], however they are not able to determine the distribution of ^{10}B in the cells, in particular to determine if the BPA is located intracellularly or extracellularly. Cellular and sub-cellular level chemical imaging is necessary to support dosimetry studies and clinical efficacy in BNCT [9] and more generally novel drug delivery research. Clinically approved imaging modalities including magnetic resonance [12] and positron emission tomography [13] lack the spatial resolution to determine *in vivo* BPA distributions on a cellular scale, hence, it is essential to develop alternative methods capable of determining the distribution of ^{10}B of BPA at the cellular level in tumour cells. Secondary ion mass spectrometry (SIMS) imaging is one such technique. A number of SIMS studies of the uptake and distribution of BPA have previously been reported in the literature (for example ref. [1]). SIMS studies have mostly focused on the application of the ion microscope technique with spatial resolution limited to ~ 0.5 μm by the ion optics of the instrument. Microprobe methods have also been applied, and combined with laser post-ionization techniques to increase sensitivity and quantification levels [14]. Most of the previous studies have been conducted on established glioma model cell lines, animal tissues or glioblastoma xenografts grown in nude mice, whereas primary GBM tissues biopsies, as investigated in this thesis, show tumour heterogeneity which can influence ^{10}B uptake in cell subpopulations [8][15].

The literature has shown that the effect of pre-treatment with tyrosine is not always successful in increasing the BPA uptake, where it has enhanced uptake in some studies [7][16]–[19], while it did not have an effect in other samples [8][20]. It is therefore important to measure the outcome of BPA exposure and treatment regimes on primary human glioma cells and ultimately imprints of human tumour biopsies to best inform clinical practice.

The results in this thesis present the most detailed and quantified BPA distribution study to-date and further demonstrate the capability of the dynamic SIMS technique to support clinical research and personalized therapy. The results are also important for research into improving the uses of SIMS for applications of biological imaging.

The following is a summary of the thesis results from Chapters 4 and 5 in terms of spatial resolution, sensitivity, and quantification in different treatment regimes which were the aims of thesis.

In terms of spatial resolution, the use of NanoSIMS with a ~ 400 nm Cs^+ beam provided greater imaging resolution at the sub-cellular level than BioToF-SIMS with ~ 1-2 µm Au^+ beam during analysis of the cell culture samples. The Cs^+ beam has the ability to chemically enhance the ionization efficiency of the samples, while there is no such effect of the Au^+ beam. The high spatial resolution of NanoSIMS in cell cultures samples enabled it to distinguish cell compartments (nucleus and cytoplasm), showing variation in the distribution of different ions between cellular parts, and determination of cell morphology and other features on the surface as well as the outer region surrounding the cell, for example, as shown in **Figure 4.9**. Again, NanoSIMS demonstrated high imaging capabilities when analysing the imprints of GBM tumour and BAT tissue biopsies, showing the variation in the distribution of ions across the imprint and distinguishing the cells from other features in the area surrounding the cells, despite the more complex morphology of the imprints than the cell cultures in terms of holes, cracks and cellular diversity (tumour, apoptotic, and unknown cells). The small size of the cells (less than 10 µm), and their low number, led to difficulty in finding cells for analysis in both instruments (see **Figure 5.3)**. Regions of interest within analysis areas were selected post-acquisition based on defined criteria in order to avoid features for instance holes, cracks, and surface contamination which could affect the measurement accuracy. Whilst bias in selecting the regions of interest could not be ruled out completely, using defined criteria to avoid damaged areas helped to minimise it. The NanoSIMS revealed a heterogeneous distribution of ^{10}B from BPA in cell cultures samples (*in vitro*), with a higher accumulation in the nuclei compared with the cytoplasmic regions, as well as an almost homogeneous distribution within cells of the imprint samples of tissue

biopsies (*in vivo*). Thus, the results of NanoSIMS imaging at the cellular and sub-cellular levels allowed determination of the preferential accumulation of ^{10}B, which is an important parameter in the success of BNCT therapy [4][21][22].

On the other hand, BioToF-SIMS with an Au^+ primary beam was unable to achieve the above level of detail necessary to determine the subcellular distribution of ^{10}B. In both Chapters 4 and 5, the optical camera in the BioToF-SIMS instrument was used to identify cells, whether with cell cultures or biopsy imprints samples. Cell location was confirmed using the resulting SIMS images after analysis, where high sodium and potassium levels and low silicon levels showed the presence of the biological material. The BioToF-SIMS imaging performance in cell cultures was however limited to only showing the distribution and intensity of ion signals at the cellular level, without distinguishing the cell compartments or morphological features on the surface, or revealing details of the external area around the cell accurately (see **Figure 4.39)**. The lack of spatial resolution was also very clear in the BioToF-SIMS images of the imprint samples. Thus, the results of BioToF-SIMS imaging revealed only a semi-homogeneous distribution of ^{10}B in all the samples without determining the preferred accumulation of BPA (**Figure 5.16).**

In terms of sensitivity, NanoSIMS was able to determine the distribution sites of low-abundance ions in the sample's images. This was evident during the detection of boron isotopes in the control samples for the two types of cell cultures (GBM tumour and BAT), as seen in **Figures 4.1** and **4.3**. This sensitivity of NanoSIMS led to more accurate quantitative measurements of boron isotopes that corresponded to the level of the natural ratio [23][24]. Whereas, the BioToF-SIMS images of the control samples showed only very weak signals, without any clear pattern of distribution, as in **Figure 4.26**. The boron isotope signals for the control samples in the BioToF spectrum, as in **Figure 4.25**, overlapped with the background noise signals, which led to a reduction in the accuracy of the quantitative measurement of signals that were very low in abundance. Moreover, the NanoSIMS images showed small accumulations of low signal intensity in the imprint samples, as in **Figure 5.12**, which were not shown in the BioToF-SIMS images (**Figure 5.16)**.

In terms of the quantitative data interpretation presented in Chapters 4 and 5, both SIMS instruments presented similar performance in measuring relative boron levels. These measurements support the imaging results of the SIMS systems. In the cell culture experiments, the following conclusions were reached when normalising the data from the NanoSIMS (**Figure 4.23, Tables 4.2 & 4.4**) and BioToF-SIMS (**Figure 4.57, Tables 4.6 & 4.7)** to ^{12}C intensity. The data indicated higher uptake of BPA in the GBM tumour and BAT

cells compared with the control samples. Accumulation of ^{10}B was greater in B2 treated with BPA only, followed by that preloaded with tyrosine B3 and then that exposed to an efflux process B4. An inconsistent outcome was found for the BAT samples, for which NanoSIMS analysis indicated that there is no significant difference in ^{10}B levels accumulated of BPA between D2-treated with BPA only and D3-preloaded with tyrosine, whereas BioToF analysis indicated a high level of ^{10}B in D3 compared with other BAT samples. This difference in ^{10}B accumulation levels in D3 was attributed to factors influencing the distribution pattern and uptake as mentioned below. In addition, the comparison between BAT and GBM tumour cells in the different treatment methods yielded a similar result from both SIMS instruments, which was that D3 cells pre-treated with tyrosine and D4 cells exposed to efflux from BAT had a higher accumulation of BPA compared with B3 and B4 from the GBM tumour. Subcellular concentrations of ^{10}B (in nucleus and cytoplasm) were determined using $^{10}B^-/^{12}C^-$ ratios measured by NanoSIMS and an appropriate RSF as shown in **Tables 4.3** and **4.5**, results showed there is no significant difference in mean ^{10}B concentrations between the B2 and D2 samples. Pre-loading of tyrosine reduced the concentration of ^{10}B in the B3 sample but not in the D3 sample. Concentrations of ^{10}B in B4 and D4 samples decreased as a result of the efflux process but did not reach the concentrations calculated in the control samples B1 and D1, indicating that the efflux process is slower than the uptake process. The BioToF-SIMS results on the normalisation with $^{11}B^+$ (**Figure 4.58**) were not very accurate due to low intensities of $^{11}B^+$, so $^{12}C^+$ was used to give greater confidence in the normalisation due to the high and constant signal intensity of $^{12}C^+$.

For the imprint samples from the GBM tumour and BAT tissue biopsies derived from two different patients, the quantitative measurements of both SIMS instruments, whether normalised to $^{12}C^{14}N^-$ for NanoSIMS data or normalised to $^{12}C^+$ for BioToF-SIMS data, showed one consistent result: the accumulation of BPA was higher in GBM tumour cells than BAT cells. It was not possible to calculate the ^{10}B concentrations using the $^{10}B^{12}C^-/^{12}C^-$ ratios from cell cultures or $^{10}B^-/^{12}C^{14}N^-$ ratios from imprint samples measured with NanoSIMS, nor the $^{10}B^+/^{12}C^+$ ratios measured with BioToF-SIMS in both type of samples because no appropriate RSF values were available from a reference identical or close to the freeze-dried cell sample. Coating the surface of one of the GBM tumour imprint samples with 10 nm Pt did not significantly improve ion yields, particularly $^{10}B^-$ and $^{10}B^+$ ions, or help with potential charging effects.

Comparing the results of the analysis of samples using NanoSIMS and BioToF-SIMS with the literature, the following conclusions can be drawn:

- The NanoSIMS image quality (spatial resolution) for all the samples in the thesis when using a Cs^+ beam was better due to the coaxial ion optics compared to other SIMS instruments in the literature. Conversely the quality of the BioToF-SIMS images with a Au^+ beam had the lowest spatial resolution, this was due to the sensitivity requirement of this experiment.
- The distribution pattern and accumulation levels for ^{10}B from BPA in cells at the sub-cellular, cellular, and imprint levels may be affected by several factors, such as drug dose, method of receiving the samples for treatment (*in vivo – in vitro*), histological tumour type and anatomical location of the tumour, type and size of the observed cells, activity of LAT-1 expression, particularly in cells infiltrating to BAT, and the cell's proliferation status. All these effects would require further work with clearly defined samples.
- Pre-loading of tyrosine prior to pharmacotherapy in the samples did not enhance the BPA uptake in the cell cultures of BAT and GBM tumours. This result corresponded with studies that indicated that the effect of pre-loading with tyrosine varies from one patient to another according to the location and histological type of the tumour and the activity of LAT-1 expression in the transfer of L-amino acids. However, this result contrasted with other studies, most of which were conducted on animal cell lines (*in vivo - in vitro*), which differed in their nature from the heterogeneous and complex human cells used in the research reported in this thesis.
- The exposure of primary cell cultures of BAT and GBM tumours to the efflux process resulted in decreased levels of BPA accumulating in the cells. However, after the 4h efflux process the cells retained the lethal concentration level of ^{10}B and the levels of ^{10}B remained higher than for the control samples. This result is consistent with the literature, confirming that the efflux process is an exchange between the inside and outside the cell and is slower than the uptake process.
- The wet weight concentrations of ^{10}B measured using NanoSIMS in cell cultures of GBM tumour and BAT confirms an increased BPA concentration in cellular nuclei compared to the cytoplasm. This result is important in achieving higher efficacy of the BNCT treatment. The nuclear concentration of ^{10}B in cell cultures of GBM and BAT samples treated only with BPA (~200 μg per g wet wt) was similar to that reported in the literature on cell lines or in animal models using different SIMS instruments, whereas the concentrations in the cytoplasm were ~ 50% of those measured in previous studies. The concentrations calculated in the treatments with pre-loading of tyrosine and efflux process confirm the observations summarized above in this regard.

- The quantitative results of NanoSIMS and BioToF-SIMS in imprint samples were consistent with literature in that the ^{10}B accumulated in GBM tumour cells was twice as high as that accumulated in tumour cells infiltrating normal brain tissue BAT. The homogeneous distribution of ^{10}B at the imprint level as imaged by BioToF-SIMS, and cell level in NanoSIMS is similar to some studies presented in the literature conducted on animal tissue sections (*in vivo - in vitro*), but other studies show a heterogeneous distribution.

Thus, the use of human-derived materials further demonstrated the ability of SIMS to image heterogeneous and complex samples, particularly the imprint samples that contain other cell types alongside tumour cells: fibroblast, apoptotic, and necrotic cells [25]. It may seem that the imprint method is not the optimum sample preparation method for the biopsy samples, but the analysis with high-resolution NanoSIMS imaging gave confidence in determining the localisation of selected species and the possibility of obtaining valid data as shown in the Chapter 5 results. It is also clear, the extent to which NanoSIMS imaging was superior to BioToF-SIMS for this type of experiment, in terms of spatial resolution and sensitivity, whereas the quantitative measurement ability remained similar between the SIMS instruments. Thus, the results of the BioToF-SIMS in this thesis play a supportive role to the NanoSIMS outcomes. One advantage of the BioToF-SIMS is the ability to measure all *m/z* values in parallel. This can help confirm quantitative conclusions e.g. by measuring multiple ion ratios such as $^{10}B^+/^{11}B^+$ and $^{10}B^+/^{12}C^+$, and can also provide additional signals which could help to characterise the sample. The real power of ToF-SIMS comes in molecular characterisation, but that was not the focus of this study.

Thus, the novelty of this research is imaging and quantifying the ^{10}B distribution of BPA in primary human cells cultures and the imprints of tissue biopsies. Furthermore, the study of the effect of pre-treatment with tyrosine and the efflux process on the BPA uptake has not been previously reported in the literature.

6.2 Future work

The following are the future studies and suggestions to improve and support the outputs of the thesis which could not have been performed within the timescale of this project:

- Analyse more samples to improve the reliability of the data, this would help to determine the differences between the types of samples and treatments regimes more accurately.

- Sample preparation of primary biopsies should be optimised using better freezing methods such as high pressure freezing, but there are limitations on what can be achieved due to restrictions on the procedures in the operating theatre. The preparation method for primary cellular cultures described in the thesis could be improved by using Cellattice^{TM} plastic cover slips coated with 10 nm Pt to the substrate prior to cell culture. This type of grid is numbered, which helps locate cells and makes it easy to analyse the same cells with multiple instruments. This approach would be useful in saving experiment time and the lifetime of the primary ion beam. This grid was previously used by Lau *et al.* during the analysis of HeLa cells [26]. It is also possible to use the sandwich-fractured-freeze-dried method in the preparation of cultures from primary human cells, as this method was proven successful in maintaining ion distribution and analysis with SIMS systems in the Chandra *et al*. studies [27]–[29]. It would then be possible to compare the effect of different preparation methods on BPA uptake in primary human cells cultures with the thesis results as well as with the findings of Chandra's studies.
- A cell cycle synchronization process could be used for the primary human cell cultures to bring cells in different phases of the cell cycle into a specific phase. This would reduce the uncertainty in the data by allowing the collection of data from a sufficient number of cells within one phase hence giving more confidence in the quantitative SIMS analysis as well as allowing an assessment of the BPA uptake in different phases. A number of references illustrate methods of cell synchronization in cell cultures depending on the type of phase to be studied [30]–[33]. A number of studies were reviewed in Chapter 2 that addressed the BPA uptake in specific phases of cell lines, for example references [34]–[36].
- To obtain quantitative information from the imprints of tissue biopsies (Chapter 5), it is necessary to extend the work with NanoSIMS on these samples to measure $^{10}B^{-}/^{12}C^{-}$ ratios instead of $^{10}B^{-}/^{12}C^{14}N^{-}$ and then apply the same method used to quantify data the cell cultures in Chapter 4. Furthermore, instead of using the RSF of PMMA standards, the quantification method could be optimised by establishing appropriate calibration standards for the research samples. One method would be to add BPA to a homogeneous cellular or tissue material and measure the concentration by a quantitative technique such as ICP-MS. The RSF for ^{10}B, considering C or CN as the matrix element, could then be determined by the correlation of each individual instrument and the ICP-MS analysis of homogeneous cellular materials. A number of references provide an explanation of how to find the RSF [37][38].

- Better methods for cell identification in the imprint samples need to be found. Histological staining prior to NanoSIMS or BioToF-SIMS analysis is not compatible but a histologist may be able to identify particular cells from the optical or SIMS images alone. Unknown cells showing an accumulation of ^{10}B from BPA that appeared in the imprint samples from BAT and GBM tumour biopsies with high signal intensities of CN and S, but low P signals would be interesting to investigate further as they may create a competitive environment with tumour cells to absorb the BPA. SEM imaging of high pressure frozen and microtomed samples may be a way to achieve a higher rate of cell identification.
- Ascertaining the effect of morphological changes on the surface of the cultured cells, such as the branch-like features and groups of small bright dots, which may be salt crystals originating from the buffer solution used in sample washing or ice crystals from a freezing artefact. It might help to use scanning electron microscopy (SEM) to determine the shape of features and energy-dispersive X-ray microanalysis (EDX) to identify the component elements of the features prior to SIMS analysis. SEM and EDX were used by Oyedepo *et al.* to verify a similar issue [39]. It would be interesting to link any changes in surface morphology to the results of BPA uptake.
- The nature of the outer edge of the cells needs further investigation. This could be achieved by studying the localisation of Na^+ and K^+ using NanoSIMS and determining the localisation of phospholipid and lipid molecules using BioToF-SIMS, and then determining the thickness of the edge. Again, SEM could be useful to provide high-resolution morphological images.
- Verifying the effectiveness of using laser post-ionization experiments with BioToF-SIMS analysis using an Au^+ beam to study the accumulation of BPA in human cells in order to increase the measurement sensitivity and enhance the ion yields from low-abundance boron isotopes, which may improve the quality of the images and reveal accumulations of ^{10}B in cellular structures more precisely. Fartmann *et al.* have shown the promise of this approach, although it comes with added experimental complexity [14].
- To increase the sensitivity of the measurement and improve the secondary ion yields with BioToF-SIMS, metal-assisted SIMS could be tested by adding a thin layer of silver on the sample surface and then conducting the static-SIMS analysis. The use of silver-coating with ToF-SIMS analysis has previously proved effective in increasing the intensity of secondary signals resulting from organic [40][41], polymer [40][42], and biological [43][44] materials. With dynamic NanoSIMS technique, adding a thick layer of silver may be required on the samples surface, then the effectiveness of this is verified.

In addition, platinum-coating has been tested once with imprint sample of tissue biopsies, but it can be tested again on cell culture samples to verify the possibility of increased sensitivity with both SIMS instruments.

- The interpretation of NanoSIMS-imaging results encountered some difficulties, especially the interpretation of ion distributions in the imprint samples from BAT and GBM tumour tissue biopsies. This highlights the need to also study the localisation of positive ions of importance in cellular structures on the same samples used in this project. This can be performed using O^- beam from a duoplasmatron ion source but the measurement sensitivity of the BPA was too low with this source (see Chapter 3), and provides lower spatial resolution compared to the Cs^+ source [45]. Instead, this aim could now be achieved using the Manchester NanoSIMS 50L, which was upgraded in 2018 with a new O^- Hyperion^{TM} source which has the unique advantages reviewed in section 3.6.2.1. It would be interesting to operate a Hyperion^{TM} source with an oxygen beam (O^-) and resolution of 50 nm in studying the localisation of Na^+ and K^+, in order to confirm the nuclei sites of the cytoplasm and to investigate the nature of the outer edge of the cells, the observed cell type, cell size, and the integrity of the preparation method. It would also be interesting to track the increase in Mg^+ accumulation and the decrease in Ca^+, which are important markers in the differentiation of tumour cells from other cells, along with the monitoring of $^{10}B^+$ distribution. Comparing that study with the existing work would add further confirmation of the results of this thesis and allow further interpretation of the patterns of boron accumulation. It would also be instructive to compare the spatial resolution and sensitivity of O^- beam imaging with the results of the Cs^+ imaging presented in the thesis in the area of detecting the distribution and localisation of BPA molecules in biological samples.

6.3 References

[1] D. R. Smith, S. Chandra, R. F. Barth, W. Yang, D. D. Joel, and J. A. Coderre, "Quantitative imaging and microlocalization of boron-10 in brain tumors and infiltrating tumor cells by SIMS ion microscopy: Relevance to neutron capture therapy," *Cancer Res.*, vol. 61, no. 22, pp. 8179–8187, 2001.

[2] K. Yokoyama *et al.*, "Analysis of boron distribution in vivo for boron neutron capture therapy using two different boron compounds by secondary ion mass spectrometry.," *Radiat. Res.*, vol. 167, no. 1, pp. 102–109, 2007.

[3] R. D. Alkins, P. M. Brodersen, R. N. S. Sodhi, and K. Hynynen, "Enhancing drug delivery for boron neutron Capture Therapy of Brain Tumors With Focused Ultrasound," *Neuro. Oncol.*, vol. 15, no. 9, pp. 1225–1235, 2013.

[4] M. J. Luderer, P. De La Puente, and A. K. Azab, “Advancements in Tumor Targeting Strategies for Boron Neutron Capture Therapy,” *Pharm. Res.*, vol. 32, no. 9, pp. 2824–2836, 2015.

[5] S. Chandra, “SIMS ion microscopy as a novel, practical tool for subcellular chemical imaging in cancer research,” *Appl. Surf. Sci.*, vol. 203–204, pp. 679–683, 2003.

[6] A. Portu *et al.*, “Inter-comparison of boron concentration measurements at INFN-University of Pavia (Italy) and CNEA (Argentina),” *Appl. Radiat. Isot.*, vol. 106, pp. 171–175, 2015.

[7] A. Wittig, W. A. Sauerwein, and J. A. Coderre, “Mechanisms of Transport of p-Borono-Phenylalanine through the Cell Membrane In Vitro,” *Radiat. Res.*, vol. 153, pp. 173–180, 2000.

[8] A. Detta and G. S. Cruickshank, “L-Amino Acid Transporter-1 and Boronophenylalanine-Based Boron Neutron Capture Therapy of Human Brain Tumors,” *Cancer Res.*, vol. 69, no. 5, pp. 2126–2132, 2009.

[9] A. Wittig *et al.*, “Laser postionization secondary neutral mass spectrometry in tissue : a powerful tool for elemental and molecular imaging in the development of targeted drugs,” *Am. Assoc. Cancer Res.*, vol. 7, pp. 1763–1772, 2008.

[10] C. L. Schütz *et al.*, “Intercomparison of inductively coupled plasma mass spectrometry, quantitative neutron capture radiography, and prompt gamma activation analysis for the determination of boron in biological samples,” *Anal. Bioanal. Chem.*, vol. 404, pp. 1887–1895, 2012.

[11] F. Basilico, W. Sauerwein, F. Pozzi, A. Wattig, R. Moss, and P. L. Mauri, “Analysis of ^{10}B antitumoral compounds by means of flow-injection into ESI-MS/MS,” *J. Mass Spectrom*, vol. 40, pp. 1546–1549, 2005.

[12] K. Ishiwata, “4-Borono-2-^{18}F-fluoro-l-phenylalanine PET for boron neutron capture therapy-oriented diagnosis: overview of a quarter century of research,” *Ann. Nucl. Med.*, vol. 33, pp. 223–236, 2019.

[13] P. Bendel, R. Margalit, N. Koudinova, and Y. Salomon, “Noninvasive Quantitative In Vivo Mapping and Metabolism of Boronophenylalanine (BPA) by Nuclear Magnetic Resonance (NMR) Spectroscopy and Imaging,” *Radiat. Res.*, vol. 164, pp. 680–687, 2005.

[14] M. Fartmann, C. Kriegeskotte, S. Dambach, A. Wittig, W. Sauerwein, and H. F. Arlinghaus, “Quantitative imaging of atomic and molecular species in cancer cell cultures with TOF-SIMS and Laser-SNMS,” *Appl. Surf. Sci.*, vol. 231, no. 232, pp. 428–431, 2004.

[15] M. Dahlstrom, J. Capala, P. Lindstrom, A. Wasteson, and A. Lindstrom, “Accumulation of boron in human malignant glioma cells in vitro is cell type dependent,” *J. Neurooncol.*, vol. 68, pp. 199–205, 2004.

[16] M. Papaspyrou, L. E. Feinendegen, and H.-W. Muller-Gartner, “Preloading with L-Tyrosine Increases the Uptake of Boronophenylalanine in Mouse Melanoma Cells1,” *Cancer Res.*, vol. 54, pp. 6311–6315, 1994.

[17] B. Wingelhofer *et al.*, “Preloading with L-BPA, L-tyrosine and L-DOPA enhances the uptake of [^{18}F]FBPA in human and mouse tumour cell lines,” *Appl. Radiat. Isot.*,

vol. 118, pp. 67–72, 2016.

[18] S. Capuani *et al.*, “L-DOPA Preloading Increases the Uptake of Borophenylalanine in C6 Glioma Rat Model: A New Strategy to Improve BNCT Efficacy,” *Int. J. Radiat. Oncol. Biol. Phys.*, vol. 72, no. 2, pp. 562–567, 2008.

[19] S. Capuani *et al.*, “Boronophenylalanine uptake in C6 glioma model is dramatically increased by L-DOPA preloading,” *Appl. Radiat. Isot.*, vol. 67, pp. S34–S36, 2009.

[20] C. Grunewald *et al.*, “On the applicability of [^{18}F]FBPA to predict L-BPA concentration after amino acid preloading in HuH-7 liver tumor model and the implication for liver boron neutron capture therapy,” *Nucl. Med. Biol.*, vol. 44, pp. 83–89, 2017.

[21] R. F. Barth, P. Mi, and W. Yang, “Boron delivery agents for neutron capture therapy of cancer,” *Cancer Commun.*, vol. 38, no. 35, pp. 1–15, 2018.

[22] R. D. Alkins, P. M. Brodersen, R. N. S. Sodhi, and K. Hynynen, “Enhancing drug delivery for boron neutron capture therapy of brain tumors with focused ultrasound,” *Neuro. Oncol.*, pp. 1–11, 2013.

[23] R. N. Sah and P. H. Brown, “Isotope ratio determination in boron analysis.,” *Biol. Trace Elem. Res.*, vol. 66, no. 1–3, pp. 39–53, 1998.

[24] M. F. L’Annunziata, *Handbook of Radioactivity Analysis*, 3rd ed. Elsevier Inc., 2012.

[25] A. Detta, “personal communication,” 2018.

[26] K. H. Lau, M. Christlieb, M. Schröder, H. Sheldon, A. L. Harris, and C. R. M. Grovenor, “Development of a new bimodal imaging methodology : a combination of fluorescence microscopy and high-resolution secondary ion mass spectrometry,” *J. Microsc.*, vol. 240, pp. 21–31, 2010.

[27] S. Chandra and D. R. Lorey II, “SIMS ion microscopy imaging of boronophenylalanine (BPA) and $^{13}C^{15}N$-labeled phenylalanine in human glioblastoma cells : Relevance of subcellular scale observations to BPA-mediated boron neutron capture therapy of cancer,” *Int. J. Mass Spectrom.*, vol. 260, pp. 90–101, 2007.

[28] S. Chandra, T. Ahmad, R. F. Barth, and G. W. Kabalkab, “Quantitative evaluation of boron neutron capture therapy (BNCT) drugs for boron delivery and retention at subcellular-scale resolution in human glioblastoma cells with imaging secondary ion mass spectrometry (SIMS),” *J. Microsc.*, vol. 254, no. 3, pp. 146–156, 2014.

[29] D. R. Lorey, G. H. Morrison, and S. Chandra, “Dynamic secondary ion mass spectrometry analysis of boron from boron neutron capture therapy drugs in co-cultures: Single-cell imaging of two different cell types within the same ion microscopy field of imaging,” *Anal. Chem.*, vol. 73, no. 16, pp. 3947–3953, 2001.

[30] G. Banfalvi, “Overview of cell synchronization,” in *Methods in Molecular Biology*, vol. 1524, 2016, pp. 3–27.

[31] J. V. Harper, “Synchronization of Cell Populations in G1/S and G2/M Phases of the Cell Cycle,” in *Cell cycle control: Mechanisms and Protocols*, T. Humphrey and G. Brooks, Eds. New Jersey: Humana Press Inc., 2005, pp. 157–166.

[32] C. K. Osborne, D. H. Boldt, and P. Estrada, “Human Breast Cancer Cell Cycle

Synchronization by Estrogens and Antiestrogens in Culture," *Cancer Res.*, vol. 44, no. 4, pp. 1433–1439, 1984.

[33] P. K. Davis, A. Ho, and S. F. Dowdy, "Cell-Cycle Synchronization of Mammalian Cells," *Biol. Methods*, vol. 30, no. 6, pp. 1322–1330, 2001.

[34] S. Chandra, W. Tjarks, D. R. Lorey, and R. F. Barth, "Quantitative subcellular imaging of boron compounds in individual mitotic and interphase human glioblastoma cells with imaging secondary ion mass spectrometry (SIMS)," *J. Microsc.*, vol. 229, no. 1, pp. 92–103, 2008.

[35] T. Sasajima, T. Miyagawa, T. Oku, J. G. Gelovani, R. Finn, and R. Blasberg, "Proliferation-dependent changes in amino acid transport and glucose metabolism in glioma cell lines," *Eur. J. Nucl. Med. Mol. Imaging*, vol. 31, no. 9, pp. 1244–1256, 2004.

[36] F. Yoshida *et al.*, "Cell cycle dependence of boron uptake from two boron compounds used for clinical neutron capture therapy," *Cancer Lett.*, vol. 187, no. 1–2, pp. 135–141, 2002.

[37] W. A. Ausserer, Y. Ling, S. Chandra, and G. H. Morrison, "Quantitative Imaging of Boron, Calcium, Magnesium, Potassium, and Sodium Distributions in Cultured Cells with Ion Microscopy," *Anal. Chem.*, vol. 61, pp. 2690–2695, 1989.

[38] R. G. Wilson, G. E. Lux, and C. L. Kirschbaum, "Depth profiling and secondary ion mass spectrometry relative sensitivity factors and systematics for polymers/organics," *J. Appl. Phys.*, vol. 73, no. 5, p. 2524, 1993.

[39] A. C. Oyedepo, S. L. Brooke, P. J. Heard, J. C. C. Day, G. C. Allen, and H. Patel, "Analysis of boron-10 in soft tissue by dynamic secondary ion mass spectrometry," *J. Microsc.*, vol. 213, no. August 2003, pp. 39–45, 2004.

[40] L. Adriaensen, F. Vangaever, and R. Gijbels, "Metal-assisted secondary ion mass spectrometry: Influence of Ag and Au deposition on molecular ion yields," *Anal. Chem.*, vol. 76, no. 22, pp. 6777–6785, 2004.

[41] A. Delcorte and P. Bertrand, "Interest of silver and gold metallization for molecular SIMS and SIMS imaging," *Appl. Surf. Sci.*, vol. 231–232, pp. 250–255, 2004.

[42] P. A. Zimmerman and D. M. Hercules, "Time-of-Flight Secondary Ion Mass Spectrometry of Poly(alkyl methacrylates)," *Anal. Chem.*, vol. 65, pp. 983–991, 1993.

[43] J. W. Park *et al.*, "Multi-dimensional TOF-SIMS analysis for effective profiling of disease-related ions from the tissue surface," *Sci. Rep.*, vol. 5, no. June, pp. 1–9, 2015.

[44] H. NYGREN, "Bioimaging TOF-SIMS: localization of cholesterol in rat kidney sections," *FEBS Lett.*, vol. 566, no. 1–3, pp. 291–293, 2004.

[45] J.-L. Guerquin-Kern, T. Wu, C. Quintana, and A. Croisy, "Progress in analytical imaging of the cell by dynamic secondary ion mass spectrometry (SIMS microscopy)," *Biochim. Biophys. Acta*, vol. 1724, pp. 228–238, 2005.